Further developments in performance prediction techniques of adiabatic diesel engines

Rasihhan, Yavuz

Award date:
1990

Awarding institution:
University of Bath

FURTHER DEVELOPMENTS IN PERFORMANCE PREDICTION TECHNIQUES OF ADIABATIC DIESEL ENGINES

submitted by

Yavuz Rasihhan
for the Degree of PhD
of the University of Bath
1990

ProQuest LLC
789 East Eisenhower Parkway
P.O. Box 1346
Ann Arbor, MI 48106-1346

Dedicated to my PARENTS

ACKNOWLEDGMENTS

I would like to gratefully acknowledge the help given by the following people:-

Professor F.J. Wallace for his supervision, understanding and persistence during the writing up stages of this volume.

Mr W.D. Alexander for his technical advice and assistance, especially with the instrumentation.

Dr S.J. Charlton for his assistance with the engine cycle simulation program.

Finally, I would like to thank my sponsors, Eastern Mediterranean University in Turkish Republic of Northern Cyprus without who this work would not have been possible.

ABSTRACT

The development of fast computers led to the birth of engine cycle simulation programs which provide a useful tool in engine performance prediction. The cycle simulation program 'SPICE', developed at Bath University, has been used extensively for the insulated diesel engine research. However, the computer models related to engine heat transfer are very simple and are not very suitable for insulated diesel engine simulation. The present study introduces more comprehensive engine heat transfer models to the simulation program 'SPICE', thus enabling us to study the insulated engine heat transfer and performance characteristics in more detail.

The new version of 'SPICE' separates the gas to wall heat transfer into two parts, convective and radiative. For this purpose, a detailed radiative heat transfer model which considers both the flame (gas and soot) and wall to wall radiative heat transfer is written. The previous engine resistance model is refined and replaced by a more detailed resistance model which considers piston-liner conduction heat transfer and 2-D heat flow in the liner. The wall surface temperature swing is also included in the engine heat transfer calculations which is quite significant in low conductivity ceramic insulated engines. A 1-D FD model is written for the transient heat transfer region of the wall and linked to the engine resistance model.

This new version of 'SPICE' is used to predict the insulated engine heat transfer and performance for the experimental Petter PH1W engine for various insulation levels and schemes. An answer to the controversy of increase in engine heat loss with insulation is looked for. The effect of wall deposits on engine heat transfer and its significance to the insulated engine is highlighted.

CONTENTS

PART 2

NOTATION

Units are SI unless stated.

a	Absorption coefficient
A	Area
AT	Aluminium titanate
a	Absorption coefficient
AB	Total band absorptivity
AB^*	Dimensionless integrated band absorptivity
A/F	Air fuel ratio
AFBR	Apparent fuel burning rate
bs	Self-broadening coefficient
Bi	Biot number
BDC	Bottom dead centre
BDUR	Burning duration
c	Speed of light
C	Gas velocity
C_d	Discharge coefficient
C_f	Skin friction coefficient
Cp	Specific heat capacity
CA	Crank angle
CI	Cast iron
CR	Compression ratio
CV	Control volume
CO	Carbon monoxide
CO_2	Carbon dioxide
CFD	Computational fluid dynamics
CRL	connecting rod length
D	Diameter
E	Blakbody emissive power
EF	Absorption efficiency
ER	Extra resistance
f	Frequecy
f(u)	Fractional function of dimensionless parameter u

f_v	Soot volume fraction
F	Overall Fourier number
F_{j-k}	Geometric configuration factor between surfaces j and k
Fo	Fourier number
FD	Finite difference
FF	Friction force
FF^*	Amplitude of friction force FF
F/A	Fuel/air ratio
FMEP	Friction mean effective pressure
g_k	Statistical weight for the k'th vibrational quantum number
h	Planck's constant
hr	Ratio of heat release to the injected fuel energy
htc	Heat transfer coefficient
H	Enthalpy
ΔH_f	Enthalpy of evaporation for fuel
HC	Hydogen to carbon atomic ratio
HL_j	Ratio of piston heat loss through ring j to total piston heat loss
HLC	Ratio of piston heat loss to oil to total piston heat loss
H_2O	Water vapour
HPSC	Hot pressed silicon carbide
HPSN	Hot pressed silicon nitride
i	$\sqrt{-1}$
I	Directional radiation intensity
IC	Influence coefficient
ID	Ignition delay
k	Conductivity
$\bar{k}$	Absorption index of soot
k_B	Boltzmann's constant

KE	Kinetic energy
L_m	Mean beam length
L_s	Engine stroke
m	Mass
$\bar{m}$	Complex refraction index of soot
mt	Total band number
mv	Number of vibrational transition
M	Molecular weight
M_1	Mean molecular weight correction function due to temperature
M_2	Mean molecular weight correction function due to pressure
$\bar{n}$	Refractive index of soot
nj	Number of junctions
nn	Number of nodes
nr	Number of rings and skirt section on the piston
ns	Number of surfaces
nt	Total number of gas specie
N	Group of variables defined in eqn.6.40
Ne	Engine speed
Nu	Nusselt number
NO_x	Nitrogen oxide
NIS	Number of integration steps
P	Pressure
P^*	Dimensionless pressure
Pr	Prandtl number
PC	Percentage change
PR	Period of a cycle
PRF	Piston ring friction ratio
PSF	Piston skirt friction ratio
PSZ	Partially stabilized zirconia
q	Heat flux
Q	Heat transfer

r	Radius
R	Thermal resistance Gas constant
R_1	Gas constant without dissociation
R_2	Represents the effect of dissociation on gas constant
Re	Reynolds number
R1	Conductivity ratio ($k_{i,l}/k_{i,r}$)
R2	Thermal diffusivity ratio ($\alpha_{i,l}/\alpha_{i,r}$)
R3	Displacement ratio ($\Delta x_{i,i-1}/\Delta x_{i,i+1}$)
R4	Conductivity ratio ($k_{i,i-1}/k_{i,l}$)
R5	Conductivity ratio ($k_{i,i+1}/k_{i,r}$)
R6,R7,R8,R9	Displacement groups for spherical and cylindrical coordinate systems (eqns.6.28 and 6.29)
RR	Ratio R2/(R1*R3)
$RATP_{i,j}$	Relative ratio of contact time of ring j with liner node i
$RATL_{i,j}$	Ratio of contact time of ring j with liner node i
s	Directional distance in space Axial distance in a cylinder Entropy
S	Total length in direction s
S^*	Space
SD	Size distribution
SH	Piston skirt height
$S(3,a^*,u)$	Function used to obtain the exact solution of integral equation of soot emissivity and absorptivity
S(3,0,u)	Function used to obtain the exact solution of integral equation of gas emissivity and absorptivity

t	Time
T	Temperature
T^*	Dimensionless temperature
ΔT	Temperature difference
	Amplitude of temperature wave
TF_i	Time factor for liner node i
TDC	Top dead centre
TPD	Thermal penetration depth
u	Specific internal energy
	Dimensionless parameter defined by $hc\nu/k_BT$
U	Internal energy
U_1	Internal energy without dissociation
U_2	Represents the effect of dissociation on internal energy
V	Volume
	Velocity
W	Work
x	Wall thickness
X_n	Mole fraction for gas specie n
Y	Ratio 0.5*D/s
Z	Ratio s/D

Greek Letters

α	Thermal diffusivity
	Absorption coefficient
$\bar{\alpha}_{\lambda, j-k}$	Geometric – mean spectral absorptivity
$\alpha(T_g)$	Integrated band intensity
β	Mode of burning proportionality factor
$\beta(T_g)$	Line width parameter

δ_k	Vibrational transition of k'th vibrational quantum number
δ_{kj}	Kroncker delta function for surfaces j and k
Δ	Increment Difference
ε	Emissivity
$\bar{\varepsilon}_{\lambda, j-k}$	Geometric-mean spectral emissivity
ϕ	Phase angle Phase function Equivalence ratio
$\phi(T_g)$	Temperature dependent function for line width parameter
γ	Specific heat ratio
Γ	Gama function defined by; $\Gamma(m+1)=m\Gamma(m)$
η	Line width parameter
φ	Excess air ratio
λ	Wavelength
μ	Viscosity Micron, 10^{-4} cm
ν	Wavenumber
π	3.1415927
Π	Multiplication factor
θ	Crank angle Azimuth angle
ρ	Density Reflectivity

ρCp	Thermal inertia
σ	Stefan-Boltzmann constant
	Scaterring coefficient
	Particle effective crossection area
Σ	Summation sign
τ	Transmittance
	Dimensionless crank angle
$\bar{\tau}_{\lambda,j-k}$	Geometric-mean spectral transmissivity
τ_H	Optical depth at the gas band head or most intense spectral location
υ	Vibrational quantum number
$\omega(T_g)$	Band width parameter
Ω	Solid angle
ψ	Circumferential angle
$\Psi(T_g)$	Temperature dependent function for integrated band intensity

Subscripts

a	Air
ab	Absorption
ad	Adiabatic
app	Apparent
b	Burned
	Black body
c	Ceramic
	Corrected
ch	Characteristic
cl	Clearence
cn	Centre
co	Coolant

cy	Cylinder
cond	Conduction
conv	Convection
d	Diffusion flame burning
e	Effective
f	Fuel
fl	Flame
fric	Friction
g	Gas
h	Hydraulic
i	CV i
	Node i
	Injected
i,l	Left side of CV i
i,r	Right side of CV i
i,i-1	Regions between nodes or CV's i and i-1
i,i+1	Regions between nodes or CV's i and i+1
in	Inner or in
int	Internal
j	Surfaces j
j-k	From surface j to k
k	Surface k
	k'th vibrational quantum band
lw	Lower
l	Liner
m	Gas band number
	Metal
mb	Midboiling point
max	Maximum
min	Minimum
n	n'th gas specie
p	Piston
p,j	Piston region j
pr	Premixed
r	Piston ring
rad	Radiation

s	Direction s
sc	Scattering
sk	Piston skirt
so	Soot
sp	Sphere
st	Stoichiometric
sw	Swept
t	Total
	Turbulence
u	Initial mixture
up	Upper
w	Wall
w,k	Wall region k
w,l	Postion l within wall (x=l)
w,0	Wall surface (x=0).
0	Reference
λ	Spectral
λb	Spectral black body
λi	Spectral arriving at (in)
λo	Spectral leaving (out)
ν	Spectral

Superscripts

-	Previous value
+	Future values
_	Average or mean value.
.	Rate of change with time

CHAPTER 1
INTRODUCTION

1.1 OVERVIEW

In this chapter, a brief description of adiabatic diesel engines is given and the significance of R & D and of the application of high performance ceramics is explained. The present research at Bath University is briefly described and finally the structure of the thesis is presented.

1.2 ADIABATIC DIESEL ENGINE

A diesel engine is a reciprocating internal combustion engine which is working on the principle of igniting the fuel in hot compressed air. The combustion gases cause a sharp rise in the cylinder pressure and push the piston to provide useful work through the piston-crank mechanism. During combustion some of the heat is lost to the engine walls which causes a reduction in the cylinder pressure and thus a reduction in the work output. An adiabatic diesel engine is one which has virtually no heat transfer between the gas and the wall, and hence converts the maximum amount of heat to work.

To design an adiabatic diesel engine requires a special material which has almost no thermal inertia, so that with only a small amount of heat transfer between the gas and the wall, the wall temperature reaches the gas temperature and stops the heat transfer. Such a material is purely theoretical and the present available materials do not provide the above condition. Thus a true adiabatic diesel engine is an engineering dream.

Since the instantaneous wall temperature, due to inherent material thermal properties, can't be made to follow the gas temperature, the mean temperature can

nevertheless be raised to high levels to reduce the heat loss during the combustion period of the cycle and achieve a better fuel economy. With the standard all metallic engine, this simply means the failure of the engine due to metallurgical problems. Thus new materials which withstand high temperatures are necessary, viz. ceramics. In the literature, the terms adiabatic or insulated diesel engines are used which simply refer to engines with suppressed heat loss from combustion gases and partial elimination of the cooling system.

1.3 ENGINEERING CERAMICS

Engineering ceramics have, in the past decade, attracted worldwide interest for the application in gas turbines and in reciprocating diesel engines. They are not only important for engine insulation, but also due to their special properties such as high hardness, high temperature strenght, low friction and density as well as excellent corrosion and wear resistance, they are good candidates for replacing certain metallic parts of engines.

Engineering ceramics have also political and economic significance. The basic elemental constituents of ceramics are aluminium, silicon, zirconia, oxygen, nitrogen and carbon. Unlike some high performance metals which are expensive, scarce and strategically important such as nickel, tungsten and cobalt, they are readily available in the whole of the Earth's crust and atmosphere. Thus engineering ceramics provide the political and economic independency over other raw material supplying countries. Japan is an excellent example, where a high level of technology exists with limited raw material resources, and it was one of the first countries to realize the importance of engineering ceramics.

The US and Japan are the leading countries in the R & D of engineering ceramics. The annual funding levels

are shown in Table 1.1. Although they appear to be spending similar amounts on R & D, the US programmes have been heavily funded by the government, whereas in Japan industry has provided the bulk of the funding. The US in overall terms is probably still ahead of Japan but Japan leads in production and applications technology, and is catching up rapidly in areas such as basic R & D and engine application.

In the UK the R & D activity of engineering ceramics compared to US and Japan is quite low. Although the UK pioneered the development of silicon based ceramics and their application in engines and is still among the leaders in the development of certain ceramic materials such as sialons, it seriously lags in the application development activity. The level of R & D activity in different countries as a function of time is shown in Fig.1.1.

The current limitation of ceramics in engine applications include brittleness, design and fabrication problems, whereas the long term problems to be solved are process technology and product reliability. An 'all ceramic engine' is not likely to be a commercially viable proposition within the next two decades. Short term applications are likely to be substitution for metal parts which do not require extensive modification to engine design. A small number of ceramic components are likely to be introduced in the market within a few years, such as diesel injector nozzles, ceramic pads for tappet followers, rocker arms and valve seat inserts. The evolution of engine materials is presented schemattically in Fig.1.2.

1.4 RESEARCH AT BATH UNIVERSITY

The research at Bath University into insulated diesel engines started with theoretical work and later developed into the experimental stage. The first theoretical work was carried out in order to understand

the mechanism of insulation and predict insulated engine performance [4-7].

The initial theoretical analysis was performed using the cycle simulation package CSP, a finite element package written by Kao [7] and Fourier methods as the primary computational tools. The finite element package was used to analyse the performance of an experimental air-gap piston, whereas CSP was used to study different insulated engine schemes such as turbocharged, turbocompound and with bottoming cycles.

The theoretical work was later applied to ceramic components. The stress levels in disc shaped ceramic components were studied for both monoliths and zirconia coatings under both steady state and transient loadings. The work was completed using both the program package ANSYS and a program written by Manton [10].

The first insulated engine tests at Bath University were done using an air-gap all metal piston in a single cylinder Petter PH1W engine [8,9]. The piston has an aluminium body fitted with a nimonic crown which led to a reduction in heat flow of over 50%. Later, the experimental work developed to the stage where ceramic components could be tested in 3 different rigs, as follows:-

1) A thermal shock test rig: This rig was designed and manufactured at Bath University by W. Alexander [110]. The rig uses high power quartz halogen lamps and focusing devices to heat one side of a ceramic specimen. By this means, high levels of thermal stress comparable to the thermal loadings in a diesel engine environment are produced at the front face of the ceramic disc and hence the resistance of the material to the thermal shock is studied.

2) A simulation rig: This rig is a modified single cylinder Petter PH1W engine with a new cylinder head designed to accomodate the ceramic specimen. The rig operates only under motored conditions but the high

boost pressure and heating the inlet air produce gas pressure and temperature peaks similar to those in a fired diesel engine.The description of the rig is given in Chapter 8.

3) A fired diesel engine: The ceramic specimens which survive the first two tests are finally ready to be tested in the actual fired diesel engine. The rig is a heavily instrumented single cylinder Petter PH1W engine and it is described in Chapter 8.

1.5 THESIS STRUCTURE

The thesis is divided into 3 main parts as follows:-

1) General - Chapters 1, 2, 3
2) Theoretical Part - Chapters 4, 5, 6
3) Overall Results - Chapters 7, 8, 9

The first part of the thesis comprises the introduction, a past literature survey and the explanation of the cycle simulation program. The benefits of engine insulation are explained and for ceramic engine simulation the required modifications in the cycle simulation program are pointed out. The possible ceramic candidates and their thermal and mechanical properties are presented.

In the second part of the thesis, the theories of the written simulation models, such as radiation heat transfer, engine thermal resistance and the surface temperature transient behaviour, are explained in detail.

In the final part of the thesis, the simulation results of the experimental Petter PH1W engine for standard and various insulation cases are produced by using the new version of the cycle simulation package (adopted especially for ceramic engines). An explanation to the controversy of increase in engine heat loss with insulation is searched, and the significance of soot deposits on engine heat transfer is discussed. The

experimental methods and results are presented and finally the conclusion and the recommendation for future work are given.

CHAPTER 2
LITERATURE SURVEY

2.1 INTRODUCTION

In this chapter the published literature on insulated diesel engines is reviewed. Although research into the subject was started about 12-14 years ago, the literature is vast. The main interest areas, related to the thesis subject are explained; they are heat transfer, thermal analysis and performance of the adiabatic engine, and the methods of insulation, candidate insulation materials and their properties.

2.2 HEAT TRANSFER AND THERMAL ANALYSIS

Heat transfer and thermal analysis in the combustion chamber is very significant in adiabatic engine studies for both understanding the benefits of insulation and from a structural design point of view. In current metal engines, a controlled amount of heat transfer is provided by the cooling system to ensure that the internal surface temperatures lie below their critical limits even at the highest thermal loadings. The heat loss to the coolant decreases the thermodynamic efficiency of the diesel cycle and also reduces the energy availability of the exhaust gases. Hence, in the design of conventional metal engines a compromise between cycle efficiency and structural strength is aimed at.

In insulated diesel engines, by the elimination of the cooling system and by applying low conductivity materials to the walls of the combustion chamber, it is possible to raise the internal surface temperatures upto 1300 K, depending on the insulation level. Although materials such as ceramics can withstand these high temperature levels, the huge temperature gradient

created across the material is one of the major problem in engine component design. Due to the low conductivity of ceramics, even the temperature gradients across the combustion chamber surface are expected to be high enough to create local thermal stress concentrations, and incidentally to affect the heat transfer calculations. It is important to understand current heat transfer and thermal analysis methods for conventional engines, and to modify them before applying them to the insulated engine. The main topics of interest can be listed as follows:-

1) Convective heat transfer from gas to wall.
2) Radiation heat transfer from diesel flame to wall.
3) Conduction heat transfer through the engine walls.

2.2.1 Convective Heat Transfer

The convective heat transfer at a particular location on the inside surface of the engine is defined by the local gas to wall temperature difference and local heat transfer coefficient as follows:-

$$Q(\theta,S^*) = htc(\theta,S^*) * Area * \left[T_g(\theta,S^*) - T_w(\theta,S^*)\right] \quad (2.1a)$$

where (θ,S^*) shows the time and space dependent property of the function.

The above heat transfer equation requires a knowledge of the local heat transfer coefficients and local gas temperatures which are not easy to obtain. In existing cycle simulation packages a space mean heat transfer coefficient and gas temperature are used for all the internal surface which simplifies eqn.2.1a to:-

$$Q(\theta,S^*) = htc(\theta) * Area * \left[T_g(\theta) - T_w(S^*)\right] \quad (2.1b)$$

where the wall temperature is assumed to be independent of time but space dependent.

In a conventional metal engine, the constant wall temperature assumption throughout the cycle is quite

reasonable since the wall temperature fluctuations is only about ±10 K, i.e. about 1% of the gas temperature fluctuation. However, for low conductivity materials such as ceramics, the wall temperature fluctuation may increase upto ±150 K which invalidates the constant wall temperature assumption. Thus for ceramic engine applications, $T_w(S^*)$ should be replaced by $T_w(\theta, S^*)$ in eqn.2.1b.

The heat transfer coefficient term $htc(\theta)$, in eqn.2.1b has a strong influence on engine performance. Although different htc functions can produce the same amount of heat loss over a cycle, the engine performance can be quite different. If, for example, instead of a transient htc a constant cycle mean value is used, it will reduce the volumetric efficieny and exhaust temperature but increase the brake power.

The highly unsteady and complex nature of the flow in the cylinder, makes it very difficult to model htc from basic principles. Engineers have been trying to model htc by simple correlations from experimental engine data. Generally, the approaches adopted can be gathered into 3 groups, viz. dimensional, dimensionless and flow based models.

The dimensional models are the first generation of models used for internal combustion engines which date back over 60 years. The first model, proposed by Nusselt [11] in 1923 who based his correlation on experiments carried out in a spherical bomb, is given by:-

$$htc(\theta) = a\left[P^2(\theta)\,T(\theta)\right]^{1/3}\left(b_1 + b_2\bar{V}_p\right) \qquad (2.2)$$

where:-

$P(\theta)$ and $T(\theta)$ are the combustion chamber pressure and temperature.

$\bar{V}_p$ is the mean piston velocity.

a, b_1 and b_2 are the constants to be fitted to the experimental data.

Another example of the early type of dimensional model is that proposed by Eichelberg [12] in 1939:-

$$htc(\theta) = a\left[P^2(\theta)T(\theta)\right]^{1/2}\left(\bar{V}_p\right)^{1/3} \tag{2.3}$$

where constant a is determined by experimental engine data.

In both models, the main drawback is the lack of physics and the difficulty in scaling such models for a particular engine.

The second generation of models are of the dimensionless type which makes their application more general. The first correlation is the one proposed by Elser [13] in 1955:-

$$Nu = a\,Re^{0.5}\,Pr^{0.5} \tag{2.4}$$

where Nu, Re and Pr are the Nusselt, Reynolds and Prandtl numbers, respectively, and are conventionally defined by:-

$$Nu = \frac{htc * D_{cy}}{k_g} \tag{2.5}$$

$$Re = \frac{\rho_g \bar{V}_p D_{cy}}{\mu_g} \tag{2.6}$$

$$Pr = \frac{Cp_g \mu_g}{k_g} \tag{2.7}$$

where:-

D_{cy} is the cylinder diameter.

$\bar{V}_p$ is the mean piston speed.

k_g is the gas conductivity.

μ_g is the gas viscosity.

Cp_g is the gas specific heat capacity.

ρ_g is the gas density.

Later, use of the well known Reynolds analogy between heat and momentum in fully developed turbulent boundary layers led Annand [14] in 1963 to propose the proper dimensionless form:-

$$Nu = a\,Re^b \tag{2.8}$$

where the Reynolds number is based on the mean piston velocity. The values suggested for constant a is between 0.35 and 0.80, depending on the intensity of the charge motion, whereas b is suggested to be 0.7.

The widely used Woschni correlation [16] which was proposed in 1967 is similar in form to Annand's but with an exponent 0.8. However, the mean piston velocity in the Reynolds term was replaced by the characteristic velocity which is defined by:-

$$V_{ch} = c_1 \bar{V}_p + \text{additional gas velocity} \tag{2.9}$$

where c_1 is 6.18 and 2.28 during open and closed periods, respectively. The second term is calculated from the instantaneous pressure difference between the firing and motoring cases. For the motored case the second term is zero and Woschni's correlation reverts to the general form proposed by Annand.

A comparison of the Woschni and Annand htc models at various engine operating conditions are shown in Fig.2.1.

The third generation of htc models are flow based. Earlier models represent the fluid motions in the cylinder by the mean piston velocity which is a very crude measure of gas velocity. As is well known, the gas velocities inside the combustion chamber are a function of both time and space. The proposed models are still insensitive to several engine design details that are

well known to enhance heat transfer, such as valve size and shape, and piston crown geometry.

This deficiency was recognized by some researchers who proposed different definitions for the characteristic velocity to replace the mean piston velocity in the Reynolds term. Knight [15] was the first to investigate the problem and he defined a mean gas velocity calculated by the mean kinetic energy of the gas:-

$$V_{ch} = \sqrt{\frac{KE}{2m_g}} \tag{2.10}$$

where the kinetic energy KE is defined by:-

$$\left(\dot{m_g} KE\right) = \sum \dot{m}_{g,in} \frac{C_{in}^2}{2} + \text{squish} \quad KE - \dot{m}_{g,out} KE \tag{2.11}$$

where $\dot{m}_{g,in}$ and $\dot{m}_{g,out}$ are the gas mass flow rate into and out of the cylinder and C is the gas velocity.

Other researchers [17] defined the Reynolds number by only using the swirl:-

$$Re = \frac{\rho_g \omega r_{cy}^2}{\mu_g} \tag{2.12}$$

where r_{cy} is the cylinder radius and ω is the swirl angular velocity which can be obtained by solving the equation of conservation of angular momentum. Some researchers [19,20] attempted to include the turbulence terms in their models but none of these formulations include all the key fluid motions.

A more detailed htc model has been developed recently by Morel and Keribar [21]; this considers the time and space variations. In the model, htc was assumed to be related to the strength of the fluid motions through the Colburn analogy:-

$$htc = 0.5 C_f \rho_b C_e Cp P^{-2/3} \qquad (2.13)$$

where:-

C_f is the skin friction coefficient for which a mean correlation for fully developed flat plate or pipe flow was used.

ρ_b is the boundary layer mean density.

C_e is the effective gas velocity outside the boundary layer.

Cp and P are the specific heat and pressure.

The effective gas velocity is defined by:-

$$C_e = \left(C_x^2 + C_y^2 + KE_t\right)^{0.5} \qquad (2.14)$$

where C_x and C_y are the gas velocity components parallel to the particular surface of interest and KE_t is the kinetic energy of turbulence. The combustion chamber is divided into 3 regions defined as the squish area above the piston crown, the cup volume and the region above the cup lip as shown in Fig.2.2. In each region the radial, axial, swirl and turbulence intensity and length scale were solved and the effective velocity for each surface was calculated.

The model is far more complex and advanced than the previous ones and provides a tool to predict the benefits of selective insulation of the combustion chamber. However, the implementation of such detailed models in simulation packages increases the computational time enormously, while the accuracy of the results is questionable until they are validated experimentally. Typical htc values calculated for different regions of the combustion chamber and area averaged htc are shown in Figs.2.3 and 2.4,respectively.

2.2.2 Radiative Heat Transfer

In diesel engines, radiative heat transfer forms

a significant part of the total heat transfer compared to spark ignition engines. Soot particles are the main source of radiation; these are generated during the diffusion mode of burning. A small amount of radiation is also emitted by carbon dioxide and water molecules and by intermediate chemical species formed during combustion, mainly in narrow spectral bands.

In an adiabatic diesel engine the role of the radiative heat transfer is more significant. Insulating the combustion chamber raises the wall temperatures which results in a drastic decrease in the convective part of the heat transfer. However, the effect on the radiative component is very difficult to judge. Radiative heat transfer is a function of the fourth power of absolute temperature which makes the flame temperature the dominant variable. Higher wall temperatures will slightly decrease the radiative heat transfer to the walls, but a slight increase in the flame temperature is also expected. As a result of insulation, the ignition delay period is shorter and the combustion mode shifts from the premixed towards the diffusion burning mode, which is largely responsible for soot formation. Thus, the overall effect of insulation can even be higher radiative heat transfer than in a conventional engine. There is no doubt that the percentage of the radiative component of heat transfer will significantly increase with insulation and should be considered separately in adiabatic engine simulation studies.

Nusselt was one of the first to attempt to estimate the radiative heat transfer in diesel engines by using a combustion bomb; he reported that it can vary between 5 to 55% of the total heat transfer. The radiative component of heat transfer has far long been the subject of discussion and most of the researchers such as Eichelberg, Pflaum, Nusselt, Sitkei and Woschni

considered it as part of the convection term [22]. However, Annand expressed it separately in his correlation in a simple way with the Stefan-Boltzmann equation:-

$$q_{rad} = \varepsilon \sigma \left(T_g^4(\theta) - T_w^4 \right) \qquad (2.15)$$

where:-

ε is the emissivity.

σ is the Stefan – Boltzmann constant.

T_w and $T_g(\theta)$ are the wall and gas temperatures.

Annand suggested a value of 1.5 for the emissivity to compensate for the loss caused by the lower gas mean temperature value which is substituted for the flame temperature. This is a very crude way of expressing the radiative heat transfer in a diesel engine which is a strong function of both time and space.

Ebersole [22] was the first to measure the radiative heat transfer in an operating diesel engine in 1963 by covering the thermocouple at the cylinder gas to wall interface with a sapphire window. He reported that the radiative heat transfer accounts for 5 to 10% of the total heat transfer at low engine load, and 35 to 45% at near maximum load (Fig.2.5). The suggested percentages are cycle mean values and therefore higher values are expected during combustion and expansion period of the cycle.

Oguri and Inaba [24] also measured the radiative heat transfer using the same method as Ebersole and reported that the radiative heat transfer is about 10 to 30% of the total heat loss depending on the fuelling; their result is shown in Fig.2.6.

The instantaneous radiative heat flux in a diesel engine was measured by Flynn et al [23] in 1972 using a photodetector and infrared monochromator. Tests were done for a wide range of engine operating conditions and fuels, and an empirical correlation for instantaneous

radiative heat flux was presented. It was observed that the radiative heat flux exhibited a shape and duration similar to the heat release. Therefore a Wiebe function was chosen for the correlation; this is given by:-

$$q_{rad} = 2\bar{q}_{rad}\, b(a+1)\left(\frac{\theta-\theta_1}{360}\right)\exp\left[-b\left(\frac{\theta-\theta_1}{360}\right)^{a+1}\right] \qquad (2.16)$$

where θ is the crank angle and $\bar{q}_{rad}$, a, b and θ_1 are the functions defined by the engine speed, equivalence ratio, fuel injection timing and inlet manifold pressure, and should be scaled for that particular engine. Correlations for these functions were presented in [23].

The recorded radiative heat flux, flame temperature and emissivity, and heat release rate for different engine speeds, equivalence ratios and boost levels are shown in Figs.2.7 to 2.9. It can be seen that the radiative heat flux can be as high as 2 MW/m^2.

Although the correlation proposed by Flynn is sensitive to certain engine parameters such as speed, equivalence ratio, boost pressure and injection timing which makes it very attractive to use, it is not well suited to adiabatic engine applications. The lack of flame and wall temperatures, and flame emissivity terms are the main drawbacks.

The model proposed by Sitkei and Ramanaiah [25] in 1972, concentrates on the flame emissivity which is expressed as:-

$$\varepsilon_{fl} = \varepsilon_i\left[1-\exp(-aPL_m)\right] \qquad (2.17)$$

where:-

ε_i is the emissivity of infinitely thick radiating agent suggested to be 0.8.

a is the absorption coefficient.

P is the pressure in bars.
L_m is the mean path length in metres, and is defined as:-

$$L_m = 3.6 \frac{V(\theta)}{A(\theta)} \qquad (2.18)$$

where $V(\theta)$ and $A(\theta)$ are the instantaneous volume and surface area of the combustion chamber.

The flame absorption coefficient was derived from the experimental data as a function of equivalence ratio which is shown in Fig.2.10. The black body temperature of the flame as a function of load and crank angle was measured by using a quick response photoelectric pyrometer. It was assumed that the flame temperature does not vary greatly with load and type of engine; the flame emissivity was calculated from its definition:-

$$\varepsilon_{fl} = \left(\frac{T_b}{T_{fl}} \right)^4 \qquad (2.19)$$

where subscripts b and fl denotes the black body and actual flame, respectively. The flame temperatures are obtained from Belinskiy's data which is shown in Fig.2.11. After calculating the flame emissivity the absorption coefficient is evaluated from eqn.2.17.

Using a suitable flame temperature such as Belinskiy's, as suggested by Sitkei and Ramanaiah, and the calculated flame emissivity, the instantaneous radiant heat flux can be obtained by:-

$$q_{rad} = \sigma \varepsilon(\theta) T_{fl}^4(\theta) \qquad (2.20)$$

The model suggested by Kunitomo [26] in 1975 is similar to that of Sitkei and Ramanaiah's. However, the flame emissivity was here defined in terms of gas and soot emissivity, ε_g and ε_{so}, such that:-

$$\varepsilon_{fl}(\theta) = 1 - \left(1 - \varepsilon_g(\theta)\right)\left(1 - \varepsilon_{so}(\theta)\right) \qquad (2.21)$$

The gas emissivity is defined by:-

$$\varepsilon_g(\theta) = 1 - \prod_n \left[1 - \varepsilon_{g,n}(\theta)\right] \qquad (2.22)$$

where $\prod$ is a multiplication sign and $\varepsilon_{g,n}(\theta)$ is the emissivity of each infrared active gas such as CO_2, H_2O and CO. However, calculating $\varepsilon_{g,n}(\theta)$, the effective optical depth of the flame is necessary which is defined by Kunitomo as:-

$$L_{m,e}(\theta) = hr(\theta)\,P(\theta)\,L_m(\theta)\,X_n \qquad (2.23)$$

where:-

$hr(\theta)$ is the ratio of cumulative heat release to the total injected fuel energy.

$P(\theta)$ is the gas pressure in atm.

L_m is the mean beam length.

X_n is the total mole fraction of gas n and is calculated by using the air-fuel ratio.

The mean beam length is defined slightly differently than that proposed by Sitkei's and Ramanaiah's, viz.:-

$$L_m(\theta) = 3.5\frac{V(\theta)}{A(\theta)} \qquad (2.24)$$

The soot emissivity term was derived from the experimental data obtained from luminous flames at atmospheric pressure. It was found that the ratio of soot to gas emissivity $(\varepsilon_{so}/\varepsilon_g)$ depends mainly on the fuel properties and the excess air ratio φ:-

$$\left(\frac{\varepsilon_{so}}{\varepsilon_g}\right)_{P=1} = \frac{0.09}{\varphi - \rho_f^2 + 0.35\rho_f - 0.38} + 6.8\,\rho_f - 5.95 \qquad (2.25)$$

where ρ_f is the specific gravity of the fuel.

The soot emissivity at high pressures was obtained by using the following relation for the absorption coefficient, a_{so}:-

$$a_{so} = (a_{so})_{P=1} P^m \tag{2.26}$$

where $(a_{so})_{P=1}$ is given by:-

$$(a_{so})_{P=1} = -\frac{1}{L_m} \ln\left[1 - (\varepsilon_{so})_{P=1}\right] \tag{2.27}$$

P is the pressure in atm. and m is the exponent given by:-

$$m = \frac{4.95}{\varphi_e + 1.5} - 0.25 \tag{2.28}$$

where φ_e is the effective excess air ratio and suggested to be a value between 1.0 and 1.2.

Using the definition of emissivity $(1-\exp(-aL_m))$ and eqns.2.25 to 2.27, the soot emissivity can be expressed by:-

$$\varepsilon_{so}(\theta) = 1 - \exp\left\{-P^m(\theta) \ln\left[1 - (\varepsilon_g(\theta))_{P=1}\right.\right.$$

$$\left.\left.\left(\frac{0.09}{\varphi_e^2 - \rho_f^2 + 0.35\rho_f - 0.38} + 6.8\rho_f - 5.95\right)\right]\right\} \tag{2.29}$$

The flame temperature was suggested to be 2400 K upto the point where 90% of the heat is released; thereafter it gradually approaches the gas mean temperature.

A more detailed model was proposed by Chang and Rhee [28], to compute the radiative heat flux at a

particular location in the combustion chamber. The gas in the chamber was considered to be composed of many small volumes, each of them at constant temperature and having the corresponding equilibrium chemical composition. The model requires time and space resolved species data to calculate the burned fuel-air ratio, and the flame temperature distribution inside the chamber.

The flame emissivity was calculated as in Kunitomo's model by eqn.2.21. However, the wide band model proposed by Edwards and Balakrishnan [32] was used to obtain the gas emissivities for CO_2 and H_2O. For soot emissivity, first the spectral absorption coefficient (by using the optical constants of soot particles) and then the spectral emissivity, were calculated. The radiative heat flux at a particular point was obtained by superimposing the radiant heat transfer from all volumes, expressed as:-

$$q_{rad} = \sigma \int_{A_j} F_{j-k} \varepsilon_{fl} T_{fl}^4 \, dA \qquad (2.30)$$

where F_{j-k} is the shape factor connecting the emitting area A_j with the receiving area A_k.

Multidimensional modelling of radiative heat transfer in a diesel engine was studied by Menguc et al [29]. The monochromatic radiative heat transfer equation for an absorbing, emitting and anisotropically scattering gas-particle mixture in a cylinder was solved by the first (P_1) and third (P_3) order spherical harmonics approximations. It is reported that the scattering due to fuel droplets during the combustion period is negligible. The resultant radiative heat flux on the cylinder head and piston surfaces are shown in Fig.2.13. The very low radiative heat flux on the head near the centre is due to the low temperature and optically thick characteristic of the adjacent gas zone.

The model is purely theoretical and requires assumed temperature, soot and fuel droplet distributions to be representative of the conditions in a diesel engine during combustion.

2.2.3 Conductive Heat Transfer

Conductive heat transfer through the engine walls is composed of transient heat transfer in the thin layers of the material adjacent to the combustion chamber and steady state heat transfer within the rest of the engine body (at constant engine operating condition). The transient heat transfer is caused by the highly unsteady cycle conditions with concentrated bursts of high heat flux from gases during combustion followed by relatively long periods of low heat flux rates for the rest of the cycle. The transient gas to wall heat flux causes the wall temperaure to fluctuate about a mean value. As mentioned earlier, for low conductivity materials the temperature swing can reach ±150 K. The magnitude of the wall temperature swing is important in relation to heat transfer and thermal stress analysis.

The transient temperature wave propagates into the structure for only a limited distance, before being damped out by thermal inertia of the material. The thermal penetration depth (TPD), defined as the position in the material which has 1% of the total surface temperature swing, is of the order of 0.5 to 2.5 mm depending on the thermal inertia and conductivity of the material. However, the temperature gradients across this thin layer are very high and for low conductivity ceramics can reach 300 K/mm. This makes a one dimensional analysis of transient conductive heat transfer perpendicular to the surface quite appropriate. This approach was adopted by previous researchers, such as Bradish, Shamah, Wallace and Morel [118,119,4,67].

Bradish et al studied the effects of the deposits

on heat transfer and wall temperature by solving the one dimensional conductive heat transfer equation numerically. Shamah tried to discover the effects of temperature fluctuation on engine performance. Wallace et al investigated the effects of different materials on surface temperature fluctuations, and engine performance by expanding the heat flux input as a Fourier series. However, for simplicity they only considered the fundamental frequency component, giving lower temperature fluctuation values. Morel and Keribar solved the one dimensional conduction equation by finite difference numerical method and coupled it with thermodynamic cycle code to investigate the wall temperature fluctuations for ceramic components under realistic engine operating conditions.

The surface temperature has been measured by several researchers [69,75-78], using thin film surface thermocouples. Such data provide valuable local heat flux values inside the engine from which local gas heat transfer coefficient can be obtained. The accuracy of the results depends on the thickness of thermocouple junction, i.e. thermal inertia. A surface thermocouple of thickness less than 5 microns can give virtually undamped signals. The accuray of the thermocouple reading is also affected by the method of thermocouple attachment to substrate.

The steady state conduction heat problem for the engine body can be solved quite accurately by using available 3-D finite element (FE) models, providing that the true boundary conditions are specified. These free standing FE models are mainly used for detailed thermal analysis and design of engine components, rather than as part of cycle simulation packages, because of the enormous increase in the computational time. 2-D thermal analysis in r-z co-ordinates of axisymmetric piston using the FE program developed by Kao at Bath University [6,7] is shown in Fig.2.14.

In cycle simulation packages, the engine body is represented by simple resistance networks so that the wall temperatures can be approximately computed within a short computational time for the heat transfer calculations. By adjusting the resistance values, a temperature distribution inside the engine can be generated to provide adequately accurate heat transfer results. A typical engine resistance network used in simulation packages is shown in Fig.2.15.

2.3 INSULATED ENGINE PERFORMANCE

Early insulated engine performance investigations were carried out by simulation. Various insulation levels were chosen by the researchers, approximately 40% heat supression to the coolant being selected as probably representing a realistic target in terms of component design. The engine insulation was modelled by the simplest method either increasing the resistance values of the engine thermal resistance network or simply by raising the wall temperatures. Other engine processes such as heat transfer, heat release and friction were assumed to be essentially unchanged.

It was well understood from these early adiabatic engine performance predictions that suppressing heat loss to coolant simply transfers energy to the exhaust gas. Naturally aspirated engines do not benefit from insulation because the increased exhaust energy cannot be recovered and higher wall temperatures decrease the volumetric efficiency and thus reduce the engine performance drastically. This fact is generally accepted by all researchers. However, for the turbocharged case, substantial improvement in engine performance with an increase of about 10% in thermal efficiency has been estimated [4,42,43]. Using turbocompound engine schemes the greatest benefit of insulation can be obtained with thermal efficiencies reaching upto 46%, provided that highly efficient turbomachinery is used. By also using

an organic Rankine bottoming cycle after the power turbine in the exhaust system, the overall thermal efficiency can be raised to over 50%. However, the cost, complexity and maintenance problems of the Rankine system do not make it an attractive approach.The development of new and advanced ceramics will also provide new methods of engine lubrication which will make it possible to design a minimum friction adiabatic diesel engine with a brake thermal efficiency of 56%. Schematic diagrams for various engine schemes are shown in Figs.2.16 and 2.17.

Adiabatic diesel engine research was later extended to the experimental stage where different kinds of insulation techniques, such as thermal barrier coatings, monolithic ceramics and air-gaps were implemented. Both selective and complete insulation of the combustion chamber have been investigated and tested by various researchers such as Kamo, Yoshimitsu, Wallace, Woschni and Alkidas [48,54,8,69,72]. Most of them reported significant increase in fuel consumption with insulation. The thermal efficiency of the insulated engine was found to worsen with increasing load and decreasing engine speed; typical isfc values for both standard and insulated engines are shown in Fig.2.22.

It is well known that ignition delay periods are shorter in an insulated engine, thus reducing the premixed combustion spike. The tests performed by Isuzu Motors Limited [81] in a Si_3N_4 engine showed that ignition delay periods reduced by about 40% which caused a sharp drop in the maximum rate of pressure rise from 10 Bar/CA to 5.6 Bar/CA. It was also reported that the period of heat release took longer, i.e. at slower rates; this was thought to be the cause of the higher observed bsfc, especially at low speeds and high loads. It was suggested that the drop in maximum pressure rise might have caused a poorer and more prolonged combustion. Typical curves of ignition delay and maximum

pressure rise as a function of engine speed are shown in Fig.2.18.

Performance tests carried out by Alkidas [72,82] in an air-gap insulated engine showed the same trends as those of Isuzu Motors Ltd. However, the deterioration of the bsfc with increasing load was thought to be due to a degradation of the injection process resulting from elevated injector temperatures. Higher wall temperatures caused lower viscosity and increased clearence of the injector, both of which might have caused a reduction in the fuel injection rate. As a result of this, prolonged combustion might have taken place, causing an increase in bsfc. To prove the point, the 8 hole injector was replaced by a 9 hole injector and a different injector seal design was adopted to reduce heat transfer from the firedeck. The performance of the uncooled engine was significantly improved, being as good as the performance of the water-cooled engine except at high load, low speed conditions (Figs.2.20 and 2.21). The heat release duration was substantially shorter in the uncooled engine than in the water-cooled engine for the same mass of fuel per cycle. This result contadicts the prolonged combustion hypothesis employed previously to explain the deterioration of bsfc experienced by the uncooled engine at high loads. Pumping and friction losses were found to be lower in the uncooled engine which resulted in a much larger difference in isfc for the two types of engine (Fig.2.22). It was concluded that the increase in isfc at high loads is caused by the higher heat losses during the combustion and expansion periods of the cycle.

A loss of volumetric efficiency with insulation of about 5 to 10% was experienced depending on the insulation level of the engine (Fig.2.23).

Exhaust temperatures were raised by 50 to 150 K with insulation and the increase is more pronounced at high load conditions (Fig.2.24).

Engine insulation has also significant effects on

the exhaust emissions. Due to higher flame temperatures, nitric oxide emissions increase and the unburned hydrocarbons decrease. Smoke does significantly change in the low load conditions but at high loads it increases slightly (Fig.2.25).

2.4 DOES INSULATION INCREASE OR DECREASE ENGINE HEAT LOSS?

Until now, engine tests have indicated that insulation increases the fuel consumption which contradicts the previous theoretical predictions. This led to a debate among researchers as to the cause of this apparent paradox.

Woschni [69] in 1987 was the first to reach the conclusion that engine insulation, instead of decreasing the gas to wall heat transfer during the combustion period of the cycle, which is crucial to engine performance, actually increases it. He accepted the fact that insulation decreases the gas to wall temperature difference but suggested that high wall temperatures enhances the gas htc, so that overall heat transfer to the wall during the combustion period is greater than in the uninsulated case. He explained the enhancement of htc at high wall temperatures by the approach of the flame towards the wall which increases temperature gradients and turbulance within the boundary layer. He modified his htc model for the combustion period by expressing the constant C_2 as a function of wall temperature T_w, as follows:-

$$htc = C_3 D^{-0.2} P^{0.8} T^{-0.53} \left[C_1 \bar{V}_p + C_2 \frac{V_{sw} T_1}{P_1 V_1} \left(P - P_1 \right) \right]^{0.8} \qquad (2.31)$$

$$C_2 = 3.24 \times 10^{-3} \quad (m/sK) \qquad \text{for} \quad T_w < 600 \text{ K}$$

$$C_2 = 2.30 \times 10^{-5} \left(T_w - 600 \right) + 0.005 \quad (m/sK) \qquad \text{for} \quad T_w \geq 600 \text{ K}$$

where P, T, V and D are the cylinder pressure, temperature, volume and diameter, respectively, and subscripts sw and 1 denote the swept and trapped conditions. C_1, and C_2 are constants given in [16].

Woschni supported his argument by using Germerdonk's and Nguyen's work [79] which suggested that if an exothermic reaction occurs within the boundary layer, the htc increases by a factor greater than two, this being referred to as 'convection vive'. To create such a reaction in the boundary layers requires wall temperatures above 620 K. This fact is well-proved experimentally using a premixed propane-air flame [79]. The ratio of 'convection vive' to normal htc showed a linear relation to the wall temperature (Fig.2.26). However, the combustion in a diesel engine is based on a highly turbulent diffusion type flame and it is not yet known whether 'convection vive' phenomenan could apply to it.

Since Woschni's hypothesis clearly has to be considered, in connection with engine insulation, it is very important to understand which methods he implemented in his investigations and how he reached his crucial conclusion. He based his hypothesis on the experimental data obtained by 3 different routes which are listed as follows:-

1) Heat balance in the cylinder.
2) Transient wall surface temperature data.
3) Steady state heat flux data.

In the internal heat balance, the heat release was obtained from the cylinder pressure data using the same htc term for both conventional and insulated engines (Fig.2.27). It was observed that the total heat release was less than the injected fuel energy in the insulated engine from which Woschni concluded that the energy loss was caused by the additional heat loss to the walls by the 'convection vive' phenomenon during combustion. This seems to be a premature conclusion because the extra

energy loss could be caused or partly affected by other factors, such as inefficient combustion, changes in fuel injection rate and characteristics, loss in volumetric efficiency, increase in radiation heat transfer, reduced maximum pressure rise rate and burning of the wall deposits. However, Woschni strongly defends his point by claiming that the loss in volumetric efficieny was compensated by adjusting the inlet manifold pressure, and the combustion efficiency was checked by the exhaust gas analysis and no significant changes were recorded. On the other hand Alkidas's work [82] showed that modifying the fuel injection system for insulated engines could improve their performance.

Woschni proved that the higher fuel consumption in insulated engines occurs because of the high wall temperatures and not the process temperature. The process temperature in a conventionally cooled engine was raised by heating the inlet air to a point where the exhaust temperature was equal to that of the insulated engine and no further increase in fuel consumption was observed. However, it is not very easy to decide which process in the engine is affected by hot walls.

Woschni further supported his argument by the wall surface temperature data obtained from a similar engine (cooled) with one of the exhaust valves replaced by an air cooled heat flux probe. By changing the air flow rate, the probe mean surface temperature was varied within the limits of 650-1100 K without changing the engine operating conditions. Since the probe area was small, it's temperature change could hardly affect in-cylinder conditions. Using the transient surface temperature data, the htc's were computed which showed higher values for the hot wall by a factor of 4 to 5 (Fig.2.28). If the surface temperature data is carefully examined, it is seen that the amplitude of the temperature waves is almost the same for both cold and hot surfaces, and with hot surface, the rate of

temperature rise or the response of the thermocouple is slighty higher than the cold one which caused a sharp increase in Woschni's computed htc. Woschni did not mention any temperature dependent material properties and wall deposit effects on the fluctuating wall temperature and the author believes that cold soothy and hot clean surface thermocouples can produce similar temperature waves with the same gas boundary conditions.

A hot clean surface thermocouple produces higher response, i.e. steeper temperature rise and records the true heat flux. On the other hand, in the cold soothy surface thermocouple case, the response is slightly slower and the rate of temperture rise is not as steep as with the clean thermocouple; the calculated heat flux will be less because of the damping characteristic of the wall deposits, thus recording smaller surface fluctuations. If the temperature dependent material properties, $k\rho Cp$, are also considered, the hot surface produces higher temperature swing than the cold surface under the same gas to wall heat flux condition. Thus, it is possible to obtain similar temperature waves at the cold and hot surfaces without drastic change in the gas side boundary conditions (T_g, htc).

Woschni's mean heat flux measurements obtained from the cooled engine showed that the mean heat flux dropped steadily with insulation upto 700 K and that further insulation did not make any change at all which supports Woschni's argument (Fig.2.29).

However, the heat flux measurements obtained from an open-chamber diesel engine by Huang and Borman [77] with an instrumentation plug which can incorporate plates of various materials on the gas side, showed that a significant reduction of cycle mean heat flux was achieved with both zirconia and with insulated metal surfaces (Fig.2.30,2.31). On the other hand, the peak values of surface transient heat flux during combustion for the insulated metal surface were reported to be

higher than those for the uninsulated metal which supports Woschni's argument. But a reduction of 50% in peak values of surface transient heat flux were observed for zirconia surface over the uninsulated metal which contradicts Woschni's hypothesis. It was suggested that the reason for the higher peak values of the transient surface heat flux on the insulated metal was probably because of the burning of wall deposits.

Further tests performed on a DI engine with Loex and ceramic pistons (SSN, HPSN) by Furuhoma and Enomoto [75] showed that ceramics can reduce the cycle mean heat flux levels and makes it possible to reduce the cooling capacity of the engine. However, the peak heat flux values during combustion for the ceramics were found to be higher than the Loex piston. Their conclusion was same as Woschni, i.e. insulation increases gas htc's.

Morel et al [84] also measured the surface heat flux in a single cylinder, DI diesel engine with zirconia coated components. Their results showed both mean and peak surface heat fluxes were consistently reduced as the wall temperatures rose from 500 to 950 K. Heat flux measurements with an air cooled surface temperature probe were also carried out in a metallic engine similar to that in Woschni's tests. The probe mean surface temperature was reduced from 667 to 564 K and an increase in mean heat flux was observed. Although this finding contradicts Woschni's result, it is not conclusive because the probe mean surface temperature was kept relatively at a lower temperatures than in Woschni's tests.

There is no doubt that engine insulation decreases the cycle mean heat flux because if a coolant boundary condition near to adiabatic condition is chosen, i.e. elimination of cooling system and introducing air-gap or ceramic insulation, the reduction is inevitable even if the gas side boundary conditions become more severe. However, the change in gas to wall

peak heat flux values with insulation during combustion, which is very crucial for the engine performance, is debatable and further experiments should be performed to reveal the situation.

2.5 INSULATION METHODS AND MATERIALS

The main objective of engine insulation is to suppress heat loss to the coolant, to increase the thermal efficiency directly or indirectly by such means as turbocompounding and bottoming cycles, and to reduce or eliminate the cooling system of the engine. Different insulating techniques are applied to diesel engines, mainly depending on the insulation level required. These could be listed in order of increasing insulation levels as follows:-

1) Minimum cooled engine.
2) Air-gap insulation.
3) Ceramic insulation.

2.5.1 Minimum Cooled Engine

Although minimum cooled engines do not represent an insulation technique, an effort is made to suppress the heat loss to the coolant and the technique is therefore briefly explained. The cooling system design can be optimized by eliminating the excessive cooling of certain regions and by minimizing the combustion chamber surface area. Further reduction in cooling capacity can be achieved by replacing the aluminium piston with a cast iron piston which has a 75% lower thermal conductivity. The heat loss to the coolant can be reduced to 8% of the fuel energy input without involving air-gap or ceramic insulation techniques [40]. In the engine component design, the minimum cooling rate is determined by careful consideration of the following factors:-

1) The critical surface temperature.
2) The critical temperature gradient across the

material.

3) The maximum lubricant operating temperature.

2.5.2 Air-Gap Insulation

The air-gap insulation technique uses a thin layer of stagnant air trapped in a sealed enclosure immediately beneath the component surface. The thickness of the air layer is in the order of few millimeters and its very low conductivity value (k=0.067 W/mK), makes it a very good insulator. This kind of insulation technique has the advantage of not involving ceramic component design where design techniques are still not fully established.

The air-gap insulated components can incorporate high temperature alloys such as nickel/chrome, e.g. nimonic. The air-gap piston designed at Bath University [9] has a nimonic crown bolted on top of the aluminium piston with an air gap in between. The air-gap insulation technique was first used for pistons and later applied to other components such as the firedeck, the top part of the liner and exhaust ports where the whole cooling system was eliminated. The air-gap insulated test engine used by General Motors [72] is shown in Fig.2.32. Although the air-gap insulation technique is very effective, it is limited by the surface temperature of the metallic parts unless it is used in conjuction with ceramic components.

2.5.3 Ceramic Insulation

Ceramics are non-metallic, inorganic materials and are primarily based on silicates. The advanced ceramics include oxides, carbides, nitrides and borides which require high level production technology. Ceramics are well known for their low conductivity and temperature resistant properties which make them excellent candidates for diesel engine insulation. However, their brittleness and poor reliability

characteristics which can lead to sudden and catastrophic failure are the main drawbacks. Improvement of the mechanical properties of advanced ceramics is still in the development stage.

Ceramics can be used either as monolithic components or as coatings on the metal surface to insulate the combustion chamber. Due to the brittle nature of ceramics, monolithic components require special attention in the design and mechanical clamping systems. Ceramic coatings offer an easier solution to the problem without making any major changes in the engine components design. The possible candidate materials for both monolithics and ceramic coatings are listed in Table 2.1.

Plasma sprayed zirconia (PSZ) is the most widely used ceramic coating applied to a metal substrate with a suitable bond coating. Zirconia with yttria additive, ZrO_2-0.08 Y_2O_3, as a thermal barrier coating and Ni-16.8, Cr-5.8, Al-11.8, Y_2O_3 bond coatings offer an attractive thermal barrier coating system for adiabatic engines. In order to have a strong bond between the ceramic layer and the metal substrate within a wide temperature range, the thermal expansion coefficients of both the coating and the substrate should be closely matched. For this reason, zirconia coating of aluminium pistons is very difficult and usually ends in failure, whereas coating of cast iron pistons produces better results. The insulating properties of ceramic coatings are quite good when compared to their monolithic counterpart because of high degree of porosity. To achieve meaningful insulation levels a minimum of 3 mm zirconia coating seems to be required. However, one of the difficulties with plasma spraying is the inability to deposit a thick layer.

Monolithic ceramics can provide very good heat insulation for diesel engines. They can either be mechanically joined to the metal surface or simply

replace the metal component, depending on the application and on the mechanical properties of the ceramic. Some typical desired ceramic properties for an adiabatic diesel engine application are listed in Table 2.2. However, no monolithic ceramics, having all these properties are known.

The properties of ceramics are strongly dependent on microstructure, composition and manufacturing technique. In considering the properties of ceramics, it is important to distinguish between their intrinsic and extrinsic properties. Intrinsic properties are determined by the microstructure and are invariant with the method of test. They are density, specific heat, thermal expansion, thermal conductivity and elastic moduli. The extrinsic properties are those which vary according to the precise condition of the test and include strength, hardness, friction, wear, fracture toughness, thermal shock, oxidation, corrosion, fatigue and creep, i.e. the principal thermo-mechanical properties of interest for engine application. Therefore, one should be very careful in using the available extrinsic property data and should refer to the type of the test for which the data is produced. The properties of possible candidate ceramics and some metals used predominantly in the automotive industry are presented in Tables 2.3 and 2.4.

From an insulation point of view, the best ceramic is the one with intrinsic properties which allow surface temperature to follow the gas temperature as closely as possible in the cylinder and thus to reduce the heat loss during the combustion period. This requires a ceramic with low values of conductivity, density and specific heat capacity, i.e. aluminium titanate (AT), cordierite (MAS), zirconia. In the engine, such a ceramic component experiences very large cyclic thermal stresses within a thin layer near the material surface because of the high surface temperature

fluctuation which makes the thermal shock resistance property very important. Assesment of the thermal shock and thermal fatigue resistance of ceramics is a complex problem. The values given in Table 2.3b are based on simple quench tests and are valid only a comparative basis. Fatigue behaviour is best for materials of low expansion coefficient and high thermal conductivity where the temperature gradients and thermal strains are least. AT is a good example with almost zero expansion coefficient and having the best thermal shock resistance of about 1000 K.

Ceramics are much harder than most metal alloys. They are very wear resistant under lubricated conditions but vary widely in performance under non-lubricated conditions, much depending on the physical, mechanical and chemical properties of the wearing surfaces.

Ceramics are oxidation and corrosion resistant materials. However, the non-oxide ceramics such as silicon nitrides, silicon carbides and sialon form a thin oxide layer at temperatures above 1250 K and suffer changes in all properties that rely on surface characteristics.

The strength of ceramic materials compared to metal alloys is poorer and is controlled by a large number of parameters. Data are normally obtained from laboratory tests on small samples, usually in bending where the volume of material placed under stress is very small. The results always show a scatter and there is a finite probability of failure at stress levels much lower than the mean failure stress. The surface finish and the duration and environment of loading can influence the result. Strenght tends to fall as the temperature is raised (Fig.2.33). With non-oxide ceramics, strength will also be altered by the period and temperature of exposure to oxygen, this is normally significant above 1250 K. The effective strength of ceramics also tends to decline with time under load, due

to the phenomenan of subcritical crack growth which is termed static fatigue.

Advanced ceramics are used not only to insulate the combustion chamber but also applied to other engine components, such as valves, rocker arms, inlet and exhaust ports and manifolds, tappets and turbochargers. Different ceramics are chosen for the specific applications which are shown in Table 2.5.

CHAPTER 3
METHOD OF ENGINE PERFORMANCE PREDICTION

3.1 INTRODUCTION

This chapter gives an outline description of an engine simulation program 'SPICE' developed at Bath University [109] in which have been incorporated the various submodels for radiant heat transfer, unsteady wall effects, including refined thermal resistance network, etc.,described in the subsequent chapters.

Prediction methods for the performance of internal combustion engines have developed at an accelerating rate over the last 30 years, due to the application of the digital computer to the problem [98-101]. Although diesel engines obey the principles of energy, mass and momentum conservation, due to the complex nature of diesel engine processes, accurate performance prediction is very difficult. To develop the mathematical models of air flow, combustion and heat transfer in a combustion chamber from the basic principles is a formidable task. Simple empirical correlations derived experimentally for related groups of engines are generally used for modelling their complicated processes. However, for a specific engine better performance prediction can be obtained by tuning these models using the available correlation constants, by matching simulated and experimental results.

The analysis of performance using such cycle simulation programs, enables the research engineer to predict the power output of engines at the design stage. By varying certain parameters of the engine, such as bore, stroke, valve timing, etc., it is possible to reach an optimum design and reduce engine testing time. However, the present cycle simulation programs are not

powerful enough to predict the effect as engine performance of detail design changes such as piston crown and manifold shapes, which limit their usefulness.

In the present work, the cycle simulation package program 'SPICE', developed at Bath University, is used in the performance analysis of both a standard and an insulated Petter PH1W single cylinder Diesel engine. Due to engine insulation several models have to be added to, or modified within, the program. The present chapter explains in detail the theory of the simulation package and points out the weak parts of the program for the insulated engine case. Since the Petter PH1W test engine is operated under simulated turbocharged conditions, i.e. constant manifold pressure, models for the turbocharger are not required.

3.2 PROGRAM STRUCTURE

The simulation program 'SPICE' regards an engine as a system of thermodynamic control volumes where each control volume (CV), describes a specific engine component such as a cylinder, manifold, compressor or turbine. The CV's, within the program, are appropriately linked to each other by junctions and/or shafts so that mass and/or energy transfer between them can be represented. The main processes taking place within the program can be classified as:-

1) Air flow between the CV's.
2) Combustion and heat transfer in each CV.

The air flow through the engine can be modelled in several ways as listed below, in order of increasing complexity:-

1) Quasi-steady.
2) Filling and emptying.
3) Wave action.

The simplest, i.e. quasi-steady method, considers the engine and turbocharger as a series of interconnected components, the air flow between them

being generated by the relevant pressure ratios. Apart from the cylinder itself, mass accumulation is not allowed anywhere in the system.

In the filling and emptying method, the manifolds are considered to have finite volume and are capable of accumulating gas. Thus, the system components are not linked by a common air mass flow rate, as in the quasi-steady analysis.

On the other hand, wave action techniques involve the solution of the unsteady compressible gas flow equations and allow spatially varying pressure levels to exist throughout the intake and exhaust manifolds. The solution of differential equations of such flow conditions even for a single spatial dimension is tedious and requires enormous computational time.

In the cycle simulation program 'SPICE' the air flow through the engine is calculated by using the filling and emptying technique which is the common approach adopted by many research engineers [98-101]. By this means, mass accumulation between engine components is allowed without any involvement of the physical shape of the manifolds. The CV representation of a turbocharged diesel engine is shown in Fig.3.1.

Having represented the engine by CV's, the solution of the diesel cycle is performed by dividing it into finite time steps, usually 1°CA, where thermodynamic equilibrium and ideal gas behaviour are assumed to exist. The contents of CV's is considered as homogeneous; with the quasi-steady approach, 3 first order coupled differential equations are obtained for each CV by considering mass, energy and equivalence ratio balance. These three differential equations are solved throughout the cycle at every time step, and an acceptable solution is obtained after a certain number of cycles by comparing the start and end cycle calculations. In the solution of coupled differential equations certain submodels are required to supply

necessary additional information, such as for heat transfer, friction, gas properties, etc., as explained later in the chapter.

Energy Equation

The conservation of energy equation for a CV is given by:-

$$\frac{d(mU)}{d\theta} = -P\frac{dV}{d\theta} + \frac{1}{6Ne}\sum_{i=1}^{ns}\dot{Q}_i + \frac{1}{6Ne}\sum_{i=1}^{nj}\dot{m}_i H_i \qquad (3.1)$$

where:-

$\frac{d(mU)}{d\theta}$ is the rate of energy change w.r.t. crank angle within the CV.

$P\frac{dV}{d\theta}$ is the work done by the gas on the surroundings.

$\sum_{i=1}^{ns}\dot{Q}_i$ is the total heat transfer rate from the surrounding surfaces (ns).

$\sum_{i=1}^{nj}\dot{m}_i H_i$ is the total enthalpy transfer rate into the CV from the CV juntions (nj).

The internal energy and gas constant of the gases inside the CV are functions of pressure P, temperature T , and equivalence ratio ϕ. In differential form they are expressed as:-

$$\frac{dU}{d\theta} = \frac{\partial U}{\partial T}\frac{dT}{d\theta} + \frac{\partial U}{\partial P}\frac{dP}{d\theta} + \frac{\partial U}{\partial \phi}\frac{d\phi}{d\theta} \qquad (3.2)$$

$$\frac{dR}{d\theta} = \frac{\partial R}{\partial T}\frac{dT}{d\theta} + \frac{\partial R}{\partial P}\frac{dP}{d\theta} + \frac{\partial R}{\partial \phi}\frac{d\phi}{d\theta} \qquad (3.3)$$

Using the equation of state, the rate of change of pressure can be expressed as:-

$$\frac{dP}{d\theta} = \frac{mRT}{V}\left[\frac{1}{m}\frac{dm}{d\theta} + \frac{1}{R}\frac{dR}{d\theta} + \frac{1}{T}\frac{dT}{d\theta} - \frac{1}{V}\frac{dV}{d\theta}\right] \qquad (3.4)$$

Substituting eqns.3.2, 3.3 and 3.4 into eqn.3.1 yields an expression for the rate of change of temperature w.r.t. crank angle in the CV as:-

$$\frac{dT}{d\theta} = \frac{\left\{-\frac{P}{m}\frac{dV}{d\theta} + \frac{1}{m}\left[\frac{1}{6Ne}\sum_{i=1}^{ns}\dot{Q}_i + \frac{1}{6Ne}\sum_{i=1}^{nj}\dot{m}_i H_i - U\frac{dm}{d\theta} - m\frac{dU}{d\phi}\frac{d\phi}{d\theta}\right] - D\right\}}{\left[\frac{\partial u}{\partial T} + \frac{C}{B}\frac{P}{T}\frac{\partial u}{\partial P}\right]} \qquad (3.5)$$

where:-

$$B = 1 - \frac{P}{R}\frac{\partial R}{\partial P}$$

$$C = 1 + \frac{T}{R}\frac{\partial R}{\partial P}$$

$$D = \frac{P}{B}\frac{\partial u}{\partial P}\left[\frac{1}{m}\frac{dm}{d\theta} - \frac{1}{V}\frac{dV}{d\theta} + \frac{1}{R}\frac{R}{\phi}\frac{d\phi}{d\theta}\right]$$

Mass Equation

The mass conservation equation for a CV is given by:-

$$\frac{dm}{d\theta} = \frac{1}{6Ne}\sum_{i=1}^{nj}\dot{m}_i \qquad (3.6)$$

where nj is the number of junctions for the CV.

Equivalence Ratio Equation

The mass of burned fuel in the CV is given by:-

$$m_{f,b} = \left(\frac{(F/A)_{st} \phi}{1 + (F/A)_{st} \phi} \right) m \qquad (3.7)$$

where the equivalence ratio ϕ, is defined as:-

$$\phi = \frac{m_{f,b}}{(F/A)_{st} \left(m_a - m_{f,b} \right)} \qquad (3.8)$$

where $(F/A)_{st}$ is the stoichiometric fuel air ratio, and m_a is the mass of air inside the CV.

The conservation of combustion gases in the CV is expressed similarly to eqn.3.6 as:-

$$\frac{dm_{f,b}}{d\theta} = \frac{1}{6Ne} \sum_{i=1}^{nj} \left(\frac{(F/A)_{st} \phi_i}{1 + (F/A)_{st} \phi_i} m_i \right) + \frac{dm_{f,i}}{d\theta} \qquad (3.9)$$

where $\frac{dm_{f,i}}{d\theta}$ is the fuel injection rate, and is assumed to be ignited instantaneously and thus equal to the apparent fuel burning rate.

The differential equation for the equivalence ratio is obtained by differentiating eqn.3.8 and substituting eqns.3.7 and 3.9, giving:-

$$\frac{d\phi}{d\theta} = \left(\frac{1 + (F/A)_{st} \phi}{(F/A)_{st} m_t} \right) \left[\left(1 + (F/A)_{st} \phi \right) \left(\frac{A}{6Ne} + \frac{dm_{f,b}}{d\theta} \right) - (F/A)_{st} \phi \frac{dm}{d\theta} \right] \qquad (3.10)$$

where:-

$$A = \sum_{i=1}^{nj} \left(\frac{(F/A)_{st} \phi_i}{1 + (F/A)_{st} \phi_i} \right) m_i$$

Eqns.3.5, 3.6 and 3.10 form the three basic differential equations for each CV which are solved degree by degree throughout the diesel cycle.

3.3 GAS PROPERTIES

The gas internal energy and constants as functions of temperature, pressure and equivalence ratio are presented by Krieger and Borman [102]. The internal energy is formulated as a single equation on the lean burning side, i.e. for equivalence ratios less than 1, whereas on the rich burning side it is expressed by several equations which are applicable to specific ranges of equivalence ratios, the value at the desired equivalence ratio being obtained by linear interpolation. The internal energy U, and gas constant R are defined as:-

$$U = U_1 + U_2 \qquad (3.11a)$$

$$R = R_1 + R_2 \qquad (3.11b)$$

where:-

U_1 and R_1 are the internal energy and gas constant, respectively, without dissociation.

U_2 and R_2 represents the effects of dissociation on the internal energy and gas constant, respectively.

The equations of U_1, U_2, R_1 and R_2 for the lean burn side are given as follows:-

$$U_1 = a(T) - b(T)\,\phi \qquad (3.12)$$

where a(T) and b(T) are fourth and fifth degree polynomials of temperature and are given in [102].

$$R_1 = 0.28703 + 0.020046\phi \quad \left(\frac{kJ}{kgK}\right)air \qquad (3.13)$$

The effect of dissociation is given by:-

$$U_2 = D_1 \exp\left(D_2 + D_3 + D_4\right) \qquad (3.14)$$

where:-

$$D_2 = f(\phi)$$
$$D_3 = f(\phi,T)$$
$$D_4 = f(\phi,T,P)$$

$$R_2 = E_1 \exp(E_2) \tag{3.15}$$

where $E_2 = f(T,P,\phi)$ and functions D_2, D_3, D_4, E_2, and constants D_1 and E_1 are given in [102].

The equations of internal energy and gas constant for the rich side are given as follows:-

$$U_1 = 2.326\left(a_1 + a_2 T + a_3 T^2 + a_4 T^3 + a_5 T^4 + a_6 T^5 + a_7 T^{1.5} + \frac{a_8}{1 + T/3000}\right) \tag{3.16}$$

$$U_2 = 2.326\left[\frac{A(T)}{P^{D(T)}} + \frac{C(T)}{P^{D(T)}}\right] \tag{3.17}$$

$$R = \frac{4.428}{(M + M_1 + M_2)} \tag{3.18}$$

where:-

M is the molecular weight and is a function of equivalence ratio.

M_1 and M_2 are the mean molecular weight correction functions due to temperature and pressure, respectively.

The constants a_1, a_2, a_3, a_4, a_5, a_6, a_7 and a_8, and functions A(T), C(T), D(T), M, M_1 and M_2 are specified at certain equivalence ratios in [102].

3.4 GAS FLOW

The gas flow between CV's is modelled as a quasi-steady one dimensional flow through a defined

orifice area which represents either a valve or port. The flow through the orifice is assumed to be isentropic, the minimum static pressure at the orifice being equal to the downstream CV pressure, i.e. zero pressure recovery. The effects of non-isentropic flow are allowed for by using an effective area instead of the actual flow area, defined as the product of a discharge coefficient C_d, obtained experimentally, and the geometric orifice area. The steady flow energy equation between the upstream volume (1) and orifice (2), as shown in Fig.3.2, is given by:-

$$\frac{dQ}{dt} - \frac{dW}{dt} + \frac{dH}{dt} + \frac{1}{2}\frac{dC^2}{dt} = 0 \qquad (3.19)$$

Since no work is done on the surroundings and for an isentropic flow, eqn.3.19 becomes:-

$$\frac{dH}{dt} = -\frac{1}{2}\frac{dC^2}{dt} \qquad (3.20)$$

where H is the enthalpy and C is the gas velocity.
For an isentropic flow the relation becomes:-

$$T\frac{ds}{dt} = \frac{dH}{dt} - \frac{1}{\rho}\frac{dP}{dt} = 0 \qquad (3.21)$$

Eqns.3.20 and 3.21 yield:-

$$\frac{1}{\rho}\frac{dP}{dt} = -\frac{1}{2}\frac{dC^2}{dt} \qquad (3.22)$$

Using the relation, $\frac{P}{\rho^{\gamma}} = K = \text{Constant}$, the density is defined as:-

$$\rho = \left(\frac{K}{P}\right)^{(1/\gamma)} \qquad (3.23)$$

Substituting eqn.3.23 into eqn.3.22 gives:-

$$-\frac{1}{2}\frac{dC^2}{dt} = \left(\frac{K}{P}\right)^{(1/\gamma)}\frac{dP}{dt} \qquad (3.24)$$

Integrating eqn.3.24, assuming that the upstream velocity is negligible compared to the orifice velocity, and replacing the constant K from eqn.3.23, gives the following relation for the gas velocity through the orifice:-

$$C_2^2 = \left(\frac{2\gamma}{\gamma-1}\right)\left(\frac{P_1}{\rho_1}\right)\left[1-\left(\frac{P_2}{P_1}\right)^{(\gamma-1)/\gamma}\right] \qquad (3.25)$$

The mass flow rate ρAC, is expressed as:-

$$\frac{dm}{dt} = A_2\sqrt{\left(\frac{2\gamma}{\gamma-1}\right)\left(\frac{P_1}{\rho_1}\rho_2^2\right)\left[1-\left(\frac{P_2}{P_1}\right)^{(\gamma-1)/\gamma}\right]} \qquad (3.26)$$

Using the isentropic relation $\left(\frac{\rho_1}{\rho_2}\right)=\left(\frac{P_1}{P_2}\right)^{(1/\gamma)}$, and the equation of state, $\frac{P}{\rho}=RT$, eqn.3.26 becomes:-

$$\frac{dm}{dt} = A_2\frac{P_1}{\sqrt{T_1}}\frac{2\gamma}{(\gamma-1)R}\sqrt{\left(\frac{P_2}{P_1}\right)^{(2/\gamma)}-\left(\frac{P_2}{P_1}\right)^{(\gamma+1)/\gamma}} \qquad (3.27)$$

Assuming that the velocity head is lost on entering the downstream volume (3), and using a discharge coefficient C_d to allow for non-isentropic flow, eqn.3.27 becomes:-

$$\frac{dm}{dt} = C_d A_2\frac{P_1}{\sqrt{T_1}}\frac{2\gamma}{(\gamma-1)R}\sqrt{\left(\frac{P_2}{P_1}\right)^{(2/\gamma)}-\left(\frac{P_2}{P_1}\right)^{(\gamma+1)/\gamma}} \qquad (3.28)$$

The pressure ratio for sonic flow conditions is given

by:-

$$\frac{P_2}{P_1} = \left(\frac{\gamma+1}{2}\right)^{\gamma/(\gamma-1)} \qquad (3.29)$$

Substituting eqn.3.29 into 3.28 gives the mass flow rate for sonic conditions as:-

$$\left(\frac{dm}{dt}\right)_{sonic} = C_d A_2 \frac{P_1}{\sqrt{T_1}} \sqrt{\left(\frac{\gamma}{R}\right)\left(\frac{2}{\gamma+1}\right)^{(\gamma+1)/(\gamma-1)}} \qquad (3.30)$$

3.5 COMBUSTION

Combustion is the source of all external thermal energy inputs into an engine, and therefore its model plays an important role in accurate engine performance prediction. The combustion process in a diesel engine starts by the injection of the fuel into the hot compressed air, followed by fuel mixing, evaporation and ignition. The development of time and space dependent detailed combustion models for diesel engines from basic principles is based on computational fluid dynamics (CFD), but such models are still unsuitable for inclusion in complete cycle simulations. Instead, current simulation programs use simple heat release models which are derived from experimental cylinder pressure data. Heat release curves are obtained, by analysing experimental cylinder pressure to obtain 'shape factors' which are supplied as data to cycle analysis programs. Gas homogenity and instantaneous thermal equilibrium are assumed to exist throughout the cycle. Combustion is thus represented in a simple manner which allows rapid computation. However, this approach unlike CFD, is not sensitive to detail design changes, such as piston geometry, flow conditions, etc.

The heat release curve for a diesel engine is characterized by an early premixed 'spike' followed by diffusion burning and eventually late burning or 'tail

burning', as shown in Fig.3.3. There are two delay periods which retard the onset of ignition, namely injection and ignition delay. The injection delay period is the time interval between the start of pumping and the start of fuel injection into the cylinder. The ignition delay period is the time interval between the start of fuel injection into the cylinder and the start of positive heat release from fuel to surroundings. During the ignition delay period the injected fuel is prepared for combustion; it is thought to consist of a physical and a chemical delay periods. The ignition delay period which depends on the mixing temperature and pressure, air turbulence, fuel properties, influences both heat release and engine performance. Longer ignition delay periods result in a higher premixed spike, and thus higher maximum cylinder pressure and engine noise.

In the simulation package 'SPICE', the formula proposed by Wolfer [103] is used to evaluate the ignition delay period, and is given by:-

$$ID = a_1 \exp\left(\frac{a_2}{\bar{T}}\right)\bar{P}^{a_3} \quad \text{(msec)} \qquad (3.31)$$

where:-

$\bar{T}$ and $\bar{P}$ are the mean temperature and pressure, respectively, during ignition delay period.

a_1, a_2 and a_3 are the related constants given in [103].

The first heat release model, proposed by Wiebe in 1956 [104], represents the heat release curve by a single mathematical expression named as Wiebe function. Later, researchers [105,120] found out that the total heat release curve is expressed far better by a weighted sum of the two curves, one representing the premix burning and the other the diffusion burning. The premixed and diffusion burning components are combined by using a mode of burning proportionality factor β,

defined as:-

$$\beta = \frac{m_{f,pr}}{m_{f,d}} \tag{3.32}$$

where subscripts f,pr and f,d denotes fuel burned in the premixed and diffusion modes, respectively.
The total apparent fuel burning rate ($AFBR_t$) is given by:-

$$AFBR_t = \beta AFBR_{pr} + (1-\beta) AFBR_d \tag{3.33}$$

where the premix and diffusion components are defined by the following Wiebe type expressions:-

$$AFBR_{pr} = C_{pr,1} C_{pr,2} \tau^{C_{pr,2}-1} \exp\left(-C_{pr,1} \tau^{C_{pr,2}}\right) \tag{3.34a}$$

$$AFBR_d = C_{d,1} C_{d,2} \tau^{C_{d,2}-1} \exp\left(-C_{d,1} \tau^{C_{d,2}}\right) \tag{3.34b}$$

Although, some researchers accepted the above form, others, such as Marzouk and Watson [105], suggested that the following curve better represents the premixed combustion mode:-

$$AFBR_{pr} = C_{pr,1} C_{pr,2} \tau^{C_{pr,1}-1} \left(1-\tau^{C_{pr,1}}\right)^{C_{pr,2}-1} \tag{3.34c}$$

In the cycle simulation package 'SPICE' both models are included, thus provides the user with the option.

The coefficients $C_{pr,1}$, $C_{pr,2}$, $C_{d,1}$ and $C_{d,2}$ are expressed in empirical correlations as functions of the basic engine parameters of ignition delay ID, trapped equivalence ratio ϕ_{tr}, and engine speed Ne. In general the following correlations have been found to apply:-

$$C_{pr,1} = A + B(ID.Ne)^{C} \tag{3.35}$$

$$C_{pr,2} = D \tag{3.36a}$$

$$C_{pr,2} = E + F\left(C_{pr,1}\right)^{G} \tag{3.36b}$$

where A, B, D, E, F and G are correlation constants. Eqns.3.36a and 3.36b are for the Marzouk (D=5000) and Wiebe type expressions, respectively.

The formulation of the diffusion combustion coefficients seem to be less agreement than the above two coefficients. In sources [105] and [120] they are given as follows:-

$$C_{d,1} = H\phi_{tr}^{J} \tag{3.37a}$$

$$C_{d,2} = KC_{d,1}^{L} \tag{3.37b}$$

and

$$C_{d,1} = M + \frac{N\left[\frac{1-\beta}{\phi_{tr}^{P}}\right]^{Q}}{1 + R\left(1 - \frac{S}{Ne}\right)^{T}} \tag{3.38a}$$

$$C_{d,2} = U + V\left(C_{d,1}BDUR\right)^{W} \tag{3.38b}$$

where H, J, K, L, M, N, Q, R, S, T, U, V and W are correlation constants, obtained experimentally. BDUR is the burning duration and is defined as:-

$$BDUR = X + Y\phi_{tr}^{Z} \tag{3.39}$$

where X, Y and Z are correlation constants.

The mode of burning proportionality factor β, in

eqn.3.33, is correlated as:-

$$\beta = 1 - B^{*} \phi_{tr}^{D^{*}} ID^{C^{*}} \qquad (3.40)$$

where B^{*}, C^{*} and D^{*} are correlation constants.

3.6 HEAT TRANSFER

Heat transfer in a diesel engine plays as important a role as heat release in the correct prediction of engine performance. Although heat transfer models may predict the cycle mean heat flux, this does not mean that the effect of heat transfer on engine performance is truly represented. The distribution of heat loss from gas to wall throughout the cycle also has a major influence on engine performance. Heat transfer during the intake and compression strokes influences the engine volumetric efficency and start of ignition respectively, whereas heat transfer during the combustion, expansion and exhaust phases of the cycle affects the power output and exhaust temperature, respectively. In the insulated engine case, heat transfer is of even greater importance in engine simulation.

Heat transfer in a diesel engine can be divided into two parts, viz. transient and steady. The transient heat transfer region includes the gas to wall boundary layer and a thin layer of wall adjacent to the combustion chamber; steady state heat transfer occurs beyond the transient wall region and includes the coolant heat transfer.

The gas to wall heat transfer consists of convective and radiative components. The detailed modelling of both convective and radiative heat transfer from basic principles as a function of time and space is a difficult task. Current simulation programs usually ignore the radiation component of heat transfer and use empirical correlations for the convective component.

These correlations represent a space mean convective htc which is used together with the space mean gas temperature to calculate the instantaneous gas to wall heat transfer. This is very crude approximation to the actual heat transfer process taking place in the combustion chamber, and needs to be refined for greater accuracy. The htc and radiative models proposed by various researchers are given in Chapter 2.

For engine simulation purposes, the steady state heat transfer through the engine walls is usually represented by simple resistance networks, while the transient thermal analysis of the wall region adjacent to the combustion chamber is ignored. A steady state heat transfer balance is used at the end of each cycle to update the wall gas side surface temperatures which are used to calculate the instantaneous gas to wall heat transfer during the following cycle.

The simulation package 'SPICE' calculates the gas to wall heat transfer by alternative htc models proposed by Eichelberg [12], Annand [14], Woschni [16] and Hohenberg [106], depending on the program user's choice. The radiative heat transfer component is included implicitly in the proposed htc models but an explicit formulation is ignored. However, the author has developed a radiation model based on soot and combustion gases concentration, and flame temperature, which is then incorporated in 'SPICE'. A detailed explanation of the radiation model is given in Chapter 4.

In 'SPICE',the steady state heat transfer through the engine walls is calculated by using a simple resistance model which is presented in Fig.5.1. The author developed a more comprehensive thermal resistance network adapted specifically to insulated engine simulation studies, which is explained throughly in Chapter 5.

A transient wall temperature analysis is also considered both in the thermal resistance network and

the instantaneous gas to wall heat transfer calculations. This is particularly relevant to insulated engine simulation. The models related to transient thermal analysis are explained in detail in Chapter 6.

3.7 PISTON-CRANK MECHANISM

In determining the time derivative of cylinder temperature from eqn.3.5, the rate of change of volume w.r.t. time is required. This value is obtained by using the piston-crank mechanism geometry which is shown in Fig.3.4. The instantaneous cylinder volume $V_{cy}(\theta)$, is given as:-

$$V_{cy}(\theta) = \frac{\pi D_{cy}^2}{4}\left\{1 + r_{ca} - r_{ca}\,Cos\theta - \left[CRL^2 - r_{ca}^2\,Sin^2\theta\right]^{0.5}\right\} + V_{cl} \tag{3.41}$$

and the volume derivative is given as:-

$$\frac{dV_{cy}(\theta)}{d\theta} = \frac{\pi^2 D_{cy}^2}{4}\left\{r_{ca}\,Sin\theta + r_{ca}\,Sin\theta Cos\theta\left[CRL^2 - r_{ca}^2\,Sin^2\theta\right]^{-0.5}\right\} \tag{3.42}$$

where:-

D_{cy} is the cylinder diameter.

r_{ca} is the crank arm radiaus.

CRL is the connecting rod length.

V_{cl} is the clearence volume.

3.8 SOLUTION METHOD

The three differential eqns.3.5, 3.6 and 3.10 describing the change in temperature, mass and equivalence ratio w.r.t. CA are solved simultaneously using the modified Euler predictor-corrector method which has the virtues of computational simplicity and speed. The numerical solution starts at inlet valve

closure IVC, where assumed values for temperature, mass and equivalence ratio are used initially. At the end of each cycle these initial values are replaced by the final cycle values and the calculations are repeated. An acceptable numerical solution is obtained when final cycle values are equivalent to those of the previous cycle; this usually requires about 5 to 6 successive cycle evaluations.

CHAPTER 4
RADIATION HEAT TRANSFER

4.1 INTRODUCTION

Radiation heat transfer contributes about 10 to 40% of the total heat loss in diesel engines depending on the engine type and operating conditions. However, for simplicity it was always grouped together with the convective component of heat transfer and an explicit formulation for the radiative heat transfer was then ignored. As already mentioned in Sec.2.2.2, the role of radiative heat transfer in adiabatic diesel engines is much more pronounced than in conventional engines and its percentage may under certain conditions be expected even higher than the convective component. This makes it necessary to model radiative heat transfer separately in order to carry out realistic heat transfer analysis in a highly insulated diesel engine. The proposed models and the experimental work in connection with radiative heat transfer in diesel engines has been explained in Sec.2.2.2.

The present study makes an attempt to model the radiative heat transfer in diesel engines and incorporates it in the cycle simulation package 'SPICE'. The model includes the radiative heat transfer from soot particles which are formed during the diffusion flame burning mode, and from the combustion gases CO_2 and H_2O. Due to low concentration levels, the radiative heat transfer from other chemical species formed during combustion, such as CO and NO_x, are not considered. A simple mean-beam length model is used for cycle simulation purposes. A more extensive zone model was also partially developed for studying the effects of soot concentration and gas temperature variations in a cylindrical enclosure, but is not yet completed.

4.2 FORMULATION OF THE RADIATIVE HEAT TRANSFER

The diesel flame inside the combustion chamber emits, absorbs and scatters radiation, and therefore it is very convenient to express radiative heat transfer to the walls in terms of radiation intensity which is defined as the radiation energy falling onto unit projected area per unit time. Thus for projected unit area $dA\cos\theta$, and for solid angle $d\Omega$, the one-way heat transfer dQ on the area dA, is given by:-

$$dQ = I(\theta,\psi)\, dA\, \cos\theta\, d\Omega \qquad (4.1)$$

where the radiation intensity $I(\theta,\psi)$, is a function of the ray direction and is fixed by the circumferential angle ψ, and the azimuth angle θ (Fig.4.1). The radiation intensity is evaluated by integrating the spectral intensity over the whole wavelength spectrum.

$$I(\theta,\psi) = \int_0^\infty I_\lambda(\theta,\psi,\lambda)\, d\lambda \qquad (4.2)$$

In order to calculate the radiative heat transfer at a particular location on the combustion chamber surface, the spectral intensity I_λ, should be determined by solving the equation of radiative heat transfer in space. While the radiation energy is travelling through a participating medium in a certain direction, it loses some of its energy by absorption and gains some energy in that direction by emission of the medium. Energy loss and gain in the same direction also occurs due to scattering. The equation of radiative transfer at a particular point in space and in a certain direction is given by:-

$$\underbrace{\frac{dI_\lambda(s)}{ds}}_{\text{Rate of change of intensity in direction s.}} = \underbrace{-a_\lambda I_\lambda(s)}_{\text{Energy loss by absorption}} + \underbrace{a_\lambda I_{\lambda b}(s)}_{\text{Energy gain by emission in direction s}} - \underbrace{\sigma_\lambda I_\lambda(s)}_{\text{Energy loss by scattering}}$$

$$+ \underbrace{\frac{\sigma_\lambda}{4\pi}\int_0^{4\pi} I_\lambda(\Omega, s)\phi^*_{sc}(\lambda, \Omega, \Omega_{sc})\, d\Omega_{sc}}_{\text{Energy gain by scattering in direction s}} \qquad (4.3\,a)$$

where:-

$I_{\lambda b}$ is the black body spectral intensity.

s is the distance in a certain direction.

a_λ is the spectral absorption coefficient.

σ_λ is the spectral scattering coefficient.

Ω and Ω_{sc} are the solid angles for radiation and scattering.

ϕ^*_{sc} is the phase function for scattering.

The scattering of radiation in the combustion chamber is caused by the soot particles and fuel droplets. However, the scattering coefficient is much smaller than the absorption coefficient of the soot particles and can be neglected (See Sec.4.4.1). The effect of scattering by the fuel droplets in a diesel engine environment as reported by Menguc et al [29] is not significant. Thus, radiative heat transfer in an absorbing and emitting medium may be expressed, by reducing eqn.4.3a, as:-

$$\frac{dI_\lambda(s)}{ds} = -a_\lambda I_\lambda(s) + a_\lambda I_{\lambda b}(s) \qquad (4.3b)$$

The general solution of eqn.4.3b for a diesel combustion chamber is a formidable task, because of the multidimensional spatial dependence compounded by spectral dependence. However, since the above equation is a first-order linear differential equation, its solution along path s can easily be obtained by the use

of an integrating factor $\exp\left(\int_0^S a_\lambda ds\right)$ and is given by:-

$$I_\lambda(s) = I_{\lambda o}\exp\left(-\int_0^S a_\lambda ds\right) + \int_0^S a_\lambda I_{\lambda b}(T_g)\exp\left(-\int_0^S a_\lambda ds^*\right)ds \quad (4.4a)$$

where:-

ds^* is a dummy variable of integration.

S is the total path length.

$I_{\lambda o}$ is the spectral intensity at s=0, and it is referred to the energy leaving a surface (out).

T_g is the gas temperature.

One of the common approaches in radiative heat transfer is to assume that the pressure, temperature and composition of the gas over a finite space are constant, which simplifies eqn.4.4a to:-

$$I_\lambda(s) = I_{\lambda o}\exp(-a_\lambda s) + I_{\lambda b}(T_g)\left[1 - \exp(-a_\lambda s)\right] \quad (4.4b)$$

or

$$I_\lambda(s) = I_{\lambda o}\tau_\lambda(s) + I_{\lambda b}(T_g)\,\varepsilon_\lambda(s) \quad (4.4c)$$

where $\tau_\lambda(s)$ and $\varepsilon_\lambda(s)$ are the transmissivity and emissivity of the gas volume in direction s at the mean gas temperature and are expressed as:-

$$\tau_\lambda(s) = \exp(-a_\lambda s) \quad (4.5)$$

$$\varepsilon_\lambda(s) = 1 - \exp(-a_\lambda s) \quad (4.6)$$

It is also useful to define the spectral absorptivity of the gas volume in direction s which is complementary to

the emissivity,

$$\alpha_\lambda(s) = 1 - \tau_\lambda(s) \qquad (4.7a)$$

or

$$\alpha_\lambda(s) = 1 - \exp\left(-a_\lambda s\right) \qquad (4.7b)$$

Because the energies emitted or absorbed by a volume of gas depend on the size and shape of the volume in addition to its physical properties and temperature, the gas absorptivity and emissivity are extensive properties. To show this property, the -ance suffix is used by some sources [36], to make the terms absorptance and emittance. However, most of the published work on diesel engine radiation heat transfer adopts the terms gas absorptivity and emissivity and therefore to prevent any complications the general terms absorptivity and emissivity are used in this text.

The spectral absorptivity and emissivity of a gas volume are equal. However, the total absorptivity and emissivity values which are obtained by integrating the spectral functions over the whole spectrum differ unless the gas is grey, i.e. the absorption coefficient a_λ is independent of wavelength.

Using eqn.4.4c, the radiative heat transfer from an isothermal gas volume with soot particles in an enclosure can be treated by analogy to radiation exchange between surfaces in the absence of an intervening medium. This is the general approach adopted by various workers [35,36]. The gas and soot radiation effects are introduced to the system by the emissivity, transmissivity and absorptivity terms which are defined for gas volumes of uniform temperature and compostion; their values also depend on the gas volume size and shape.

The radiation exchange between two isothermal

surfaces A_j and A_k is formulated by considering the differential surface elements dA_j and dA_k (Fig.4.2). The spectral radiation energy arriving at surface dA_k from dA_j in terms of radiation intensity is given by:-

$$dQ_{\lambda i,j-k} = I_{\lambda i,j-k}\, dA_k \cos\theta_k\, d\Omega_k\, d\lambda \qquad (4.8)$$

where the subscript $\lambda i,j-k$ denotes the spectral energy arriving at surface k from j.
The differential solid angle is given by:-

$$d\Omega_k = \frac{dA_j \cos\theta_j}{s^2} \qquad (4.9)$$

Substituting eqns.4.4c and 4.9 into eqn.4.8 and integrating over surfaces A_j and A_k gives the total spectral radiation energy falling onto surface A_k from A_j,

$$Q_{\lambda i,j-k} = \int_{A_k}\int_{A_j}\left[I_{\lambda o}\tau_\lambda(s) + I_{\lambda b}(T_g)\,\varepsilon_\lambda(s)\right]\left(\frac{dA_k\, dA_j \cos\theta_k \cos\theta_j}{S^2}\right)d\lambda \qquad (4.10)$$

The walls are assumed to be diffuse, i.e. reflection and emission are independent of direction, and the spectral intensity leaving surface A_j is defined as:-

$$I_{\lambda o,j} = \frac{q_{\lambda o,j}}{\pi\, d\lambda} \qquad (4.11)$$

where $q_{\lambda o,j}$ is the spectral energy flux leaving surface j.
The gas emissive radiation intensity in direction s is given by:-

$$I_{\lambda b,g} = \frac{E_{\lambda b,g}(T_g)}{\pi} \qquad (4.12)$$

where $E_{\lambda b,g}$ is the black body gas emissive power at T_g. Substituting eqns.4.11 and 4.12 into eqn.4.10 gives:-

$$Q_{\lambda i,j-k} = \int_{A_j}\int_{A_k}\left[q_{\lambda o,j}\tau_\lambda(s) + E_{\lambda b,g}(T_g)\,d\lambda\,\alpha_\lambda(s)\right]\frac{Cos\theta_j Cos\theta_k}{\pi S^2}dA_j dA_k \qquad (4.13)$$

The wall and gas temperatures are constant and therefore $q_{\lambda o,j}$ and $E_{\lambda b,g}(T_g)d\lambda$ can be taken out of the integral. Using the definitions of the geometric-mean transmissivity $\bar{\tau}_{\lambda,j-k}$ and geometric-mean absorptivity $\bar{\alpha}_{\lambda,j-k}$, eqn.4.13 can further be simplified to:-

$$Q_{\lambda i,j-k} = A_j F_{j-k}\left[\bar{\tau}_{\lambda,j-k}\,q_{\lambda o,j} + \bar{\alpha}_{\lambda,j-k}E_{\lambda b,g}(T_g)\,d\lambda\right] \qquad (4.14)$$

where $\bar{\tau}_{\lambda,j-k}$ and $\bar{\alpha}_{\lambda,j-k}$ are given by:-

$$\bar{\tau}_{\lambda,j-k} = \frac{1}{A_j F_{j-k}}\int_{A_k}\int_{A_j}\tau_\lambda(s)\frac{Cos\theta_j Cos\theta_k}{\pi S^2}dA_j dA_k \qquad (4.15a)$$

$$\bar{\alpha}_{\lambda,j-k} = \frac{1}{A_j F_{j-k}}\int_{A_k}\int_{A_j}\alpha_\lambda(s)\frac{Cos\theta_j Cos\theta_k}{\pi S^2}dA_j dA_k \qquad (4.15b)$$

F_{j-k} is the geometric configuration factor between surface j and k and is defined as:-

$$F_{j-k} = \frac{1}{A_j}\int_{A_k}\int_{A_j}\frac{Cos\theta_j Cos\theta_k}{\pi S^2}dA_j dA_k \qquad (4.16)$$

The geometric-mean transmissivity and absorptivity are related to each other as in equation 4.7a by:-

$$\bar{\alpha}_{\lambda,j-k} = 1 - \bar{\tau}_{\lambda,j-k} \tag{4.17}$$

In eqn.4.14, the first term on the RHS is the spectral energy reaching surface k from j, and the second term is the spectral energy emitted from the isothermal gas volume between the surfaces and absorbed by surface k. For cool walls the first term in eqn.4.14 can be ignored, however here it is kept in the model because of high wall temperatures caused by insulation.

The total spectral energy falling onto surface k is the summation of the spectral energies arriving from all directions. Assuming that the gas enclosure has N surfaces, eqn.4.14 becomes, for the total spectral energy flux on surface k:-

$$Q_{\lambda i,k} = q_{\lambda i,k} A_k = \sum_{j=1}^{N} \left[A_j F_{j-k} \bar{\tau}_{\lambda,j-k} q_{\lambda o,j} + A_j F_{j-k} \bar{\alpha}_{\lambda,j-k} E_{\lambda b,g}(T_g) d\lambda \right] \tag{4.18}$$

The net energy absorbed by surface k which is conducted through the material is the difference between the outgoing and incoming energy fluxes of surface k and is given by:-

$$q_{\lambda,k} = q_{\lambda o,k} - q_{\lambda i,k} \tag{4.19}$$

The outgoing spectral flux is composed of emitted and reflected energy, i.e.

$$q_{\lambda o,k} = \varepsilon_{\lambda,k}(\lambda, T_k) E_{\lambda b,k} d\lambda + \rho_{\lambda,k}(\lambda, T_k) q_{\lambda i,k} \tag{4.20}$$

where $\varepsilon_{\lambda,k}$ and $\rho_{\lambda,k}$ are the spectral emissivity and reflectivity of surface k and are related by:-

$$\rho_{\lambda,k} = 1 - \varepsilon_{\lambda,k} \tag{4.21}$$

The relation between the geometric configuration factors is given by:-

$$A_j F_{j-k} = A_k F_{k-j} \tag{4.22}$$

From the symmetry of integrals in eqns.4.15a and 4.15b and the reciprocity relation given by eqn.4.22, it can be shown that:-

$$\bar{\tau}_{\lambda,j-k} = \bar{\tau}_{\lambda,k-j} \tag{4.23a}$$

$$\bar{\alpha}_{\lambda,j-k} = \bar{\alpha}_{\lambda,k-j} \tag{4.23b}$$

Eqns.4.18, 4.19 and 4.20 form a set of equations with three unknowns fluxes $q_{\lambda o,k}$, $q_{\lambda i,k}$ and $q_{\lambda,k}$. These three equations are solved for net energy flux $q_{\lambda,k}$ and the resulting equation is further simplified by the use of eqns.4.21 to 4.23. The final form of the net radiation flux equation to any surface j, is given by:-

$$\sum_{j=1}^{N}\left(\frac{\delta_{kj}}{\varepsilon_{\lambda,j}} - F_{k-j}\frac{1-\varepsilon_{\lambda,j}}{\varepsilon_{\lambda,j}}\bar{\tau}_{\lambda,k-j}\right)q_{\lambda,j} = \sum_{j=1}^{N}\left[\left(\delta_{kj} - F_{k-j}\bar{\tau}_{\lambda,k-j}\right)E_{\lambda b,j}\,d\lambda - F_{k-j}\bar{\alpha}_{\lambda,k-j}E_{\lambda b,g}\,d\lambda\right] \tag{4.24}$$

where δ_{kj} is the Kronecker delta and is expressed by:-

$$\delta_{kj} = 1 \qquad \text{when } k = j$$

$$\delta_{kj} = 0 \qquad \text{when } k \neq j$$

If eqn.4.24 is written for each surface of the enclosure, it forms a set of N equations with a set of

2N unknown quantities $q_{\lambda,j}$ and $E_{\lambda b,j}$. However, if the wall surface temperature, which can be obtained from the heat balance of the engine thermal resistance network, are specified the set of unknowns can be reduced to N and the solution of $q_{\lambda,j}$ is possible. This solution is for a particular wavelength and the total energy flux on each surface can be evaluated by repeating the solution over the whole wavelength spectrum and then summing up the results.

In order to avoid the repetition of the solution process of eqn.4.24 over the whole spectrum which will increase the computing time, eqn.4.24 is expressed over the whole spectrum as follows:-

$$\sum_{j=1}^{N}\left(G_j\delta_{kj} - F_{k-j}B_{j-k}\right)q_j = \sum_{j=1}^{N}\left(\delta_{kj}E_{b,j} - F_{k-j}C_{k-j} - F_{k-j}D_{k-j}\right) \tag{4.25}$$

where:-

$$G_j = \frac{\int_0^{\infty}\frac{q_{\lambda,j}}{\varepsilon_{\lambda,j}}d\lambda}{q_j} \tag{4.26a}$$

$$B_{j-k} = \frac{1}{q_j}\int_0^{\infty}\frac{1-\varepsilon_{\lambda,j}}{\varepsilon_{\lambda,j}}\bar{\tau}_{\lambda,k-j}q_{\lambda,j}\,d\lambda \tag{4.27a}$$

$$C_{k-j} = \int_0^{\infty}\bar{\tau}_{\lambda,k-j}E_{\lambda b,j}\,d\lambda \tag{4.28a}$$

$$D_{k-j} = \int_0^{\infty}\bar{\alpha}_{\lambda,k-j}E_{\lambda b,g}\,d\lambda \tag{4.29a}$$

For grey walls where the wall emissivity is independent of wavelength, eqn.4.26a reduces to:-

$$G_j = \frac{1}{\varepsilon_j} \tag{4.26b}$$

The wall reflection term which is given by eqn.4.27a, includes the radiation originally emitted from the flame and walls which have different wavelength regions. However, since the flame radiation is the dominant component, a mean value for the spectral geometric-mean transmissivity term $\tau_{\lambda,k-j}$ in eqn.4.27a and defined by eqn.4.15 is used; this is evaluated for soot particles at the flame temperature. In this way, it is possible to eliminate the spectral radiation flux term in eqn.4.27a and simplify it to:-

$$B_{j-k} = \frac{1-\varepsilon_j}{\varepsilon_j}\bar{\tau}_{k-j} \tag{4.27b}$$

where $\bar{\tau}_{k-j}$ is the mean value for the geometric-mean transmissivity of the soot particles and is given by:-

$$\bar{\tau}_{k-j} = \frac{1}{(\lambda_2 - \lambda_1)}\int_{\lambda_1}^{\lambda_2}\bar{\tau}_{\lambda,k-j}\,d\lambda \tag{4.30}$$

where $\bar{\tau}_{\lambda,k-j}$ is given by eqn.4.15a, as already stated.

The terms C_{k-j} and D_{k-j} can also be expressed in terms of gas absorptivity and emissivity observed at surface k, which are given by:-

$$C_{k-j} = \left(1-\alpha_{k-j}\right)\sigma T_j^4 \tag{4.28b}$$

$$D_{k-j} = \varepsilon_{k-j}\sigma T_g^4 \tag{4.29b}$$

where α_{k-j} and ε_{k-j} are the gas absorptivity and

emissivity between surfaces j and k, and are given by:-

$$\alpha_{k-j}\left(T_j, T_g\right) = \frac{\int_0^\infty \bar{\alpha}_{\lambda,k-j} E_{\lambda b,j}\, d\lambda}{\sigma T_j^4} \qquad (4.31\,a)$$

$$\varepsilon_{k-j}\left(T_g\right) = \frac{\int_0^\infty \bar{\alpha}_{\lambda,k-j} E_{\lambda b,g}\, d\lambda}{\sigma T_g^4} \qquad (4.31\,b)$$

Eqn.4.25 for the net radiation heat flux can be rearranged and expressed in terms of gas absorptivity and emissivity as follows:-

$$\sum_{j=1}^{N}\left(\frac{\delta_{kj}}{\varepsilon_j} - F_{k-j}\frac{\left(1-\varepsilon_j\right)}{\varepsilon_j}\bar{\tau}_{k-j}\right)q_j = \sum_{j=1}^{N}\left(\delta_{kj}E_{b,j} - F_{k-j}\left(1-\alpha_{k-j}\right)\sigma T_j^4 - F_{k-j}\varepsilon_{k-j}\sigma T_g^4\right) \qquad (4.32)$$

If eqn.4.32 is written for all surfaces, it forms a matrix system as follows:-

$$\begin{array}{c} \\ k\downarrow \end{array}\overset{\rightarrow j}{\begin{bmatrix} a_{11} & a_{12} & \cdots & & \\ a_{21} & a_{22} & \cdots & & \\ \vdots & \vdots & \ddots & & \\ \cdots & a_{kj} & \cdots & a_{kk} & \cdots \\ & & & & \ddots \\ & & & & a_{nn} \end{bmatrix}}\begin{bmatrix} q_1 \\ q_2 \\ \vdots \\ q_k \\ \vdots \\ q_n \end{bmatrix} = \begin{bmatrix} b_1 \\ b_2 \\ \vdots \\ b_k \\ \vdots \\ b_n \end{bmatrix} \qquad (4.33)$$

where:-

$$a_{kj} = -F_{k-j}\frac{\left(1-\varepsilon_j\right)}{\varepsilon_j}\bar{\tau}_{k-j} \qquad (4.34\,a)$$

$$a_{kk} = \frac{1}{\varepsilon_k} - F_{k-k}\frac{(1-\varepsilon_k)}{\varepsilon_k}\bar{\tau}_{k-k} \qquad (4.34b)$$

$$b_k = E_{b,k}(T_k) - \sigma\sum_{j=1}^{N} F_{k-j}\left\{\left[1-\alpha_{k-j}(T_j,T_g)\right]T_j^4 + \varepsilon_{k-j}(T_g)T_g^4\right\} \qquad (4.34c)$$

The absorptivity and emissivity values are specified as functions of the related temperatures.

The above matrix system requires the solution of N simultaneous equations unless the reflection terms given by eqn.4.34a are ignored. The matrix system for an enclosure considered as a single surface reduces to:-

$$q_w = \left[\alpha_g(T_w,T_g)\varepsilon_w\sigma T_w^4 - \varepsilon_g(T_g)\varepsilon_w\sigma T_g^4\right]\frac{1}{1-(1-\varepsilon_w)\tau} \qquad (4.35)$$

where the subscripts w and g refer to wall and gas.

Eqn.4.35 was also used by Balakrishnan [32] to calculate the radiative heat transfer from the combustion gases to the walls in a cylindrical enclosure where the value for τ was taken 0.33 which represents the strongest emission and absorption band of 6.3μ wavelength for water vapour. With a wall emissivity value of 0.75, the reflection term increased the radiative heat flux falling onto the walls by 9%. However, in a diesel engine environment where the combustion gases together with soot particles form the medium, the transmissivity term τ, is expected to be close enough to zero and to reduce significantly the effect of incoming reflected rays from the other surfaces. Soot particles play an important role in this process, and greatly increase the medium absorptivity. With values of 0.1 and 0.75 for τ and ε_w, the reflection term introduces a 2.5% (approximately) contribution to

the radiative heat flux. Therefore, for simplicity the reflection term given by eqn.4.34a is ignored in the following calculations and the expressions for a_{kj} and a_{kk} are simplified to:-

$$a_{kj} = 0$$

$$a_{kk} = \frac{1}{\varepsilon_k}$$

By this means, the matrix A becomes a diagonal matrix, and eqn.4.33 can be directly solved.

4.3 MEAN BEAM LENGTH

In order to calculate the radiative heat flux falling on each surface using eqn.4.33, the gas absorptivity α_{k-j} and emissivity ε_{k-j} terms are needed; this requires the evaluation of the geometric-mean absorptivity term. The geometric-mean absorptivity term given by eqn.4.15b can also be expressed as [35,36]:-

$$\bar{\alpha}_{\lambda,k-j} = 1 - \exp\left(-a_\lambda L_{m,j-k}\right) \qquad (4.36)$$

where $L_{m,j-k}$ is the characteristic length called the mean beam length between surfaces j and k. The exact value for the mean beam length for the related surfaces can be obtained by simultaneous solution of eqns.4.15b and 4.16. However, for simplicity the mean geometric distance between the surfaces can also be considered as the mean beam length. Although this is a crude approximation, the advantage is that the evaluation of the double integrals containing the exponential term α_λ is thereby eliminated. This is very convenient for cycle simulation studies.

In the engine thermal resistance network, explained in Chapter 5, the combustion chamber is

considered as piston, cylinder head and 26 liner nodes distributed along the cylinder axis. Even with the simplified mean beam length model, the calculation of radiative heat flux falling on each surface using eqn.4.34c, at every degree CA, requires enormous computational time. For this reason the flame to wall and wall to wall radiative heat transfers in eqn.4.34c are seperated. The net radiative heat exchange between the flame and surface k, at every degree CA, is calculated by the following equation:-

$$Q_{rad} = \sigma A_k \varepsilon_k \left[\varepsilon_{fl,k} T_{fl}^4 - \alpha_{fl,k} T_{w,k}^4 \right] \qquad (4.37)$$

where $\varepsilon_{fl,k}$ and $\alpha_{fl,k}$ are the flame (or gas) emissivity and absorptivity related to surface k.

The summation of net flame radiative heat transfer to all surfaces gives the total gas radiative heat loss. In the calculation of flame emissivity and absorptivity for various surfaces the following simple mean beam lengths are adopted:-

$$L_m = s + 0.5 D_{cup} \quad \text{for piston and cylinder head} \qquad (4.38a)$$

$$L_m = 0.63 D_{cy} \quad \text{for liner} \qquad (4.38b)$$

where D_{cy} and D_{cup} are the cylinder and piston cup diameters, and s is the instantaneous piston position measured from the cylinder head.

The flame absorptivity and emissivity terms for surface k are obtained by substituting eqn.4.36 into eqns.4.31a and 4.31b, respectively:-

$$\alpha_{fl,k}\left(T_{w,k}, T_{fl}\right) = \frac{\int_0^\infty \left[1 - \exp\left(-a_\lambda L_{m,k}\right)\right] E_{\lambda b,w,k}\, d\lambda}{\sigma T_{w,k}^4} \qquad (4.39a)$$

and

$$\varepsilon_{fl,k}\left(T_{fl}\right) = \frac{\int_0^{\infty}\left[1 - \exp\left(-a_{\lambda} L_{m,k}\right)\right] E_{\lambda b,fl}\, d\lambda}{\sigma T_{fl}^{4}} \qquad (4.39b)$$

These equations are general and can be used to evaluate both gas and soot absorptivity and emissivity, providing that the appropriate absorption coefficients are used, i.e. $a_{\lambda,g}$ and $a_{\lambda,so}$.

The wall to wall radiative heat transfer is calculated at the end of each simulation cycle by considering the combustion chamber as piston, cylinder head and 26 liner nodes. By this means, the influence of hot parts of the chamber are also included on thermal resistance network solution. Although some of the wall to wall radiative heat transfer is absorbed by the combustion gases, the gas absorptivity is significant during the high pressure combustion period, which occupies about 40 to 50°CA of the 720°CA diesel cycle. In the expansion and exhaust strokes the gas absorptivity is around 0.1, which is not significant. The wall to wall radiative heat transfer for surface k, derived from eqn.4.34c is given by:-

$$Q_k = \sigma\varepsilon_k\left[A_k T_k^4 - \sum_{j=1}^{N} F_{k-j} A_j T_j^4\right] \qquad (4.40)$$

The configuration factors are evaluated for a right circular finite cylinder and are defined for end to end, end to side and side to side by eqns.4.41a, 4.41b and 4.41c, respectively:-

$$F_{end-end} = 0.5\left[\frac{1}{Y^2} + 2 - \frac{1}{Y}\sqrt{4 + \frac{1}{Y^2}}\right] \qquad (4.41a)$$

$$F_{side-end} = \frac{Z^2 + 0.5}{\sqrt{Z^2 + 1}} - Z \qquad (4.41b)$$

$$F_{side-side} = 1 - \frac{2Z^3 - 3Z}{2(Z^2+1)^{1.5}} \qquad (4.41c)$$

where Y and Z are ratios, defined as:-

$$Y = 0.5\frac{D}{S}$$

$$Z = \frac{S}{D}$$

where D is the diameter and s is the axial position of the circular ring element.

4.4 FLAME ABSORPTIVITY AND EMISSIVITY

The flame absorptivity $\alpha_{fl,k}$, and emissivity $\varepsilon_{fl,k}$, for surface k are calculated for soot particles and combustion gases separately and are then superimposed by the following relation:

$$\alpha_{fl,k} = 1 - (1 - \alpha_{so,k})(1 - \alpha_{g,k}) \qquad (4.42a)$$

$$\varepsilon_{fl,k} = 1 - (1 - \varepsilon_{so,k})(1 - \varepsilon_{g,k}) \qquad (4.42b)$$

where fl, so and g denotes flame, soot and combustion gases, respectively.

4.4.1 Soot Absorptivity and Emissivity

Soot plays an important role in flame absorptivity and emissivity. It is generated in flames due to incomplete combustion of fuel and emits thermal radiation in a continuous spectrum in the visible and infrared regions. The nucleation and growth of soot particles is not well understood at this time. Soot can be in the form of spherical particles, agglomerated masses, or long filaments and its size generally ranges from 50 to 1000 Angstroms in diameter, with agglomerated

masses sometimes being even larger.

Scattering σ_{sc}, and absorption σ_{ab}, cross sections of small particles are described as [33]:-

$$\sigma_{sc} = \left(\frac{\pi D_{so}}{\lambda}\right)^4 \qquad \sigma_{ab} = \left(\frac{\pi D_{so}}{\lambda}\right)$$

and the condition for a small particle is given by:-

$$\frac{\pi D_{so}}{\lambda} \leq 0.25$$

where D_{so} and λ are respectively, the soot diameter and wavelength of thermal radiation.

The size of the soot particles produced in a hydrocarbon flame lies well within the small particle region which makes the scattering cross section negligible compared to the absorption cross section. Thus, the extinction coefficient of soot particles can be considered as the absorption coefficient.

The absorption coefficient for the soot particles is expressed by using the Milne-Eddington absorption coefficient [33], in which it is considered as a product of a function only of radiation frequency and of the path variables. This approximation is well suited to the present formulation of the radiation heat transfer, where the soot concentration, pressure and temperature are assumed to be constant over a finite volume. The soot spectral absorption coefficient $a_{\lambda,so}$, is given by:-

$$a_{\lambda,so} = \int_0^\infty EF_{\lambda,so} A_{so} SD(D_{so}) dD_{so} \qquad (4.43)$$

where:-

A_{so} is the cross sectional area of soot particles, $\frac{\pi}{4} D_{so}^2$.

$SD(D_{so})$ is the size distribution of soot particles. $EF_{\lambda,so}$ is the spectral absorption efficiency of the soot particles and is defined for small particles as:-

$$EF_{\lambda,so} = \frac{24\pi D_{so}}{\lambda} \frac{\bar{n}\bar{k}}{\left[\left(\bar{n}^2 - \bar{k}^2\right) + 2\right]^2 + 4\bar{n}^2\bar{k}^2} \qquad (4.44)$$

where $\bar{n}$ and $\bar{k}$ are the refractive index and absorption index of the complex index of refraction $\bar{m}$, given by:-

$$\bar{m} = \bar{n} - i\bar{k}$$

where i is $\sqrt{-1}$.

Substituting eqn.4.44 and soot cross section area in eqn.4.43 gives:-

$$a_{\lambda,so} = \left(\frac{36\pi}{\lambda}\right)\left\{\frac{\bar{n}\bar{k}}{\left[\left(\bar{n}^2 - \bar{k}^2\right) + 2\right]^2 + 4\bar{n}^2\bar{k}^2}\right\} f_v \qquad (4.45)$$

where f_v is the total volume fraction of soot particles and is given by:-

$$f_v = \int_0^\infty V(D_{so})\, SD(D_{so})\, dD_{so} \qquad (4.46)$$

where $V(D_{so})$ is the volume of soot particles with diameter D_{so}.

The optical properties of soot particles are obtained from Dalzell's and Sarofim's work [34] which produced experimentally from acetylene and propane soot at room temperature in the 0.4 to 0.8 and 2.5 to 10 microns wavelength region (Table 4.1). However, it was mentioned that the temperature dependence of optical properties is not significant, thus the experimental results can be applied to high flame temperatures.

In the present work, a solution method proposed by Chang and Rhee [28] is used to find the exact solutions of eqns.4.39a and 4.39b for absorptivity and emissivity. In the solution, the optical constants are assumed to be constant in the intervals of integration. The soot emissivity or absorptivity for surface k is transformed to:-

$$\varepsilon_{so,k} = 1 - \frac{15}{\pi^4}\int_0^{\infty} \exp(-a^* u)\frac{u^3}{[\exp(u)-1]}\,du \qquad (4.47)$$

where u is the dimensionless parameter defined by:-

$$u = \frac{hc\nu}{k_B T_{so}} \qquad (4.48)$$

where:-

h is the Planck's constant.

c is the speed of light.

ν is the wave number of thermal radiation.

k_B is the Boltzmann's constant.

T_{so} is the soot temperature in K.

and

$$a^* = \left\{\frac{36\pi\bar{n}\bar{k}}{\left[\left(\bar{n}^2-\bar{k}^2\right)+2\right]^2 + 4\bar{n}^2\bar{k}^2}\right\} f_v L_{m,k}\frac{k_B T_{so}}{hc} \qquad (4.49)$$

where $L_{m,k}$ is the mean beam length for surface k.

The exact solution of eqn.4.47 is given by:-

$$\varepsilon_{so,k} = 1 - \frac{15}{\pi^4}\sum_{i=1}^{M}\left[S\left(3,a_i^*,u_i\right) - S\left(3,a_i^*,u_{i+1}\right)\right] \qquad (4.50)$$

where M is the number of intervals in the integral range and a_i^* and u_i are the parameters at the i'th interval.

The function $S(3,a_i^*,u_i)$ is defined by:-

$$S(3,a_i^*,u_i) = \sum_{N=1}^{\infty} \exp[-(N+a^*)u] \sum_{i=0}^{3} \frac{\Gamma(3+1)}{\Gamma(3-i+1)} (N+a^*)^{-i-1} u^{3-i} \tag{4.51}$$

where Γ is the gamma function defined as $\Gamma(m+1)=m*\Gamma(m)$ and $\Gamma(1)=1$.

In the soot absorptivity and emissivity calculations, the soot volume fraction f_v, and soot temperature are also needed, as explained in sections 4.5 and 4.6.

4.4.2 Gas Absorptivity and Emissivity

The absorptivity and emissivity of CO_2 and H_2O mixtures can be obtained from the emissivity charts and the CO_2-H_2O mixture correction charts presented by Hottel [35]. However, the available charts are for atmospheric pressure and using them at high pressures will introduce a significant error. They can also be obtained from spectral calculations using detailed information about the mean line intensity and mean line width to mean line spacing ratio at each spectral location, which requires long and tedious calculations. A third alternative, which can be employed for a variety of gas mixture components, is to use wide-band absorption relations. In the present model, an exponential wide-band absorption model proposed by Edwards and Balakrishnan [32] is employed. The model assumes a block approximation that calls for black-body properties in the bands and is transparent oterwise. The total band absorptivity AB_m, based on the band width of the m'th band, is defined by:-

$$AB_m = \int_{band\ m} \alpha_\nu d(\nu - \nu_m) \qquad (4.52)$$

where:-

α_ν is the spectral band absorptivity.

ν is the wave number.

ν_m is the wave number at the centre of the m'th band.

The model provides for each radiating gas a semi empirical correlation of the integrated band intensity $\alpha(T_g)$, the band width parameter $\omega(T_g)$, the line width parameter $\beta(T_g)$, and the effective pressure P_e. The integrated intensity of each band is given by:-

$$\alpha(T_g) = \alpha_0 \frac{\left[1 - \exp\left(-\sum_{k=1}^{mv} \pm u_k \delta_k\right)\right]\Psi(T_g)}{\left[1 - \exp\left(-\sum_{k=1}^{mv} \pm u_{0,k} \delta_k\right)\right]\Psi(T_0)} \qquad (4.53)$$

where u_k and $u_{0,k}$ are the dimensionless groups defined by the following equations:-

$$u_k = \frac{hc\nu_k}{k_B T_g} \qquad (4.48a)$$

$$u_{0,k} = \frac{hc\nu_k}{k_B T_0} \qquad (4.48b)$$

The temperature dependent band absorption function is given by:-

$$\Psi(T_g) = \frac{\sum_{k=1}^{mv} \sum_{\upsilon_k=\upsilon_{0,k}}^{\infty} \frac{(\upsilon_k + g_k + \delta_k - 1)!}{(g_k - 1)!\upsilon_k!} \exp(-u_k \upsilon_k)}{\sum_{k=1}^{mv} \sum_{\upsilon_k=0}^{\infty} \frac{(\upsilon_k + g_k - 1)!}{(g_k - 1)!\upsilon_k!} \exp(-u_k \upsilon_k)} \qquad (4.54)$$

where:-

α_0 is a band absorption parameter.

δ_k is vibrational transition.

υ_k is vibrational quantum number.

g_k is the statistical weight.

mv is the number of vibrational transition.

ν_k is the wave number.

T_0 and T_g are the reference $(T_0 = 100\ K)$ and gas temperatures, respectively.

Subscript k denotes the k'th vibrational quantum number.

The values of α_0, δ_k, υ_k, g_k, mv and ν_k are given in Table 4.2. The value of $\upsilon_{0,k}$ in $\Psi(T_g)$ function is defined by:-

$$\upsilon_{0,k} = 0 \qquad \text{if} \qquad \delta_k \geq 0$$
$$\upsilon_{0,k} = \delta_k \qquad \text{if} \qquad \delta_k < 0$$

The absolute value of the vibrational transition δ_k, is used in all equations except in the integrated band intensity equation.

The bandwidth parameter is given by:-

$$\omega(T_g) = \omega_0 \left(\frac{T_g}{T_0} \right)^{0.5} \tag{4.55}$$

where ω_0 is constant and is given in Table 4.2.

The line width parameter $\beta(T_g)$, is expressed as:-

$$\beta(T_g) = \beta_0 \left(\frac{T_0}{T_g} \right)^{0.5} \left(\frac{\phi(T_g)}{\phi(T_0)} \right) \tag{4.56}$$

where β_0 is constant and is presented by Table 4.2.

The function $\phi(T_g)$ is given by:-

$$\phi(T_g) = \frac{\left\{\sum_{k=1}^{mv}\sum_{\upsilon_k=\upsilon_{0,k}}^{\infty}\left[\frac{(\upsilon_k + g_k + \delta_k - 1)!}{(g_k - 1)!\upsilon_k!}\exp(-u_k\upsilon_k)\right]^{0.5}\right\}^2}{\sum_{k=1}^{mv}\sum_{\upsilon_k=\upsilon_{0,k}}^{\infty}\frac{(\upsilon_k + g_k + \delta_k - 1)!}{(g_k - 1)!\upsilon_k!}\exp(-u_k\upsilon_k)} \quad (4.57)$$

In the calculations of the integrated band intensity $\alpha(T_g)$, and line width parameter $\beta(T_g)$, special care is needed for two particular bands of water. One is the pure rotational band (δ=0, k=1,2,3), where the two parameters are simplified as:-

$$\alpha(T_g) = \alpha_0 \quad (4.53\,a)$$

$$\beta(T_g) = \beta_0\left(\frac{T_g}{T_0}\right)^{0.5} \quad (4.56\,a)$$

The second is the 2.7μ band width which consists of three overlapping bands. The integrated band intensity $\alpha(T_g)$, is computed for each type of transition and the results then summed. On the other hand, the calculated values of each line width parameter $\beta(T_g)$ are used to obtain an averaged value as follows:-

$$\beta(T_g) = \frac{\left[\sum_{j=1}^{3}\left[\left(\alpha_j T_g\right)\beta_j(T_g)\right]^{0.5}\right]^2}{\sum_{j=1}^{3}\alpha_j(T_g)} \quad (4.58)$$

where j denotes the vibrational transitions.

The effective pressure P_e, which is responsible for the pressure broadening effect is given by:-

$$P_e = \left[\frac{P_t}{P_0} + \left(\frac{P_n}{P_0}\right)(bs - 1)\right]^{ns} \tag{4.59}$$

where:-

P_0 is the reference pressure of 1 atmosphere.

P_t is the cylinder total pressure in atmospheres.

P_n is the partial pressure of the absorbing gas.

bs and ns are self-broadening coefficients and are given in Table 4.2.

The effective pressure parameter η, and optical depth parameter τ_H, are obtained from the computed values of $\alpha(T_g)$, $\beta(T_g)$, $\omega(T_g)$ and P_e with the following relations:-

$$\eta = \beta(T_g) P_e \tag{4.60}$$

$$\tau_H = \frac{\alpha(T_g)\rho_g L_{m,k}}{\omega(T_g)} \tag{4.61}$$

where ρ_g is the gas density and $L_{m,k}$ is the mean beam length for surface k.

Using the values of η and τ_H, the dimensionless integrated band absorptivity AB^*, can be obtained from Table 4.3 and the total band absorptivity can be evaluated from:-

$$AB = AB^* \omega(T_g) \tag{4.62}$$

Once the total band absorptivity of each species at the specified spectral locations have been evaluated,

the total gas absorptivity and emissivity for surface k can be obtained from the block approximation:-

$$\alpha_{g,k}\left(T_g, T_{w,k}, \rho_g L_{m,k}, P_t\right) = \sum_{n=1}^{nt}\sum_{m=1}^{mt}\left[f\left(u_{lw}\right) - f\left(u_{up}\right)\right]_{n,m} \quad (4.63\,a)$$

$$\varepsilon_{g,k}\left(T_g, \rho_g L_{m,k}, P_t\right) = \sum_{n=1}^{nt}\sum_{m=1}^{mt}\left[f\left(u_{lw}\right) - f\left(u_{up}\right)\right]_{n,m} \quad (4.63b)$$

where:-

subscripts n and m denotes the gas specie and band number, respectively.

nt and mt represent the total gas specie and bands.

subscripts lw and up denotes the lower and upper wavenumber of band m.

$T_{w,k}$ is the temperature of wall section k in K.

f(u) is the fractional function which is evaluated at the wall temperature for absorption and at gas temperature for emissivity.

The fractional function is given by:-

$$f(u) = \frac{15}{\pi^4}\int_u^{\infty}\frac{u^3}{\exp(u) - 1}du \quad (4.64)$$

where u is the dimensionless group given by eqn.4.48. In evaluating u, the lower and upper wave number of each band are required which are obtained from:-

$$AB_{n,m} = \nu_{up,n,m} - \nu_{lw,n,m} \quad (4.65\,a)$$

$$\nu_{up,n,m} = \nu_{cn,n,m} + 0.5\,AB_{n,m} \quad (4.65b)$$

$$\nu_{lw,n,m} = \nu_{cn,n,m} - 0.5\,AB_{n,m} \quad (4.65\,c)$$

where $\nu_{cn,n,m}$ is the central wave number of band m of specie n.

In Table 4.2 either the central, lower or upper wave number of each band is given and the rest is calculated from eqns.4.65a to 4.65c. The lower and upper wave numbers of each band form a block of black bands and this should be checked for any overlapping with the other block of black bands before computing the fractional function f(u). If overlapping is discovered, the minimum and the maximum wave numbers of the overlapping bands are considered and the rest are ignored. The possible overlapping bands for CO_2 and H_2O are:-

CO_2	15μ	2.7μ	1.9μ
H_2O	Rotational	2.7μ	1.87μ

The exact solution of the integral function f(u), for band m is obtained from [28]:-

$$f(u_{lw}) - f(u_{up}) = \frac{15}{\pi^4}\left[S(3,0,u_{lw,m}) - S(3,0,u_{up,m})\right] \quad (4.66)$$

where:-

$$S(3,0,u) = \sum_{N=1}^{\infty}\exp(-Nu)\sum_{i=0}^{3}\frac{u^{3-i}\Gamma(3+1)}{N^{i+1}\Gamma(3-i+1)} \quad (4.67)$$

where Γ is the gamma function, defined in the previous section.

4.5 SOOT CONCENTRATION

As already mentioned in the previous section, the soot concentration in the combustion chamber is directly related to the flame absorptivity and emissivity, and the accuracy of the results is highly dependent on it. The soot concentration during the combustion period which is both time and space dependent mainly depends on the type of fuel, the mixing characteristics of the fuel

jet and air, and the combustion temperature and pressure. Predictions from basic principles are extremely difficult.

Experimental data on soot concentration are obtained either by direct sampling or two-color methods (Fig.4.4). The soot is formed just after the start of the diffusion combustion phase and peaks around the end of injection, then it is oxidized rapidly, followed by the termination of oxidation when the flame temperature drops 1800 K. However, there is no published empirical correlation which describes the soot concentration in a diesel engine as a function of engine operating conditions and crank angle.

Sitkei and Ramanaiah [25] measured radiation heat transfer in a diesel engine at various operating conditions, and from the apparent flame emissivity they deduced an extinction coefficient which is given in Fig.2.10. Morel and Keribar [31] used their data at the maximum extinction coefficient value to produce the maximum soot volume fraction as a function of engine equivalence ratio (Fig.4.5), where it is also used in this study. A curve similar to the experimental ones is chosen to represent the soot mass fraction as a function of CA (Fig.4.6). The soot mass fraction is assumed to peak at around 40% of combustion duration after the start of diffusion burning, and gradually decrease to the exhaust level which is considered to be 20% of the maximum value. The duration of combustion which is obtained from the cycle simulation heat release model is used to scale the x-axis of Fig.4.6 while the y-axis is scaled by Fig.4.5.

4.6 COMBUSTION MODEL

In order to evaluate radiation heat transfer in the cycle simulation package, a combustion model is required to supply the flame temperature and the partial pressures of CO_2 and H_2O. These values can be obtained by

assuming chemical equilibrium of the species throughout the combustion process. Thus, for a given fuel, air temperature and pressure, the mass action equations can be solved directly for species concentrations from which the flame temperature and other thermodynamic properties can be derived. An alternative method is to calculate the species concentrations that minimize the Gibbs free energy of the system. Both methods need long iteration procedures and considering that these calculations will be repeated at every degree CA, a heavy computational effort is required. In simulation studies much simpler methods with an acceptable degree of accuracy are preferred.

4.6.1 Flame Temperature

The actual flame temperature is very difficult to obtain from basic principles because of the complex nature of the heat transfer occurring in the flame. Therefore, it is usual to use the adiabatic flame temperature as a reference. This is defined as the maximum attainable flame temperature for any given initial conditions. It is a function of fuel type, fuel-air equivalence ratio, temperature of the fuel and air, and pressure. The fuel type is characterized by the enthalpy of formation or by the hydrogen to carbon ratio.

Glassman and Clark [38] presented universal graphs for adiabatic flame temperature of hydrocarbon-air systems. Chang and Rhee [39] reported functional expressions for the adiabatic flame temperature of pure hydrocarbons. However, both publications are limited to an initial mixture temperature of 298 K and low combustion pressures which restrict their use for a diesel engine. The formula proposed by Gulder [89] is used in this study; this is applicable over a wide range of equivalence ratio, temperature and pressure. The formula was obtained by fitting of the data from a

detailed chemical equilibrium code which incorporates 14 species in the combustion products, to a functional expression. The expressed formula is a function of combustion pressure, initial mixture temperature, equivalence ratio and hydogen to carbon atomic ratio of the fuel. The suggested formula is applicable to diesel fuels, gasolines, pure alkanes, aromatics and jet fuels, and is given by:-

$$T_{fl,ad} = C_1 \phi_c^{C_2} \exp\left[C_3\left(\phi_c + C_4\right)^2\right] (P^*)^x (T^*)^y HC^z \qquad (4.68a)$$

where the exponent x, y and z are defined as:-

$$x = a_1 + b_1\phi_c + c_1\phi_c^2 \qquad (4.69a)$$

$$y = a_2 + b_2\phi_c + c_2\phi_c^2 \qquad (4.69b)$$

$$z = a_3 + b_3\phi_c + c_3\phi_c^2 \qquad (4.69c)$$

and C_1, C_2, C_3, C_4, a_i, b_i and c_i are constants and are given in Table 4.4.

P^* and T^* are the dimensionless combustion pressure and initial mixture temperature, respectively, defined as:-

$$P^* = \frac{P}{P_0} \qquad T^* = \frac{T_u}{T_0}$$

and P_0, and T_0, are 0.1013 MPa and 300 K, respectively. HC is the hydrogen to carbon atomic ratio.

ϕ_c is the corrected fuel-air equivalence ratio defined as:-

$$\phi_c = \phi \qquad \text{for} \qquad \phi \leq 1.0$$

$$\phi_c = \phi - 0.7 \qquad \text{for} \qquad \phi \geq 1.0$$

and ϕ is the actual equivalence ratio of the flame.

In the above formulation, the fuel is assumed to be in vapor form and is at the same temperature as air. However, in diesel engines the injected fuel is in liquid form and its temperature is much lower than that of the hot compressed air. This requires a correction for the initial mixture temperature T_u, which is defined as:-

$$T_u = \frac{Cp_f T_f + (A/F) Cp_a T_a - \Delta H_f}{Cp_f + (A/F) Cp_a} \qquad (4.70)$$

where:-

T_f is the fuel temperature.

T_a is the mean air temperature at the ignition delay period.

Cp_f and Cp_a are the specific heats of fuel and air, respectively.

ΔH_f is the enthalpy of evaporation for the fuel.

(A/F) is the local air to fuel mass ratio and is taken as 13.5.

The specific heat of fuel is given by:-

$$Cp_f = (0.363 + 0.000467 T_f)(5 - 0.001 \rho_{f,0}) \left(\frac{kJ}{kg\,K}\right) \qquad (4.71)$$

where $\rho_{f,0}$ is the density of fuel at 288.6 K.

The enthalpy of evaporation of the fuel is defined by:-

$$\Delta H_f = \frac{360 - 0.39 T_f}{\rho_f} \left(\frac{kJ}{kg}\right) \qquad (4.72)$$

where ρ_f is the relative density of fuel.

The hydrogen to carbon atomic ratio can be obtained from the following correlation:-

$$HC = 0.9479\left(\frac{T_{mb}}{100}\right)^{0.2527} \rho_{f,20}^{-2.4063} \qquad (4.73)$$

where T_{mb} is the midboiling point of fuel and $\rho_{f,20}$ is the density of fuel at $20^{\circ}C$.

The proposed formula for adiabatic flame temperature can provide quite accurate results within 0.4% error and is applicable within the following range:-

$$\begin{aligned} 0.3 \leq \quad & \phi \quad \leq 1.6 \\ 0.1 \leq \quad & P \quad \leq 7.5 \text{ MPa} \\ 275 \leq \quad & T_u \quad \leq 950 \text{ K} \\ 0.8 \leq \quad & HC \quad \leq 2.5 \end{aligned}$$

The initial mixture temperature is calculated from eqn.4.70 where the air temperature is obtained from the cycle simulation package prior to the start of combustion. The flame is assumed to be of the shape shown in Fig.4.7, the soot being concentrated in the regions with high fuel-air equivalence ratio. An equivalence ratio of 1.5 is chosen for the adiabatic flame temperature. After the injection process stops, ignition of the fuel still continues at lower rates, the actual local equivalence ratios and flame temperatures being very difficult to predict. As the mass of fuel in the chamber decreases the flame temperature approaches the mean gas temperature. For these reasons the following relation is adopted for the flame temperature:-

$$T_{fl} = \left(\frac{m_{f,b}}{m_{f,i}}\right)^4 T_g + \left[1 - \left(\frac{m_{f,b}}{m_{f,i}}\right)^4\right] T_{fl,ad} \qquad (4.74)$$

where:-

$T_{fl,ad}$ and T_g are the adiabatic flame and mean gas temperatures, respectively.

$m_{f,b}$ and $m_{f,i}$ are the burned and total injected fuel masses which are obtained from the heat release model in the cycle simulation.

4.6.2 Partial Pressures of Carbon Dioxide and Water Vapor

The partial pressures of CO_2 and H_2O are required in the prediction of gas radiation. Gulder [90] proposed the following formula for the partial pressures P_n, of CO_2 and H_2O in flames, which is similar to the adiabatic flame temperature formula presented in the previous sub-section. It is given by:-

$$\left(\frac{P_n}{P}\right) = C_1 \phi_c^{C_2} \exp\left[C_3\left(\phi_c + C_4\right)^2\right] (P^*)^x (T^*)^y HC^z \qquad (4.68b)$$

where P is the total cylinder pressure and the exponents x, y and z are defined in eqns.4.69a to 4.69c, and constants C_1, C_2, C_3, C_4, a_i, b_i and c_i are given in Table 4.5.

The corrected fuel-air equivalence ratio ϕ_c, is defined for CO_2 same as in the previous sub-section, whereas for H_2O it is equal to the actual equivalence ratio, i.e. no correction is needed. The rest of the terms are explained in the previous sub-section.

In the calculation procedure for the partial pressures of CO_2 and H_2O, the combustion pressure, initial air-fuel mixture temperature and fuel-air equivalence ratio values are needed. From the cycle simulation package, pressure, gas temperature and heat release data can be obtained. The latter is used to determine the total burned fuel and to obtain the fuel-air equivalence ratio as a function of crank angle by the following relation:-

$$\phi = \frac{\left(\frac{m_{f,b}}{m_a}\right)}{\left(\frac{m_{f,i}}{m_a}\right)_{st}} \qquad (4.75)$$

where m is the mass and subscripts f,b, f,i, a and st refer to fuel burned, fuel injected, air and stoichiometric, respectively.

4.7 NEW RADIATION SUB-MODELS

The following four sub-models were developed for radiation heat transfer and tested before incorporating them in the cycle simulation package 'SPICE':-

1) Soot.For; Evaluates the soot emissivity and absorptivity.

2) Gas.For; Evaluates the combustion gases emissivity and absorpivity.

3) Flame1.For; Evaluates the adiabatic flame temperature.

4) Flame2.For; Evaluates the partial pressures of H_2O and CO_2.

The flowcharts and sample outputs for these models are presented in Figs.4.8 to 4.11 and Tables 4.6 to 4.9.

The soot emissivity as a function of soot temperature is shown in Fig.4.12, where the same curve can also be used for soot absorptivity if soot temperature is replaced by the wall temperature. The soot emissivity showed an increase at high temperatures. The soot emissivity and absorptivity as functions of soot volume fraction and mean beam length are also shown in Fig.4.13 and 4.14. As expected, the emissivity and absorptivity increase at high values of soot volume fraction and mean beam length, and approach unity.

The gas emissivity and absorptivity as functions of pressure, temperature, mean beam length and mole fractions of H_2O and CO_2 are presented in Figs.4.15 to

4.18. Raising the values of pressure, mean beam length and mole fractions of H_2O and CO_2 increases the gas emissivity and absorptivity. However, due to the overlapping effects of the individual absorption bands, the gas emissivity decreases with increasing gas temperature.

The adiabatic flame temperature as a function of H/C atomic ratio at various temperatures and pressures is shown in Fig.4.19. It is also expressed as a function of equivalence ratio which is presented in Fig.4.20. As expected, the peak flame temperature occurs close to an equivalence ratio of 1.0; however at higher temperatures and pressures, it shifts towards the right, where the equivalence ratio has a value of about 1.05.

The partial pressures of H_2O and CO_2 as functions of H/C atomic ratio and equivalence ratio are shown in Figs.4.21 to 4.23. The maximum value for the partial pressure of H_2O shifts towards the right and down with increasing air temperature and decreasing pressure. Temperature and pressure have similar effects on the mole fraction of CO_2 but without any significant change in the position of the peak value.

4.8 INCORPORATING THE RADIATION SUB-MODELS IN 'SPICE'

In the cycle simulation package program 'SPICE', the gas heat transfer calculations are performed in subroutine 'Woschni.For', which evaluates the gas convective htc using the Woschni htc empirical correlation [16]. This subroutine is modified to accept the radiation model, fluctuating wall temperature model and new Woschni htc correlation (enhanced htc). Its flowchart is presented in Fig.4.26. For radiation heat transfer, the following two subroutines are developed:-

1) Radd.For: Evaluates the instantaneous flame temperature and mole fractions of H_2O and CO_2.

2) Rad.For: Evaluates the instantaneous mean beam lengths, gas, soot and total emissivities for each section of the combustion chamber.

The flowchart for these models are shown in Figs.4.27 and 4.28. The 'Radd.For' subroutine uses the necessary heat release data as input and calls the two subroutines 'Flame1.For' and 'Flame2.For'. However, the 'Rad.For' subroutine uses simple equations for soot and gas emissivities, which are derived by using the models 'Soot.For' and 'Gas.For', to calculate the total flame emissivity. By this means, the computational time is kept to minimum in the cycle simulation package 'SPICE'.

Since soot has a continuous emission spectrum, its emissivity is expressed by an exponential function of soot volume fraction f_v, soot temperature T_{so} and mean beam length L_m as follows:-

$$\varepsilon_{so} = 1 - \exp(K f_v T_{so} L_m) \qquad (4.76)$$

where K is constant and has value of 8.781 $K^{-1} cm^{-1}$. The logaritmic function of the soot emissivity is shown in Fig.4.24 where its slope is K.

The combustion gases do not have a continuous emission spectrum and therefore it is not possible to express the gas emissivity by an exponential function. Using the idea developed by Hottel and Sarofim [35], the gas emissivity is expressed as a function of gas temperature at various values of the variable group $P_t(X_{H2O}+X_{CO2})L_m$ as shown in Fig.4.25. The equations for the curves are obtained by using curve fitting techniques which are given in Appendix 1. Thus, for a given gas temperature, the gas emissivity is calculated by linear interpolation between the nearest $P_t(X_{H2O}+X_{CO2})L_m$ curves. The same curves are also valid for gas absorptivity, if the gas temperature is replaced by the wall temperature.

The necessary radiation data is transferred to the appropriate subroutines such as 'Linat.For' for liner and 'Rest.For' for piston, cylinder head, valves and other parts; using the Stefan-Boltzmann equation the radiation heat flux is evaluated for each separately. The flowcharts for 'Linat.For' and 'Rest.For' are given in Figs.6.82 and 6.83, respectively.

Using the radiation heat transfer model, the convective htc is scaled until the heat losses with and without the radiation model are the same assuming that combined convection and radiation in 'normal' engines are correctly represented by the original Woschni formulation. It is concluded that 20% reduction in Woschni htc during combustion and exhaust strokes compensates the radiation heat loss. In order not to affect the volumetric efficiency of the engine, htc is kept same at the intake and compression strokes of the cycle.

The results of the radiation heat transfer model in a diesel engine, i.e. incorporated in simulation package 'SPICE', are presented in Chapter 7.

CHAPTER 5
STEADY STATE HEAT TRANSFER THROUGH ENGINE WALLS

5.1 INTRODUCTION

The heat transfer through the engine walls consists of a very thin transient layer at the gas side, which is explained in Chapter 6 in detail, and a steady state heat transfer at the rest of the walls. In simulation studies, the steady state part of the heat transfer is solved by using a thermal resistance network which models the engine structure. This resistance network plays an important role in predicting the true surface temperatures of each part of the combustion chamber and thus to obtain accurate gas to wall heat transfer.

In the cycle simulation package 'SPICE', a simple 1-D thermal resistance model is used as shown in Fig.5.1, which is quite sufficient for simulation studies. Better thermal resistance networks can be written in 2-D or 3-D by using finite element methods, but this will increase the complexity of the package program and the computing time enormously with a little gain in accuracy. On the other hand, in cycle simulation packages space mean gas htc's are calculated and such an effort is not justified.

The model used in 'SPICE' considers each part of the combustion chamber as a thermal resistance and uses a cycle mean gas htc and a cycle mean gas temperature on the gas side. The liner is divided into 15 regions where the top, 13 intermediate, and the bottom parts are regarded as 3 different resistances, allowing for the fact that the liner is thicker at the top and bottom. The cylinder head is represented by three resistances, two for the inlet and exhaust valves, and one for the

rest of the cylinder head. The piston is considered as one resistance and the fraction of heat conducted from the piston to the liner is specified by the user. The liner absorbs heat from the combustion gases, by piston conduction and by friction. In the model the piston conduction and friction heat is assumed to be evenly distributed on the liner. The gas heat transfer is calculated by modifying the cycle mean htc for each liner region by multiplying it by the ratio of time of exposure to the combustion gases during the cycle to the total cycle time. Using this method the lower regions on the liner obtains more heat than the actual case because the gas heat transfer is not only a function of ratio of exposure time to the combustion gases but also a function of start and end of exposure time during the cycle.

Although the model is quite simple and useful for simulation studies, it has certain disadvantages which limit the use for adiabatic engine applications. The piston is dealt with in a very simple way where the fraction of heat conducted to the liner is specified by the user. Under normal conditions, heat is expected to be conducted from piston to liner but with insulated piston and insulated liner, cooler piston rings and hotter liner than in the conventional cooled engine are expected which will probably reverse the conduction of heat from liner to piston, especially at the top part of the liner. Thus the fraction of heat conducted from piston to liner is a strong function of the insulation level of the piston and liner, and should be included in the solution of the thermal resistance network.

The liner 1-D resistance model is quite sufficient for standard and surface coated liner simulation studies. However, if the insulation layer is used away from the surface, somewhere in the liner, or if part of the insulation is achieved by reducing the cooling capacity of the coolant, then the 1-D model is

not valid any more. The reason is simply that the thermal resistance across the liner is big enough to divert some of the heat flow in the axial direction along the liner surface, assuming that the liner surface has high conductivity, and makes it necessary to have a 2-D resistance model. To have a detailed 2-D resistance model for cycle simulation studies is not very convenient in terms of computing time and therefore the simple 2-D resistance model shown in Fig.5.2a is adopted. (Fig.5.2b applies specifically to ceramic coated liners).

The modified resistance model is more complicated for piston and liner and is kept the same for the cylinder head. The piston resistance network which represents the piston rings and the skirt as separate resistances is considered to be moving in axial direction and distributing conduction and friction heats to the nodes on the liner, and allowing the convective and radiative heat fluxes to apply at the nodes. A more detailed piston resistance network can be used as shown in Fig.5.3 to include piston to ring and ring to liner resistances, but to obtain the true resistance values of piston to ring, and ring to liner is quite difficult. Therefore, a single resistance is found to be more practical to represent the whole heat path between the internal piston node and the liner. The internal node in the piston is an imaginary node which provides approximately the same temperature difference between the rings and the liner, so that the direction of the instantaneous piston conduction heat flux can be correctly obtained.

The liner is represented by a simple 2-D resistance model and to achieve a better accuracy, nodes are used on the liner rather than dividing it into finite zones; the heat inputs to these nodes, i.e. convection, radiation, piston conduction and friction, are functions of crank angle. Thus, better liner surface

temperature distribution can be obtained which is quite important in terms of heat transfer and tribology in an insulated diesel engine.

5.2 SOLUTION OF PISTON-LINER RESISTANCE NETWORK

The solution of piston-liner resistance network, shown in Fig.5.2a, is obtained by applying the Kirchoff law at nodes 1, 2 and 3 as follows:-

Node 1: Piston Surface

$$q_p = \frac{T_{p,up} - T_{p,int}}{R_{p,1}} \tag{5.1}$$

where:-

q_p is the piston cycle mean heat flux.

$R_{p,1}$ is the piston top internal resistance.

$T_{p,up}$ and $T_{p,int}$ are the piston upper surface and internal node temperatures, respectively.

The cycle mean heat flux for the piston is given by:-

$$q_p = \frac{1}{PR}\int_0^{PR}\left[htc_p\left(T_g - T_{p,up}\right) + \left(\varepsilon_{fl,p}T_{fl}^4 - \varepsilon_p T_{p,up}^4\right)\right]d\theta$$

or

$$q_p = \frac{1}{PR}\int_0^{PR} htc_p T_g\, d\theta - \frac{1}{PR}\int_0^{PR} htc_p T_{p,up}\, d\theta + \frac{1}{PR}\int_0^{PR}\varepsilon_{fl,p}T_{fl}^4\, d\theta - \frac{1}{PR}\int_0^{PR}\varepsilon_p T_{p,up}^4\, d\theta \tag{5.2a}$$

where:-

PR is the period of the cycle, i.e. 720° CA.

htc_g is the gas heat transfer coefficient for piston.

T_g and T_{fl} are the mean gas and flame temperatures.

$\varepsilon_{fl,p}$ and ε_p are the flame and wall emissivities related to piston.

The wall radiation term can be neglected compared with the flame radiation and convection terms and thus the piston heat flux in the above equation can be expressed as a linear function of the wall temperature. For the constant wall temperature case, the heat flux term becomes:-

$$q_p = \frac{1}{PR}\int_0^{PR} htc_p T_g \, d\theta + \frac{1}{PR}\int_0^{PR} \varepsilon_{fl,p} T_{fl}^4 \, d\theta - T_{p,up}\frac{1}{PR}\int_0^{PR} htc_p \, d\theta \qquad (5.2b)$$

and q_p can be expressed in a simpler form as:-

$$q_p = \overline{htc_p T_g} + \overline{\varepsilon_{fl,p} T_{fl}^4} - T_{p,up}\,\overline{htc_p} \qquad (5.2c)$$

where:-

$$\overline{htc_p T_g} = \frac{1}{PR}\int_0^{PR} htc_p T_g \, d\theta \qquad (5.3)$$

$$\overline{\varepsilon_{fl,p} T_{fl}^4} = \frac{1}{PR}\int_0^{PR} \varepsilon_{fl,p} T_{fl}^4 \, d\theta \qquad (5.4)$$

$$\overline{htc_p} = \frac{1}{PR}\int_0^{PR} htc_p \, d\theta \qquad (5.5)$$

Using eqns.5.1 and 5.2c:-

$$T_{p,up} = \frac{\left(\overline{htc_p T_g} + \overline{\varepsilon_{fl,p} T_{fl}^4}\right) R_{p,1} + T_{p,int}}{\overline{htc_p} R_{p,1} + 1} \qquad (5.6)$$

Node 2: Piston Internal Node

$$A_{p,up}\left(\frac{T_{p,up}-T_{p,int}}{R_{p,1}}\right)=A_{p,lw}\left(\frac{T_{p,int}-T_{p,co}}{R_{p,2}+R_{p,co}}\right)+\sum_{i=1}^{nn}\sum_{j=1}^{nr}A_{r,j}RATP_{i,j}\left(\frac{T_{p,int}-T_{l,i}}{R_{p,j+2}}\right) \quad (5.7)$$

where:-

the summation term is the conduction heat from piston to liner through the piston rings and the skirt, and nn and nr are the number of nodes on the liner and the number of rings and skirt sections on the piston, respectively.

$A_{p,up}$ and $A_{p,lw}$ are the piston upper and lower surface areas.

$A_{r,j}$ is the surface area of ring j.

$T_{p,co}$ is the piston coolant temperature.

$T_{l,i}$ is the liner surface temperature at node i.

$R_{p,2}$ and $R_{p,co}$ are the piston coolant side resitances.

$R_{p,j+2}$ is the resistance for piston ring or skirt region j.

$RATP_{i,j}$ is the relative ratio of time for ring j in contact with liner node i and is given by:-

$$RATP_{i,j}=\frac{\theta 2_{i,j}-\theta 1_{i,j}}{\sum_{i=1}^{nn}\left(\theta 2_{i,j}-\theta 1_{i,j}\right)} \quad (5.8)$$

where $\theta_{i,j}$ and $\theta 2_{i,j}$ are the start and end of contact time in degree CA of ring j with liner node i, in 1 stroke of the cycle. $\theta 1_{i,j}$ and $\theta 2_{i,j}$ are obtained by using the

equation of motion for piston-crank mechanism together with the resistance network, shown in Fig.5.2a. (Fig.5.2b refers to the insulated liner, section 5.7).

Using eqn.5.7, piston internal node temperature can be expressed as:-

$$T_{p,int} = \frac{\frac{T_{p,up}}{R_{p,1}} + \frac{A_{p,lw}}{A_{p,up}}\left(\frac{T_{p,co}}{R_{p,2}+R_{p,co}}\right) + \sum_{i=1}^{nn}\sum_{j=1}^{nr}\left(\frac{A_{r,j}}{A_{p,up}}\right)\left(\frac{RATP_{i,j}}{R_{p,j+2}}\right)T_{l,i}}{\frac{1}{R_{p,1}} + \frac{A_{p,lw}}{A_{p,up}}\left(\frac{1}{R_{p,2}+R_{p,co}}\right) + \sum_{i=1}^{nn}\sum_{j=1}^{nr}\left(\frac{A_{r,j}}{A_{p,up}}\right)\left(\frac{RATP_{i,j}}{R_{p,j+2}}\right)} \qquad (5.9)$$

Node 3: Node i on the Liner

$$q_{l,i} = q_{l,i,conv} + q_{l,i,rad} + q_{l,i,cond} + q_{l,i,fric} - q_{l,i,oil}$$

$$= \frac{T_{l,i} - T_{l,co,i}}{R_{l,i}+R_{l,co}} - \frac{T_{l,i-1} - T_{l,i}}{R_{l,i,i-1}} + \frac{T_{l,i} - T_{l,i+1}}{R_{l,i,i+1}} \qquad (5.10)$$

where:-

$q_{l,i}$ is the cycle mean heat flux at liner node i and subscripts conv, rad, cond, fric and oil denotes the gas convective and radiative, piston rings conduction and friction, and heat flux absorbed by the oil film, respectively.

$T_{l,i}$ and $T_{l,co,i}$ are the liner and liner coolant temperatures corresponding to liner node i.

$R_{l,i}$ $R_{l,i,i-1}$ are the liner radial and axial resistances related to node i, and i,i-1.

Convection and radiation terms are the same as in eqn.5.2c:-

$$q_{l,i,conv} + q_{l,i,rad} = \overline{htc_{l,i}}\,T_g + \overline{\varepsilon_{fl,l,i}\,T_{fl}^4} - \overline{htc_{l,i}}\,T_{l,i} \qquad (5.11)$$

The conduction term is similar to the term in

eqn.5.7:-

$$q_{l,i,cond} = \sum_{j=1}^{nr} RATL_{i,j} \frac{T_{p,int} - T_{l,i}}{R_{p,j+2}} \qquad (5.12)$$

where $RATL_{i,j}$ is the ratio of contact time of ring j and the node i in 1 stroke of the cycle, and is given by:-

$$RATL_{i,j} = \frac{\theta 2_{i,j} - \theta 1_{i,j}}{180} \qquad (5.13)$$

The heat flux absorbed by the oil film from node i $q_{l,i,oil}$, is assumed to be a function of the temperature difference between oil and liner and the time during which the node i is covered with oil and is defined as:-

$$q_{l,i,oil} = TF_i \frac{T_{l,i} - T_{oil}}{R_{oil}} \qquad (5.14)$$

where R_{oil} is the oil film thermal resistance and TF_i is the time factor of node i and expressed as:-

$$TF_i = 0 \qquad \text{for liner nodes above top ring TDC.}$$

$$TF_i = \frac{\theta 1_{i,j}}{180} \qquad \text{for liner nodes below top ring TDC.} \qquad (5.15)$$

The friction heat flux term $q_{l,i,fric}$, is assumed to be independent of liner temperature and only a function of CA and FMEP which will be explained later in the chapter.

Eqns.5.11, 5.12 and 5.14 are substituted into eqn.5.10 and solved for $T_{l,i}$:-

$$T_{l,i} = \frac{A_i^* + B_i^* + \sum_{j=1}^{nr} RATL_{i,j} \frac{T_{p,int}}{R_{p,j+2}}}{C_i^*} \qquad (5.16)$$

where:-

$$A_i^* = \overline{htc_{l,i} T_g} + \overline{\varepsilon_{fl,l,i} T_{fl}^4} + \frac{TF_i}{R_{oil}} T_{oil} + q_{l,i,fric} + \frac{T_{l,co,i}}{R_{l,i} + R_{l,co}}$$

$$B_i^* = \frac{T_{l,i-1}}{R_{l,i,i-1}} + \frac{T_{l,i+1}}{R_{l,i,i+1}}$$

$$C_i^* = \frac{1}{R_{l,i} + R_{l,co}} + \frac{1}{R_{l,i,i-1}} + \frac{1}{R_{l,i,i+1}} + \overline{htc_{l,i}} + \sum_{j=1}^{nr} \frac{RATL_{i,j}}{R_{p,j+2}} + \frac{TF_i}{R_{oil}}$$

Eqns.5.6 and 5.16 are substituted into eqn.5.9 and solved for the piston internal node temperature, $T_{p,int}$:-

$$T_{p,int} = \frac{D^* - \sum_{i=1}^{nn}\sum_{j=1}^{nr}\left(\frac{A_{r,j}}{A_{p,up}}\right)\left(\frac{RATP_{i,j}}{R_{p,j+2}}\right)\left(\frac{B_i^*}{C_i^*}\right)}{E^* \times F^*} \qquad (5.17)$$

where:-

$$D^* = \frac{\overline{htc_p T_g} + \overline{\varepsilon_{fl,p} T_{fl}^4}}{\overline{htc_p} R_{p,1} + 1} + \left(\frac{A_{p,lw}}{A_{p,up}}\right)\left(\frac{T_{p,co}}{R_{p,2} + R_{p,co}}\right) + \sum_{i=1}^{nn}\sum_{j=1}^{nr}\left(\frac{A_{r,j}}{A_{p,up}}\right)\left(\frac{RATP_{i,j}}{R_{p,j+2}}\right)\left(\frac{A_i^*}{C_i^*}\right)$$

$$E^* = \frac{1}{R_{p,1}} + \left(\frac{A_{p,lw}}{A_{p,up}}\right)\left(\frac{1}{R_{p,2} + R_{p,co}}\right) + \sum_{i=1}^{nn}\sum_{j=1}^{nr}\left(\frac{A_{r,j}}{A_{p,up}}\right)\left(\frac{RATP_{i,j}}{R_{p,j+2}}\right)$$

$$F^* = 1 - \frac{1}{R_{p,1}\left(\overline{htc_p} R_{p,1} + 1\right)E^*} - \frac{\sum_{i=1}^{nn}\sum_{j=1}^{nr}\left(\frac{A_{r,j}}{A_{p,up}}\right)\left(\frac{RATP_{i,j}}{R_{p,j+2}}\right)\sum_{j=1}^{nr}\left(\frac{RATP_{i,j}}{R_{p,j+2}}\right)\frac{1}{C^*_i}}{E^*}$$

The terms A^*_i, C^*_i, D^*, E^* and F^* can easily be calculated for a given piston-liner resistance network for any given engine operating condition. However, for the term B^*_i a liner temperature distribution should be assumed which leads to an iterative solution for $T_{p,int}$. To avoid this complication, the liner resistance model is assumed to be radial only and the piston internal node temperature is solved sraightforwardly. As observed from experimental liner temperature data, the temperature gradients in the axial direction are small in the region where the rings travel, thus suggesting that 1-D resistance model is quite satisfactory in that region. Therefore, for the calculation of $T_{p,int}$, B^*_i is taken zero, thus reducing C^*_i and $T_{p,int}$ to:-

$$C^*_i = \frac{1}{R_{l,i} + R_{l,co}} + \overline{htc_{l,i}} + \sum_{j=1}^{nr}\frac{RATL_{i,j}}{R_{p,j+2}} + \frac{TF_i}{R_{oil}}$$

$$T_{p,int} = \frac{D^*}{E^* \times F^*} \qquad (5.17a)$$

Once $T_{p,int}$ is obtained, the piston surface temperature can be calculated by using eqn.5.6, whereas for the liner temperature distribution the solution is not straigtforward because eqn.5.16 is coupled with the surrounding node temperatures, i.e. the B^*_i term. Eqn.5.16 forms a set of equations which are solved simultaneously by applying the Gaussian elimination

method. This is done by arranging eqn.5.16 in the following form:-

$$a_i T_{l,i-1} + b_i T_{l,i} + c_i T_{l,i+1} = d_i \qquad (5.18)$$

where:-

$$a_i = -\frac{1}{R_{l,i,i-1}}$$

$$b_i = C_i^*$$

$$c_i = -\frac{1}{R_{l,i,i+1}}$$

$$d_i = A_i^* + \sum_{j=1}^{nr} RATL_{i,j}\left(\frac{T_{p,int}}{R_{p,j+2}}\right)$$

The boundary conditions at the top and bottom ends of the liner are assumed to be adiabatic, which makes the coefficients a_1 and c_n zero (n is the last liner node). The solution of eqn.5.18 is given by:-

$$T_{l,i} = \gamma_i - \left(\frac{c_i}{\beta_i}\right) T_{l,i+1} \qquad (5.19)$$

where:-

$$\beta_i = b_i - \frac{a_i c_i}{\beta_{i-1}}$$

$$\gamma_i = \frac{d_i - a_i \gamma_{i-1}}{\beta_i}$$

The solution for $T_{l,i}$ is obtained by first calculating β_i and γ_i values for the nodes starting from the first node

and advancing towards the last node and later calculating $T_{l,i}$ starting from the n'th node and marching backwards.

5.3 FRICTION HEAT FLUX MODEL

The friction heat flux term $q_{l,i,fric}$, is calculated by assuming that all the heat generated by the piston rings and the skirt friction is absorbed by the liner. The total mechanical friction losses in an engine are about 8 to 10% of the total energy input, or 20 to 25% of the indicated power of which, in turn, approximately 19 and 25% are generated at the piston rings and the skirt, respectively. These figures are average values for engines with different numbers of cylinders, auxilaries, types of combustion, speed and load characteristics, and are obtained from [91]. In the cycle simulation package 'SPICE', the mechanical friction is expressed in terms of pressure as friction mean effective pressure (FMEP), and is calculated at the end of each cycle by using the Chen and Flynn (eqn.5.20a), or the Millington and Hartles (eqn.5.20b) empirical correlations, which are defined as:-

$$FMEP = 0.137 + 0.005 P_{max} + 0.162 \bar{V}_p \qquad (5.20a)$$

or

$$FMEP = \frac{CR - 4}{14.5} + 0.0004288 Ne \qquad (5.20b)$$

where:-

FMEP is in bars.

CR is the compression ratio.

P_{max} is the maximum cylinder pressure in bars.

$\bar{V}_p$ is the mean piston speed in m/s, and is given by:-

$$\bar{V}_p = \frac{L_s \times Ne}{30} \qquad (5.21)$$

where L_s is the stroke of the engine in m.

The friction heat flux term for an evenly distributed case is:-

$$q_{l,i,fric} = \frac{10^5 * FMEP * A_p * \bar{V}_p}{A_l} (PRF + PSF) \qquad (5.22)$$

where PRF and PSF are the piston ring and skirt friction fraction, which are taken as 0.19 and 0.25 respectively, and A_p and A_l are the piston and liner surface areas. Substituting the expressions for A_p, A_l and $\bar{V}_p$ in eqn.5.22:-

$$q_{l,i,fric} = 366.6 \times FMEP \times D_p \times Ne \qquad (5.23)$$

where D_p is the piston diameter in m.

In the present model the friction generated heat flux $q_{l,i,fric}$, is calculated from instantaneous friction force and piston velocity. The instantaneous oil film thickness and friction force was measured for each ring and piston assembly in an engine with a bore of 80 mm and a stroke of 102 mm, which is almost the same size as that of the present test rig engine, and reported in [92]. The measured instantaneous normalized friction force is represented by the graph shown in Fig.5.6. The amplitude of the friction force FF^* for the piston assembly was discovered to be a linear function of FMEP and is given by:-

$$FF^* = 291.5\,FMEP - 6.75 \qquad (5.24)$$

where FF^* is in N/m^2.

In the thermal resistance model, the piston lateral surface is divided into rings and skirts sections as shown in Fig.5.5. The ratios of the frictional force generated at the rings and skirt to the

total piston friction force are taken as 0.44 and 0.56 respectively, as suggested in [92]. The friction forces generated at each ring starting from top to oil ring, are chosen as 20, 16, 20 and 44% of the total ring force [92]. Thus, the amplitude of the individual ring forces are expressed as follows:-

$$FF^*_{r,1} = 0.088 FF^* \tag{5.25a}$$

$$FF^*_{r,2} = 0.070 FF^* \tag{5.25b}$$

$$FF^*_{r,3} = 0.088 FF^* \tag{5.25c}$$

$$FF^*_{r,4} = 0.193 FF^* \tag{5.25d}$$

where subscript r,i represents ring i.

The friction force at each piston skirt region j ($FF^*_{sk,j}$), is assumed to be proportional to the surface area and expressed as:-

$$FF^*_{sk,j} = 0.56\left(\frac{SH_j}{SH_t}\right)FF^* \tag{5.25e}$$

where SH_j and SH_t are the heights of skirt region j and total skirt region, respectively.

The total friction heat flux on a liner node i is the summation of the friction heat flux from different parts of the piston, and is expressed as:-

$$q_{l,i,fric} = \sum_{j=1}^{nr}\sum_{k=1}^{NIS}\frac{FF(\theta_k)\times FF^*_{r,j}\times V_p(\theta_k)}{A_{r,j}\times NIS} + \sum_{j=1}^{nr}\sum_{k=1}^{NIS}\frac{FF(\theta_k)\times FF^*_{sk,j}\times V_p(\theta_k)}{A_{sk,j}\times NIS} \tag{5.26}$$

where:-

$FF(\theta_k)$ and $V_p(\theta_k)$ are the instantaneous friction force (obtained from Fig.5.6), and piston velocity,

respectively.

$A_{r,j}$ and $A_{sk,j}$ are the surface areas of ring and skirt region j.

NIS is the number of integration steps.

θ_1 and θ_{NIS} are $\theta 1_{i,j}$ and $\theta 2_{i,j}$, i.e start and end of the interaction between liner node i and piston region j.

The instantaneous piston velocity $V_p(\theta_k)$, is obtained from the time derivative of the equation of motion for piston-crank mechanism, and is given by:-

$$V_p(\theta_k) = \left(\frac{\pi r_{ca} Ne}{30}\right)\left[\mathrm{Sin}\left(\frac{\pi}{180}\theta_k\right) + \frac{r_{ca}\,\mathrm{Sin}\left(\frac{\pi}{90}\theta_k\right)}{2\sqrt{CRL^2 - r_{ca}^2\,\mathrm{Sin}^2\left(\frac{\pi}{180}\theta_k\right)}}\right] \tag{5.27}$$

where r_{ca} and CRL are the crank arm radius and connecting rod length in m, respectively.

5.4 EVALUATION OF PISTON THERMAL RESISTANCES

Although the above formulation is quite detailed, the correct prediction of piston temperature and liner temperature distribution depends on the values of the thermal resistances used in the network. For this reason a computer program is written to provide the values of the thermal resistances in the network for a given set of piston temperature, liner temperature distribution, and gas and coolant side boundary conditions. The formulation of the model is the same as above, the only difference being that instead of specifying the resistances, the temperatures are input and the resistances are obtained. The flowchart of the program is shown in Fig.5.7.

The program is run interactively so that the user can see the effect of various options on the results.

The liner temperature data used are obtained experimentally from 2 sets of thermocouples embedded in the liner. Each set contains 22 thermocouples which are respectively 1 mm and 6 mm away from the liner surface. The related test rig and its instrumentation together with the experimental results are explained in Chapter 8. The liner surface temperature is interpolated from the experimental data by assuming 1-D heat conduction between the thermocouples.

The internal node in the piston is responsible for providing the true temperature difference across the piston and the liner, which makes its position in the piston quite important. It can be chosen at the extreme positions, either at the top or bottom surface of the piston. Choosing it at the top surface produces a high temperature difference between piston and liner and the heat always flows from piston to liner even if the piston and liner are insulated. On the other hand, choosing it at the lower surface results in a negative temperature diffence between the piston and liner, and heat always flows from liner to piston. Therefore, the internal node should be chosen somewhere in the piston which will possess a realistic temperature, i.e. close to the ring package temperature. By this means, the effect of piston and liner insulation on piston-liner conduction heat flux can be correctly observed. The temperature distribution of piston rings and piston is measured with thermocouples in a high speed diesel engine under actual operating conditions and reported in [93]. The measured ring temperatures, shown in Fig.5.8, are used as a reference for the internal node temperature.

In determining the piston internal resistances, the percentage of heat conducted through each part of the piston must also be known. The piston rings play an extremely important part in the piston cooling and it is reported that about 70% of the piston crown heat,

irrespective of the engine operating condition, flows out through the ring zone in the direction of the cylinder [93]. The rest of the piston crown heat is lost through the pin boss, the undercrown surface and the skirt which are shown in Fig.5.9. Although the surface area of the skirt is much greater than that of the rings, the heat transfer is extremely small (about 5%), because of a large clearance beween the skirt and the cylinder wall [93].

The piston internal resistances are expressed in terms of known temperatures as follows:-

Node 1

Using eqns.5.1 and 5.2c:-

$$R_{p,1} = \frac{T_{p,up} - T_{p,int}}{\overline{htc_p T_g} + \overline{\varepsilon_{fl,p} T_{fl}^4} - \overline{htc_p} T_{p,up}} \qquad (5.28)$$

Node 2

Heat loss from the piston to the cooling oil is given by:-

$$A_{p,lw}\left(\frac{T_{p,int} - T_{p,co}}{R_{p,2} - R_{p,co}}\right) = HLC \times A_{p,up}\left(\frac{T_{p,up} - T_{p,int}}{R_{p,1}}\right) \qquad (5.29a)$$

Simplifying:-

$$R_{p,2} + R_{p,co} = \left(\frac{A_{p,lw}}{A_{p,up}}\right)\left(\frac{T_{p,int} - T_{p,co}}{T_{p,up} - T_{p,int}}\right)\left(\frac{R_{p,1}}{HLC}\right) \qquad (5.29b)$$

where HLC is the ratio of piston heat loss to cooling oil through the under crown surface to total piston heat loss, and is taken as 0.25, as suggested in [93].

The heat loss through each piston ring to the liner is expressed as follows:-

$$\sum_{i=1}^{nn} A_{r,j}\,RATP_{i,j}\left(\frac{T_{p,int}-T_{l,i}}{R_{p,j+2}}\right)=HL_j A_{p,up}\left(\frac{T_{p,up}-T_{p,int}}{R_{p,1}}\right) \tag{5.30a}$$

Simplifying:-

$$R_{p,j+2}=\left(\frac{A_{r,j}}{A_{p,up}}\right)\left(\frac{R_{p,1}}{HL_j}\right)\sum_{i=1}^{nn} RATP_{i,j}\left(\frac{T_{p,int}-T_{l,i}}{T_{p,up}-T_{p,int}}\right) \tag{5.30b}$$

where HL_j is the ratio of the heat conducted through ring j to total piston crown heat loss, and is shown in Fig.5.9.

5.5 EVALUATION OF LINER COOLANT HEAT TRANSFER COEFFICIENT

The liner coolant flows in a concentric annular duct which receives heat from the inner surface and loses some of its heat through the outher surface, as shown in Fig.5.4. The continuity, momentum and energy equations were solved in [94] for the case where fully developed laminar flow exists in the annulus with constant heat flux at both surfaces. The local Nusselt numbers for the inner and outer surfaces are given as:-

$$Nu_{in}=\frac{Nu^*_{in}}{1-\left(\frac{q_{w,in}}{q_{w,out}}\right)IC_{in}} \tag{5.31a}$$

$$Nu_{out}=\frac{Nu^*_{out}}{1-\left(\frac{q_{w,out}}{q_{w,in}}\right)IC_{out}} \tag{5.31b}$$

where:-

IC_{in} and IC_{out} are defined as influence coefficients.

Nu^*_{in} and Nu^*_{out} are the Nusselt numbers of the inner and outer surfaces, respectively, when only the one surface is heated.

$\left(\frac{q_{w,in}}{q_{w,out}}\right)$ is the inner to outer wall heat flux ratio.

The values for IC_{in}, IC_{out}, Nu^*_{in} and Nu^*_{out} were obtained from [94], which are expressed in graphical form as a function of outer to inner diameter ratio, D_{out}/D_{in}. The inner to outer wall heat flux term is assumed to be 0.05, i.e. 5% of the absorbed heat is lost through the engine body. The hydraulic diameter D_h, which is used in the Reynolds and Nusselt expressions is defined as:-

$$D_h = D_{out} - D_{in} \tag{5.32}$$

Using the definition of the Nusselt number, the heat transfer coefficient is given by:-

$$htc_{co} = \frac{k_{co} Nu_{in}}{D_h} \tag{5.33}$$

where k_{co} is the coolant conductivity.

The Reynolds number is obtained by using the experimental coolant mass flow rate, assuming that the flow is well within the laminar region. Thus, the above formulation is used to calculate the coolant inner surface heat transfer coefficient which is found to be 655 W/m^2K. When this value was tested in the written resistance model, it raised the liner temperature considerably and did not raise the liner coolant temperature much, suggesting that engine coolant htc is higher than the calculated value. Therefore, a second method was tried to obtain the liner coolant htc where the experimental liner temperature distribution and the coolant inlet and outlet temperatures are used as data.

A heat balance is considered for a concentric annular water element around the liner, as shown in Fig.5.4:-

$$dQ_{co} = htc_{co}\pi D_{in}\left[T_{w,co}(s) - T_{co}(s)\right]ds \qquad (5.34a)$$

Then, the total energy absorbed by the cooling water is given by:-

$$Q_{co} = htc_{co}\pi D_{in}\int_0^S\left[T_{w,co}(s) - T_{co}(s)\right]ds \qquad (5.34b)$$

where $T_{w,co}(s)$ and $T_{co}(s)$ are the liner coolant side wall and coolant temperatures, respectively, and S is the total axial length of the liner.

The coolant side wall temperature term can be expressed in terms of measured temperatures. The second set of thermocouple temperatures near the coolant side are used to describe the 1-D heat flux through the liner. The energy absorbed by the coolant is given by:-

$$Q_{co} = \pi D_{in}\int_0^S\left[\frac{T_{1,2}(s) - T_{w,co}(s)}{R_{1,2-co}}\right]ds \qquad (5.35a)$$

where the integral of coolant side wall temperature can be expressed as:-

$$\int_0^S T_{w,co}(s)ds = \int_0^S T_{1,2}(s)ds - \left(\frac{R_{1,2-co}}{\pi D_{in}}\right)Q_{co} \qquad (5.35b)$$

where:-

$T_{1,2}(s)$ is the second set thermocouple temperatures.

$R_{1,2-co}$ is the liner radial thermal resistance between the second set of thermocouple and liner coolant surface.

The energy absorbed by the coolant is calculated from its mass flow rate and temperature rise which are obtained experimentally,

$$Q_{co} = (\dot{m}Cp\,\Delta T)_{co} \qquad (5.36)$$

Substituting eqns.5.35b and 5.36 into eqn.5.34b and solve for htc_{co}:-

$$htc_{co} = \frac{\pi D_{in}}{(\dot{m}Cp\Delta T)_{co}} \int_0^s \left[\frac{T_{1,2}(s)}{R_{1,2-co} + 1} - T_{co}(s) \right] ds \qquad (5.37a)$$

or expressing in terms of the summation:-

$$htc_{co} = \frac{\pi D_{in}}{(\dot{m}Cp\Delta T)_{co}} \sum_{i=1}^{nn-1} \left(\frac{\bar{T}_{1,2,i}}{R_{1,2-co} + 1} - \bar{T}_{co,i} \right) (s_{i+1} - s_i) \qquad (5.37b)$$

where:-

nn is the number of nodes on the liner.

s_i is the coordinate of node i from the cylinder head.

$\bar{T}_{1,2,i}$ and $\bar{T}_{1,co,i}$ are the average temperatures for the region between the nodes and are defined as:-

$$\bar{T}_{1,2,i} = \frac{T_{1,2,i} + T_{1,2,i+1}}{2}$$

$$\bar{T}_{co,i} = \frac{T_{co,i} + T_{co,i+1}}{2}$$

Eqn.5.37b is solved by iteration. First, a coolant temperature distribution $T_{co}(s)$ is assumed and the coolant htc and the new coolant temperature distribution are obtained. Using the new coolant temperature distribution, a new value of htc for the coolant is calculated and so on. The new coolant temperatures are obtained by considering the heat absorbed by the water as it rises in the annulus:-

$$T_{co}(s - ds) = T_{co}(s) + \frac{\pi D_{in}}{(\dot{m}Cp)_{co}} \left[\frac{T_{1,2}(s) - T_{co}(s)}{R_{1,2-co}} \right] ds \qquad (5.38a)$$

Expressing in terms of nodes:-

$$T_{co,i} = T_{co,i+1} + \frac{\pi D_{in}}{(\dot{m}Cp)_{co}} \frac{\left(\bar{\bar{T}}_{1,2,i} - \bar{\bar{T}}^{-}_{co,i}\right)}{R_{1,2-co}} \left(s_{i+1} - s_i\right) \quad (5.38b)$$

where:-

$$\bar{\bar{T}}^{-}_{co,i} = \frac{T^{-}_{co,i} + T_{co,i+1}}{2}$$

and $T^{-}_{co,i}$ is the previous value for $T_{co,i}$.

Specifying the coolant inlet temperature, the coolant temperature distribution can be obtained from eqn.5.38b, and the coolant exit temperature can be checked with the experimental value. A small computer program was written to obtain the coolant htc. The results showed that the coolant exit temperature converged in 4 to 5 iterations, and it is almost equal to the experimental value. The calculated coolant htc is 2450 W/m^2K, and when it is used in the engine thermal resistance model a better liner temperature distribution was obtained.

The 1-D heat flux in the liner could be directly obtained from the two sets of thermocouple readings but this would increase the potential error in the calculations. The temperature difference between the two thermocouple readings at the same axial postion is only a few degrees (0 to 3 K), and if the heat flux equation is considered, slight temperature reading errors will produce big heat flux errors. However, using a higher temperature difference, such as that between the liner and the coolant will decrease the effect of these experimental errors.

5.6 MODEL CHECKING AND MODIFICATIONS

Using the solution of the piston-liner resistance network, a computer program was written to predict the

piston surface temperature and liner surface temperature distribution, and its flowchart is given in Fig.5.10. To check the model, the predicted liner temperature distribution is compared with the experimental values obtained at 1000 rpm engine speed and A/F ratio of 25:1. The gas side boundary conditions, gas temperature, gas htc and flame radiation used in the model are obtained from the simulation package 'SPICE' at the specified engine operating conditions, which are presented in Figs.5.11 to 5.14. Although the model is quite detailed and the resistance values have been obtained as accurately as possible, the experimental and predicted liner temperature distributions do not match well as shown in Fig.5.15. This is not surprising, because the model is not complete due to the following reasons:-

1) The gas htc for the liner is expected to be lower than the calculated mean spatial value of the combustion chamber, and this difference resulted in higher liner temperatures at the top part of the liner where gas to wall heat transfer is the primary heat source.

2) The liner region where the ring pack stays over it around TDC is cooled by oil evaporation due to high gas temperatures.

3) The lower part of the liner is cooled by oil splash.

4) Some heat is absorbed by the oil film between the piston and the liner, and transferred to the oil sump as the piston reciprocates.

It is quite difficult to write the mathematical models for the above events. Thus, simple terms and scaling factors are introduced to the model to represent them. The modified theoretical and experimental liner temperature distributions, based on scaling htc's and resistance values, are shown in Fig.5.16. As can be seen, they are well matched except for the lower part of the liner which can be due to the complex oil splash and/or due to entrance effects of the coolant. However, this part of the liner temperature is not significant at

all for both gas to wall and piston-liner conduction heat transfer calculations.

In matching the experimental and theoretical liner temperature distribution, two gas htc scaling factors are used for liner regions 1 and 2, shown in Fig.5.5, to control the temperatures at the top part of the liner. The effect of ignoring the htc scaling factors on liner temperature distribution is presented in Fig.5.17, which is obtained by fixing the values of htc scaling factors to 1. This caused a temperature increase mainly in the top part of the liner, since the convective component is the dominant heat transfer mode in this region. The temperature at the cylinder head and liner junction is raised by about 40 K higher than the experimental value, introducing an error of 12%. For a ceramic liner, not implementing the gas htc scaling factors, is expected to raise the difference between the predicted and actual temperature distribution further. However, ignoring the htc scaling factors in the resistance model affected very little the temperature distribution in the middle and lower parts of the liner, raising it by about 2 to 3 K. This is not surprising, since the piston-liner conduction and friction are the dominant heat fluxes in these regions.

The effects of scaling factors are also investigated separately. It is assumed that there is no convective heat transfer in the liner region 2, shown in Fig.5.5, and thus the value of the htc scaling factor for this region was set to zero. The matching of experimental and theoretical liner temperature distributions is achieved by using a higher htc scaling factor for liner region 1, and the result is presented in Fig.5.18. Comparing Figs.5.16 and 5.18, suggests that the gas htc applies equally to liner regions 1 and 2, and therefore the same htc scaling factors should be used for both regions, being 0.44 for this specific engine condition.

The oil evaporative cooling is represented by using a high coolant htc for the liner region covered by the ring pack TDC position and is expressed linearly as:-

$$R_{co} = \left(\frac{R_{co} - R_{co,TDC}}{0.25 L_s} \right) (s - s_{TDC}) + R_{co,TDC} \qquad (5.39)$$

for the liner region $s_{TDC} < s < s_{TDC+0.25L_s}$.

where:-

R_{co} is the liner coolant convective resistance.

$R_{co,TDC}$ is the value of R_{co} at TDC, obtained by matching the experimental and theoretical results.

L_s is the engine stroke.

s is the axial distance measured from the cylinder head.

The effect of oil evaporative cooling is demonstrated in Fig.5.19. Keeping the coolant htc constant over the entire liner length, raises the gas side liner temperature by about 0 to 8 K depending on the axial position, in the vicinity of the ring pack TDC position. This suggests that, for certain reasons, excessive cooling occurs in this region, being most probably caused by oil evaporation after coming into contact with the hot combustion gases. This effect is controlled by using the higher coolant htc given by eqn.5.39.

The heat absorbed by the oil film between piston and liner and by oil splash, has already been included in the solution of the resistance network in eqn.5.10, and is defined by a simple term in eqn.5.14. The results showed that the assumed relation had to be modified and expressed as proportional to the cube of time factor TF_i, to adjust the excessive cooling of the lower part of the liner by oil splash. It is defined as:-

$$q_{l,i,oil} = TF_i^3 \frac{T_{l,i} - T_{oil}}{R_{oil}} \qquad (5.14a)$$

where TF_i is given by eqn.5.15. The value of the oil film resistance R_{oil} is determined through the matching exercise of the experimental and theoretical values.

The effects of different oil film cooling terms, i.e. eqns.5.14 and 5.14a, can be seen in Figs.5.16 and 5.21. Eqn.5.14a seems to represent the oil film cooling better except at the bottom end of the liner which is in the oil splash region and is very difficult to model. The difference between the experimental and theoretical values at this end of the liner could also be due to entrance effects of the cooling water. Since the combustion gases do not come into contact with lower part of the liner, the temperature distribution in this region is not significant at all in gas heat loss calculations.

The effect of not using an oil film cooling term, causing higher temperatures of about 5 to 15 K in the lower part of the liner is also demonstrated in Fig.5.20.

In order to observe the influence of axial resistances on the solution, the temperature distribution for the liner with only radial resistances is presented in Fig.5.22. As can be seen the predicted temperature curve is not as smooth as the original curve given in Fig.5.16, because of the missing conduction term in the axial direction. Differences between predicted and experimental temperatures are mainly in the top part of the liner; where the liner joins the cylinder head this difference approaches 20 K.

For higher coolant htc's, the experimental and theoretical liner temperature distributions can be matched by raising the coolant temperature, as shown in Fig.5.23. Although the matching is not as good as for

the original case shown in Fig.5.16, it is still satisfactory. This underlines the significance of using the true value of coolant htc in the matching studies, in order to obtain the correct values for the scaling factors and thermal resistances. The method of obtaining the coolant htc has already been explained in the previous section.

In the model, the liner coolant inlet temperature is specified, and the coolant temperature distribution in the axial direction is evaluated by using the following equation:-

$$T_{co,i} = T_{co,i+1} + \frac{\pi D_{in}}{(\dot{m}Cp)_{co}} \frac{\left(\bar{T}_{l,i} - \bar{T}_{co,i}\right)}{\left(R_l + R_{l,co}\right)} \left(s_{i+1} - s_i\right) \quad (5.38\,c)$$

which is the same as eqn.5.38b, except that the experimental mean liner temperature $\bar{T}_{l,2,i}$, is replaced by the calculated mean liner temperature $\bar{T}_{l,i}$, i.e. mean temperature of nodes i and i + 1.

In the computational code, an iterative solution is adopted to evaluate the liner and coolant temperature distributions. Initially, a coolant temperature distribution is assumed in the axial direction, and the liner and updated coolant temperature distributions are calculated. This is repeated several times until the coolant temperature distribution has converged; this takes about 4 to 5 iteration cycles. The obtained coolant temperature distribution is almost linear and is presented in Fig.5.24.

The effect of constant and variable coolant temperature on the liner temperature distribution is shown in Fig.5.25. The value used for the constant coolant temperature is the mean bulk temperature of the variable coolant temperature case. Using the method which accounts for the actual coolant temperature increase within the cooling channel produced higher liner temperatures in the top part and lower

temperatures in the bottom part of the liner of about 4 K. At higher loads and engine speeds where the coolant temperature difference between the inlet and exit is expected to rise, the difference between the liner temperatures obtained by constant and variable coolant temperature methods will further increase.

The total piston-liner conduction heat flux and its components for each ring and skirt are shown in Fig.5.26. The oil ring is ignored because it is near the bottom end of the piston and thus its temperature is much lower than that of the other rings. Even if it is near the ring pack, as stated in [93], more than 70% of its heat flows into the oil sump with the oil, rather than to the liner. The piston-liner conduction heat flux is higher around TDC and BDC since the piston stays for longer periods over these positions. The conduction heat flux at BDC is higher than at TDC because the ring (internal node) to liner temperature difference is higher at BDC.

The liner total mean heat flux and its components, i.e. radiation, convection, friction generated heat and piston-liner conduction heat flux, as a function of axial distance are shown in Fig.5.27. Radiation and convection heat transfer forms the main heat source for the top part of the liner, whereas for the region where the rings travel piston-liner conduction is the dominant heat source for the liner. Friction heat flux seems to be not very significant, however its influence is expected to increase at higher loads and engine speeds.

The effects of oil film cooling and oil evaporative cooling on total heat flux are shown in Fig.5.28. They are obtained by matching the theoretical and experimental results and as it can be seen their magnitudes are quite high compared with the total heat flux falling on the liner surface.

The axial heat flux on the liner surface is

expressed as the axial heat flux arriving at and leaving the nodes, and their difference and they are given in Fig.5.29. At the top and bottom parts of the liner the axial heat flux component is quite important, whereas in the middle it is almost zero. The difference of axial heat fluxes arriving at and leaving a node shows the amount of heat transferred from the axial to the radial direction or vice versa, depending on the sign of the difference. In the regions where oil evaporative and oil splash cooling occurs, some of the axial heat flux is absorbed due to excessive cooling effect, and as a result of this high positive flux peaks occur in these regions.

The net radial heat flux conducted to the liner coolant for each node is the summation of the net radial heat flux input from the gas side and the difference in axial fluxes arriving at and leaving the node. These fluxes are given in Fig.5.30. The net coolant radial heat flux has almost the same shape as the liner temperature curve.

The piston is divided into several rings and skirts sections; the friction heat fluxes generated by each section and their total are shown in Fig.5.31. The generated frictional heat flux for each section is obtained by the multiplication of the instantaneous frictional force, piston velocity and contact time between that region and the liner node. Their overall effect almost results in a constant frictional heat flux on the liner from each section of the piston. The total frictional heat flux at each liner node mainly depends on the postions of the rings on the piston.

The effects of the combined radiation plus convection, friction and piston-liner conduction heat fluxes on the liner temperature distribution are given in Fig.5.32. The value of the liner coolant inlet temperature is chosen as 335 K. The radiation and convection terms are effective mainly in the top part of

convection terms are effective mainly in the top part of the liner and contribute little to the rest of the liner. The piston-liner conduction and friction heat fluxes are the main heat sources for the middle and lower parts of the liner. However, conduction and friction heat fluxes also influence top liner temperatures amounting for a shift of about 8 K upwards (Fig.5.32), because of reduced conduction heat transfer in the axial direction.

5.7 THE POSITION OF AXIAL RESISTANCES IN AN INSULATED ENGINE

Undoubtedly, in a ceramic coated liner, the axial resistances at the ceramic surface are much higher than the axial resistances in the metal substrate. However, the axial temperature gradients are greater at the ceramic surface than in the metal substrate. In order to understand whether the axial heat flux is dominant on the ceramic surface or in the metal substrate, the thermal resistance model is modified to include an option, so that the position of the axial resistances can either be on the ceramic surface or at the ceramic-metal interface. The solution of the thermal resistance network with axial resistances at the ceramic-metal interface (Fig.5.2b), is obtained by taking heat balances around internal and surface nodes i and i', respectively:-

Node i

$$-\frac{T_{l,i'}-T_{l,i}}{R_c}-\frac{T_{l,i-1}-T_{l,i}}{R_{l,i,i-1}}+\frac{T_{l,i}-T_{l,i+1}}{R_{l,i,i+1}}+\frac{T_{l,i}-T_{l,co,i}}{R_{l,i}+R_{l,co}}=0 \qquad (5.40a)$$

Re-arranging eqn.5.40a:-

$$\frac{T_{l,i-1}}{R_{l,i,i-1}} + \left(\frac{1}{R_c} + \frac{1}{R_{l,i,i-1}} + \frac{1}{R_{l,i,i+1}} + \frac{1}{R_{l,i}+R_{l,co}}\right)T_{l,i} - \frac{T_{l,i+1}}{R_{l,i,i+1}} - \frac{T_{l,i'}}{R_c} - \frac{T_{l,co,i}}{R_{l,i}+R_{l,co}} = 0 \quad (5.40b)$$

where R_c is the thermal resistance of the ceramic layer and the other notations are explained in the previous resistance network solution.

Node i'

$$q_{l,i',conv} + q_{l,i',rad} + q_{l,i',cond} + q_{l,i',fric} - q_{l,i',oil} = \frac{T_{l,i'} - T_{l,i}}{R_c} \quad (5.41)$$

where the heat flux terms are given in eqns.5.11, 5.12, 5.14 and 5.26. Substituting only the flux terms which are functions of liner surface temperature and solving for liner surface temperature, gives:-

$$T_{l,i'} = \frac{\overline{htc_{l,i'}}\,T_g + \overline{\varepsilon_{fl,l,i'}}\,T_{fl}^4 + \sum_{j=1}^{nr} RATL_{i',j}\frac{T_{p,int}}{R_{p,j+2}} + q_{l,i',fric} + TF_{i'}\frac{T_{oil}}{R_{oil}} + \frac{T_{l,i}}{R_c}}{\overline{htc_{l,i'}} + \sum_{j=1}^{nr}\frac{RATL_{i',j}}{R_{p,j+2}} + \frac{TF_{i'}}{R_{oil}} + \frac{1}{R_c}} \quad (5.42)$$

Substituting eqn.5.42 into eqn.5.40b and expressing it in the following form, as already shown in Sec.5.2:-

$$a_i T_{l,i-1} + b_i T_{l,i} + c_i T_{l,i+1} = d_i \quad (5.18)$$

yields the following coefficients:-

$$a_i = -\frac{1}{R_{l,i,i-1}}$$

$$b_i = \frac{1}{R_c} + \frac{1}{R_{l,i,i-1}} + \frac{1}{R_{l,i,i+1}} + \frac{1}{R_{l,i} + R_{l,co}} - \frac{1}{R_c^2\left(\overline{htc}_{l,i'} + \sum_{j=1}^{nr}\frac{RATL_{i',j}}{R_{p,j+2}} + \frac{TF_{i'}}{R_{oil}} + \frac{1}{R_c}\right)}$$

$$c_i = -\frac{1}{R_{l,i,i+1}}$$

$$d_i = -\frac{\overline{htc}_{l,i'}T_g + \overline{\varepsilon}_{fl,l,i'}T_{fl}^4 + \sum_{j=1}^{nr}RATL_{i',j}\frac{T_{p,int}}{R_{p,j+2}} + q_{l,i',fric} + TF_{i'}\frac{T_{oil}}{R_{oil}}}{R_c\left(\overline{htc}_{l,i'} + \sum_{j=1}^{nr}\frac{RATL_{i',j}}{R_{p,j+2}} + \frac{TF_{i'}}{R_{oil}} + \frac{1}{R_c}\right)} + \frac{T_{l,co,i}}{R_{l,i} + R_{l,co}}$$

The matrix eqn.5.18 is solved by the Gaussian elimination method as mentioned before and the internal node temperatures $T_{l,i}$'s are obtained. Then, the internal node temperatures are used to obtain the surface temperatures $T_{l,i'}$'s, from eqn.5.42.

The liner is insulated with 3 mm PSZ coating and tested for both solutions. The result is shown in Fig.5.33, which suggests that the axial resistances on the surface give better prediction since it has less steep temperature gradients in the axial direction. Therefore, it is concluded that axial resistances should be kept at the liner surface for both standard and insulated liner.

5.8 LINER TEMPERATURE DISTRIBUTION WITH VARIOUS INSULATION SCHEMES

The piston-liner resistance model is used to obtain the liner temperature distribution for different

insulation schemes, and thus to observe the influence of piston and/or liner insulation.

In the solution of the thermal resistance network, the piston internal node temperature is calculated by ignoring the axial heat flow in the liner region where the piston rings travel (Eqn.5.17). By this means, an error of about 0 to 5% is introduced in the piston heat balance for both standard and surface insulated parts. However, for an externally insulated liner, i.e. liner with reduced cooling capacity, the piston heat balance error rises upto 37%. This is not surprising, since the axial conduction heat flux gains more importance with this type of insulation. Thus, an iteration loop is added to the thermal resistance model to update the piston internal node temperature, and hence reduce the piston heat balance error to zero. The results without and with corrected piston internal node temperatures are shown in Tables 5.1 and 5.2, respectively.

Various combinations of piston and liner insulation, which can be seen in Tables 5.1 or 5.2 together with piston temperature and heat flux data, are used to show their effects on the liner temperature distribution. In all cases, two insulation levels of 1.5 and 3.0 mm PSZ coating with an assumed conductivity of 0.6 W/mK are used. The same gas side boundary conditions are applied, irrespective of the insulation type, and are shown in Figs.5.11 to 5.14. However, in practice, engine insulation raises the gas htc, temperature and flame radiation, and the final effect of insulation can only be fully assessed when the wall model is linked with the cycle simulation package 'SPICE'. The present insulation study in this chapter, simply shows the significance of insulating the different parts of the combustion chamber and their possible effects on piston and liner temperature distribution.

The piston temperature and flux data for all types of insulation schemes is shown in Table 5.2. The piston mean surface temperature is raised from 473.1 K to 805.8 K and 978.4 K for the two specified piston insulation levels, i.e. 1.5 and 3.0 mm PSZ coating. By this means, the piston mean heat flux is reduced to 68.4 and 51.9%, respectively, of its original value. However, piston internal node temperature is reduced from 418.5 K to 395.0 K and 382.8 K, respectively, with piston insulation, thus decreasing the temperature difference between piston and liner. As a result of this, liner temperatures are reduced by about 2 to 8 K, especially in the middle section. The effect of piston insulation on liner temperature and flux distribution is given in Figs.5.34 to 5.36. The total piston liner conduction heat flux is reduced to 66.5 and 49.2%, respectively, of its original value with the two insulation levels.

The effect of liner insulation on the liner temperature and flux data is given in Figs.5.37 to 5.39. The liner temperature distribution, as expected, is shifted upwards, top liner temperature being raised to 820 K. Due to the higher liner temperatures created by insulation, the piston-liner conduction heat flux changes direction, i.e. heat flows from liner to piston, in the TDC ring pack region. However, with increasing insulation the overall heat loss from the liner which is calculated from the liner coolant temperature rise, drops. A decrease of 69.5 and 53.4%, respectively, in the liner heat loss is found for the two specified insulation levels. However, this does not mean that the same degree of heat loss reduction occurs in the case of gas to wall heat transfer, since the main heat sources for the liner are piston-liner conduction and friction heat fluxes. Insulation of the liner, especially in the middle and lower parts, simply diverts the heat path from piston-liner to piston-undercrown oil. Insulation of the liner with 3 mm PSZ increases the piston oil heat

loss from 25 to 47% of the total piston heat loss. The only benefit obtained by insulating the middle and lower parts of the liner is the increase in the piston internal node temperature, which reduces the gas to piton crown heat flux. A 3 mm PSZ coating on the liner surface causes a 6% reduction in piston heat flux. However, this effect is expected to reduce drastically with piston insulation.

The effect of piston plus liner insulation on the liner temperature and flux distribution is shown in Figs.5.40 to 5.42. The piston and liner insulation leads to an increase in piston mean surface temperature of approximately 25 K, compared with the piston only insulated case, reducing the gas to piston crown heat flux by a further 2.3%, based on the uninsulated case. Due to insulation of the piston, the piston internal node temperature decreases, and insulation of the liner further reduces the positive temperature difference between piston and liner in the lower part and actually making it negative in the upper part. Thus, the total conductive heat flux from piston to liner reduces drastically to 26.7% of the uninsulated case. The cooling effect of the rings in the top part of the liner is so high that, the net or total heat flux in this region almost approaches zero. The heat loss from the piston to piston cooling oil increases from 25 to 59.3% of the total piston heat loss for the 3 mm PSZ coated case, indicating the significant change in the heat path.

The liner temperature distribution for the insulated piston plus liner and for the other insulation types is shown in Fig.5.43. The top part of the liner which is not in contact with the rings, has almost the same temperatures as in the case where only the liner is insulated. The temperatures for the region where the piston rings travel are lower than in the liner only insulated case because of the reduction in the

piston-liner heat conduction.

The effects of insulating only the top part of the liner on the liner temperature and flux distributions are shown in Figs.5.54 to 5.46. The temperatures in the top part of the liner increases and, as expected, no change occurs over the rest of the liner and piston. The total liner heat loss is reduced to 94.3 and 92.0%, respectively, of its original value by the two insulation levels.

The results of insulating both the top part of the liner and piston are shown in Figs.5.47 to 5.49. The temperatures in the top part of the liner increases as in the previous case, whereas in the region which is in contact with the piston rings, there is a slight drop of about 2 K because of the reduction in piston-liner heat conduction.

The liner temperature distributions for the three cases of uninsulated liner, insulated liner top section, and an insulated liner top section plus insulated piston are given in Fig.5.50. Insulation of the piston causes a slight decrease in the middle and lower parts of the liner.

Finally, the liner is insulated externally, i.e. reduction of cooling capacity. The results for both liner insulation only and liner plus piston insulation are presented in Figs.5.51 to 5.57. External insulation increases the axial heat flux component at the surface of the liner, and produces a smooth liner surface temperature curve. It is quite difficult with this form of insulation to raise the temperature of the top part of the liner; this has a strong effect on the gas heat loss. The temperatures in the middle and bottom sections of the liner are higher than in the internally insulated case. As a result of this, excessive cooling of the top part of the liner occurs in the region of the TDC ring pack section so that the net heat flow in this region is from liner to piston (Fig.5.56). The piston to oil heat

flux increases from 25 to 69.4% of the total piston heat flux, indicating the significant change in the heat path. Due to the high conductivity of the liner surface, piston insulation decreases the liner temperature distribution by about 30 to 40 K all over the liner surface (Fig.5.57).

5.9 INCORPORATING THE PISTON-LINER RESISTANCE MODEL IN SPICE

After testing the piston-liner resistance model with varios insulation schemes in the previous section, it was modified and adopted to the simulation package 'SPICE'. By this means, the liner temperature distribution can be predicted at various engine operating conditions. The direction of the heat path between the piston and a liner node, which is dependent on the axial liner node position and the level of insulation of both piston and liner, is determined within the model. This characteristic of the model together with the detailed interaction between the piston and liner nodes makes the resistance model particularly suitable for insulated engine applications. The predicted liner temperature disribution, especially in the TDC ring pack section, can give us the necessary information about oil film temperature conditions which become very significant in insulated diesel engines. The flowchart of the piston-liner thermal resistance model for 'SPICE' is presented in Fig.5.58.

Although the resistance model is very comprehensive, its effect on the total simulation computing time is not significant, because the calculations are performed at the end of each cycle. The mean cycle frictional heat flux for each liner node is provided to the model by the 'Fric.For' subroutine which is generated from the instantaneous piston-liner friction force data. The cycle cumulative values for the gas side boundary conditions at each liner node are

calculated throughout the cycle by the subroutine 'Resdat.For', and averaged at the end of the cycle in the resistance model. The flowcharts for 'Fric.For' and 'Resdat.For' are given in Figs.5.59 and 5.60.

CHAPTER 6
TEMPERATURE TRANSIENTS ON ENGINE COMBUSTION CHAMBER WALLS

6.1 INTRODUCTION

In IC engines, due to highly unsteady nature of the gas to wall heat transfer, as mentioned in Sec.2.2.3, temperature transients are produced within a thin layer of the wall adjacent to the combustion chamber. This thin layer is referred to as the thermal penetration depth or thickness (TPD), and it is in the range of 0.5 to 10 mm, depending on the thermal properties of the material.

The wall surface temperature fluctuates about a mean value, where the magnitude of the temperature swing for metals is in the order of 10 to 20 K which is about 1% of the cylinder gas temperature swing. Thus, in cycle simulation studies, the constant wall surface temperature assumption for heat transfer calculations is quite appropriate. However, with the concept of the adiabatic diesel engine where low conductivity materials will be used for the combustion chamber, the wall temperature swing can reach ±150 K. This makes the constant wall temperature assumption for heat transfer calculations inappropriate.

The transient temperature wave produced at the gas-wall interface propagates through the TPD before being damped out by the thermal inertia of the material (Fig.6.1). Comparing the temperature gradients perpendicular and parallel to the surface, it is obvious that the temperature gradients across the material are much more severe. This makes 1-D analysis of the transient heat conduction within the TPD quite sufficient and this is the general approach adopted by most researchers.

To study the effects of the wall temperature swing on engine performance, a 1-D time dependent finite difference (FD) heat conduction model was developed. The model has the capability to handle different material layers together with temperature dependent thermal properties. A free standing 1-D FD model which is also applicable for cylindrical and spherical coordinate systems was first developed and tested. Then, a modified version of FD model was incorporated in the cycle simulation package 'SPICE', by joining it to the engine resistance network shown in Fig.5.2. The free standing FD model is a more general code which can be applied to a wide range of boundary conditions. It can also perform the Fourier analysis of any input function and calculate the wall temperature swing for the required harmonic function.

Although the developed FD model produces more accurate heat transfer calculations for cycle simulation, it can also provide us with the temperature wave through the material which is quite significant for thermal stresses. The maximum surface temperature provided by the model can also help us to predict the liner lubrication conditions and material failure under insulated conditions.

6.2 FINITE DIFFERENCE FORMULATION

The 1-D unsteady state heat conduction problem may be formulated by using one of three different FD methods which are known as the explicit, implicit and Crank-Nicholson method. The difference in these methods arises from the time derivative of temperature $\partial T/\partial t$, which can be approximated in terms of central, backward, or forward differences. Each method has different error levels and stability properties.

The explicit method which uses the forward difference approach yields uncoupled FD equations, and therefore is easy to solve for the temperature

distribution. However, its solution is not always stable and it introduces a restriction on the time and displacement intervals. The implicit method which employs a backward difference approach produces coupled equations, and is therefore difficult to solve. However, its solution is always stable. The third, Crank-Nicholson method uses the arithmetic average of the explicit and implicit equations which results in slightly more complicated equations than the implicit method. On the other hand, the solution is stable for all values of time and displacement intervals, and it is more accurate than the other two methods. The truncation errors introduced by discretizing the displacement and time domains are in the order of magnitude of $[\Delta t+\Delta x^2]$ for the explicit and implicit methods, and $[\Delta t^2+\Delta x^2]$ for the Crank-Nicholson method. For reasons of better accuracy, the Crank-Nicholson method was chosen in this project.

The FD equations can be directly obtained by discretizing the 1-D unsteady state heat conduction equation. However, in this study, inorder to accommodate the temperature dependent material properties and variable grid sizing, the more general approach, i.e. the energy balance and rate equations are used to derive the FD equations. The variable grid sizing which is shown in Fig.6.2, allowed the use of very thin layers near the surface and thicker layers within the material. By this means, the computing time is kept to minimum.

6.2.1 Internal Nodes

The FD equation for the internal nodes is obtained by using an energy balance for the control volume (CV) around node i, where unit lengths are considered in the y and z directions (Fig.6.2). The equation is given as:

$$\frac{k_{i,i-1}\left(T_i - T_{i-1}\right)}{\Delta x_{i,i-1}} - \frac{k_{i,i+1}\left(T_i - T_{i+1}\right)}{\Delta x_{i,i+1}} = -\frac{m_i Cp_i\left(T_i - T_i^+\right)}{\Delta t} \tag{6.1}$$

where:-

T_i, T_{i-1} and T_{i+1} are the temperatures at nodes i, $i-1$ and $i+1$, respectively.

$k_{i,i-1}$ and $k_{i,i+1}$ are the thermal conductivities between nodes i, $i-1$ and i, $i+1$.

$\Delta x_{i,i-1}$ and $\Delta x_{i,i+1}$ are the distances between nodes i, $i-1$, and i, $i+1$.

m_i is the mass of CV i.

Cp_i is the specific heat capacity of CV i.

Δt is the time interval.

+ denotes the future values.

Assume that the left and right side of node i are different materials, then the $m_i Cp_i$ term can be expressed by:-

$$m_i Cp_i = \rho_{i,l} V_{i,l} Cp_{i,l} + \rho_{i,r} V_{i,r} Cp_{i,r} \tag{6.2}$$

where ρ and V are density and volume, and subscripts i,l and i,r represent the left and right side of CV i.

Thermal Diffusivity is defined by:-

$$\alpha = \frac{k}{\rho Cp} \tag{6.3}$$

Using eqn.6.3 and replacing volume terms by nodal distances, eqn.6.2 can be expressed by:-

$$m_i Cp_i = \left(\frac{k}{\alpha}\right)_{i,l}\left(\frac{\Delta x_{i,i-1}}{2}\right) + \left(\frac{k}{\alpha}\right)_{i,r}\left(\frac{\Delta x_{i,i+1}}{2}\right) \tag{6.4}$$

Substitute eqn.6.4 into eqn.6.1 and rearrange it:-

$$T_i^+ - T_i = -\frac{2k_{i,i-1}\left(T_i - T_{i-1}\right)\Delta t}{\Delta x_{i,i-1}^2\left(\frac{k}{\alpha}\right)_{i,l}\left[1+\left(\frac{k_{i,r}}{k_{i,l}}\right)\left(\frac{\alpha_{i,l}}{\alpha_{i,r}}\right)\left(\frac{\Delta x_{i,i+1}}{\Delta x_{i,i-1}}\right)\right]}$$

$$-\frac{2k_{i,i+1}\left(T_i - T_{i+1}\right)\Delta t}{\Delta x_{i,i+1}^2\left(\frac{k}{\alpha}\right)_{i,r}\left[\left(\frac{k_{i,l}}{k_{i,r}}\right)\left(\frac{\alpha_{i,r}}{\alpha_{i,l}}\right)\left(\frac{\Delta x_{i,i-1}}{\Delta x_{i,i+1}}\right)+1\right]} \quad (6.5)$$

The above equation suggests that two Fourier numbers should be defined for node i, one for the left and the other for the right side:-

$$Fo_{i,l} = \frac{\alpha_{i,l}\Delta t}{\Delta x_{i,i-1}^2} \quad (6.6a)$$

$$Fo_{i,r} = \frac{\alpha_{i,r}\Delta t}{\Delta x_{i,i+1}^2} \quad (6.6b)$$

Using a simpler notation for the ratios in eqn.6.5:-

$$R1 = \frac{k_{i,l}}{k_{i,r}} \quad (6.7a)$$

$$R2 = \frac{\alpha_{i,l}}{\alpha_{i,r}} \quad (6.7b)$$

$$R3 = \frac{\Delta x_{i,i-1}}{\Delta x_{i,i+1}} \quad (6.7c)$$

$$R4 = \frac{k_{i,i-1}}{k_{i,l}} \quad (6.7d)$$

$$R5 = \frac{k_{i,i+1}}{k_{i,r}} \quad (6.7e)$$

Substituting eqns.6.6 to 6.7e into eqn.6.5 yields:-

$$T_i^+ - T_i = -\frac{2\left(T_i - T_{i-1}\right)Fo_{i,l}\,R4}{\left(1+\frac{R2}{R1\times R3}\right)} - \frac{2\left(T_i - T_{i+1}\right)Fo_{i,r}\,R5}{\left(\frac{R1\times R3}{R2}+1\right)} \quad (6.8)$$

Defining RR by:-

$$RR = \frac{R2}{R1\times R3} \quad (6.9)$$

Subsituting eqn.6.9 into eqn.6.8 and rearranging it:-

$$T_i^+ - T_i = 2\frac{Fo_{i,l}\,R4}{(1+RR)}T_{i-1} - 2\left[\frac{Fo_{i,l}\,R4}{(1+RR)} + \frac{Fo_{i,r}\,R5\times RR}{(1+RR)}\right]T_i + 2\frac{Fo_{i,r}\,R5\times RR}{(1+RR)}T_{i+1} \quad (6.10)$$

Defining an overall Fourier number for the left and right side of node i, as:-

$$F_{i,l} = \frac{Fo_{i,l}\,R4}{(1+RR)} \quad (6.11a)$$

and

$$F_{i,r} = \frac{Fo_{i,r}\,R5\times RR}{(1+RR)} \quad (6.11b)$$

Using eqns.6.11a and 6.11b, eqn.6.10 can be reduced to:-

$$T_i^+ - T_i = 2F_{i,l}\,T_{i-1} - 2\left(F_{i,l}+F_{i,r}\right)T_i + 2F_{i,r}\,T_{i+1} \quad (6.12)$$

Applying Crank-Nicholson method which uses the arithmetic mean of the explicit and implicit methods yields:-

$$T_i^+ - T_i = \frac{1}{2}\Big[2F_{i,l}T_{i-1} - 2\big(F_{i,l}+F_{i,r}\big)T_i + 2F_{i,r}T_{i+1} + 2F_{i,l}T_{i-1}^+ - 2\big(F_{i,l}+F_{i,r}\big)T_i^+ + 2F_{i,r}T_{i+1}^+\Big] \quad (6.13)$$

Arranging eqn.6.13 in the following form:-

$$a_i T_{i-1}^+ + b_i T_i^+ + c_i T_{i+1}^+ = d_i \quad (6.14)$$

gives the coefficients by:-

$$a_i = -F_{i,l} \quad (6.15a)$$

$$b_i = F_{i,l} + F_{i,r} + 1 \quad (6.15b)$$

$$c_i = -F_{i,r} \quad (6.15c)$$

$$d_i = F_{i,l}T_{i-1} - \big(F_{i,l} + F_{i,r} - 1\big)T_i + F_{i,r}T_{i+1} \quad (6.15d)$$

6.2.2 Gas Side Boundary Conditions

The gas side boundary conditions for the wall are convective and radiative heat fluxes. The radiative heat flux equation is non-linear and therefore expressing it in terms of flame and wall temperatures requires an iterative solution, which will greatly increase the computing time. In this project, a simpler solution is adopted by using a net radiative heat flux at the wall boundary which is calculated at every degree CA from the radiative equation by using the wall temperature at the previous time step (CA). By this means, the solution is kept simple and the accuracy of the results is hardly affected since the wall temperature changes only slightly between each time step, and for radiative heat transfer where the flame temperature is the dominant one, this has no significance at all.

Using the energy balance for the CV 1 shown in Fig.6.2:-

$$-htc\left(T_1 - T_g\right) + q_{rad} - \left(\frac{k_{1,2}}{\Delta x_{1,2}}\right)\left(T_1 - T_2\right) = \frac{m_1 Cp_1\left(T_1^+ - T_1\right)}{\Delta t} \tag{6.16}$$

Using eqn.6.4 and multiplying eqn.6.16 by $\left(\frac{\Delta x_{1,2}}{k_{1,2}}\right)$ gives:-

$$-\left(\frac{htc \times \Delta x_{1,2}}{k_{1,2}}\right)\left(T_1 - T_g\right) + q_{rad}\left(\frac{\Delta x_{1,2}}{k_{1,2}}\right) - \left(T_1 - T_2\right) = \left(\frac{\Delta x_{1,2}}{2}\right)\left(\frac{\Delta x_{1,2}}{k_{1,2}}\right)\left(\frac{k}{\alpha}\right)_{1,r} \frac{\left(T_1^+ - T_1\right)}{\Delta t} \tag{6.17}$$

The Biot number is defined by:-

$$Bi = \frac{htc \times \Delta x}{k} \tag{6.18}$$

Using the definitions of Biot number, right Fourier number and ratio R5, eqn.6.17 can be reduced to:-

$$T_1^+ - T_1 = 2Fo_{1,r} R5\left[Bi_1 T_g - \left(Bi_1 + 1\right)T_1 + T_2 + q_{rad}\left(\frac{\Delta x_{1,2}}{k_{1,2}}\right)\right] \tag{6.19}$$

Applying the Crank-Nicholson method and arranging the equation in the form presented by eqn.6.14, gives the following coefficients:-

$$a_1 = 0 \tag{6.20a}$$

$$b_1 = Fo_{1,r} R5\left(Bi_1^+ + 1\right) + 1 \tag{6.20b}$$

$$c_1 = -Fo_{1,r} R5 \tag{6.20c}$$

$$d_1 = Fo_{1,r} R5\left(Bi_1 T_g + Bi_1^+ T_g^+\right) - \left[\left(Bi_1 + 1\right)Fo_{1,r} R5 - 1\right]T_1$$
$$+ Fo_{1,r} R5 \times T_2 + Fo_{1,r} R5\left(\frac{\Delta x_{1,2}}{k_{1,2}}\right)\left(q_{rad} + q_{rad}^+\right) \quad (6.20d)$$

The applied boundary conditions are suitable for the piston and cylinder head. However, for the liner nodes where the piston reciprocates over them, the boundary conditions can be either convective plus radiative, only convective, or conductive and frictional heat fluxes, depending on the position of the piston. The above derived equations are still valid for the three types of gas side boundary conditions. For liner region 2 which is shown in Fig.5.5, the q_{rad} and q^+_{rad} terms are taken as zero. For positions below region 2, the radiative heat flux is replaced by the frictional heat flux and the Biot number is modified for the conductive heat flux by:-

$$Bi_1 = Bi_1^+ = \frac{\Delta x_{1,2}}{R_{p,j} k_{1,2}} \quad (6.21)$$

where $R_{p,j}$ is the internal resistance of the piston passing through ring j (Chapter 5). The present and future Biot numbers are equal because the piston internal node temperature is constant throughout the cycle.

The present and future gas temperatures T_g and T_g^+ in eqn.6.20d are replaced by the piston internal node temperature $T_{p,int}$, and eqn.6.20d simplifies to:-

$$d_1 = 2Fo_{1,r} R5 \times Bi_1 T_{p,int} - \left[\left(Bi_1 + 1\right)Fo_{1,r} R5 - 1\right]T_1$$
$$+ Fo_{1,r} R5 \times T_2 + Fo_{1,r} R5\left(\frac{\Delta x_{1,2}}{k_{1,2}}\right)\left(q_{fric} + q_{fric}^+\right) \quad (6.20d')$$

6.2.3 Coolant Side Boundary Condition

Beyond the TPD there is virtually no temperature swing. Thus a constant wall temperature is assumed for the coolant side boundary condition at the TPD. The rest of the wall is treated as thermal resistance where the steady state heat conduction equation is applied. Assuming that the coolant boundary condition applies to (n+1)th node, then the energy balance for the CV n gives:-

$$a_n = -F_{n,l} \tag{6.22a}$$

$$b_n = F_{n,l} + F_{n,r} + 1 \tag{6.22b}$$

$$c_n = 0 \tag{6.22c}$$

$$d_n = F_{n,l} T_{n-1} - \left(F_{n,l} + F_{n,r} - 1\right) T_n + 2F_{n,r} T_{n+1} \tag{6.22d}$$

6.3 SOLUTION OF FD EQUATIONS

The derived FD equations for n nodes form a set of n equations with n unknown nodal temperatures which can be expressed in matrix form as follows:-

$$\begin{bmatrix} b_1 & c_1 & 0 & 0 & 0 & \cdots & \cdots \\ a_2 & b_2 & c_2 & 0 & 0 & \cdots & \cdots \\ 0 & a_3 & b_3 & c_3 & 0 & \cdots & \cdots \\ \cdots & \cdots & \cdots & \cdots & \cdots & \cdots & \cdots \\ \cdots & \cdots & 0 & a_k & b_k & c_k & 0 \\ \cdots & \cdots & \cdots & \cdots & \cdots & \cdots & \cdots \\ \cdots & \cdots & \cdots & \cdots & \cdots & 0 & a_n \; b_n \end{bmatrix}_{n \times n} \begin{bmatrix} T_1^+ \\ T_2^+ \\ T_3^+ \\ \cdots \\ T_k^+ \\ \cdots \\ T_n^+ \end{bmatrix} = \begin{bmatrix} d_1 \\ d_2 \\ d_3 \\ \cdots \\ d_k \\ \cdots \\ d_n \end{bmatrix} \tag{6.23}$$

The above square matrix is a tridiagonal matrix, i.e. the only non zero terms arise along the diagonal and on either side of it. Thus, it can be solved by an

algorithm based on Gaussian elimination, often known as the Thomas algorithm, which is explained in Chapter 5 (eqn.5.19).

6.4 TEMPERATURE DEPENDENT MATERIAL PROPERTIES

The available literature shows that the variations of both the thermal inertia and conductivity can be quite substantial over the anticipated temperature range of 300 to 1200 K. The 1-D unsteady state conduction heat transfer equation with temperature dependent material properties forms a non-linear differential equation which is difficult to solve. However, the temperature dependent material properties are included in FD equations by considering different conductivities and thermal inertias at the left and right side of each node. The thermal properties of any region are calculated at the temperature which is determined by linear interpolation of the temperatures at the surrounding nodes.The conductivity $k_{i,i-1}$ is evaluated at temperature:-

$$\bar{T}_{i,i-1} = \frac{T_i + T_{i-1}}{2} \qquad (6.24a)$$

The conductivity $k_{i,l}$ and thermal inertia $(\rho Cp)_{i,l}$ are evaluated at:-

$$\bar{T}_{i,l} = \frac{3T_i + T_{i-1}}{4} \qquad (6.24b)$$

and $k_{i,r}$ and $(\rho Cp)_{i,r}$ are evaluated at:-

$$\bar{T}_{i,r} = \frac{3T_i + T_{i+1}}{4} \qquad (6.24c)$$

In fact the above method does not cover all the temperature effects on thermal properties. The true mean temperature at which the thermal properties should be

evaluated is that defined by the spatial and temporal average. It is shown schematically in Fig.6.3 and the equation is given by:-

$$\bar{T}_{i,i-1} = \frac{\left(\frac{T_i + T_{i-1}}{2}\right) + \left(\frac{T_i^+ + T_{i-1}^+}{2}\right)}{2} \qquad (6.25)$$

where + denotes future values.

In eqn.6.25, the present and future node temperatures are required and thus an iterative solution is needed which will make the solution procedure rather complicated.

On the other hand, in order to have a non-oscillating solution which is determined by the Fourier number (less than 1), the nodal distances should be chosen accordingly with respect to the time interval. The time interval used in the FD code is 1 degree CA so that it is compatible with the simulation package 'SPICE'. This resulted in nodal distances of the order of 0.01 mm. For such conditions, the temperature difference between two successive nodes at a specific time is much greater than the temperature difference of a node during a time step, i.e.:-

$$\left(T_i - T_{i-1}\right) >> \left(T_i^+ - T_i\right) \text{ or } \left(T_{i-1}^+ - T_{i-1}\right)$$

and thus,

$$\frac{T_i^+ + T_{i-1}^+}{2} \cong \frac{T_i + T_{i-1}}{2} \qquad (6.26)$$

which reduces eqn.6.25 to eqn.6.24a.

The above condition is also checked and verified by the developed FD computational code.

6.5 FD EQUATIONS IN CYLINDRICAL AND SPHERICAL COORDINATE SYSTEMS

The derived equations in Sec.6.2 are in the cartesian system, and therefore the length of the left and right side of CV i, where the heat flows in and out, are equal (Fig.6.2). However, in cylindrical and spherical geometries, the surface for the incoming flux is smaller than the surface where the flux leaves, assuming that heat flows radially outward (Fig.6.4). Thus, more heat is absorbed by the material as the heat wave propagates through it, and consequently the wave may be affected. To investigate this geometry effect, the FD equations are also derived for cylindrical and spherical coordinate systems by using an energy balance for the CV's shown in Fig.6.4. These two coordinate systems are used as an option in the free standing FD code and the results are presented in Sec.6.10.

The definitions used in the cartesian coordinate system for certain ratios, and the left and right Fourier numbers of a node (eqns.6.6a to 6.7e and 6.9), are also valid in the cylindrical and spherical coordinate systems. The only difference, is the nodal distance term Δx which is replaced by Δr in the Fourier numbers. On the other hand, the defined overall Fourier numbers for the cylindrical and spherical coordinate systems are different from the ones described by eqns.6.11a and 6.11b, and are given by:-

$$F_{i,l} = \frac{R4_i R6_i}{\left(R8_i + RR_i R9_i\right)} Fo_{i,l} \qquad (6.27a)$$

$$F_{i,r} = \frac{R5_i R7_i}{\left(R8_i + RR_i R9_i\right)} Fo_{i,r} \qquad (6.27b)$$

where $Fo_{i,l}$, $Fo_{i,r}$, $R4_i$ and $R5_i$ are defined in eqns.6.6a, 6.6b, 6.7d and 6.7e, respectively. R6, R7, R8 and R9 are

defined for the cylindrical coordinate system as follows:-

$$R6_i = r_i - 0.5\,\Delta r_{i,i-1} \tag{6.28a}$$

$$R7_i = r_i + 0.5\,\Delta r_{i,i+1} \tag{6.28b}$$

$$R8_i = r_i - 0.25\,\Delta r_{i,i-1} \tag{6.28c}$$

$$R9_i = r_i + 0.25\,\Delta r_{i,i+1} \tag{6.28d}$$

For the spherical coordinate system:-

$$R6_i = \left(r_i - 0.5\,\Delta r_{i,i-1}\right)^2 \tag{6.29a}$$

$$R7_i = \left(r_i + 0.5\,\Delta r_{i,i+1}\right)^2 \tag{6.29b}$$

$$R8_i = r_i^2 - 0.5\,r_i\,\Delta r_{i,i-1} + \frac{1}{12}\Delta r_{i,i-1} \tag{6.29c}$$

$$R9_i = r_i^2 + 0.5\,r_i\,\Delta r_{i,i+1} + \frac{1}{12}\Delta r_{i,i+1} \tag{6.29d}$$

For the internal nodes, the coefficients a_i, b_i, c_i and d_i in eqn.6.14 are also the same for these two coordinate systems and are given by eqns.6.15a to 6.15d. The gas side boundary condition for the cylindrical system is defined by the following coefficients:-

$$a_1 = 0 \tag{6.30a}$$

$$b_1 = \frac{R5_1}{R9_1} Fo_{1,r}\left(r_1^2 Bi_1^+ + R7_1\right) + 1 \tag{6.30b}$$

$$c_1 = -\frac{R5_1 R7_1}{R9_1} Fo_{1,r} \tag{6.30c}$$

$$d_1 = \frac{R5_1}{R9_1} Fo_{1,r} \left[r_1 \left(Bi_1 T_g + Bi_1^+ T_g^+ \right) - \left(r_1 Bi_1 + R7_1 - \frac{R9_1}{R5_1 Fo_{1,r}} \right) T_1 + R7_1 T_2 + r_1 \frac{\Delta r_{1,2}}{k_{1,2}} \left(q_{rad} + q_{rad}^+ \right) \right] \quad (6.30d)$$

For the spherical coordinate system:-

$$a_1 = 0 \quad (6.31a)$$

$$b_1 = \frac{R5_1}{R9_1} Fo_{1,r} \left(r_1^2 Bi_1^+ + R7_1 \right) + 1 \quad (6.31b)$$

$$c_1 = - \frac{R5_1 R7_1}{R9_1} Fo_{1,r} \quad (6.31c)$$

$$d_1 = \frac{R5_1}{R9_1} Fo_{1,r} \left[r_1^2 \left(Bi_1 T_g + Bi_1^+ T_g^+ \right) - \left(r_1^2 Bi_1 + R7_1 - \frac{R9_1}{R5_1 Fo_{1,r}} \right) T_1 + R7_1 T_2 + r_1^2 \frac{\Delta r_{1,2}}{k_{1,2}} \left(q_{rad} + q_{rad}^+ \right) \right] \quad (6.31d)$$

The coolant side boundary condition, i.e. constant wall temperature, is defined by the coefficients given in eqns.6.22a to 6.22d, which are the same for the cylindrical and spherical coordinate systems.

6.6 EXACT SOLUTION OF 1-D UNSTEADY STATE CONDUCTION HEAT EQUATION

The 1-D unsteady state conduction heat equation with constant thermal properties is given by:-

$$\frac{k}{\rho Cp} \frac{\partial^2 T}{\partial x^2} = \frac{\partial T}{\partial t} \quad (6.32)$$

In order to have an analytical solution for eqn.6.32, it is necessary to apply boundary conditions at both ends of the wall. As is already known, the combustion chamber walls are subjected to periodic gas

convective and radiative heat fluxes on the gas side and constant coolant convective heat flux on the outside. The gas side boundary conditions make it virtually impossible to solve eqn.6.32 analytically.

In order to check and validate the developed FD model, eqn.6.32 is solved by using a constant htc and sinusoidal gas temperature function at the gas side boundary, and a constant wall temperature at the coolant side. The periodic gas temperature inside the cylinder can be expressed as the summation of sine and cosine functions by a double Fourier series as follows:-

$$T_g = \bar{T}_g + \sum_{n=1}^{\infty}\left[A_n \mathrm{Sin}(n\omega t) + B_n \mathrm{Cos}(n\omega t)\right] \qquad (6.33)$$

where $\bar{T}_g$ is the gas mean temperature and ω is given by:-

$$\omega = 2\pi f$$

where f is the engine frequency.

Thus, the overall effect of the gas temperature on wall temperature swing can be obtained by the summation of the solutions for each individual harmonic. The solution of eqn.6.32 with the following sinosoidal gas temperature:-

$$T_g = \bar{T}_g + \Delta T_g \mathrm{Sin}(\omega t + \phi) \qquad (6.34)$$

is given by:-

$$T_w = \bar{T}_{w,0} + \frac{x}{l}\left(T_{w,l} - \bar{T}_{w,0}\right) + \Delta T_{w,0}\exp\left(-\sqrt{\frac{\omega}{2\alpha}}\,x\right)\mathrm{Sin}\left(\omega t - \sqrt{\frac{\omega}{2\alpha}}\,x\right) \qquad (6.35)$$

where:-

ϕ is the phase angle between gas and wall temperatures.

x is the distance measured from the wall surface.

T_w is the time and space dependent wall temperature.
$\bar{T}_{w,0}$ is the wall surface mean temperature ($x = 0$).
$T_{w,l}$ is the constant wall temperature at $x = l$, i.e. oscillations are heavily damped.
α is the thermal diffusivity.
$\Delta T_{w,0}$ is the amplitude of the wall temperature swing.

6.6.1 Amplitude and Phase Angle

The amplitude and phase angle for the wall surface temperature can be obtained by equating the convective and conductive heat fluxes at the wall surface (i.e. x=0):-

$$-k\left(\frac{\partial T_w}{\partial x}\right)_{x=0} = htc\left(T_g - T_{w,0}\right) \qquad (6.36)$$

Using eqns.6.34 and 6.35, eqn.6.36 can be expressed by:-

$$\Delta T_{w,0}\left[k\sqrt{\frac{\omega}{2\alpha}}\left(Sin\left(\omega t + \frac{\pi}{4}\right) + Sin(\omega t)\right)\right] = htc\left(\bar{T}_g - \bar{T}_{w,0}\right)$$

$$- k\left(\frac{\bar{T}_{w,0} - T_{w,l}}{l}\right) + htc\Delta T_g Sin(\omega t + \phi) \qquad (6.37)$$

where the gas and the wall steady state heat fluxes are equal:-

$$htc\left(\bar{T}_g - \bar{T}_{w,0}\right) = k\left(\frac{\bar{T}_{w,0} - T_{w,l}}{l}\right) \qquad (6.38)$$

and reduces eqn.6.37 to:-

$$\Delta T_{w,0} = \frac{\Delta T_g Sin(\omega t + \phi)}{\frac{1}{N}\left(Sin\left(\omega t + \frac{\pi}{4}\right) + Sin(\omega t)\right)} \qquad (6.39)$$

where N is given by:-

$$N = \frac{htc}{k}\sqrt{\frac{\alpha}{\omega}} \qquad (6.40)$$

The phase angle ϕ, is obtained by using $\omega t=-\phi$, where the instantaneous gas temperature is equal to the mean gas temperature and eqn.6.39 reduces to:-

$$\frac{\Delta T_{w,0}}{N}\left[\mathrm{Sin}\left(-\phi+\frac{\pi}{4}\right)+\mathrm{Sin}(-\phi)\right]=0$$

Since wall temperature amplitude $\Delta T_{w,0}$ can't be zero, it can be eliminated, thus:-

$$\frac{1}{N}\left[\mathrm{Sin}\left(-\phi+\frac{\pi}{4}\right)+\mathrm{Sin}(-\phi)\right]=0$$

where the phase angle ϕ can be expressed by:-

$$\phi=\tan^{-1}\left(\frac{1}{1+\sqrt{2}N}\right) \qquad (6.41)$$

The maximum wall temperature occurs at $\omega t=\pi/2$, which reduces eqn.6.39 to:-

$$\Delta T_{w,0}=\Delta T_g\left(\frac{\sqrt{2}N}{1+\sqrt{2}N}\right)\mathrm{Cos}\phi$$

Using eqn.6.41 and right angle triangle relation:-

$$\mathrm{Cos}\phi=\frac{1+\sqrt{2}N}{\sqrt{2+2\sqrt{2}N+2N^2}}$$

Thus, the wall temperature swing can be expressed in terms of N, as:-

$$\Delta T_{w,0}=\Delta T_g\left(1+\sqrt{2}N^{-1}+N^{-2}\right)^{-0.5} \qquad (6.42)$$

6.6.2 Thermal Penetration Depth (TPD)

The TPD is defined as the distance from the wall

surface where the fluctuating wall temperature amplitude decays to 1% of the surface temperature amplitude. From eqn.6.35, the amplitude of the wall temperature through the material is given by $\Delta T_{w,0}\exp\left(-\sqrt{\frac{\omega}{2\alpha}}\,x\right)$, and using the definition of TPD, the following expression is derived for it:-

$$x_{TPD} = 2.6\sqrt{\frac{k}{f\rho Cp}} \qquad (6.43)$$

where f is the engine frequency.

6.6.3 Wall Mean Surface Temperature

In order to compare the numerical and exact solutions and to determine the number of cycles necessary for the numerical solution to reach steady state, the wall mean surface temperature is obtained from eqn.6.38 and is given by:-

$$\bar{T}_{w,0} = \frac{htc\bar{T}_g + \frac{k}{l}T_{w,l}}{\frac{k}{l} + htc} \qquad (6.44)$$

6.7 DEVELOPED FD COMPUTATIONAL CODE

A general purpose FD computational code was generated to check and validate the numerical method, and to study the effects of certain parameters on the temperature wave under different boundary conditions. The developed FD code is capable of solving for the temperature wave in cartesian, cylindrical and spherical coordinate systems. The analytical solution procedure of Sec.6.6 is also included in the system, and is used to validate the numerical method as explained in the next section. The analytical solution option can also provide the Fourier harmonics for given gas temperature data to obtain the total solution. The flowchart for the main computer program is presented in Fig.6.30 and the list of its subroutines and their functions are listed in

Table 6.2. A typical tabular output is presented in Table 6.1.

The developed model can either be used with constant or temperature dependent thermal properties depending on the input data. It can also handle combinations of several different material layers. Thus, a surface thermocouple on a ceramic surface with a metallic substrate can easily be modelled by the code. The effect of soot deposits on the thermocouple reading can also be included in the problem.

Different boundary conditions such as convective, radiative, adiabatic or constant wall temperature can be applied to the wall. The convective and radiative boundary conditions can either be constant, sine wave, square wave, any periodic function in data form, or engine data. Step changes in boundary conditions can also be applied by choosing appropriate options.

The developed FD model is capable of simulating the temperature wave on a ceramic surface in the thermal shock rig (which is part of a wider ceramic investigation in the School of Mechanical Engineering [110]), simulation rig and fired engine rig. Although it could be argued that gas to wall heat flux variation over a ceramic surface is not adequately covered by a 1-D FD model, the temperature gradients through the material are much more severe than along the surface, obviating the need for a 2-D transient heat flow model.

The initial wall temperature distribution which can be constant or linear, the time interval, and the total time for the transient analysis are specified by the user. The time step can be adjusted to obtain an accurate and stable solution. For periodic boundary conditions, the data for successive cycles can be printed to see the effect of number of cycles on the numerical solution.

The temperature and flux data at any node as a function of time, or at any time in the cycle through

the material are generated for plotting. The developed FD computational code is a useful tool to investigate the fluctuating wall temperature under different conditions.

6.8 VALIDATION AND GRID OPTIMIZATION

In order to check and validate the developed FD model, the computational code is used to obtain the fluctuating wall temperature by both analytical and numerical methods. The FD analysis is restricted to a wall thickness of 1.2*TPD. Beyond that point, the heat flow is steady, hence a FD analysis is not necessary, and a simple thermal resistance network can be used to solve the heat transfer problem. On the other hand, extending FD analysis into the whole thickness of the material increases the number of cycles necessary for the numerical solution to reach a steady state and is computationally uneconomical. By comparing the numerical and exact solutions an optimum grid sizing is obtained. In the analysis, the following criteria for accuracy are chosen:-

1- The maximum difference between the numerical and exact solutions at any node at any time.

2- The difference between the numerical and exact surface temperature swings.

3- The difference between the numerical and exact phase angle.

First, the developed FD model is tested with a constant htc and sinusoidal gas temperature variation. In the test, the layer thickness ratio ($R3=\Delta x_{i,i-1}/\Delta x_{i,i+1}$) and the first layer thickness are chosen as 0.9 and 0.01*TPD respectively, which are later optimized. The choice of these values is determined by considerations of numerical accuracy and computational economy. The value R3=0.9 (see eqn.6.7c) implies that the thickness of successive layers increases in geometric progression, with the thinnest layers nearest the gas side surface.

The applied boundary conditions are given by:-

Gas Side	Coolant Side
$T_g = 1000 + 500\mathrm{Sin}(2\pi ft)$ K	$x_1 = 1.2*TPD$
$htc = 1000$ W/m^{2}K	$T_{w,1} = 1000$ K
$q_{rad} = 0$	

where x_1 is the wall thickness and f is the engine frequency which is taken as 10 cps, equivalent to 1200 rpm engine speed.

The initial wall temperature distribution are chosen as 1000 K, which is the mean gas temperature. By this means, the numerical solution can reach the steady state in few cycles, thus facilitating comparison with the exact solution. The effect of using a value other than the mean gas temperature for the initial mean wall temperature, such as 500 K, on the number of cycles necessary for the numerical solution to reach steady state is shown in Fig.6.15. In the test, low conductivity (1 W/mK), and thermal inertia (10^6 Jkg/m^3) values are used which are typical thermal properties of ceramics for diesel engine insulation. The obtained wall surface temperature together with gas temperature are shown in Fig.6.5, where it can be seen that they are out of phase by 11%.

The exact and numerical solutions at various nodes throughout the cycle, and through the material at certain times in the cycle are compared and are presented in Figs.6.6 and 6.7. These tests showed that the numerical and analytical solutions are in good agreement which suggests that the developed FD code is quite accurate.

Subsequently the FD model was tested for a cylinder gas temperature (Fig.6.8), obtained from the cycle simulation package 'SPICE', which was represented by a Fourier series as shown in Fig.6.9. The coolant side boundary condition is set to the mean gas

temperature value. The gas temperature wave is decomposed into its Fourier harmonics and for each component the wall surface temperature swing is analytically calculated, as shown in Fig.6.12. It can be seen that the higher gas harmonics such as the 20th, have almost negligible effect on the wall temperature swing. The total solution for the wall temperature swing is obtained by summing the individual gas harmonic solutions as shown in Fig.6.13. The numerical method is sufficiently powerful to yield a solution close to the analytical solution of the wall temperature wave. The exact and numerical solution of the temperature wave through the material (spatial variation) is also checked as shown in Fig.6.14, which proved that the FD code has a high accuracy.

Once the numerical method is validated, an optimum grid sizing is sought to achieve an economical computing time. By this means, the developed FD code can be incorporated into the cycle simulation package 'SPICE' without drastic increase in computational time. In this connection, the first layer thickness and layer thickness ratio R3, are varied to investigate the effect on the number of the nodes required for accurate FD analysis. The numerical tests are performed for both low and high conductivity materials such as ceramic and aluminium, where the wall temperature swing varies enormously. The same boundary conditions are used, as specified at the beginning of this section.

The effect of layer thickness ratio on numerical solutions for both types of materials are shown in Fig.6.16 and 6.17. The percentage errors in the surface temperature swing and phase angle are given in Figs.6.18 and 6.19. As expected, the percentage error in the numerical solution increases at low values of layer thickness ratio. The effect of layer thickness ratio on the number of nodes is given in Fig.6.24. Comparing Fig.6.24 and 6.18, one can reach the conclusion that the

layer thickness ratio R3 must be in the region 0.7 to 0.9. Increasing R3 beyond 0.9 improves the percentage error very slightly, but increases the number of nodes greatly. Decreasing R3 below 0.7 raises the percentage error with a slight decrease in the number of nodes.

The effect of first layer thickness on the numerical solutions for both types of materials is given in Fig.6.20. and 6.21. Increasing the first layer thickness reduces the wall temperature swing and increases the phase shift. The percentage errors for the surface temperature swing and phase angle are shown in Figs.6.22 and 6.23. As expected, varying the first layer thickness to TPD ratio , has greater influence for aluminium than ceramic, since aluminium has a TPD about 10 times bigger than ceramic.

The effect of first layer thickness on the number of nodes is presented in Fig.6.25. Comparing Figs.6.22 to 6.24 a value of 0.02 for the ratio DELX1/TPD seems to be quite appropriate.

Using engine simulation data for gas temperature, htc and radiation heat flux, as shown in Figs.6.8, 6.10 and 6.11, the surface temperature fluctuations for ceramic and aluminium walls are obtained for two different node numbers, and are given in Figs.6.26 and 6.27. It was decided that ratios R3 and DELX1/TPD, have respectively optimum values of 0.75 and 0.02. This produces an accurate numerical solution with 12 nodes and has an economical computing time. Further reduction in the ratios will slightly reduce the node numbers which will improve the computing time very little, but raise the percentage error in the numerical solution enormously.

The effect of the Fourier number on the numerical solution is also investigated. A 10 mm ceramic wall with an initially uniform temperature distribution of 500 K, is subjected to suddenly applied heat flux of 1000 W/m^2 on one surface. The other surface is kept at 500 K. The

numerical solutions for the wall surface temperature for different Fourier numbers are presented in Figs.6.28 and 6.29. Using Fourier numbers greater than one introduces damped oscillations in the numerical solution which requires long periods of time for the oscillations to vanish. As seen in Fig.6.29, the numerical solution in a long time scale with Fourier number of 100 is quite satisfactory, whereas even with smaller Fourier numbers in a small time scale these oscillations can become a big problem in the numerical solution as shown in Fig.6.28. Considering engine speeds of 1000 and 2500 rpm, where each cycle takes about 0.06 to 0.024 seconds, these damped oscillations will create a problem in the numerical solution, and therefore Fourier numbers should be kept below 1.0.

The developed FD code implements a self-generating grid sizing where the minimum layer thickness depends on the TPD, and the optimum value is found to be:-

$$\Delta x_1 = 0.02 * x_{TPD} \tag{6.45}$$

where x_{TPD} is given by eqn.6.43.

Using the definition of Fourier number,

$$Fo = \frac{\alpha \Delta t}{\Delta x^2} \tag{6.6}$$

where α is the thermal diffusivity given by eqn.6.3, and Δt is the time interval which for cycle simulation studies is generally that for 1°CA and is given by:-

$$\Delta t = \frac{1}{6Ne} \tag{6.46}$$

Substituting eqn.6.45 and 6.46 into eqn.6.6 and using eqn.6.43, a Fourier number of 0.513 is obtained which

produces a stable numerical solution.

6.9 PREDICTION OF TEMPERATURE WAVES AND HEAT FLUX LEVELS ON DIFFERENT MATERIAL SURFACES

The developed FD model is used to predict the temperature waves and heat flux levels in different materials which are used, or are possible candidates, for the automotiv industry. Their thermal properties are given in Tables 2.3 and 2.4. First, the effect of the coolant side boundary condition on the mean wall temperature and temperature swing is investigated.

6.9.1 The Effect of Coolant Side Boundary Condition on Temperature Wave

The transient thermal analysis is performed for a low conductivity and low thermal inertia ceramic ($k=1$ W/mK, $\rho Cp=10^6$ J/m^{3}K), and aluminium through a thickness of 1.2*TPD, i.e. 1 and 10 mm respectively. The applied gas side boundary conditions are the same engine simulation data as used in Sec.6.8 and shown in Figs.6.8 to 6.11. The coolant side boundary conditions are either fixed at a constant temperature of 300 K to represent an extremely cooled case or engine cold start, or are taken as adiabatic. The results are presented in Fig.6.31 to 6.36.

Applying an adiabatic condition on the coolant side boundary simply shifts the wall temperature upwards as expected, as shown in Figs.6.32 and 6.34. However, the surface temperature swing for both materials drops in the adiabatic case by about 50% as shown in Figs.6.31 and 6.33. This is not surprising since the mean wall temperature is increased by insulation which reduces the transient gas to wall heat transfer and results in a corresponding reduction in the surface temperature swing. From a thermal stress point of view, it is better to cancel the cooling system totally for ceramic applications and thus to reduce the level of cyclic

thermal stresses created by the wall temperature swing.

Although aluminium can't withstand the calculated temperatures created by insulation, this study merely explores the effect of coolant side boundary conditions on materials with various conductivities. If Fig.6.32 and 6.34 are compared, it can be seen that the aluminium mean wall temperature for the adiabatic is slightly higher than the ceramic one. However, the apparent wall surface temperature, defined as steady state equivalent temperature and explained in Sec.6.13, is the same for both materials (1317.4 K).

The heat flux levels for the cooled and adiabatic cases are shown in Figs.6.35 and 6.36. Although for the adiabatic case, the mean heat flux for both materials is zero, heat transfer between gas and wall in both directions still takes place throughout the cycle. With insulation, the peak heat fluxes are reduced compared with the cooled case by about 50% for ceramic and slightly more for aluminium. The peak heat flux value for the ceramic wall is slightly lower than for the aluminium wall, as expected, because of the higher temperature swing of the ceramic which reduces the gas to wall temperature difference. For the adiabatic case, except for the combustion period, heat transfer is from wall to gas, and the overall cycle mean heat flux is zero. True adiabatic condition where gas to wall heat transfer is zero throughout the cycle can be approximated only by using a low conductivity and thermal inertia material such as air, so that the wall temperature follows the gas temperature throughout the cycle.

6.9.2 Application of FD Model on Various Metals and Ceramics

The thermal analysis is then carried out for various metals and ceramics which are already used or are potential candidates in the design of diesel

engines, such as aluminium, aluminium alloy, cast iron, steel, nimonic, partially stabilized zirconia (PSZ), aluminium titanate (AT), cordierite, sialon, hot pressed silicon nitride (HPSN), and hot pressed silicon carbide (HPSC). A wall of 10 mm thickness is chosen to study the effects of different materials on surface temperature swings and heat flux levels. The coolant side boundary conditions are specified in Fig.6.37 where for metals a higher cooling rate is applied to ensure safe operation. However, for ceramics the external cooling system is eliminated and it is assumed that cooling is applied only by natural convection and radiation, and thus a low heat transfer coefficient value of 50 W/m^2K is used.

The gas side boundary conditions which are obtained from cycle simulation are given in Figs.6.8 to 6.11. Although using different wall materials in an engine affects the heat transfer through the engine walls and hence the gas side boundary conditions, in this study the same gas side boundary conditions are assumed for all types of materials. Thus, this is not a true represantation of the heat transfer through the engine walls. However, this study indicates how different materials would behave under similar engine conditions. The exact behaviour in an engine can only be predicted by incorporating the FD model in the cycle simulation package itself, as explained in Sec.6.13, with the corresponding results presented in Chapter 7.

The wall surface temperature and its swing for metals and ceramics are given in Figs.6.39 to 6.42, and in Tables 6.3. and 6.4. As expected, metals have lower temperature swings than ceramics due to their higher conductivity and thermal inertia values. Table 6.3 shows material thermal properties and groups of thermal properties together with thermal penetration depth and temperature swing. Nimonic, among the metals has the highest surface temperature swing with 33.9 K and aluminium the lowest with 10.2 K. The level of the

surface temperature is governed by the conductivity of the material since it is the only effective thermal property in the dominant steady state part of the wall. As shown in Fig.6.40, the surface temperature shifts upwards for low conductivity metals.

Among ceramics, PSZ and AT have the highest surface temperature swing of about 92 K and HPSC has the lowest with 10.2 K. The dominant variable in the steady state section of the wall is the coolant side heat transfer coefficient which has been deliberately fixed at a very low value for the ceramic materials. In the case of those ceramics with relatively high conductivities (Sialon, HPSN, HPSC) the thermal resistance of the coolant side boundary layer is dominant, and the mean gas side temperature is hardly affected by changes of material. On the other hand, for the ceramics with low conductivity (PSZ and AT) the wall resistance is compareable with the boundary layer resistance, and the mean gas side temperature is affected.

Although the thermal property group $k\rho Cp$ for steel is slightly higher than for cast iron, one expects a slightly higher temperature swing than for steel, yet the temperature swings for both materials are nearly the same (Table 6.3). The reason is that steel has a slightly lower conductivity which shifts the surface temperature upwards (Fig.6.40), as a result of which slightly less heat is transferred from gas to surface. Thus, the overall effect on the temperature waves is similar.

PSZ and AT walls are also found to possess almost the same surface temperature and same temperature swing. PSZ and AT have different densities and specific heat capacities. However, their thermal inertias are almost the same and with the same conductivity values, the final outcome is not surprising (Table 6.3).

In Table 6.4, wall surface mean and apparent

temperatures and extra resistance values for various materials are also given. The apparent wall surface temperature which is defined as the steady state equivalent temperature, is almost equal to the mean surface temperature for materials with small temperature swings, such as aluminium. For high temperature swings such as occur at the surface of PSZ and AT walls, the difference reaches upto 18.8 K. The term called 'extra resistance' which is evaluated by the difference between the apparent and time mean surface temperatures and mean heat flux, is also a strong function of the temperature swing and vanishes for constant surface temperature. The terms 'apparent wall surface temperature' and 'extra resistance' and their use are fully explained in Sec.6.13.

The heat flux data are presented in Fig.6.43 and Table 6.5. Cancelling the cooling system and using ceramics reduces maximum heat flux values by 52.3, 53.7, 55.5, 57.0 and 57.2% respectively for ceramics PSZ (or AT), cordierite, sialon, HPSN and HPSC (relative to aluminium alloy). Considering the conductivities of ceramics used which vary beween 1 and 100 W/mK, the differences in percentage reduction of maximum heat flux with different ceramics are not significant. This is simply because cancelling the cooling system introduces a high level of insulation and further insulation can be achieved only by using very low conductivity and thermal inertia materials, i.e. one depends on the temperature swing to decrease the gas to wall temperature difference during the combustion.

Due to the high level of temperatures on the ceramic surfaces, the minimum, i.e. negative, heat flux from wall to gas is increased by 25 to 26.8 times compared to aluminium alloy. The pumped heat for metals during the exhaust stroke is virtually zero. However, for ceramics this value varies between 13.9 to 12.3 W/m^2, depending on the ceramic, and will raise the

exhaust temperature. On the other hand, the pumped heat during the intake stroke relative to aluminium alloy, increases by about 27 times which is expected to drop volumetric efficiency drastically and make the turbocharger a necessity for engines with partial insulation. The mean heat flux levels drop to about 13.5 to 19.5% of those for aluminium alloy walls for the above mentioned ceramics.

The computational test simply shows that cancelling the cooling system provides a good insulation in terms of mean and maximum heat flux values irrespective of the wall material. Further reduction in the mean flux levels requires very low conductivity materials ($k<2$ W/mK), or use of an air gap within the material. To reduce the maximum heat flux which has a crucial effect on engine performance, is only possible by using very low conductivity and thermal inertia materials which produce high temperature swings. However, this introduces very large cyclic thermal stresses which limit the ability of the material to survive. With present materials, a ceramic which withstands high temperatures of about 1500 K, having slightly higher conductivity, solves the cyclic thermal stress problem without greatly reducing the level of thermal insulation is the best candidate material. The benefits of insulation can be realized in different engine schemes such as turbocharging, turbocompounding or Rankine bottomming cycle.

6.9.3 The Effect of Enhanced htc on The Temperature Wave

Computational tests were also carried out for more severe gas side boundary conditions. Woschni reported that insulation increases the htc within the combustion chamber and causes higher heat transfer rates than those for conventionally cooled engines, during the combustion period, (See Chapter 2). In order to explore

the effect of higher htc's on the wall surface temperature, temperature swing and heat flux, the present convective htc data is multiplied by 2 during the combustion and expansion period of the cycle, as shown in Fig.6.38. The gas temperature and radiative heat flux data are kept the same. The wall surface temperature and swing are presented in Figs.6.44 and 6.45, and Table 6.6. The mean surface temperatures and their swings for the specified ceramics are raised by 8.7 to 11.2% and 25.4 to 30.4%, respectively, compared to the original Woschni htc correlation.

The mean and maximum heat fluxes are increased by 12.2 to 15.3%, and 25.5 to 29.8%, respectively. The pumped heat during the exhaust stroke is increased significantly by 58.4 to 66.4%. During intake, the pumped heat is raised by 15.4 to 21.2%. In Fig.6.46 and 6.47, the instantaneous heat fluxes for the original and modified Woschni htc correlations are shown for the low and high conductivity ceramics, PSZ and HPSC.

Comparing Fig.6.43 with Figs.6.46 and 6.47, it can be seen that the maximum heat flux values are still lower for the modified Woschni htc by about 66.4 and 74.3% for PSZ and HPSC respectively, compared to aluminium alloy. Thus, there is no evidence to support Woschni's argument that, because insulation raises htc values, it also increases gas to wall heat transfer during the combustion period to higher levels than for the standard metallic engine.

In the present calculations, the cylinder gas temperature is kept the same, while with insulation it is expected to increase to higher levels with an effect on heat transfer. A full understanding of the problem is achieved by running the FD model together with simulation package 'SPICE', the results being presented in Chapter 7. On the other hand, the mean heat flux values with the modified Woschni htc are still low and are not expected to rise. The higher pumped heat

transfer rates during the exhaust stroke will increase the availability of the exhaust gas which will be partly recovered by the downstream turbocharger and turbocompound turbines.

6.9.4 The Effect of Ceramic Wall Thickness on Cycle Mean Heat Flux

The effect of wall thickness on the apparent wall temperature and mean heat flux levels are also investigated and presented in Figs.6.48 and 6.49. Reduction in mean heat flux is possible only by using very low conductivity materials. Increasing wall thickness from 10 to 20 mm for PSZ or other materials with conductivity of the order of 1 W/mK reduces mean heat flux by 22%. For materials with conductivities higher than 10 W/mK, the reduction is not significant at all. For further reduction in cycle mean heat flux values, air-gap cushion within ceramic components is a promising solution.

6.10 THE EFFECT OF GEOMETRY ON THE TEMPERATURE WAVE

The developed FD computational code is used to investigate the effect of wall geometries such as plane, cylindrical and spherical, on surface temperature swings. The cross sectional are perpendicular to heat flux for a plane wall is constant throughout its thickness. However, for a cylindrical and spherical wall, assuming 1-D heat conduction in the radial direction, the heat flux area changes with radius and affects the heat flux. This could be significant for the surface temperature fluctuations.

The percentage change of area between the inner and outer surfaces of a cylinder with a wall thickness of TPD is given by:-

$$PC_{cy} = \frac{200\,TPD}{D_{in}} \qquad (6.47)$$

and for a sphere:-

$$PC_{sp} = \frac{400\,TPD\left(D_{in} + TPD\right)}{D_{in}^{2}} \qquad (6.48)$$

where D_{in} is the inner diameter of the cylinder or sphere.

The percentage change between the inner and outer surfaces of the transient heat flow section of the wall is a function of TPD and diameter. Thus, it strongly depends on the material type as well as on the geometry and size. In Fig.6.52, the variation of TPD with material thermal properties is shown at different engine speeds.

The percentage changes in areas for PSZ, cast iron and aluminium are shown as a function of size for both cylinder and sphere in Fig.6.50 and 6.51. It can be seen that change in cross sectional areas is less significant in low conductivity materials, such as PSZ.

In order not to include the effects of the steady state section of the wall, the thermal analysis is limited to a wall thickness of 1.1 TPD. To avoid the coolant side boundary effects on the solution, the same constant temperature is assigned at coolant side surface temperature which is obtained from the thermal analysis of a 10 mm thickness plane wall with the boundary conditions shown in Fig.6.37. In this way, the change in the flux areas within the transient wall region is tested under the same conditions. The dimensions used in the thermal analysis for the cylinder and sphere are the Petter PH1W engine cylinder and piston bowl diameters (87 and 50 mm, see also Chapter 8). The results are presented in Figs.6.53 to 6.56.

Although aluminium has a high TPD of about 9 mm, the change in the surface temperature swing for both geometries is almost negligible. However, the level of

the surface temperature is shifted slightly downwards by about 0.6 K for the cylinder and 2.1 K for the sphere (Fig.6.54).

PSZ which has a small TPD of about 0.6 mm shows no significant change in the temperature swing and surface temperature levels for either cylindrical or spherical walls (Figs.6.55 and 6.56).

After showing that the effect of geometry on the solution within the transient wall region is not significant, the thermal analysis is carried out for the whole wall thickness of 10 mm for PSZ. The surface temperature swing is increased by about 2.5 K and 6 K for cylindrical and spherical walls, respectively (Fig.6.57). The wall surface temperature levels are reduced by about 23 K and 84 K for the cylindrical and spherical wall, respectively (Fig.6.58). This big difference in the surface temperature levels is due to the steady state heat transfer region of the wall which is related to the actual thickness of the wall, and is also responsible for the slight increase in the temperature swings.

As a result of geometry variations the apparent wall surface temperature is different and this affects the gas to wall heat transfer. The effect of geometry types and sizes on the apparent wall surface temperature and mean surface heat flux is shown for a 10 mm thick wall of material type aluminium, cast iron and PSZ in Figs.6.59 to 6.64. The highest differences in both variables occur in low conductivity materials. This also explains why the temperature swings for a 10 mm thick PSZ wall are slightly higher for cylindrical and spherical walls.

6.11 THE EFFECTS OF TEMPERATURE DEPENDENT MATERIAL PROPERTIES

For particular boundary conditions, conductivity and thermal inertia determine the magnitude of the

temperature swing on the wall surface. However, the thermal properties for most ceramics are strong functions of temperature and their effect on the wall temperature dynamics and surface swings should be considered.

In Table 2.3, the thermal properties of ceramics at various selected temperatures are presented; it can be seen that their differences are quite substantial for most ceramics. For PSZ, AT, cordierite, sialon, HPSN and HPSC the specific heat capacity increases respectively by 40.4, 48.6, 71.2, 91, 91.2 and 88.1% through a temperature range of 300 to 1300 K.

The temperature distribution across the materials at certain positions are obtained by using the data in Tables 6.4 and 6.5; the results are presented in Table 6.8. For low conductivity materials such as PSZ an AT, not only in the transient heat flow region but also in the steady state part of the wall, the temperature variations are quite high. PSZ or AT have temperature differences of about 99.3 K, 266 K and 365.3 K in the transient, steady state and overall wall regions, respectively. For sialon, HPSN and HPSC the maximum temperature differences within the wall are respectively 49.7 K, 24.8 K and 11.7 K. With an adiabatic coolant side boundary condition the temperature difference in the steady state section reduces to zero; the only temperature variation is within the transient region and is equal to the surface temperature swing.

To study the effect of temperature dependent material properties on the temperature dynamics of the wall, a hypothetical reference material with a low conductivity and thermal inertia of 1 W/mK and 10^6 J/m^{3}K is chosen which produces a reasonably high temperature swing. First, the thermal analysis is applied to the wall shown in Fig.6.37, with constant material properties. The apparent surface temperature (1189.7 K) obtained from the solution is used as a reference point

to define the temperature dependent thermal properties of the hypothetical material as shown in Fig.6.65. It is assumed that for every 500 K conductivity reduces and thermal inertia rises by an amount equal to the reference point value.

In order to distingish the effect of the temperature dependent properties within the transient and steady state wall, a set of thermal analyses is first performed for a wall thickness of 1.1*TPD. A constant wall temperature of 1132.3 K which is obtained from the constant material property results produced previously, is applied to the coolant boundary condition. The computer runs are made for cases of either varying conductivity or thermal inertia, or both. Subsequently the thermal analysis is performed for the whole wall thickness including the steady state part, again with temperature dependent properties. The results are presented in Figs.6.66 to 6.69.

The inclusion of the temperature dependent material properties in the solution had little effect on the results. The surface temperature swings increased by 1.9, 1.5 and 3.6 K respectively for temperature dependent conductivity, thermal inertia and for both, as shown in Fig.6.66 and 6.67. The surface temperatures for different cases are shown in Fig.6.68. Confining the temperature dependent properties to the transient layer has no significant effect on the solution. However, extending the temperature dependent properties also to the steady state part of the wall reduces the surface temperature by about 7 K without any change in the temperature swing.

The effect of temperature dependent conductivity in the steady state section of the wall is demonstrated by Figs.6.70 and 6.71. Higher temperature variation within the wall shifts the surface temperature down, resulting in slight increase in the mean heat flux. These results are for the poorly cooled case (Fig.6.37);

for a highly cooled wall the temperature dependent conduction will have more significance. On the other hand, for an adiabatic coolant side boundary condition this effect is zero.

The temperature waves through the material for various cases are also presented in Fig.6.69. The differences due to temperature dependent properties are similar to the ones observed for surface temperatures.

In Fig.6.72 and 6.73 the surface temperatures and swings for various ceramics with temperature dependent material properties are presented. The applied coolant side boundary condition is again shown in Fig.6.37. Similar results were obtained previously with constant material properties (evaluated at room temperature); these were shown in Figs.6.41 and 6.42. Applying temperature dependent properties, the surface temperature swings are reduced by 16.0, 36.4, 22.0 and 9.2% respectively for PSZ, AT, cordierite and sialon. Conversely, for HPSN and HPSC an increase of 1.0 and 9.8% is observed. The reduction or increase of the temperature swing depends on the resultant effect of the rate of change of conductivity and thermal inertia within the working temperature range. The large differences in temperature swings are direct result of using property values at room temperature for the constant material property case (Figs.6.41 and 6.42). The previous results also suggest that FD runs using the constant material property option yield almost the same results as those using the temperature dependent material property option when the properties are evaluated at the apparent surface temperature. The surface temperature and flux data are also presented in tabular form and are shown in Tables 6.9 and 6.10.

6.12 THE EFFECT OF MATERIAL PROPERTIES

As already mentioned, for particular wall boundary conditions, conductivity k, and thermal inertia

ρCp, are the two material properties which govern the surface temperature swing. In this section, the property group $k\rho Cp$ is varied widely between 10^3 and 10^9 J^2/m^4K^2s, to discover its effect on the surface temperature fluctuation.

The required value for the property group $k\rho Cp$ can be obtained by various combinations of k and ρCp. As long as $k\rho Cp$ is kept constant within the TPD without any change in the steady state part of the wall, the surface temperature and its swing remain unchanged. However, including the changes in k and ρCp also in the steady state part, where ρCp has no effect , produces different values of surface temperature and swing. This is not surprising, because variations in k affect the steady state resistance network which shifts the surface temperature levels up or down. This influences the gas to wall heat transfer resulting in different surface temperature swings. In order to observe the influence of $k\rho Cp$ on the temperature swing, excluding the steady state effects, the change of $k\rho Cp$ is limited to the TPD. This can be done either by assigning a constant temperature at the TPD for all $k\rho Cp$ values which means imposing different coolant side boundary conditions for each case, or by having an adiabatic coolant side boundary condition.

In this section, for simplicity an adiabatic coolant side boundary condition is chosen. Both convective and convective plus radiative gas side boundary conditions are separately applied to reveal their differences at low $k\rho Cp$ values. As stated earlier, the radiation heat flux data obtained from the cycle simulation package 'SPICE', shown in Fig.6.11, are again

used as in the previous cases. However, these radiative fluxes had to be corrected by subtracting the wall emission which plays an important role at low values of $k\rho Cp$, where the wall surface temperature approaches the flame temperature.

The absolute surface temperature together with gas temperature are shown in Figs.6.75 and 6.77, the former for convective heat transfer only, and the latter for convective plus radiative. The temperature swings are shown separately in Figs.6.74 and 6.76, again for convective and combined convective and radiative heat transfer, respectively. Reducing $k\rho Cp$ increases the temperature swing drastically. For a $k\rho Cp$ value of 10^3, the temperature swings are about 1000 K and 900 K for convective, and convective plus radiative gas boundary conditions, respectively. Therefore, the surface temperature of a wall having low $k\rho Cp$ value tends to follow the gas temperature and provide a situation close to a true adiabatic case, where gas to wall heat transfer stops.

As expected, with convective gas boundary conditions the wall surface temperature is always lower than the cylinder gas temperature. However, Fig.6.77 shows that applying convective and radiative gas boundary conditions for low values of $k\rho Cp$, produced peak surface temperatures slightly higher than the peak gas temperatures and shifted towards the left relative to the latter. This is not surprising, because the radiation heat flux is emitted from the diesel flame at temperatures reaching approximately 2500 K, and still the wall surface temperature is lower than the source temperature. The wall surface temperature is close enough to the gas mean temperature to reduce drastically or even stop the gas to wall convective heat transfer, thus leaving the radiation component of heat transfer as

the dominant mode. This is also evident for higher values of $k\rho Cp$ which raise the influence of the convective heat transfer and thus shift the surface temperature peaks towards the right, i.e. towards the gas temperature peak.

Although a low value of $k\rho Cp$ is desired to provide an approach towards the ideal of a true adiabatic case, this undoubtedly creates huge cyclic thermal stresses determined by the large temperature swings. Even if a material could be produced with a very low $k\rho Cp$ value - which is unlikely in the near future - this will introduce serious mechanical problems from a thermal stress point of view.

Providing that the property group $k\rho Cp$ is constant, separate changes in k and ρCp values within the TPD have no influence on the surface temperature and swing. However, various combinations of k and ρCp produce different TPD's within the material. The TPD is a linear function of the property group $(k/\rho Cp)^{0.5}$, and thus the outcome is not surprising. The TPD's at various engine speeds are presented in Fig.6.52. Ceramics with low conductivities have smaller TPD's in the order of 0.5 to 1.0 mm. Conversely, for metals this value is higher; for aluminium it is of the order of 10 mm.

The magnitude of the surface temperature swing depends on the gas and coolant side boundary conditions, and the material properties. The gas side boundary condition is composed of periodic convective and radiative heat transfer data generated at a specific engine operating condition. The engine speed determines the frequency of the surface temperature wave and thus affects the amplitude of the wave. Although convective and radiative heat fluxes vary with engine speed, in this specific study it is assumed that they remain

constant. Using the gas boundary conditions given in Figs.6.8 to 6.11, surface temperature and flux data at 1000 and 2000 rpm are generated with and without radiative heat transfer. By this means, the differences due to engine frequency only, can also be observed.

Fig.6.78 shows the surface temperature fluctuation as a function of $\log_{10}k\rho Cp$ with convective and convective plus radiative gas boundary conditions at 1000 and 2000 rpm. The temperature swing is found to be lower at higher engine speed and this difference increases at small values of $k\rho Cp$ reaching 110 K. At a more realistic low value of $k\rho Cp$ of 10^6 J^2/m^4K^2s, the temperature swing difference due to engine speed is about 25 K. However, in a real engine environment where more severe gas boundary conditions occur at higher engine speeds, this difference most probably is covered and even higher swings can be produced. These results are presented in Chapter 7, where the FD model and cycle simulation package 'SPICE' runs are made concurrently. The temperature swing curves shift downwards for the gas boundary conditions without radiation. This shift is high at low $k\rho Cp$ values and is almost negligible for large values of $k\rho Cp$, such as 10^9 J^2/m^4K^2s.

In Fig.6.79 the mean and apparent surface temperatures as a function of $\log_{10}k\rho Cp$ are given. Since the surface temperature swings are very small at high values of $k\rho Cp$, the mean and apparent surface temperatures are almost equal irrespective of engine speed. At low values of $k\rho Cp$ the differences between the mean and apparent surface temperatures are bigger and reach 250 to 300 K for $k\rho Cp$ values of 10^3 J^2/m^4K^2s. Higher swings produce lower mean surface temperatures and in the ideal adiabatic case the wall mean surface

temperature is equal to the gas mean temperature. This effect can also be seen in Figs.6.75 and 6.77. For the same reason, the mean temperatures are slightly raised for higher engine speeds. The apparent surface temperature for the convective gas boundary condition is constant, whereas for convective plus radiative gas boundary it drops with decreasing $k\rho Cp$ value, because of the increasing amount of wall radiative emission.

In Figs.6.80 and 6.81 the wall mean pumped heat fluxes for the exhaust and inlet strokes are shown with respect to $\log_{10} k\rho Cp$. At low values of $k\rho Cp$, where wall surface temperature tends to follow the gas temperature, the pumped heat fluxes drop. It is obvious that the pumped heat during the inlet stroke is much higher than for the exhaust stroke due to higher wall to gas temperature differences. The pumped heat for the inlet stroke causes a reduction in the volumetric efficency which is undesirable. However, during the exhaust stroke it raises the exhaust gas temperature and thus the availability.

6.13 INCORPORATING THE FD MODEL IN 'SPICE'

After testing and validating the FD model, it was incorporated in the cycle simulation package 'SPICE', allowing the surface temperature swings to be obtained in a real insulated engine environment at various operating conditions.

In the previous version of Spice the gas to wall heat transfer is computed by assuming a constant surface temperature. This is an acceptable approximation for metal walls. However, as explained in Sec.6.9, for low conductivity ceramics where the temperature swings reach approximately 100 K, this assumption does not hold any more. Implementing a time dependent wall temperature model improves the gas to wall cycle mean heat flux values, and especially the instantaneous heat flux

values. In this way, the gas to wall heat transfer process during the combustion period which is crucial for engine performance, is represented correctly.

As mentioned in Chapter 4, Sec.4.8, in the cycle simulation program Spice the gas to wall heat transfer calculations start in the subroutine 'Woschni.For' (see flowchart in Fig.4.26). In this subroutine, the instantaneous gas htc is computed by using the empirical correlation proposed by Woschni [16]. Then, the flame radiation data is generated by calling the 'Radd.For' and 'Rad.For' subroutines which are explained in Sec.4.8. The heat transfer from gas to wall for each section of the combustion chamber is computed in subroutines 'Linat.For' and 'Rest.For' called by 'Woschni.For'. 'Linat.For' calculates the heat loss to the liner which is represented by 26 nodes, its flowchart being given in Fig.6.82. 'Rest.For' evaluates the heat transfer to piston, cylinder head, valves and other extra areas specified by the user and its flowchart is shown in Fig.6.83.

The FD model is modified and superimposed on the steady state engine resistance network which is presented in Chapter 5. The transient thermal analysis is kept within the TPD, and the rest of the wall is represented by thermal resistances which are used in the steady state heat flux equations at the end of each cycle. The coolant side boundary condition is represented by a constant temperature at the TPD; at the end of each cycle, its value is updated so that the heat balance to and from the wall is sustained.

According to the user's input data for Spice, when a time dependent wall temperature analysis is required, the FD model is used for the heat transfer calculations by calling 'Fd.For' from either 'Linat.For', or 'Rest.For'. It is also possible to apply selective FD model options to certain parts of the combustion chamber. The subroutine 'Fd.For' calls the

necessary subroutines 'Input.For', 'Laygen.For', 'Matp.For' and 'Fds.For', their flowcharts being shown in Figs.6.84 to 6.88. 'Input.For' handles the input data file and calculates the possible maximum TPD's. 'Laygen.For' generates the FD nodes within the TPD and treats the rest of the wall as thermal resistances. 'Matp.For' computes the material properties if they are temperature dependent, and stores the values of thermal diffusivity for the FD equations. 'Fds.For' is the subroutine that generates a set of simultaneous FD equations for each section of the combustion chamber, and calls subroutine 'Tridag.For' to solve them, and thus obtains the temperature distribution within the TPD.

The transient thermal analysis in the liner not only includes the convective and radiative heat flux components, but also conduction through the rings and friction fluxes. The detailed piston geometry and its complex interaction with the liner nodes is considered in the thermal analysis by the use of the piston crank mechanism. For this purpose, the subroutine 'Fricfd.For' has been written to supply the instantaneous friction flux to the liner nodes from the related piston region (Fig.6.89). The transient piston-liner conduction heat flux is evaluated from the temperature difference created between the piston internal node and the related liner node. The temperature of the piston internal node is constant throughout the cycle, whereas for the liner node it is a function of time.

While the transient thermal analysis is performed throughout the cycle, the gas heat transfer aggregates are stored to be used at the end of the cycle in the subroutine 'Resist.For'. This subroutine has been written to check the heat balance to and from the walls of the chamber, and update the surface temperatures for the constant wall temperature option, or the temperatures at the TPD's for the transient wall

temperature option. 'Resist.For' is well explained for the steady state engine resistance network in Chapter 5, and its flowchart is given in Fig.5.58. The proposed engine resistance model shown in Fig.5.2 is modified for the transient thermal analysis to include the resistances associated with the ceramic coating. A new term called 'extra resistance (ER)' which is dependent on the amplitude of the surface temperature swing is defined by:-

$$ER = \frac{T_{app} - \bar{T}_{w,0}}{\bar{q}} \qquad (6.49)$$

where:-

T_{app} is the apparent wall surface temperature.

$\bar{T}_{w,0}$ is the wall surface mean temperature.

$\bar{q}$ is the cycle mean heat flux obtained from the heat transfer aggregates.

The apparent surface temperature is derived from the instantaneous gas to wall heat transfer equation which is given by:-

$$q(\theta) = htc(\theta)\left(T_g(\theta) - T_{w,0}(\theta)\right) + q_{rad}(\theta) \qquad (6.50a)$$

or

$$q(\theta) = htc(\theta)\left(T_g(\theta) - T_{app}\right) + q_{rad}(\theta) \qquad (6.50b)$$

and expressed as:-

$$T_{app} = \frac{\overline{htcT_g} + \bar{q}_{rad} - \bar{q}}{\overline{htc}} \qquad (6.51)$$

where $\overline{htc}$, $\overline{htcT_g}$ and $\bar{q}_{rad}$ are the cycle mean values as defined in eqns.5.3 to 5.5.

The cycle mean heat flux calculated from wall to coolant is given by:-

$$\bar{q} = \frac{\bar{T}_{w,0} - T_{co}}{R_c + R_m + R_{co}} \qquad (6.52)$$

where R_c, R_m and R_{co} are the thermal resistances for ceramic, metal and coolant, respectively.

From FD results, it is proven that the mean heat flux calculated from eqn.6.52 and from cumulative transient heat flux are same. Therefore, it is concluded that, in order to write an overall steady state heat flux equation from gas to coolant, the temperature difference created by the apparent and mean surface temperatures can be represented by an imaginary resistance on the ceramic layer, which is called 'extra resistance', ER, and which has already been defined by eqn.6.49.

The apparent and mean surface temperatures and ER are demonstrated in Figs.6.92 and 6.93. For a non-fluctuating wall temperature, where the two temperatures are equal, ER becomes zero. However, for materials with low $k\rho Cp$ values, the difference between the apparent and mean temperatures is high due to bigger temperature swings. The cycle mean heat flux values are also expected to reduce a great deal, and as eqn.6.49 suggests the role of ER becomes significant in the steady state heat transfer calculations.

The importance of the ER term can also be explained by considering two materials having the same $k\rho Cp$ value, where one has high k and low ρCp values, and the other has low k and high ρCp values. Applying the same boundary conditions to the TPD and gas side produces the same mean heat flux values for both materials. However, a steady state heat transfer analysis yields a higher mean heat flux for the higher conductivity material, unless ER is included in the resistance network.

Once ER is evaluated, the apparent surface

temperature can be updated by using the heat balance from gas to wall and from wall to coolant, where the equation is given by:-

$$T_{app} = \frac{\left(\overline{htcT_g} + \bar{q}_{rad}\right)\left(ER + R_c + R_m + R_{co}\right)}{\left[1 + \overline{htc}\left(ER + R_c + R_m + R_{co}\right)\right]} \qquad (6.53)$$

The temperature at the TPD, T_n, is updated by the following equation:-

$$T_n = T_{app} - \left(\overline{htcT_g} + \bar{q}_{rad}\right)\left(ER + R_{TPD}\right) \qquad (6.54)$$

A subroutine called 'Exres.For' is written to compute the ER's of the various parts and its flowchart is presented in Fig.6.90.

For particular gas and coolant side boundary conditions, the FD numerical solution, depending on the initial conditions and the insulation level, requires about 10 to 20 cycles to reach steady state as shown in Fig.6.15. For this reason, at the end of each cycle the FD model is applied several times with coarser time interval of 5°CA, at the required combustion chamber walls to shift the temperature wave up or down. These calculations are performed in a subroutine named 'Fdcy.For' which is called by the subroutine 'Resist.For'. Its flowchart is given in Fig.6.91. However, in the last simulation cycle these calculations are excluded to reveal the true temperatures which are used for the heat transfer calculations.

CHAPTER 7
CYCLE SIMULATION RESULTS

7.1 INTRODUCTION

In this chapter, the cycle simulation results obtained by the new version of 'SPICE' which includes the models explained in Chapters 4, 5 and 6 are presented. The simulation runs are made for the experimental Petter PH1W engine geometry. In the first section of the chapter, the results of a standard engine and an engine with a nominal 1.5 mm PSZ coating on all combustion chamber surfaces are compared at various air-fuel ratios, engine speeds and boost pressure levels. The effect of engine insulation on radiative, convective and total heat fluxes, wall temperature distribution and performance are studied. Later a systematic approach is adopted to find an answer to the Woschni controversy concerning increase in heat loss with engine insulation. The significance of enhanced heat transfer coefficient (htc) and wall deposits on engine heat loss and performance is pointed out. The simulation runs for the 1.5 mm PSZ coated engine are repeated with enhanced htc at various engine operating conditions, and its effect on engine heat loss and performance are studied. Then, the effects of different monolithic ceramics on engine heat loss and performance are compared. Finally, the surface temperature swings during the engine start-up period are obtained to show their relevance to ceramic component failures.

7.2 1.5 mm PSZ COATED ENGINE

In this section, the piston, cylinder head, valves and top part of the liner, i.e. all engine internal surfaces except the liner section over which the piston rings slide, are considered to be coated with

1.5 mm PSZ. In order to save computing time, the ceramic properties are taken as constant and evaluated at 500°C (Table 2.3). The simulation runs are made for both standard and insulated engines at 3 air-fuel ratios, engine speeds and boost pressure levels which are summarized in Table 7.1. This section is concerned with the behaviours of the new models under various engine operating conditions.

The engine energy distribution for both standard and insulated engines at various engine operating conditions is shown in Table 7.2. As expected, increasing engine speed decreases the gas heat loss and raises the exhaust energy content and frictional losses. On the other hand, there is no significant change in heat loss and exhaust energy percentages by varying air-fuel ratio or boost level. In the present study, the gas heat loss in the standard engine is reduced from 32.5 to 19.8% by raising the engine speed from 1000 to 2000 rpm (Runs 2 and 5). As a result of this, exhaust energy and friction work are increased from 27.7 to 36.2%, and 6.1 to 9.6%, respectively. The engine brake thermal efficiency lies between 32.8 to 36.5% depending on the engine operating conditions, reaching its maximum at the highest boost condition.

Engine insulation reduces the gas heat loss by between 12.2 and 21.3%, the maximum occuring at the highest boost and lowest speed condition. As a result of this, thermal efficiency and exhaust energy increases by between 0.9 and 4.7%, and 5.5 and 15.4% respectively, thus suggesting that a turbocompound engine scheme is a suitable solution for further increase in engine overall efficiency. The insulated engine performance can be understood better by studying the effect of engine insulation on instantaneous heat fluxes which are explained in the following sub-sections.

The total gas heat loss per cycle and its distribution among the various parts of the combustion

chamber are shown in Table 7.3. The piston and cylinder head surfaces absorb between 41 and 45%, and between 34 and 36% of the total gas heat loss, respectively. The top part of the liner which is about 10% of the total liner area receives 12% of the total gas heat loss, whereas the rest of the liner absorbs between 7 and 13%, depending on the engine operating condition. Insulation of piston, cylinder head and top part of liner has no significant effect on heat loss distribution among the various parts of the chamber. The heat loss distribution through the piston and the cylinder head reduces by about 2%, whereas in the top part and rest of the liner they increase by about 1.5 and 2.5%, respectively. Although the lower part of the liner is not insulated, the heat loss in this region has not risen much. This is not surprising because of the rapid drop in gas temperature and htc, as a result of expansion of the combustion gases. This effect is well presented by instantaneous radiative, convective and total heat fluxes at various positions on the liner which are explained in the following sub-sections.

7.2.1 Radiative Heat Transfer

The results of the proposed radiative heat transfer model for the diesel engine, explained in Chapter 4, are given in Figs.7.1 to 7.15 and Tables 7.4 and 7.5. The net radiative heat flux at the piston surface as a function of crank angle (CA) at various engine operating conditions for both standard and insulated engines is shown in Figs.7.1 to 7.3.

There is a time lag of about 5°CA between the start of heat release and radiative heat transfer, i.e. no radiative heat transfer takes place in the premixed combustion mode, and this can be seen by comparing the heat release and heat flux curves shown in Figs.7.34 and 7.1, respectively.

The radiative heat flux curve rises sharply just

prior to the TDC, i.e. with the start of diffuse flame burning, and decays in a short time of about 40 to 50°CA. After combustion, a small amount of radiative heat transfer takes place during the expansion and exhaust strokes. However, its significance to the total gas to wall heat transfer is small. Due to rapid expansion of combustion gases in the cylinder, the flame and space mean temperatures drop sharply during and after combustion, thus reducing the radiative heat transfer drastically.

As the air-fuel ratio is reduced the radiative heat flux curve rises and the peak values reaches upto 1.5 MW/m^2. Under boosted conditions the maximum radiative flux value can further increase to a value of about 2 MW/m^2. There is no significant change with engine speed, except for sideways shifting of the radiative flux curve due to changes in the ignition delay periods. The values and trends of the radiative flux curves agree well with the experimental results published by Flynn et al [23]. However, their results do not show significant differences in the peak heat flux values at various air-fuel ratios and boost levels. Since the present radiation heat transfer model is based on the soot concentration levels published by Sitkei and Ramanaiah [25], which are functions of engine equivalence ratio as shown in Fig.7.6, it makes the flame emissivity and thus radiative heat flux sensitive to engine overall air-fuel ratio. The flame temperature is also higher at low air-fuel ratio, as shown in Fig.7.12, thus further raising the radiative heat flux. Under boosted conditions with the same air-fuel ratio the flame emissivity remains almost the same; however, radiative heat transfer is higher because of the increased flame temperatures as shown in Fig.7.14.

The cycle mean heat flux values and the percentages of the radiative and convective components for different parts of the combustion chamber are given

in Tables 7.4 and 7.5. In the standard engine, the cycle mean radiative heat loss varies between 23.4 and 16.4% of the total heat loss when the air-fuel ratio is varied from 20 to 40. The results published by Ebersole [22] and Oguri [24] which are shown in Figs.2.5 and 2.6 (Chapter 2), suggest that the percentage of radiative heat transfer is higher at rated engine conditions, thus supporting the model predictions.

Engine insulation raises the radiative heat flux both in absolute value and as a percentage of total heat loss. This effect is more pronounced at low air-fuel ratios and high boost conditions. The reason for the higher radiative heat flux with engine insulation, undoubtedly is the rise in flame temperature which is shown in Figs.7.12 to 7.14. The absolute value of cycle mean radiative heat flux at the piston surface for air-fuel ratios 40, 25 and 20 increases with insulation by 0.2, 5.6 and 9.1% respectively, whereas the radiative heat loss for the piston surface at various engine operating conditions rises from between 16.4 and 23.4%, to a higher level of between 20.0 and 33.9%, as shown in Table 7.4. However, engine insulation reduces the convection heat transfer and the overall engine heat loss reduces by an amount of between 12.2 and 21.3% (Table 7.2), depending on the engine operating condition.

The absolute cylinder head cycle mean radiative heat flux, as well as its percentage value are similar to the values for the piston (Table 7.4). The cycle mean radiative heat flux is less in the top part of liner and reduces further to very low levels in the lower part of the liner (Table 7.5).

The wall to wall radiative heat flux is also presented as a component of the net surface heat flux in Tables 7.4 and 7.5. The negative sign shows the energy leaving the surface, whereas the positive sign means the opposite. Due to low levels of wall surface temperature

inside the uninsulated engine, the wall to wall radiative heat flux is negligible. However, engine insulation is expected to raise its significance. With the present engine insulation level, maximum mean surface temperatures reaching 812 K (Table 7.6), there is no large increase in its percentage. The wall to wall radiative heat transfer becomes very crucial in heat flux calculations in a highly insulated engine and/or selectively insulated engine which are presented in the next section.

The radiative heat transfer model considers emission both from soot particles and from CO_2 and H_2O. The typical instantaneous mole fractions and partial pressures of CO_2 and H_2O at various air-fuel ratios are presented in Figs.7.4 and 7.5. The soot mass fraction as a function of CA is shown in Fig.7.6, where the exhaust level soot concentration after the completion of burning is taken as 20% of the peak soot concentration value and left constant until the gas exchange period commences. The soot volume fraction which is the product of soot mass fraction and gas density is shown in Fig.7.7, which emphasises the importance of gas expansion on soot volume fraction and thus on soot emissivity. Under insulated engine conditions lower volumetric efficiencies produce lower gas densities, thus slightly reducing the soot volume fraction.

The total flame emissivity and its components, i.e. gas and soot emissivity, observed at piston surface as a function of CA, are shown in Fig.7.8. For the early stages of the combustion the soot emissivity which follows a similar curve as soot volume fraction (Fig.7.7), is dominant. However, in the late burning, expansion and exhaust phases it loses its importance and gas emissivity takes over. After combustion, although the total emissivity has a value between 0.1 and 0.2, the radiative heat flux is not significant because of the drastic reduction in gas temperatures. Engine

insulation causes a slight reduction in emissivity values because of the loss in volumetric efficiency.

The total flame emissivities observed at various parts of the combustion chamber as a function of CA are shown in Fig.7.9. Due to the larger mean beam length of the liner compared with piston and cylinder head around compression and exhaust TDC, the flame emissivity observed at the liner is higher, leading to higher heat fluxes for the liner. However, around expansion BDC the mean beam lengths for piston and cylinder head are slightly higher than for the liner, thus leading to slightly higher emissivities for piston and cylinder head.

The flame and gas spatial mean temperatures as a function of CA for standard and insulated engines are shown in Fig.7.10. The flame temperature has a maximum value of about 2400 K, and rapidly approaches the space mean gas temperature value within 50°CA. The flame temperature is a function of burned to total fuel ratio which is expressed in eqn.4.74 (Chapter 4), and therefore after combustion it is equal to the space mean value. Engine insulation raises both the cylinder gas and flame temperatures, with a smaller effect on the latter.

The net total radiative heat flux at the piston surface and its components, i.e. soot and gas radiation, are shown as a function of CA in Fig.7.11. The gas radiative heat flux has a maximum value of about 0.18 MW/m^2, whereas the maximum soot radiative heat flux is about 1.38 MW/m^2, i.e. 7.7 times higher. Furthermore, the overall radiative heat flux which is calculated from the total flame emissivity expressed by eqn.4.42 (Chapter 4), is almost equal to the soot radiative heat flux, showing that the gas radiation has only small effect on the overall result. Engine insulation raises the radiative heat flux only in the early stages of combustion, due to higher flame temperatures.

The flame temperatures which are very important for radiative heat flux, at various air-fuel ratios, speeds and boost conditions for both standard and insulated engines are shown in Figs.7.12 to 7.14. The flame temperatures rise with reduction in air-fuel ratio and higher boost conditions, but there is no significant change with engine speed. Engine insulation raises flame temperatures, thus resulting in higher radiative heat flux, and this effect is more pronounced at low air-fuel ratio and high boost conditions. Although the difference between the radiative source temperatures for standard and insulated engines is higher after combustion, there is no significant change in radiative heat fluxes because of the low level of absolute temperatures. However, the difference in flame temperatures, as a result of engine insulation, is crucial in the early stages of combustion, producing bigger radiative heat flux changes.

Finally, the radiative heat flux at the piston, cylinder head and at various positions on the liner surface for both standard and insulated engines are shown as a function of CA in Fig.7.15. The liner-cylinder head junction receives higher radiative heat flux because as mentioned earlier a higher flame emissivity is applied to it caused by longer mean beam length (Fig.7.9). At an axial position of 10.4 mm from the cylinder head, the liner surface starts to receive radiative heat transfer around 35°CA after TDC, with a peak flux value of 0.2 MW/m^2. The axial position 16.7 mm which marks the end of the top part of liner, i.e. where the piston top ring rests at TDC, has a relatively small radiative heat input. This graph shows that especially for the middle and lower parts of the liner, the radiative heat flux has no significance at all. This effect can also be seen with mean cycle radiative heat flux values given in Table 7.5.

7.2.2 Convective Heat Transfer

The computer predictions showed that in a standard engine the convective heat transfer at piston and cylinder head surfaces contributes about 77 to 84% of the total heat loss, depending on the engine operating condition; being a maximum under low load conditions (Table 7.4). However, its percentage is slightly higher for the liner regions, where radiative heat transfer plays a less significant role because of the protective radiation shield formed by the combustion chamber geometry. The convective heat transfer forms between 79 and 89%, and between 83 and 95% of the total gas heat loss for the top and lower parts of the liner, respectively (Table 7.5).

The convective heat flux at the piston surface at various engine operating conditions for standard and insulated engines as a function of CA is shown in Figs.7.16 to 7.18. The magnitude of the instantaneous heat flux at specific points of the diesel cycle has a significantly different effect on engine performance. Higher heat flux during the inlet and compression strokes reduces the volumetric efficiency and ignition delay period, respectively. On the other hand, during combustion they cause a reduction in brake power.

The cycle peak heat flux increases with air-fuel ratio and with high boost conditions, reaching 4.5 MW/m^2. However, changes with the engine speed are not very significant. Engine insulation raises the wall temperatures upto 950 K, as shown in Tables 7.6 to 7.8, thus reducing the convective heat flux significantly. The maximum reduction in peak convective heat flux occurs at high load conditions which contradicts the experimental findings of Woschni et al [88]. Since the original Woschni htc is used in the performance predictions, this outcome is not surprising. However, the model predictions are supported by the published experimental flux data by Morel [111] and Cheng [112],

which show a reduction in flux levels with engine insulation.

As a result of engine insulation radiative heat flux increases and convective heat flux decreases, thus reducing the convective component of heat transfer significantly. For piston and cylinder head, the predictions showed that the convection component drops to a value of between 67 and 81%, depending on the engine operating condition, whereas for the top part of the liner lies between 75 and 88%. On the other hand, there is no significant change for the lower part of the liner where it ranges between 83 and 95%.

The instantaneous convective heat fluxes at piston, cylinder head and various axial positions on the liner surface are shown in Fig.7.19. Since the same htc is applied to the cylinder head and piston, the cylinder head having slightly lower temperatures, the resulting heat flux to the cylinder head is slightly higher than to the piston. The convective heat flux at the liner surface is quite low compared to piston and cylinder head because htc used for this region is multiplied with a scaling factor of 0.44 which is obtained experimentally (Chapter 5). The convective heat flux in the middle and lower parts of the liner, over which the piston rings travel, reduces significantly as shown in Fig.7.19. The main heat sources for these regions are friction and conduction provided by the piston rings, and are presented in Table 7.5.

7.2.3 Total Heat Transfer

The total heat flux falling on the combustion chamber walls is obtained by the summation of the convective and radiative heat fluxes. The instantaneous and cycle mean total heat flux values at various engine operating conditions for standard and insulated engines are presented in Figs.7.20 to 7.22, and Tables 7.4 and 7.5, respectively.

Since convective heat transfer in both types of engines is the major component, the total heat flux curve is dominated by it. The heat flux rises sharply at rich mixtures and high boost conditions reaching upto 5.8 MW/m^2 for the standard build. Cycle mean values vary between 114.8 and 312.4 kW/m^2, depending on the engine operating condition. Although engine insulation raises the radiative heat flux, its overall effect on total heat flux is a significant reduction. As mentioned previously, engine insulation reduces the total gas heat loss by an amount of between 12.2 and 21.3%, being a maximum at the highest loading. The cycle mean values drop to a level of between 93.9 and 218.6 kW/m^2.

The total instantaneous heat fluxes at the piston, cylinder head and at several positions on the liner surface are shown in Fig.7.23. The flux curves are the combinations of net radiative and convective heat flux curves shown in Figs.7.15 and 7.19. Considering the shape of the combustion chamber, some regions on the liner surface are always in contact with combustion gases. As the piston moves down, these regions are also exposed to the radiative flame, thus causing a sudden jump in the flux curve. This effect is well documented in Fig.7.23. The liner regions which are covered by the piston when it is at TDC, first come into contact with the combustion gases as the piston slides down, and later are exposed to see the radiative flame. This causes two jumps in the flux curve. However, the second jump caused by the radiative flux is not significant at all in these regions because of the rapidly decaying characteristic of the radiative flux as shown in Fig.7.15. The first sudden increase in heat flux also affects the surface temperature fluctuations at the liner, as shown in Figs.7.25 and 7.26.

In Fig.7.24, the radiative, convective and total heat fluxes for the high load and low speed condition, as a function of CA, for both types of engines, are also

shown together. These flux curves show the relative magnitude of radiative, convective and total fluxes and the effect of engine insulation on them.

7.2.4 Engine Temperature Distribution

The engine temperature distribution on the internal surfaces required for gas heat loss calculations also provides a rough estimate of temperature levels in an operating engine, thus giving an indication of failure probability of critical components. The engine resistance and transient wall models, as presented in Chapters 5 and 6, form a complete model to provide both steady state and transient temperature data of the engine.

Transient and steady state temperature data, i.e. surface minimum, maximum, time mean, apparent and ceramic-metal interface temperatures, as well as surface wave amplitude, at various engine operating conditions and for various parts of the combustion chamber, are presented for both types of engines in Tables 7.6 to 7.8. The apparent surface temperature is the steady state equivalent value which is used in the steady state heat transfer calculations, and it is always higher than the mean surface temperature.

In the standard engine, aluminium alloy thermal properties are used for the piston and cast iron for remaining surfaces. Since the thermal group $k\rho Cp$ for the piston is the highest, its surface temperature fluctuation is lower than for the cylinder head, varying between 7.4 and 19.9 K, depending on the engine operating conditions. For the cylinder head the surface temperature swing lies in the range 10.9 to 29.8 K. The swings on the liner surface are the lowest because of the lower heat flux falling on this surface. The liner-cylinder head junction which receives the highest heat flux on the liner surface, has a temperature swing of between 7.2 and 18.2 K. The mean surface temperatures

for the piston, cylinder head and at the liner-cylinder head junction lie between 410.2 and 537.9 K, 388.2 and 476.2 K, and 369.4 and 430.4 K, respectively.

Engine insulation raises the surface temperature swings for the PSZ coated piston, cylinder head and liner-cylinder head junction to a level of between 76.7 and 186.0 K, 77.6 and 190.1 K, and 55.4 and 132.5 K, respectively. Slightly higher swings for the cylinder head than for the piston result from the higher heat flux falling on the cylinder head, caused by its lower mean surface temperatures. The mean surface temperatures at the piston, cylinder head and liner-cylinder head junction are raised to a level of between 538.3 and 811.9 K, 524.1 and 780.6 K, and 466.8 and 673.8 K, respectively. However, the peak temperatures for these engine parts are much higher than the mean values. For the piston, under full load conditions, it becomes 954.3 K (Table 7.6).

The surface temperature of various parts of the combustion chamber, both for the standard and the PSZ coated engines, as a function of CA are shown at a particular engine operating condition in Figs.7.25 and 7.26. The double peaks occurring in the temperature curves of the top part of the liner can be seen; these are a direct result of sudden exposure to radiative heat flux, as mentioned in the previous section.

The effect of engine operating conditions on the surface temperature swing can be studied both in Tables 7.6 to 7.8 and Fig.7.27, which apply to a PSZ coated piston. As expected, increasing engine equivalence ratio and boost level more than double the temperature swing. On the other hand, it is reduced considerably at high engine speeds.

The propagation of the temperature wave through the material at various points of the cycle, and for specific engine operating conditions, for both types of engine is presented in Figs.7.28 to 7.30. Since the

aluminium alloy piston has the highest kρCp value, the thermal penetration depth (TPD) for this component is the highest of about 7.3 mm, almost double that for cast iron. For the PSZ coating the TPD is low, being only 0.54 mm at this particular engine operating condition. The PSZ coating has very high temperature gradients across the TPD, especially during the combustion period, indicating severe thermal stresses.

Finally, liner surface mean temperature distributions in the axial direction at various engine operating conditions, and for both types of engines are presented in Figs.7.31 to 7.33. As expected, the highest liner temperature occurs at the liner-cylinder head junction under full load conditions, having a value of 432.0 and 700.6 K respectively, for the standard and insulated engines. In the insulated engine, the liner temperature curve shows a sharp drop at a location about 17 mm below the cylinder head, corresponding to the end of the ceramic coating. The liner temperature distribution in the lower part of the liner, over which piston rings slide, is lower in the insulated engine. Thus piston-liner lubrication is not expected to be a problem with this type of engine insulation. This outcome is not surprising because in an insulated engine cooler piston rings lead to a reduction of conductive heat to the liner surface.

7.2.5 Engine Performance

Various engine performance parameters for both standard and insulated engines are presented in Table 7.10. Engine insulation reduces the isfc by 1.4 to 4.5%, thus raising the standard thermal efficiency of between 32.8 and 36.5%, to a higher level of between 33.5 and 38.2%. The greatest benefit of insulation is obtained under full load conditions.

The absorbed and pumped heat transfers for each stroke of the cycle are also given in Table 7.9, which

allows changes in certain engine performance parameters to be understood better. In the insulated engine, the hot walls raise the pumped heat for the inlet stroke by between 106.2 and 185.7%, thus reducing the volumetric efficiency by between 3.1 and 4.3%, the maximum occurring at full load. The heat loss for the exhaust stroke reduces by between 41.1 and 54.9%, thus leading to an increase in exhaust gas temperature of between 3.5 and 6.7%. By this means, more exhaust energy is provided for turbocharging or turbocompounding. As a result of the reduced volumetric efficiency of the insulated engine, the engine fuelling is adjusted in the simulation runs until the desired air-fuel ratio, as described in Table 7.1, is obtained. This causes a slight reduction in insulated engine power output (Table 7.10). However, higher exhaust temperatures will rise the boost level in a real turbocharged engine, thus compensating for the loss of volumetric efficiency.

The effect of engine insulation on the instantaneous and the mean gas htc and on pressure is very small, as shown in Table 7.10 and Figs.7.35 and 7.36. On the other hand, both cycle mean and instantaneous cylinder gas temperatures are influenced considerably, raising the mean value by between 2.7 and 5.1%, with the maximum at full load. The instantaneous gas temperatures at various air-fuel ratios are shown in Fig.7.37.

The engine combustion data, i.e. mean temperature and pressure during ignition delay, ignition delay and premixed combustion fraction are presented in Table 7.11. Engine insulation raises the mean ignition delay temperatures by upto 67 K which reduces the ignition delay period, as well as the premixed combustion fraction. The heat release curves for various air-fuel ratios for both types of engine are presented in Fig.7.34, which shows a significant reduction in the premixed combustion spike.

7.3 DOES INSULATION INCREASE OR DECREASE ENGINE HEAT LOSS?

In the previous section, it was shown that there is a significant drop in the engine heat loss with insulation. However, the experimental results published by researchers, such as Wallace [8] and Woschni [69,88], suggest that engine insulation, rather than reducing heat loss to coolant, actually raises it. The highest rise occurs under low engine speed and full load conditions, as explained in Sec.2.4. The experiments, by the named researchers, were performed with an air-gap heat barrier piston which was designed to reduce piston heat loss by about 55% of its original value.

In the heat barrier piston engine, the gas htc was suggested by Woschni to have higher values than the conventional engine, thus leading to higher heat losses. He modified his htc correlation by making it a function of the wall surface mean temperature. However, his conclusion is premature at this stage of the research. The observed increase in engine heat loss and reduction in power output can be the result of one or more of the possible reasons, as already discussed in Sec.2.4, viz. the selective insulation, increase in radiative heat transfer, changes in combustion characteristic and wall deposits. In the sub-sections these possibilities are considered and investigated throughly to identify the root of the problem. For this reason, the Petter PH1W engine equipped with a 1.5 mm air-gap insulated piston is simulated under high load and low speed conditions (A/F=20, Ne=1000 rpm). The effect of enhanced htc on engine heat loss and performance with heavy insulation is also studied. The description of the simulation runs performed for this section is presented in Table 7.12.

The heat transfer across the air-gap piston occurs both in the conductive and radiative modes, the radiative component being a significant portion. In order to model the air-gap piston correctly, a slight

modification was made to the piston thermal resistance network. The air-gap is considered as two parallel thermal resistances representing both the conductive and radiative heat transfers. The conductive resistance is given by the air-gap thickness to conductivity ratio (x/k), whereas the radiative resistance is calculated by:-

$$R_{rad} = \frac{\Delta T}{q_{rad}}$$

where ΔT and q_{rad} are the temperature drop and radiative heat flux across the air gap, respectively. To obtain the correct radiative thermal resistance and thus the steady state temperature distribution across the piston, an iterative solution, needing about 6 iterations to reach the correct solution, is applied. The wall emissivities for the Nimonic cap and aluminium body are approximately 0.6 and 0.1, respectively. However, in the present simulation the emissivity of the walls surrounding the air-gap is taken as 0.8, because the tests performed with the air-gap piston engine at Bath University showed that, soot deposits had accumulated within the air-gap space.

7.3.1 The Effect of Selective Insulation

This sub-section is included to indicate the effect of selective insulation, i.e. piston insulation only, on heat flux in other parts of the combustion chamber. In the analysis, both the original and modified Woschni htc correlations are used and the results are compared. As a result of piston insulation, the gas temperature can rise to such levels that the heat losses to other surfaces of the combustion chamber increase considerably. Thus, even with the original Woschni htc correlation, the overall heat loss of the selectively insulated engine is higher than that of the standard

engine.

The simulation runs included in this sub-section are numbered from 1 to 4 in Table 7.12. The first three runs are the main ones, the results being presented in Figs.7.38 to 7.50 and Tables 7.13 to 7.21. On the other hand, the fourth simulation run, was made with a low air-gap wall emissivity of 0.1 to demonstrate the importance of air-gap wall emissivity on piston heat loss. These latter results are given in Figs.7.51 and 7.52, and in the above mentioned tables.

The gas htc and temperature for the first 3 runs are shown in Figs.7.38 and 7.39. For the modified Woschni htc correlation, the peak and cycle mean htc's on the piston surface increase by 350 and 120% of their original values, respectively. The piston insulation using the original Woschni htc, the peak and cycle mean gas temperatures rise by 5.4 and 8.4%, respectively. In the modified Woschni htc case, lower increases in peak and cycle mean values of 3.0 and 7.4% respectively, are obtained. The resulting gas to wall heat fluxes, with their radiative and convective components, for the piston, cylinder head and the top part of liner (x=0.0 mm) are shown in Figs.7.40 to 7.42. The changes in the radiative component with piston insulation have little effect on total surface heat flux and are dominated by the convective component.

Piston insulation using the original Woschni htc, raises the cycle mean heat flux at the cyclinder head and for the top part of the liner by 15.7 and 10.5%, respectively. On the other hand, the mean heat flux at the piston surface and in the lower part of the liner are reduced by 63.3 and 10.5%, respectively (Tables 7.15 and 7.16). The decrease in heat flux in the lower part of the liner is the result of reduced piston-liner conduction.

Using the modified Woschni htc, the cycle mean heat flux at the cylinder head and in the top part of

the liner are increased by 20.3 and 15.3%, respectively. The mean heat flux at the piston surface and in the lower part of the liner is reduced respectively by 37.2 and 7.5%. Irrespective of the type of Woschni htc, the cycle mean heat flux for the piston is lower than in the uninsulated case (Table 7.15). This outcome is not surprising because the 1.5 mm air-gap is the dominant thermal resistance in the piston resistance network.

However, the transient heat fluxes at the insulated piston surface, computed with the original and modified Woschni htc correlations, differ widely from each other (Fig.7.40). The high peak heat flux caused by the modified Woschni htc during the combustion period reduces brake power and thermal efficiency considerably, as shown in Table 7.21. High rates of heat transfer from wall to gas during the intake stroke decrease the volumetric efficiency drastically.

The radiative heat exchange between the piston and the rest of the combustion chamber surfaces constitutes more than 30% of the net heat conducted through the piston which underlines its importance in selective and heavy insulation schemes. For the low air-gap wall emissivity case (Run 4), the radiated energy from the piston surface is greater than the net heat conducted through it, and has a cycle mean value of approximately 86 kW/m^2 (Table 7.15).

After studying the effect on surface heat flux, of piston insulation with the original and modified Woschni htc correlations, the work was extended to total heat loss from gas to wall. The gas heat losses to different parts of the combustion chamber in the standard engine are shown in Fig.7.43. The main heat loss is to the piston and cylinder head surfaces, whereas only a small amount of heat is transferred to the top and lower parts of the liner. The heat losses to the piston and cylinder head for the specifed three cases are shown in Figs.7.44 and 7.45, which are similar

to the flux curves. The heat losses to the top and lower parts of the liner are presented in Fig.7.46. the effect of piston insulation using the original and modified Woschni htc's has very little effect on the liner heat loss. For a better understanding, the heat loss curves in these two liner regions are also shown with their radiative and convective components in Fig.7.47.

The instantaneous cumulative heat losses to all parts of the combustion chamber for the specified three cases are shown in Fig.7.48. For the insulated piston using the modified Woschni htc, higher rates of pumped heat and peak flux are very evident. However, the cycle mean values for both insulated cases are lower than for the uninsulated case (Table 7.15).

In Fig.7.49 the effect of piston insulation on piston-liner conduction heat flux is presented. Piston insulation reduces the piston ring temperatures, thus providing a cooling effect in the top part of the liner, such that heat is transferred from the liner to the piston rings. The resulting liner temperature distribution is shown in Fig.7.50. The hotter gas temperatures in the insulated engine raise the liner temperature at the top end. On the other hand, temperatures in the mid-liner region are about 10 K lower than for the standard engine because of the reduced piston-liner conduction heat transfer.

The effect of reducing the air-gap wall emissivity on the piston surface heat flux and on total gas to wall heat loss are shown in Figs.7.51 and 7.52. Reducing the air-gap wall emissivity to 0.1 (Run 4), increases the piston mean surface temperature drastically upto 1424.2 K (Table 7.17), thus increasing the pumped heat during the intake and compression strokes of the cycle, as shown in the figures. On the other hand, there is a slight reduction in the piston peak heat flux, suggesting that heavy engine insulation makes the enhanced heat transfer effect during

combustion ineffective after some point.

The engine energy distributions for the specified cases are shown in Table 7.13. In the insulated engine, with the original Woschni htc, the engine gas heat loss decreases considerably from 32.74 to 28.09% of the fuel energy. As a result of this both brake thermal efficiency and exhaust energy rise from 33.92 and 28.18% to 34.44 and 32.12%, respectively. This suggests that the increase in engine heat loss reported by the previous researchers is not due to the selective insulation.

In the insulated engine, with the modified Woschni htc, the engine heat loss increases to 33.02%. The thermal efficiency reduces drastically to 30.89%, because of the greater peak heat flux during combustion. The exhaust energy content rises to 30.75%. This supports the experimental findings of Wallace [8] and Woschni [69,88].

The simulation run with low air-gap wall emissivity (Run 4), shows that the engine heat loss decreases even with selective insulation and modified Woschni htc (Table 7.13). However, the drop in thermal efficiency is unavoidable because of the enhanced htc during combustion. By changing the air-gap wall emissivity from 0.8 to 0.1 for the modified Woschni htc case, piston net cycle mean heat flux reduces from 145.4 to 66.8 kW/m^2 (Table 7.15). On the other hand, piston surface mean radiative heat flux increases from 56.3 to 86.1 kW/m^2 which underlines the significance of wall radiation in selectively insulated engines.

The effect of piston insulation on the gas heat loss distribution between different parts of the combustion chamber is shown in Table 7.14.Piston insulation reduces significantly the gas heat loss percentage of the piston. Contrariwise, the heat loss to other parts, mainly to the cylinder head, increases because of the raised gas temperatures in the cylinder.

The engine gas side wall temperature data are given in Tables 7.17 to 7.19. Air-gap insulation raises piston mean surface temperature from 485.7 to 1076.5 and 1281.9 K respectively, for the original and modified Woschni htc cases. There is also an increase in other parts, mainly the cylinder head mean surface temperature because of higher heat flux rates to these regions due to piston insulation.

The absorbed and pumped heats for each stroke of the cycle are shown in Table 7.20. Due to piston insulation, the significant increase in pumped heat for the inlet and compression strokes can be seen; this reduces the volumetric efficiency from 94.2 to 88.7 and 86.6% respectively, for the specifed three cases (Table 7.21), thus reducing the brake power output at constant air-fuel ratio significantly.

7.3.2 The Effect of Heavy Engine Insulation

In the previous section, it was shown that it is still possible to reduce the heat loss to coolant in a selectively insulated engine even when using the modified Woschni htc (Run 4). The wall radiation becomes a significant heat transfer mode in such a case. In order to observe the effect of enhanced htc in a heavily insulated engine and to reduce the wall radiation effect by total insulation, the piston, cylinder head and the top part of the liner are now insulated with a 1.5 mm air-gap. The air-gap is placed between the base metal and a 2 mm thick Nimonic section. To increase the effect of insulation, the air-gap wall emissivities are chosen as 0.1. The simulation runs are made with the original and modified Woschni htc correlations, as numbered 5 and 6 in Table 7.12.

Such engine insulation raises the piston and cylinder head mean surface temperature levels to 1350 and 1550 K respectively, for the original and modified Woschni htc's, (Table 7.17 to 7.19). The resulting wall

surface heat flux and gas heat loss are shown in Figs.7.53 and 7.54. Due to these high wall temperatures, the pumped heat during the compression stroke around TDC increases enormously, as shown in the figures and in Table 7.20.

The modified Woschni htc produces a lower piston surface peak heat flux in the heavily insulated engine than in the partially insulated case (Fig.7.53). This suggests that the effect of enhanced htc stops beyond a certain degree of insulation. However, the total gas to wall heat loss has a higher peak value in the heavily insulated case, because of the increase in peak heat flux in other parts of the combustion chamber, i.e. cylinder head and top part of liner. In the heavily insulated engine, the difference in peak surface heat flux created by the original and modified Woschni htc's are enormous (Fig.7.53).

With such heavy insulation, the cycle mean heat fluxes at the piston and cylinder head surfaces reduce drastically to levels of 60 to 80 kW/m^2. Flame radiation rather than convection becomes the main component of cycle mean heat flux. Wall radiation which is mainly exchanged between piston and liner, and cylinder head and liner still plays a significant role in cycle mean heat flux values.

The cycle mean heat flux at the top part of the liner increases from 109.1 to 112.4 and 149.9 kW/m^2 respectively,for the two types of htc's. This is not surprising because such liner insulation does not raise liner temperature as easily as in the piston or cylinder head (Table 7.17 to 7.19), because the axial heat flow down the liner surface becomes significant with this insulation type. Thus, the heat loss to the top part of the liner slightly increases with insulation. In order to reduce it, a low conductivity material should be used for the air-gap instead of Nimonic.

In the heavily insulated engine, the enhanced htc

reduces both the thermal efficency and gas to wall heat loss from 33.92 and 32.74 respectively, to 29.13 and 25.33% (Table 7.13). As a result of this, almost all the excess energy is transferred to the exhaust gas, increasing its energy from 28.18 to 39.26%, implying that with enhanced htc to obtain any benefit from engine insulation, heat recovery in the exhaust system via a low pressure turbine and/or Rankine bottoming cycle should be adopted.

The engine heat loss distribution between various parts of the combustion chamber becomes more evenly distributed in the heavily insulated case, compared to the standard engine (Table 7.14). This is mainly caused by the wall to wall radiative heat exchange. The gas heat loss percentages to the top and bottom parts of the liner rises considerably, as shown in the table.

The engine power output of such a heavily insulated engine decreases drastically because of the huge loss in volumetric efficiency, and makes turbocharging essential (Table 7.21).

The effect of engine insulation with a 1.5 mm PSZ coating on the liner surface cycle mean temperature distribution has already been discussed in Sec.7.2.4. As a result of such relatively low insulation levels, the temperature distribution in the lower part of the liner, over which the piston slides is slightly reduced (Figs.7.31 to 7.33). However, in a heavily insulated engine, especially with enhanced htc, the piston and cylinder head temperatures rise greatly, making the wall radiative heat exchange between these parts and the liner very important. As a result of this and higher gas temperatures, in the heavily insulated engine an increase in the liner temperature distribution, especially around ring pack TDC, is expected. With the effect of axial heat flow down the liner surface, even higher liner temperature rises around TDC can be obtained, thus creating piston-liner lubrication

problem.

The liner surface mean temperature distributions in the heavily insulated engine are given in Fig.7.60. The liner temperature difference between the standard and insulated engines at the top ring TDC is more than 50 K, for the two types of htc. In order to reveal the reasons behind this increase, the net heat flux falling on the liner surface and its components are plotted in Figs.7.55 to 7.59.

The engine insulation causes a slight increase in flame radiative heat flux over the lower part of the liner surface (Fig.7.55). However, the increase in the top part of the liner is more significant. The wall to wall radiative heat flux, especially for the modified Woschni htc case, rises drastically, reaching more than the double flame radiative value around top ring TDC (Fig.7.56).

The change in the convective heat transfer component at the lower part of the liner is not significant (Fig.7.57). However, in the top part of the liner, with the original Woschni htc, the insulated wall receives a lower convective heat flux than in the uninsulated case because of the higher wall temperatures. In this liner region, the convective heat flux increases as it is moved away from the cylinder head because of the reduction in wall temperatures. With the modified Woschni htc, the convective heat flux in the top part of the liner is much higher than in the other cases. However, a sudden drop in the flux curve towards the lower end of this top liner region shows that the liner temperature has reached 600 K, and enhanced heat transfer stops.

The piston-liner conductive heat flux is shown in Fig.7.58. Engine insulation, as already stated, changes the heat flow direction around TDC, and rings act as cooler for the liner.

The total heat flux distribution on the liner

surface is shown in Fig.7.59. In the insulated engine, the net heat flux around piston ring-pack TDC is lower than in the standard case. Thus, lower liner temperatures in this region would be expected, but this is not the case as shown in Fig.7.60. The reason is simply that the air-gap insulation in the top part of the liner forms a high resistance for radial heat flow through the cylinder walls. On the other hand, Nimonic with relatively higher conductivity than the air-gap, creates a better heat path along the liner surface, thus raising the net heat flux at the liner nodes around ring-pack TDC. This raises the liner temperatures in that region and could create piston-liner lubrication problems. To reduce this risk, the insulation of the top part of the liner should be effective both radially and axially, with similar levels of thermal resistance; alternatively Nimonic should be replaced by a low conductivity material ($k<2$ W/mK).

As already mentioned, the effect of enhanced htc stops beyond a certain level of insulation (Runs 3 and 6). In order to show this effect clearly, the surface heat fluxes for the air-gap insulated piston and the 1.5 mm PSZ coated piston (which is relatively a lower level of insulation) are compared (Runs 3 and 7). The results are shown in Figs.7.61 and 7.62. 1.5 mm PSZ coating raises the piston surface mean temperature to 864.3 K, thus increasing the peak heat flux during combustion. On the other hand, cooler wall temperatures reduce the pumped heat drastically, especially around TDC, compared to the air-gap insulated piston. The graphs clearly demonstrates the disadvantage of low level insulation for enhanced htc.

7.3.3 The Effect of Flame Radiation

The effect of engine insulation on radiative heat flux at various engine operating conditions has already been discussed in Sec.7.2.1. It was shown that, as a

result of engine insulation flame temperatures rise in the engine, thus increasing the flame radiative heat flux.

The flame emissivity has two components, soot emissivity, the dominant component, and gas emissivity which is a strong function of engine equivalence ratio. Engine insulation has almost no effect on flame emissivity. However, in an actual insulated engine, due to changes in combustion conditions within the engine, the soot concentration levels are expected to vary and thus affect the flame emissivity. This may be the reason for the reported increase in engine heat loss with insulation. For this reason, the air-gap piston engine was simulated with a flame emissivity of 1.0 throughout the cycle (Run 8), and these results were compared with the standard engine.

The surface heat flux at the piston and cylinder head both with their convective and radiative components, are shown in Figs.7.63 and 7.64. The peak heat flux at the air-gap insulated piston surface, with the original Woschni htc correlation and flame emissivity of unity, has still lower value than for the uninsulated piston case. On the other hand, at the cylinder head surface, due to increase in both convective and radiative heat fluxes, the net surface peak heat flux rises considerably. The overall effect of flame emissivity on gas to wall heat loss, as shown in Fig.7.66, is not very great. The engine heat loss increases slightly from 32.74 to 33.01% of the fuel energy, which is the same as with the modified Woschni htc case (Run 3). The thermal efficiency reduces from 33.92 to 32.72%, and its drop is not as drastic as in the modified Woschni htc case (Run 3), because of the smaller peak heat flux.

Although the flame emissivity is kept at unity throughout the cycle, the flame radiation is mainly influenced during the combustion period. This is not

surprising because of the rapid drop in flame temperature during and after combustion (Fig.7.65), makes the influence of flame emissivity on total heat flux for the rest of the cycle virtually negligible.

7.3.4 The Effect of Combustion

In the engine simulation program, the combustion process is represented by heat release curves as explained in detail in Chapter 3. Engine insulation raises the ignition delay mean temperature which reduces the ignition delay period and hence also the magnitude of the premixed combustion 'spike'. This effect has already been explained in Sec.7.2.5 and shown in Fig.7.34 and Table 7.11. However, these heat release curves are empirical correlations obtained on standard engines, and may not fully represent the insulated engine case. Furthermore, the combustion in the experimental insulated piston engine may not be as efficient as in the standard engine, thus causing a reduction in power output and increase in engine heat loss. In order to highlight the effect of combustion in insulated engines, simulation runs with extended and reduced heat release durations (HRD) were made for the air-gap insulated piston engine (Runs 9 and 10). To reduce the maximum cylinder pressure in the reduced HRD case, the premixed combustion spike is reduced by using a low ignition delay period in the heat release correlation. The resulting heat release curves are shown in Fig.7.69.

The effect of HRD, using the original Woschni htc correlation, on piston and cylinder head surface heat fluxes are given in Figs.7.67 and 7.68. These graphs demonstrate the importance of heat release curves on surface heat flux and thus engine heat loss. Reducing the HRD raises the peak heat flux, the opposite being the case when it is extended. However, the increase in surface peak heat flux for the insulated piston with the

reduced HRD, is still lower than for the uninsulated case, i.e. it is not similar to the modified Woschni htc case (Run 3). In order to have higher peak heat flux at the insulated piston surface, the HRD should be reduced further but this will raise the peak cylinder pressure (Table 7.21), which is not supported by the experimental pressure data obtained at Bath University [9].

The changes in surface heat flux at various locations in the combustion chamber influence the total gas to wall heat loss, as shown in Fig.7.70. The peak gas to wall heat loss in the insulated piston engine with reduced HRD has almost the same value as in the standard engine. However, the cycle mean heat loss percentage is still lower than in the standard engine (Table 7.13).

The effect of HRD on engine energy distribution can be seen in Table 7.13. In the insulated piston engine, increasing HRD reduces both the thermal efficiency and engine heat loss percentage (Run 2 and 9). The excess energy is transferred to the exhaust gases. Comparing the insulated engine having extended HRD with the standard engine (Run 1 and 9), reductions in both thermal efficiency and heat loss occur in the insulated engine, which does not support the experimental results published by Woschni and Wallace with respect to heat loss.

On the other hand, in the engine with the insulated piston only, reducing HRD raises both the thermal efficiency and engine heat loss (Runs 2 and 10). As a result of this, the exhaust energy content reduces. Comparing the insulated engine having reduced HRD with the standard engine (Runs 1 and 10), increase in thermal efficiency and decrease in heat loss are obtained in the insulated engine. This again contradicts the previous experimental findings.

Thus, the main conclusion is that the combustion process in the insulated engine may not be as efficient

as in the standard engine and re-optimization may be required. However, combustion optimization will not solve the crucial problem of increase in engine heat loss by insulation.

7.3.5 The Effect of Wall Deposits

During the combustion process soot particles are produced some of which adhere to the surface of the combustion chamber and form deposits. In spark ignition engines, these wall deposits not only influence gas to wall heat transfer, but also cause premature ignition and detonation, whereas in diesel engines the main concern is with the gas to wall heat transfer.

The thickness and thermal properties of the wall deposits considerably affect the gas to wall heat transfer. However, it is very difficult to obtain their values experimentally and to apply them universally for all engines. The thickness and thermal properties of the deposits depend on such factors as combustion characteristics, fuel type, wall type and temperature, etc. The variation in thermal property data of wall deposits, given in Table 7.22, also underlines the difficulties associated with this problem. The conductivity and thermal inertia vary between 0.04 and 0.8 W/mK, and between $6.45*10^4$ and $4*10^7$ J/m^3K, respectively. It is also shown that the thermal properties obtained by Anderson [114], of the initial transient and a fully formed steady state deposit layers as numbered 1 and 2, and 3 and 4 respectively in Table 7.22, show significant differences.

7.3.5.1 The Effect of Wall Deposit Thickness

First the effect of deposit thickness on wall temperature dynamics is investigated separately by using the FD code, discussed in Chapter 6. In the thermal analysis, two extreme groups of thermal properties are used, as indicated in Table 7.22, so that the full range

of deposit effects on gas to wall heat transfer can be covered. In order to include different wall material effects, the results are produced for both aluminium and PSZ walls.

The thermal analysis is performed for a 10 mm wall thickness. The gas side boundary conditions, including both convective and radiative heat transfer are obtained from standard engine simulation runs, e.g. Run 1 in Table 7.12. The gas temperature, htc and radiative heat flux are shown as functions of CA in Figs.7.38 to 7.40. The coolant side boundary condition is convective and has a htc value of 5000 W/m^2K. The coolant temperature is taken as 350 K. The results of the thermal analysis are presented in Figs.7.71 to 7.80.

The temperature dynamics of the wall deposit, i.e. maximum, minimum and mean temperatures, as well as swing amplitude, are plotted against deposit thickness in Figs.7.71 to 7.74. The wall deposit with the higher $k\rho Cp$(conductivity*thermal inertia) value, i.e. Deposit 2, has a smaller effect on the wall temperature dynamics. On the other hand, Deposit 1 which has a very low $k\rho Cp$ value has a significant effect on the wall temperature dynamics. Increasing thickness of Deposit 1, raises the maximum deposit surface temperature to over 1800 K (Fig.7.71). Beyond 0.1 mm deposit thickness, the maximum surface temperature remains almost constant and the wall material effect becomes insignificant. It may be thought that it is not possible for wall deposits to survive such high temperatures during combustion. However, during the combustion and expansion periods of the cycle, the oxygen availability could be quite limited, thus preventing the complete burn out of deposits.

The minimum surface temperature reduces with deposit thickness for Deposit 1, whereas the opposite occurs for Deposit 2 (Fig.7.72). Unlike the maximum

surface temperature, it is greatly influenced by the wall material.

Surface temperature swings exceeding 1400 K occur with Deposit 1, as against less than 100 K with Deposit 2 (Fig.7.73). Due to the lower surface temperature levels at the aluminium wall compared to PSZ, higher surface temperature swings are obtained at the aluminium wall for the same deposit type.

The deposit mean surface temperature increases steadily with deposit thickness for the aluminium wall, whereas for the PSZ wall, with Deposit 2 it remains almost constant. With Deposit 1, it reduces upto a 0.1 mm deposit thickness and then gradually increases. The drop in mean surface temperature with deposit thickness for Deposit 1 for the PSZ wall is a result of the huge temperature swings created at the surface. This effect can be understood better if the minimum surface temperature graphs in Fig.7.72 are studied.

The deposit-wall interface temperature swing and its peak timing are given in Figs.7.75 and 7.76. These graphs are particularly important for interpreting experimental surface thermocouple readings, and also determine the wall deposit thickness. As expected, increasing deposit thickness reduces the deposit-wall interface temperature swing and retards its peak timing. This effect is more pronounced with deposits having higher $k\rho Cp$ value.

The peak heat fluxes at the deposit surfaces are given as functions of deposit thickness in Fig.7.77. Deposit 1 reduces the surface peak heat flux drastically both on the aluminium and PSZ walls, whereas Deposit 2 has little effect on it.

The peak heat fluxes at the deposit-wall interfaces are given as functions of deposit thickness in Fig.7.78. Deposit thickness reduces the peak heat flux considerably at the deposit-wall interface for both deposit types, underlining the effect of soot deposits

on thermocouple readings.

Finally, the apparent or steady state equivalent temperatures and cycle mean heat fluxes as functions of deposit thickness are plotted in Figs.7.79 and 7.80. As expected, Deposit 1 which has low $k\rho Cp$ value has a higher effect on both variables, this effect being more pronounced for the aluminium wall.

7.3.5.2 Determining The Thickness and Thermal Properties of Combustion Chamber Deposits

After studying the effect of deposit thickness on wall temperature dynamics and gas to wall heat transfer, it was concluded that possible deposit thicknesses vary between 10 and 20 microns. This is also supported by the published experimental surface temperature data by various researchers [77,88,112], which suggest that the peak temperature timing is around 30°CA after firing TDC. Thicker soot deposits at surface thermocouple junctions would probably retard the peak temperature timing by more than that value, as shown in Fig.7.76.

Inclusion of wall deposits in wall transient heat transfer calculations with the original Woschni htc, reduces both the surface peak and cycle mean heat fluxes drastically (Fig.7.77 and 7.80). In order to have the same surface peak and cycle mean heat fluxes as in the clean wall case, the gas htc should be raised. The original Woschni htc correlation was obtained by considering only the wall thermal resistances, but ignoring wall deposit effects. Therefore, inclusion of wall deposits in heat transfer calculations requires an adjustment of the original Woschni htc correlation.

The more comprehensive theoretical gas convective htc model developed for diesel engines by Morel and Keribar [21] also suggests that the peak values of space mean gas convective htc are much higher than the values produced by the original Woschni htc correlation, reaching 12000 W/m^2K. Their predictions are similar to

the values obtained with the modified Woschni htc for hot walls (T_w>1100 K). Therefore, it is concluded that engine insulation instead of enhancing gas htc, can also cause a reduction in wall deposit thickness or even vanishing it, thus raising the gas to wall heat transfer.

The modified Woschni htc correlation is expressed as a function of wall surface mean temperature. On the other hand, deposit thickness is also expected to depend on the wall surface temperature. Tests performed for cleaner exhuast gas showed that soot disappears heating the exhaust gas beyond 1200 K [107]. Therefore, it is logical to conclude that soot deposits on combustion chamber walls become thinner and finally disappears with increasing insulation level, thus leaving combustion chamber walls directly in contact with the combustion gases. If the wall deposit thermal property group $k\rho Cp$ has a high value as for Deposit 2, then reduction in deposit thickness produces little effect on the gas to wall heat transfer. However, for the opposite case, i.e. with thermal properties similar to Deposit 1, then significant changes occur with reduction in wall deposit thickness.

The presence of wall deposits and their effects on gas to wall heat transfer is also supported by the experimental results published by Huang and Borman [77]. The experiments performed to measure metal surface temperature swings showed that there is a drastic decrease of up to 40% in surface temperature swings with increasing equivalence ratio. However, the opposite effect was expected because of the more severe gas boundary conditions occuring at higher equivalence ratios. This effect of engine air-fuel ratio on surface temperature swing, has already been presented in Fig.7.27 for clean walls. The apparent reduction in surface temperature swings at high equivalence ratios, as suggested by Huang and Borman, is probably the result

of higher soot production and its accumulation on thermocouple junctions during the combustion, thus damping the thermocouple output.

The experimental surface temperature swings at cold and hot walls presented by Woschni [88] also support the above argument. The surface temperature swings on uninsulated and insulated metal walls have almost the same amplitude, but the latter show a very sharp rise at the start of combustion. This simply indicates the effect of soot deposits on thermocouple readings. However, Woschni concluded that this sharp rise in surface temperature at the insulated metal is a result of enhanced gas htc.

It is possible that the heat flux predictions for insulated walls using the modified Woschni htc correlation are of the right order. However, this increase in wall heat flux is not caused by the enhanced gas htc but rather by wall deposit effects. Arguably, the reasons for the increase in heat flux with insulation are less important than the recognition of their existence. However, understanding the gas to wall heat transfer phenomenan with insulated walls will enable research to be directed into more fruitful areas.

For this reason an investigation was carried out for a 10 mm thick aluminium wall subjected to gas and coolant side boundary conditions as described in the previous sub-section. The thermal analysis is performed for both clean and sooty walls with the FD code described in Chapter 6. In the thermal analysis, gas htc values used for clean and sooty walls are obtained from the original and modified Woschni htc correlations respectively, as shown in Fig.7.38.

The thermal analysis of sooty walls was performed for 2 deposit thicknesses, 10 and 20 microns, having various conductivity and thermal inertia values. The surface peak and cycle mean heat fluxes as functions of deposit conductivity for various deposit thermal

inertias are plotted in Figs.7.81 and 7.82. Comparing these two graphs the thickness, conductivity and thermal inertia of the deposits are chosen such that the surface peak and cycle mean heat fluxes for both clean and sooty walls have the same values. The selected two deposit types which satisfy the above condition are described as follows:-

x=10 microns, k=0.042 W/mK, $\rho Cp=10^6$ J/m^3K

x=20 microns, k=0.032 W/mK, $\rho Cp=2*10^6$ J/m^3K

Although the above two types of deposits produce similar surface peak and cycle mean heat fluxes, their effects on the deposit-wall interface temperature wave are quite different, as shown in Figs.7.83 and 7.84. The second deposit type reduces the interface temperature swing and retards its peak timing considerably. Therefore, in terms of peak temperature timing at deposit-wall interface as recorded by surface thermocouples, the first deposit type is more realistic.

In order further to compare the two deposit types, the surface temperature and heat flux for both deposit types are plotted, as shown in Figs.7.85 and 7.86. The surface temperature of the first deposit decays faster, thus providing higher heat flux rates during the late burning and expansion periods of the cycle. As a result of this, slightly higher cycle mean heat fluxes are obtained with this deposit type. Although the first deposit type provides more realistic thermocouple readings, the second deposit type is chosen for engine simulation purposes because its surface heat flux curve is more similar to the clean wall case. It should also be noted that the wall deposits slightly shift the surface heat flux curve towards the left.

It is believed that the wall deposit thickness is varying about a mean value throughout the cycle. During

the combustion process soot accumulates on the walls, even if the wall is highly insulated, especially for rich mixtures where oxygen is less abundant, while during the intake and compression strokes, most probably some of the wall deposits are burned by the fresh incoming air. For insulated hot walls the burning rates of wall deposits are expected to be faster than for uninsulated cold walls, thus making the wall deposit thinner. Under heavy insulated conditions, it is also possible to reduce the deposit thickness to zero during the intake and compression strokes, thus leaving the bare wall in contact with the combustion flame. This makes the modelling of soot deposits in heat transfer calculations very difficult. On the other hand, considering the temperature changes experienced by the soot deposits and their influence on the thermal properties, greatly adds a further complication to the problem. Therefore, at the present level of modelling, the selection of soot deposit type 2 by just considering the surface heat flux and not the deposit-wall interface peak temperature timing can be considered as the optimum choice.

7.3.5.3 Heat Loss to Cold and Hot Walls

After determing the wall deposit thickness and thermal properties in the previous sub-section, the gas heat loss to cold and hot walls is compared in the presence of soot deposits. In order to include different material property effects on gas to wall heat transfer, metal and ceramic walls which can withstand high temperatures are chosen; they are Nimonic and PSZ walls. It is assumed that the cold walls are covered with 20 microns soot deposits, whereas the hot walls are free of any deposits. The thermal analysis for simplicity, is limited to the TPD, i.e. 0.6 mm for PSZ and 1.7 mm for Nimonic, and it is performed with the free standing FD code. The coolant side boundary conditions are assumed

to be constant temperature, 350 and 1000 K for cold and hot walls respectively.

The surface temperatures at the cold and hot walls are shown in Fig.7.87. With the effect of soot deposits, the surface temperatures at cold walls during combustion are higher than for soot free hot walls. The resulting surface heat fluxes are shown in Fig.7.88. The huge peak of the surface heat flux at the soot free hot Nimonic wall is clearly seen. Conversely, at the hot PSZ wall, this peak heat flux is relatively lower because of higher surface temperature swing at this wall.

The cycle mean heat fluxes through the cold and hot Nimonic walls are 260.3 and 336.7 kW/m^2, respectively. However, the cycle mean heat flux at cold and hot PSZ walls are 235.2 and 235.5 kW/m^2. Although the peak heat fluxes for the cold and hot PSZ walls differ considerably, their mean heat flux values are almost the same.

The deposit-wall interface temperatures and heat fluxes are also shown in Figs.7.89 and 7.90. In order to obtain reasonable peak temperature timing at the deposit-wall interface, the first deposit type, as explained in Sec.7.3.5.2 is used in the thermal analysis. For the hot walls which are assumed to have no deposits, the surface and interface values are same. As expected, the deposit-wall interface temperatures for the cold walls are much lower than the surface temperatures for the hot walls. The peak heat flux value at the interface also drops considerably, as shown in Fig.7.90.

7.3.5.4 Application of Wall Deposits to Engine Simulation Package 'SPICE'

After investigating the effects of soot deposits on gas to wall heat transfer separately by using the free standing FD code, these effects are now studied by using the engine simulation package 'SPICE',(See

simulation runs 11, 12 and 13 in Table 7.12). The engine internal surfaces, except for the liner region over which the piston slides, are assumed to be covered with a wall deposit of 20 microns thickness.

The first simulation run 11 is made with the original Woschni htc correlation for a soot covered standard engine. Wall deposits cause very large surface temperature swings during combustion, thus reducing the gas to wall heat transfer significantly. Piston and cylinder head cycle mean heat fluxes reduce from 231.7 and 243.1 kW/m^2 to 168.0 and 175.4 kW/m^2, respectively (Table 7.15). As a result of this, the engine energy distribution changes significantly as shown in Table 7.13. The engine gas heat loss reduces from 32.74 to 25.38%. Thermal efficiency and exhaust energy rise from 33.92 and 28.18% to 37.71 and 31.86%, respectively.

As already known, the Woschni htc correlation was obtained without considering any soot deposits on the engine walls. Therefore, for the purpose of correct cycle simulation the above results suggest that the gas htc should be raised in a sooty engine so that soot free and sooty standard engines give similar heat transfer results, assuming that in a real standard engine walls are always covered with soot. The second simulation run 12 is carried out for the sooty standard engine with adjusted Woschni htc correlation, i.e. the constant in the Woschni htc correlation for the closed period is increased so that similar gas htc values are obtained as in the modified Woschni htc case in the insulated piston engine, represented by Run 3 in Table 7.12. The htc curves as functions of CA are shown in Fig.7.92. The surface heat fluxes in various parts of the combustion chamber are compared with the results produced by the original Woschni htc in the soot free engine case (Run 1 and 12), as shown in Fig.7.91. The piston and cylinder head surface heat fluxes in both cases are very similar. The curves produced for the sooty engine have shifted

slightly to the 'left' because of the wall deposit effect; as also shown in Fig.7.86. The surface heat fluxes for the top and lower parts of the liner are higher for the soot covered engine because of different htc values used in these regions. However, the total gas to wall heat transfer curves for both cases are very similar. In order to understand the surface heat flux changes better, gas temperature and radiative heat flux for both cases are also presented in Figs.7.93 and 7.94.

The surface temperatures for clean and soot covered walls show large differences, as shown in Fig.7.95. These large differences in surface temperatures for heat transfer calculations are compensated by using higher htc values as shown in Fig.7.92. The resulting engine energy distributions for both cases (Runs 1 and 12) are similar and are given in Table 7.13.

Finally, the insulated-piston engine is simulated (Run 13) by assuming that the deposits on the piston surface dissappear due to the effect of insulation. As a result of this, piston surface peak heat flux increases drastically as shown in Fig.7.96, whereas the cycle mean value reduces from 215.3 to 139.1 kW/m^2 (Table 7.15). The selective insulation raises the heat transfer in other parts of the combustion chamber (Table 7.15 and 7.16), thus the heat loss rises from 34.92 to 35.95% (Table 7.13).

The gas to wall heat transfer curves for the three cases are shown in Fig.7.97. The disadvantage of piston insulation and absence of soot deposits can clearly be seen. As a result of this, a significant reduction in engine thermal efficiency from 33.10 to 29.83% is observed (Table 7.13).

The gas temperatures for the three cases (Runs 11, 12 and 13) and for the insulated-piston only engine with the modified Woschni htc case (Run 3) are shown in Fig.7.98. It is clearly seen that simulation

runs 3 and 13 produced almost the same gas temperature curves, thus indicating that enhanced htc and wall deposit effect can yield similar results.

Finally, the piston surface temperatures for clean and deposit covered walls with various versions of the Woschni htc are shown in Fig.7.99. The effect of soot deposits on piston surface temperature is clearly seen in this figure.

7.3.6 Conclusion

The published experimental results for selectively and fully insulated air-gap metallic engines by Woschni [69,88], Wallace [8] and Alkidas [72,82] showed that there was a significant drop in engine power output and thermal efficiency, accompanied by an increase in engine heat loss and exhaust energy, especially in selectively insulated engines. In the previous sub-sections, after investigating throughly all possible reasons to understand why engine insulation raises the heat loss to coolant, the following conclusions are drawn:-

1- Due to enhanced htc and/or wall deposit effect or an unknown phenomenon, engine insulation raises the surface peak heat flux during combustion, thus reducing engine power output and thermal efficiency.

2- At present, since the modified Woschni htc correlation is the only one readily available for insulated engines, it is provisionally accepted for simulation purposes until new models are proposed.

3- The insulation level has significant effect on both surface peak and cycle mean heat fluxes being greater on the latter. This is clear from the following argument:-

i) Low levels of engine insulation, such as 1.5 mm PSZ coatings, raise both surface peak and cycle mean heat fluxes. As a result of this, thermal efficiency drops and engine heat loss and exhaust energy increase.

ii) High levels of engine insulation, e.g. 1.5 mm air-gap, still raise the surface peak heat flux, but not as much as for PSZ coated surfaces. Thus, indicating that the effect of enhanced htc is reversed beyond a certain degree of wall insulation. On the other hand, the cycle mean heat flux reduces drastically because of the higher rates of pumped heat from wall to gas. As a result of this, thermal efficiency and engine heat loss decreases, and exhaust energy increases considerably (Table 7.13, Run 6). If exhaust energy is recovered in turbocompound and/or Rankine bottoming cycle engine schemes, a higher overall engine efficiency can still be obtained.

7.4 1.5 mm PSZ COATED ENGINE WITH ENHANCED GAS HTC

After showing the significance of enhanced gas htc on low level engine insulation in the previous section, the simulation runs made for the 1.5 mm PSZ coated engine in Sec.7.2., for various engine operating conditions as desribed in Table 7.1, are repeated in this section with the enhanced Woschni gas htc. The results are presented in Tables 7.23 to 7.29 and in Figs.7.100 to 7.107, and can be compared with the results in Sec.7.2, produced by using the original Woschni htc, given in Figs.7.20 to 7.22, and 7.31 to 7.33, and Tables 7.2 to 7.10.

The engine energy distribution data, given in Tables 7.2 (top part) and 7.23, shows that there is a significant increase in gas heat loss in the insulated engine, except at the low load and speed condition. At this engine operating condition, the surface mean temperatures of the combustion chamber walls are below 600 K (Table 7.27), which marks the start of the enhanced htc, as suggested by Woschni [69,88]. Thus, the benefit of insulation at low load is seen as an increase of 2.1% in thermal efficiency.

The highest increase in heat loss with engine insulation occurs at high load and low speed with a value of 8.5%. This finding is also supported by the published results of Woschni [88]. The highest wall temperatures occur at this engine operating condition, and with the enhanced htc which is a function of wall surface mean temperature, high heat flux rates are produced. As a result of this, the thermal efficiency at this engine operating condition reduces by 10.9%, while the the exhaust energy increases by 2.9%.

The gas htc's and temperatures at various air-fuel ratios obtained with the modified Woschni htc for both standard and insulated engines are given in Figs.7.100 and 7.101. For rich mixtures, the high htc peaks which reduce the peak gas temperature to uninsulated engine levels are clearly seen. In insulated engines, heat is pumped from the hot walls to the gas during the exhaust stroke, thus raising the exhaust gas temperature.

The instantaneous piston heat flux at various engine operating conditions for the standard and insulated engine are shown in Figs.7.102 to 7.104. The reduction in peak heat flux value at low load, and increase at high load and boost conditions are seen. The cycle mean flux values for different component surfaces are given in Tables 7.25 and 7.26 (compare with Tables 7.4 and 7.5). At the lowest air-fuel ratio and engine speed, the cycle mean heat flux at the piston and cylinder head increases from 231.7 and 243.1 kW/m^2 to 246.7 and 253.2 kW/m^2, respectively, while cycle mean flux for the top part of liner reduces from 109.1 to 92.7 kW/m^2, because even at this high loading the temperatures for most positions of the liner are below 600 K (Fig.7.105). Therefore, the enhanced htc is not very effective in this region. This effect can also be seen in Table 7.24, which describes the heat loss distribution among different surfaces. Comparing Tables

7.3 and 7.24, it is seen that there is a slight increase in heat loss through the piston and cylinder head, whereas a slight decrease occurs in the top and bottom parts of the liner.

The absorbed and pumped heat data is presented in Table 7.28. Comparing it with the data obtained with the original Woschni htc in Sec.7.2 (Table 7.9), shows that there is a significant increase in pumped heat during the inlet and exhaust strokes, because of the higher wall temperatures.

As a result of enhanced htc, higher peak heat fluxes occur during combustion and thus reduce the brake power drastically, especially for the full load condition, by 16.6% (Table 7.29).

The enhanced gas htc increases both the surface mean temperature and the temperature swing considerably, especially at the low speed and high load condition (Tables 7.6 and 7.27). For the piston, at this engine operating condition (A/F=20, Ne 1000 rpm, N.A.), the surface mean temperature increases from 738.7 to 863.6 K, whereas the surface temperature swing rises from 147.6 to 217.4 K, i.e. 47% rise. This shows the significance of the htc type used in thermal stress analysis of ceramic coatings and monolthic components.

7.5 ENGINE INSULATION BY USING MONOLITHIC CERAMICS

The temperature dynamics and heat transfer of different ceramic walls, having 10 mm thickness, have already been presented in Chapter 6 (Sec.6.9). The thermal analysis was performed by using the separate FD code with gas boundary conditions obtained from the engine simulation package. In this section, different ceramic materials are assessed, based on the Petter PH1W engine, by using the new version of the engine simulation package 'SPICE'. However, before investigating the effect of different ceramic materials

on engine heat loss and performance, the role of ceramics as heat insulators is discussed in the following sub-section.

7.5.1 The Role of Ceramics as Heat Insulators

It seems probable that low heat loss engines will appear in the market first with reduced cooling capacity and later with the cooling system completely eliminated. Reducing or eliminating the cooling system reduces the parasitic losses, such as those for the water pump and cooling fan, and thus directly raises the engine overall efficiency. This also provides a high level of engine insulation, irrespective of wall material, and raises the combustion chamber gas side surface temperatures above 1300 K. The coolant side boundary effect has already been explained in Sec.6.9.1 and is shown in Figs.6.32 and 6.34.

In order for combustion chamber walls to survive such high temperature levels, caused by the elimination of the cooling system, they should be made from high temperature materials, such as ceramics. Ceramics have a wide range of thermal properties and their effect on engine heat transfer and performance can vary widely. In the present sub-section this is discussed, based on Sec.6.9, to explain the role of different ceramics in engine heat insulation.

The effect of wall thickness on heat transfer for various ceramic walls has already been discussed in Sec.6.9.4. It is shown that increasing the thickness of a ceramic wall which has conductivity less than 2 W/mK, further reduces the cycle mean heat flux. Conversely, for ceramics having higher conductivity, such as sialon or HPSN, the wall thickness has virtually no effect on cycle mean heat flux (Fig.6.49). These conclusions are based on calculations for a ceramic wall with fixed coolant side boundary conditions (htc=50 W/m^2K, T_{co}=300 K). Further significant reductions in cycle mean

heat flux can be achieved by introducing an air-gap within the ceramic component or using a coolant side boundary condition close to adiabatic. Under such conditions the ceramic conductivity becomes insignificant in reducing the cycle mean heat flux. Therefore, the surface temperature levels within the combustion chamber can easily be controlled by the coolant side boundary condition, irrespective of the ceramic type and thickness. Wall conductivity and thickness gain importance in highly cooled engines.

The coolant side boundary condition also plays a significant role in reducing the surface peak heat flux, which directly influences the engine power output and thermal efficiency. This effect has already been shown for aluminium and a hypothetical low conductivity, low thermal inertia material ($k=1$ W/mK, $\rho Cp=10^6$ J/m^{2}K), in Figs.6.35 and 6.36 respectively. It was shown that the wall surface peak heat flux reduced by about 50% of its original value by the elimination of the cooling system, irrespective of the wall material type. In the uncooled case, the difference in surface peak heat flux created by the two materials is very small, but becomes greater in the cooled case. In order to reduce the surface peak heat flux further in the uncooled case, ceramic walls having low $k\rho Cp$ values, such as wall deposits (as explained in Sec.7.3.5) should be used. However, with currently available candidate ceramic materials which have considerably higher $k\rho Cp$ values than the wall deposits (Tables 2.3 and 7.22), it is not possible to reduce the wall surface peak heat flux drastically.

The coolant side boundary condition has a marked effect on both steady state and transient temperature gradients created within the wall which control thermal stresses. Cancelling the cooling system raises the wall temperature both on the gas and coolant side. However, for a particular material, the steady state temperature

difference across the wall drops due to the lower cycle mean heat flux. This effect has already been explained in Sec.6.11, the wall temperature distribution is given in Table 6.8. As a result of higher wall temperature levels, the surface temperature swing, irrespective of wall material, reduces by about 50%, as shown in Figs.6.31 and 6.33.

It was mentioned that introducing an air-gap within a ceramic component further reduces the cycle mean heat flux. An air-gap also divides the wall into two parts, viz. hot and cold, the former adjacent to the combustion chamber, and the latter to the coolant side. The large temperature drop across the air-gap simplifies component design.

A 1.5 mm PSZ coated engine with a cooling system can be shown as an example of severe thermal gradients created within the wall. Using the enhanced htc, the steady state temperature difference across a 1.5 mm PSZ coating can be as high as 562.6 K (Table 7.27); the associated surface temperature swing being 286.9 K. These large steady state and transient thermal gradients can be reduced by using thicker coatings, if possible, and by reducing or cancelling the cooling system.

The best insulation method from a thermal efficiency and thermal stress point of view can be described as a monolithic ceramic component attached to a metal base separated by an air-gap, in conjunction with the total elimination of the cooling system. By this means, the cycle mean heat flux will drop considerably to very low levels, assuming that a proper air-gap design is adopted. In order to reduce the surface peak heat flux which greatly affects power output, a material having low $k\rho Cp$ value, such as wall deposits, should be used. However, such material properties produce large surface temperature swings resulting in severe cyclic thermal stresses. Therefore, in selecting the ceramic type a compromise should be

made between the low surface peak heat flux and low cyclic thermal stresses.

7.5.2 The Effect of Different Monolithic Ceramics on Engine Heat Loss and Performance

As already explained in the previous sub-section, the cycle mean heat flux can easily be controlled by the coolant side boundary condition. Therefore, the comparison of different ceramics relative to engine heat loss and performance is based on the peak heat flux which is a function of the wall surface temperature swing. Of the six ceramics investigated in Sec.6.9, the monolithic ceramics cordierite, HPSN and HPSC are chosen for the present simulation study so that a wide range of material conductivity is covered. In order to maximize the surface temperature swing effect on peak heat flux, a low speed, high load and high boost engine operating condition is chosen (A/F=20, Ne=1000 rpm, 2 Bar boost). By using the same insulation levels for all ceramics, the gas side wall surface mean temperature levels are kept close to each other. The difference created in insulation levels by the use of different ceramics is compensated by adjusting the coolant side htc. By this means, the difference produced in the peak surface heat flux for different ceramics is a function only of surface temperature swing.

The engine internal surfaces, piston, cylinder head and top part of the liner are covered with monolithic ceramics. The insulation level, i.e. wall thickness and coolant side htc values are chosen such that the maximum surface temperature is around 1500 K. Since cordierite has the highest surface temperature swing, the insulation level is based on this ceramic. The simulation runs are made with both the original and the modified Woschni htc correlations. The ceramic wall thickness is taken as 10 mm for the original Woschni htc case. The coolant htc values for cordierite, HPSN and

HPSC are 416.5, 119.3 and 113.4 W/m^2K, respectively (Table 7.30). The coolant side htc values are obtained from the cordierite thickness required to raise the cylinder head peak surface temperature to about 1500 K in the cooled engine. This value corresponds to 13 mm, where 10 mm is accounted for by the wall thickness and an additional 3 mm cordierite insulation is assumed to be supplied on the coolant side. For other ceramics, 10 mm ceramic wall and coolant side boundary condition supplies an overall insulation level equivalent to 13 mm of cordierite wall in a cooled engine.

The piston coolant side boundary condition is kept the same. Even if it is altered, rather than insulating the piston it simply changes the heat path within the piston towards the rings. Therefore, the piston is always assumed to be insulated with a thermal resistance equivalent to 10 mm cordierite. For high conductivity ceramics such as HPSN and HPSC, this insulation level can be considered as a 10 mm ceramic wall seperated from the main piston body by an air-gap to give the necessary insulation level.

The simulation runs made with the modified Woschni htc correlation required a lower insulation level to keep the peak surface temperature to approximately 1500 K. This corresponds to a cordierite wall thickness of 3 and 3.5 mm, for the piston and the remaining components respectively, in the cooled engine. For cordierite of 3 mm wall thickness a coolant htc value of 1363.4 W/m^2K was chosen. However, for HPSN and HPSC the wall thickness is kept the same as before, i.e. 10 mm. In order to provide the same insulation level, the coolant htc values for HPSN and HPSC were taken as 489.3 and 402.3 W/m^2K, respectively (Table 7.30).

Using high conductivity ceramics for the top part of the liner and cylinder head leads to further reduction or total elimination of the cooling system. This is an advantage because of the reduction or

elimination of parasitic losses of the engine. On the other hand, low conductivity ceramics can be considered advantageous for piston insulation as they eliminate the need for an air-gap, ceramic piston design. For materials which can withstand very high temperatures, the cooling system will be eliminated irrespective of the ceramic type. In such a case materials with a low $k\rho Cp$ value will be chosen to reduce the peak heat flux further.

Surface temperatures and heat fluxes of ceramic pistons calculated with both types of Woschni htc correlation are shown in Figs.7.108 to 7.111. The peak surface temperature for the cordierite piston in both cases is about 100 to 120 K higher than for the other ceramic pistons. As a result of this, in the original Woschni htc case the peak surface heat fluxes for the different ceramic pistons vary only slightly. On the other hand, the differences in the peak surface heat fluxes obtained by using the modified Woschni htc are very large. The advantage of a high surface temperature swing, such as occurs with the cordierite piston using the enhanced htc, is very evident. This reduces the peak surface heat flux by 2 MW/m^2, compared with the HPSC piston. However, peak heat fluxes for all ceramic pistons are still higher than for the uninsulated aluminium alloy piston.

Energy distributions for ceramic engines are presented in Table 7.31. Results obtained with the original Woschni htc correlation show sigificant reduction in engine heat loss, with an increase in engine thermal efficiency and exhaust energy content. Conversely, use of the enhanced htc reduces engine thermal efficiency drastically. As a result of this, engine coolant and exhaust energy contents increase.

The gas heat loss distribution between different parts of the combustion chamber is shown in Table 7.32. There is no significant change for the modified Woschni

htc case. However, with the original Woschni htc significant reductions in piston and cylinder head heat loss percentages are observed. The heat loss for the lower part of the liner rises by about 2.6 times compared with the standard engine.

The cycle mean heat fluxes and their components for various parts of the engine are given in Tables 7.33 and 7.34. The influence of the original and modified Woschni htc correlations on cycle mean heat fluxes is shown clearly. Although the insulation levels are kept the same, in the enhanced htc case the high surface temperature swing produced at the cordierite wall reduces the cycle mean heat flux by 6.7%. Almost identical cycle mean heat fluxes are obtained for the rest of the cases.

Temperature data for ceramic engines is given in Table 7.35. The high temperature swing obtained at the low conductivity cordierite surface is 160.9 K for this particular high load and high boost condition. With enhanced heat transfer it is almost doubled, reaching 312.7 K.

Gas to wall heat transfer for the various strokes of the cycle is shown in Table 7.36. The increase in wall to gas heat transfer percentages with engine insulation for the intake and exhaust strokes is clearly seen. On the other hand, gas to wall heat loss percentage during combustion rise with engine insulation, this being the only period of the cycle with gas to wall heat transfer.

Ceramic engines performance parameters are given in Table 7.37. Due to lower volumetric efficiency caused by engine insulation, engine power output reduces. However, higher exhaust gas temperatures can be used to provide either higher boost level or recover energy via a low pressure turbine, and thus raise the engine power output.

The effect of different ceramics on liner

temperature distribution for both types of the Woschni htc are shown in Figs.7.112 and 7.113. At TDC the position of the top ring centreline is 18.05 mm below the cylinder head, and marks a sharp drop in the liner temperature distribution for cordierite. This shows the beneficial effect of using low conductivity ceramics for top part liner insulation, on the lubrication of the piston ring pack around TDC. For relatively higher heat conductivity ceramics, the axial heat flux gains importance, thus raising the liner temperature around the piston ring pack TDC, and possibly causing serious lubrication problems. Since the insulation level in the modified Woschni htc case is reduced to 27% of the original Woschni htc case to maintain the peak surface temperatures at below 1500 K, lower temperatures resulted at the top part of the liner.

7.6 The Effect of The Engine Start-Up Period on Wall Surface Temperature Fluctuation

During the engine start-up period, the combustion chamber walls are cold and engine speed is much lower than under normal engine operating conditions. As a result of this, for a particular set of gas and coolant side boundary conditions (which are also valid in normal engine operation), higher surface temperature fluctuations are expected during the engine start-up period.

Ignition in the experimental Petter PH1W engine starts at approximately 200 rpm, engine speed thus reaches idling speed of approximately 800 rpm, in 5 to 10 cycles. During this start-up period, the gas side boundary conditions and wall temperature distribution change continuously, making it very difficult to model the actual gas to wall heat transfer. However, previous studies with the cycle simulation package showed that the peak gas temperature and htc values, which greatly affect the surface temperature swings, do not change

significantly with engine speed, being strong functions of air-fuel ratio. The surface heat flux curves produced at various engine speeds also support this view, as shown in Fig.7.21. Thus, it was decided to use the available gas side boundary data at 1000 rpm of the standard engine, which has relatively cold walls, in conjuction with the free standing FD code to obtain the possible surface temperature fluctuations during the engine start-up period.

During this period, fuelling can be low or high depending on the engine operator. Even if low fuelling is used, before ignition takes place, i.e. during cranking, some of the fuel is expected to be absorbed by the cold combustion chamber walls, especially by ceramic walls which are relatively more porous. The fuel wall wetting could create local rich air-fuel pockets near the wall surfaces. It is thus possible to have rich air-fuel mixtures in the vicinity of the wall surfaces during the engine start-up period, even if the overall engine equivalence ratio is low. For these reasons, the thermal analysis is performed for two air-fuel ratios of 20 and 40 to observe possible surface temperature swings generated during this period.

The thermal analysis is performed for a cordierite wall and is limited to the TPD, i.e. 2 mm at 200 rpm. First, the effect of successive firing cycles on wall surface temperature during engine start is investigated at an engine speed of 200 rpm and an air-fuel ratio of 20, as shown in Fig.7.114. The coolant side boundary temperature and initial wall temperature distribution are both chosen as 293 K, so that the cold wall condition is satisfied. The wall surface temperature rises quickly and reaches its steady mean state in 15 cycles with the specified boundary and initial conditions. Due to the low engine speed and high fuelling, the surface temperature swing is very high, especially during the first firing cycle reaching

315.4 K. This value is similar to the surface temperature fluctuation produced with enhanced htc at 1000 rpm, high load and 2 bar boost level, as shown in Table 7.35. The surface temperature fluctuations decrease with the number of cycles, dropping to 283.1 K at the 15th cycle.

The actual wall surface temperature dynamics during the engine start-up period may be obtained by assuming that for every firing cycle, engine speed rises by 100 rpm. Thus, the engine reaches idling speed of approximately 800 rpm in 7 cycles. The surface temperature swing at a particular engine speed is represented by the specified cycle number at that engine speed. The coolant side boundary temperature and initial wall temperature distribution are taken as 293 K. The results are obtained for air-fuel ratios of 20 and 40 and presented in Figs.7.115 and 7.116. The rapid change in surface temperature swing during the engine start-up period is clearly seen. Surface temperature swings change from 315.4 to 155.8 K and from 165.7 to 81.4 K for air-fuel ratios of 20 and 40, respectively. Such high surface temperature swings occuring during the engine start-up could well result in crack initiation within ceramic components. Crack growth can then continue even if the ceramic component is subjected to less severe gas side boundary conditions, and could well result failure of the component.

In order to reduce surface temperature swings during the engine start-up period, a thermal analysis for two preheated wall cases of 500 and 1000 K at air-fuel ratio of 20 were also performed. The results are shown in Figs.7.117 and 7.118. As a result of wall preheating, the surface temperature swings are reduced from between 315.4 and 155.8 K to 278.9 and 139.7 K, and to 195.9 and 101.7 K for the initial wall temperature distribution of 500 K and 1000 K, respectively.

CHAPTER 8
EXPERIMENTAL STUDY

8.1 INTRODUCTION

This chapter details the experimental work carried out during this project and describes its associated test rigs and instrumentation. The programme consisted of two main parts as:-

1- Measurement of surface temperature swings on ceramic disks.

2- Measurement of cycle mean axial liner temperature distribution.

The first part of the programme was carried out in the simulation test rig which is explained in the next section. The surface temperature fluctuations on ceramic components were attempted to be measured in order to derive the cyclic thermal stress levels from the temperature data. The transient gas side boundary conditions can also be calculated from the transient wall surface temperature and thus provide us with valuable data in the adiabatic engine component design. Unfortunately, the tests were not successful. The research in this field at Bath University is still continuing.

The second part of the programme was performed in the fired engine rig which is explained in Sec.8.5. By this means, the heat flux levels on the cylinder liner can be observed and a better engine thermal model can be built which will predict the axial liner temperature distribution and heat flux levels under various insulated engine conditions.

8.2 SIMULATION TEST RIG

This test rig was designed by the previous research student S. Manton and his colleague W.

Alexander for endurance testing of ceramic components [10]. The rig is a single cylinder Petter PH1W engine with a completely new cylinder head design which accommodates the ceramic specimen. By keeping the ceramic piece stationary in the cylinder head a catastrophic failure of the specimen and thus serious damage to the rig is prevented. The test rig is further protected from damage by a retaining grid which is incorporated immediately below the ceramic piece to prevent any ceramic fragments from entering the cylinder space.

In the design of the test rig the main consideration was to mimic the temperature and pressure fluctuations present in a fired diesel engine. Thus typical mechanical and thermal loadings generated in a diesel engine can be applied to the ceramic specimen. In order to increase the cylinder peak pressures, the compression ratio is increased from 16.5 to 19.5 by using a raised flat top piston. The piston top is very close to the top end of the cylinder at TDC and therefore further raising its height is not possible. Although this kind of piston arrangement is expected to increase the compression ratio higher than 19.5, the particular cylinder head design makes it necessary to leave some space between the retaining grid and ceramic specimen in the cylinder head, resulting in the specified compression ratio. The test rig is connected to a high pressure air supply system which is at 80 psi gauge pressure. By using boost pressure levels of about 3 bars, it is possible to generate peak cylinder pressures in excess of 140 bars. The pressure of the system is controlled by a manual pressure regulator and a dome valve. The schematic layout of the system is given in Fig.8.1.

Since the compression ratio of the test rig is not high enough to raise the gas temperature by compression to the level in a fired engine, an air

heater is used to increase the engine inlet air temperature so that higher temperatures can be produced within the engine. To decrease the energy consumption in the air heater a closed air loop system is adopted (Fig.8.1). By controlling the engine air inlet temperature, the desired thermal loading can be applied to the ceramic component. The cylinder peak temperatures can be raised to 1200°K which may seem well below the temperatures in a fired engine but still provides a means of testing the ceramic piece before using it in the actual fired engine. The detailed description of the rig and its components is given in [10].

The engine is powered by an 8 kW three phase electrical motor. A manually operated variable speed belt drive system is used to provide an engine speed range of 800 to 2000 rpm. The photograph of the simulation test rig is presented in Fig.8.2.

8.3 MODIFICATIONS TO THE SIMULATION TEST RIG

The simulation test rig was first designed and built for endurance testing of ceramic components. Later in the programme, it was modified and instrumented to measure the temperature fluctuations occurring at the ceramic surface due to thermal loading. Although the tests were not successful, a brief description of the work done during the project is given.

The engine speed and thermal loading range of the rig were increased. For this reason one of the pulleys of the manually operated variable speed belt drive system was changed and the previous 4 kW electric motor was replaced by an 8 kW motor. The reed valves of the rig were replaced by new ones made of stainless steel which can survive high temperatures. Thus the full capacity of the air heater which can raise the air inlet temperature to 250°C could be used in the tests. By thi means, the peak cylinder temperatures could reach

1500 K, approximately.

The cylinder head was drilled as shown in Fig.8.3, to provide a passage for the thermocouple wires to link to the data acquisition system. A nose section was machined to provide the sealing of the cylinder head.

In the previous arrangement the ceramic specimen was held in a three piece chuck. However for the instrumented ceramic disc, for instrumentation reasons it was replaced with a simpler one piece chuck which is shown in Fig.8.10.

8.4 INSTRUMENTATION OF THE SIMULATION RIG

The simulation test rig was first built for endurance testing of ceramic components and therefore its initial instrumentation was limited to a failure detection system. Later in the programme, temperature fluctuations at the ceramic surface were measured and thus the related instrumentation such as thermocouples and data logging system were introduced to the test rig.

8.4.1 Failure Detection System

The endurance testing of a ceramic component requires it to be left under cyclic loading in the simulation rig for considerable periods. This makes it very impractical to run the rig in the presence of a responsible person throughout the test. For this reason, in case of a component failure to prevent excessive damage to the test rig by seizure, a failure detection system was installed. The system contains 8 channels which monitor the rig's behaviour througout the test, such as sudden change of engine speed, failure in the cooling water system or air heater system. In case of a failure the power of the electric motor which turns the engine is immediately shut down to prevent further damage to the rig. The detailed description of the system is given in [10].

8.4.2 Surface Thermocouples

To measure the ceramic surface temperature swing under fluctuating gas boundary conditions requires a low mass thermocouple junction which provides very fast response and accuracy. This type of thermocouple is referred as surface thermocouple and it is usually very fragile which it makes very difficult to handle in experiments. Since the mass or thickness of the thermocouple junction plays an important role in accurate surface temperature measurements, its effect on accuracy of readings was investigated by using the 1-D FD model which is explained in Chapter 6. A 10 mm thick cordierite ceramic disk having a gold-platinum surface thermocouple of varying thickness was subjected to the gas and coolant side boundary conditions which are shown in Figs.6.8 to 6.11 and 6.37 (Chapter 6). The predicted surface thermocouple readings for various thermocouple junction thicknesses are shown in Fig.8.4, indicating the significance of thermocouple junction thickness. The percentage error in surface temperature swing obtained by different surface thermocouple types at various thermocouple junction thicknesses is also shown in Fig.8.5. This graph clearly demonstrates the importance of thermal properties of the thermocouple on surface temperature swing readings. Gold-platinum and chromel-alumel provides the maximum error, whereas antimony-bismuth has the least error for this particular ceramic substrate.

The effect of ceramic type on the accuracy of surface thermocouple readings is also investigated. The thermal properties of the ceramic substrate are varied and the percentage errors in surface temperature swing obtained with a gold-platinum thermocouple are presented in Fig.8.6. Ceramics having a higher $k\rho Cp$ (Conductivity* thermal inertia) value result in a lower percentage error in reading the surface temperature swing.

Foil thermocouples as thin as 5 microns are

available in the market and are well suited for the task. However, their application to the ceramic substrate involves the use of an intermediate material which affects the thermal response characteristic of the sensor. For this reason, thermocouples which can be directly deposited on the ceramic surface are preferred and the techniques available to achieve this are listed as follows:-

1- Vacuum deposition methods, which are:-
   a) Evaporation.
   b) Sputtering.
   c) Molecular/ion beam.
   d) Plasma assisted chemical vapour.
2- Electroless deposition.
3- Plasma spray.

At present, the deposition technique available in the Material Science Department at Bath University is sputtering. This technique makes use of low pressures. The vacuum chamber is filled with an inert gas having a pressure of about 100 mTorr. When a sufficient voltage is placed across the vacuum, a glow discharge forms as electrons are ejected from the cathode surface. The electron-atom collisions that occur result in the formation of ions. When these ions impinge on a surface, they can cause surface atoms to be ejected and coat any nearby surface. By this means, using appropriate masks and thermocouple materials in the target, it is possible to deposit surface thermocouple junctions as thin as 0.5 microns on the ceramic surface.

In the early stages of the research programme, while the work on sputtering deposition techniques was carried out in the Material Science Department, 5 microns thickness foil thermocouples of the K type (chromel-alumel) were attached to silicon nitride (Si_3N_4) disks. High temperature capability and linear output were the prime reasons for choosing this type of thermocouple. After cleaning the ceramic surface

throughly with ethyl alcohol, the foil thermocouple was attached to the ceramic surface by using a ceramic adhesive which can withstand high temperatures. Since the thermal properties of the adhesive are different from the ceramic substrate, the thermocouple output will be affected. However, knowing the thickness and the thermal properties of the thermocouple, adhesive and substrate it is possible to model the instrumented ceramic disk with the 1-D FD model and interpret the experimental results. The surface thermocouple reading with and without ceramic adhesive are presented in Fig.8.7. An adhesive thickness of 30 microns with the provided thermal properties produces good surface temperature reading. However, the thermal properties and the thickness of the ceramic adhesive play a significant role in the correct measurement of surface temperature swing, as shown in Fig.8.8, and one should be careful to use the correct thermal properties and thickness of the ceramic adhesive.

The instrumented silicon nitride disk was assembled in the cylinder head of the simulation rig and tests were started. The experimental results showed that the temperature fluctuation is far bigger than the expected value, about ±300 K, and the trend of the temperature wave was almost the same as the cylinder gas temperature. It was obvious that the thermocouple was measuring the gas temperature rather than the wall surface temperature, suggesting that the thermocouple had peeled off the surface. When the cylinder head was taken off it was observed that the thermocouple together with the ceramic adhesive were no longer attached to the ceramic surface. After repeating the test once more and finding the same result it was decided to cancel these tests and concentate on thermocouples deposited by sputtering. Most probably the reason for the failure of these tests was the mismatch of the thermal properties of the adhesive and the substrate. However it is very

difficult to find an adhesive which has thermal properties very close to the substrate.

After solving the technical problems in the sputtering unit, in the Material Science Department, deposition of chromel-alumel type thermocouples on the ceramic surfaces was attempted. Although successful thermocouple deposition was achieved, the alloy composition in the thermocouple could not be maintained and this resulted in thermocouples with high resistance values. Later in the programme, gold-nickel thermocouple deposition was tried and good results were obtained. However, the tests in the furnace revealed that nickel at temperatures higher than 450°C started cracking and thus destroyed the thermocouple junction. Considering the high temperature application of these thermocouples in a diesel engine, it was decided to use a gold-platinum type. Successful deposition of such thermocouples on ceramic surfaces was achieved and the tests in the thermal shock rig showed that the sensor under fluctuating heat flux survived upto 700°C without failure.

A cordierite ceramic disk and the required masks for sputtering were supplied to the Material Science Department for gold-platinum thermocouple deposition. The instrumented cordierite disk shown in Fig.8.9, was used to measure the surface temperature swings in the simulation rig. The contact between the thermocouple legs and wires that lead out of the engine were formed at the edge of the ceramic specimen holder by positioning the ceramic disk over the wires as shown in Fig.8.10. For this purpose the previous ceramic disk holder which was a three piece chuck was replaced by a simpler 1 piece chuck with an extended edge. The thermocouple leads are electrically insulated from the chuck by coating its extended edge with a 50 micron thickness of plasma sprayed PSZ. The instrumented cordierite disk was assembled into the cylinder head and

the wiring was checked to make sure that there was no short circuit, and that contact at the thermocouple legs and wires still existed. However, after mounting the cylinder head in the rig and starting the engine for tests, it was discovered that the contact between the thermocouple legs and wires had been lost. The cylinder head was taken off, disassembled and assembled back, making sure that the thermocouple circuit was complete. Unfortunately, using this procedure several times did not change the result and the contact beween the thermocouple legs and wires was always lost. Finally the deposited platinum leg was broken in the continuous process of assembling and disassembling. An attempt was made to repair it by using a platinum frit in the furnace at 800°C, but this caused the deposited gold le to diffuse into the ceramic and thus losing the thermocouple. At the end it was concluded that this method was not practical with the present cylinder head and it was decided to cancel the experiments.

Later in the programme the simulation rig was converted to IDI operation by replacing its piston and cylinder head. Transient temperature measurements on ceramic surfaces are planned to be carried out by designing a surface thermocouple probe placed in an instrumented plug in the prechamber passage. By this means, easier assembling will provide better protection and longer life for these fragile sensors. The research in this field is still continuing at Bath University.

8.4.3 Data Logging System

Advances in micro-computer technology have enabled microprocessor based systems to be developed for the purpose of accurately recording large quantities of transient engine signals. A high speed data acquisition system has been developed at Bath University to measure and record the transient engine data from the fired engine rig. This system, using a CBM microcomputer,

records and transfers the transient engine data to a tape cassette which is used to load the University's main frame computer for analysis. The high speed data acquisition system is shown in Fig.8.11.

The system has five independent channels each having the same maximum sampling rate. Each channel is capable of recording and storing an analogue signal having a maximum value of ±10 Volts, and convert it to a digital approximation with maximum conversion rate of 30 kHz, i.e. 30,000 data points per second. In terms of engine speed this is equivalent to 5000 rpm with 1°CA resolution. The system also has the capability of 0.5 and 0.25°CA resolution which results in a lower engine speed range. Each channel can store 288,000 data points, average and transfer them to disk which is equivalent to 40 successive engine cycles with 1°CA resolution. Before transferring the data to disk it can be observed on the oscilloscope screen and checked for possible errors.

Since the high speed data acquisition system is designed for the fired engine where combustion takes place, high resolution of the engine transient signals is required where the resolution pulses are supplied by the shaft encoder. On the other hand, in the simulation rig which is motored, coarser resolution of the engine signals is sufficient. Also considering the cost, a 90 teeth wheel was assembled on the engine shaft. The wheel together with an opto-switch supplies the necessary resolution signal of 4°CA to the data acquisition system. The detailed explanation of the high speed data acquisition system is given [9].

The schematic instrumentation diagram for the simulation rig is shown in Fig.8.12. The analogue signals coming from the pressure transducer and surface thermocouples are amplified in the charge and thermocouple amplifiers to the data acquisition digitizing voltage level of ±10 Volts. The signals coming from the opto-switches where their related flags

are mounted on the crankshaft and camshaft are fed into the trigger box. An inverter and AND logic gates in the trigger box convert the opto-switch signals to a single signal which is used to trigger the oscilloscope at every engine cycle. Although the opto-switch and the flag on the camshaft provide the necessary trigger signal at every cycle, due to backlash on the camshaft another set of flag and opto-switch is used on the crankshaft. By this means a trigger pulse can be produced at every cycle with a maximum error of 0.25°CA. The timing diagrams for the camshaft and crankshaft opto-switches together with the trigger box output is given in Fig.8.13.

8.5 FIRED ENGINE RIG

A fired engine rig was designed by a previous research student A.Cole [9] and his colleague W. Alexander for assessing insulating components in the engine and thus reveal their effect on the overall engine performance. An air-gap insulated piston with a Nimonic crown has already been tested in this engine. The engine is a water cooled single cylinder Petter PH1W, direct injection diesel with a recommended speed range of 1000 to 2000 rpm. The engine specification in its standard form is detailed in Table 8.1. The overall schematic layout and the picture of the rig are given in Figs.8.14 and 8.15, respectively.

The large receivers placed upstream and downstream of the inlet and exhaust manifolds respectively, dampen pressure pulsations within the manifold so presenting the flow measuring orifice plate with substantially steady flow.

The engine can run under both naturally aspirated and boosted conditions. For boosted conditions the engine intake system is connected to the laboratory air compressor which supplies a constant air pressure of 80 psig. The inlet manifold pressure is controlled by using

a pressure regulator and a dome valve. The inlet air temperature can also be raised to the desired temperature (max 50°C) by using the air heater in the intake receiver. The exhaust back pressure is controlled by a hand operated 1" diameter gate valve which is located downstream of the damping exhaust receiver.

The engine load is applied through a direct current dynamometer where the generated electric energy is dissipated in the resistance banks placed in the water tank. The dynamometer can also be used to motor the engine by supplying the required voltage to it, hence making it very convenient.

The engine cooling system is a closed loop and its heat is transferred to an open loop cooling system which draws water from the storage tank. The heat transfer occurs in a shell and tube heat exchanger. The close loop cooling system has also 3 kW heater which is used to warm up the water and thus reduce the engine warm up period. The oil cooling system is similar to the engine coolant system where the closed loop is cooled through a heat exchanger by the open loop water.

8.6 INSTRUMENTATION OF THE FIRED ENGINE RIG

The fired engine rig is heavily instrumented so that the necessary data can be obtained for the analysis of engine performance, steady state energy distribution and heat release. By this means, the effect of engine insulation can be studied extensively. The detailed description, installation, method of calibration and expected measurement errors of each instrument are explained thorougly in [9]. In this section the instrumentation related to the measurement of the liner temperature distribution is briefly explained.

8.6.1 The Engine Operating Condition

The engine operating condition is described by the engine speed, air-fuel ratio and boost level. The

engine speed is measured by a non-contact inductive transducer which is placed above the flywheel starter motor teeth. As the flywheel turns its magnetic field is disturbed by each tooth and a pulse is created which is amplified in a d.c. amplifier and counted by a tachometer and then displayed as revolutions per minute on a digital display.

The air-fuel ratio is calculated from the engine fuel and air mass flow rates. Fuel flow rate is measured volumetrically using a simple burette and a stop watch. In order to reduce the percentage error in fuel flow rate, the measurement time is kept around 2 minutes. The air mass flow rate is measured by a bevel edged orifice plate which is located upstream of the damping receiver. Two plate/pipe assemblies are used to cover the expected flow range from naturally aspirated to engine boost conditions. The pressure difference across the orifice is obtained from water manometers and together with the fuel flow rate is used as input data for the data reduction program written by A. Cole [9],to provide the engine air-fuel ratio.

The inlet manifold temperature is measured by a sheathed chromel-alumel thermocouple placed in the inlet air receiver. The inlet manifold pressure is measured using a static tapping on the air receiver connected to either a water or mercury manometer depending on the receiver pressure (naturally aspirated or boosted). The exhaust back pressure is measured by a static pressure tapping piezometric ring which placed downstream of the damping receiver. Regular checking and cleaning of the tappings are required due to the carbon deposit blockage.

8.6.2 Engine Coolant Flow Rate and Temperature Measurements

The closed loop engine coolant flow rate is measured by using a bevel edged orifice plate and a

differential water manometer. Although its calibration was done by the previous research student [9], it was repeated to see if it had been affected during this period by scale deposits in the pipe circuit. Almost the same calibration curve was obtained as the previous one. The calibration was performed by opening the pipe circuit to the outside and measuring a range of timed deliveries into a beaker on a calibrated balance.

The water inlet and exit temperatures of the liner were measured by two groups of three 1 mm diameter sheated chromel-alumel thermocouples, each group being located within a machined housing. The group thermocouples are connected in parellel to the cold junction/display unit, thus giving a mean temperature of the water flowing through each housing.

8.6.3 Liner Thermocouples

The axial liner temperature distribution was measured by 22 pairs of chromel-alumel kapton covered thermocouples which are placed in the liner body. Each pair of thermocouples is placed in the same radial position of 1 mm and 6 mm from the gas side surface, as shown in Fig.8.16a. For each pair of thermocouples a single hole is drilled in the liner and a spacer metal piece is used to fill the 5 mm gap between the two thermocouples. Epoxy resin is used to form a good thermal contact between the thermocouples and the liner, thus preventing any errors which would be introduced by an air gap. The first and last thermocouple pairs are placed at an axial position of 4.4 mm and 155.8 mm respectively, from the cylinder head to cover almost the whole of the liner. The intermediate thermocouple pairs are distributed between the end pairs with increasing distance between them down the liner. The thermocouple leads are taken out through the water gallery and a single hole in the engine block as shown in Fig.8.16b. The thermocouples are sealed in place with rubber gasket

coated with one part silicon rubber.

8.6.4 Data Acquisition System

As already mentioned in Sec.8.4.3 a high speed data acquisition system is available for the fired engine test rig. However, for this specific application which involves only the steady state temperature measurements, such a system is not convenient. A slow speed data acquisition system developed at Bath University was used for this purpose. The system allows the measurement and storage of liner temperature distribution at every cycle for the user's specified number of cycles. The data is averaged and is shown on the screen of the Pet Commodore computer where a copy can be obtained either by printing it on paper or saving it on a floppy disk. The schematic diagram of the slow speed data acquisition system is shown in Fig.8.17.

The 44 thermocouple leads from the engine block are connected to 3 24-way switch boxes which are under the control of the computer. These switch boxes enable the connection of each thermocouple to the CIL thermocouple converter unit. The switch boxes are operated automatically by the signals sent from the computer. These signals are first passed through the interface unit where they are amplified to provide necessary magnetic turning force for the rotary solenoid switches. The voltage generated at the thermocouple junctions in the liner are amplified, conditioned and converted to digital signals in the CIL thermocouple converter unit. The digital data is transferred to the computer through the IEEE data bus as shown in Fig.8.17. The cold junction temperature compensation is provided by a precision platinum resistance thermometer for each channel where the signal is fed to the multiplexer, to be added by software.

8.6.5 Liner Temperature Data

The liner temperature distributions obtained with the front and back row thermocouples at 1000 and 2000 rpm engine speeds are shown in Fig.8.18. It is clearly seen that the temperature differences across the two sets of thermocouples do not follow a unidirectional trend for the accurate determination of heat flux distribution on the liner surface. However, the front row of thermocouples which are 0.5 mm below the gas side liner surface, give an indication of the possible liner surface temperature distribution in a firing diesel engine. Using the liner temperature data, a better engine thermal resistance model can be produced and used in the cycle simulation package 'SPICE', to predict the liner surface temperature distribution in an insulated diesel engine. The analysis of the liner temperature data has already been discussed in Chapter 5.

The experimental liner surface temperature data at various air-fuel ratios and engine speeds for naturally aspirated and 2 bar boost conditions are presented in Figs.8.19 to 8.22. The upward shift of the liner surface temperature curve at higher engine outputs is obvious because of more severe gas side boundary conditions and higher piston-liner conductive and frictional heat inputs.

CHAPTER 9
CONCLUSION

9.1 OVERVIEW

Earlier research at Bath University [9] in a selectively insulated diesel engine with an air-gap piston was mainly concentrated on the change of heat release characteristics with engine insulation, and its effect on engine performance. The present study is concerned with its prediction by simulation of the effect of insulation on performance. These simulations applied to the experimental engine, showed that the simulation and test results differ widely. Instead of the predicted reduction in engine heat loss and increase in engine thermal efficiency, the air-gap piston actually caused an increase in engine heat loss and a reduction in engine thermal efficiency. These experimental findings are also supported by various researchers such as Woschni [69,88] and Alkidas [72,82]. The reported changes in engine heat release characteristics, especially the reduced premixed combustion spike, undoubtedly influence engine performance. However, the increase in engine heat loss with insulation cannot be explained solely by the observed level of change in heat release curves. An explanation of the phenomenon of increase in engine heat loss with insulation can only be obtained by a more detailed engine heat transfer analysis.

The present study fulfills the above requirement to a certain extent. New methods in engine heat transfer calculations are introduced which aid understanding and predict the behaviour of insulated engines better. Although the project included a considerable amount of experimental work, especially the measurement of the instantaneous heat flux on metallic and ceramic

surfaces, unfortunately due to various difficulties as explained in Chapter 8, the tests had to be cancelled. Thus, the project developed mainly into a theoretical study dealing with engine heat transfer in detail. By adding more comprehensive heat transfer models to the cycle simulation package 'SPICE', a powerful package especially applicable to insulated diesel engines was produced. Using this new program, the effect of the engine insulation on engine heat transfer and performance was studied in detail for various insulation schemes. The enhanced heat transfer hypothesis of Woschni was also investigated in detail.

9.2 SUMMARY

The new version of 'SPICE' separates the gas to wall heat transfer into its components, i.e. convective and radiative. A separate radiative model was written to provide the flame radiative heat flux falling on each surface of the combustion chamber, as explained in Chapter 4. Wall to wall radiative heat exchange which is crucial to selective insulation schemes, and accurate prediction of the liner temperature distribution are also included within the heat transfer calculations. The convective heat transfer component is covered by the Woschni htc correlation and its value is reduced to 80% to compensate for the radiative heat transfer contribution. The same gas htc value is used for piston and cylinder head surfaces, whereas a lower value of 44% is applied for the liner surface. This value was obtained from a detailed analysis of the experimental liner temperature distribution with the Bath Petter engine, as explained in Chapter 5. A further option was included in the cycle simulation package for the inclusion of the Woschni enhanced htc which is a function of the mean wall surface temperature.Its effect on engine heat loss and performance was also studied.

The heat transfer through the engine walls was

modelled by separating the wall into two regions, a thin layer for transient and the remainder for steady state conduction. The steady state conduction heat transfer was modelled by a thermal resistance network which as discussed in Chapter 5, replaces the old, simple networks in the original version of 'SPICE'. The new model considers 2-D heat flow in the liner, which is important in predicting the liner temperature distribution in an insulated engine. It also allows for changes of heat path direction between piston rings and liner, depending on the temperature gradient which is determined by the axial position of the piston. To raise the accuracy of the liner temperature prediction, the actual shape of the piston, i.e. rings, lands and skirt is considered in the model. By this means, piston ring conduction and friction, flame and wall radiative as well as gas convective heat fluxes can be input accurately to the liner nodes.

The transient heat transfer section of the wall was modelled by using a FD numerical solution method, as explained in Chapter 6. The FD model and thermal resistance network were joined to form a complete thermal model for the engine walls to be incorporated in 'SPICE'. A separate FD code was also produced and used to study the wall temperature dynamics under various conditions. This provides the user with surface temperature fluctuations which becomes very significant for low conductivity ceramic components, reaching over 300 K. It also makes the gas to wall heat transfer calculation more accurate, compared to the previous method based on a constant wall temperature.

The new version of 'SPICE' was used for various insulation schemes to predict the behaviour of the insulated diesel engines (Chapter 7). The simulation runs were made with both the original and enhanced Woschni htc correlations; their different effects on engine heat loss and performance were discussed.

Possible reasons for the observed increase in aggregate engine heat loss with an air-gap heat barrier piston engine were investigated throughly.

9.3 CONCLUSIONS

The most important conclusions from this research may all be abstracted from Chapter 7. They may be summarized as follows:-

1) Radiation and Convection Heat Fluxes

In insulated diesel engines, due to higher flame temperatures both the peak and cycle mean radiative heat fluxes are raised. However, the reduction in convective heat transfer caused by hot walls is not compensated for by the increase in radiative heat transfer, leading to an overall decrease in engine heat loss. In order to include the possible effects of increase in soot concentration levels in the insulated engine, as a result of inefficient combustion, the flame emissivity was taken as unity throughout the cycle for a specific simulation run. It was found that the increase in radiative heat transfer in insulated engines cannot be the explanation of the observed increase in heat loss.

2) Selective Insulation

As a result of selective insulation, i.e. piston only, cylinder gas temperature increases, thus raises the heat loss to other uninsulated surfaces. However the overall engine heat loss is still lower than for the standard engine.

3) Heat Release Duration (HRD)

The engine insulation reduces both the fuel injection rate and ignition delay period, thus affecting the combustion process. This effect on engine heat loss and performance was studied by varying HRD. Increasing HRD reduced engine heat loss further. On the other hand,

reducing it increased heat loss but also produced higher maximum cylinder pressure and thermal efficiency, contradicting the insulated engine test results.

4) Alternative Hypothesis to Woschni Enhanced HTC

The increase in engine heat loss with insulation could be caused by the enhanced gas htc as suggested by Woschni et al [69,88], and/or by reduction of the wall deposit thickness. Both hypotheses are plausible in the insulated engine environment. Hot walls could well enable the flame to approach closer to the walls, thus reducing the boundary layer thickness and causing higher gas htc. On the other hand, due to lower thermal inertia and conductivity properties of the wall deposits, reduction in wall deposit thickness as a result of insulation could well raise the heat loss without any significant changes to the gas side boundary conditions. However, to justify either hypothesis, experimental evidence is required.

5) Soot Deposit Effects

The tests performed by various researchers to reveal the effect of insulation on surface heat flux produced contradictory results. Furuhama [75] and Woschni [69,88] reported that insulation raised the peak surface heat flux. On the other hand, Borman [77], Morel [111], and Cheng [112] reported that on PSZ coated surfaces, a reduction in both peak and cycle mean heat flux values was obtained. However, no correction for possible soot deposits over thin-film surface thermocouples was mentioned in any of these references. Soot deposit thickness also depends on the position of surface thermocouple inside the combustion chamber. Therefore, thermocouples placed at different locations inside the chamber may provide contradictory data. The test results, published by Miyairi [115], showed that cylinder head and liner top part insulation reduced

bsfc, whereas piston insulation raised it. Therefore, to make comparisons of the surface thermocouple readings placed on cooled or insulated walls without considering the wall deposit effects is misleading.

6) Engine Overall Thermodynamic Efficiency

If Woschni's claims are correct, i.e. engine insulation raises heat loss, it is still possible to achieve high thermodynamic efficiency from an insulated diesel engine by other means. The simulation runs have already shown that heavy engine insulation, despite the fact that higher peak heat fluxes occurred, produces lower levels of cycle mean heat fluxes. Due to very hot walls, the gas temperature during the expansion and exhaust strokes rises and thus increases exhaust energy availability. Recovery of exhaust energy via turbo-compounding and/or a Rankine bottoming cycle could well provide an overall engine thermodynamic efficiency reaching 50%, providing that efficient heat recovery equipment is used.

7) Effective Engine Insulation

Effective engine insulation means insulation of the piston, firing deck, valves, and top part of the liner. Insulation of the lower part of the liner, stroked by the piston rings which has much greater surface area than the other parts of the combustion chamber, provides no benefit, whereas it reduces the engine volumetric efficiency drastically. Employing a ceramic liner in an insulated engine has the major advantage of complete elimination of the cooling system. However, with present ceramic materials which have limited strenght at high temperatures, some cooling is still required, especially at high boost levels, to ensure the safe operation of the ceramic components.

8) Piston-Liner Lubrication

In order to ensure the proper lubrication between piston and liner, either the top part of the liner should be insulated using a low conductivity material ($k<2$ W/mK), or a high level insulation should be applied between the top and bottom parts of the liner. By this means, the axial heat flow down the liner will be reduced and the liner temperatures, especially at the ring-pack TDC location will be at safer operating levels. It should also be noted that wall to wall radiative heat exchange in a heavily insulated engine raises the temperatures in this region to such levels as to cause lubrication problems.

9) Selection of Ceramics

At present, the selection of ceramics for insulated diesel engines should be mainly based on high temperature strength and resistance to corrosion. Engine insulation can be supplied on the coolant side or by a low conductivity layer within the ceramic component, which can either be a low conductivity ceramic or an air-gap. Thus, low conductivity ceramics like cordierite are generally not exposed directly to hot combustion gases so as to avoid severe cyclic thermal stresses. Although, a low conductivity ceramic is required for the top part of the liner to reduce the axial heat flow down the liner thus giving a better piston-liner lubrication, due to the less severe gas boundary conditions in this region the cyclic thermal stresses will be much lower.

It may be thought that low conductivity ceramics have the advantage of reducing the peak surface heat flux during combustion. However, it has already been shown that at the same insulation level the difference in peak surface heat flux for cordierite ($k=1.5$ W/mK) and HPSC ($k=35$ W/mK) is very small. In fact, if the insulation level is limited by the maximum operating temperature of the ceramic, the peak heat flux will be

smaller for the ceramic with the highest operating temperature, irrespective of its thermal properties. Therefore, at present silicon nitride and silicon carbide ceramics which have relatively high conductivities but also high temperature strength are suitable candidates for the insulated diesel engines.

10) Ideal Engine Insulation Material

The ideal insulation material for reciprocating engines, i.e. diesel and gasoline, is one possessing both low conductivity and low thermal inertia such as air, so that the wall surface temperature can be made to approach the gas temperature throughout the cycle thus providing an almost true adiabatic process. Such a material would have the advantage that it could be applied as thin coatings over metallic surfaces avoiding major changes in the combustion chamber design. The benefits of insulation are thus obtained directly within the cylinder without requiring a turbocompound engine scheme, while the engine volumetric efficiency would be unaffected. However, such a material is purely hypothetical and the present low conductivity materials such as PSZ are far removed from the ideal case.

11) Overall Conclusion

Although the arguments involving increase in engine heat loss with insulation are not completely resolved, the present simulation studies suggest that, irrespective of the enhanced gas htc, heavy engine insulation improves the engine overall thermodynamic efficiency, particularly if turbocompound and/or Rankine bottoming cycle engine schemes are adopted. The phenomenon of enhanced htc can be explained better by including the effects of soot deposit on surface thermocouple readings obtained at various locations in the combustion chamber, and for different wall materials.

REFERENCES

1. Newland, B.G., "Challenging Time for Technical Ceramics," C.M.E., January 1986, pp.28-30.
2. Millar, G.H., "Commercial Engine Development to the Year 2000 and Beyond," SAE Paper 840577, 1984.
3. McClintock, A.L.M., and Kannan, K.R., "State of the Art Report on Engineering Ceramics as Applied to Reciprocating Engines," November 1985, EAU M46, NEL Publication, Glasgow.
4. Wallace, F.J., Way and Vollmert, "Effect of Partial Supression of Coolant on the High Output Diesel Engine Cycle," SAE Paper 790823, 1979.
5. Fuad, A., "Performance Prediction for Adiabatic Compounded Diesel Engine," MSc Thesis, University of Bath, 1980.
6. Kao, T.K., "Prediction of Heat Flow and Temperature Distribution in Adiabatic Engine Components," MSc Thesis, University of Bath, 1981.
7. Kao, T.K., "Prediction of Heat Flow, Temperature and Stress in Diesel Engine Pistons Incorporating Thermal Barriers," PhD Thesis, University of Bath, 1983.
8. Wallace, F.J., "Thermally Insulated Diesel Engines," Proc. Instn. Mech. Engrs., Vol.198A, No.5, 1984.
9. Cole, A., "Diesel Engine Thermal Insulation," PhD Thesis, University of Bath, 1986.
10. Manton, S.M., "Assesment of Ceramic Materials for Thermally Insulated Reciprocating Engines," PhD Thesis, University of Bath, 1986.
11. Nusselt,W., "Der Waermeuebergang in der Verbrennungs kraftmaschine," Z. Ver. Dtsch. Ing., Vol.67, pp.692,1923.
12. Eichelberg, G., "Some New Investigations on Old Combustion Engine Problems," Engineering, Vol.148, pp.547, 1939.
13. Elser, K., "Der Instationaere Waermeuebergang in

Diesel-Motoren," Mitt. Inst. Thermodyn. Zurich, No.15,1954.
14. Annand, W.D., "Heat Transfer in the Cylinders of Reciprocating Internal Combustion Engines," Proc. Instn. Mech. Engnrs., Vol.177, No.36, pp.973,1963.
15. Knight, B.E., "The Problem of Predicting Heat Transfer in Diesel Engines," Proc. Instn. Mech. Engrs., Vol.179, pp.99,1965.
16. Woschni, G., "A Universally Applicable Equation for the Instantaneous Heat Transfer Coefficient in the Internal Combustion Engine," SAE Transactions, Vol.76, pp.3065,1967.
17. Dent, J.C., and Suliaman, S.L., "Convective and Radiative Heat Transfer in High Swirl Direct Injection Diesel Engine," SAE Paper 770407, 1977.
18. Hohenburg, G.F., "Advanced Approaches for Heat Transfer Calculations," SAE Paper 790825, 1979.
19. Borgnakke, C., Arpaci, V.S. and Tabaczynski, R.J., "A Model for Instantaneous Heat Transfer and Turbulance in a Spark Ignition Engine," SAE Paper 800287, 1980.
20. Davis, G.C. and Borgnakke, C., "The Effect of In-Cylinder Flow Process (Swirl, Squish and Turbulance) on Engine Efficiency - Model Predictions," SAE Paper 820045, 1982.
21. Morel, T. and Keribar, R., "A Model for Predicting Spatially and Time Resolved Convective Heat Transfer in Bowl-in-Piston Combustion Chambers," SAE Paper 850204, 1985.
22. Ebersole, G.D., Myers, P.S. and Uyehara,O.A., "The Radiant and Convective Components of Diesel Engine Heat Transfer," Paper 701C presented at SAE Summer Meeting, Montreal, June 1963.
23. Flynn, P., Mizusawa, M., Uyehara, O.A. and Myers, P.S., "An Experimental Determination of the Instantaneous Potential Radiant Heat Transfer Within an Operating Diesel Engine," SAE Paper

720022, 1972.
24. Oguri,T. and Inaba, S., "Radiant Heat Transfer in Diesel Engines," SAE Paper 720023, 1972.
25. Sitkei, G. and Ramanaiah, G.V., "A Rational Approach for Calculation of Heat Transfer in Diesel Engines," SAE Paper 720027, 1972.
26. Kunitomo, T., Matsuoka, K. and Oguri, T., "Prediction of Radiative Heat Flux in a Diesel Engine," SAE Paper 750786, 1975.
27. Dent, J.C. and Suliaman, S.J., "Convective and Radiative Heat Transfer in a High Swirl Direct Injection Diesel Engine," SAE Paper 770407, 1977.
28. Chang, S.L and Rhee, K.T., "Computation of Radiation Heat Transfer in Diesel Combustion," SAE Paper 831332, 1983.
29. Menguc, M.P., Viskanta, R. and Ferguson, C.R., "Multidimensional Modelling of Radiative Heat Transfer in Diesel Engines," SAE Paper 850503, 1985.
30. Oguri, T., Takeda, A., Torii, K. and Inaba, S., "Radiation Heat Transfer of Combustion Flames in a Diesel Engine," Bulletin of JSME, Vol.28, No.238, April 1985.
31. Morel, T. and Keribar, R., " Heat Radiation in a D.I. Diesel Engines," SAE Transactions, Vol.95, pp.2.1141-2.1157, 1986.
32. Edwards, D.K. and Balakrishnan, A., "Thermal Radiation by Combustion Gases," Int. J. Heat Mass Transfer, Vol.16, pp.25-40, 1973.
33. Felske, J.D., and Tien, C.L., "The Use of the Milne - Eddington Absorption Coefficient for Radiative Heat Transfer in Combustion Systems," Transactions of the ASME, Journal of Heat Transfer, Vol.99, pp.458-465, August 1977.
34. Dalzell, W.H., and Sarofim, A.F., "Optical Constants of Soot and Their Application to Heat Flux Calculations," Transactions of the ASME,

Journal of Heat Transfer, February 1969.
35. Hottel, H.C., and Sarofim, A.F., "Radiative Transfer," McGraw Hill, New York, 1972.
36. Siegel, R., and Howell, J.R., "Thermal Radiation Heat Transfer," McGraw Hill, New York, 1972.
37. Matsui, Y., Kamimoto, T., and Matsuoka, S., "Formation and Oxidation Processes of Soot Particulates in a D.I. Diesel Engine - An Experimental Study via Two-Colour Method," SAE Paper 820464, 1982.
38. Glassman, I., and Clark, G., "Universal Hydrocarbon Air Temperature Graphs," Paper No.12, Combustion Institute, Eastern Section, 1983 Fall Technical Meeting, Providence, RI, Nov.8-10, 1983.
39. Chang, S.L., and Rhee, K.T., "Adiabatic Flame Temperature Estimates of Lean Fuel/Air Mixtures," Combustion Science and Technology, Vol.3, pp.203-206, 1983.
40. Kirloskar, C.S., Chandorkar, S.B., and Narayan Rao, N.N., "The AV1 Series III Diesel - A Differentially -Cooled Semi-Adiabatic Engine Below 10 kW," SAE Paper 790844,1979.
41. Godfrey, D.J., "The Use of Ceramics in Diesel Engines," Proc. of Nato Advanced Study Inst., 1976.
42. Griffiths, W.J., "Thermodynamic Simulation of the Diesel Engine Cycle to Show the Effect of Increasing Combustion Chamber Wall Temperatures on Thermal Efficiency and Heat Rejection," Wellworhty Topics, No.63, pp.7-10.
43. Kamo, R., and Bryzik, W., "Adiabatic Turbocompond Engine Performance Prediction," SAE Paper 780068, 1978.
44. Parker, D.A., and Smart, R.F., "An Evaluation of Silicon Nitride Diesel Pistons," Proc. British Ceramic Society, No.26, 1978.
45. Kamo, R., and Bryzik, W., "Ceramics in Heat Engines," SAE Paper 790645, 1979.

46. Timoney, S.G., "No Coolant Diesel Engine," Proc. New Ways to Save Energy, Int. Sem., October 1979.
47. Valland, H., and Wyspienski, G.K., "Thermal Barriers in Combustion Engine Cylinders," Norwegian Institute of Technology, UR-80-12, 1980.
48. Kamo, R., Woods, M., Yamada, T., and Mori, M., " Thermal Barrier Coating for Diesel Engine Pistons," ASME, 80-DGP-14, 1980.
49. Murray, R.G., "Performance and Emission Characteristics of a Semi - Adiabatic Engine," ASME, 80-DGP-44, 1980.
50. Hamano, Y., "Ceramic Parts for a Diesel Engine," Proc. Int. Sym. on Automotive Propulsion Systems," Vol.2, pp.803-812, April 1980.
51. Kamo, R., and Bryzik, W., "Cummings - Taradcom, Adiabatic Turbocompound Engine Program," SAE Paper 810070, 1981.
52. Elsbett, L., and Behrens, M., "Elko's Light Duty D.I. Diesel Engines with Heat Insulated Combustion System and Component Design," SAE Paper 810478, 1978.
53. Woods, M.E., and Oda, I., "PSZ Ceramics for Adiabatic Engine Components," SAE Paper 820429, 1982.
54. Yoshimitsu, T., Toyama, K., Sato, F., and Yamaguchi, H., "Capabilities of Heat Insulated Diesel Engines," SAE Paper 820431, 1982.
55. Valland, H., and Wyspianski, G.K., "A Theoretical Analysis of Thermal Barriers in Diesel Engine Cylinders," SAE Paper 820431, 1982.
56. Kamo, R., and Bryzik, W., "Tacom/Cummins Adiabatic Engine Program," SAE Paper 830314, 1983.
57. Toyama, K., Yoshimitsu, T., Nishiyama, T., Shimauchi, T., and Nakagaki, T., "Heat Insulated Turbocompound Engine," SAE Paper 831345, 1983.
58. Coers, R.B., Fox, L.D., and Jones, D.J., "Cummins Uncooled 250 Engine," SAE Paper, Int. Congress &

Exposition, Detroit, Michigan, Feb-March 1984.
59. Kamo, R., and Bryzik, W., "Cummins/Tacom Advanced Adiabatic Engine," SAE Paper 840428, 1984.
60. Kamo, R., and Wood, J.C., "Advanced Adiabatic Diesel Engine for Passanger Cars," SAE Paper 840434, 1984.
61. Sudhakar, V., "Performance Analysis of Adiabatic Engine," SAE Paper 840431,1984.
62. Siegla, D.C., and Amann, C.A., "Exploratory Study of the Low - Heat - Rejection Diesel for Passanger - Car Application," SAE Paper 840435, 1984.
63. Hoag, K.L., Brands, M.C., and Bryzik, W., "Cummins/Tacom Adiabatic Engine Program," SAE Paper 850356, 1985.
64. Wade, W.R., Havstad, P.H., Ounsted, E.J., Trinkler, F.H., and Garwin, I.J., "Fuel Economy Opportunities with an Uncooled D.I. Diesel Engine," SAE Paper 841286, 1984.
65. Cole, R.M., and Alkidas, A.C., "Evaluation of an Air - Gap - Insulated Piston in a Divided - Chamber Diesel Engine," SAE Paper 850359, 1985.
66. Morel, T., Fort, E.F., and Blumberg, P.N., "Effect of Insulation Strategy and Design Parameters on Diesel Engine Heat Rejection and Performance," SAE Paper 850506, 1985.
67. Morel, T., Keribar, R., and Blumberg, P.N., "Cyclical Thermal Phenomena in Engine Combustion Chamber Surfaces," SAE Paper 850360, 1985.
68. Suzuki, T., Tsujita, M., Mori, Y., and Suzuki, T., "An Observation of Combustion Phenomena on Heat Insulated Turbo - Charged and Intercooled D.I. Diesel Engines," SAE Transactions, Vol.94, pp.4.804-4.819, 1986.
69. Woschni, G., Spindler, W., and Kolesa, K., "Heat Insulation of Combustion Chamber Wall - a Measure to Decrease the Fuel Consumption of I.C. Engines,"

SAE Paper 870339, 1987.
70. Kamo, R., Bryzik, W., and Glance, P., "Adiabatic Engine Trends - Worldwide," SAE Paper 870018, 1987.
71. Kamigaito, O., " Ceramic Components for Engines in Japan," SAE 870019, 1987.
72. Alkidas, A.C., "Experiments with an Uncooled Single - Cylinder Open - Chamber Diesel," SAE 870020, 1987.
73. Gatowski, J.A., Jones, J.D., and Siegla, D.J., "Evaluation of the Fuel Economy Potential of the Low - Heat - Rejection Diesel Engine for Passanger - Car Application," SAE Paper 870024, 1987.
74. Elsbett, K., and Behrens, M., "Elsbett's Cooling for D.I. Diesel Engines Without Water or Air," SAE Paper 870027, 1987.
75. Furuhama, S., and Enomoto, Y., "Heat Transfer into Ceramic Combustion Wall of Internal Combustion Engines," SAE Paper 870153, 1987.
76. Morel, T., Wahiduzzaman, S., Tree, D.R., and DeWitt, D.P., "Effect of Speed, Load, and Location on Heat Transfer in a Diesel Engine - Measurements and Predictions," SAE Paper 870154,1987.
77. Huang, J.C., and Borman, G.L., "Measurement of Instantaneous Heat Flux to Metal and Ceramic Surfaces in a Diesel Engine," SAE Paper 870155, 1987.
78. Assanis, D.N., and Badillo, E., "Transient Heat Conduction in Low - Heat - Rejection Engine Combustion Chambers," SAE Paper 870156, 1987.
79. Germerdonk, R., and Nguyen, N.N., "Increase of the Local Heat Transfer Coefficient by Convection Vive Phenomenan," Ger. Chem. Eng., Vol.8., pp.81-86, 1985.
80. Woods, M.E., Glance, P., and Schwarz, E., "In - Cylinder Components for High Temperature Diesel," SAE Paper 870159, 1987.
81. Kawamura, H., "Development Status of Isuzu Ceramic

Engine," SAE Paper 880011, 1988.
82. Alkidas, A.C., "On the Performance and Emissions of an Uncooled Heavy - Duty Single - Cylinder Diesel Engine," SAE Paper 880013, 1988.
83. Churchill, R.A., Smith, J.E., Clark, N.N., and Turton, R.A., "Low - Heat Rejection Engines - A Concept Review," SAE Paper 880014, 1988.
84. Morel, T., Wahiduzzaman, S., and Fort, E.F., "Heat Transfer Experiments in an Insulated Diesel," SAE Paper 880186, 1988.
85. Miyairi, Y., "Computer Simulation of a LHR D.I. Diesel Engine," SAE 880187, 1988.
86. Assanis, D.N., and Badillo, E., "Transient Analysis of Piston - Liner Heat Transfer in Low - Heat - Rejection Diesel Engines," SAE Paper 880189, 1988.
87. Amann, C.A., "Promises and Challanges of the Low - Heat - Rejection Diesel," ASME Journal of Engineering For Gas Turbines and Power, Vol.110, pp.475-481, 1988.
88. Woschni, G., and Spindler, W., "Heat Transfer With Insulated Combustion Chamber Walls and Its Influence on the Performance of Diesel Engines," ASME Journal of Engineering For Gas Turbines and Power, Vol.110, pp.482-502, 1988.
89. Gulder, O.L., "Flame Temperature Estimation of Conventional Future Jet Fuels," Transactions of the ASME, Vol.108, pp.376-380, April 1986.
90. Gulder, O.L., "Combustion Gas Properties: Part II - Prediction of Partial Pressures of CO_2 and H_2O in Combustion Gases of Aviation and Diesel Fuels," Journal of Engineering for Gas Turbines and Power, Vol.108, pp.455, July 1986.
91. Martin, F.A., "Friction in Internal Combustion Engines," IMechE 1985, C67/85, pp.1-19.
92. Shin, K., Tateishi, Y., and Furuhama, S. "Measurement and Characteristics of Instantaneous Piston Ring Frictional Force," ImechE 1985, C61/85,

pp.87-95.
93. Furuhama, S., and Suzuki, H., "Temperature Distribution of Piston Rings and Piston in High Speed Diesel Engine," Bulletin of the JSME, Vol.22, No.174-12, pp.1788-1794.
94. Janna, W.S., "Engineering Heat Transfer," PWS Publishers, pp.419-423.
95. Furuhama, S., "Tribology on Reciprocating Internal Combustion Engines," JSME International Jornal, Vol.30, No.266, pp.1189-1199, 1987.
96. Tada, T., and Furuhama, S., "On the Heat Flow from the Pistons in a Farm Type Gasoline Engine," Bulletin of JSME, Vol.7, No.28., pp.784-791, 1964.
97. Jones, J.D., "Heat Transfer Processes in Low - Heat -Rejection Diesel Engines," Heat Transfer Engineering, Vol.8, No.3, pp.90-99, 1987.
98. Wallace, F.J., and Way, "A Comprehensive Suite of Steady State and Transient Response Engine - Turbocharger Performance Prediction Programmes," Un.I.C.E.G., 17-18 April 1980.
99. McAulay, Wu, Chen, Borman, Myers and Uyehara "Development and Evaluation of Simulation of Compression Ignition Engines," SAE Paper 650451, 1965.
100. Streit and Borman, "Mathematical Simulation of a Large Turbocharged Two - Stroke Diesel Engine," SAE Paper 710176, 1971.
101. Marzouk, M., "Simulation of Turbocharged Diesel Engines under Transient Conditions," PhD Thesis, Imperial College, University of London, 1976.
102. Krieger and Borman, "The Computational of Apparent Heat Release for Internal Combustion Engines," ASME 66-WA/DGP-4,1966.
103. Wolfer, H.H., "Ignition Lag in the Diesel Engine," VDI, Forschungsheft, No.392., 1938.
104. Wiebe, I. I., "Habempirische Formel fur die Verbrennungsgeschrivindig Keit," Verlag der

Akadamei der Wissenschafen der VdSSR, Moscow, 1956.
105. Marzouk, M., and Watson, N.D., "A Combustion Correlation for Diesel Engine Simulation," SAE Paper 1980.
106. Hohenburg, G.F., "Advanced Approaches for Heat Transfer Calculations," SAE Paper 670931, 1967.
107. Rasihhan, Y., "Diesel-Organic Rankine Cycle Compound Engine for Truck Vehicles," MSc Thesis, University of Bath, 1984.
108. Trustrum, L.B., "An Analysis of the Market for Advanced Ceramic Products in EEC Countries," Ceramic Research Spec. Pub.
109. Charlton, S. J., "Spice User Manual" , Bath University.
110. Alexander, W.D., "The Design and Evaluation of Components For Low Heat Loss Diesel Engines," PhD Thesis, University of Bath, 1989.
111. Morel, T., and Fort, E.F., "Heat Transfer in a Cooled and an Insulated Diesel Engine," SAE Paper 890572, 1989.
112. Cheng, W.K., and Wong, V.W., "Heat Transfer Measurement Comparisons in Insulated and Non - Insulated Diesel Engines," SAE Paper 890570, 1989.
113. Assanis, D.N., and Badillo, E., "Evaluation of Alternative Thermocouple Designs for Transient Heat Transfer Measurements in Metal and Ceramic Engines," SAE Paper 890571, 1989.
114. Anderson, C.L., Uyehara, O.A., and Myers, P.S., "An In Situ Determination of the Thermal Properties of Combustion - Chamber Deposits," SAE Paper 820071, 1982.
115. Miyairi, Y., Oikawa, H., "Selective Heat Insulation of Combustion Chamber Walls for a D.I. Diesel Engine with Monolithic Ceramics," SAE Paper 890141, 1989.
116. Bruns, L., Bryzik, W., and Kamo, R., "Performance Assessment of U.S. Army Truck with Adiabatic Diesel

Engine," SAE Paper 890142, 1989.
117. Alkidas, A.C., "Performance and Emissions Achievments with an Uncooled Heavy - Duty, Single - Cylinder Diesel Engine," SAE Paper 890144, 1989.
118. Bradish, J.P., Myers, P.S., and Uyehara, O.A., "Effects of Deposit Properties on Volumetric Efficiency, Heat Transfer and Preignition in Internal Combustion Engines," SAE Paper 660130, 1966.
119. Shamah, E., "Unsteady Heat Transfer Simulation for a Diesel Engine," MSc Thesis, University of Wisconsin, 1967.
120. Baazari, "Two Staged Turbocharging of Diesel Engines Under Steady State and Transient Conditions," PhD Thesis, Imperial College, University of London, 1979.

APPENDIX 1

Gas emissivity (or absorptivity) as function of temperature at various K values:-

$$K = P_t\left(X_{H_2O} + X_{CO_2}\right) L_m$$

$\varepsilon = 1.775*10^{-8}T^2 - 2.690*10^{-4}T + 0.7856$ K=1.0

$\varepsilon = 3.201*10^{-8}T^2 - 3.071*10^{-4}T + 0.7272$ K=2.5

$\varepsilon = 4.876*10^{-8}T^2 - 3.447*10^{-4}T + 0.6459$ K= 5

$\varepsilon = 5.617*10^{-8}T^2 - 3.448*10^{-4}T + 0.5600$ K= 10

$\varepsilon = 4.774*10^{-8}T^2 - 2.782*10^{-4}T + 0.4237$ K= 20

$\varepsilon = 3.079*10^{-8}T^2 - 1.767*10^{-4}T + 0.2638$ K= 50

$\varepsilon = 1.346*10^{-8}T^2 - 8.034*10^{-5}T + 0.1238$ K=100

$\varepsilon = 3.459*10^{-9}T^2 - 1.966*10^{-5}T + 0.0289$ K=200

	Japan	USA	Western Europe	UK	Totals*
Engineering Ceramics	40-80	40-100	10-20	6	90-200
All Tecnical Ceramics	200	70-130	20-30	8	300-370

* Estimates exclude Eastern Block countries.
Figures are in million pounds every year.

Table 1.1 Estimates of global research and development effort for technical ceramics [108].

I. Bulk Ceramics
   1. Partially Stabilized ZrO_2 (PSZ)
   2. PSZ + metal or oxide dispersoid
   3. Al_2O_3 + HfO_2 dispersoid
   3. Pressureless sintered Si_3N_4 (PS Si_3N_4)
   4. Al_2O_3 + ZrO_2 dispersoid
   4. Al_2O_3 + metal dispersoid
   5. Mullite
   5. Mullite + metal or oxide dispersoid
   5. Low thermal expansion ceramics
   6. Si_3N_4/Si_3N_4 composites (Fiber/Matrix)
   7. SiC/Si_3N_4 composites
   8. SiC/SiC composites

II. Ceramic Coatings
   1. ZrO_2 base and HfO_2 base
   2. Non ZrO_2 base
   3. Boride
   3. Carbide
   3. Nitride

Table 2.1 Tentative priority listing of candidate ceramic materials for low heat loss diesel engines (Oak Ridge National Laboratory, USA).

Temperature Limit, °C	>1800
Fracture Toughness, $MN/M^{3/2}$	> 8.0
Flexural Strength, MPa	> 800
Thermal Conductivity, Cal/CM-SEC-°C	<0.01
Thermal Shock Resistance, T °C	> 500
Coefficient of Expansion x 10^{-6}/°C	> 10
Weibull Modulus	> 18
Time, Exposure, Hours	>1000

Table 2.2 Typical desired material properties for an adiabatic type diesel engine [56].

Property	Units	Material type - oxides					
		CSZ	PSZ	TTPSZ	TZP	MAS	AT
Density (range) *	Mg/m3	5.0-5.8	4.5-5.5	5.8-6.0	6.1	2.0-2.6	2.7-3.3
Total porosity	%	1-3	1-20	1-3	1-3	1-20	0-30
Open porosity	%	0	0-10	0	0	1-20	0-20
Specific heat **	J/(g.K)						
25 C		0.44-0.47	0.45	0.47	0.45	0.73	0.74
100 C		0.50-0.54	0.51	0.51	0.53	0.88	0.74
500 C		0.58-0.64	0.60	0.62	0.59	1.13	1.04
1000 C		0.62-0.68	0.66	0.66	0.64	1.25	1.10
Th. expansion	1E-6/K						
25-100 C		8.5	4-7	8.5	8.5	0	0
25-500 C		9.5	5-8	9.5	9.5	1-2	0
25-1000 C		12.0	7-10	12.0	12.0	2-4	0
Th. conductivity	W/(m.K)						
25 C		1.8	1.0	1.8	1.8	1-3	1
100 C		1.8	1.0	1.8	1.8	1-3	1
500 C		2.0	1.0	2.0	2.0	1-2	1
1000 C		2.2	1.0	2.2	2.2	1-2	2
Young's modulus	GN/m2						
25 C		200	120	200	200	80-120	50
500 C		-	110	-	-	-	80
Shear modulus	GN/m2						
25 C		80	40	80	80	30-50	30
500 C		78	-	78	-	-	-
Poisson's ratio							
25 C		-	-	-	-	-	-
500 C		-	-	-	-	-	-

* The range of densities for CSZ allows for a range of stabiliser contents as well as porosity, whereas for PSZ, MAS and AT it reflects the range of porosity.

** The range for CSZ reflects the stabiliser type, slightly lower figures being obtained for stabilisation with Y_2O_3 than for magnesia or lime.

Table 2.3a Intrinsic properties of ceramics.

Material type - non-oxidee							
RBSN	HPSN	SSN	Sialon	RBSC	HPSC[+]	SSC	AN
2.0-2.8	3.1-3.2	3.15-3.25	3.15-3.25	3.05-3.25	3.1-3.2	3.1-3.2	3.27
15-40	<1	<1	<1	<1	<1	1-3	<1
15-40	0	0	0	0	0	0	0
0.68	0.68	0.67	0.67	0.68	0.67	0.67	0.80
0.80	0.80	0.78	0.78	0.84	0.84	0.84	0.86
1.06	1.06	1.04	1.04	1.10	1.12	1.12	1.17
1.30	1.30	1.28	1.28	1.24	1.26	1.26	1.57
1.5	1.5	1.5-1.7	1.5-1.7	2.8	2.8	2.8	3.6
2.7	2.7	2.7-3.0	2.7-3.0	3.9	3.9	3.9	4.5
3.3	3.3	3.3-3.7	3.3-3.7	4.6	4.6	4.6	5.3
7-14	30.0	5-20[++]	5-20[++]	120-200	90-110	90-110	60
5-13	28.0	5-18	5-18	100-170	70-90	70-90	-
4.8-12	21.0	4-15	4-15	60-80	55-65	55-65	-
4.3-11	14.5	4-12	4-12	30-40	35-45	35-45	-
120-250	320	300	300	350-380	440	400	350
110-240	310	290	250	-	--	-	-
30-80	120	110	110	-	-	-	-
30-80	120	110	110	-	-	-	-
0.17-0.22	0.23	0.23	0.23	0.22	0.22	-	-
0.15-0.20	0.19	0.20	0.20	-	-	-	-

+ Thermal and mechanical properties are determined by the free silicon content. High free silicon gives lower moduli and strength but higher conductivity.

++ Thermal properties depend on the composition and amount of second phase. Low second-phase content gives higher thermal conductivity.

Table 2.3a Continued.

Property	Units	Material type - oxides					
		CSZ	PSZ	TTPSZ	TZP	MAS	AT
Flexural strength at 25 C, small bars	MN/m2						
ground finish		200	100	500	800	100	50
lapped finish		200	100	500	500-1000	150	50
at 1000 C, small bars ground finish		150	100	150++	200?++	60	50
Resist. to static or cyclic fatigue		?	?	?	?	poor	?
Hardness							
HV1.0		900	700	900	900	800	-
HV0.1		1200	1000	1200	1200	1000	-
HR45N		70	-	-	-	-	-
Wear resistance, rel.							
rubbing, unlubr.		poor	poor	good	good	fair	v. poor
abrasive, unlubr.		poor	v. poor	fair	fair	poor	v. poor
Fracture toughness beam method	MN/m**1.5	4	4-6	6-10	6-10	2	?
Th. shock resist.							
quench test, T	K	100	300	300?	300?	500	1000
R parameter	1E-6*m2/K	low	mod.	mod?	mod?	mod?	high
Oxidation resist.		good	good	good	good	good	good
Temp. capability							
stable microstr.	C	1800	1800	700+	250+	1200	1300
signif. creep	C	1300	1300	-	-	1000	1200
Corrosion resist. (attacked by)		acids	acids	acids	acids	acids alkalis	?

+ Maximum temperature at which material can be used in the presence of steam without transformation.

++ The short-term stregth declines progressively from room temperature to 1000 C, at which it is no stronger than CSZ. TZP may decompose completely at room temperatures below 1000 C, but is stable at 1000 C.

Table 2.3b Extrinsic properties of ceramics.

Material type - non-oxides							
RBSN	HPSN	SSN	Sialon	RBSC	HPSC	SSC	AN
100-250 100-250	350 800	250-400 500-700	250-400 800	250-400 400	350-500 350-500	300 400	500 500
120-350	400	400	400	300	400	400	?
good	mod.	mod.	mod.	good	mod.	good	good?
500-700 600-750 60-65	1500 1700 89	1300-1500 1500-1700 84	1300-1500 1500-1700 84	1900 2000 88	2000-2400 2400-2800 89	2800 3000 90	? ? ?
mod. poor	v. good v. good	v. good v. good	v. good v. good	v. good v. good	v. good v. good	v. good v. good	good? good?
4	4	4	4-6	4	4	4	?
500 high fair	500 high mod.	500 mod-high fair-mod.	500 mod-high fair-mod.	400 v. high mod.	400 high mod.	400 high mod.	? ? fair
1450 1200	1700 1100-1200	1600* 1100-1400	1600* 1100-1400	1400** 1500?	1800? 1500?	2100 >1500	1600? ?
alkalis	alkalis	acids alkalis	acids alkalis	$HF+HNO_3$ alkalis	-	-	acids steam

* Heat-treatment in the temperature range 1000-1400 C may change the nature of the secondary phases.

** Silicon melts at about 1410 C.

Table 2.3b Continued.

Property	Units	Cast Iron	Nimonic (80A)	Steel (EN 32)	Aluminium alloy (LM 27)	Aluminium
Density	g/cm3	7.2	8.2	7.87	2.75	2.72
Th. expension	1E-6/K	12.0	13.0	13.0	21.0	23.0
Specific heat	J/(kg.K)	480	461	485	915	895
Th. conductivity	W/(m.K)	54.4	12.1	50.2	155.0	250.0
Young's modulus	cPa	117	200	206	71	-
Poisson's ratio	-	-	-	0.27	0.32	-
Hardness	HB	240	200-370	450-650	100-150	-
Tensile strength	MPa	262	1100	586	150	-

Table 2.4 Properties of some metals used in automotive industry.

Adiabatic Components	Desired Characteristics							High Technology Ceramics
	Low Friction	Light Weight	Insulation	Wear Resistant	Heat Resistant	Corrosion Resistance	Expansion Coefficient	
Piston		+	+		+	+	+	Si_3N_4, PSZ, TTA
Piston ring				+	+			SSN, PSZ, coating
Cylinder liner	+			+	+	+	+	Si_3N_4, PSZ, coating
Prechamber			+		+	+		PSZ, Si_3N_4
Valve		+	+	+	+	+		SSN, PSZ, composite
Valve seat insert			+	+	+	+		PSZ, SSN
Valve guides	+		+		+	+		PSZ, SSN, SiC
Exh./Int. ports			+		+	+		ZrO_2, Si_3N_4, TiO_2, AlO_3
Manifolds			+		+	+		ZrO_2, Si_3N_4, TiO_2, AlO_3
Tappets		+		+		+		PSZ, SiC, Si_3N_4
Mechanical seals	+			+		+		SiC, Si_3N_4, PSZ
Turbocharger								
Turbine rotor		+	+		+	+	+	Si_3N_4, SiC
Turbine housing			+		+	+	+	LAS
Heat shield			+		+	+	+	ZrO_2, LAS
Ceramic bearings	+	+		+	+	+	+	SSN

Table 2.5 Ceramic components in automotive industry.

Wavelenght (microns)	Acetylene Soot		Propane Soot	
	$\bar{n}$	$\bar{n}\bar{k}$	$\bar{n}$	$\bar{n}\bar{k}$
0.4358	1.56	0.46	1.57	0.46
0.4500	1.56	0.48	1.56	0.50
0.5500	1.56	0.46	1.57	0.53
0.6500	1.57	0.44	1.56	0.52
0.8065	1.57	0.46	1.57	0.49
2.5	2.31	1.26	2.04	1.15
3.0	2.62	1.62	2.21	1.23
4.0	2.74	1.64	2.38	1.44
5.0	2.88	1.82	2.07	1.72
6.0	3.22	1.84	2.62	1.67
7.0	3.49	2.17	3.05	1.91
8.5	4.22	3.46	3.26	2.10
10.0	4.80	3.82	3.48	2.46

Table 4.1 Optical constants of acetylene and propane soots.

Gas	Vibrations (1/cm)	Bands	Pressure parameters ns	bs (To=100 K)	Spectral location (1/cm)	Band absorption parameter (m2/gm. cm)		(1/cm)
H_2O	mv=3	1. Rotation	1	●	0	5200.0	0.14311	28.4
	=3652	2. 6.30 $^{0,0,0}_{0,1,0}$ u	1	●	1600	41.2	0.09427	56.4
	=1595	3. 2.70 $^{0,2,0}_{1,0,0}$ u	1	●	3760	0.19	0.13219	60.0
	=3756					2.3		
	g_1=1					22.4		
	g_2=1	4. 1.87 $^{0,0,1}_{0,1,1}$ u	1	●	5350	3.0	0.08169	43.1
	g_3=1	5. 1.38 ^{1,0,1} u	1	●	7250	2.5	0.11628	32.0
CO_2	mv=3	1. 15.0 ^{0,1,0} u	0.7	1.3	667	19.0	0.06157	12.7
	=1351	2. 10.4 $^{-1,0,1}$ u	0.8	1.3	960	2.47E-9	0.04017	13.4
	=667	3. 9.40 $^{0,-2,1}$ u	0.8	1.3	1060	2.48E-9	0.11888	10.1
	=2396	4. 4.30 ^{0,0,1} u	0.8	1.3	2410	110.0	0.24723	11.2
	g_1=1	5. 2.70 ^{1,0,1} u	0.65	1.3	3660	4.0	0.13341	23.5
	g_2=2	6. 2.00 ^{2,0,1} u	0.65	1.3	5200	0.066	0.39305	34.5
	g_3=1							

●=8.6* (T/To) **0.5+0.5

Table 4.2 Parameters of exponential wide band model.

$\eta < 1$	and	$0 < \tau_H < \eta$	$AB^* = \tau_H$
$\eta < 1$	and	$\eta < \tau_H < \frac{1}{\eta}$	$AB^* = (4\eta\tau_H)^{0.5} - \eta$
$\eta < 1$	and	$\frac{1}{\eta} < \tau_H < \infty$	$AB^* = \ln(\eta\tau_H) + 2 - \eta$
$\eta \geqslant 1$	and	$0 < \tau_H < 1$	$AB^* = \tau_H$
$\eta \geqslant 1$	and	$1 < \tau_H < \infty$	$AB^* = 1 + \ln\tau_H$

Table 4.3 The dimensionless integrated band absorptance.

Constants	$0.3<\phi<1.0$		$1.0<\phi<1.6$	
	$0.92<T^*<2.0$	$2.0<T^*<3.2$	$0.92<T^*<2.0$	$2.0<T^*<3.2$
C_1	2361.7644	2315.7520	916.8261	1246.1778
C_2	0.1157	-0.0493	0.2885	0.3819
C_3	-0.9489	-1.1141	0.1456	0.3479
C_4	-1.0976	-1.1807	-3.2771	-2.0365
a_1	0.0143	0.0106	0.0311	0.0361
b_1	-0.0553	-0.0450	-0.0780	-0.0850
c_1	0.0526	0.0482	0.0497	0.0517
a_2	0.3955	0.5688	0.0254	0.0097
b_2	-0.4417	-0.5500	0.2602	0.5020
c_2	0.1410	0.1319	-0.1318	-0.2471
a_3	0.0052	0.0108	0.0042	0.0170
b_3	-0.1289	-0.1291	-0.1781	-0.1894
c_3	0.0827	0.0848	0.0980	0.1037

Table 4.4 Constants for adiabatic flame temperature.

Constants	H_2O $0.3<\phi<1.6$	CO_2 $0.3<\phi<1.0$	CO_2 $1.0<\phi<1.6$
C_1	0.079773	0.144553	0.012252
C_2	0.145635	-0.314334	1.375204
C_3	-1.209735	-2.182043	1.364468
C_4	-1.177786	-1.094678	-2.033584
a_1	-0.016521	0.015232	0.059804
b_1	0.046686	-0.070608	-0.144740
c_1	-0.022225	0.080495	0.086826
a_2	0.095917	-0.095054	-0.295175
b_2	-0.292738	0.406301	0.796634
c_2	0.166642	-0.429745	-0.657352
a_3	0.693161	-0.265207	-0.010408
b_3	0.031355	-0.141315	-1.260926
c_3	-0.046328	0.108863	1.048413

Table 4.5 Constants for partial pressures of H_2O and CO_2.

INPUT DATA

PTOT=100.0 BARS TGAS=2000.0 K TWALL= 500.0 K
LMEAN= 5.0 cm XH2O=0.100 XCO2=0.100

BAND ABSORPTION OF H2O AND CO2

GAS	BAND REGION (MICRONS)	BAND ABSORPTION	LOWER LIMIT WAVENUMBER	UPPER LIMIT WAVENUMBER
1.H2O	1-ROTATIONAL	1165.9	0.0	1165.9
	2-6.3	838.9	1180.5	2019.5
	3-2.7	842.2	3338.9	4181.1
	4-1.87	268.5	5215.7	5484.3
	5-1.38	235.8	7132.1	7367.9
2.CO2	1-15.0	221.8	556.1	777.9
	2-10.4	13.5	953.2	966.8
	3-9.4	13.6	1053.2	1066.8
	4-4.3	305.4	2104.6	2410.0
	5-2.7	242.0	3539.0	3781.0
	6-1.9	10.7	5194.6	5205.4

REARRANGED BAND ABSORPTION
FOR THE OVERLAPPING BANDS

LOWER LIMIT WAVENUMBER	UPPER LIMIT WAVENUMBER
0.0	1165.9
1180.5	2019.5
2104.6	2410.0
3338.9	4181.1
5194.6	5205.4
5215.7	5484.3
7132.1	7367.9

TOTAL EMISSIVITY=0.273
TOTAL ABSORPTIVITY=0.902

Table 4.6 The output of 'Gas.For'.

```
INPUT DATA
----------
TSOOT=2000.0 K   TWALL= 500.0 K   FV= 0.1E-04   LMEAN=  5.0 cm

RESULTS
-------
SOOT EMISSIVITY=0.620
SOOT ABSORPTIVITY=0.249
```

Table 4.7 The output of 'Soot.For'.

```
INPUT DATA
----------
TAIR=1000.0 K   PCOM=10.00 MPA   EQUIV. RATIO=1.00   H/C= 2.00

RESULTS
-------
INITIAL MIXTURE TEMP= 885.0
ADIABATIC TEMP=2736.1
```

Table 4.8 The output of 'Flame1.For'.

```
INPUT DATA
----------
TAIR=1000.0 K   PCOM=10.00 MPA   EQUIV. RATIO=1.00   H/C= 2.00

RESULTS
-------
PARTIAL PRESSURE OF H2O=0.123
PARTIAL PRESSURE OF CO2=0.112
```

Table 4.9 The output of 'Flame2.For'.

Insulated Parts	PSZ (mm)	$T_{p,up}$ (Deg K)	$T_{p,int}$ (Deg K)	Q_p (kW/m2)	Q_{cond} (kW/m2)	Q_{oil} (kW/m2)	% Error of Q_p	T_{co} (Deg K)
-	-	475.3	420.7	218.3	169.1	56.16	3.20	10.60
Piston	1.5	806.6	396.2	149.2	112.2	41.03	2.65	9.00
Piston	3.0	978.7	383.5	113.3	82.6	33.16	2.12	8.20
Liner	1.5	516.6	464.2	209.6	126.2	83.13	-0.15	7.26
Liner	3.0	535.4	484.0	205.7	106.6	95.37	-1.82	5.55
Piston+Liner	1.5	829.8	432.7	144.4	79.3	63.60	-1.03	6.33
Piston+Liner	3.0	1001.5	431.2	108.6	40.5	62.68	-5.03	4.52
Liner Top	1.5	475.2	420.6	218.3	170.9	56.15	4.00	10.10
Liner Top	3.0	475.3	420.7	218.3	170.0	56.15	3.61	9.80
Piston+Liner Top	1.5	806.6	396.2	149.2	114.7	41.01	4.35	8.57
Piston+Liner Top	3.0	978.7	383.5	113.3	84.7	33.15	3.95	7.48
Liner External	1.5	516.7	464.3	209.6	112.1	83.19	-6.82	7.24
Liner External	3.0	535.5	484.1	205.7	82.7	95.40	-13.41	5.37
Piston+Liner Ext.	1.5	829.8	432.8	144.4	59.4	63.66	-14.78	6.26
Piston+Liner Ext.	3.0	1001.5	431.3	108.6	56.5	62.71	-37.05	4.27

Table 5.1 Piston temperature and heat flux data for various insulation cases without corrected $T_{p,int}$ values.

Insulated Parts	PSZ (mm)	$T_{p,up}$ (Deg K)	$T_{p,int}$ (Deg K)	Q_p (kW/m2)	Q_{cond} (kW/m2)	Q_{oil} (kW/m2)	% Q_{oil} wrt Q_p	$\triangle T_{co}$ (Deg K)
-	-	473.1	418.5	218.7	163.9	54.78	25.0	10.45
Piston	1.5	805.8	395.0	149.4	109.1	40.23	26.3	8.97
Piston	3.0	978.4	382.8	113.4	80.7	32.68	28.3	8.20
Liner	1.5	516.7	464.3	209.6	126.2	83.13	39.6	7.26
Liner	3.0	537.3	486.0	205.3	109.1	96.61	47.0	5.59
Piston+Liner	1.5	830.2	433.4	144.3	80.3	64.01	44.3	6.35
Piston+Liner	3.0	1002.8	434.0	108.3	43.9	64.43	59.5	4.58
Liner Top	1.5	472.6	417.9	218.8	164.4	54.41	24.9	9.91
Liner Top	3.0	472.9	418.2	218.7	164.2	54.59	24.4	9.62
Piston+Liner Top	1.5	805.3	394.1	149.5	109.8	39.69	26.5	8.44
Piston+Liner Top	3.0	978.0	382.1	113.5	81.2	32.24	28.4	7.39
Liner External	1.5	522.2	470.1	208.5	121.7	86.75	41.6	7.42
Liner External	3.0	547.0	496.2	203.3	100.4	102.91	50.6	5.62
Piston+Liner Ext.	1.5	835.5	441.6	143.2	74.1	69.11	48.3	6.53
Piston+Liner Ext.	3.0	1010.4	449.7	106.7	32.6	74.15	69.4	4.66

Table 5.2 Piston temperature and heat flux data for various insulation cases with corrected $T_{p,int}$ values.

1-D FD ANALYSIS IN CARTESIAN COORDINATES

MATERIAL PROP.	TH(MM)	CON(W/M2-K)	DEN(KG/M3)	CP(J/KG-K)
LAYER 1	1.00	1.00	1000.00	1000.00

LHBC;CONV+RAD

RHBC;CONS TEMP

TN= 1000.0 DEG K

	MAX	MIN	MEAN	MAX POS (CA)	MIN POS (CA)	FR (HZ)
INPUT FUNCTIONS						
TGAS(K)	1744.7	309.3	659.5	15.0	490.0	8.39
HTC(W/M2-K)	2444.2	53.6	226.4	5.0	545.0	8.39
QRAD(W/M2)	1352449.0	0.0	44819.0	0.0	-140.0	8.39

CYCLE=20

TEMPERATURES(K)					
NODE= 1	1162.3	1016.8	1052.6	20.0	-10.0
NODE= 2	1149.0	1017.8	1052.1	20.0	-10.0
NODE=25	1003.7	1003.4	1003.6	-135.0	220.0
NODE=26	1000.0	1000.0	1000.0	-140.0	-140.0
HEAT FLUXES(W/M2)					
NODE= 1	2489150.8	-127260.2	52373.5	5.0	-20.0
	-2408224.5	122766.2	-52516.7	5.0	-15.0
NODE= 2	2408224.5	-122766.2	52516.7	5.0	-15.0
	-2012656.6	115055.3	-52520.4	5.0	-20.0
NODE=25	55020.0	49818.6	52680.1	-135.0	220.0
	-55020.1	-49818.8	-52679.2	-135.0	220.0
NODE=26	55020.1	49818.8	52679.2	-135.0	220.0
	-55020.1	-49818.8	-52679.2	-135.0	220.0

MEAN WALL TEMP=1052.6 DEG K APPARENT WALL TEMP=1085.2 DEG K
EXTRA RESISTANCE=0.000621 M2/(W-K)
EX. ST. PUMPED HEAT= -9817.9 W/M2
IN. ST. PUMPED HEAT=-35606.0 W/M2

Table 6.1 The output of 'FD.For'.

Analy1.For	Finds the analytical solution for a sinosoidal gas temperature.
Analy2.For	Finds the analytical solution for each individual or total Fourier gas temperature harmonics.
Foan.For	Finds the Fourier harmonics.
Endat.For	Reads cycle simulation data.
Fds1.For	Generates FD equations in cartesian coordinate system.
Fds2.For	Generates FD equations in cylindrical coordinate system.
Fds3.For	Generates FD equations in spherical coordinate system.
Laygen.For	Generates FD layers.
Matp.For	Calculates the material properties and thermal diffusivity of each CV.
Print.For	Prints the results in tabular form.
Print1.For	Prints the plotting data.
Tridag.For	Solves the set of simultaneous FD equations.

Table 6.2 Subroutines for 'FD.For'

Material	k (W/(m.K))	ρ (kg/m3)	Cp (J/(kg.K))	$\sqrt{k/\rho Cp}$ (mm)	TPD (mm)	kρCp (J2/m4.K2.s)	Temp. Swing (Deg K)
Nimonic	12.1	8200	461	1.78	1.61	4.57E7	33.9
Steel	50.2	7870	485	3.62	3.26	1.91E8	17.9
Cast Iron	54.4	7200	480	3.97	3.57	1.83E8	18.0
Aluminium Alloy	155.0	2750	915	7.85	7.06	3.90E8	12.7
Aluminium	250.0	2720	895	10.13	9.13	6.04E8	10.2
PSZ	1.0	5000	450	0.67	0.60	2.25E6	91.6
AT	1.0	3000	740	0.67	0.60	2.20E6	92.2
Cordierite	1.5	2300	730	0.94	0.85	2.52E6	87.7
Sialon	12.5	3200	670	2.41	2.17	2.58E7	28.3
HPSN	30.0	3150	680	3.74	3.37	6.43E7	18.4
HPSC	100.0	3150	670	6.83	6.19	2.11E8	10.2

Table 6.3 Thermal properties and property groups important for TPD and temperature swing are given together with TPD's and temperature swings for various metals and ceramics.

Material	T_{min} (Deg K)	T_{max} (Deg K)	Temp. Swing (Deg K)	T_{mean} (Deg K)	T_{app} (Deg K)	ER (m2.K/W)
Nimonic	503.7	537.6	33.9	510.9	519.3	0.000047
Steel	400.8	418.7	17.9	404.6	409.1	0.000022
Cast Iron	397.8	415.8	18.0	401.6	406.1	0.000022
Aluminium Alloy	375.1	387.8	12.7	377.8	381.0	0.000015
Aluminium	370.6	380.8	10.2	372.7	375.3	0.000012
PSZ	1145.7	1237.3	91.6	1171.1	1189.9	0.000658
AT	1145.5	1237.7	92.2	1171.0	1190.0	0.000662
Cordierite	1133.5	1221.2	87.7	1157.4	1175.6	0.000571
Sialon	1125.6	1153.9	28.3	1133.2	1139.1	0.000147
HPSN	1126.5	1144.9	18.4	1131.4	1135.2	0.000093
HPSC	1128.9	1139.1	10.2	1131.6	1133.7	0.000051

Table 6.4 Surface temperature data for various metals and ceramics.

Material	q_{min} (kW/m2)	q_{max} (MW/m2)	q_{mean} (kW/m2)	Exh. St. Pumped q (kW/m2)	In. St. Pumped q (kW/m2)
Nimonic	-22.7	3.93	180.5	0.0	6.27
Steel	-10.6	4.21	205.4	0.0	2.47
Cast Iron	-10.3	4.21	206.1	0.0	2.37
Aluminium Alloy	-7.6	4.28	211.8	0.0	1.64
Aluminium	-7.1	4.29	213.1	0.0	1.50
PSZ	-204.2	2.26	28.6	13.87	44.86
AT	-204.1	2.26	28.6	13.87	44.84
Cordierite	-196.0	2.30	31.9	13.36	43.93
Sialon	-190.5	2.42	40.2	12.36	42.95
HPSN	-191.1	2.44	41.0	12.27	42.96
HPSC	-192.6	2.45	41.3	12.26	43.08

Table 6.5 Surface heat flux data for various metals and ceramics.

Material	T_{min} (Deg K)	T_{max} (Deg K)	Temp. Swing (Deg K)	T_{mean} (Deg K)	T_{app} (Deg K)	ER (m2.K/W)
PSZ	1242.1	1357.4	115.3	1272.9	1306.6	0.001049
AT	1240.7	1356.9	116.2	1271.8	1305.7	0.001048
Cordierite	1233.6	1344.6	111.0	1263.0	1295.5	0.000904
Sialon	1246.9	1283.6	36.7	1256.6	1267.2	0.000231
HPSN	1251.0	1274.9	23.9	1257.3	1264.2	0.000147
HPSC	1255.1	1268.4	13.3	1258.6	1262.4	0.000080

Table 6.6 Surface temperature data for various ceramics with modified Woschni htc.

Material	q_{min} (kW/m2)	q_{max} (MW/m2)	q_{mean} (kW/m2)	Exh. St. Pumped q (kW/m2)	In. St. Pumped q (kW/m2)
PSZ	-288.8	2.84	32.1	21.97	52.02
AT	-287.4	2.84	32.4	21.91	51.93
Cordierite	-280.2	2.90	36.0	21.35	51.35
Sialon	-293.6	3.13	46.0	20.48	51.80
HPSN	-297.7	3.16	47.1	20.45	52.00
HPSC	-301.9	3.18	47.7	20.46	52.23

Table 6.7 Surface heat flux data for various ceramics with modified Woschni htc.

Material	T_{min} (Deg K)	T_{max} (Deg K)	T_{app} (Deg K)	T_n (Deg K)	$T_{w,co}$ (Deg K)
Nimonic	503.7	537.6	519.3	482.3	362.0
Steel	400.8	418.7	409.1	388.5	363.6
Cast Iron	397.8	415.8	406.1	385.3	363.7
Aluminium Alloy	375.1	387.8	381.0	366.3	364.1
Aluminium	370.6	380.8	375.3	364.2	364.2
PSZ	1145.7	1237.3	1189.9	1138.0	872.0
AT	1145.5	1237.7	1190.0	1138.1	872.0
Cordierite	1133.5	1221.2	1175.6	1129.4	938.1
Sialon	1125.6	1153.9	1139.1	1127.8	1104.2
HPSN	1126.5	1144.9	1135.2	1128.2	1120.1
HPSC	1128.9	1139.1	1133.7	1128.6	1127.4

T_n is the wall temperature at 1.2*TPD.

$T_{w,co}$ is the coolant side wall surface temperature.

T_{min}, T_{max}, T_{app} are the minimum, maximum and apparent gas side wall temperatures.

Table 6.8 Wall temperature data across various materials obtained by using the data in Tables 6.4 and 6.5.

Meterial	T_{min} (Deg K)	T_{max} (Deg K)	Temp. Swing (Deg K)	T_{mean} (Deg K)	T_{app} (Deg K)	ER (m2.K/W)
PSZ	1151.2	1228.1	76.9	1172.5	1188.3	0.000543
AT	1143.5	1201.7	58.2	1159.6	1171.6	0.000365
Cordierite	1141.4	1209.8	68.4	1160.2	1174.3	0.000438
Sialon	1129.8	1155.5	25.7	1136.7	1142.1	0.000135
HPSN	1129.1	1147.7	18.6	1134.1	1138.0	0.000095
HPSC	1129.7	1140.9	11.2	1132.7	1135.0	0.000057

Table 6.9 Surface temperature data for various ceramics with temperature dependent material properties.

Material	q_{min} (kW/m2)	q_{max} (MW/m2)	q_{mean} (kW/m2)	Exh. St. Pumped q (kW/m2)	In. St. Pumped q (kW/m2)
PSZ	-207.8	2.27	29.0	13.90	45.16
AT	-202.6	2.32	32.8	13.38	44.47
Cordierite	-201.3	2.31	32.2	13.42	44.38
Sialon	-193.3	2.41	39.5	12.48	43.25
HPSN	-192.8	2.43	40.4	12.37	43.15
HPSC	-193.2	2.44	41.1	12.31	43.15

Table 6.10 Surface heat flux data for various ceramics with temperature dependent material properties.

Run No	P_{im} (Bars)	T_{im} (Deg K)	Ne (rpm)	A/F
1	0.97	288	1000	20
2	0.97	288	1000	25
3	0.97	288	1000	40
4	0.97	288	1500	25
5	0.97	288	2000	25
6	1.49	320	1000	25
7	1.99	340	1000	25

Table 7.1 Engine operating conditions for sections 7.2 and 7.4.

Engine Type	Run No	Fuel Energy (J/Cycle)	Energy to Exhaust (%)	Gas Heat Loss to Coolant (%)	Friction Work (%)	Usefull Work (%)
Standard	1	1506.5	28.18	32.74	5.01	33.92
	2	1217.5	27.71	32.49	6.07	33.82
	3	767.9	27.23	30.85	9.25	32.84
	4	1188.0	32.44	24.31	7.72	35.54
	5	1134.0	36.16	19.76	9.58	34.46
	6	1726.7	27.85	31.61	5.01	35.54
	7	2190.0	28.49	30.50	4.46	36.53
Insulated	1	1459.8	31.43	28.59	5.18	34.72
	2	1175.9	30.72	28.35	6.29	34.62
	3	742.6	29.96	27.12	9.56	33.50
	4	1144.4	35.14	20.91	8.03	35.87
	5	1097.4	38.19	16.99	9.97	34.77
	6	1653.7	31.72	26.09	5.22	36.92
	7	2077.0	32.92	24.04	4.68	38.26

Table 7.2 Standard and insulated engines energy distributions for Sec. 7.2.

Engine Type	Run No	Total Heat Loss (J/Cycle)	Heat Loss to Piston (%)	Heat Loss to Cylinder Head (%)	Heat Loss to Liner Top Part (%)	Heat Loss to Liner Bottom Part (%)
Standard	1	493.2	43.8	35.3	12.1	8.8
	2	395.6	44.4	35.6	11.9	8.0
	3	236.9	45.1	35.9	12.0	7.0
	4	288.8	42.7	34.7	12.0	10.6
	5	224.0	41.2	34.0	12.0	12.9
	6	545.8	44.0	35.8	12.0	8.1
	7	668.1	43.5	35.8	12.1	8.7
Insulated	1	417.3	41.6	33.2	13.5	11.6
	2	333.4	42.4	33.8	13.3	10.5
	3	201.4	43.2	34.3	13.3	9.2
	4	239.4	40.6	32.7	13.3	13.4
	5	186.4	38.7	31.5	13.3	16.5
	6	431.4	41.4	33.3	13.6	11.7
	7	499.4	40.4	32.7	13.8	13.0

Table 7.3 Gas heat loss distribution among various parts of the combustion chamber for Sec. 7.2.

Engine Type	Run No	Piston						Cylinder Head			
		q_{net} (kW/m2)	$q_{rad,g}$ (%)	$q_{rad,w}$ (%)	q_{conv} (%)	q_{oil} (%)	q_{liner} (%)	q_{net} (kW/m2)	$q_{rad,g}$ (%)	$q_{rad,w}$ (%)	q_{conv} (%)
Standard	1	231.7	23.4	-0.2	76.9	25.5	74.5	243.1	22.3	0.1	77.6
	2	188.3	22.7	-0.2	77.5	25.8	74.1	196.8	21.7	0.1	78.2
	3	114.5	16.4	-0.1	83.7	27.4	72.6	118.9	15.8	0.0	84.1
	4	198.0	22.1	-0.2	78.1	27.5	72.5	209.9	20.9	0.1	79.0
	5	197.1	22.5	-0.2	77.8	29.7	70.3	211.9	21.0	0.1	79.0
	6	258.0	23.0	-0.2	77.3	25.3	74.7	273.6	21.7	0.1	78.2
	7	312.3	22.7	-0.3	77.6	25.2	74.8	335.2	21.2	0.1	78.7
Insulated	1	185.6	32.3	-1.3	69.0	26.7	73.3	193.8	31.1	-0.3	69.2
	2	151.9	30.6	-1.0	70.4	27.1	72.9	158.0	29.5	-0.3	70.7
	3	93.4	20.0	-0.6	80.6	28.9	71.1	96.5	19.4	-0.2	80.8
	4	155.7	31.0	-1.1	70.0	29.3	70.7	163.6	29.7	-0.3	70.6
	5	154.1	29.9	-1.1	71.2	32.3	67.7	163.9	28.2	-0.2	72.0
	6	190.7	32.5	-1.3	68.8	26.9	73.0	200.3	31.1	-0.4	69.2
	7	216.6	33.9	-1.6	67.7	27.1	72.9	229.2	32.3	-0.4	68.2

Table 7.4 Cycle mean heat fluxes and their components at piston and cylinder head surfaces for Sec. 7.2.

Engine Type	Run No	Top Part of Liner				Lower Part of Liner					
		q_{net} (kW/m2)	$q_{rad,g}$ (%)	$q_{rad,w}$ (%)	q_{conv} (%)	q_{net} (kW/m2)	$q_{rad,g}$ (%)	$q_{rad,w}$ (%)	q_{conv} (%)	q_{cond} (%)	q_{fric} (%)
Standard	1	109.1	19.6	0.1	80.3	48.1	3.0	0.1	16.6	51.6	28.7
	2	85.9	16.9	0.1	83.1	40.5	1.9	0.1	15.2	49.5	33.3
	3	51.9	11.2	0.1	88.8	28.4	0.8	0.0	11.9	41.7	45.5
	4	94.7	18.8	0.1	81.1	55.7	2.1	0.0	15.9	36.7	45.2
	5	97.6	20.9	0.1	79.1	72.1	2.1	0.0	15.4	27.2	55.3
	6	119.5	15.6	0.1	84.4	53.2	2.0	0.1	16.2	52.0	29.7
	7	147.7	14.9	0.1	85.0	64.4	2.1	0.1	17.8	52.2	27.8
Insulated	1	104.1	23.6	0.7	75.7	44.4	4.1	0.7	19.8	44.3	31.1
	2	81.6	19.7	0.6	79.7	37.4	2.6	0.5	18.2	42.7	36.1
	3	49.1	12.0	0.3	87.7	26.6	1.0	0.3	14.4	35.7	48.6
	4	87.6	21.9	0.6	77.5	51.7	2.6	0.4	17.7	30.4	48.8
	5	90.8	22.9	0.5	76.6	68.6	2.3	0.3	17.3	21.5	58.5
	6	108.0	19.0	0.7	80.3	47.3	2.8	0.7	20.7	42.5	33.3
	7	127.9	19.0	0.9	80.1	55.5	3.1	0.8	22.8	41.3	32.1

Table 7.5 Cycle mean heat fluxes and their components at top and bottom parts of the liner for Sec. 7.2.

Engine Type	Run No	T_{min} (Deg K)	T_{max} (Deg K)	ΔT (Deg K)	T_{mean} (Deg K)	T_{app} (Deg K)	T_{int} (Deg K)
Standard	1	482.0	496.4	14.4	485.7	488.3	-
	2	455.4	467.4	12.0	458.6	460.5	-
	3	408.1	415.5	7.4	410.2	410.8	-
	4	465.6	475.2	9.6	468.4	469.0	-
	5	472.3	480.1	7.8	474.8	474.9	-
	6	496.4	513.0	16.6	500.6	501.6	-
	7	530.8	550.7	19.9	537.9	539.1	-
Insulated	1	705.8	853.4	147.6	738.7	775.6	457.2
	2	637.4	760.5	123.1	664.2	694.1	434.7
	3	521.9	598.6	76.7	538.3	554.9	397.2
	4	657.1	757.8	100.7	680.4	698.4	443.3
	5	661.9	744.7	82.8	682.4	694.0	449.3
	6	714.5	875.2	160.7	749.5	787.3	461.5
	7	768.3	954.3	186.0	811.9	850.5	479.7

Table 7.6 Piston surface temperature data for Sec. 7.2.

Engine Type	Run No	T_{min} (Deg K)	T_{max} (Deg K)	ΔT (Deg K)	T_{mean} (Deg K)	T_{epp} (Deg K)	T_{int} (Deg K)
Standard	1	433.5	454.9	21.4	438.7	443.3	-
	2	416.3	434.0	17.7	420.6	424.1	-
	3	385.4	396.3	10.9	388.2	389.7	-
	4	420.6	434.8	14.2	424.4	426.2	-
	5	422.1	433.7	11.6	425.4	426.1	-
	6	443.9	468.5	24.6	449.7	453.1	-
	7	467.3	497.1	29.8	476.2	478.6	-
Insulated	1	676.2	826.5	150.3	709.6	747.5	417.7
	2	613.5	738.6	125.1	640.6	671.2	403.2
	3	507.4	585.0	77.6	524.1	540.9	378.7
	4	629.7	732.3	102.6	653.3	672.0	405.7
	5	631.3	715.9	84.6	652.2	664.2	405.6
	6	685.6	849.4	163.8	721.2	760.2	420.4
	7	736.4	926.5	190.1	780.6	820.9	431.9

Table 7.7 Cylinder head surface temperature data for Sec. 7.2.

Engine Type	Run No	T_{min} (Deg K)	T_{max} (Deg K)	ΔT (Deg K)	T_{mean} (Deg K)	T_{app} (Deg K)	T_{int} (Deg K)
Standard	1	401.9	415.8	13.9	405.4	408.0	-
	2	388.8	400.5	11.7	391.6	393.6	-
	3	367.5	374.7	7.2	369.4	370.0	-
	4	396.3	405.8	9.5	398.8	399.8	-
	5	402.2	410.1	7.9	404.4	404.5	-
	6	407.4	423.0	15.6	411.2	412.6	-
	7	424.3	442.5	18.2	430.4	432.0	-
Insulated	1	591.9	700.6	108.7	615.6	643.1	400.2
	2	539.8	631.0	91.2	558.8	581.1	386.4
	3	455.7	511.1	55.4	466.8	478.0	364.2
	4	560.6	635.8	75.2	576.9	590.1	389.8
	5	566.4	628.8	62.4	580.8	589.6	389.9
	6	597.3	713.4	116.1	622.2	650.2	402.1
	7	642.9	775.4	132.5	673.8	700.6	413.1

Table 7.8 Liner surface temperature data at axial position, x=0.0 mm from cylinder head, for Sec. 7.2.

Engine Type	Run No	Total Heat Loss (J/Cycle)	Heat Loss at Intake Stroke (%)	Heat Loss at Compres. Stroke (%)	Heat Loss at Expan. Stroke (%)	Heat Loss at Exhaust Stroke (%)
Standard	1	493.4	-1.4	8.0	89.6	3.7
	2	396.0	-1.5	9.9	87.8	3.8
	3	237.2	-2.0	14.5	83.6	3.8
	4	288.8	-1.9	5.7	90.0	6.3
	5	223.9	-2.2	6.7	86.3	9.1
	6	545.9	-1.5	13.1	85.0	3.4
	7	668.2	-1.5	12.6	85.4	3.5
Insulated	1	417.5	-4.0	6.8	94.3	2.8
	2	333.6	-4.3	9.6	92.0	2.6
	3	201.8	-4.9	14.6	87.7	2.6
	4	239.4	-5.5	3.6	97.1	4.8
	5	186.4	-6.4	2.2	96.5	7.7
	6	431.3	-5.0	10.9	91.8	2.2
	7	499.3	-5.6	10.1	93.4	2.1

Table 7.9 Gas to wall heat transfer at various strokes of the cycle for Sec. 7.2.

Engine Type	Run No	ISFC (g/kWh)	Brake Power (kW)	Brake Thermal Efficiency (%)	Volumetric Efficiency (%)	P_{max} (Bars)	T_{max} (Deg K)	T_{mean} (Deg K)	HTC_{mean} (W/m2.K)	T_{exh} (Deg K)
Standard	1	215.7	4.3	33.9	94.2	83.1	1890.3	706.2	266.2	758.2
	2	210.6	3.4	33.8	94.6	78.2	1716.4	648.1	249.1	698.7
	3	199.5	2.1	32.8	95.2	70.9	1430.8	552.8	220.0	562.3
	4	194.2	5.3	35.5	92.1	73.4	1758.3	685.7	287.3	745.6
	5	190.7	6.5	34.5	88.8	65.2	1768.3	711.8	243.7	789.4
	6	207.1	5.1	35.5	95.6	116.1	1799.2	681.1	338.7	704.4
	7	204.9	6.7	36.5	95.9	151.3	1859.1	709.8	409.5	731.1
Insulated	1	210.5	4.2	34.7	89.8	84.3	1987.5	755.1	267.8	819.0
	2	205.3	3.4	34.6	91.0	79.4	1787.8	685.3	250.7	721.3
	3	195.1	2.1	33.5	92.9	69.7	1470.4	574.6	220.4	582.7
	4	191.3	5.1	35.9	88.8	73.6	1822.5	720.4	289.0	776.4
	5	187.7	6.4	34.8	86.0	67.2	1825.4	741.9	319.0	811.8
	6	199.3	5.1	36.9	91.6	116.3	1878.9	725.5	335.9	750.0
	7	195.6	6.6	38.3	91.8	149.4	1935.3	756.8	402.9	780.3

Table 7.10 Performance and related parameters of standard and insulated engines for Sec. 7.2.

Engine Type	Run No	Ignition Delay Mean Pressure (Bars)	Ignition Delay Mean Temp. (Deg K)	Ignition Delay (Deg CA)	Premixed Burning Fraction (%)
Standard	1	37.2	847.2	6.35	18.92
	2	37.1	839.3	6.50	25.45
	3	37.0	822.4	6.82	38.58
	4	37.6	851.2	9.28	24.87
	5	37.2	863.9	11.98	24.32
	6	53.9	891.0	3.81	15.11
	7	70.1	934.1	2.63	6.24
Insulated	1	37.7	912.2	5.27	14.91
	2	37.5	890.4	5.57	22.95
	3	37.5	857.0	6.14	37.10
	4	37.7	904.5	7.94	21.83
	5	37.9	916.4	10.32	21.39
	6	55.2	955.3	3.22	11.40
	7	71.8	1001.2	2.23	2.55

Table 7.11 Combustion parameters for Sec. 7.2.

Run No	Insulation Type	Type of Woschni htc corr.	Emissivity		Heat (CA) Release Duration	Wall Deposits
			Air-Gap Wall	Flame		
1	Standard engine	Original, C_2=0.00324	-	f(CA)	120	-
2	Air-Gap insulated piston	Original, C_2=0.00324	0.8	f(CA)	120	-
3	Air-Gap insulated piston	Modified, C_2=f(Tw)	0.8	f(CA)	120	-
4	Air-Gap insulated piston	Modified, C_2=f(Tw)	0.1	f(CA)	120	-
5	Air-Gap insulated engine	Original, C_2=0.00324	0.1	f(CA)	120	-
6	Air-Gap insulated engine	Modified, C_2=f(Tw)	0.1	f(CA)	120	-
7	1.5 mm PSZ coated piston	Modified, C_2=f(Tw)	-	f(CA)	120	-
8	Air-Gap insulated piston	Original, C_2=0.00324	0.8	1.0	120	-
9	Air-Gap insulated piston	Original, C_2=0.00324	0.8	f(CA)	180	-
10	Air-Gap insulated piston	Original, C_2=0.00324	0.8	f(CA)	100, Reduced Spike	-
11	Standard engine	Original, C_2=0.00324	-	f(CA)	120	.02 mm all surfaces
12	Standard engine	Adjusted, C_2=0.02082	-	f(CA)	120	.02 mm all surfaces
13	Air-Gap insulated piston	Adjusted, C_2=0.02082	0.8	f(CA)	120	.02 mm all surfaces except piston

A/F=20 ; Ne=1000 rpm ; Pim=0.97 Bar ; Tim=288 K

Table 7.12 Description of simulation runs in Sec. 7.3.

Run No	Fuel Energy (J/Cycle)	Energy to Exhaust (%)	Gas Heat Loss to Coolant (%)	Friction Work (%)	Usefull Work (%)
1	1506.5	28.18	32.74	5.01	33.92
2	1432.8	32.12	28.09	5.27	34.44
3	1410.8	30.75	33.02	5.32	30.89
4	1382.6	32.65	30.33	5.44	31.56
5	1282.5	39.55	18.90	5.84	35.66
6	1202.3	39.26	25.33	6.16	29.13
7	1470.4	28.38	34.78	5.11	31.72
8	1428.9	28.92	33.01	5.27	32.72
9	1430.8	35.42	26.10	5.01	33.39
10	1422.2	31.28	28.53	5.39	34.71
11	1518.6	31.86	25.38	5.02	37.71
12	1515.6	27.02	34.92	4.95	33.10
13	1414.4	28.86	35.95	5.27	29.83

Table 7.13 Engine energy distributions for Sec. 7.3.

Run No	Total Heat Loss (J/Cycle)	Heat Loss to Piston (%)	Heat Loss to Cylinder Head (%)	Heat Loss to Liner Top Part (%)	Heat Loss to Liner Bottom Part (%)
1	493.2	43.8	35.3	12.1	8.8
2	402.5	25.9	46.5	16.1	11.4
3	465.8	39.4	38.2	13.1	9.3
4	419.4	32.6	42.4	14.7	10.3
5	242.4	31.1	23.6	22.1	23.2
6	304.6	35.3	26.9	22.4	15.4
7	511.4	46.5	33.9	11.5	8.1
8	471.6	23.3	45.6	16.3	14.8
9	373.4	25.0	44.9	16.2	13.9
10	405.8	26.0	46.8	16.1	11.0
11	385.5	40.5	32.4	14.1	13.0
12	529.3	37.1	30.3	16.5	16.1
13	508.5	34.9	30.4	18.1	16.6

Table 7.14 Gas heat loss distribution among various parts of the combustion chamber for Sec. 7.3.

Run No	Piston						Cylinder Head			
	q_{tot} (kW/m2)	$q_{rad,g}$ (%)	$q_{rad,w}$ (%)	q_{conv} (%)	q_{oil} (%)	q_{liner} (%)	q_{tot} (kW/m2)	$q_{rad,g}$ (%)	$q_{rad,w}$ (%)	q_{conv} (%)
1	231.7	23.4	-0.2	76.9	25.5	74.5	243.1	22.3	0.1	77.6
2	84.9	67.0	-32.7	65.7	34.0	66.0	281.5	23.2	6.7	70.1
3	145.4	31.4	-38.7	107.3	28.7	71.3	292.6	21.5	13.1	65.4
4	66.8	60.0	-128.9	168.9	38.2	61.8	317.5	20.7	18.5	60.7
5	60.0	96.6	-36.9	40.3	51.9	48.1	61.8	94.1	-31.5	37.4
6	81.4	52.7	-45.6	92.9	46.8	53.2	83.2	51.5	-41.4	89.9
7	245.5	21.3	-4.5	83.2	25.2	74.8	251.1	22.6	3.0	74.4
8	88.4	80.5	-34.5	54.0	35.7	64.3	323.2	34.9	6.4	58.7
9	76.3	89.6	-31.5	42.0	35.3	64.7	251.1	30.2	6.5	63.3
10	85.9	61.0	-32.8	71.8	34.0	66.3	285.8	21.2	6.7	72.1
11	168.0	32.1	-0.5	68.4	27.7	72.3	175.4	30.9	0.0	69.1
12	215.3	19.8	-0.6	80.8	28.8	71.2	229.8	18.8	0.1	81.2
13	139.1	32.3	-37.6	105.3	32.8	67.2	251.6	19.8	14.0	66.2

Table 7.15 Cycle mean heat fluxes and their components at piston and cylinder head surfaces for Sec. 7.3.

Run No	Top Part of Liner				Lower Part of Liner					
	q_{tot} (kW/m2)	$q_{rad,g}$ (%)	$q_{rad,w}$ (%)	q_{conv} (%)	q_{tot} (kW/m2)	$q_{rad,g}$ (%)	$q_{rad,w}$ (%)	q_{conv} (%)	q_{cond} (%)	q_{fric} (%)
1	109.1	19.6	0.1	80.3	48.1	3.0	0.1	16.6	51.6	28.7
2	120.7	21.6	1.5	77.0	33.4	6.0	2.8	24.2	25.7	41.2
3	117.3	19.5	3.1	77.4	40.5	3.8	4.7	20.2	37.5	33.8
4	122.6	20.1	4.5	75.4	32.9	5.5	8.8	24.5	19.5	41.7
5	112.4	26.6	11.5	61.9	36.4	7.0	10.5	27.4	17.5	37.6
6	149.9	15.3	14.7	69.9	39.6	5.1	16.8	21.6	22.4	34.1
7	108.4	19.5	0.7	79.8	49.5	2.8	0.8	15.6	53.2	27.7
8	143.1	35.7	1.4	62.9	39.0	19.8	2.7	19.7	22.7	35.1
9	112.4	32.3	1.4	66.4	32.8	8.1	2.5	26.6	23.0	39.8
10	121.6	18.8	1.5	79.7	33.5	5.4	2.9	24.0	26.0	41.8
11	99.7	24.5	0.1	75.3	42.8	4.6	0.2	21.3	41.5	32.5
12	163.9	10.3	0.1	89.6	56.3	2.4	0.3	31.6	41.5	24.3
13	171.4	10.3	1.9	87.7	48.8	2.8	3.8	35.2	30.3	27.8

Table 7.16 Cycle mean heat fluxes and their components at top and bottom parts of the liner for Sec. 7.3.

Run No	T_{min} (Deg K)	T_{max} (Deg K)	ΔT (Deg K)	T_{mean} (Deg K)	T_{app} (Deg K)	T_{int} (Deg K)
1	482.0	496.4	14.4	485.7	488.3	-
2	1067.6	1099.3	31.7	1076.5	1078.5	1056.6
3	1264.7	1328.3	63.6	1281.9	1287.9	1249.2
4	1405.2	1466.4	61.2	1424.2	1427.9	1399.8
5	1345.6	1376.4	30.8	1355.2	1358.7	1336.8
6	1532.6	1594.0	61.4	1552.2	1558.7	1533.8
7	817.4	1037.7	220.3	864.3	934.6	491.2
8	1092.9	1128.1	35.2	1102.5	1105.9	1075.8
9	1031.6	1057.1	25.5	1039.6	1043.1	1021.6
10	1071.6	1105.1	33.5	1080.6	1084.1	1060.6
11	438.5	1238.5	800.0	553.6	817.7	447.0
12	472.8	1562.1	1089.3	622.3	1188.6	483.9
13	1249.0	1310.0	61.0	1265.4	1271.3	1233.9

Table 7.17 Piston surface temperature data for Sec. 7.3.

Run No	T_{min} (Deg K)	T_{max} (Deg K)	ΔT (Deg K)	T_{mean} (Deg K)	T_{app} (Deg K)	T_{int} (Deg K)
1	433.5	454.9	21.4	438.7	443.3	-
2	446.0	469.3	23.3	451.6	458.6	-
3	465.8	492.5	26.7	473.7	478.6	-
4	476.6	504.8	28.2	485.2	490.3	-
5	1342.2	1373.2	31.0	1351.8	1355.5	1341.2
6	1533.0	1594.4	61.4	1552.7	1559.9	1534.4
7	430.5	451.8	21.3	435.7	440.4	-
8	459.7	484.8	25.1	466.3	475.4	-
9	434.5	453.1	18.6	439.5	444.4	-
10	447.6	472.1	24.5	453.3	460.9	-
11	403.6	1219.3	815.7	521.0	792.2	410.2
12	423.7	1550.6	1126.9	579.0	1168.7	431.9
13	433.1	1607.9	1174.8	592.8	1238.4	440.6

Table 7.18 Cylinder head surface temperature data for Sec. 7.3.

Run No	T_{min} (Deg K)	T_{max} (Deg K)	ΔT (Deg K)	T_{mean} (Deg K)	T_{app} (Deg K)	T_{int} (Deg K)
1	401.9	415.8	13.9	405.4	408.0	-
2	402.8	418.3	15.5	406.6	409.9	-
3	403.1	418.3	15.2	406.8	410.3	-
4	403.3	419.1	15.8	407.1	411.1	-
5	904.2	934.5	30.3	912.0	920.6	816.6
6	1094.8	1141.3	46.5	1105.5	1131.8	968.4
7	400.8	414.8	14.0	404.3	406.9	-
8	415.7	431.7	16.0	420.0	423.3	-
9	399.9	413.7	13.8	403.6	405.9	-
10	402.8	418.7	15.9	406.6	410.2	-
11	412.1	1051.4	639.3	498.9	708.7	395.4
12	440.7	1360.2	919.5	559.8	1024.3	406.2
13	445.9	1420.1	974.2	570.0	1064.0	421.0

Table 7.19 Liner surface temperature data at axial position, x=0.0 mm from cylinder head, for Sec. 7.3.

Run No	Total Heat Loss (J/Cycle)	Heat Loss at Intake Stroke (%)	Heat Loss at Compres. Stroke (%)	Heat Loss at Expan. Stroke (%)	Heat Loss at Exhaust Stroke (%)
1	493.4	-1.4	8.0	89.6	3.7
2	402.5	-4.8	6.5	96.3	2.0
3	465.8	-5.2	4.0	100.8	0.4
4	419.4	-6.5	0.7	106.2	-0.3
5	242.4	-16.5	-4.2	124.2	-3.6
6	304.6	-15.4	-15.3	138.1	-7.3
7	511.4	-2.9	8.1	92.8	2.1
8	471.6	-4.2	5.8	98.0	0.6
9	373.4	-4.9	5.1	96.4	3.3
10	405.8	-4.8	5.2	97.8	1.8
11	385.5	-1.4	9.1	87.1	5.3
12	529.3	-1.4	11.6	86.4	2.9
13	508.5	-4.6	7.6	97.0	0.0

Table 7.20 Gas to wall heat transfer at various strokes of the cycle for Sec. 7.3.

Run No	ISFC (g/kWh)	Brake Power (kW)	Brake Thermal Efficiency (%)	Volumetric Efficiency (%)	P_{max} (Bars)	T_{max} (Deg K)	T_{mean} (Deg K)	HTC_{mean} (W/m2.K)	T_{exh} (Deg K)
1	215.7	4.3	33.9	94.2	83.2	1890.2	704.5	238.2	758.5
2	211.5	4.1	34.4	88.7	83.1	1992.2	763.4	232.0	826.2
3	231.9	3.6	30.9	86.6	82.3	1947.0	756.7	633.9	816.3
4	227.0	3.6	31.5	85.4	82.2	1983.0	777.6	694.2	844.2
5	202.4	3.8	35.6	79.5	81.0	2175.8	868.3	231.9	956.3
6	238.0	2.9	29.1	76.5	79.7	2072.4	865.2	718.5	935.6
7	228.0	3.9	31.7	90.8	82.2	1887.0	717.5	425.8	773.9
8	221.1	3.9	32.7	88.3	83.0	1980.2	744.5	233.1	777.2
9	218.7	4.0	33.4	89.1	72.2	1760.3	773.3	214.5	873.7
10	209.4	4.1	34.7	88.6	87.5	2076.6	757.6	240.5	811.1
11	196.5	4.8	37.7	94.9	85.4	1965.7	734.7	244.3	820.5
12	220.7	4.2	33.1	94.1	82.2	1867.2	695.3	612.1	749.3
13	239.3	3.5	29.8	86.8	80.3	1917.1	742.5	619.7	775.5

Table 7.21 Performance and related parameters of the engine for Sec. 7.3.

Source	Material	Conductivity (W/m .K)	Thermal Inertia (J/m3.K)
	Carbon;		
Anderson	1-Pyrolytic graphite	0.070	63.6E4
	2-Lampblack	0.0021	1.3E4
	Deposits;		
Mikita	1-Leaded	0.375	-
	2-Unleaded	0.239	-
Bennethum	1-Leaded	0.10	6.45E4
	2-Unleaded*	0.04	6.8E4
Anderson	1-Unleaded	0.38	1.3E7
	2-Ca based additive	0.50	1.5E7
	3-Unleaded**	0.66	1.2E7
	4-Leaded	0.80	2E7-4E7

* Deposit 1 ** Deposit 2

Table 7.22 Thermal properties of carbon and combustion chamber deposits [114].

Run No	Fuel Energy (J/Cycle)	Energy to Exhaust (%)	Gas Heat Loss to Coolant (%)	Friction Work (%)	Usefull Work (%)
1	1418.2	29.01	35.45	5.26	30.28
2	1171.6	28.81	33.91	6.27	31.01
3	742.8	29.81	27.12	9.56	33.54
4	1129.9	33.51	25.32	8.11	33.06
5	1084.2	37.08	20.02	10.08	32.80
6	1601.8	29.81	32.26	5.29	32.63
7	2028.4	30.98	30.58	4.71	33.70

Table 7.23 1.5 mm PSZ coated engine energy distributions at various engine operating conditions with the modified Woschni htc correlation (Sec. 7.4).

Run No	Total Heat Loss (J/Cycle)	Heat Loss to Piston (%)	Heat Loss to Cylinder Head (%)	Heat Loss to Liner Top Part (%)	Heat Loss to Liner Bottom Part (%)
1	502.8	46.3	36.1	9.9	7.7
2	397.4	46.1	35.6	10.4	7.9
3	201.4	43.2	34.2	13.3	9.3
4	286.1	44.3	34.5	10.7	10.5
5	217.1	42.3	33.3	11.1	13.3
6	516.7	45.9	36.0	10.4	7.7
7	620.3	44.5	35.4	11.1	9.0

Table 7.24 Gas heat loss distribution among various parts of the combustion chamber for Sec. 7.4.

Run No	Piston						Cylinder Head			
	q_{tot} (kW/m2)	$q_{rad,g}$ (%)	$q_{rad,w}$ (%)	q_{conv} (%)	q_{oil} (%)	q_{liner} (%)	q_{tot} (kW/m2)	$q_{rad,g}$ (%)	$q_{rad,w}$ (%)	q_{conv} (%)
1	246.7	22.5	-2.0	79.5	25.1	74.9	253.2	22.2	-0.5	78.3
2	195.2	22.5	-1.4	78.9	25.6	74.4	198.1	22.4	-0.3	77.9
3	93.3	19.8	-0.6	80.8	28.9	71.1	96.4	19.2	-0.2	81.0
4	201.8	22.6	-1.5	79.0	27.4	72.6	207.0	22.2	-0.3	78.1
5	194.6	23.6	-1.5	78.0	29.8	70.1	201.5	23.0	-0.2	77.3
6	250.7	22.8	-2.0	79.1	25.3	74.7	259.7	22.3	-0.5	78.2
7	293.1	22.7	-2.5	79.8	25.4	74.6	308.3	22.0	-0.8	78.8

Table 7.25 Cycle mean heat fluxes and their components at piston and cylinder head surfaces for Sec. 7.4.

Run No	Top Part of Liner				Lower Part of Liner					
	q_{tot} (kW/m2)	$q_{rad,g}$ (%)	$q_{rad,w}$ (%)	q_{conv} (%)	q_{tot} (kW/m2)	$q_{rad,g}$ (%)	$q_{rad,w}$ (%)	q_{conv} (%)	q_{cond} (%)	q_{fric} (%)
1	92.7	22.9	1.9	75.2	49.2	2.9	1.2	14.5	53.8	27.6
2	76.6	19.1	1.3	79.6	41.4	1.9	0.8	14.8	50.2	32.3
3	49.1	11.8	0.3	87.9	26.6	1.0	0.3	14.6	35.6	48.6
4	84.9	20.6	1.2	78.1	56.3	2.0	0.6	15.6	37.1	44.7
5	89.0	22.3	1.1	76.6	72.3	2.0	0.5	15.5	26.6	55.5
6	100.5	18.6	1.9	79.5	51.7	2.3	1.2	14.6	51.9	30.0
7	130.6	16.7	2.2	81.1	62.2	2.3	1.5	17.6	50.5	28.1

Table 7.26 Cycle mean heat fluxes and their components at top and bottom parts of the liner for Sec. 7.4.

Engine Component	Run No	T_{min} (Deg K)	T_{max} (Deg K)	ΔT (Deg K)	T_{mean} (Deg K)	T_{app} (Deg K)	T_{int} (Deg K)
Piston	1	818.0	1035.4	217.4	863.6	937.2	491.6
	2	718.8	889.4	170.6	754.2	807.8	459.6
	3	521.0	597.5	76.5	537.4	553.5	396.9
	4	742.7	884.9	142.2	773.8	811.5	469.7
	5	737.5	853.4	115.9	764.4	790.2	477.5
	6	824.5	1058.7	234.2	872.2	952.3	495.0
	7	908.7	1193.8	285.1	969.5	1061.7	523.3
Cylinder Head	1	780.1	995.0	214.9	824.7	896.3	441.3
	2	685.8	852.9	167.1	720.0	770.4	419.2
	3	506.9	584.4	77.5	523.6	540.1	378.6
	4	706.0	845.6	139.6	736.2	771.4	422.8
	5	698.2	811.8	113.6	724.3	748.0	420.6
	6	788.8	1021.8	233.0	835.8	914.6	443.9
	7	871.7	1158.6	286.9	932.8	1025.9	463.3
Liner, x=0.0 mm	1	572.2	675.7	100.5	594.1	622.4	391.8
	2	532.0	620.9	88.9	550.1	571.8	382.0
	3	455.5	510.6	55.1	466.5	477.7	364.2
	4	555.7	629.7	74.0	571.6	585.0	386.4
	5	565.3	628.3	63.0	579.6	590.0	388.1
	6	605.5	736.7	131.2	632.4	675.0	402.0
	7	690.0	857.0	167.0	726.8	773.3	423.8

Table 7.27 Temperature data at various engine component surfaces for Sec. 7.4.

Run No	Total Heat Loss (J/Cycle)	Heat Loes at Intake Stroke (%)	Heat Loss at Compres. Stroke (%)	Heat Loss at Expan. Stroke (%)	Heat Loss at Exhaust Stroke (%)
1	505.3	-4.2	8.1	95.2	0.9
2	397.0	-4.4	10.5	92.7	1.2
3	201.8	-4.9	14.7	87.6	2.6
4	285.9	-5.6	3.5	99.5	2.6
5	217.2	-6.6	1.3	100.4	4.9
6	519.9	-5.3	11.1	93.8	0.3
7	620.8	-6.0	8.9	97.2	-0.1

Table 7.28 Gas to wall heat transfer at various strokes of the cycle for Sec. 7.4.

Run No	ISFC (g/kWh)	Brake Power (kW)	Brake Thermal Efficiency (%)	Volumetric Efficiency (%)	P_{max} (Bars)	T_{max} (Deg K)	T_{mean} (Deg K)	HTC_{mean} (W/m2.K)	T_{exh} (Deg K)
1	236.4	3.6	30.3	87.9	80.2	1887.6	731.2	410.5	784.3
2	225.3	3.0	31.0	89.6	77.1	1737.5	673.6	338.9	701.1
3	194.9	2.1	33.5	92.9	70.5	1468.5	572.9	201.2	568.4
4	204.0	4.7	33.1	87.6	73.1	1785.3	710.3	372.4	761.8
5	195.9	5.9	32.8	85.1	67.8	1801.1	736.0	390.2	806.4
6	221.5	4.4	32.6	90.0	111.6	1807.4	710.8	491.5	729.2
7	218.7	5.7	33.7	89.9	144.3	1873.9	746.7	657.2	765.6

Table 7.29 Performance and related parameters of the insulated engine for Sec. 7.4.

Run No	Ceramic Type	Woschni htc Type	Coolant htc (W/m2.K)
1	-	Original	2500.0
2	Cordierite	Original	416.5
3	HPSN	Original	119.3
4	HPSC	Original	113.4
5*	Cordierite	Modified	1363.6
6	HPSN	Modified	489.3
7	HPSC	Modified	402.3

* Wall thickness is reduced from 10 mm to 3 mm to decrease the gas side wall temperature levels below 1500 K.

A/F=20, Ne=1000 rpm, Pim=2.0 Bars, Tim=340 K, Pex=1.8 Bars

Table 7.30 The description of simulation runs made for Sec. 7.5.

Run No	Fuel Energy (J/Cycle)	Energy to Exhaust (%)	Gas Heat Loss to Coolant (%)	Friction Work (%)	Usefull Work (%)
1	2721.4	29.51	30.28	3.72	36.42
2	2361.2	40.26	16.37	4.27	39.03
3	2361.2	39.38	17.82	4.27	38.47
4	2369.4	39.03	18.31	4.26	38.33
5	2426.0	32.89	31.03	4.08	31.93
6	2426.0	32.18	33.39	4.08	30.26
7	2426.0	32.24	33.31	4.08	30.28

Table 7.31 Energy distributions of various ceramic engines for Sec. 7.5.

Run No	Total Heat Loss (J/Cycle)	Heat Loss to Piston (%)	Heat Loss to Cylinder Head (%)	Heat Loss to Liner Top Part (%)	Heat Loss to Liner Bottom Part (%)
1	824.0	42.9	35.4	12.3	9.4
2	386.6	35.1	24.7	15.0	25.1
3	420.8	33.3	23.7	20.4	22.6
4	433.9	32.4	23.1	22.9	21.6
5	752.9	43.3	32.7	13.9	10.0
6	810.2	44.0	33.3	13.7	9.0
7	808.0	44.7	33.9	12.5	8.9

Table 7.32 Gas heat loss distribution among various parts of the combustion chamber for Sec. 7.5.

Run No	Piston						Cylinder Head			
	q_{tot} (kW/m2)	$q_{rad,g}$ (%)	$q_{rad,w}$ (%)	q_{conv} (%)	q_{oil} (%)	q_{liner} (%)	q_{tot} (kW/m2)	$q_{rad,g}$ (%)	$q_{rad,w}$ (%)	q_{conv} (%)
1	378.6	23.2	-0.3	77.2	25.0	75.0	408.4	21.6	0.1	78.3
2	135.8	64.0	-10.8	46.8	35.5	65.1	114.3	73.5	-20.4	46.9
3	135.6	64.3	-12.6	48.2	39.6	60.4	114.7	74.0	-22.9	48.9
4	134.8	64.6	-13.0	48.4	41.7	58.3	114.4	74.1	-23.4	49.3
5	339.4	21.7	-3.9	82.2	25.8	74.2	331.5	22.0	-4.4	82.4
6	364.4	20.3	-4.8	84.6	26.7	73.3	357.0	20.5	-5.4	84.9
7	369.5	19.9	-5.1	85.2	27.1	72.9	362.4	20.2	-5.7	85.5

Table 7.33 Cycle mean heat fluxes and their components at piston and cylinder head surfaces for Sec. 7.5.

Run No	Top Part of Liner				Lower Part of Liner					
	q_{tot} (kW/m2)	$q_{rad,g}$ (%)	$q_{rad,w}$ (%)	q_{conv} (%)	q_{tot} (kW/m2)	$q_{rad,g}$ (%)	$q_{rad,w}$ (%)	q_{conv} (%)	q_{cond} (%)	q_{fric} (%)
1	185.4	17.6	0.1	82.3	76.6	3.3	0.1	19.0	53.4	24.2
2	118.2	30.0	7.6	62.5	58.7	7.0	7.2	30.4	23.9	31.5
3	172.4	24.1	7.8	68.2	58.2	6.6	6.9	29.6	25.2	31.7
4	197.6	21.8	7.3	70.9	58.1	6.6	6.7	29.2	25.7	31.8
5	200.5	14.0	3.9	82.1	74.1	3.4	3.8	19.1	49.3	24.5
6	214.3	14.3	5.4	80.3	77.1	3.1	4.3	17.5	51.6	23.5
7	196.8	16.2	6.6	77.2	78.0	3.1	4.4	17.2	52.1	23.3

Table 7.34 Cycle mean heat fluxes and their components at top and bottom parts of the liner for Sec. 7.5.

Engine Component	Run No	T_{min} (Deg K)	T_{max} (Deg K)	ΔT (Deg K)	T_{mean} (Deg K)	T_{app} (Deg K)	T_{int} (Deg K)
Piston	1	572.4	596.4	24.0	580.7	582.9	-
	2	1313.1	1474.0	160.9	1352.9	1383.1	441.9
	3	1343.2	1388.4	45.2	1355.9	1362.8	450.5
	4	1345.2	1373.0	27.8	1353.7	1357.7	454.5
	5	1172.1	1484.8	312.7	1238.2	1351.1	556.2
	6	1284.2	1381.7	97.5	1306.7	1339.6	578.3
	7	1307.3	1368.7	61.4	1322.3	1342.6	584.1
Cylinder Head	1	495.5	531.4	35.9	506.0	510.1	-
	2	1348.2	1505.0	156.8	1387.6	1409.3	385.7
	3	1373.4	1417.5	44.1	1386.0	1387.1	385.8
	4	1373.9	1401.0	27.1	1382.3	1383.0	385.8
	5	1183.3	1494.3	311.0	1249.4	1361.2	472.6
	6	1292.9	1390.0	97.1	1315.4	1347.8	482.8
	7	1315.2	1376.3	61.1	1330.2	1349.8	485.0
Liner, x=0.0 mm	1	446.0	467.6	21.6	453.1	454.0	-
	2	1280.2	1397.1	116.9	1308.1	1335.3	399.8
	3	964.8	1002.6	37.8	974.4	985.1	384.3
	4	759.3	784.4	25.1	765.8	773.0	374.0
	5	1005.7	1203.7	198.0	1047.0	1126.2	472.4
	6	825.5	880.2	54.7	837.7	864.5	440.6
	7	645.9	675.4	29.5	652.9	675.4	410.3

Table 7.35 Temperature data at various engine component surfaces for Sec. 7.5.

Run No	Total Heat Loss (J/Cycle)	Heat Loss at Intake Stroke (%)	Heat Loss at Compres. Stroke (%)	Heat Loss at Expan. Stroke (%)	Heat Loss at Exhaust Stroke (%)
1	824.0	-1.5	9.4	88.5	3.5
2	386.6	-17.0	-1.5	121.9	-3.3
3	420.8	-15.3	-0.9	119.1	-2.8
4	433.9	-14.6	-0.4	117.6	-2.5
5	752.9	-7.5	5.5	103.8	-1.6
6	810.2	-7.5	3.4	106.1	-2.0
7	808.0	-7.5	2.8	106.7	-2.0

Table 7.36 Gas to wall heat transfer at various strokes of the cycle for Sec. 7.5.

Run No	ISFC (g/kWh)	Brake Power (kW)	Brake Thermal Efficiency (%)	Volumetric Efficiency (%)	P_{max} (Bars)	T_{max} (Deg K)	T_{mean} (Deg K)	HTC_{mean} (W/m2.K)	T_{exh} (Deg K)
1	209.2	8.3	36.4	95.3	161.0	2047.2	773.0	388.5	823.3
2	193.9	7.7	39.0	83.6	160.6	2297.1	921.1	381.9	999.8
3	196.5	7.6	38.5	83.8	160.4	2280.7	911.1	380.7	987.8
4	197.2	7.6	38.3	84.0	160.3	2274.3	907.3	380.6	982.5
5	233.3	6.5	31.9	85.6	154.3	2083.5	839.4	940.3	885.9
6	244.6	6.1	30.3	84.6	154.5	2081.2	839.8	982.0	877.3
7	244.5	6.1	30.3	84.6	155.0	2085.0	840.8	996.1	878.0

Table 7.37 Performance and related parameters of ceramic engines for Sec. 7.5.

TYPE: PETTER PH1W
Water cooled single cylinder stationary
D.I. Diesel

SPEED RANGE: 1000 - 2000 rev/min

MAX RATED POWER: 8.2 bhp (11 kW) at 2000 rev/min.

CYLINDER BORE: 87.3 mm

STROKE: 110 mm

COMPRESSION RATIO: 16.5:1

FUEL INJECTION PRESSURE: 2250 - 3150 p.s.i.

FUEL INJECTION TIMING ('SPILL'): 24 - 28 BTDC
(speed dependent)

VALVE TIMING: IVO 4.5° BTDC
IVC 35.5° ABDC
evo 35.5° BBDC
evc 4.5° ATDC

'BUMPING' CLEARANCE: 0.76 - 0.91 mm

VALVE ROCKER CLEARANCE: 0.25 mm (cold).

TABLE 8.1 ENGINE SPECIFICATION

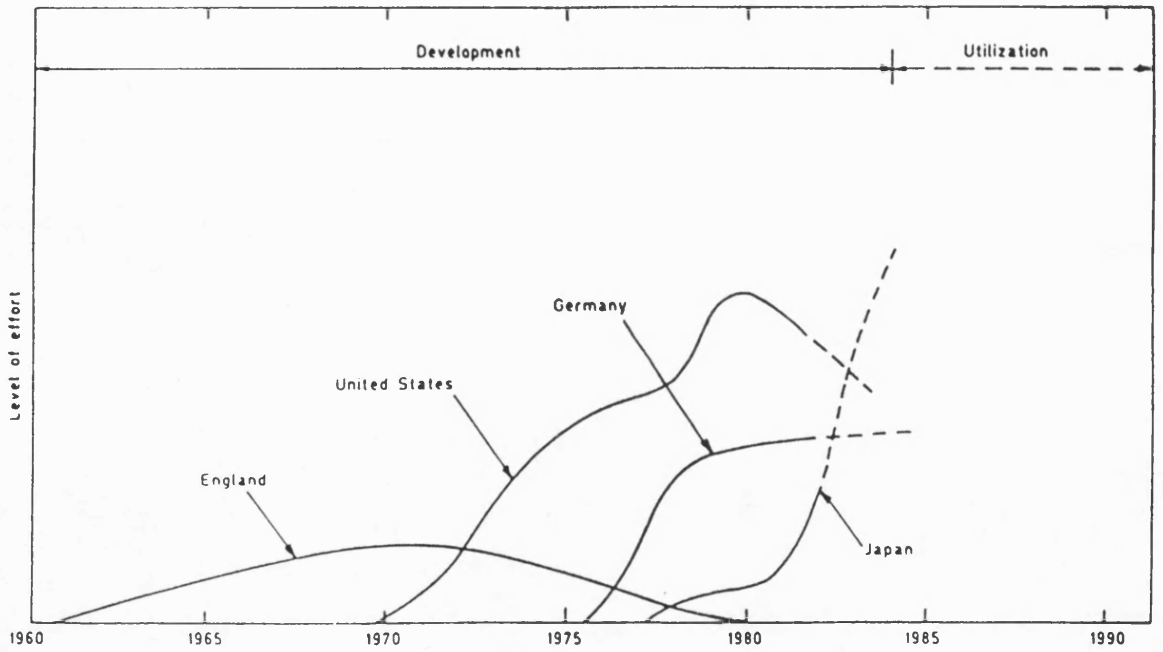

Fig. 1.1 The research and development effort on technical ceramics by various countries versus time.

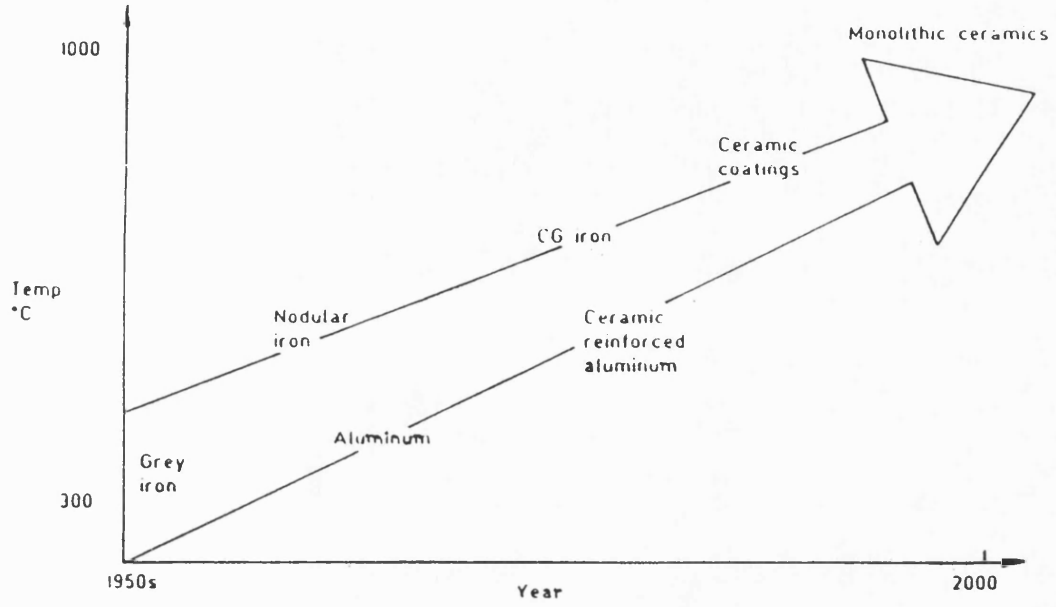

Fig. 1.2 Evolution of engine materials.

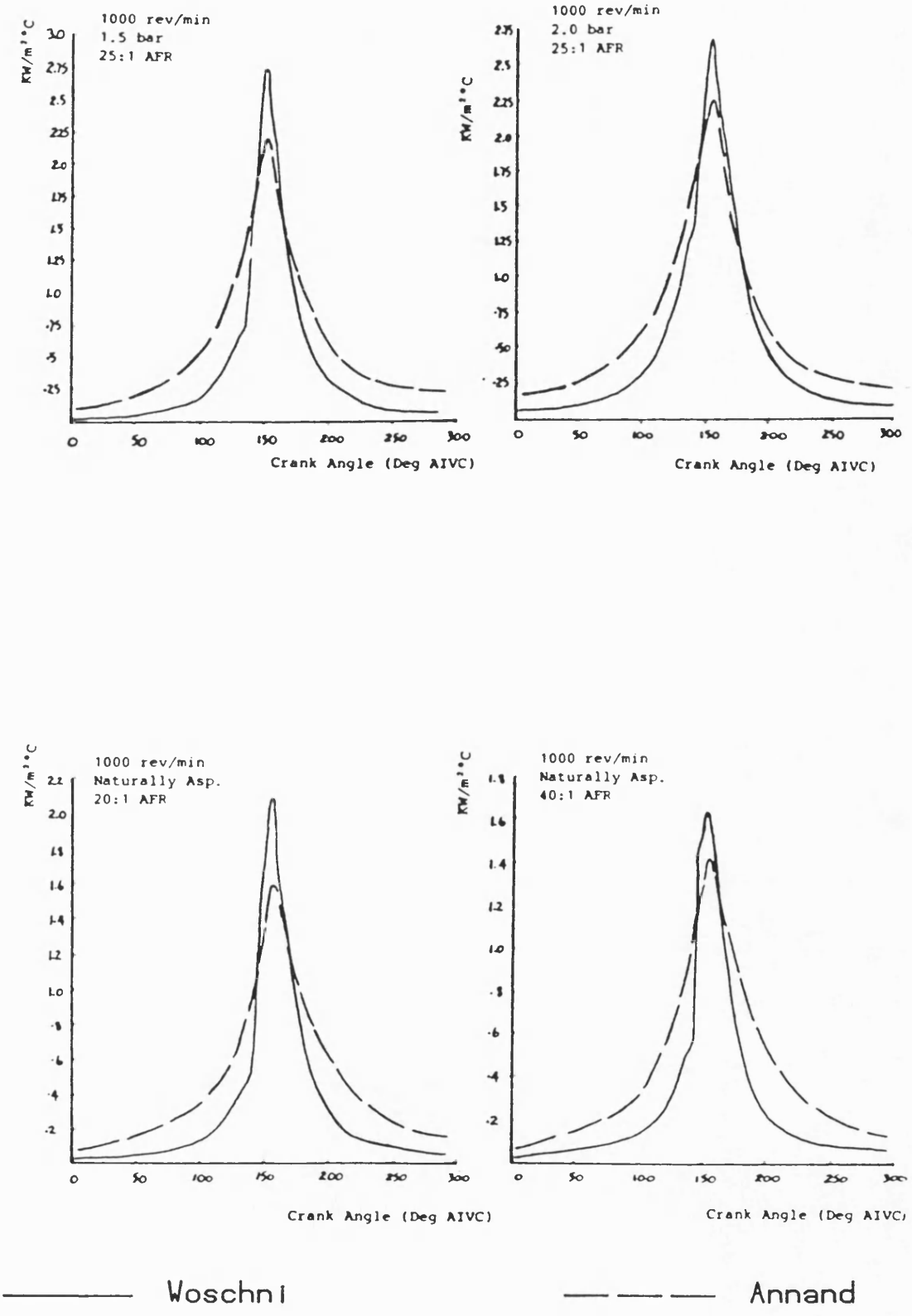

Fig. 2.1 Comparison of Woschni's and Annand's htc at various engine operating conditions [9].

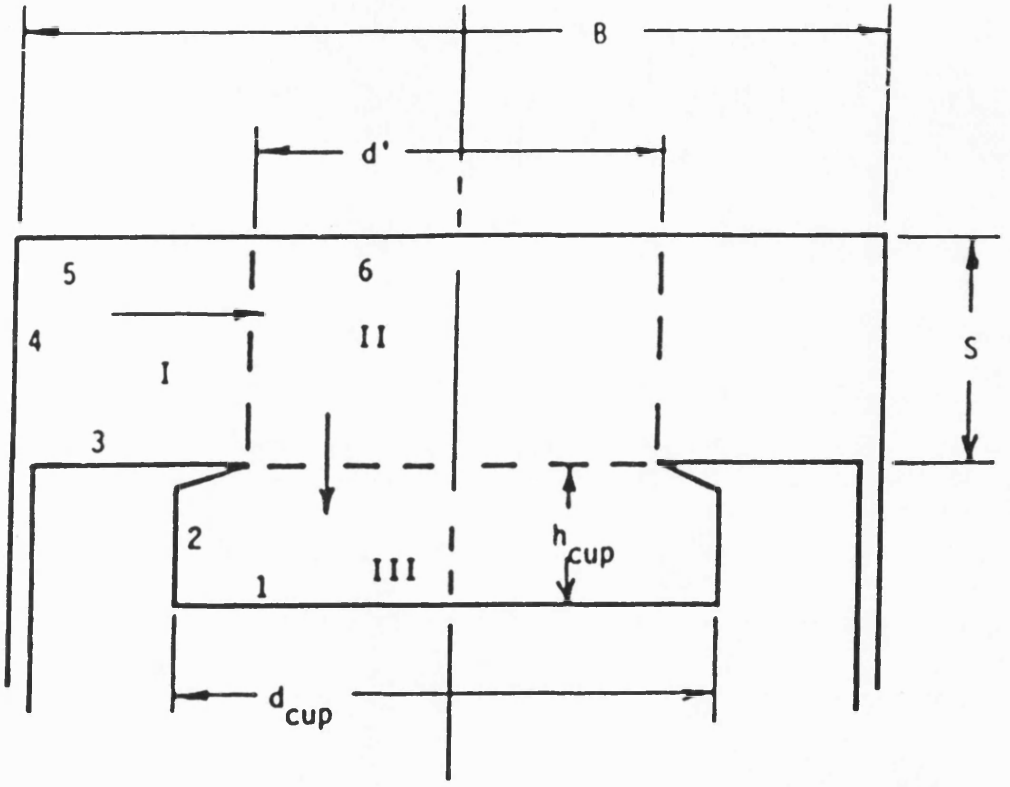

Fig. 2.2 Flow regions appropriate for typical bowl-in-piston diesel engine geometries. Arrows indicate flow directions during compression stroke. Roman numbers refer to flow regions, arabic numbers refer to the elementary surfaces bounding those regions [21].

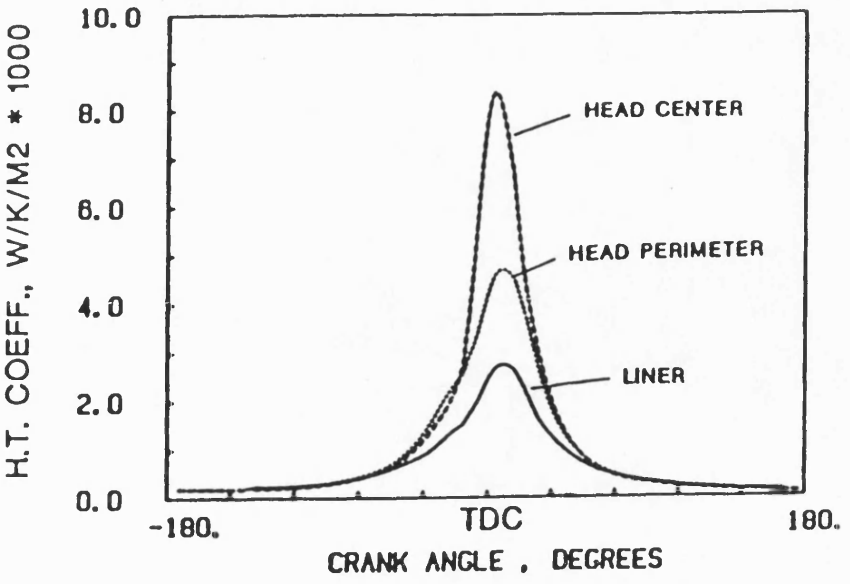

Fig. 2.3 Distribution of htc on various in-cyclinder surfaces [21].

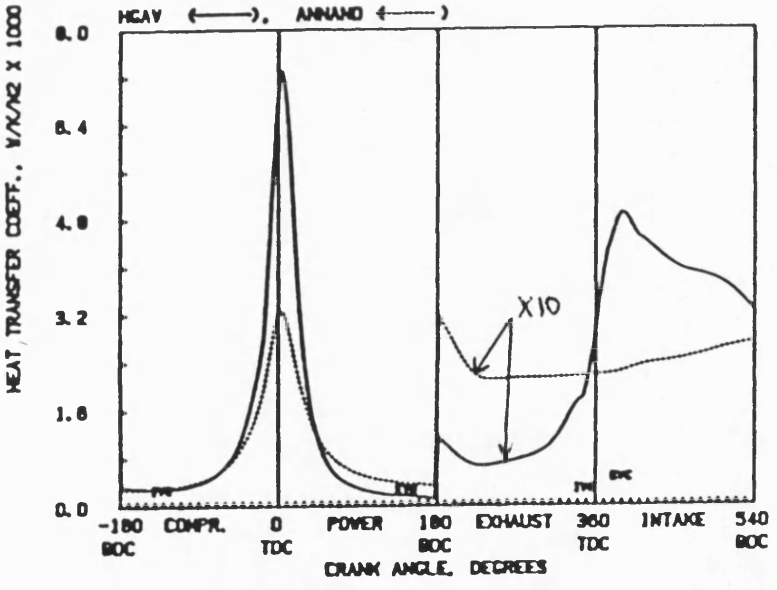

Fig. 2.4 Comparison of Morel's area averaged htc and Annand's htc correlation [21].

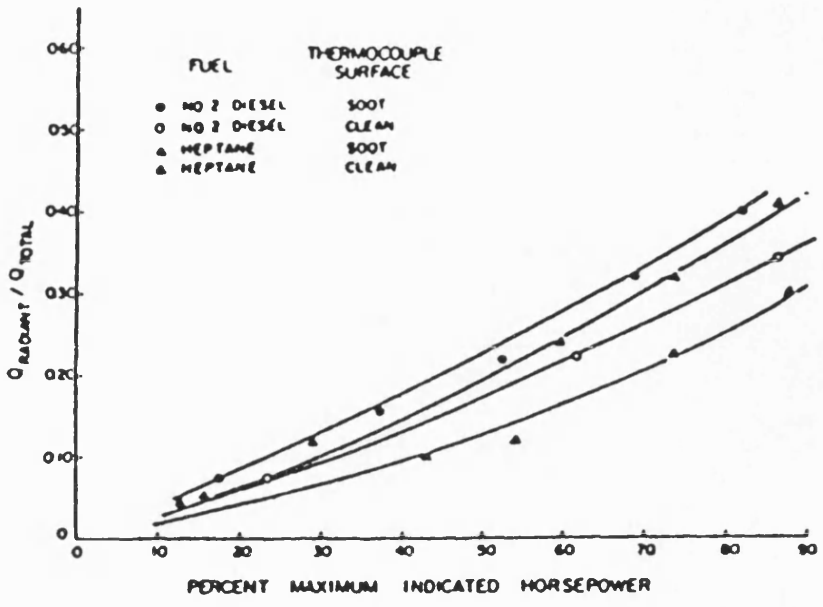

Fig. 2.5 Ratio of radiation to total heat loss versus indicated power [22].

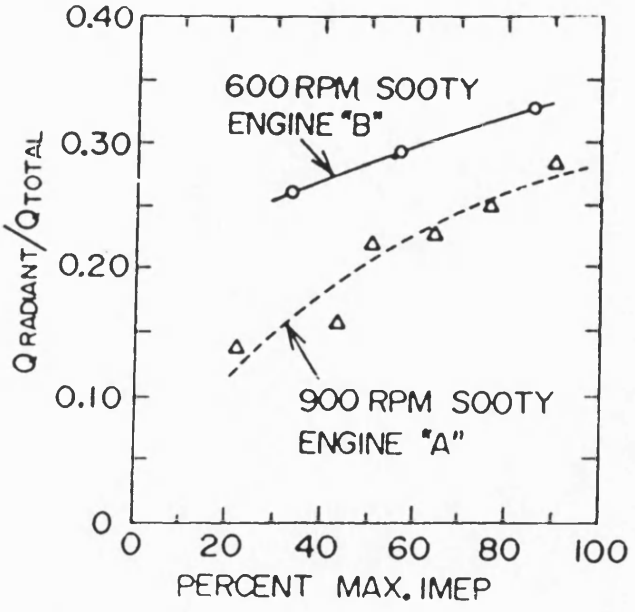

Fig. 2.6 Ratio of radiation to total heat loss versus indicated power [24].

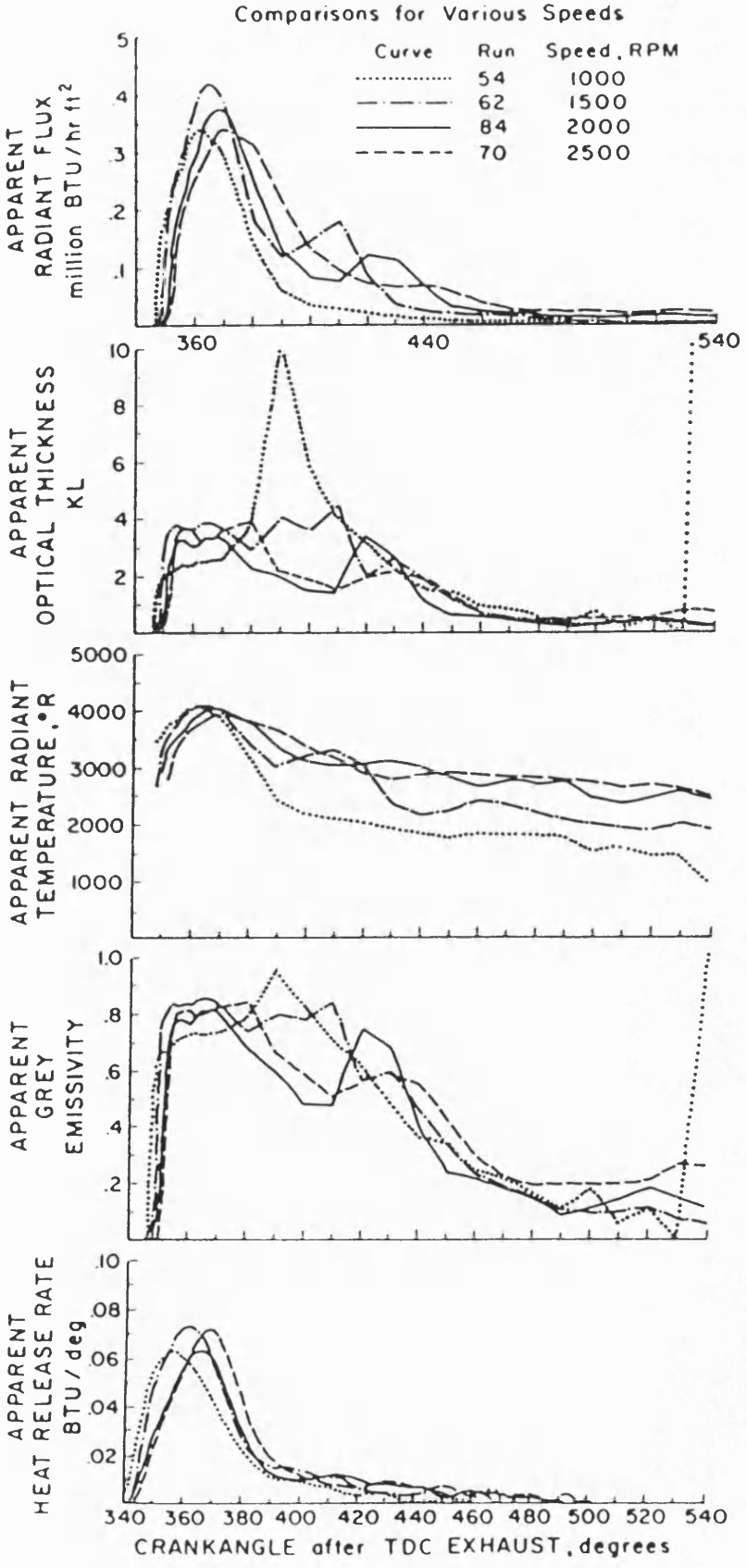

Fig. 2.7 Radiant emissions and heat release rates at various engine speeds [23].

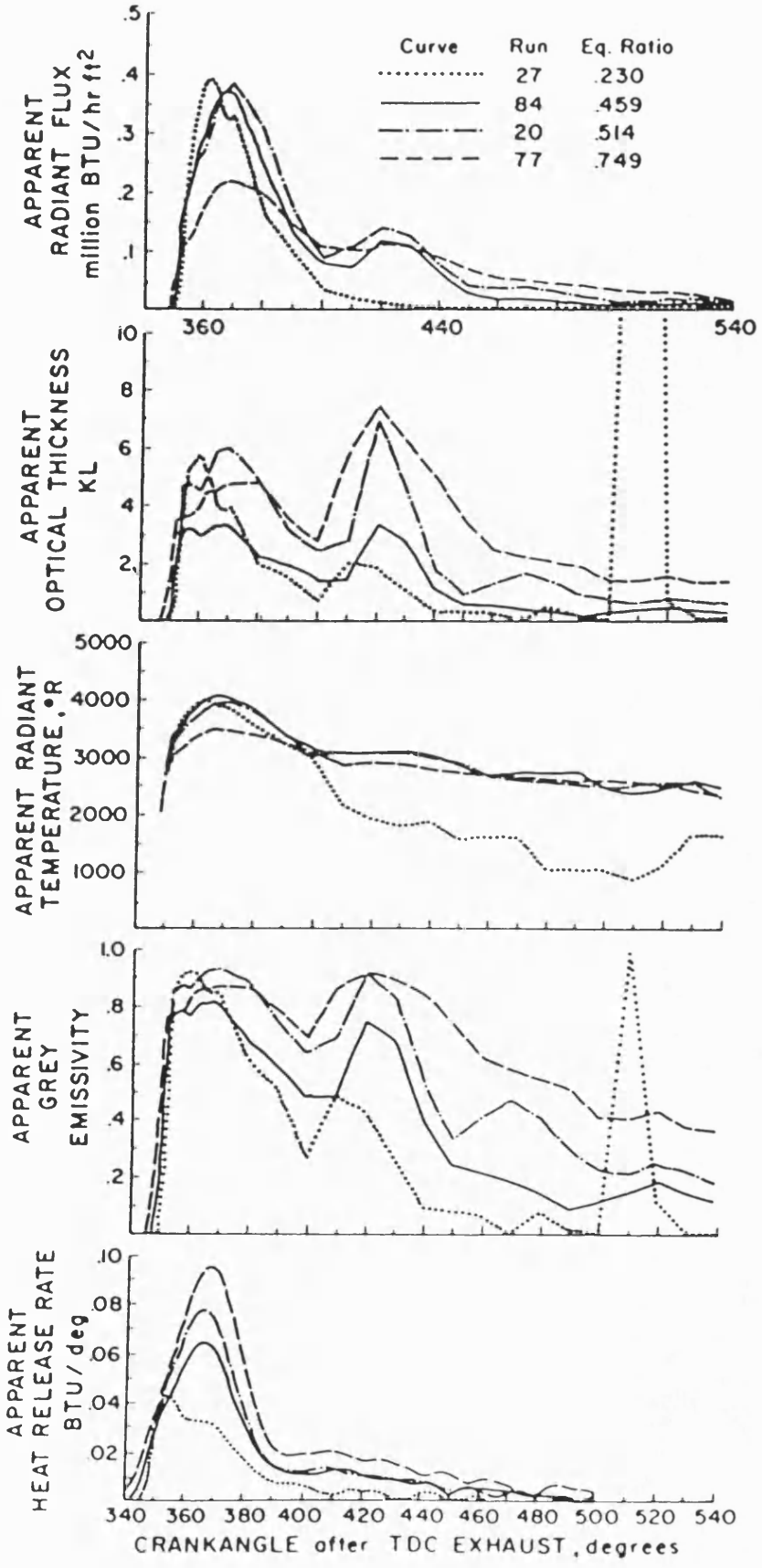

Fig. 2.8 Radiant emissions and heat release rates at various equivalence ratio [23].

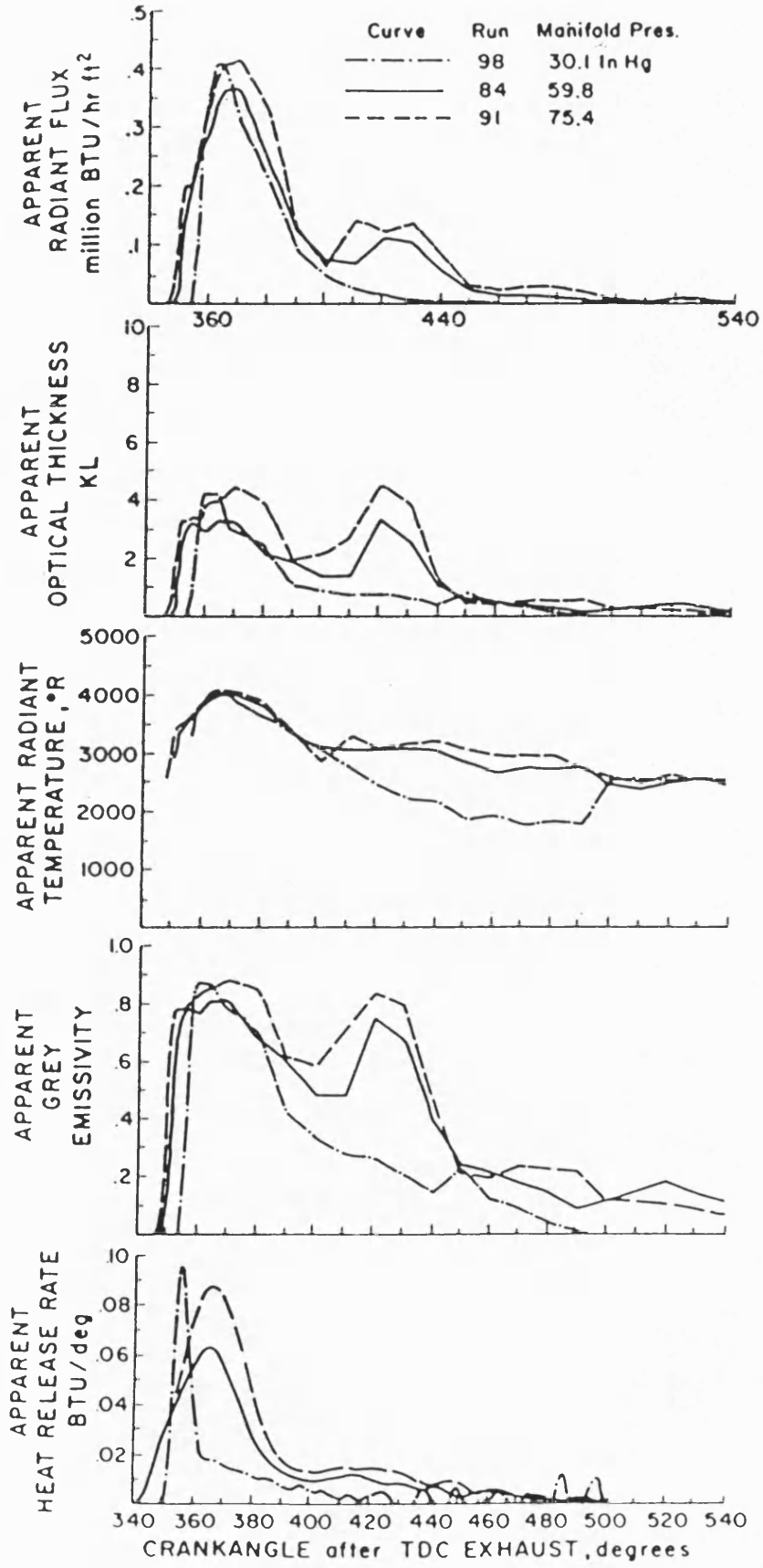

Fig. 2.9 Radiant emissions and heat release rates at various inlet manifold pressures [23].

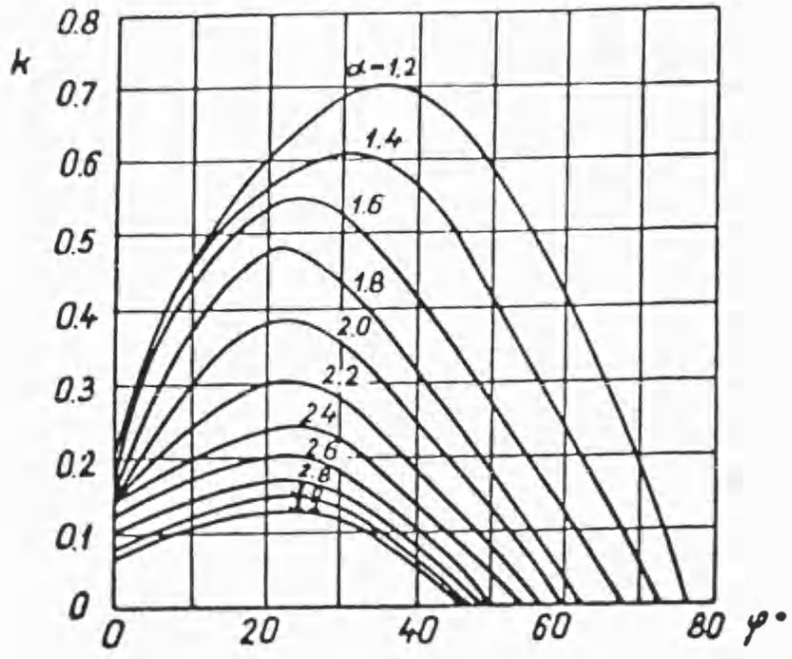

Fig. 2.10 Absorption factor versus crank angle at various excess air ratios [25].

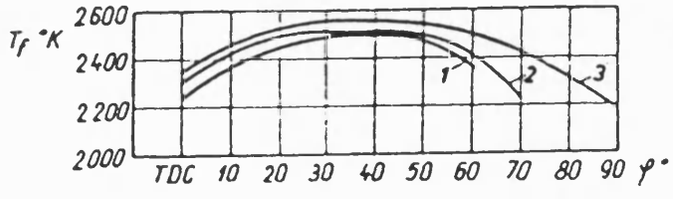

Fig. 2.11 Measured flame temperatures in diesel engines [25].

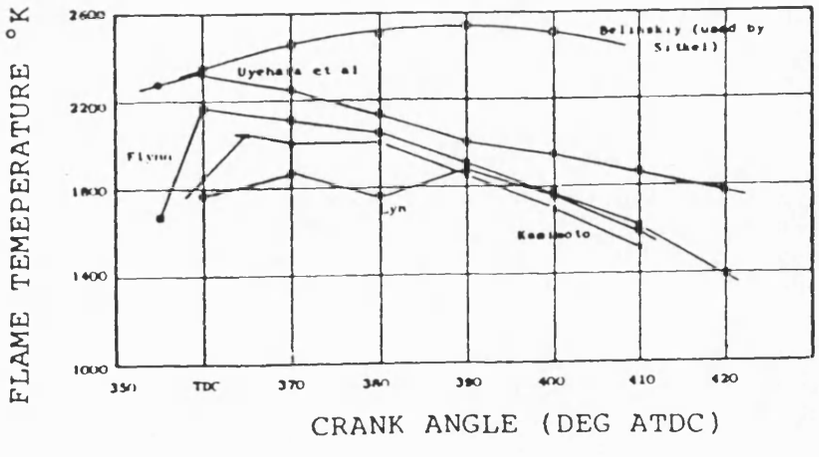

Fig. 2.12 Measured flame temperatures in diesel engines [26].

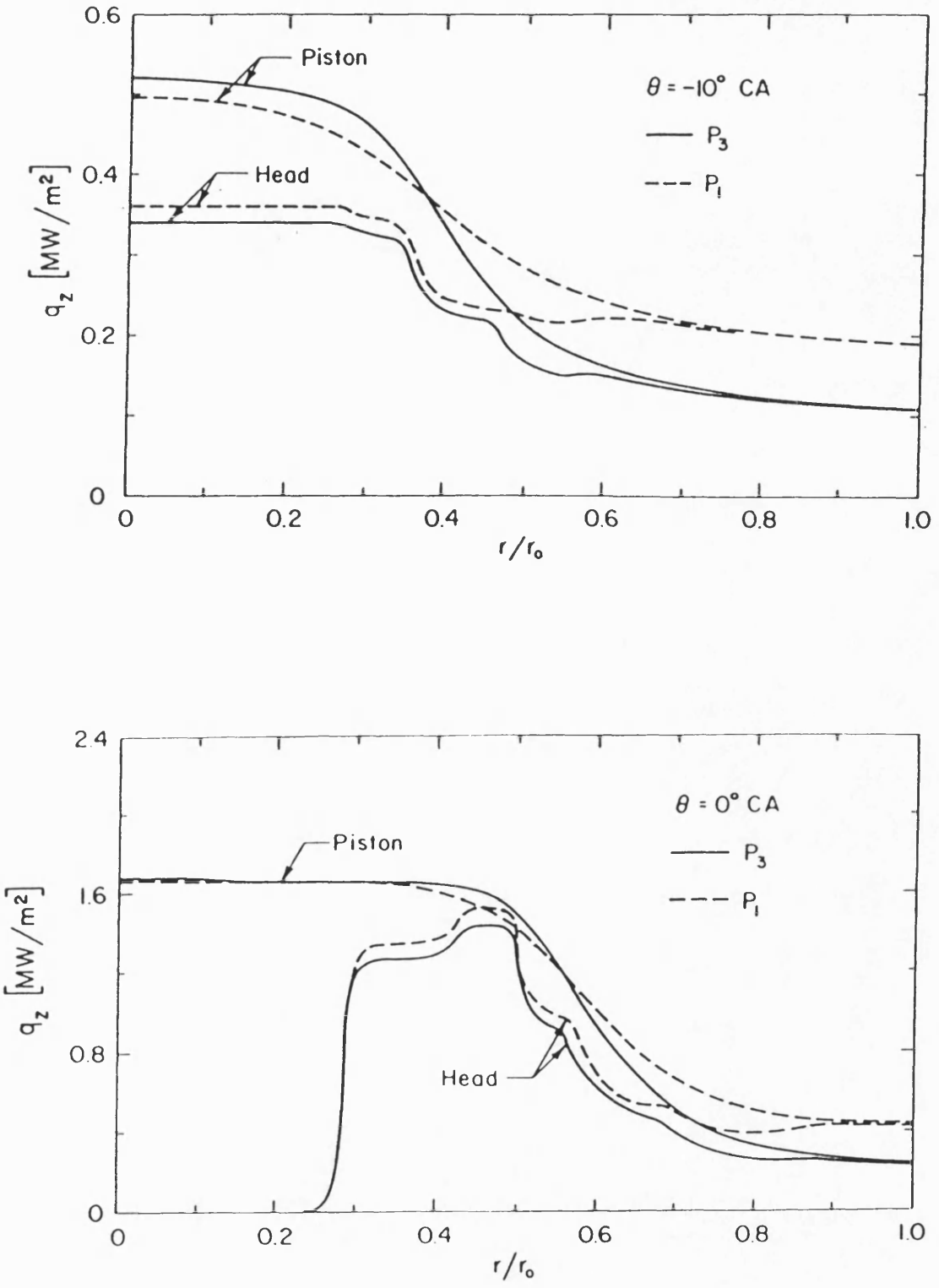

Fig. 2. 13a Radiative heat flux on the cylinder head and piston at -10 and 0 degrees CA [29].

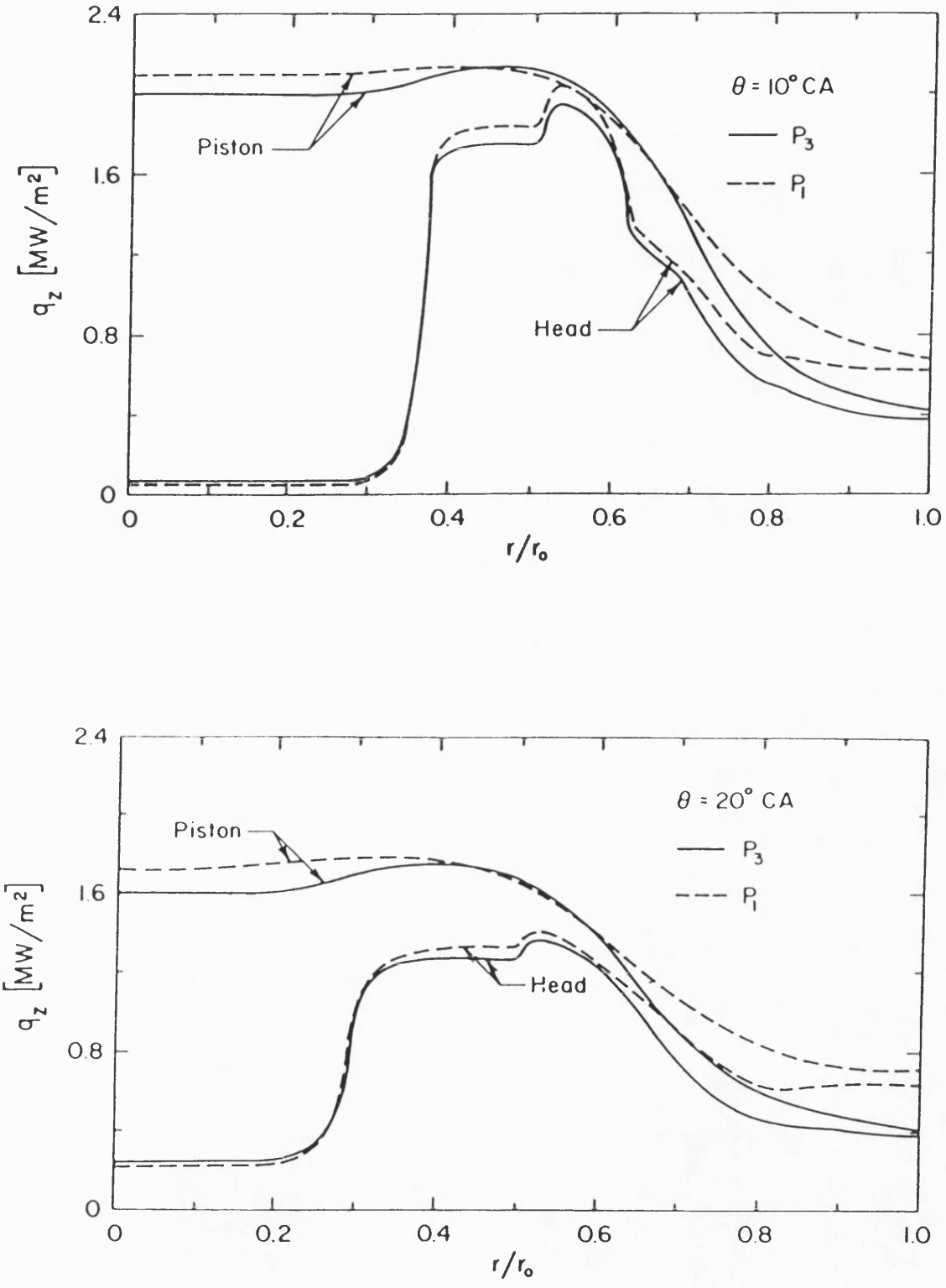

Fig. 2.13b Radiative heat flux on the cylinder head and piston at 10 and 20 degrees CA [29].

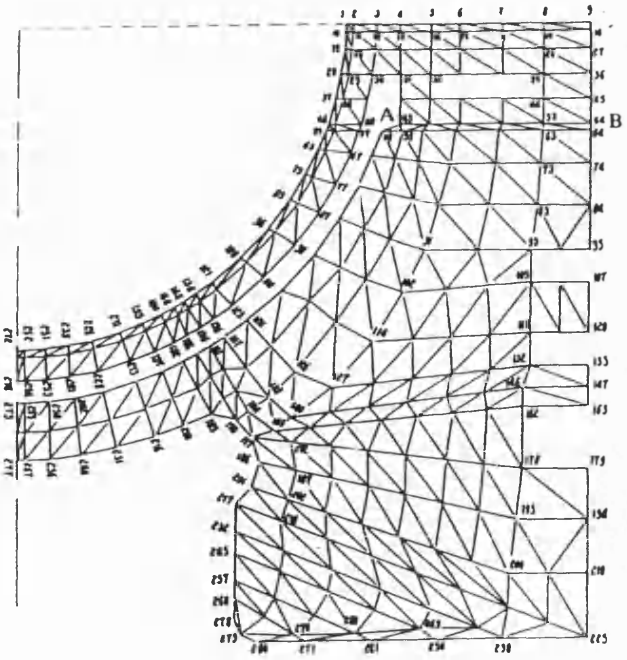

Fig. 2.14 Finite element mesh for an axisymmetric heat barrier piston [6].

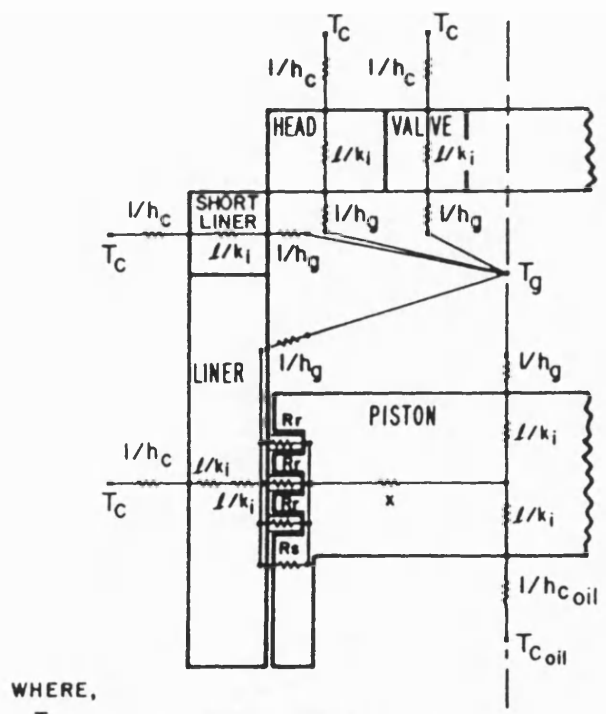

WHERE,

- T_g = AVERAGE GAS TEMPERATURE
- T_c = COOLANT TEMPERATURE (WATER)
- $T_{c\,oil}$ = COOLANT TEMPERATURE (OIL)
- l/k_i = THICKNESS DIVIDED BY THERMAL CONDUCTIVITY FOR COMPONENT,
- h_g = GAS-WALL HEAT TRANSFER COEFFICIENT
- h_c = WALL-COOLANT HEAT TRANSFER COEFFICIENT (WATER)
- $h_{c\,oil}$ = WALL-COOLANT HEAT TRANSFER COEFFICIENT (OIL)
- Rr, Rs = RING AND SKIRT THERMAL RESISTANCE

Fig. 2.15 Typical engine thermal resistance network used in cycle simulation packages [64].

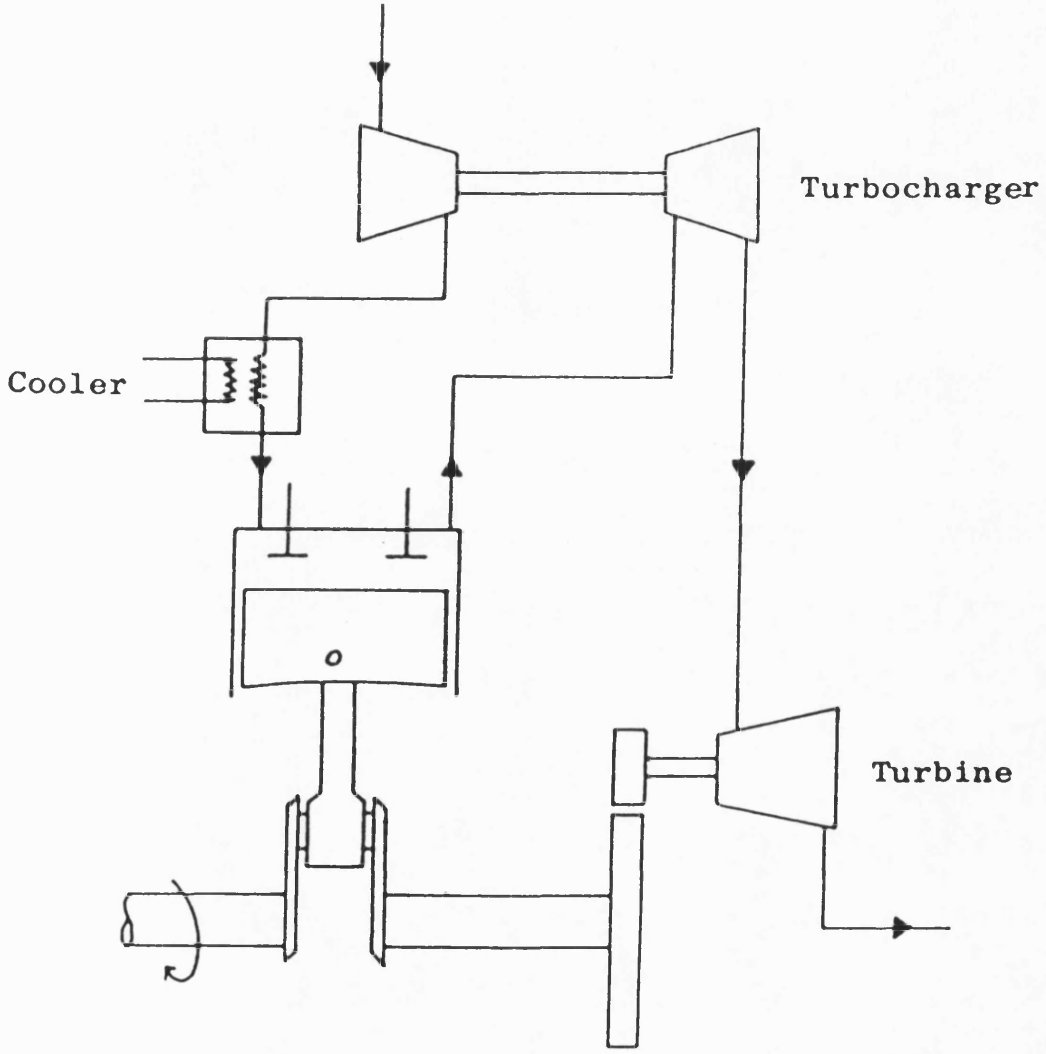

Fig. 2.16 Turbocompound diesel engine [107].

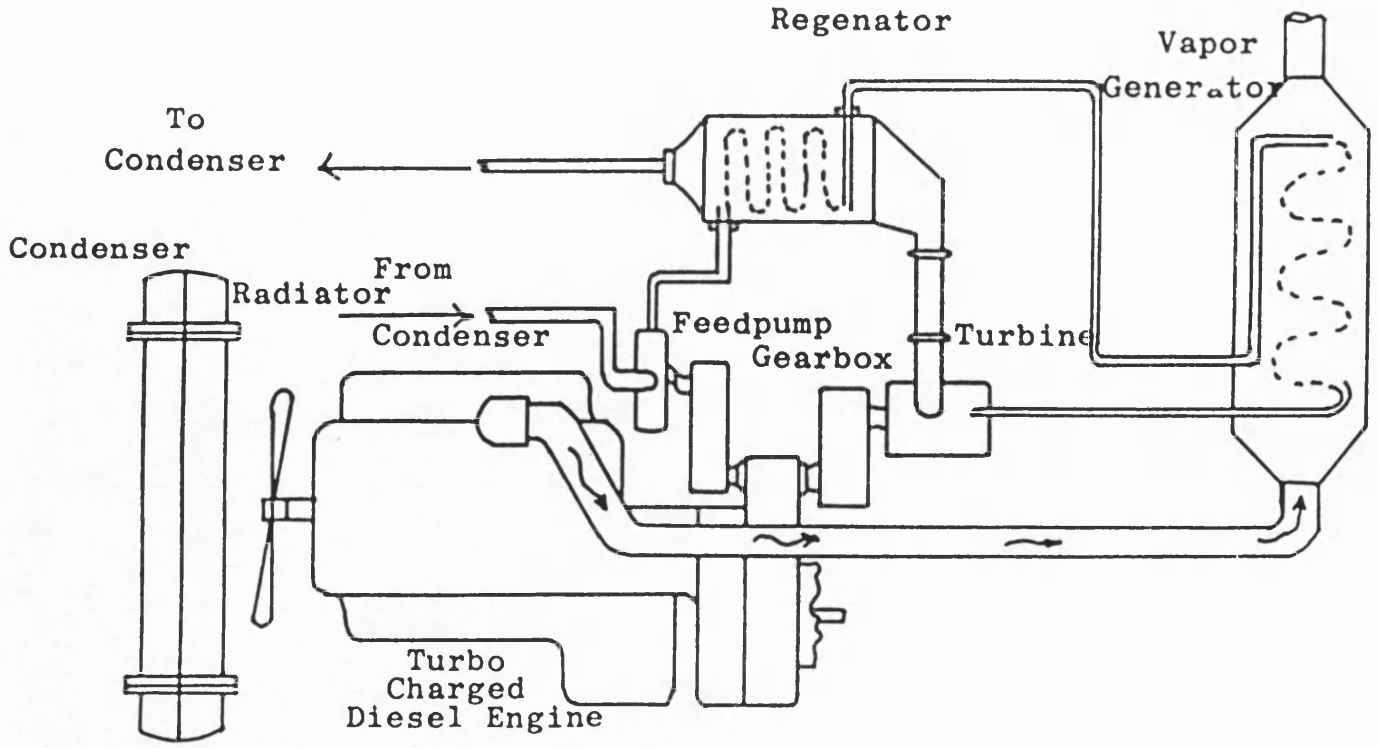

Fig. 2.17 Diesel engine with Rankine bottoming cycle [107].

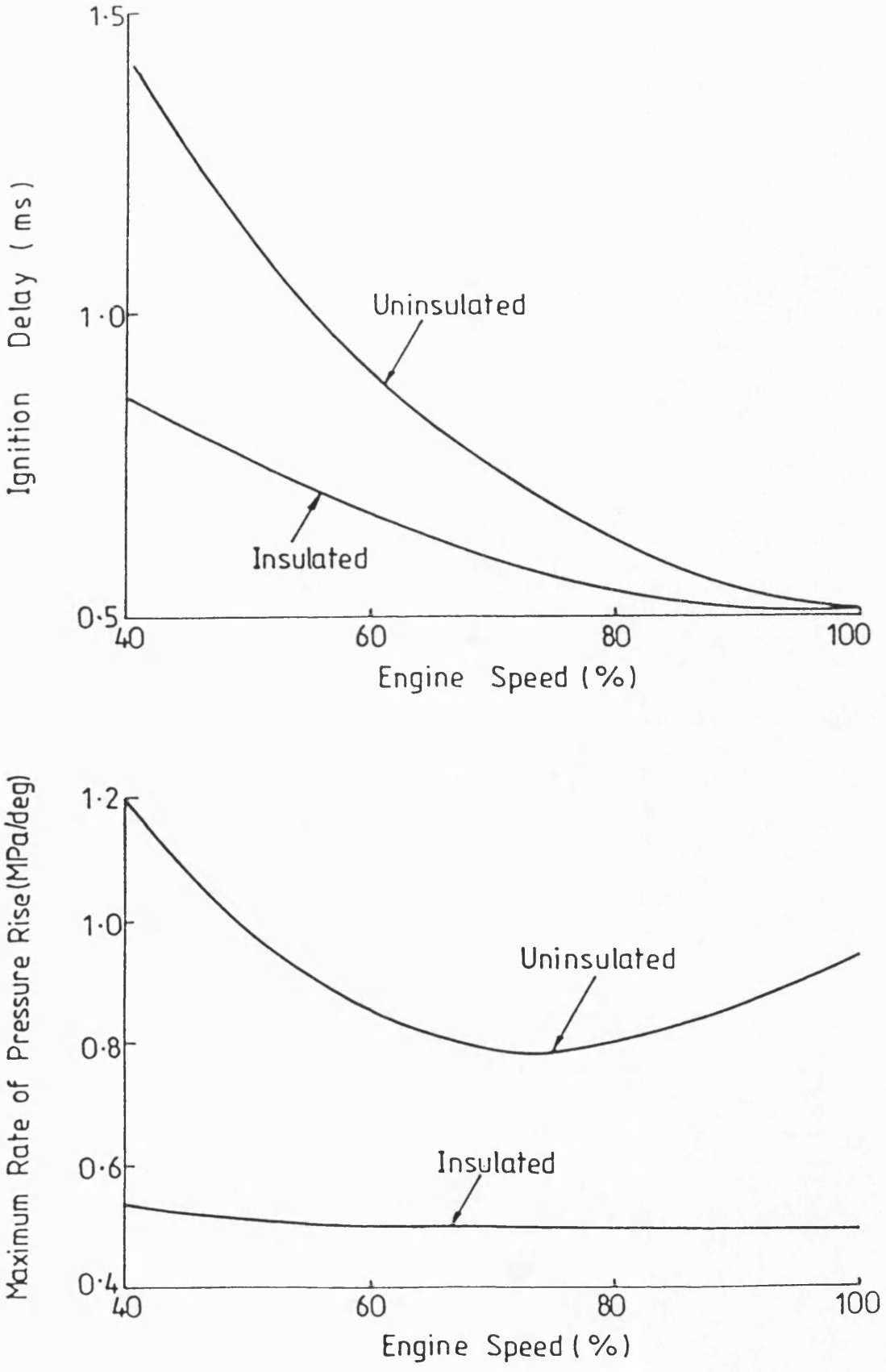

Fig. 2.18 Ignition delay and maximum rate of pressure rise versus engine speed [9].

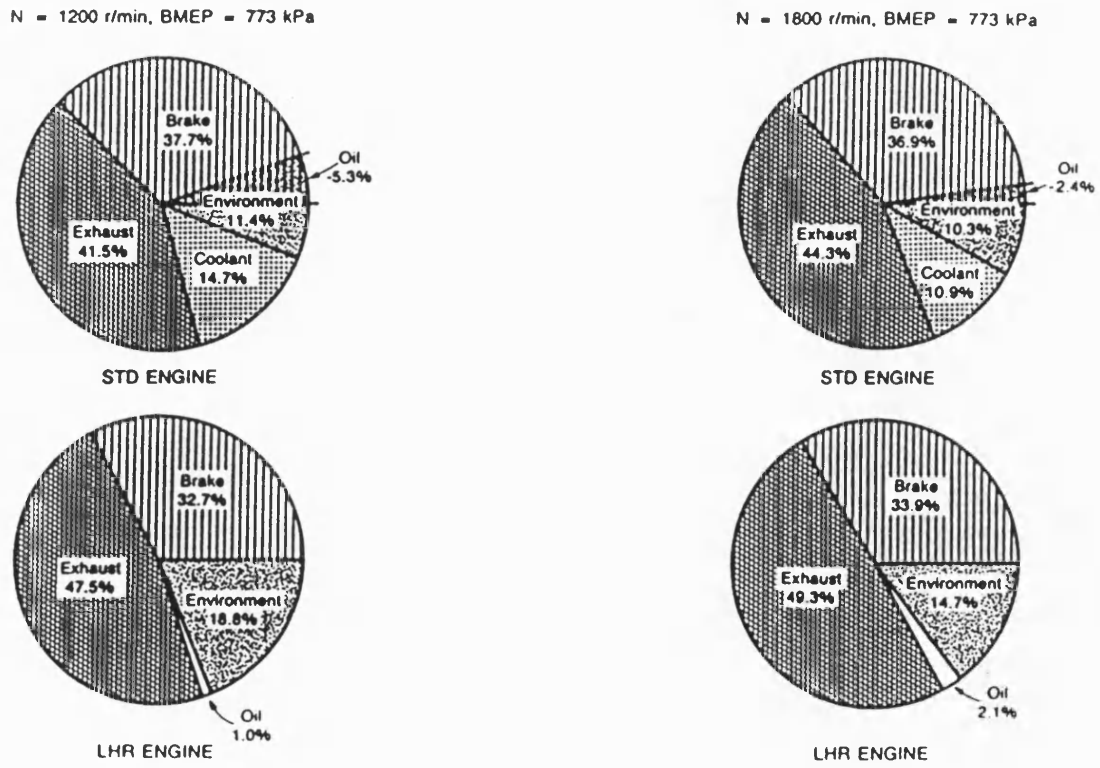

Fig. 2.19 Energy distributions for the standard and low heat rejection engines.

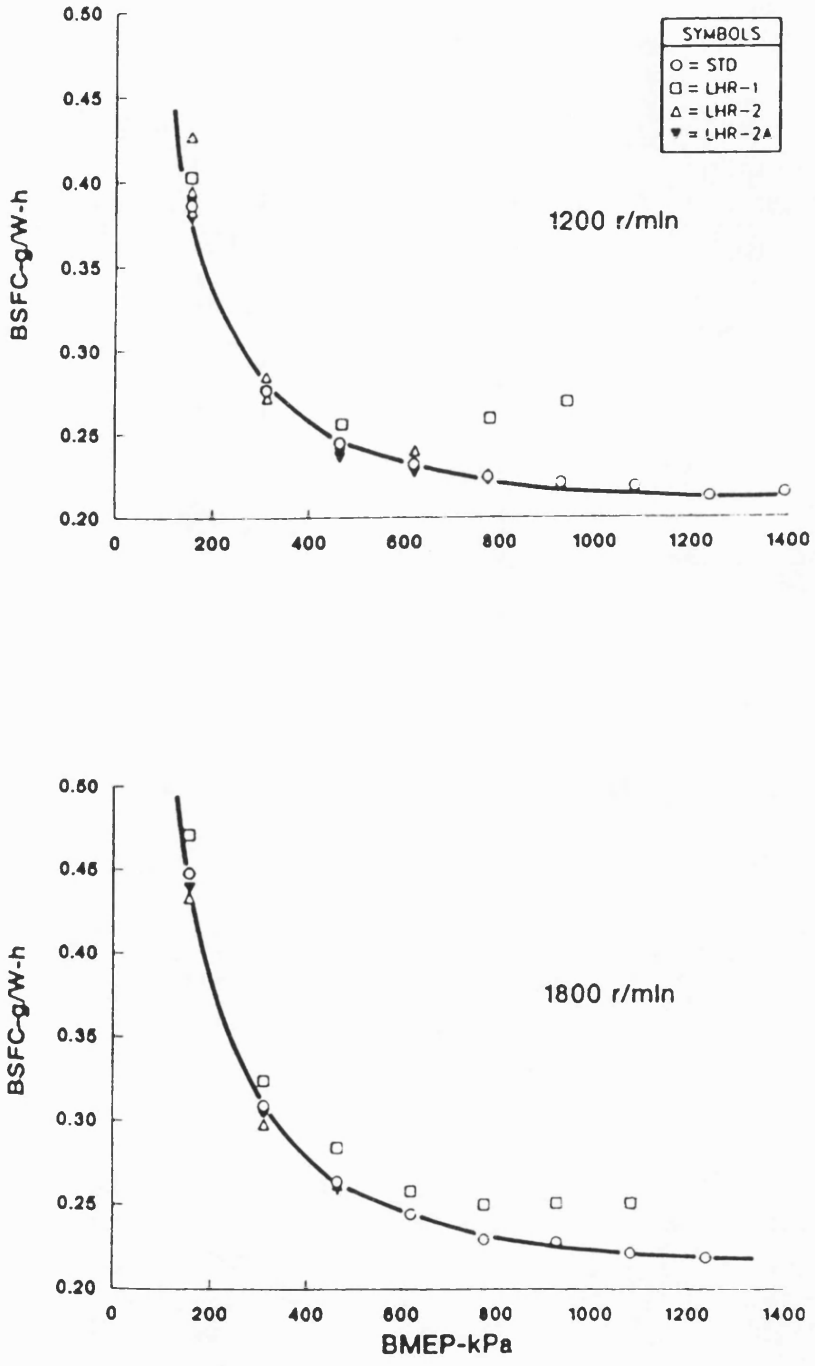

Fig. 2.20 The bsfc versus BMEP of the standard and low heat rejection engines with 8 hole fuel injector [82].

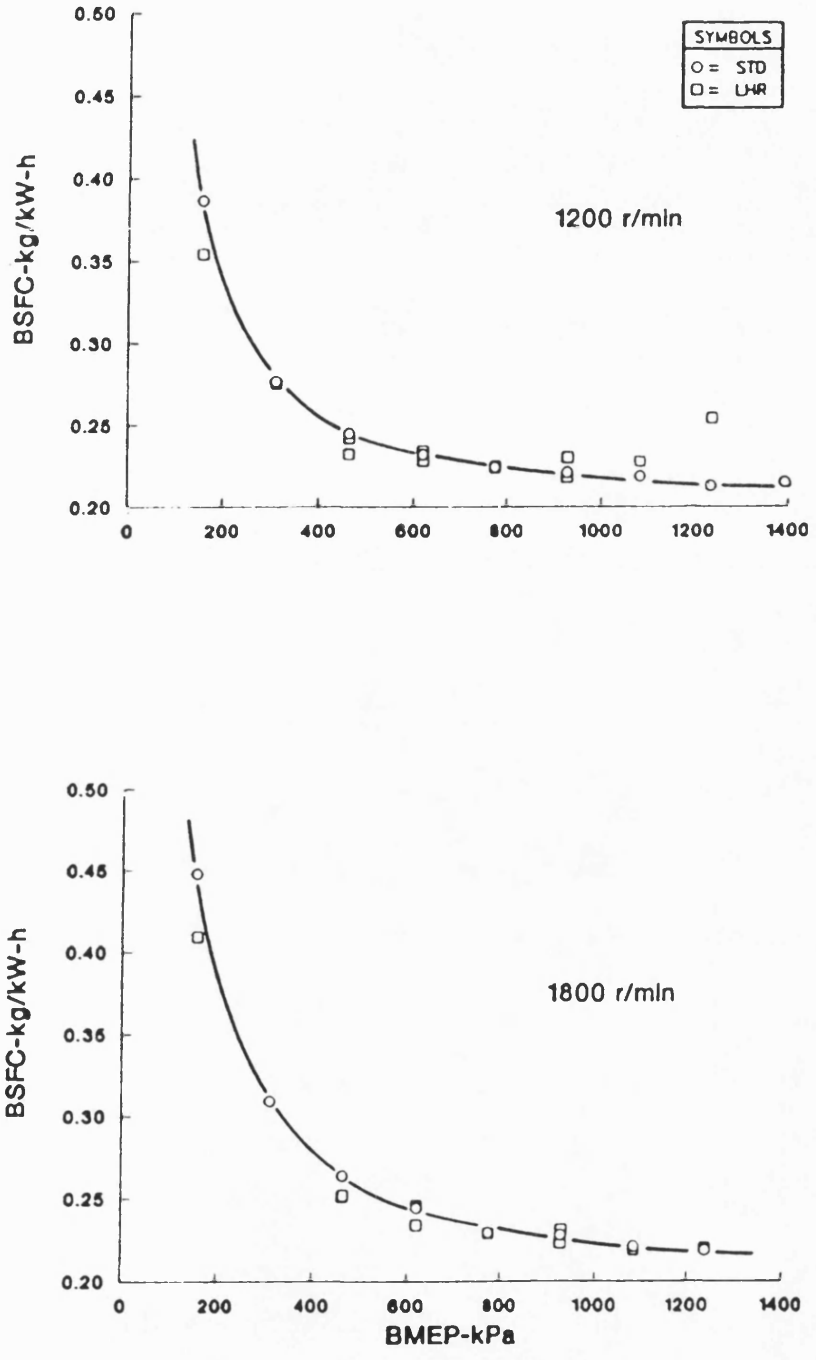

Fig. 2.21 The bsfc versus BMEP of the standard and low heat rejection engines with 9 hole fuel injector.

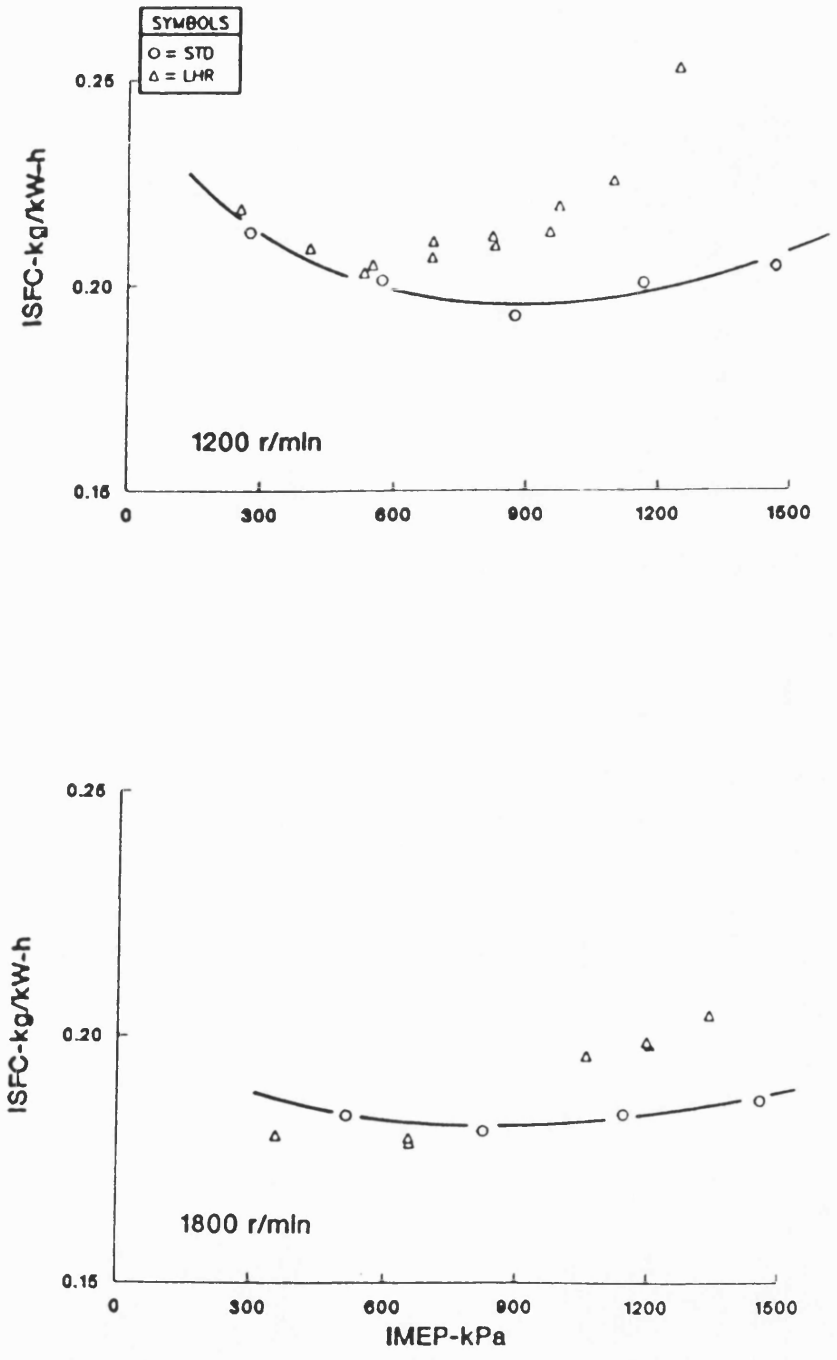

Fig. 2.22 The isfc versus IMEP of the standard and low heat rejection engines with 9 hole fuel injector.

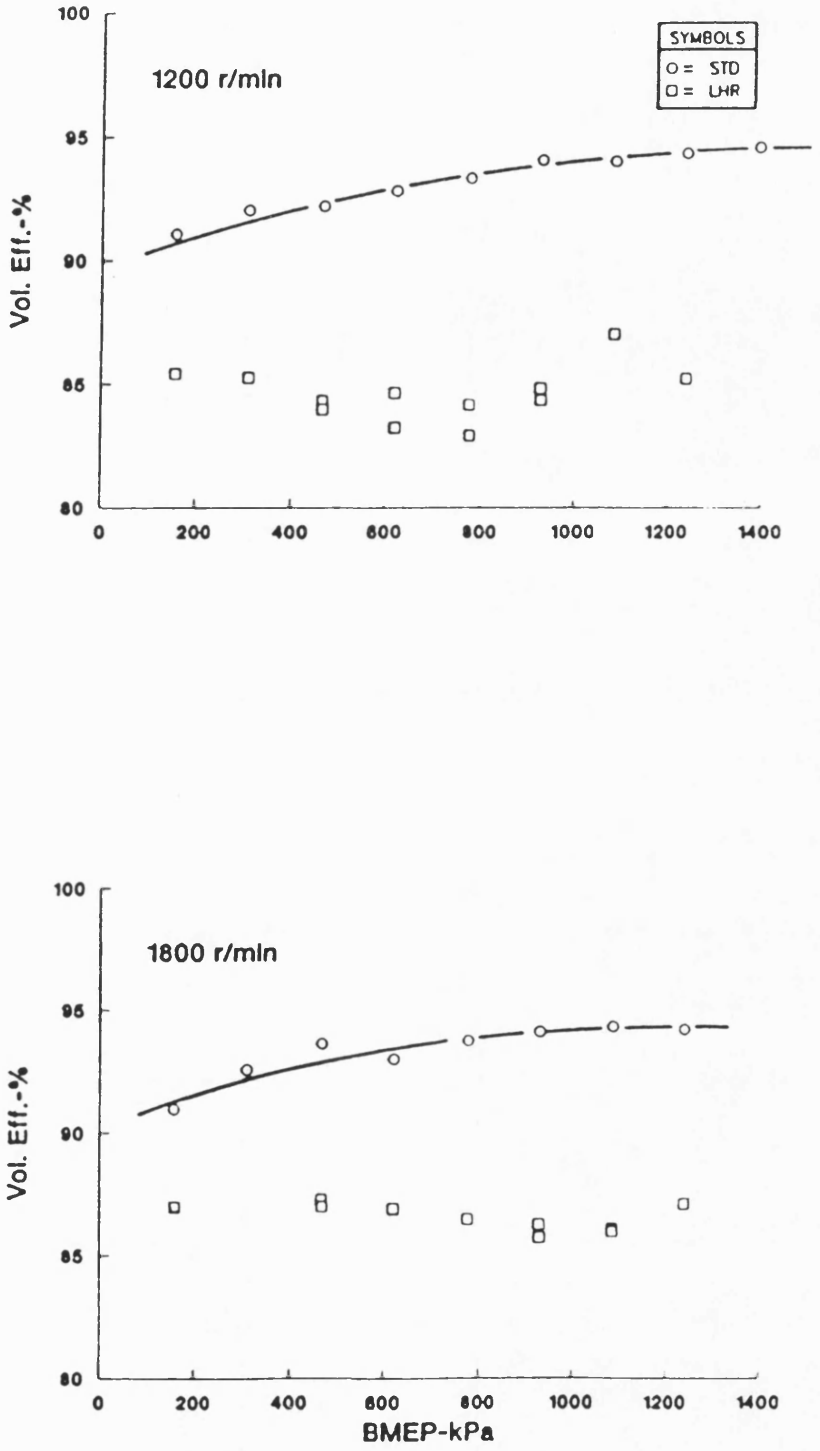

Fig. 2.23 Volumetric efficiency versus BMEP of the standard and low heat rejection engines.

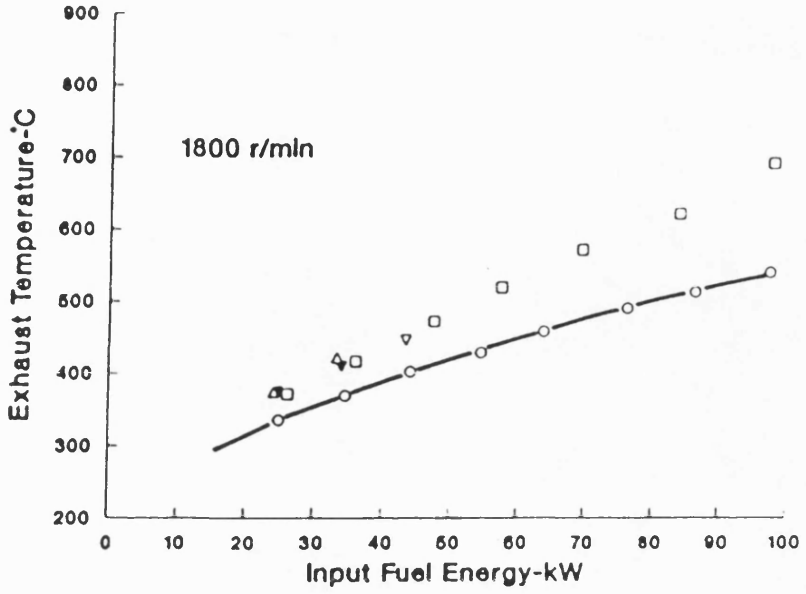

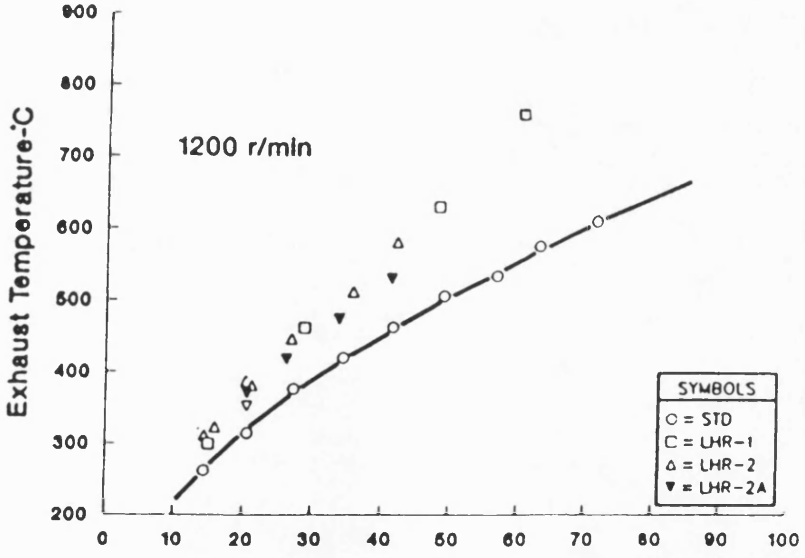

Fig. 2.24 Exhaust temperature versus input fuel energy of the standard and low heat rejection engines.

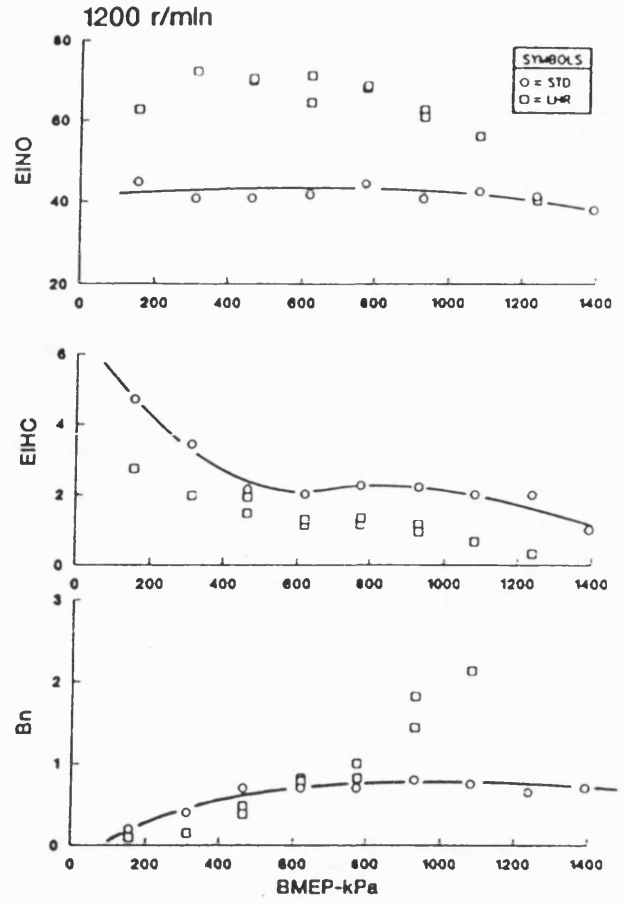

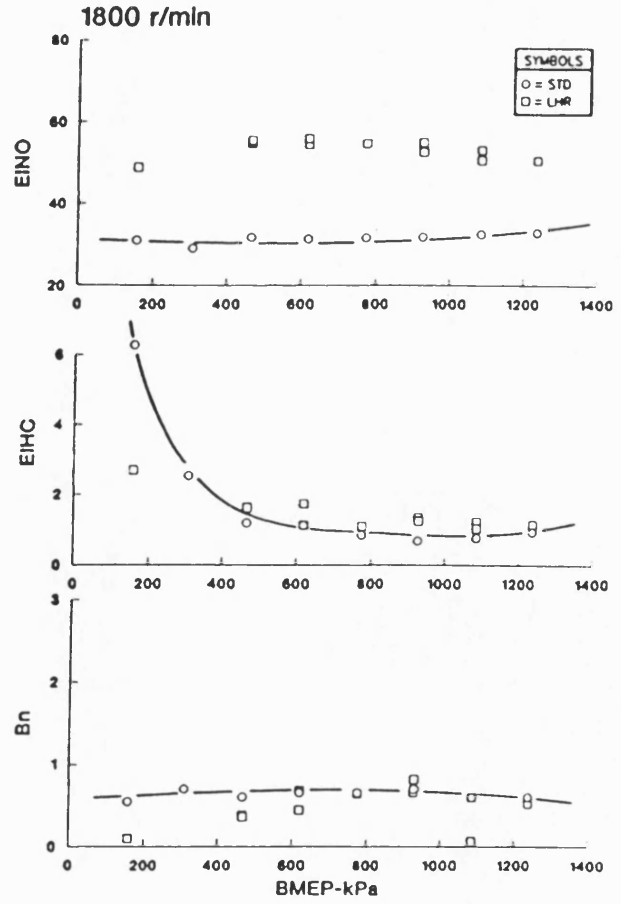

Fig. 2.25 Exhaust emissions of the standard and low heat rejection engines.

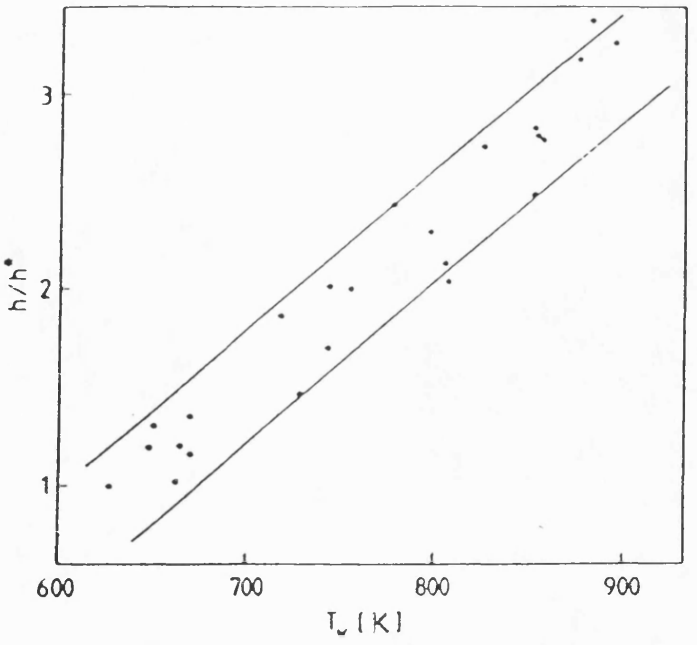

Fig. 2.26 Ratio of 'convection vive' to normal htc's versus wall surface temperature [79].

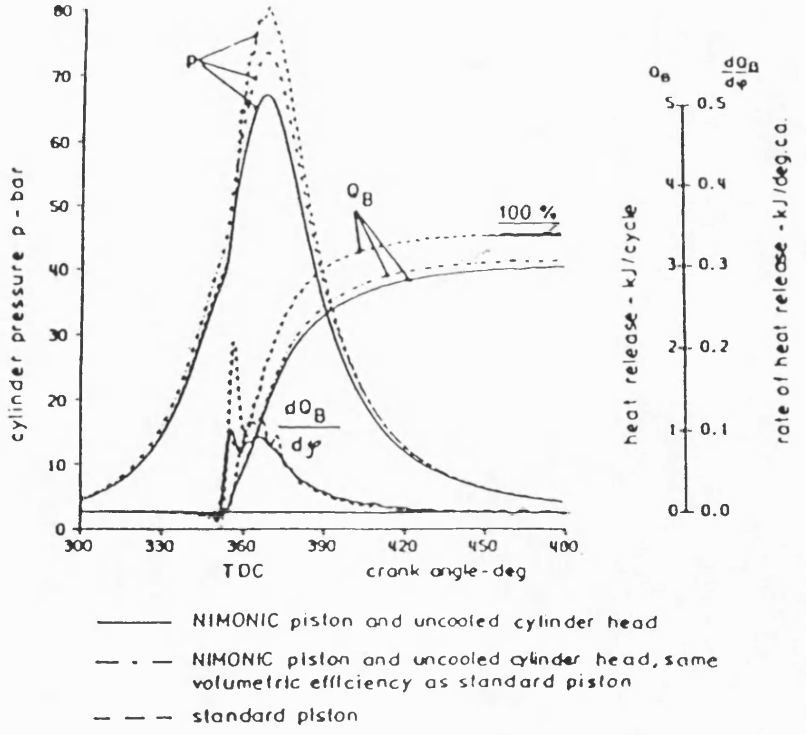

Fig. 2.27 Pressure and heat release curves for standard, insulated and insulated with modified volumetric efficiency engines [69].

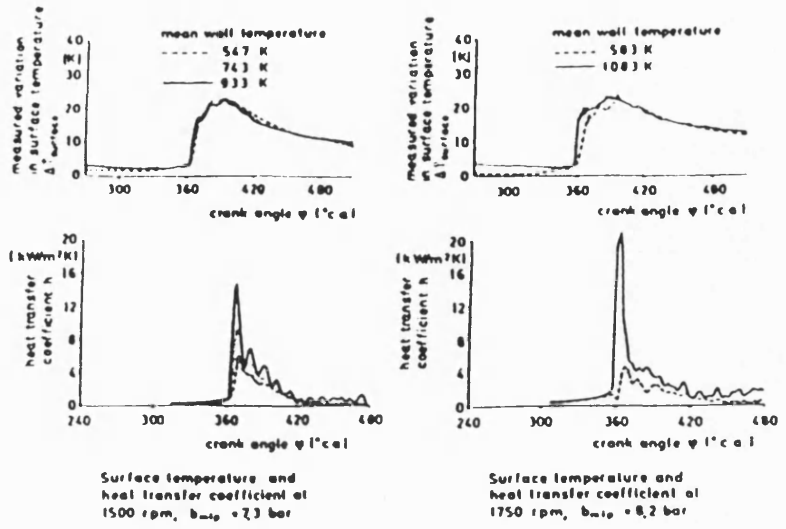

Fig. 2.28 Wall surface temperatures and gas htc's at different mean wall temperatures [67].

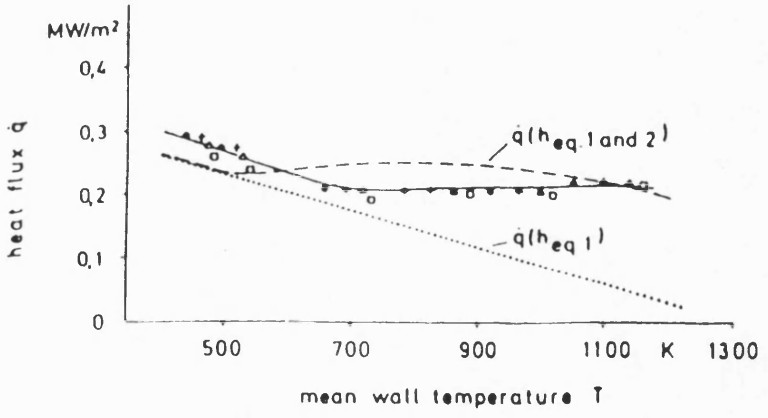

Fig. 2.29 Mean heat flux versus mean wall surface temperatures [67].

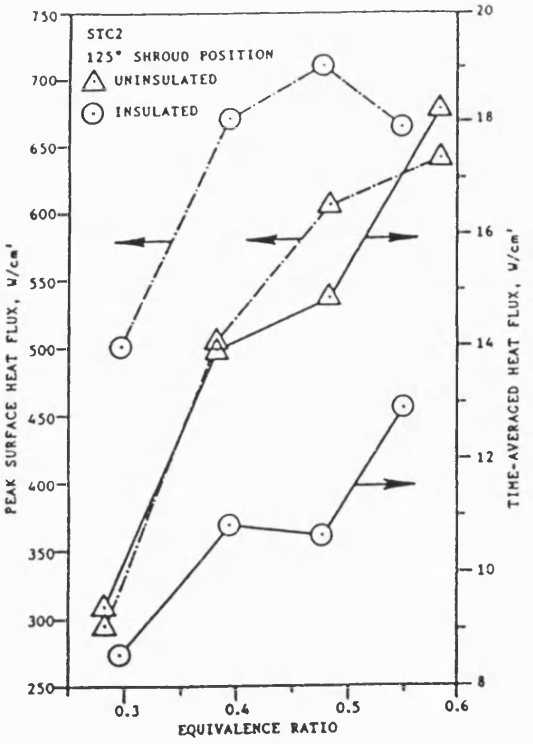

Fig. 2.30 Peak and averaged surface heat fluxes for the uninsulated and insulated metals [77].

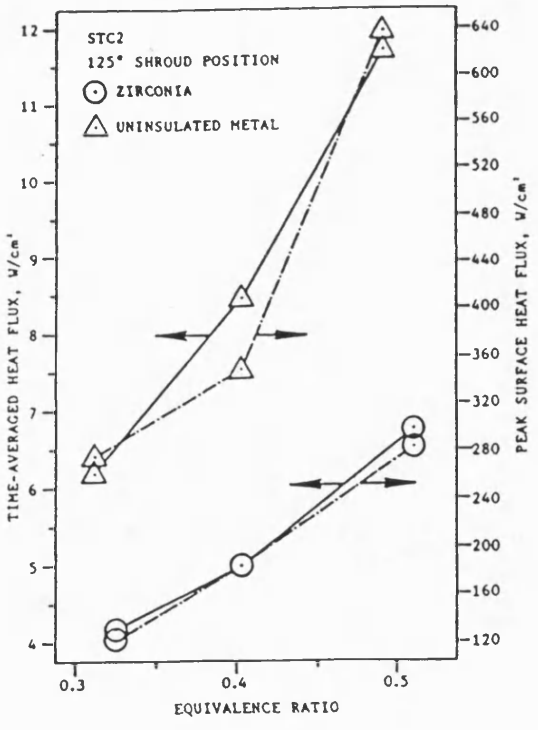

Fig. 2.31 Peak and averaged surface heat fluxes for the uninsulated metal and zirconia [77].

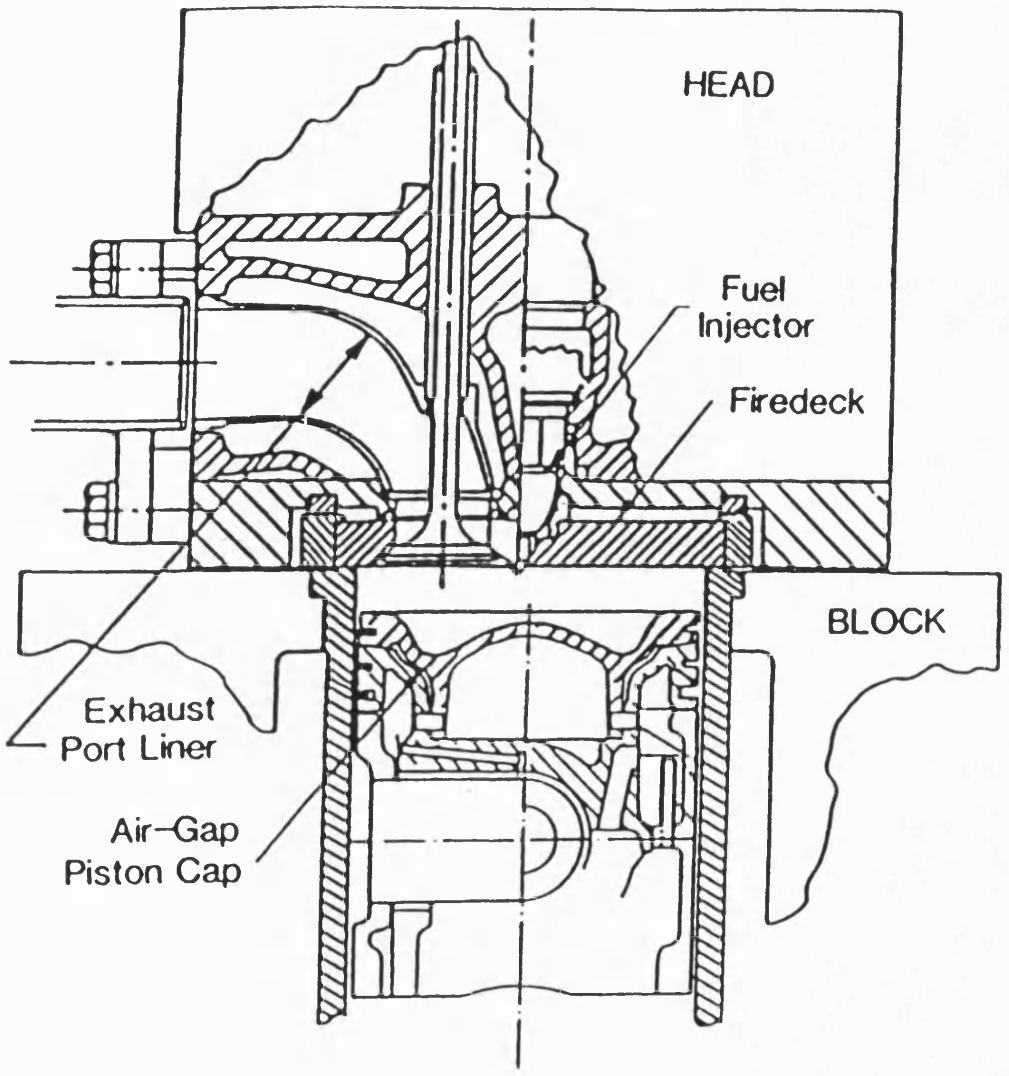

Fig. 2.32 Air-gap insulated engine [82].

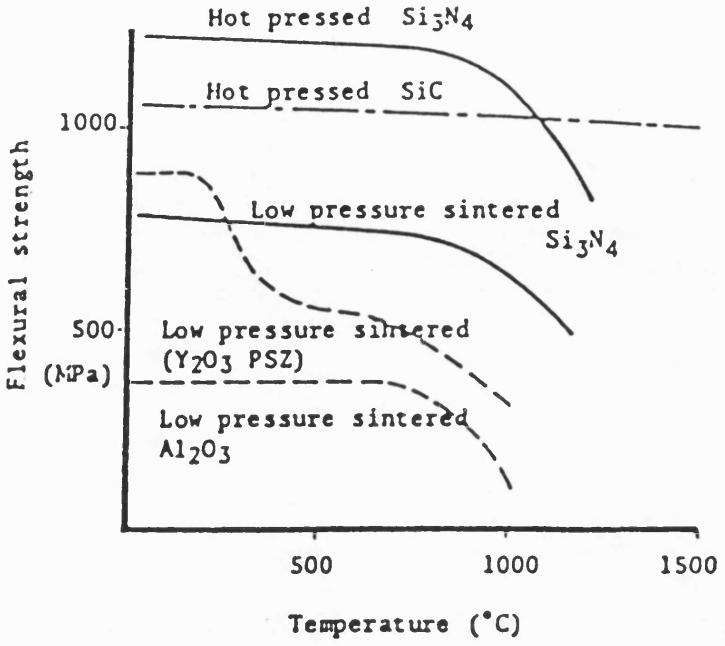

Fig. 2.33 Flexural strength versus temperature of various ceramics.

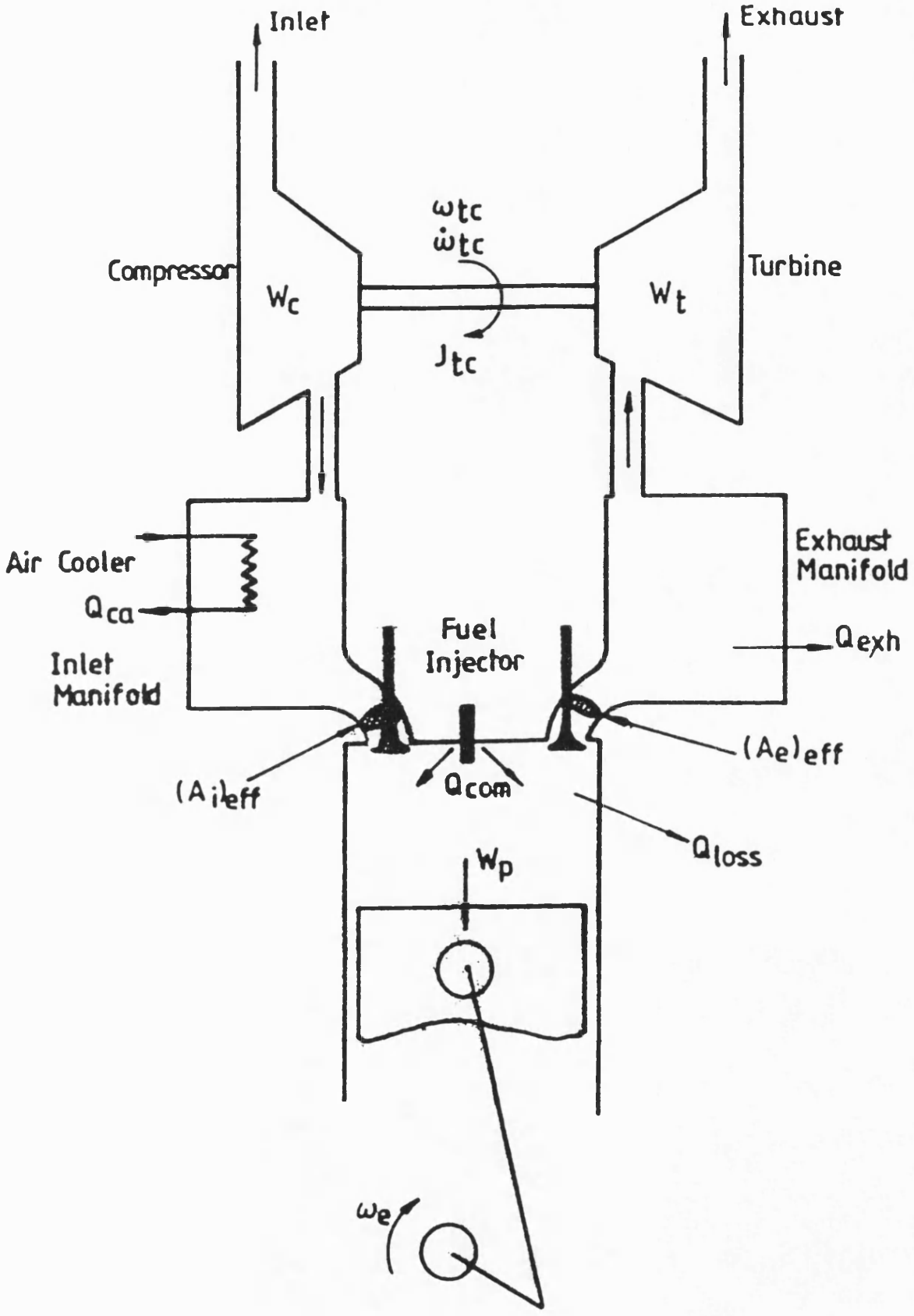

Fig. 3.1 Representation of a turbocharged diesel engine with control volumes.

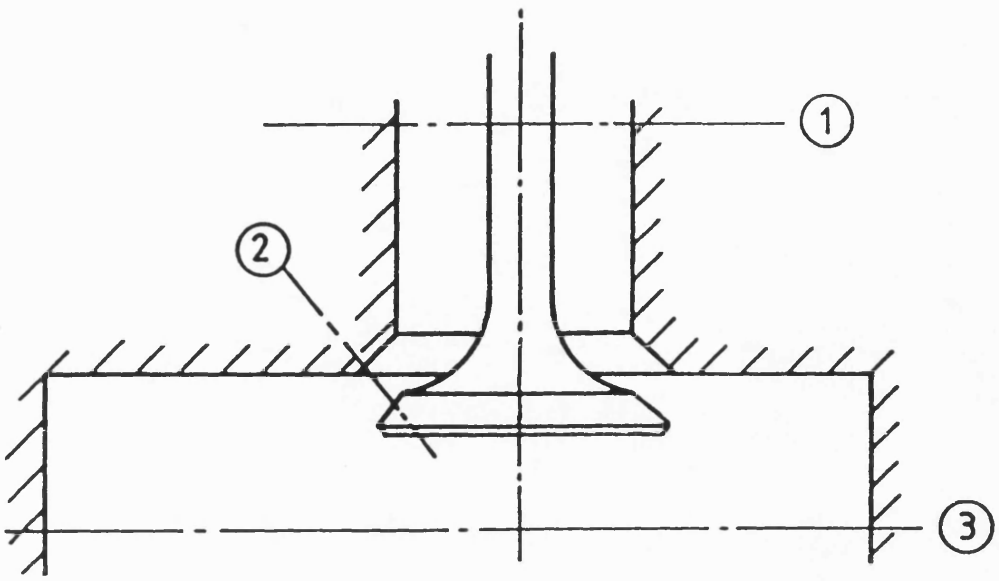

Fig. (a)

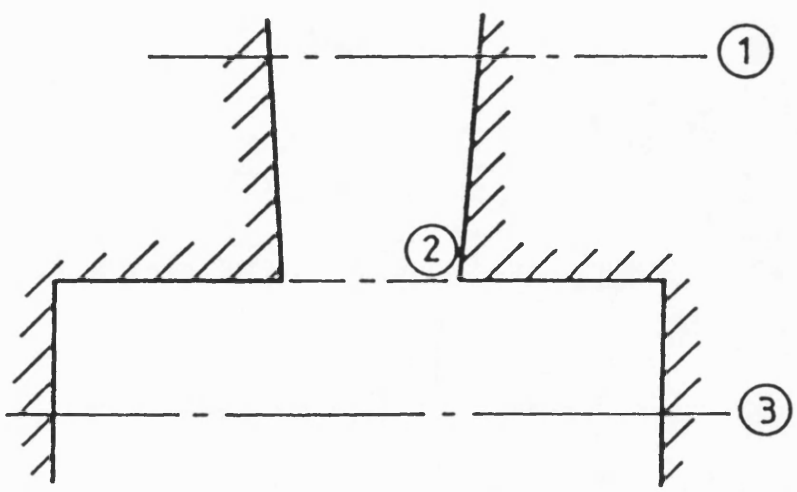

Fig. (b)

The actual annular area (2) in Fig. (a) is represented as a circular throat area (2) in Fig. (b)

Fig. 3.2 Flow modelling through the engine.

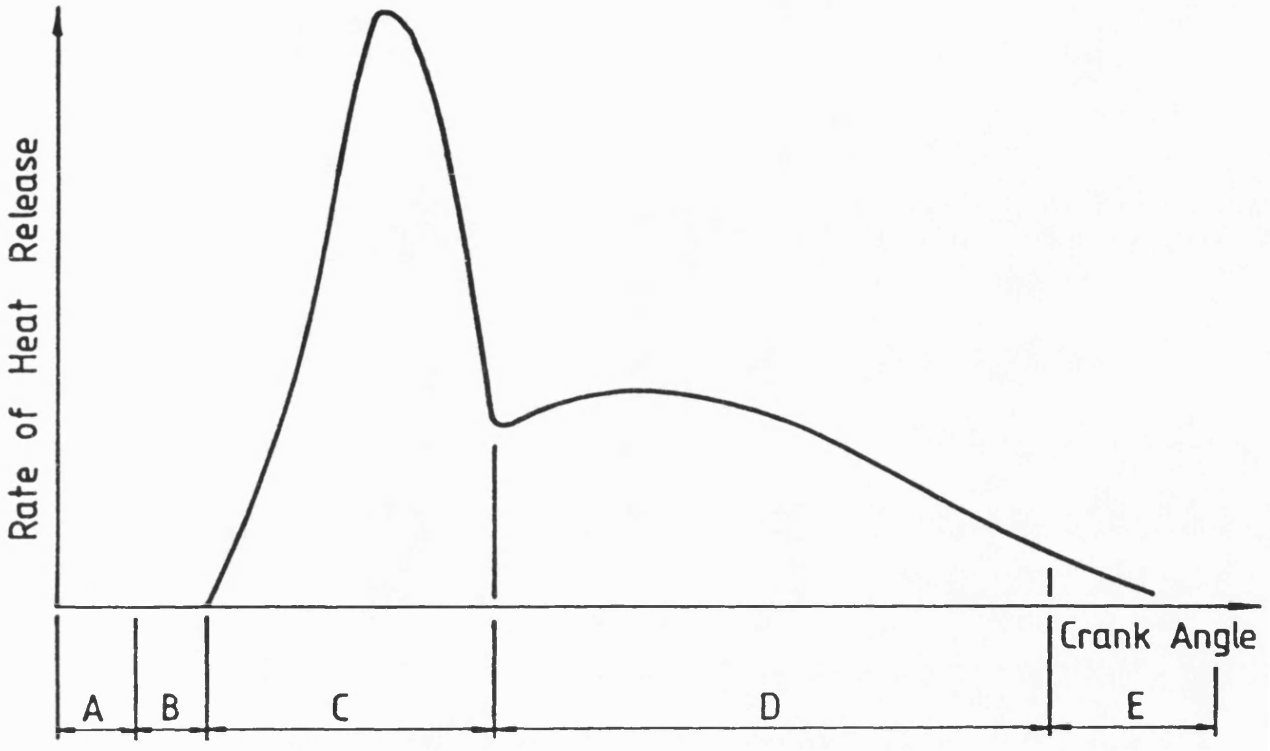

A = Injection Delay

B = Ignition Delay

C = Premix Burning

D = Diffusion Burning

E = Combustion 'Tail'

Fig. 3.3 Heat release rate in a diesel engine.

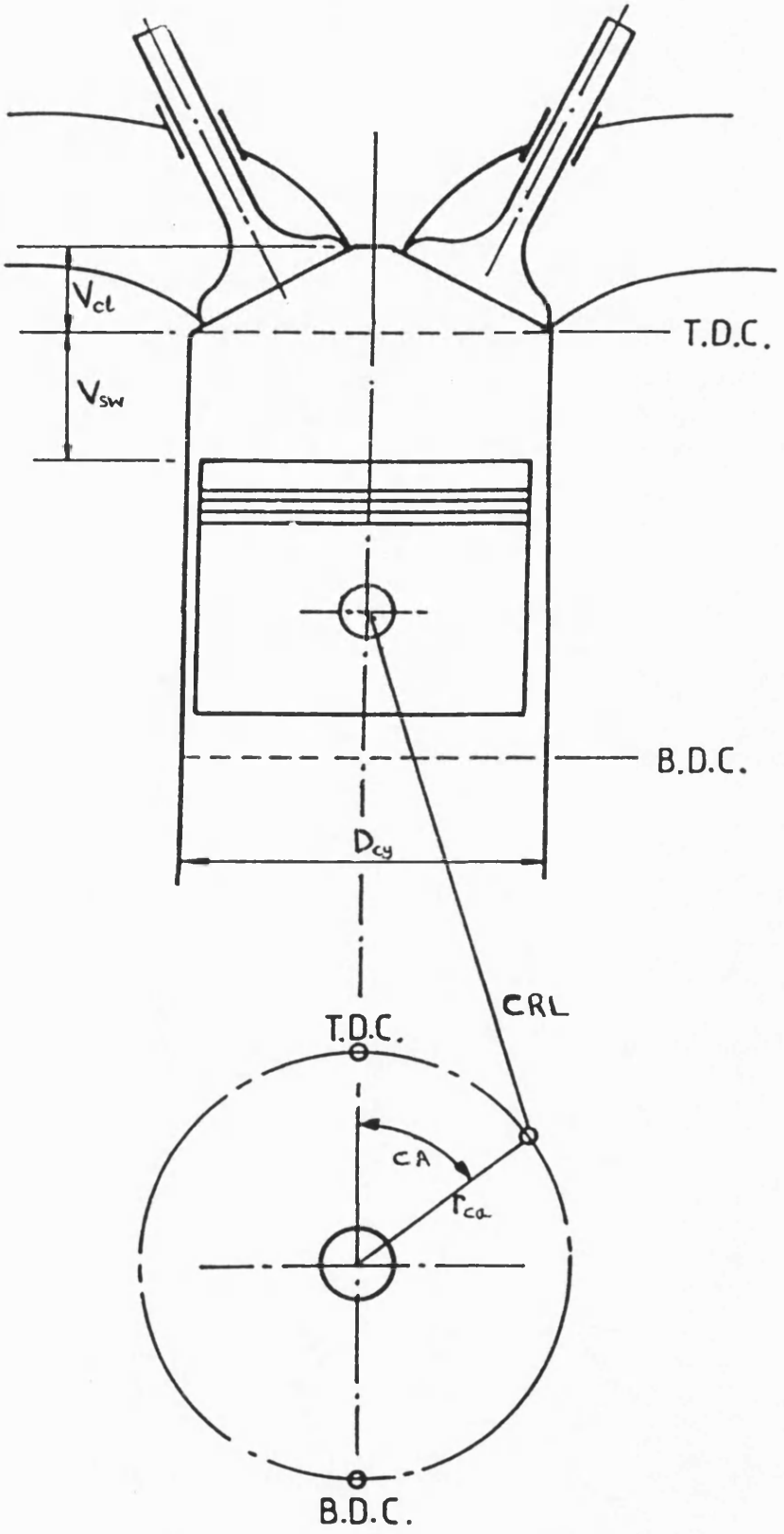

Fig. 3.4 Piston-crank mechanism.

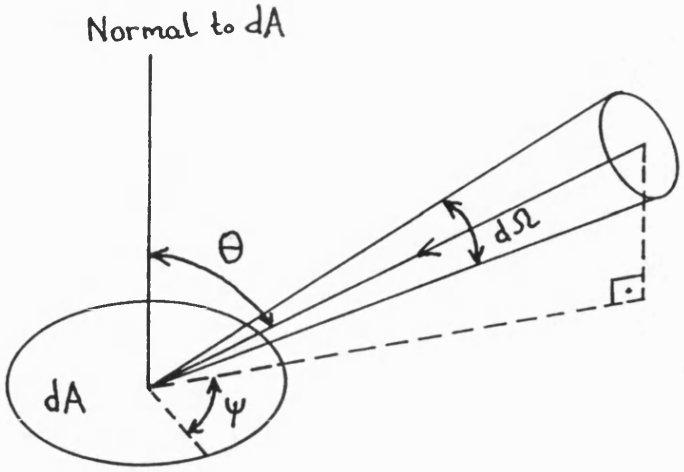

Fig. 4.1 Radiation intensity at surface dA.

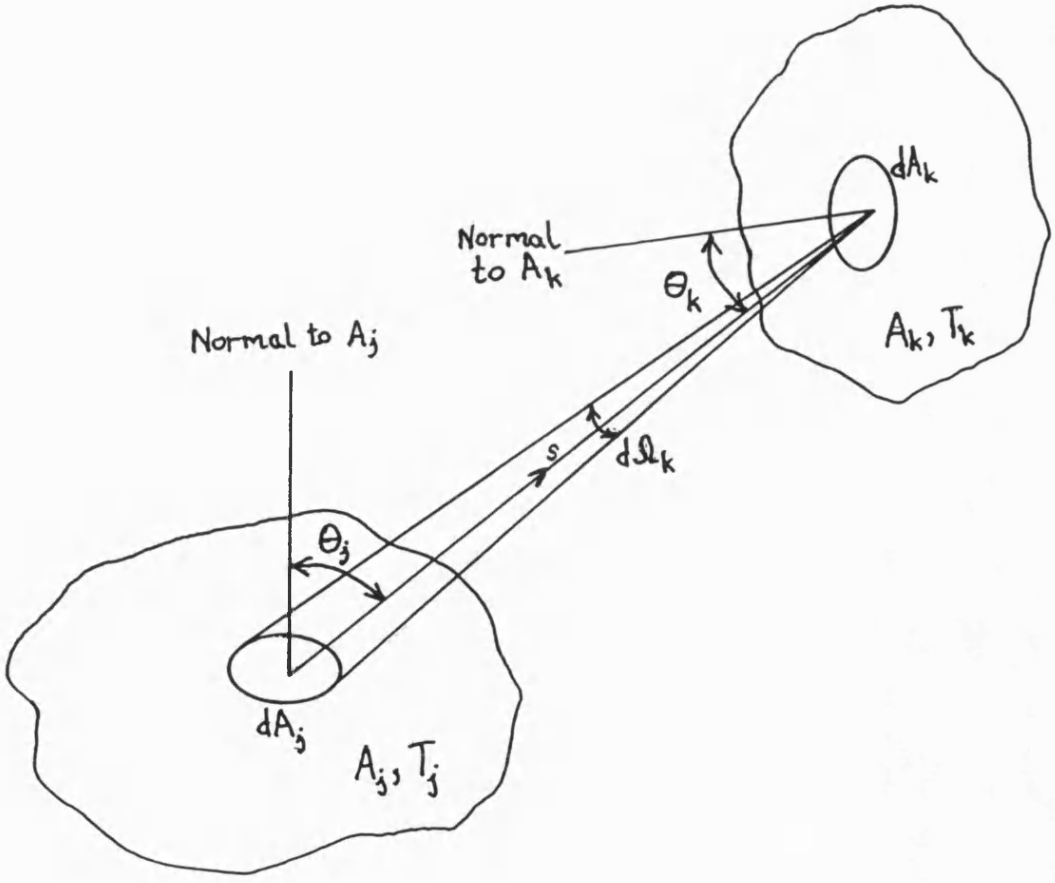

Fig. 4.2 Radiative interchange between two differential area elements dA_j and dA_k.

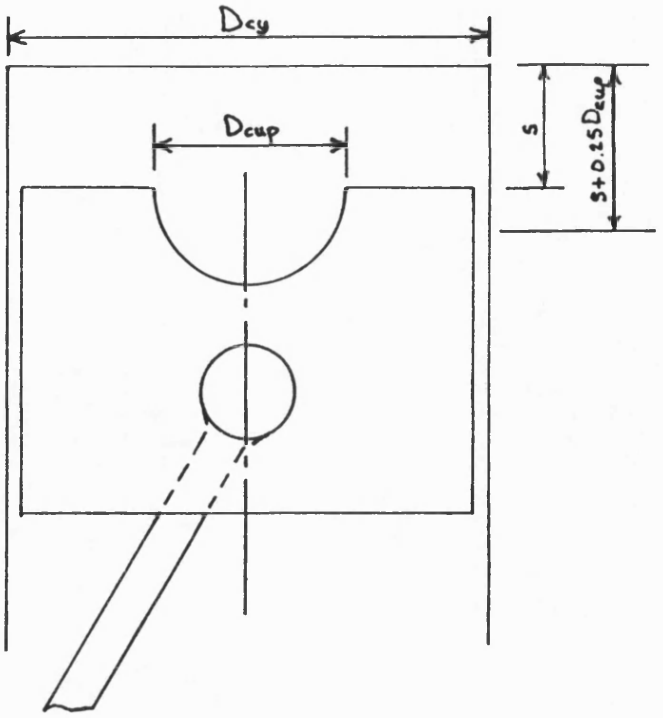

Fig. 4.3 Diesel engine combustion chamber.

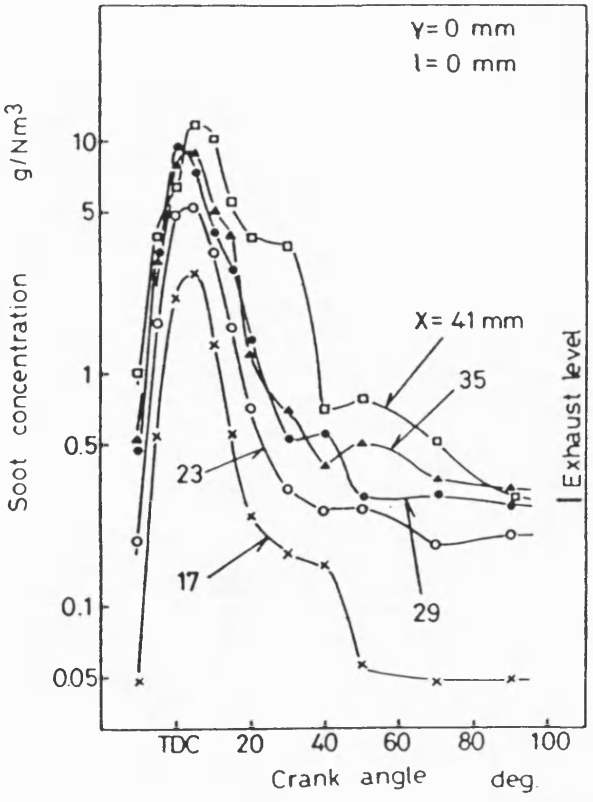

Fig. 4.4 Experimental soot concentration levels in an operating diesel engine [37].

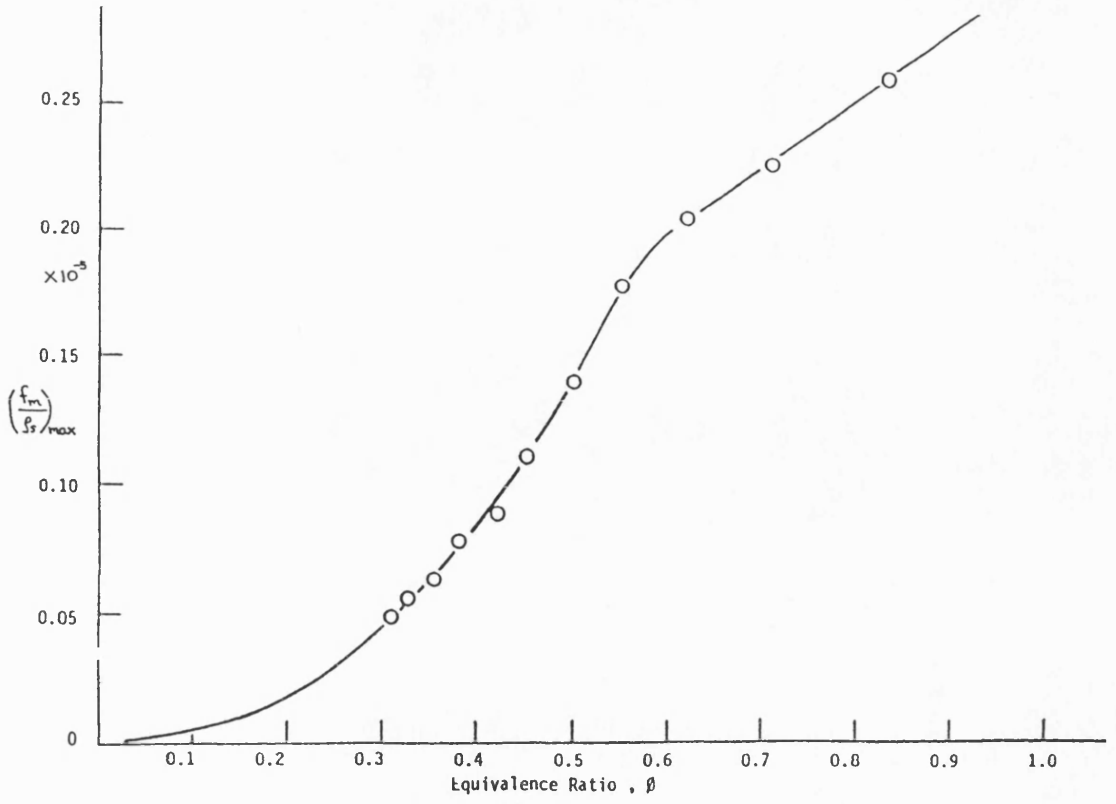

Fig. 4.5 Maximum soot concentration parameter versus equivalence ratio.

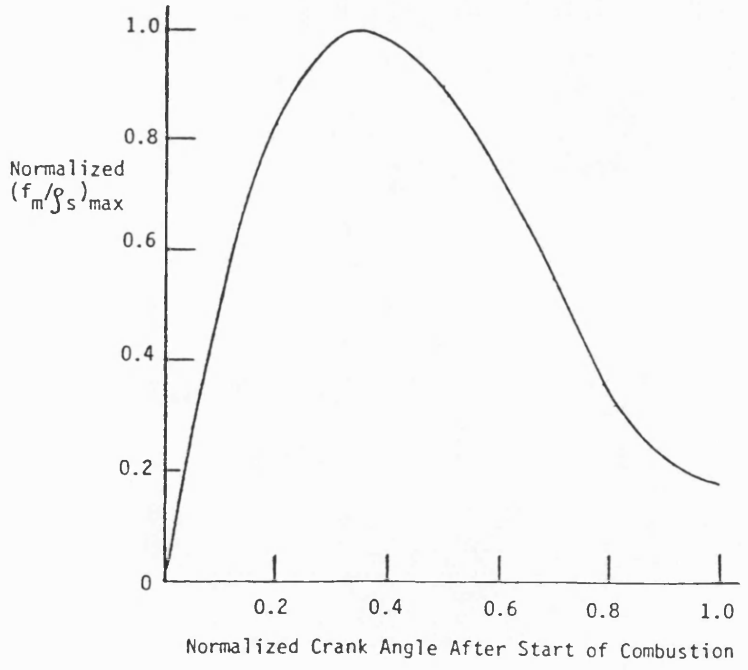

Fig. 4.6 Normalised soot concentration with its maximum value versus combustion duration.

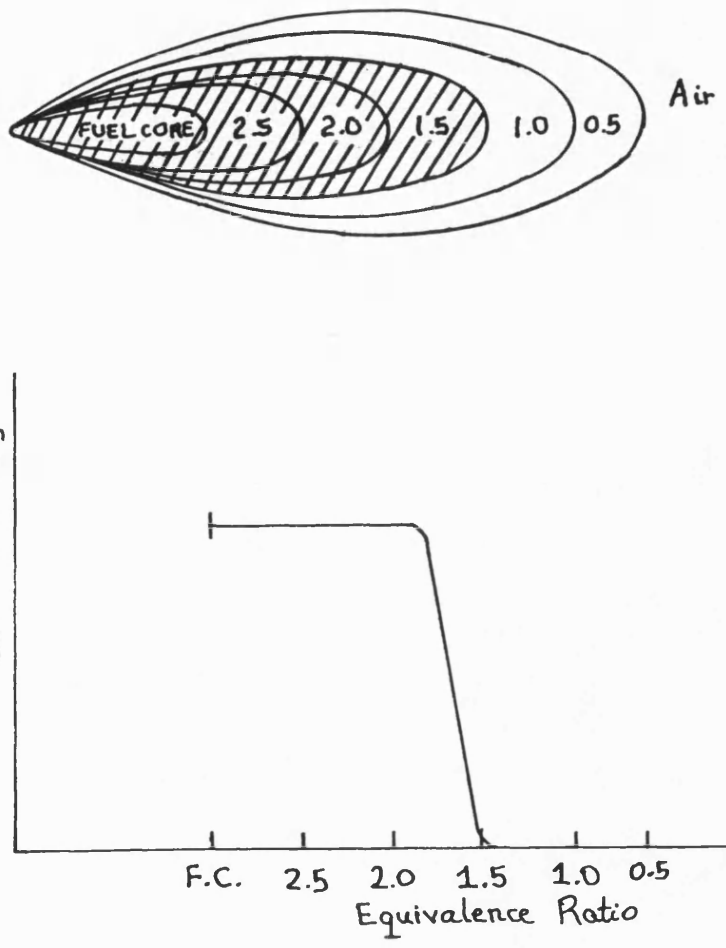

Fig. 4.7 Fuel jet model indicating assumed threshold sooting equivalence ratio.

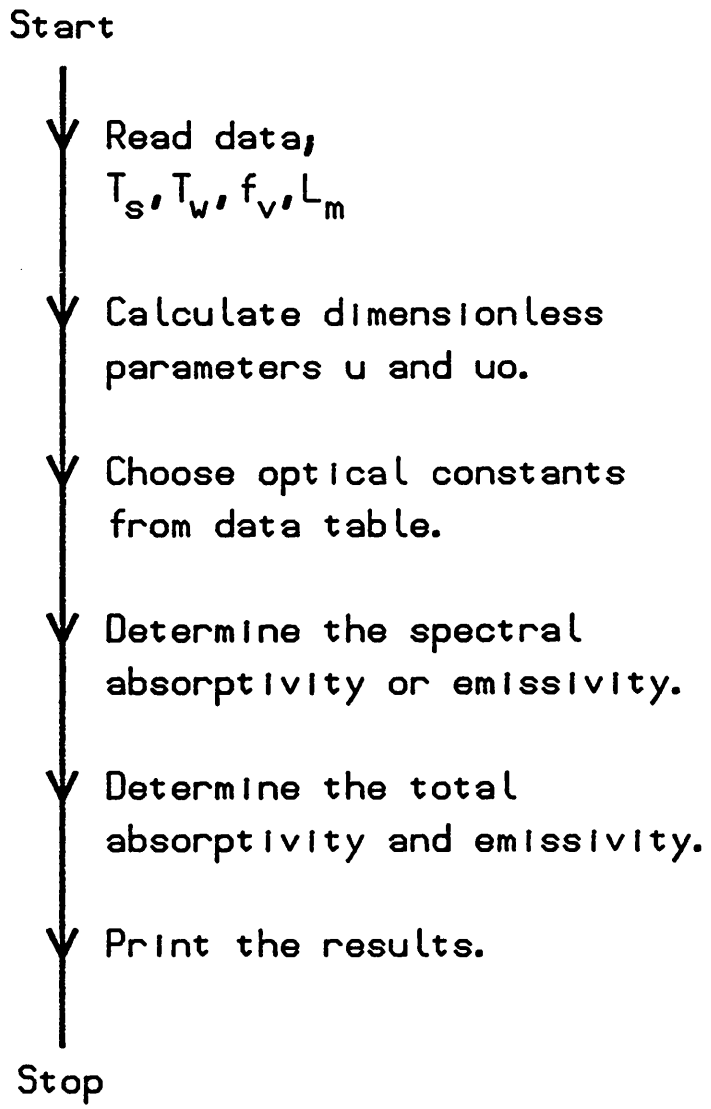

Fig. 4.8 The flowchart for Soot.For.

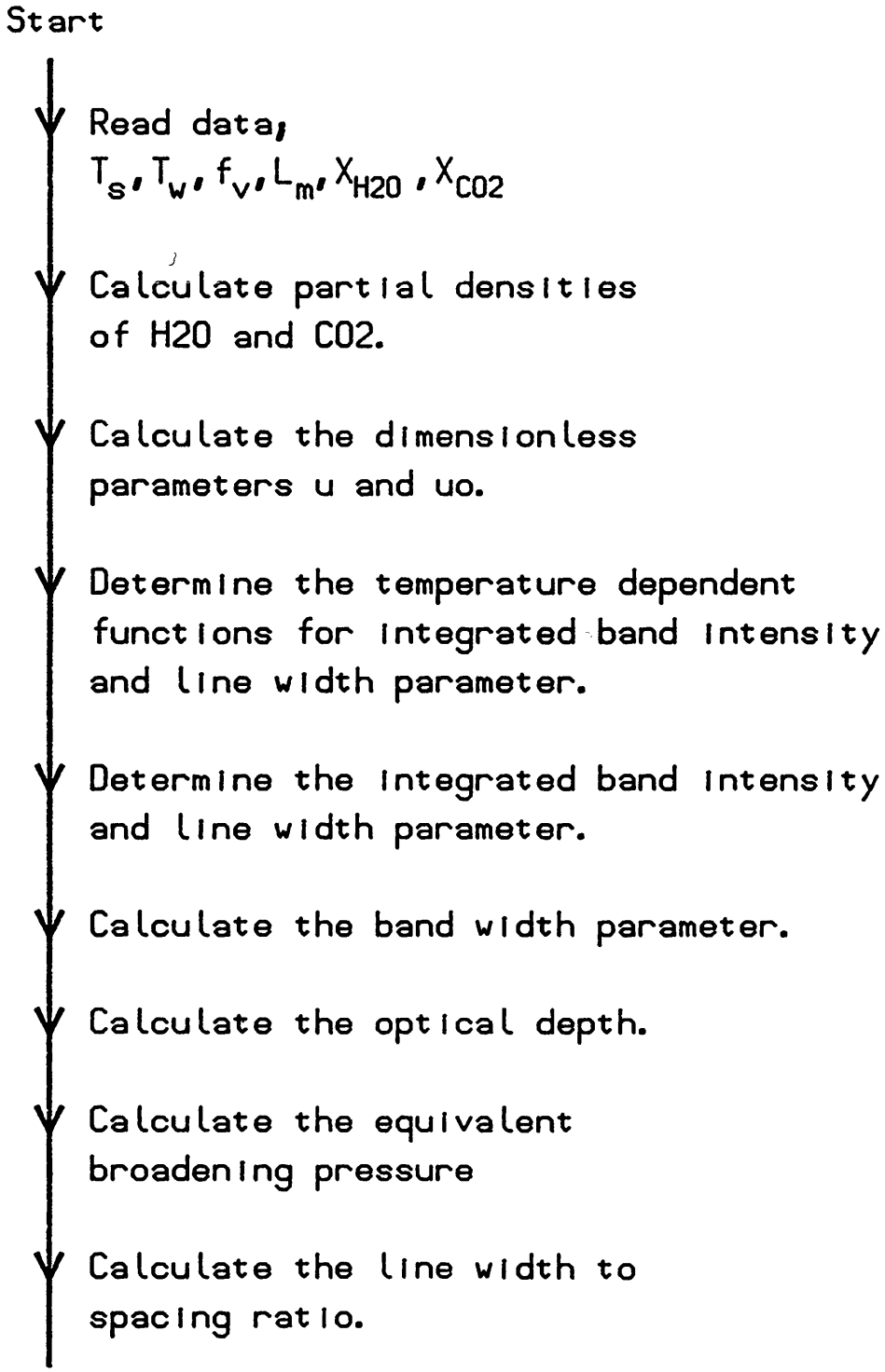

Fig. 4.9 The flowchart for Gas.For.

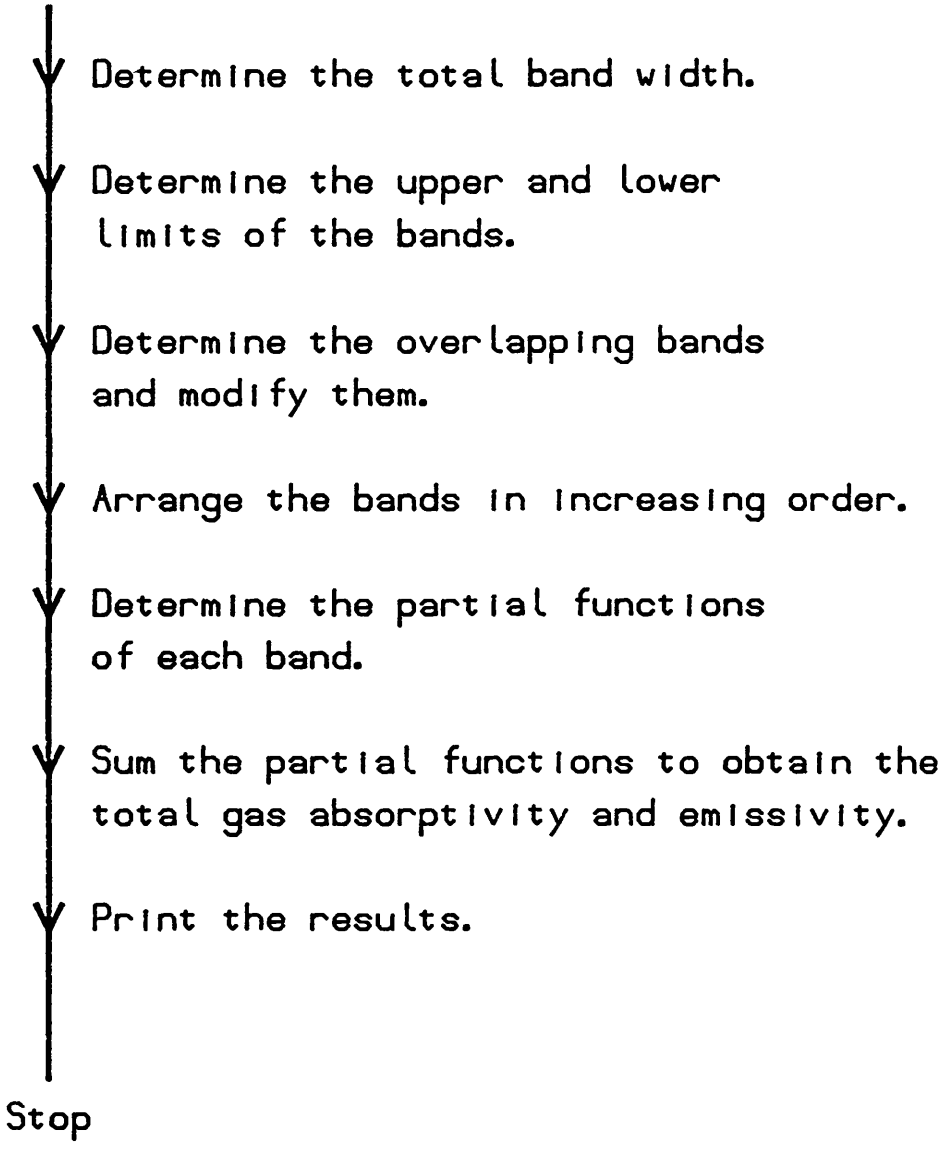

Fig. 4.9 Continued.

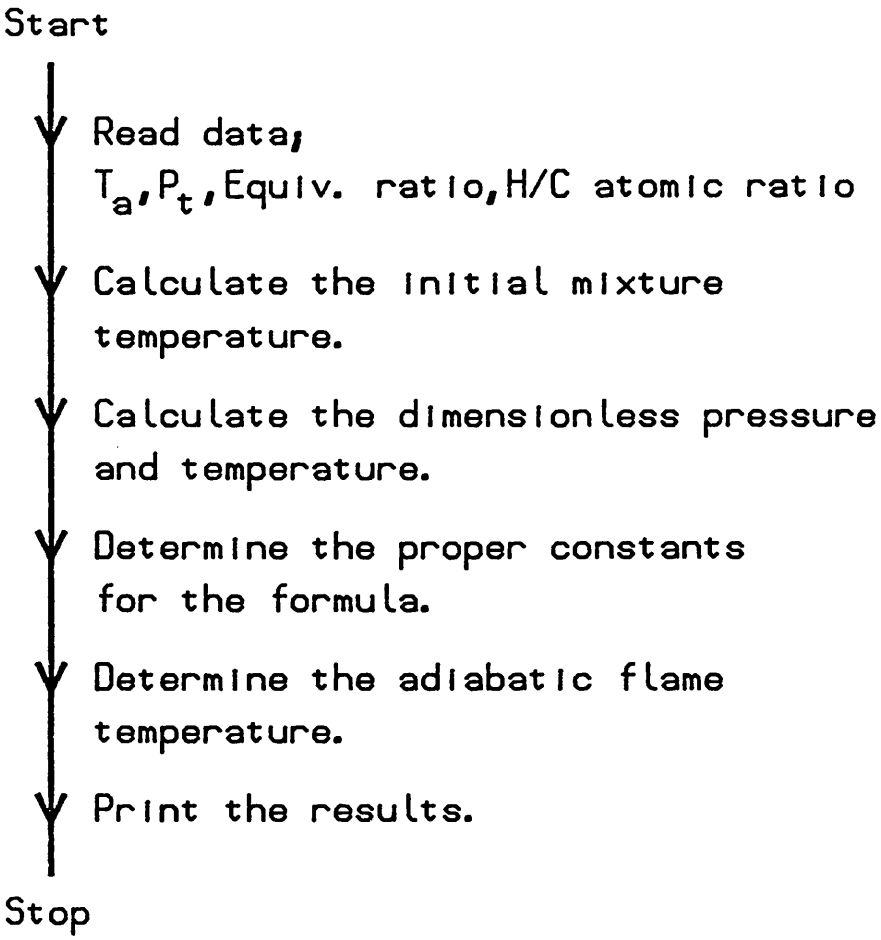

Fig. 4.10 The flowchart for Flame1.For.

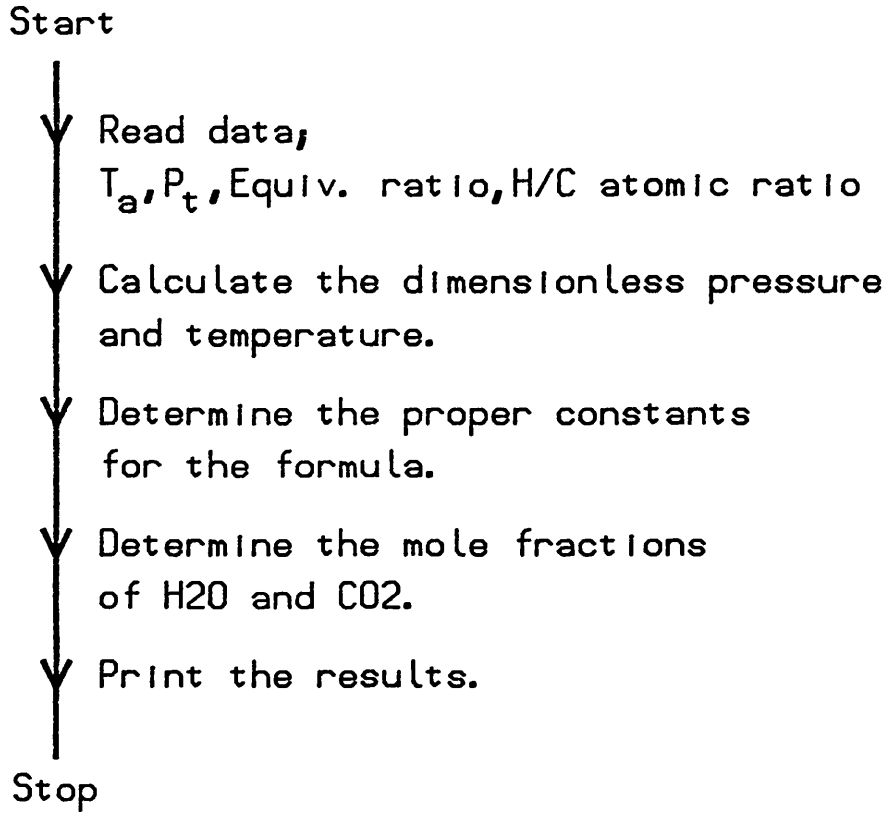

Fig. 4.11 The flowchart for Flame2.For.

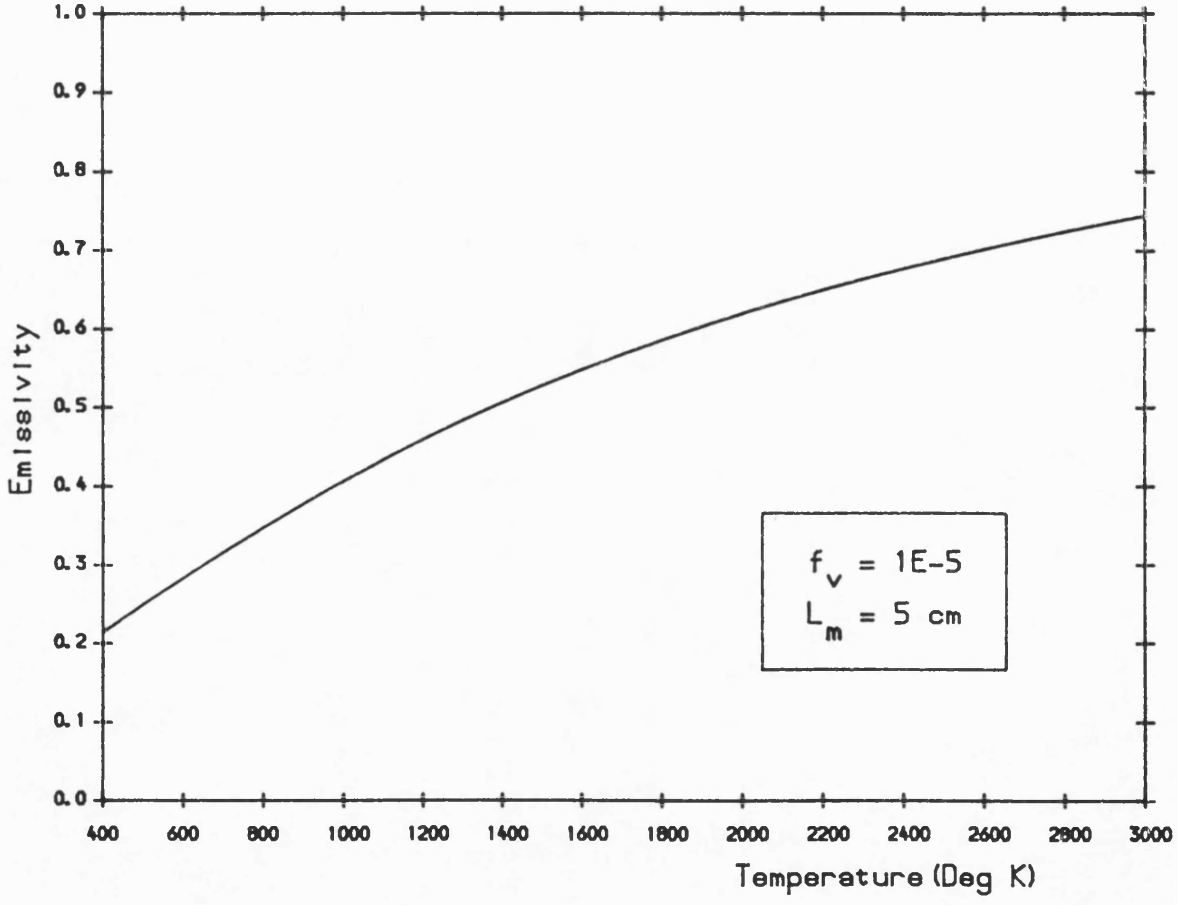

Fig. 4.12 Soot emissivity versus soot temperature (or soot absorptivity versus wall temperature).

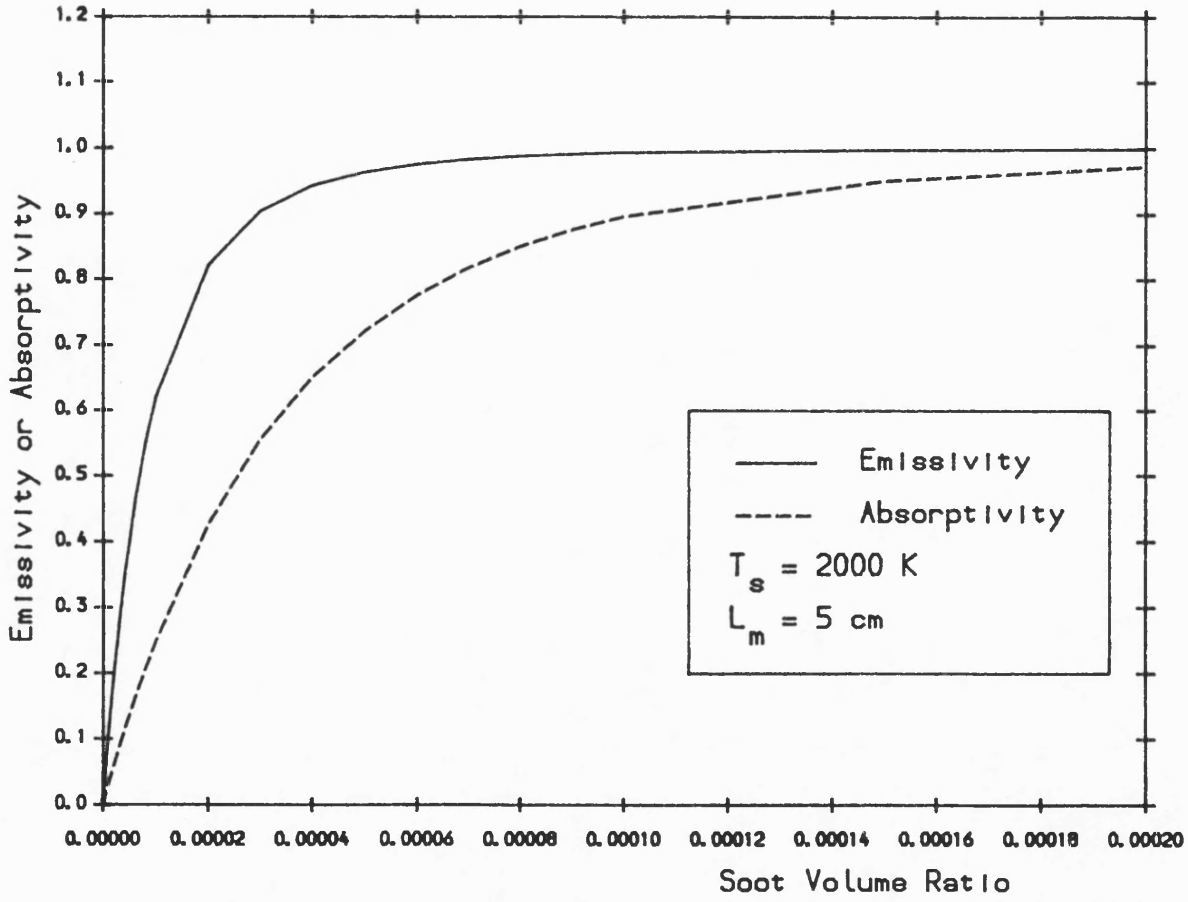

Fig. 4.13 Soot emissivity and absorptivity versus soot volume fraction.

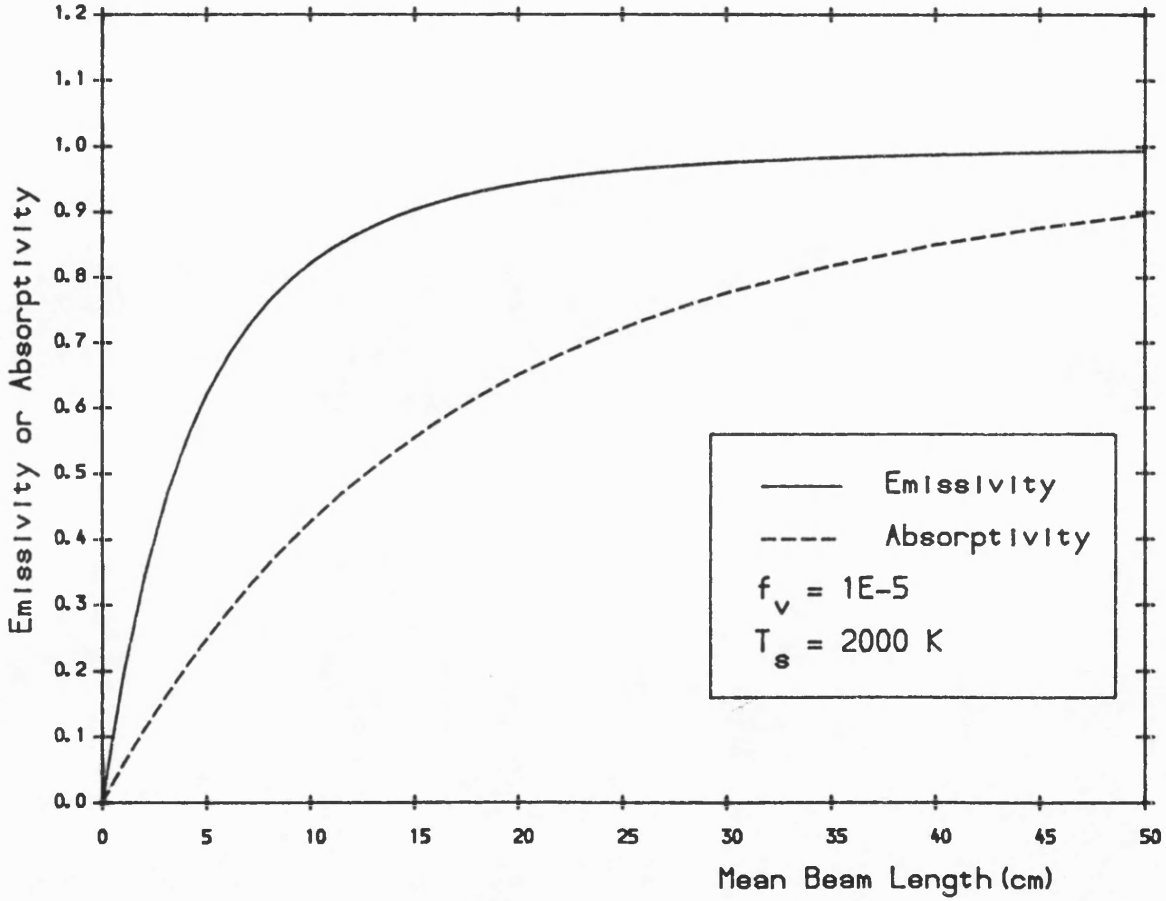

Fig. 4.14 Soot emissivity and absorptivity versus mean beam length.

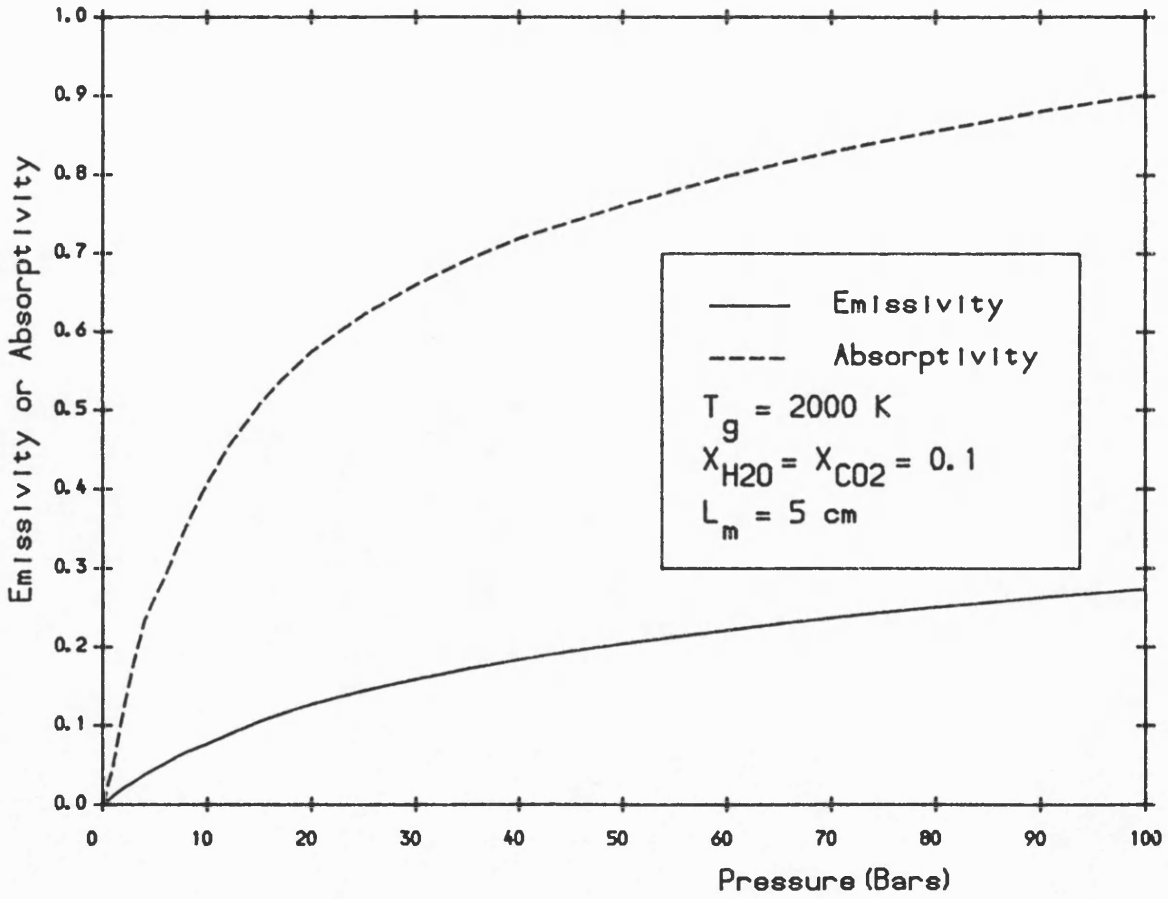

Fig. 4.15 Gas emissivity and absorptivity versus pressure.

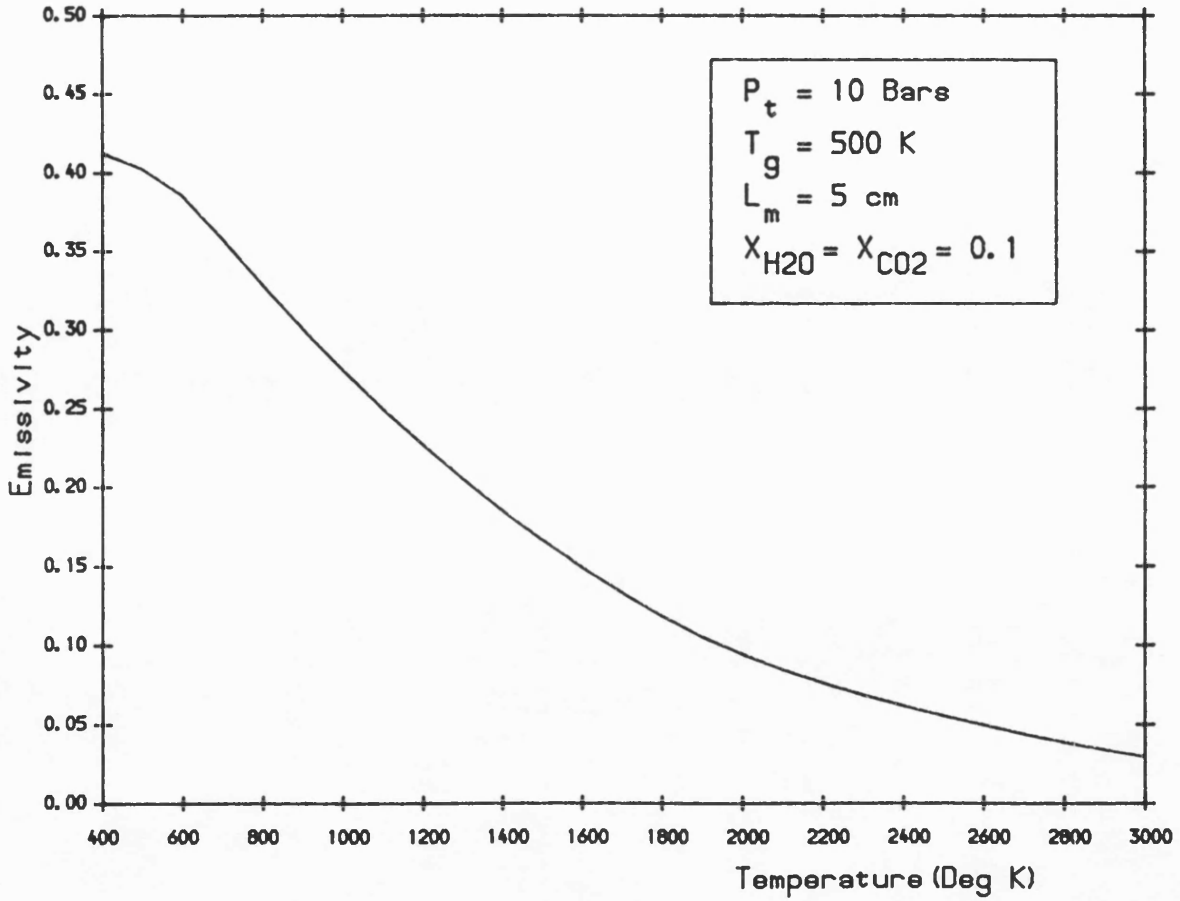

Fig. 4.16 Gas emissivity versus gas temperature (or gas absorptivity versus wall temperature).

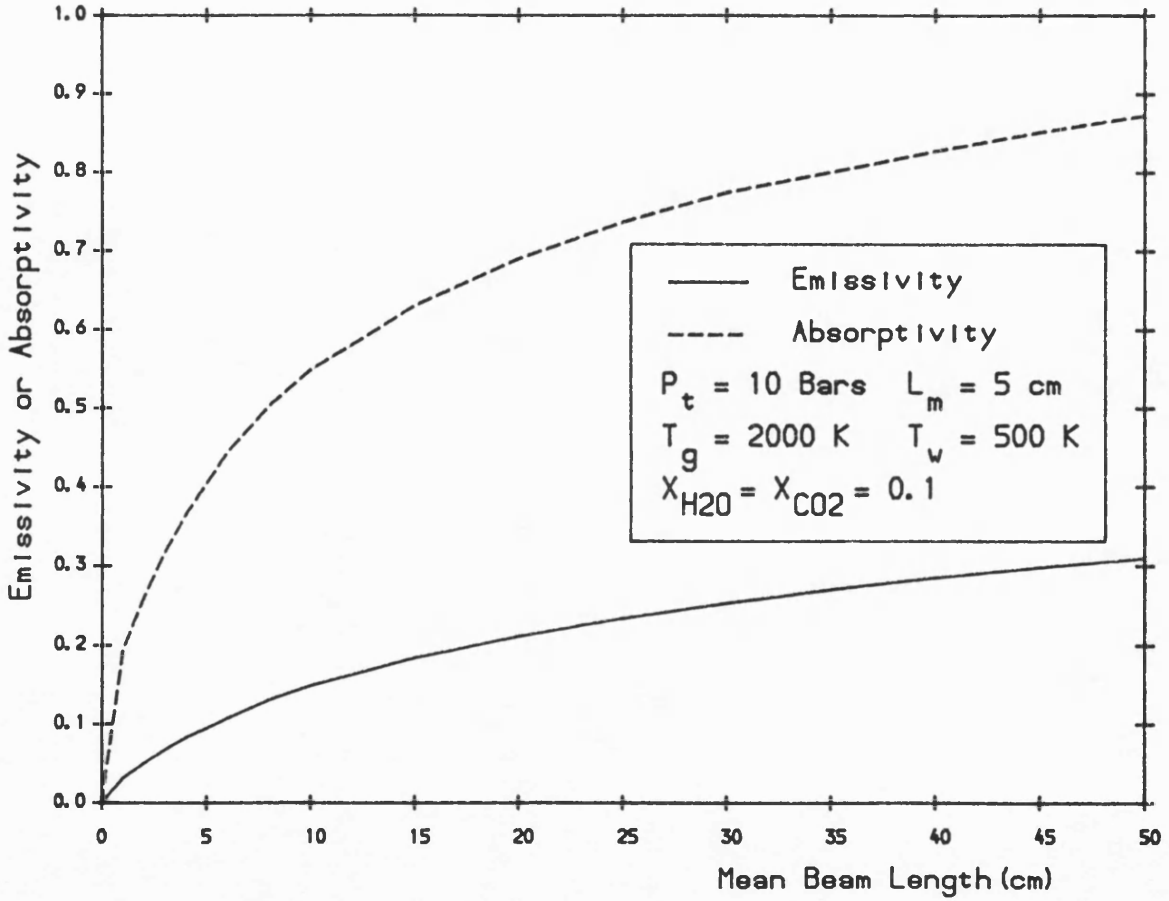

Fig. 4.17 Gas emissivity and absorptivity versus mean beam length.

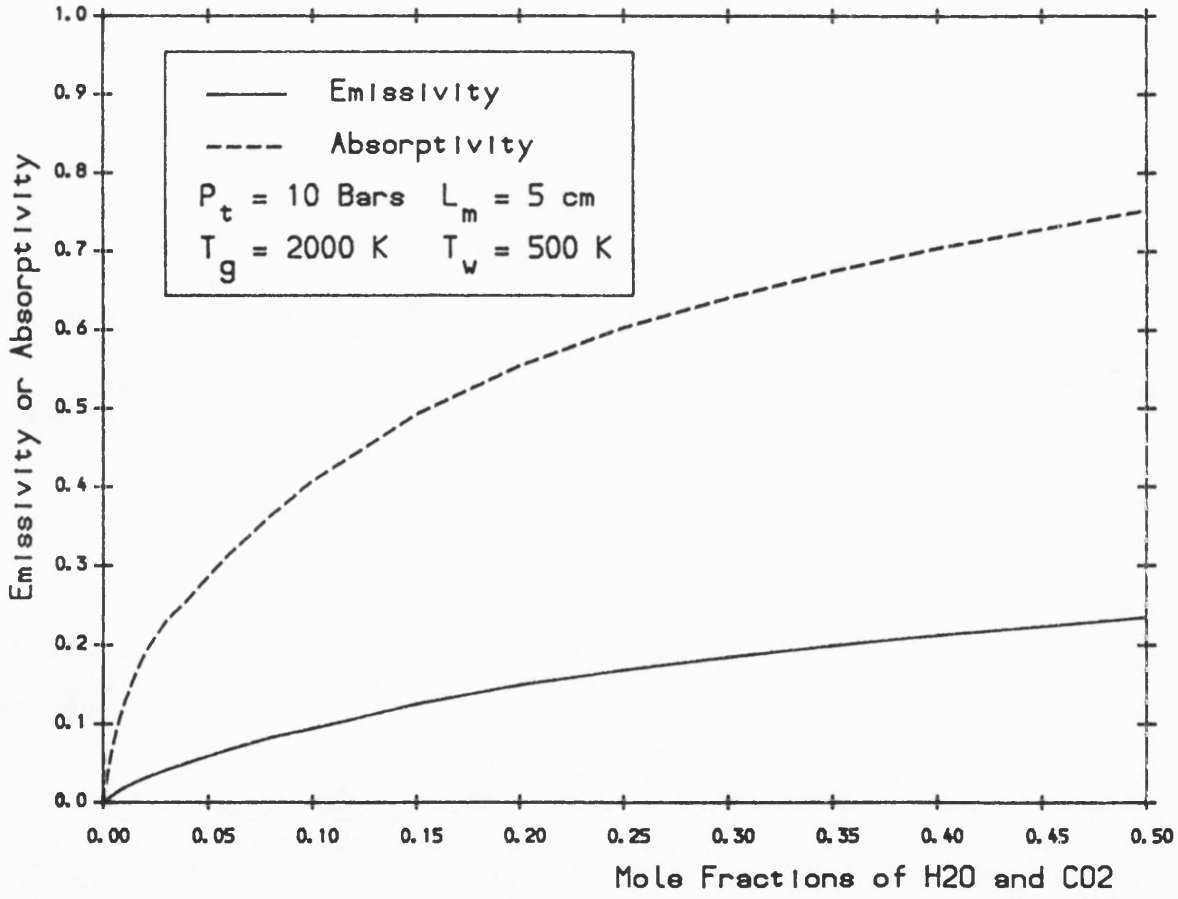

Fig. 4.18 Gas emissivity and absorptivity versus mole fractions of H2O and CO2.

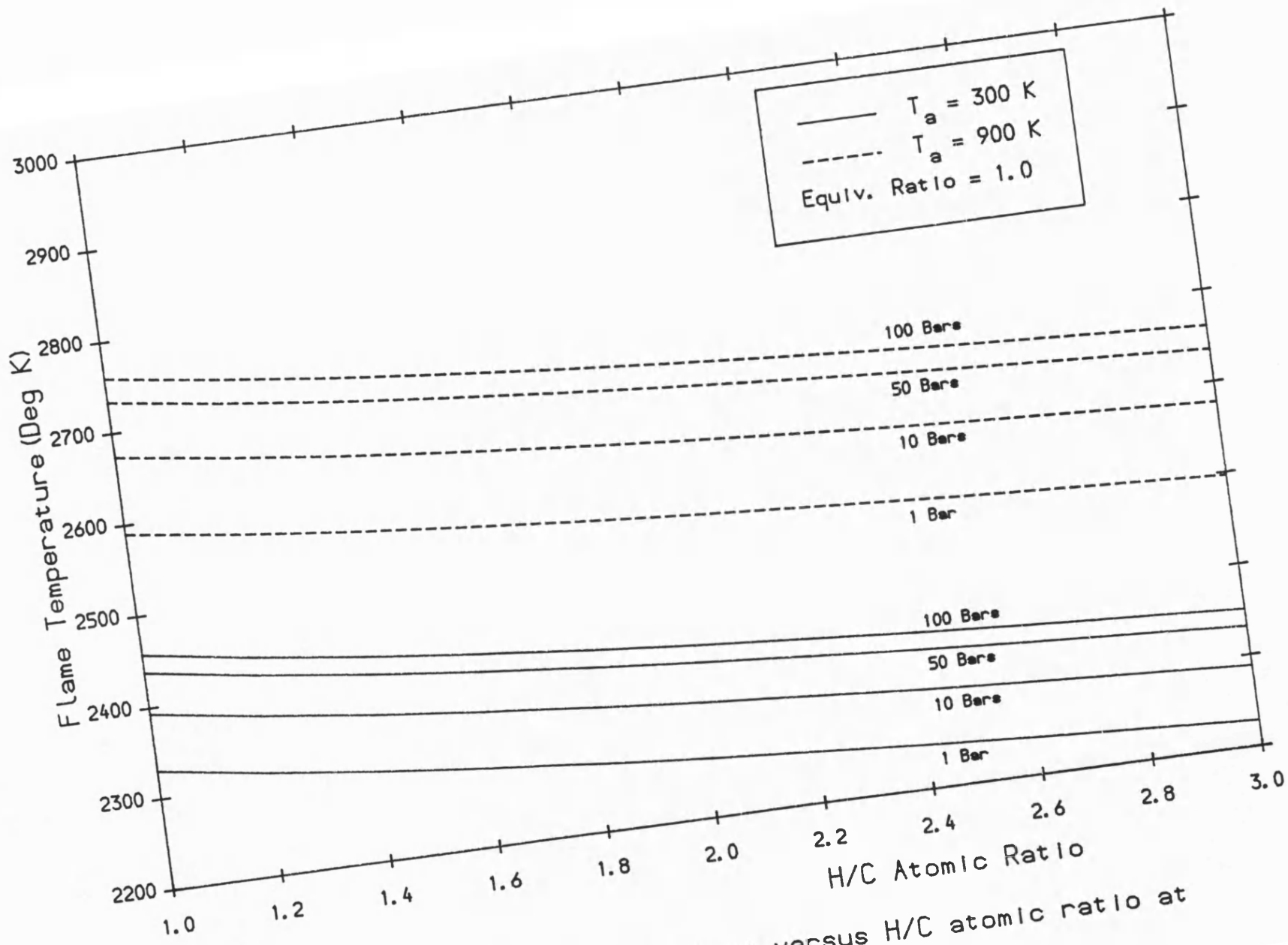

Fig. 4.19 Adiabatic flame temperature versus H/C atomic ratio at various air temperature and pressure.

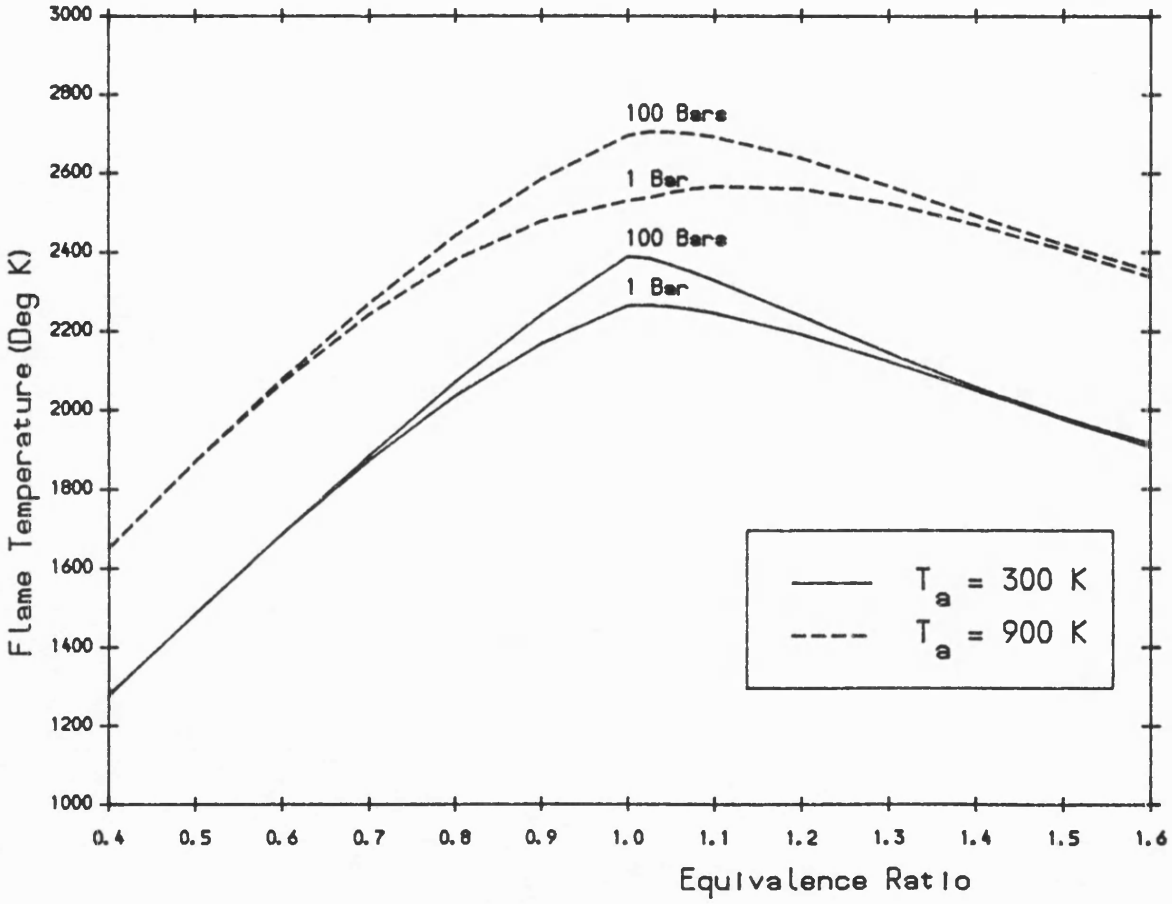

Fig. 4.20 Adiabatic flame temperature versus equivalence ratio at various air temperature and pressure.

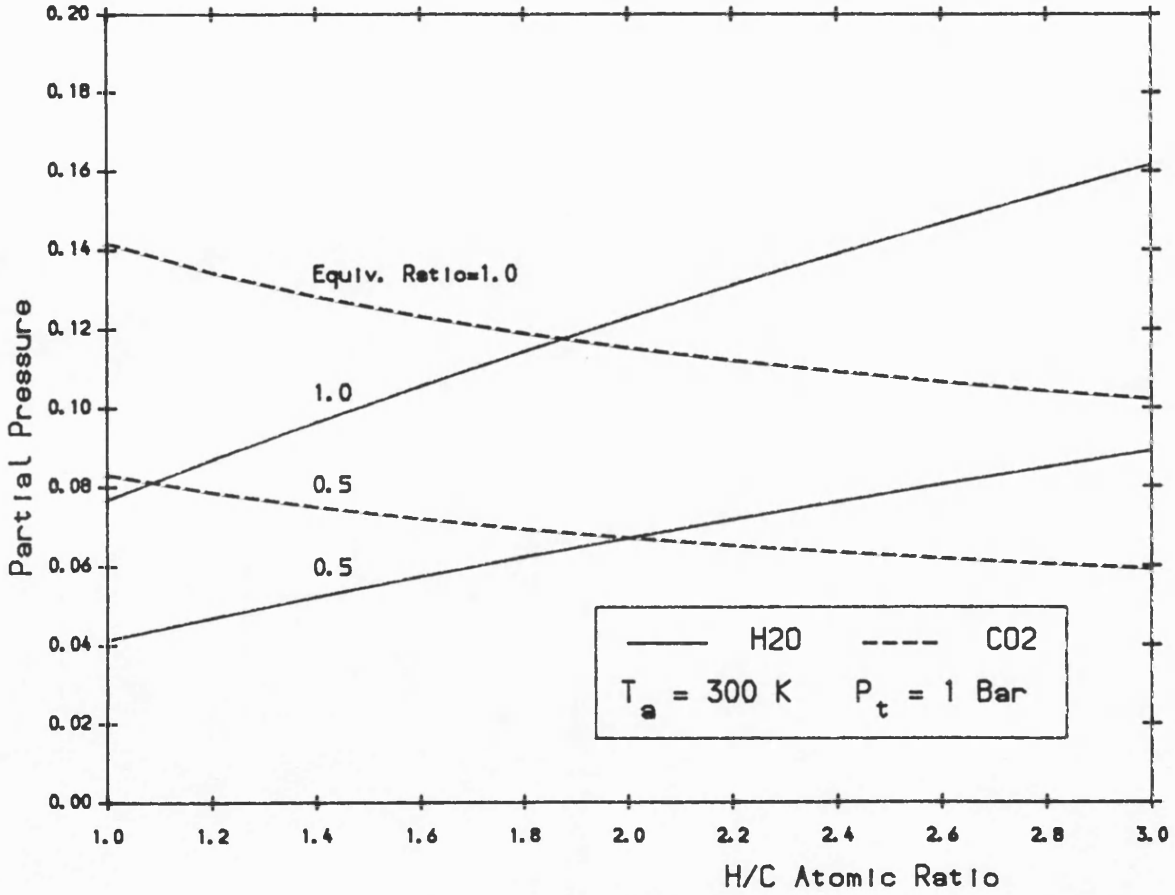

Fig. 4.21 Partial pressures of H20 and C02 versus H/C atomic ratio at 2 different equivalence ratio.

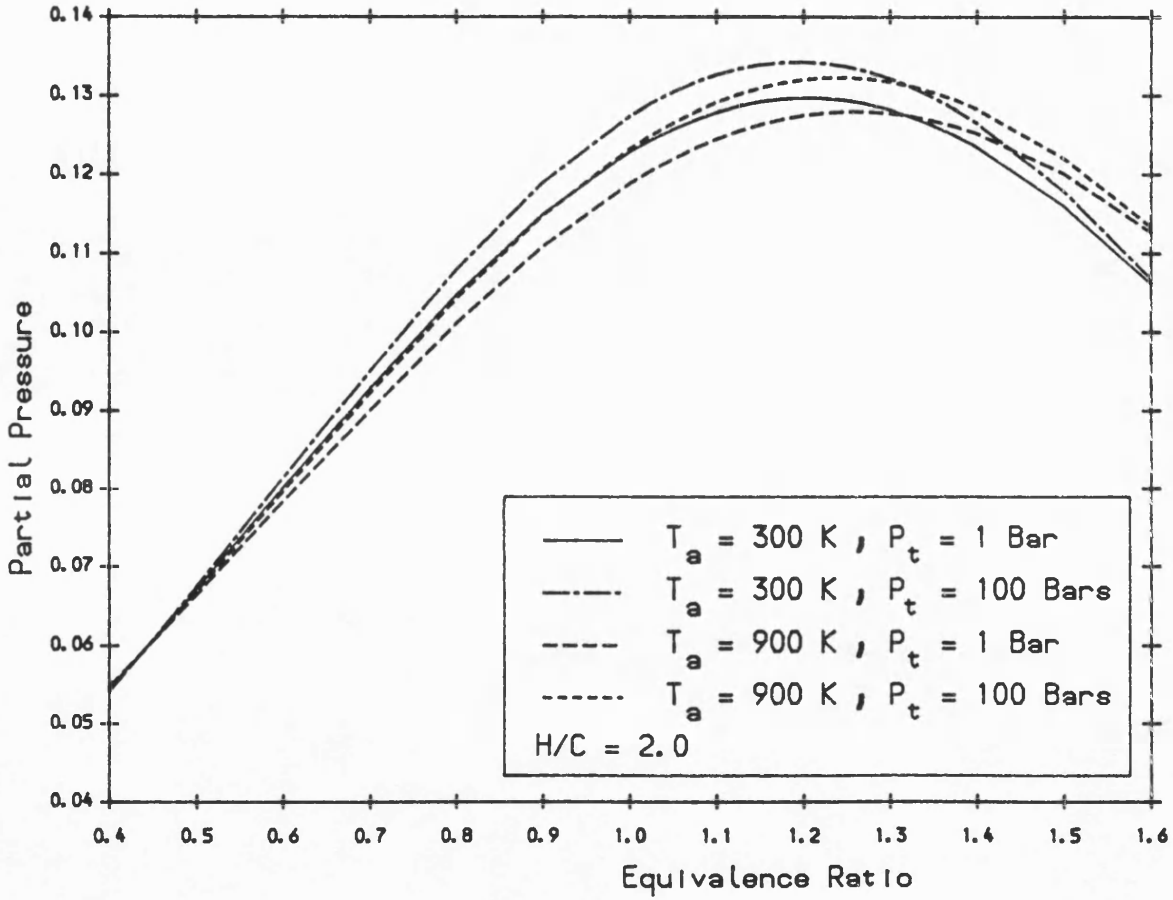

Fig. 4.22 Partial pressure of H20 versus equivalence ratio at various air temperature and pressure.

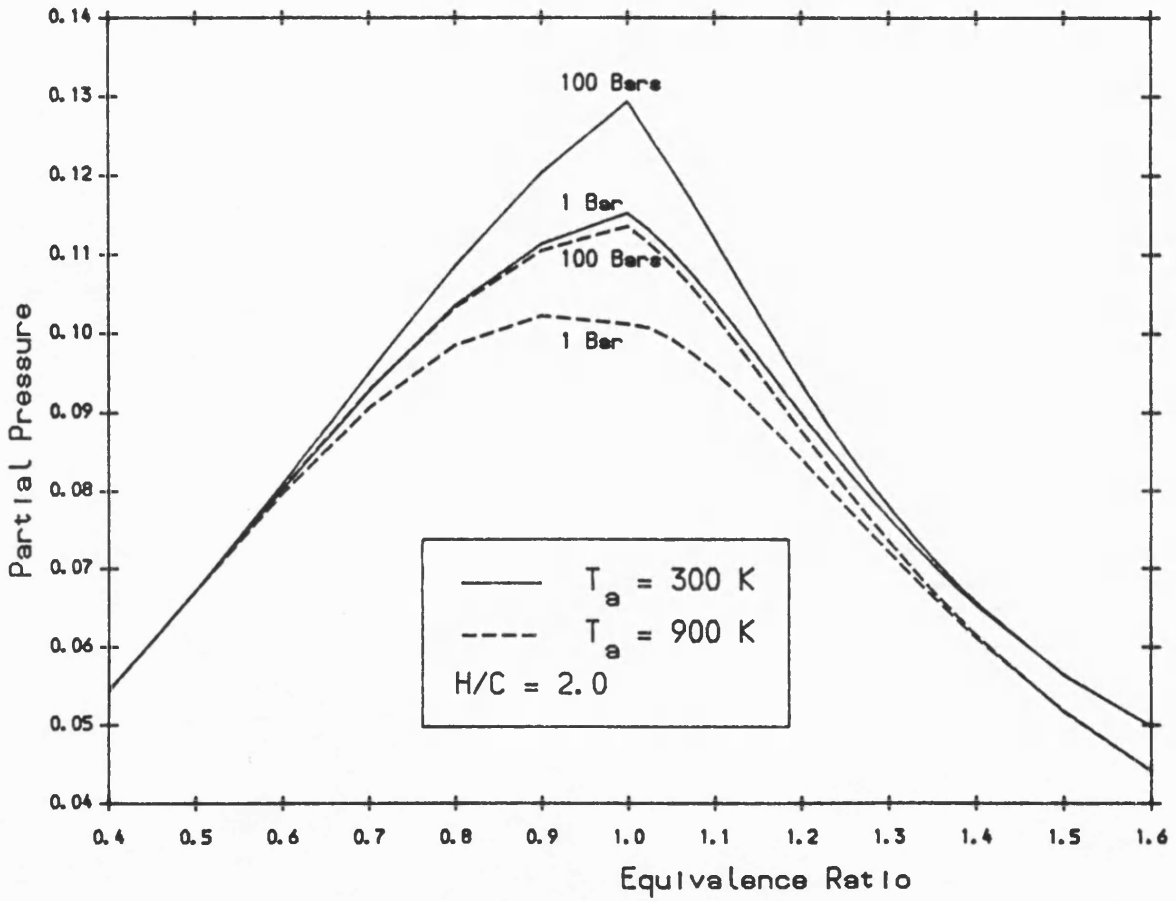

Fig. 4.23 Partial pressure of CO2 versus equivalence ratio at various air temperature and pressure.

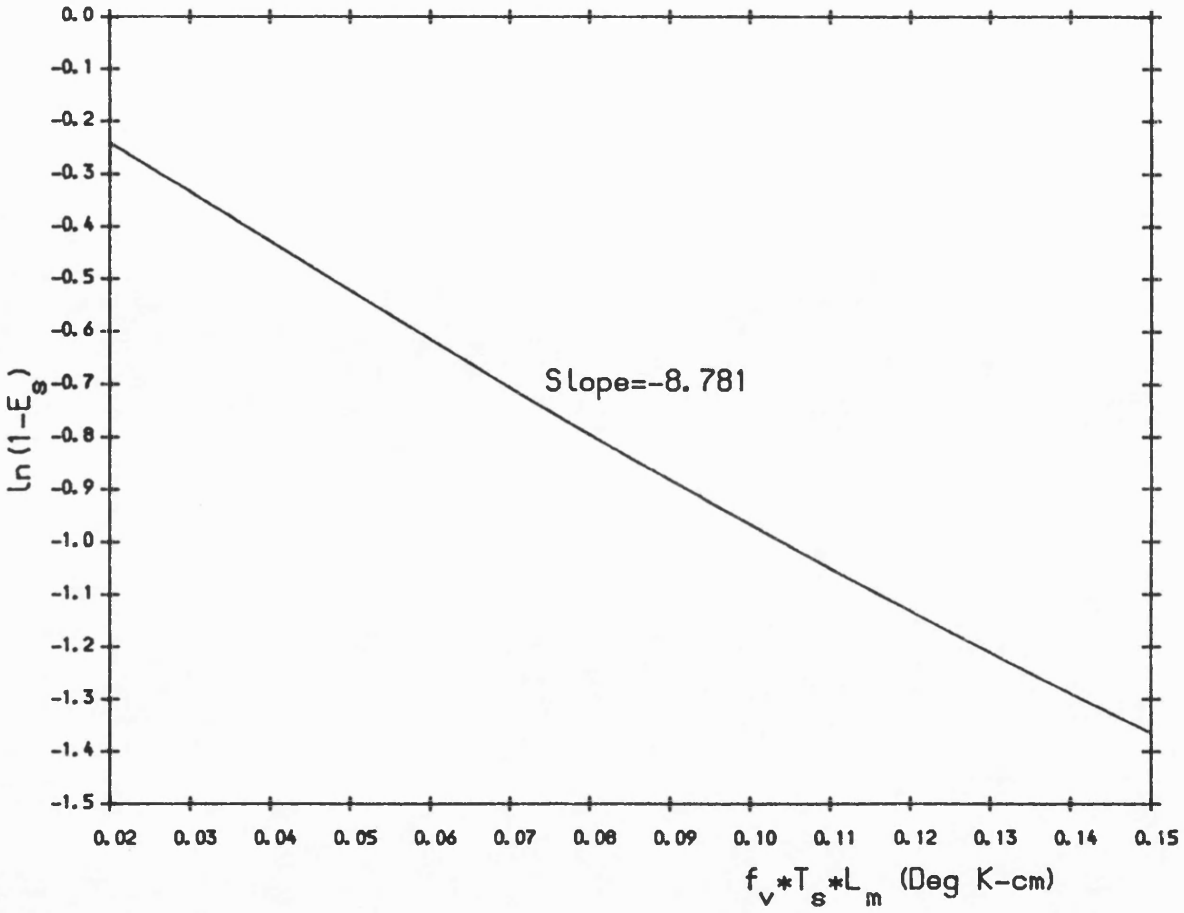

Fig. 4.24 The natural logarithmic function of soot emissivity versus the group of variables, soot volume fraction, temperature, and mean beam length.

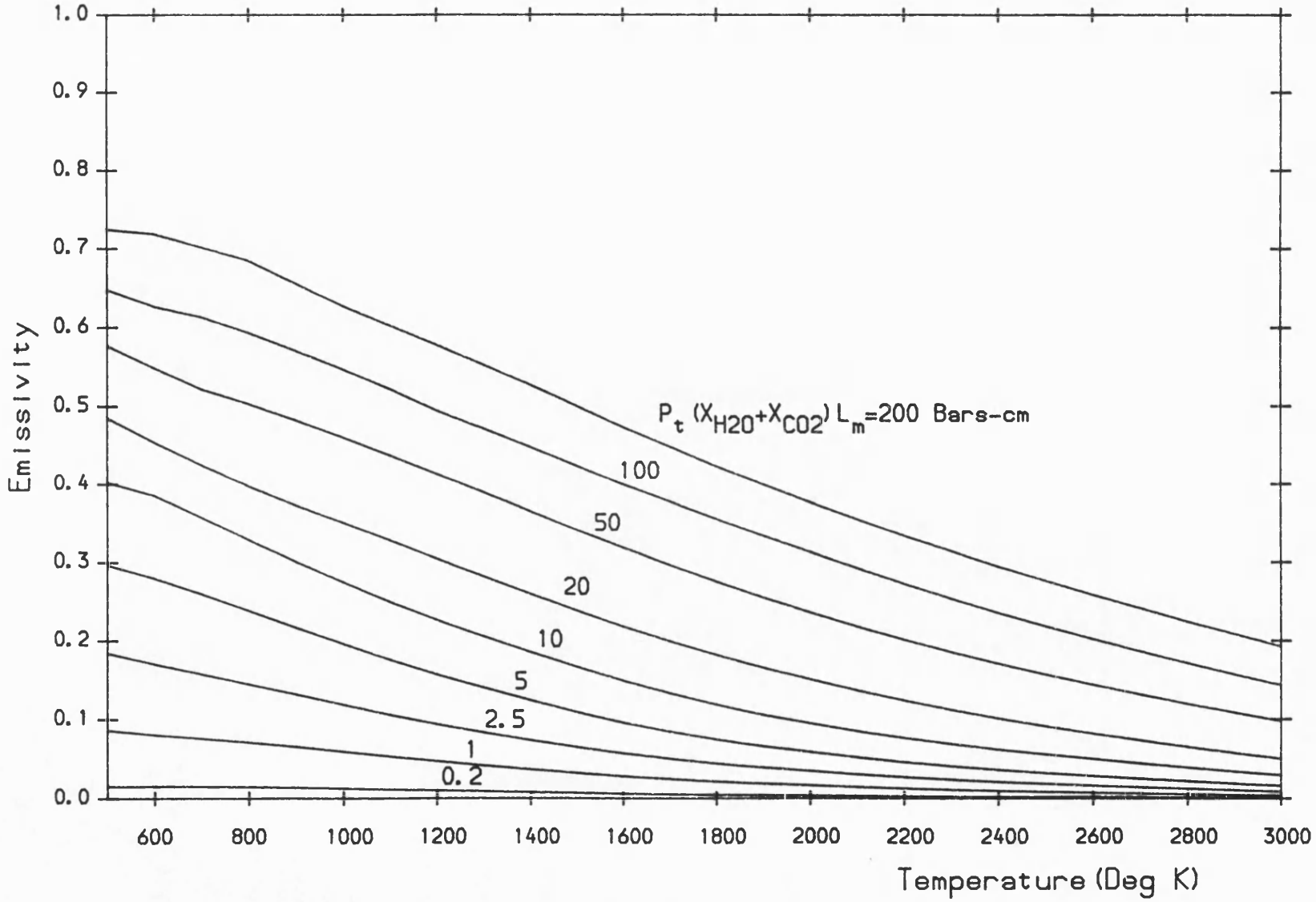

Fig. 4.25 Total gas emissivity versus gas temperature at various combinations of pressure, mean beam length and mole fractions.

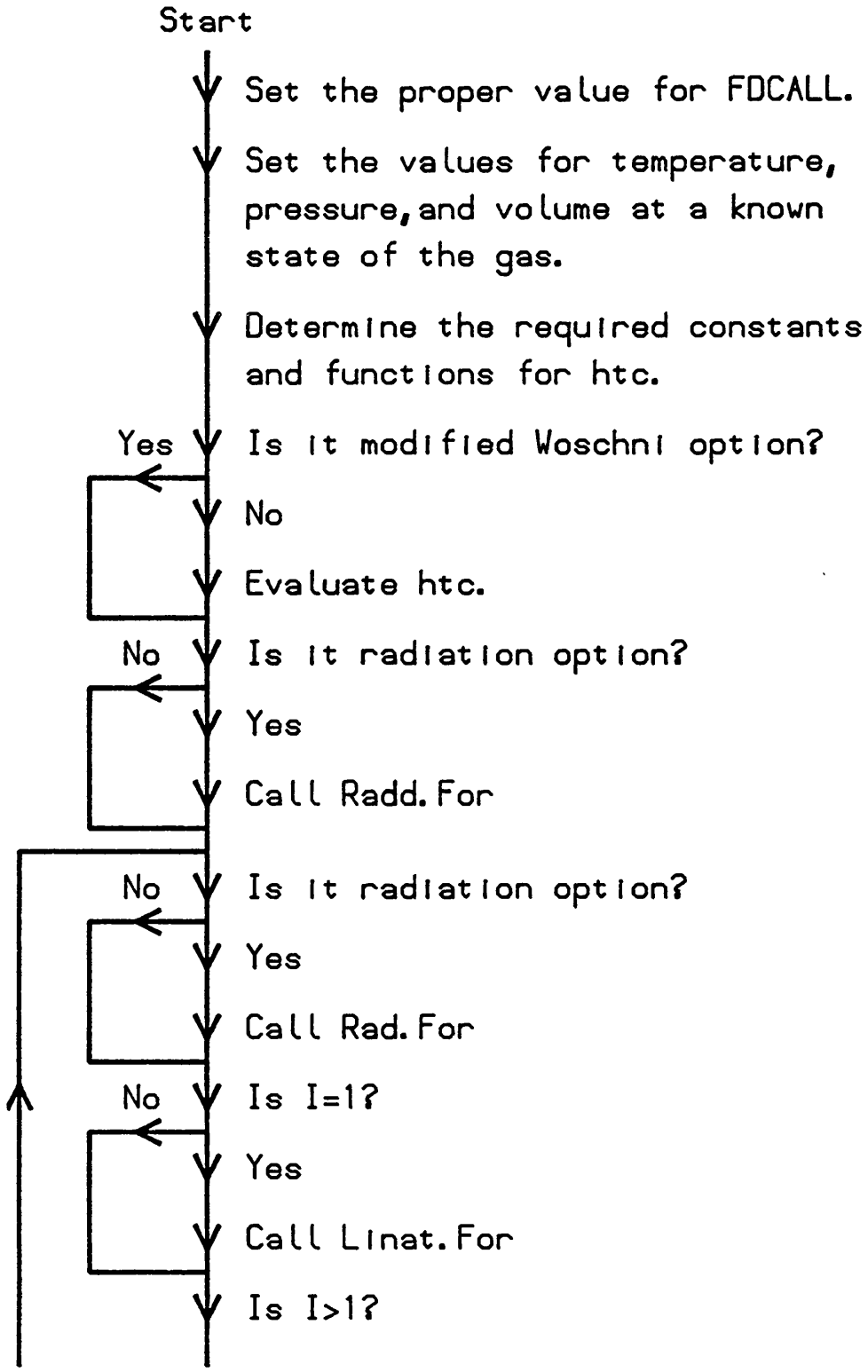

Fig. 4.26 The flowchart for Woschni.For.

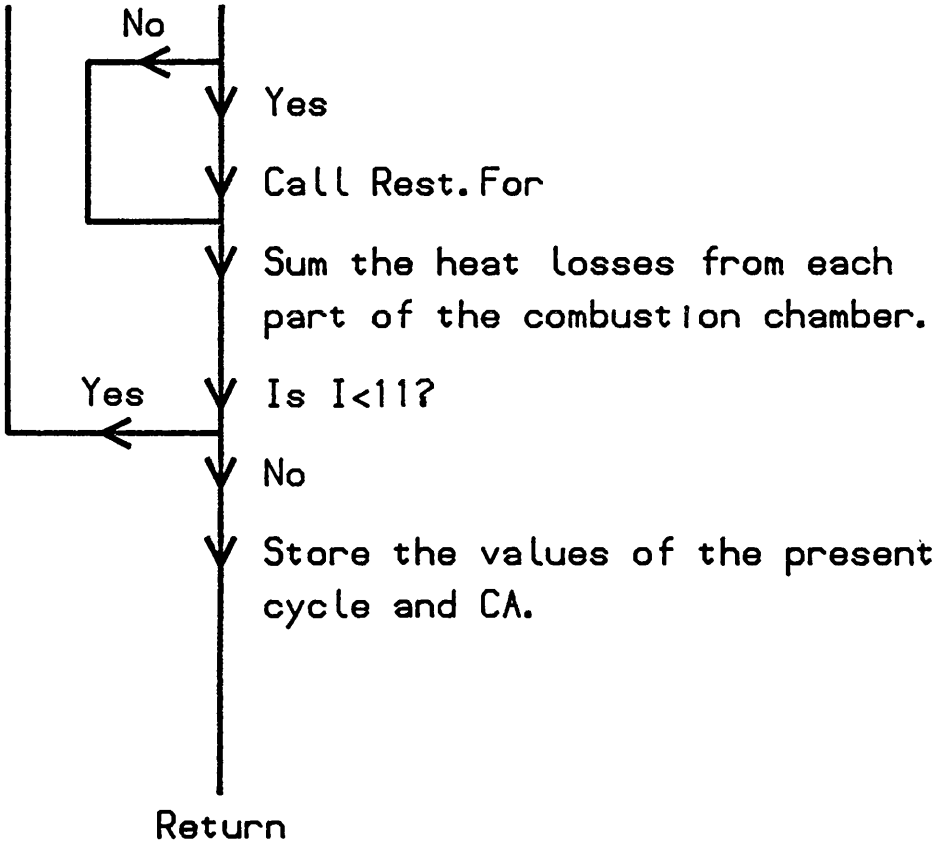

Fig. 4.26 Continued

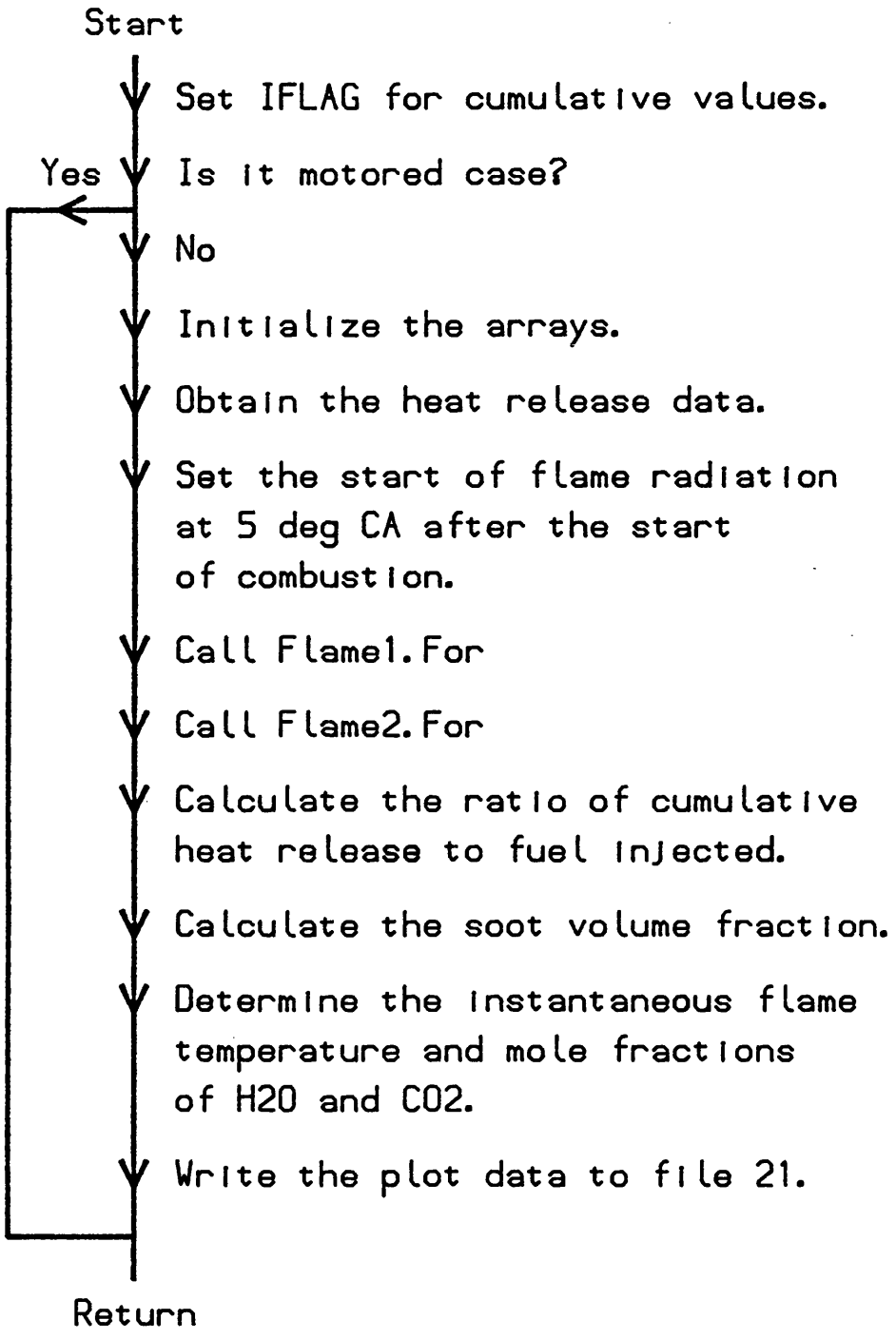

Fig. 4.27 The flowchart for Radd.For.

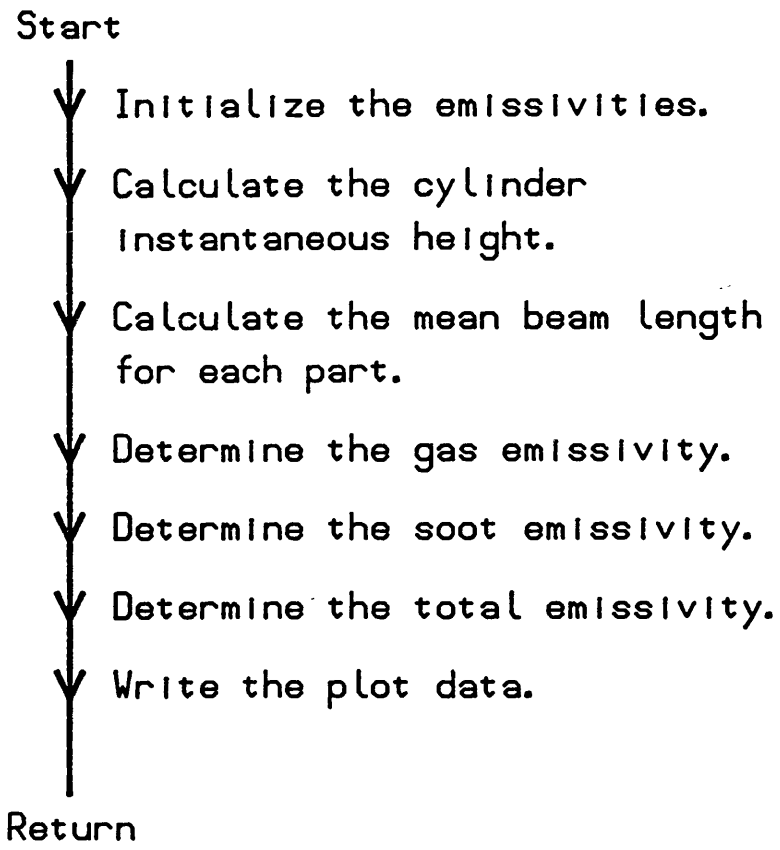

Fig. 4.28 The Flowchart for Rad.For.

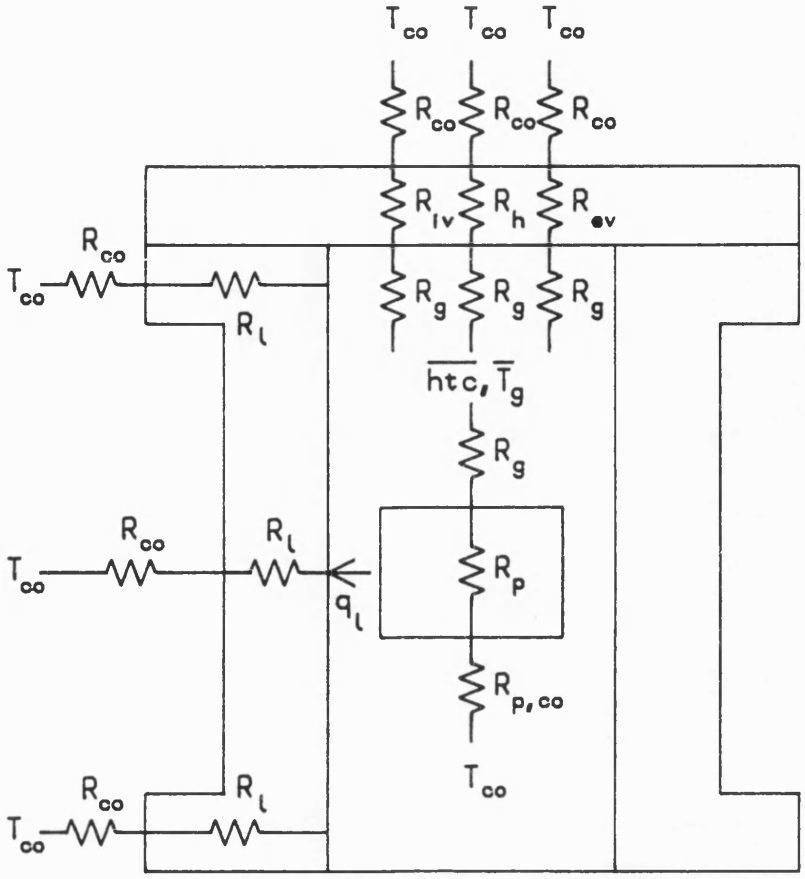

R_g is the gas side convective resistance.

R_{co} is the coolant side convective resistance.

$R_{p,co}$ is the piston coolant resistance.

R_{iv}, R_{ev} are the inlet and exhaust valve resistances.

R_h is the cylinder head resistance.

R_l is the liner resistance.

$T_{p,co}$ is the piston coolant temperature.

T_{co} is the coolant temperature.

$\overline{T}_g$ is the mean gas temperature.

q_l is the piston-liner conduction heat flux.

Fig. 5.1 Engine thermal resistance network in Spice.

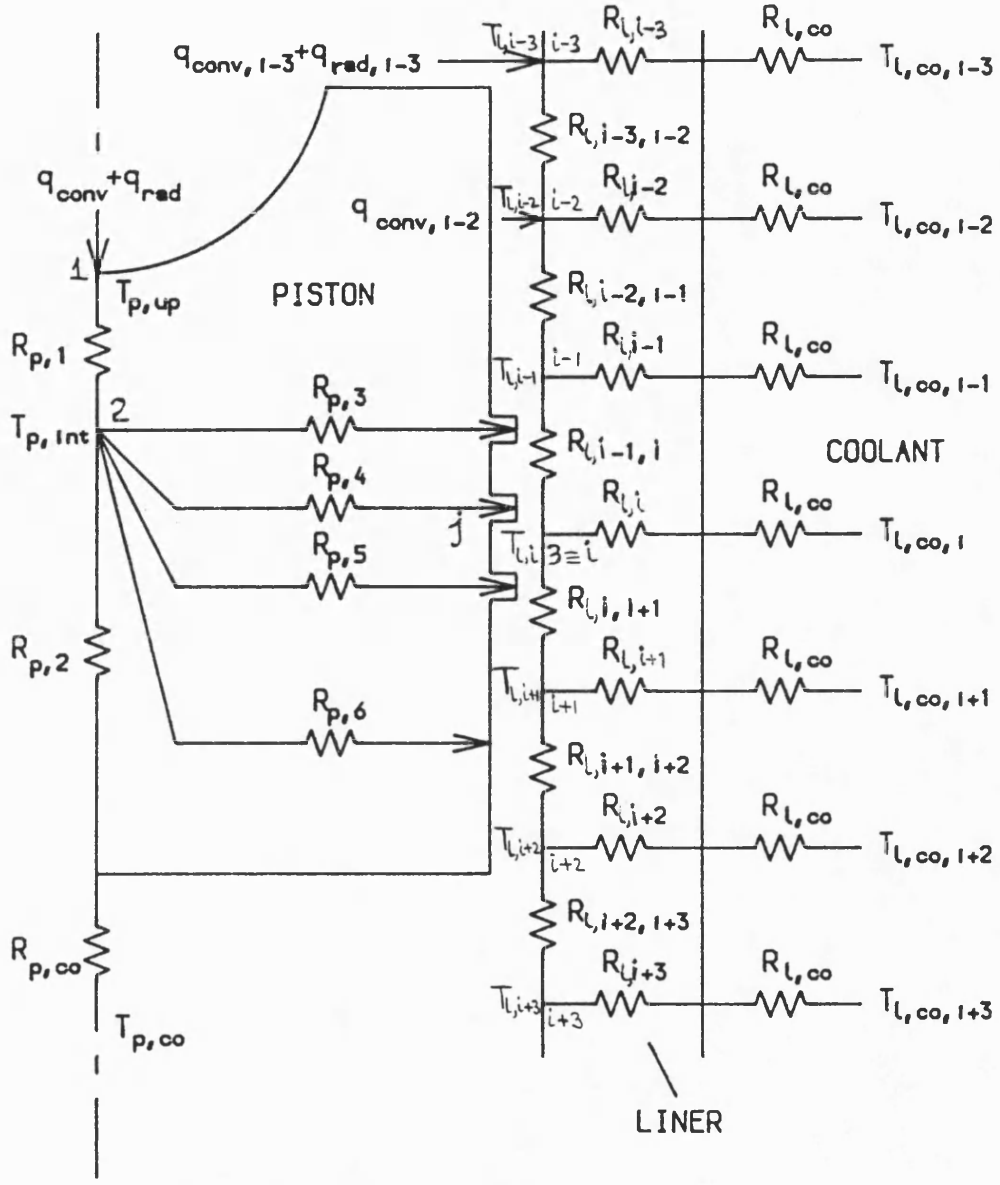

$R_{p,i}$ is the piston internal resitance i.

$R_{l,i}$, $R_{l,i,i+1}$ are the liner radial and axial resitances.

$T_{p,up}$, $T_{p,int}$ are the piston upper surface and internal node temperatures.

$T_{p,co}$, $T_{l,co}$ are the piston and liner coolant temperatures.

q_{conv}, q_{rad} are the convective and radiative fluxes.

Fig. 5.2a The new piston-liner thermal resistance model.

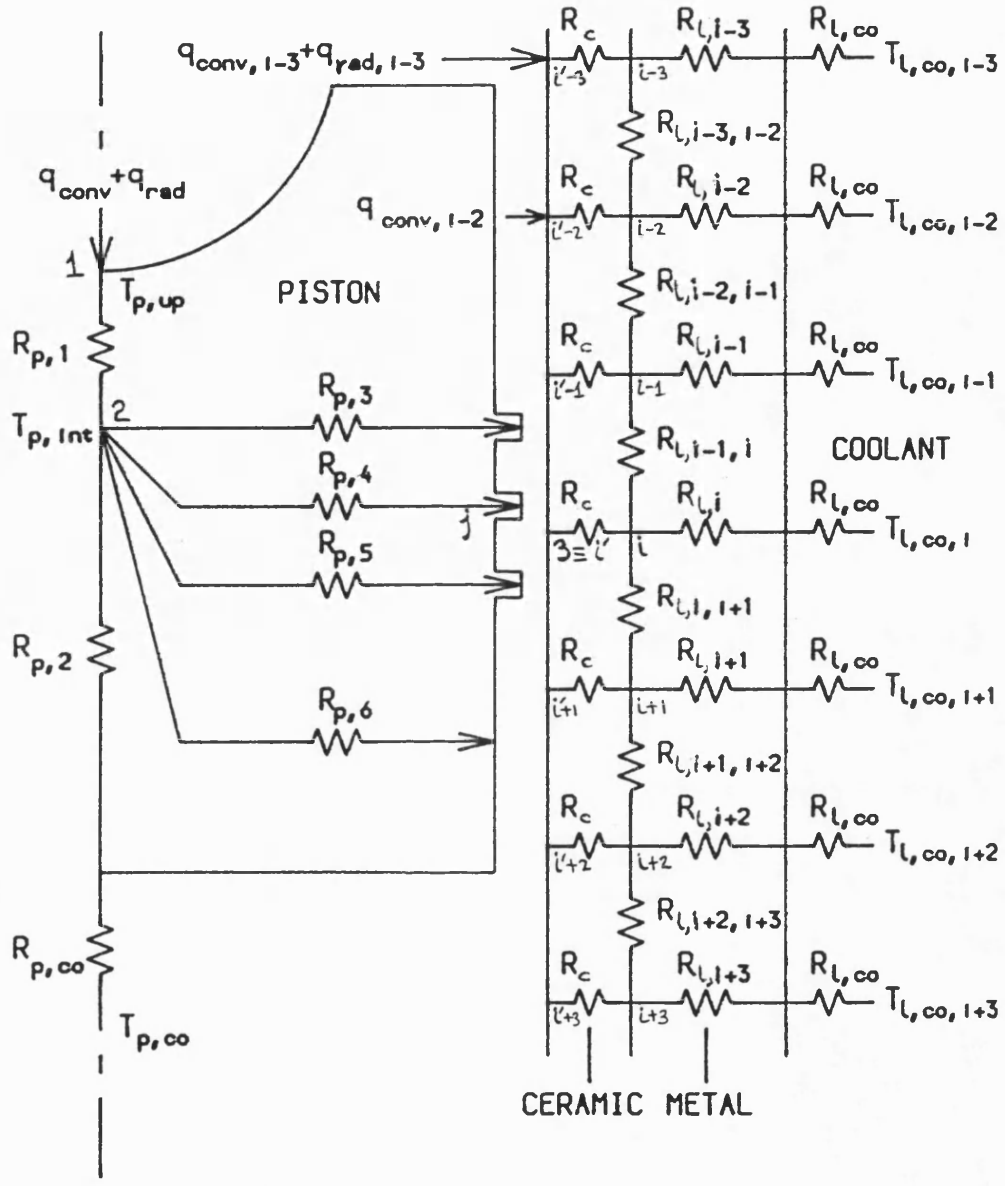

R_c is the ceramic layer resistance related to node i.

Fig. 5.2b Piston-liner thermal resistance network with axial resistances at the ceramic-metal interface.

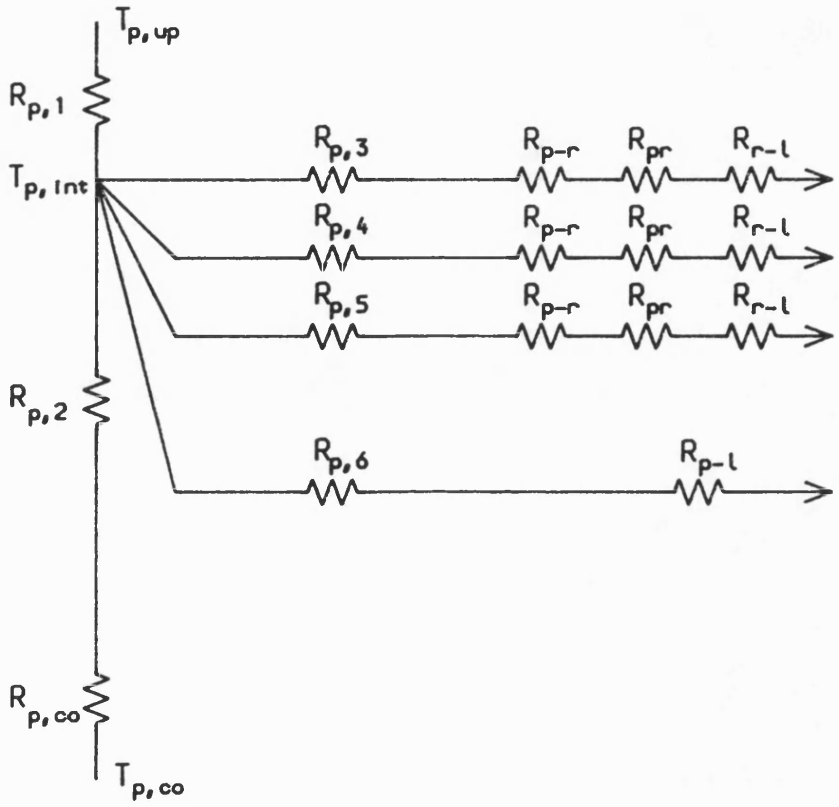

R_{p-r} is the thermal resistance between piston and ring.

R_{pr} is the piston ring thermal resistance.

R_{r-l} is the thermal resistance between ring and liner.

R_{p-l} is the thermal resistance between piston and liner.

Fig. 5.3 Piston thermal resistance model including piston to ring, ring and ring to liner resistances.

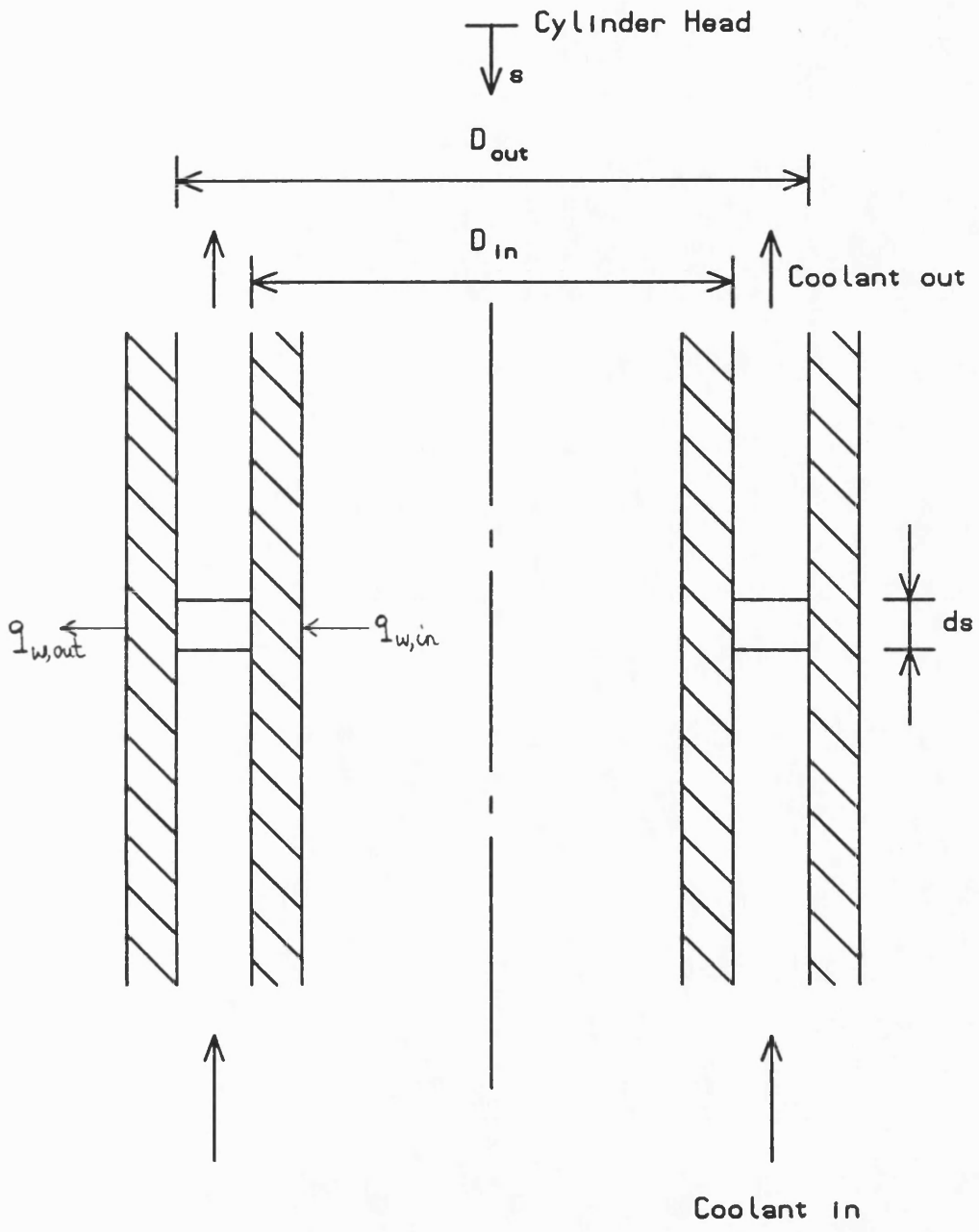

Fig. 5.4 A concentric circular coolant element around the liner.

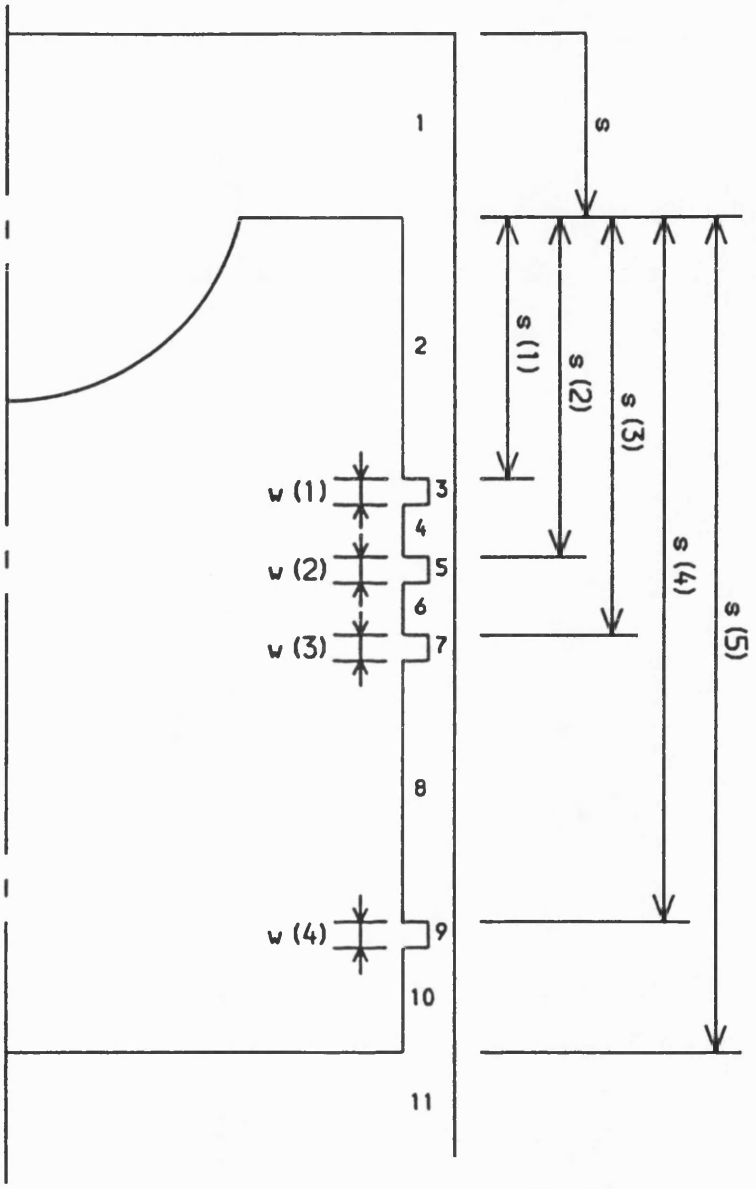

s is the instantaneous piston position from cylinder head.

s(i) is the position of ring i from top of the piston.

w(i) is the width of ring i.

1,2,3,.....,10,11 are the piston regions.

Fig. 5.5 Type of piston region in contact with the liner nodes.

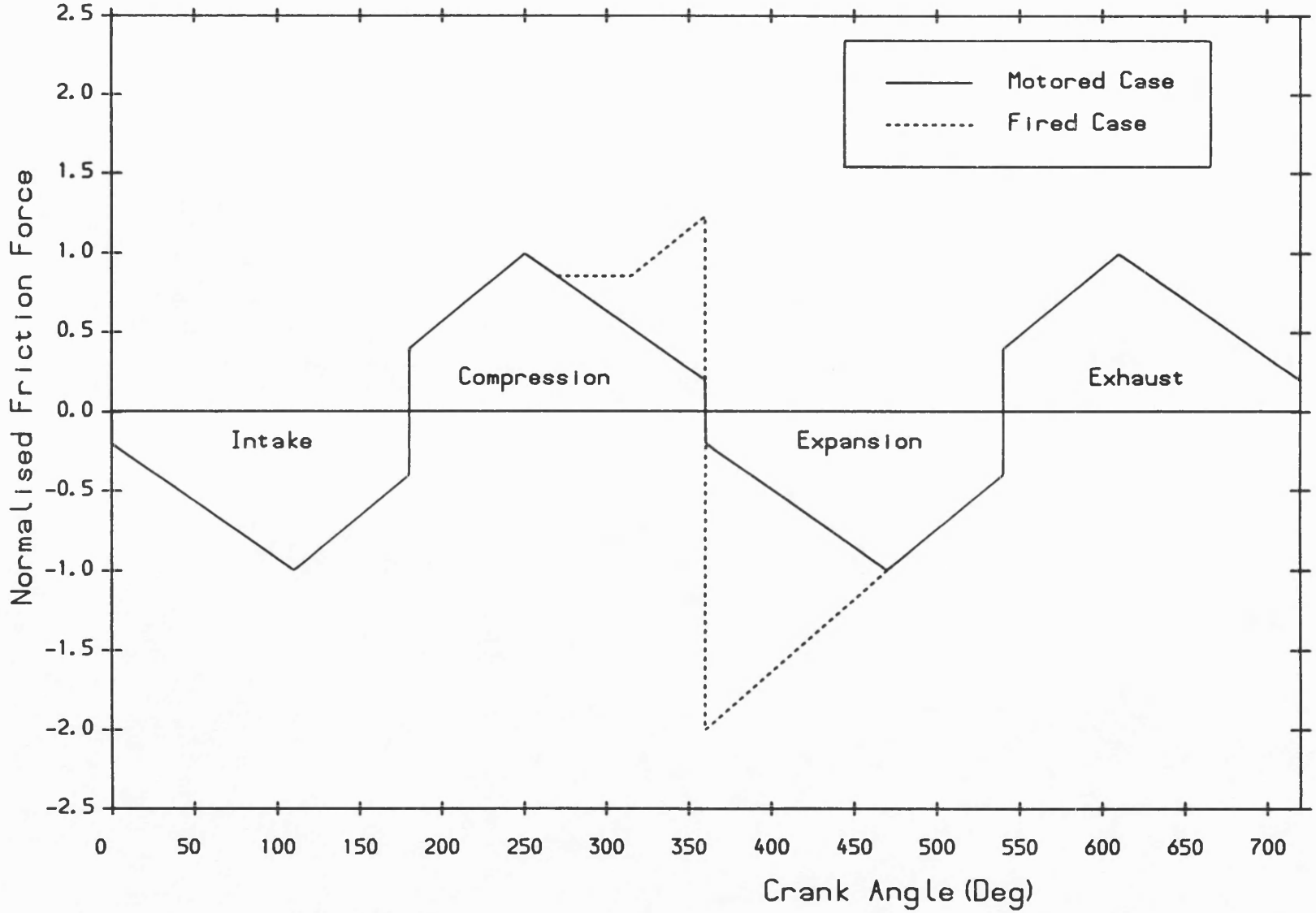

Fig. 5.6 Normalised instantaneous piston friction force in a typical diesel engine, based on maximum friction force at motoring.

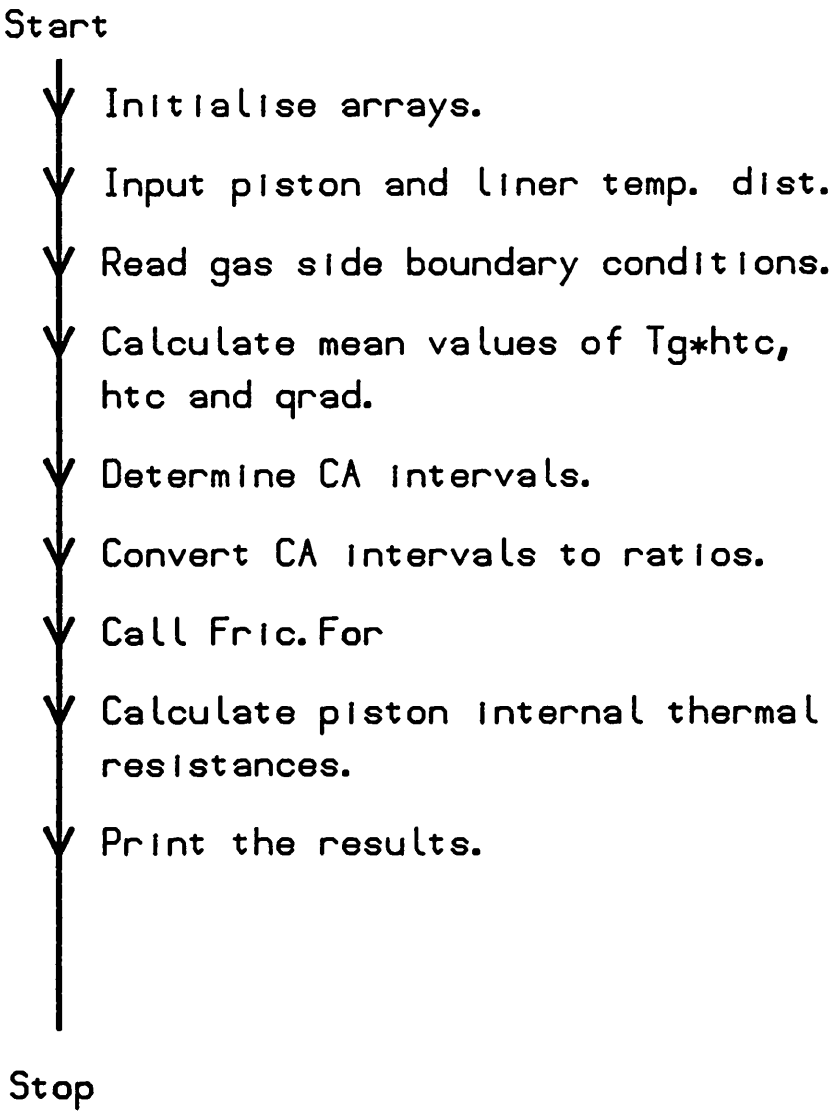

Fig. 5.7 The flowchart for Pistres.For.

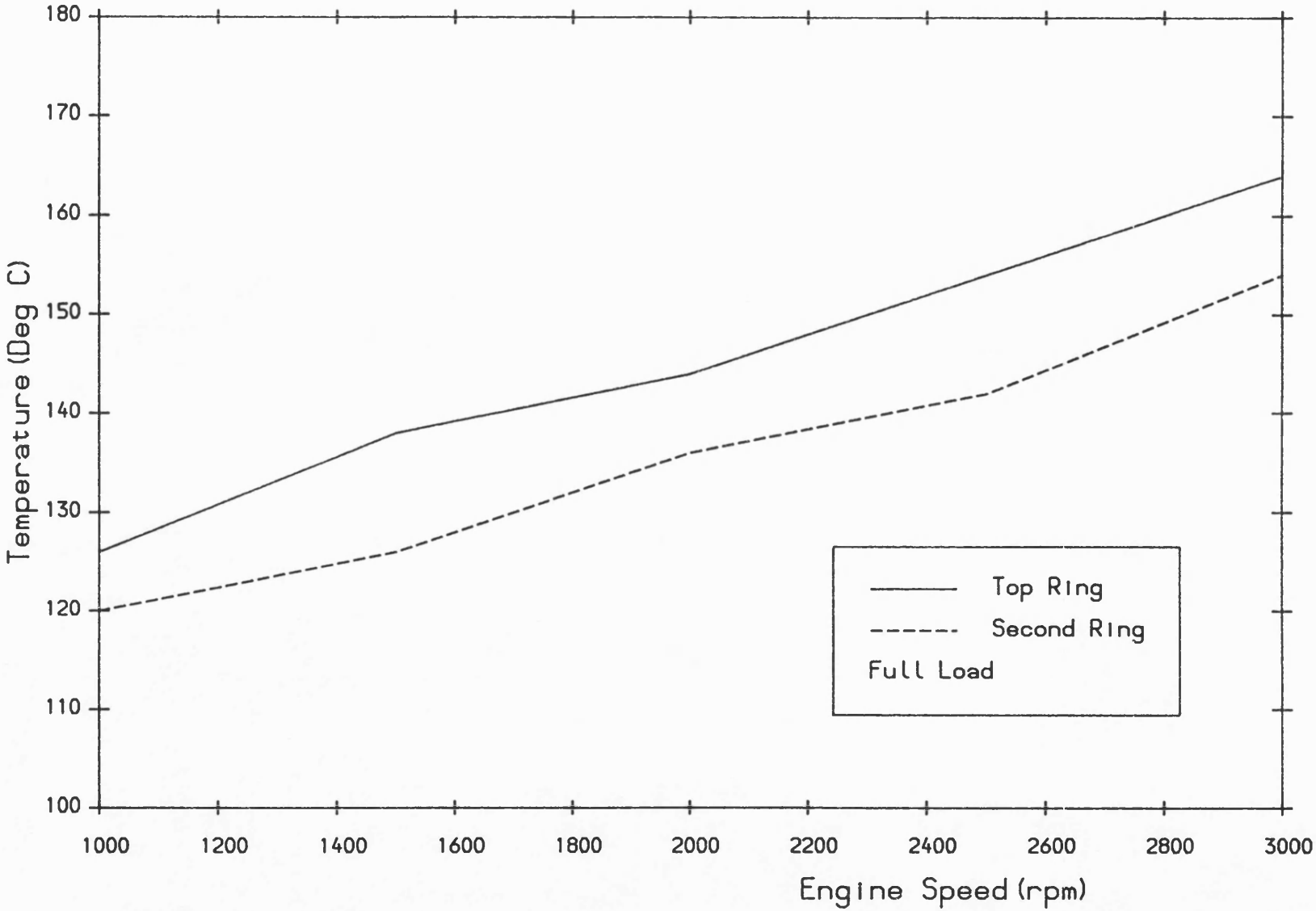

Fig. 5.8 Piston rings temperatures versus engine speed [Ref. 93].

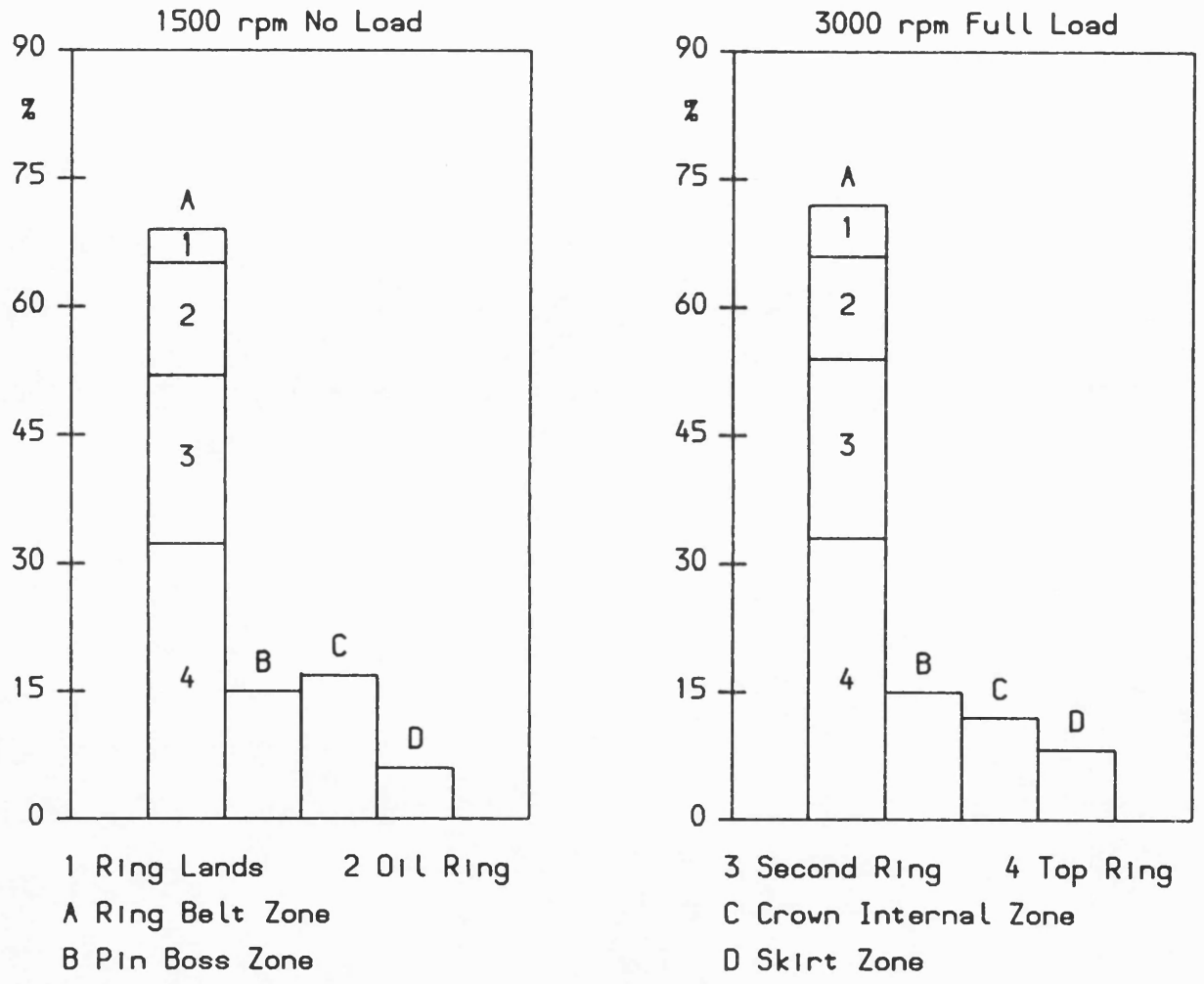

Fig. 5.9 Piston heat loss percentages through various piston zones [Ref. 93].

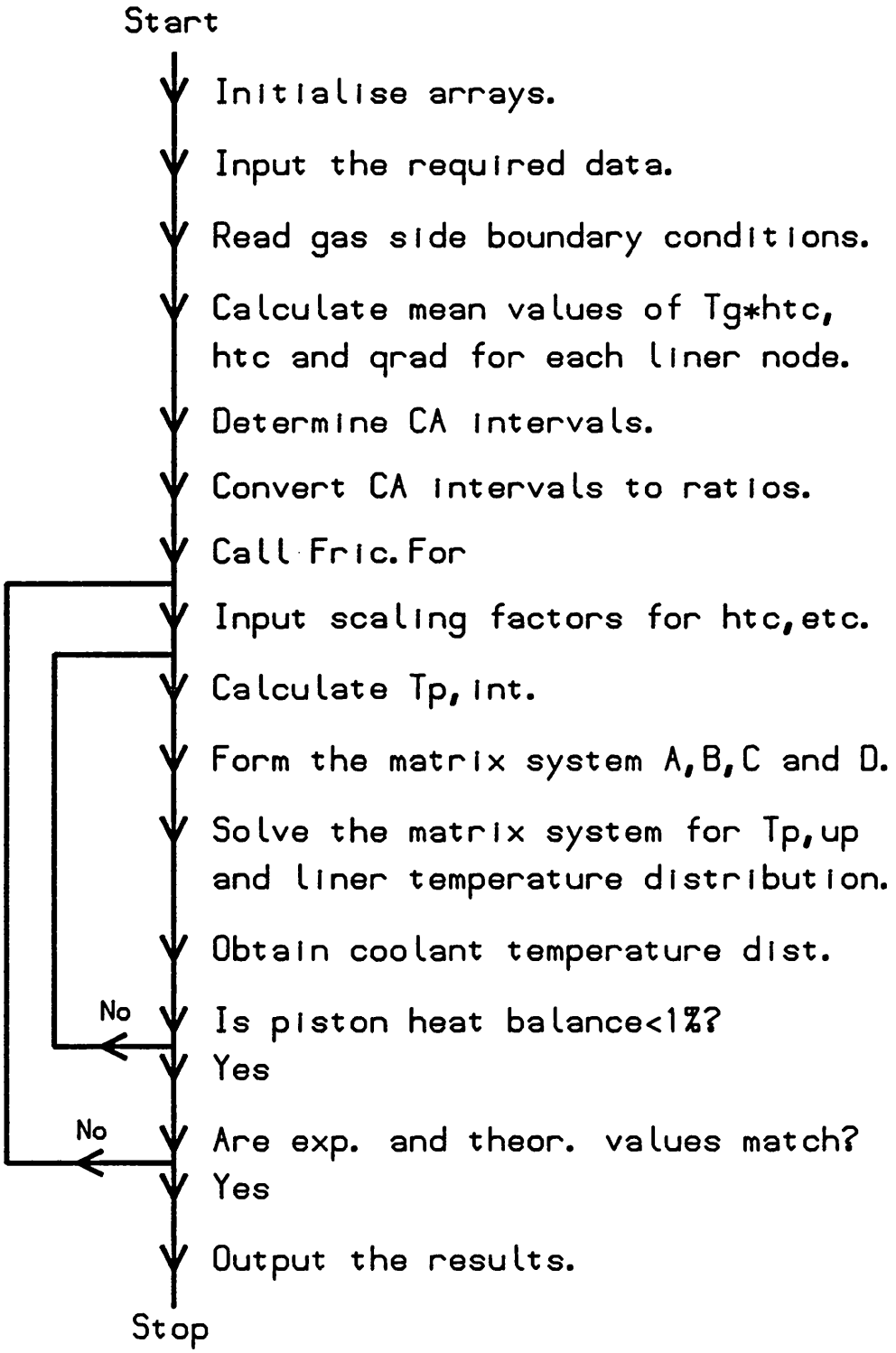

Fig. 5.10 The flowchart for Plresist.For.

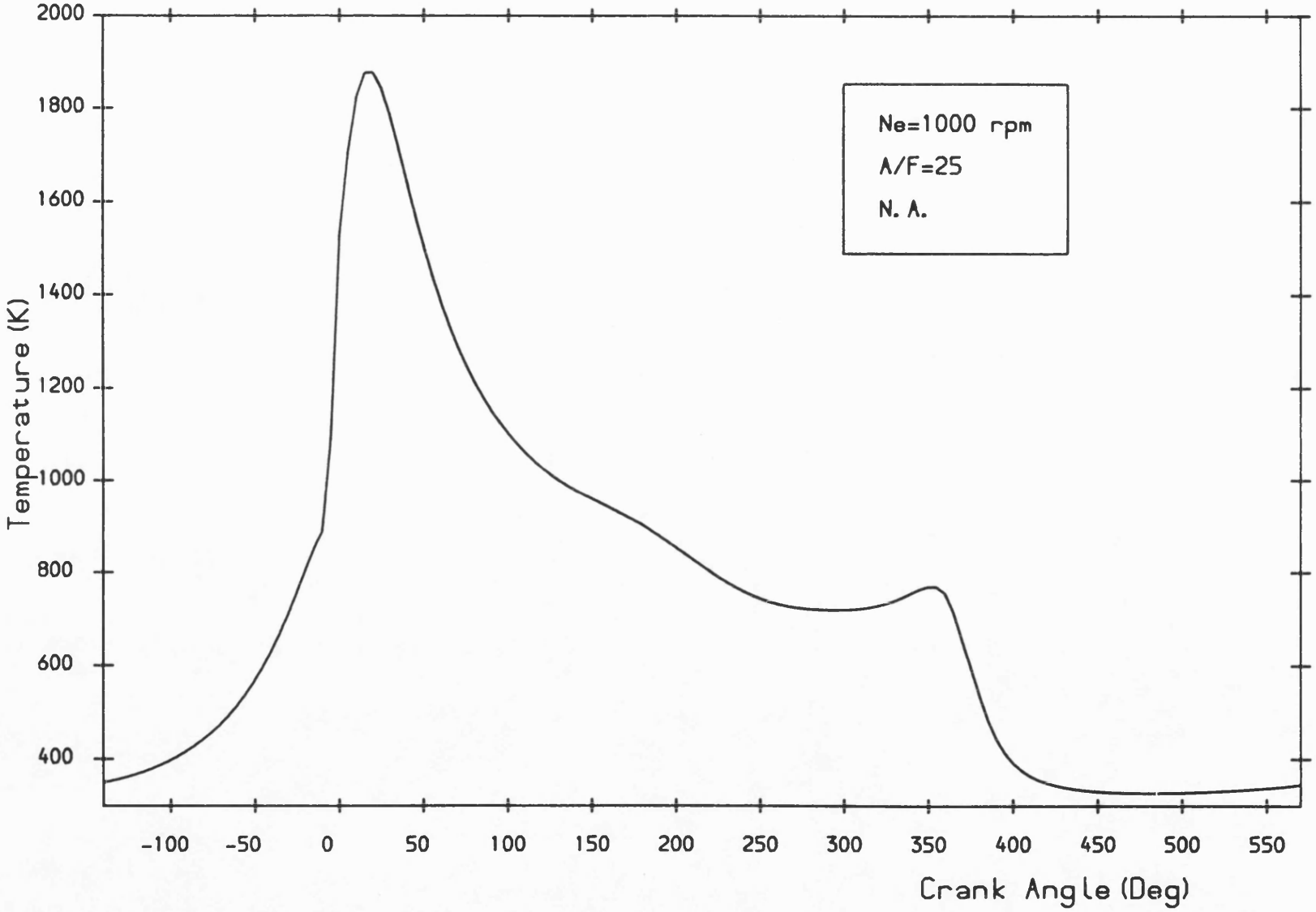

Fig. 5. 11 Cylinder gas temperature versus crank angle.

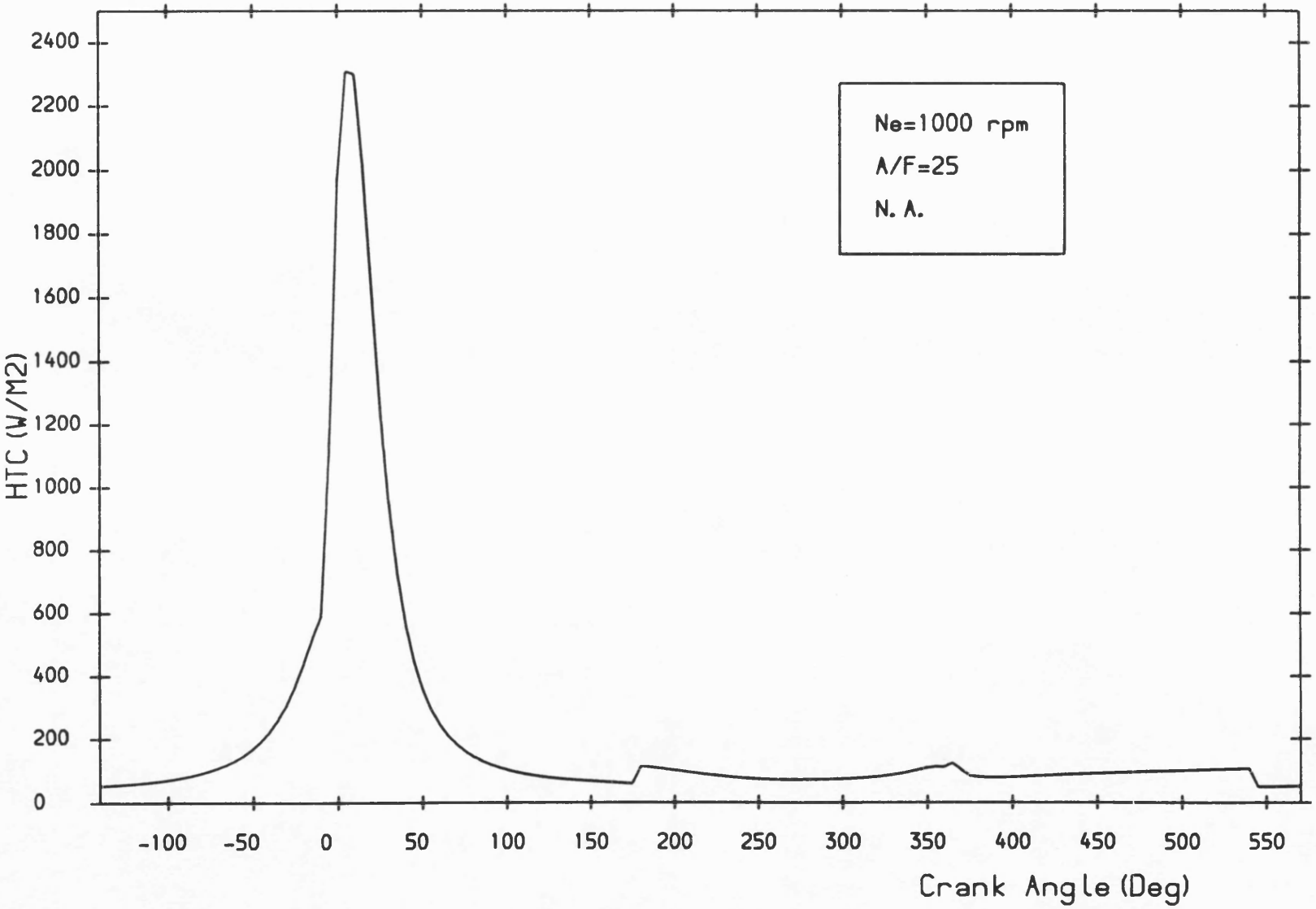

Fig. 5. 12 Gas heat transfer coefficient versus crank angle.

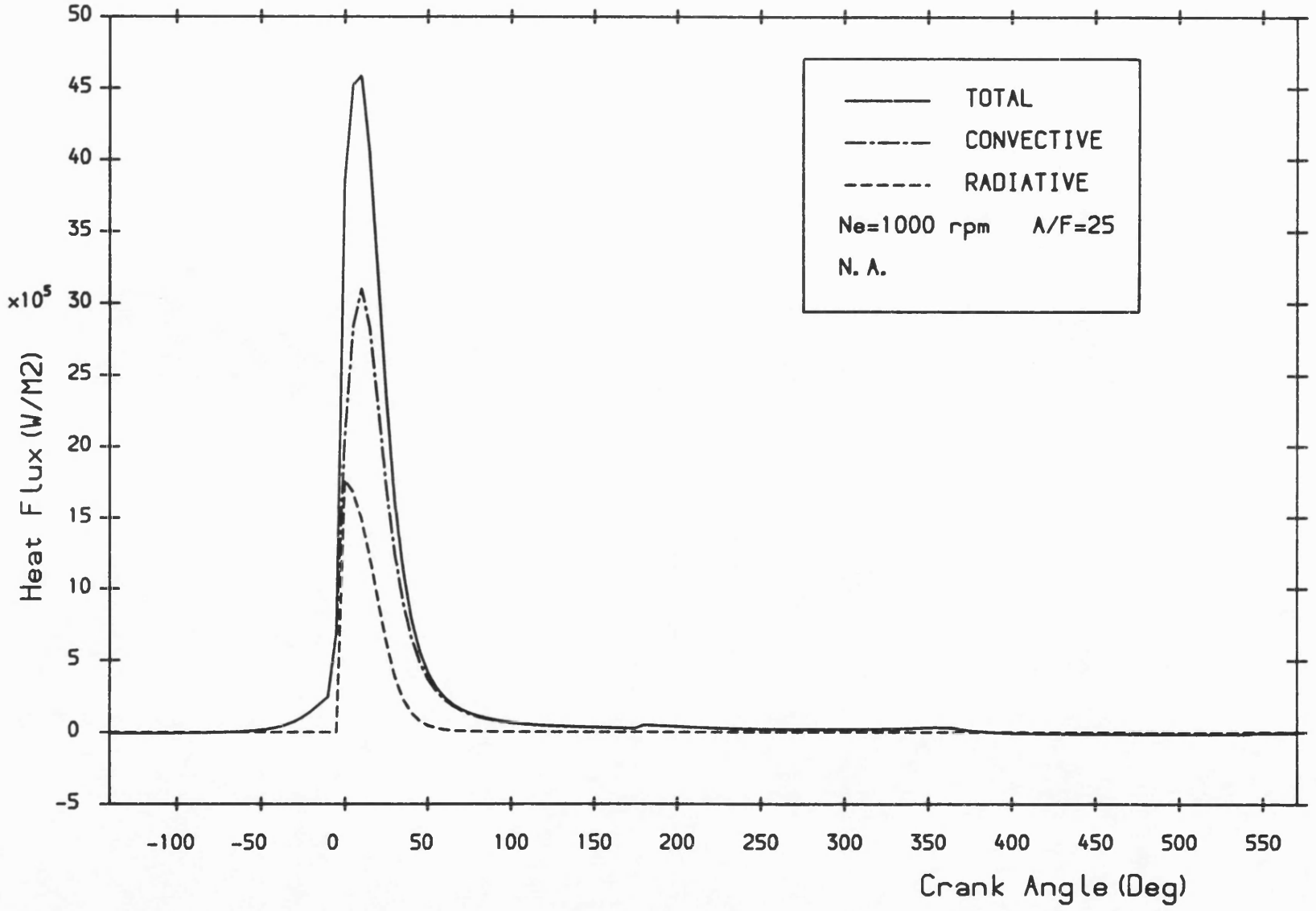

Fig. 5. 13 Radiative, convective and total heat flux at the piston surface versus crank angle.

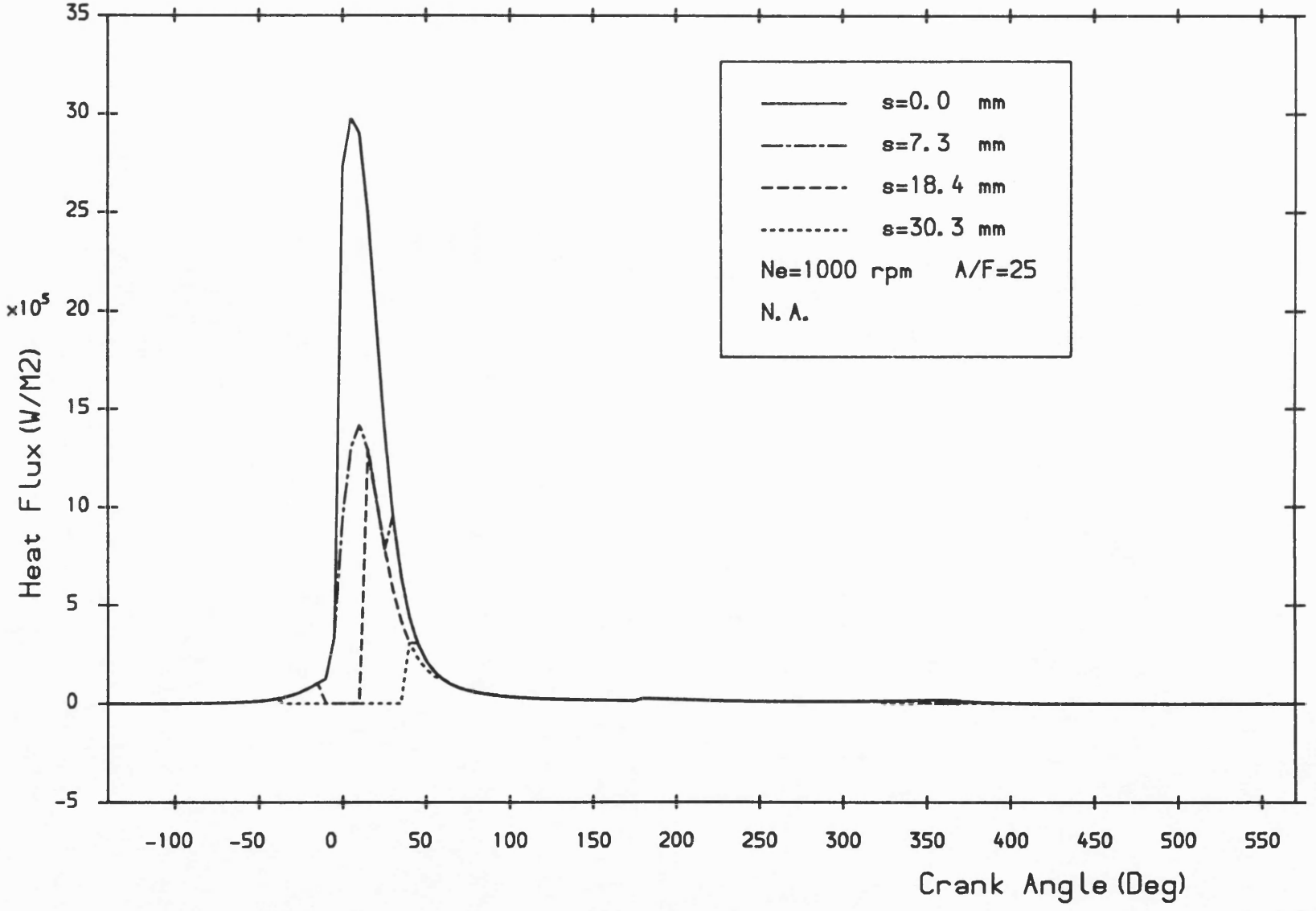

Fig. 5.14 Convective plus radiative heat flux at various positions on the liner surface versus crank angle.

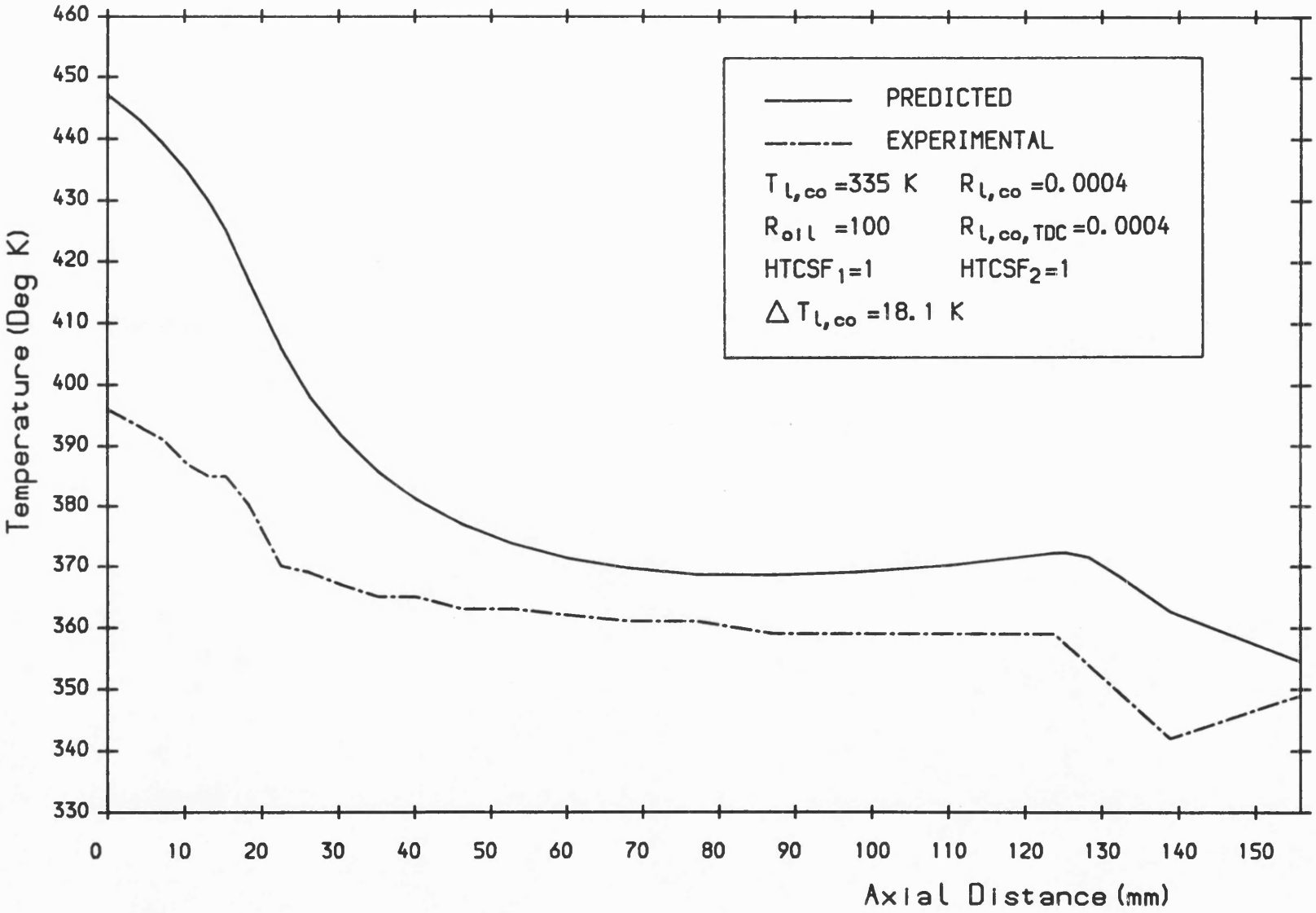

Fig. 5.15 Theoretical and experimental liner mean cycle surface temperatures versus axial distance.

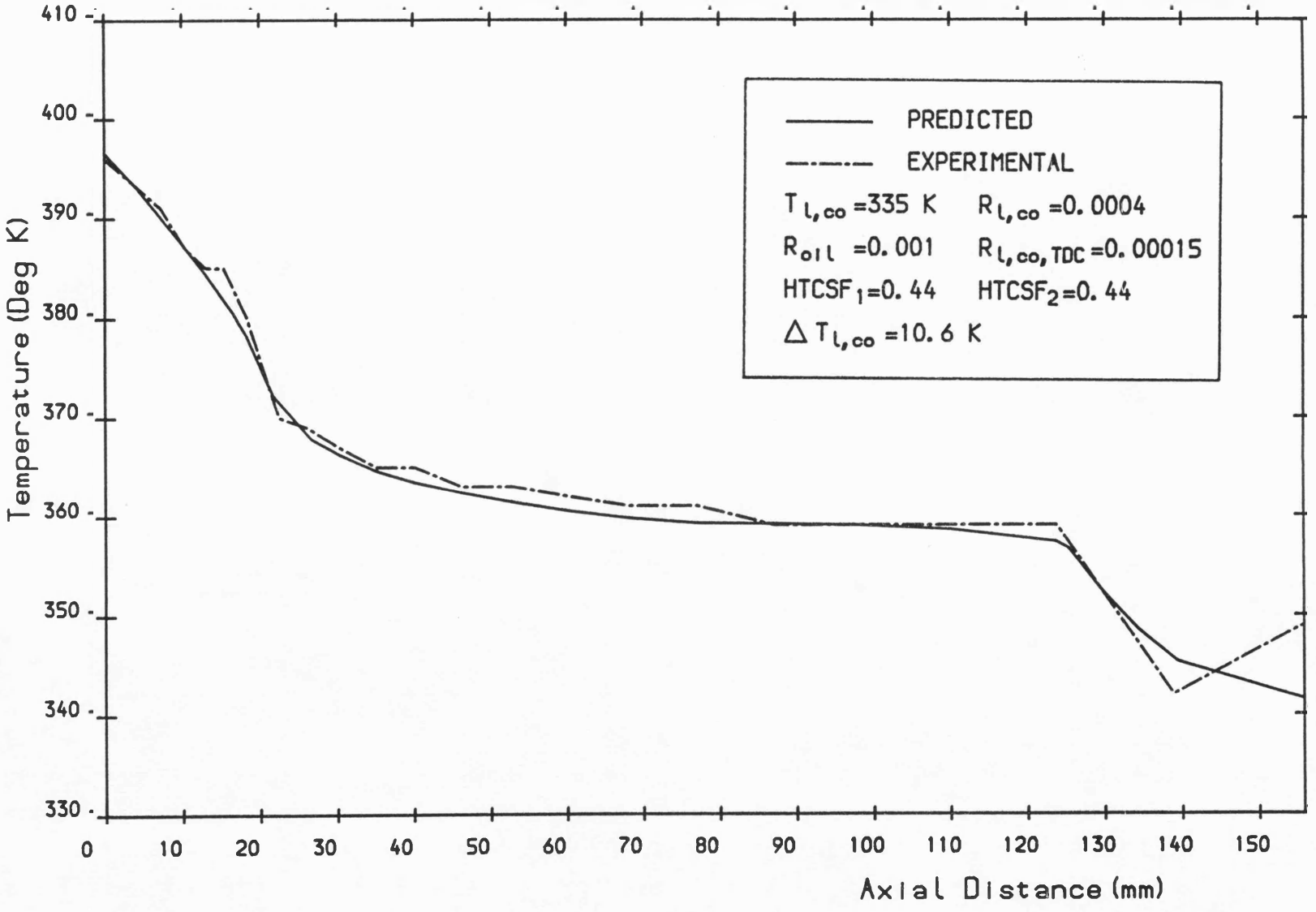

Fig. 5.16 Modified theoretical and experimental liner mean cycle surface temperatures versus axial distance.

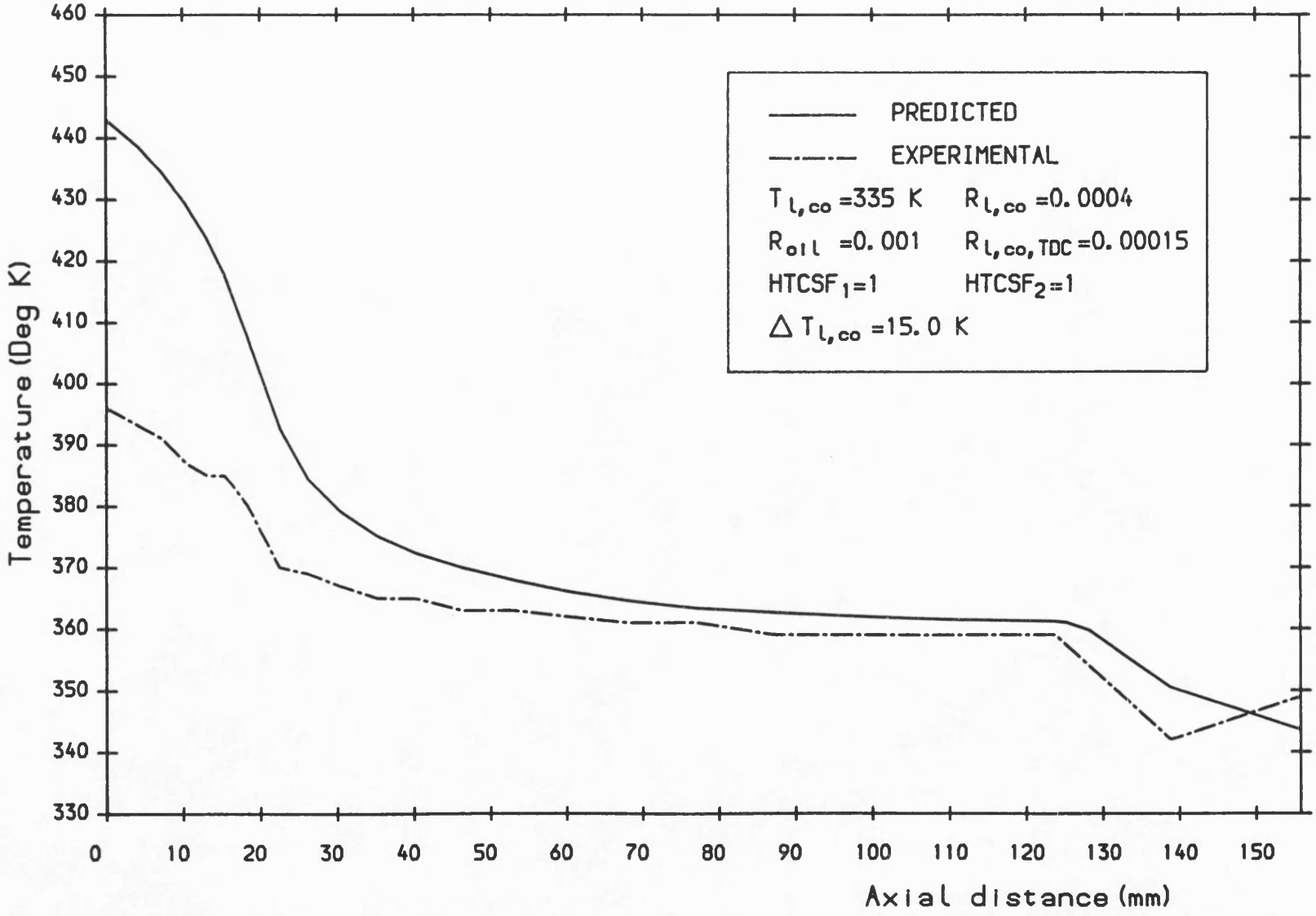

Fig. 5.17 The effect of htc scaling factors on the liner surface temperature distribution.

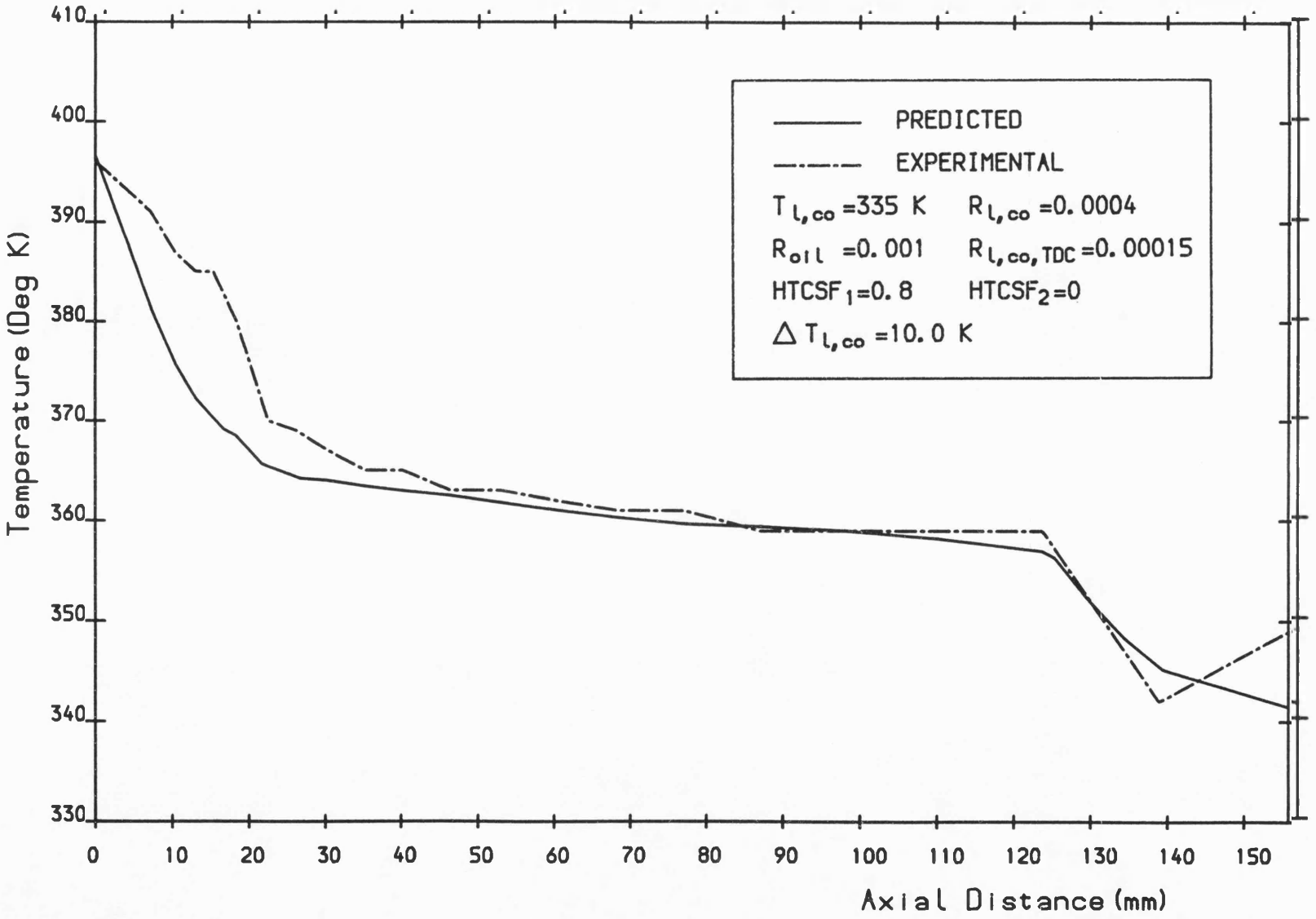

Fig. 5.18 Liner surface temperature distribution obtained without heat transfer from combustion gases between piston skirt and liner.

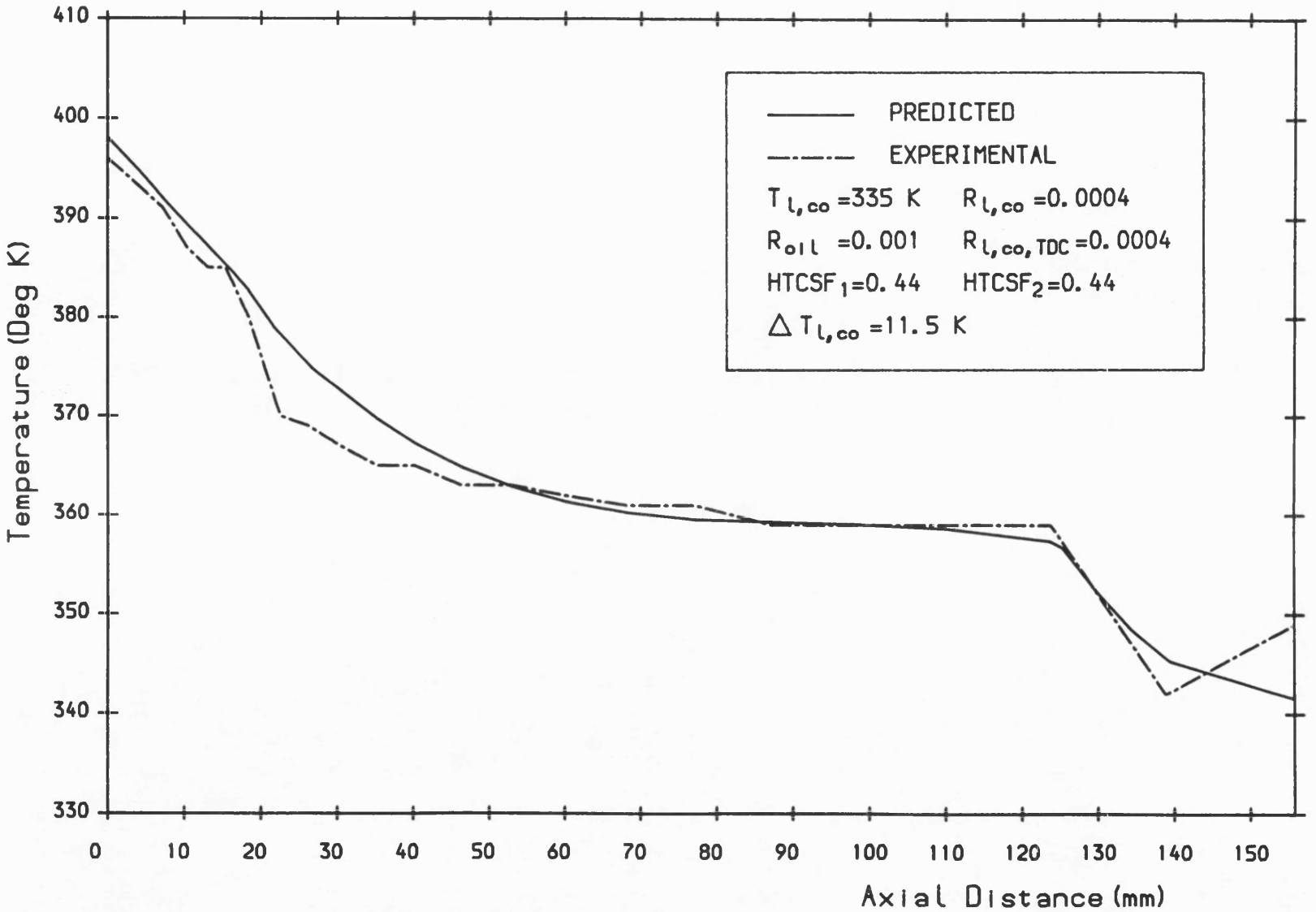

Fig. 5.19 The effect of the oil evaporation term on the liner surface temperture distribution.

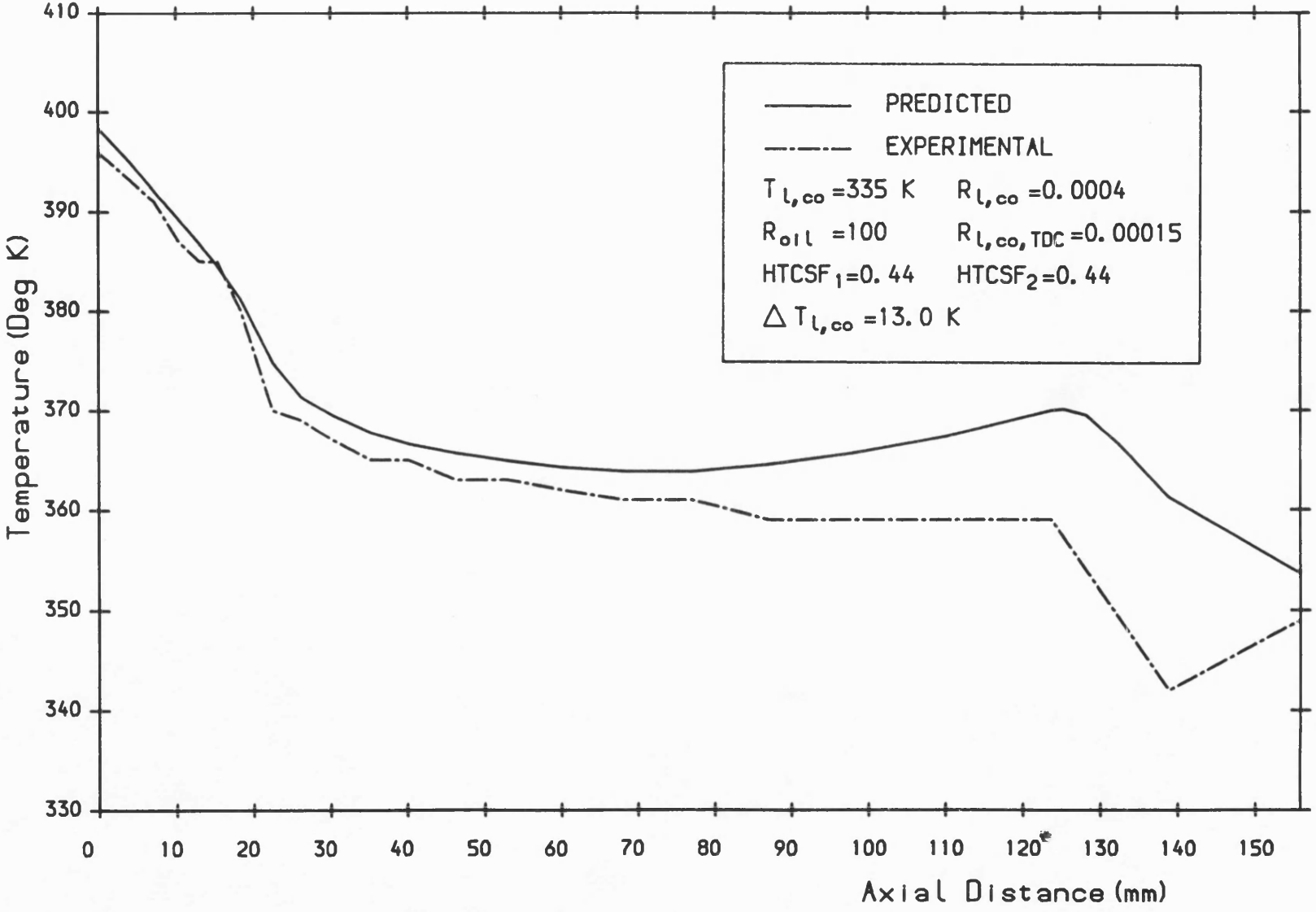

Fig. 5.20 The effect of the oil cooling term on the liner surface temperature distribution.

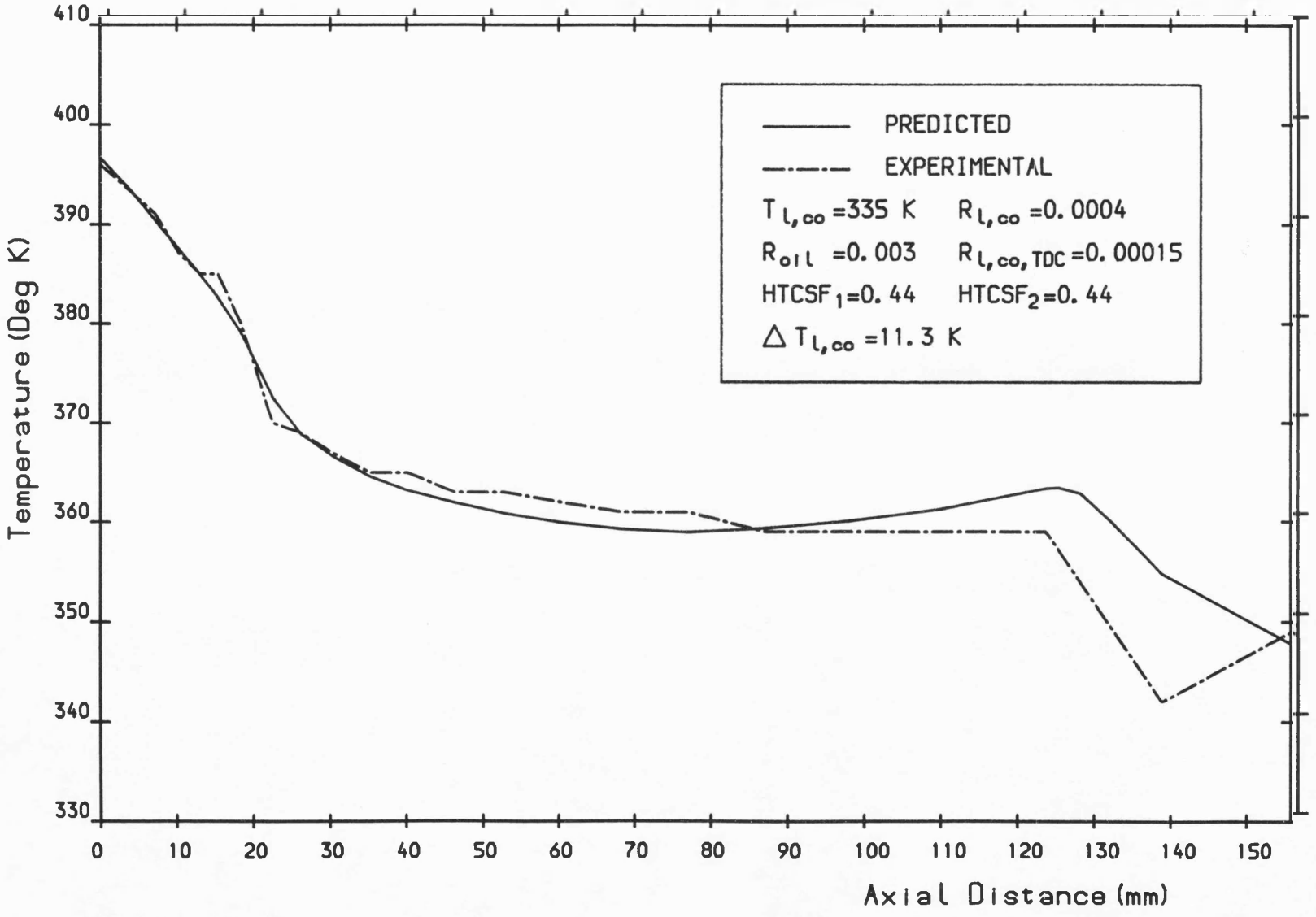

Fig. 5.21 Liner surface temperature distribution obtained with a linear oil cooling term.

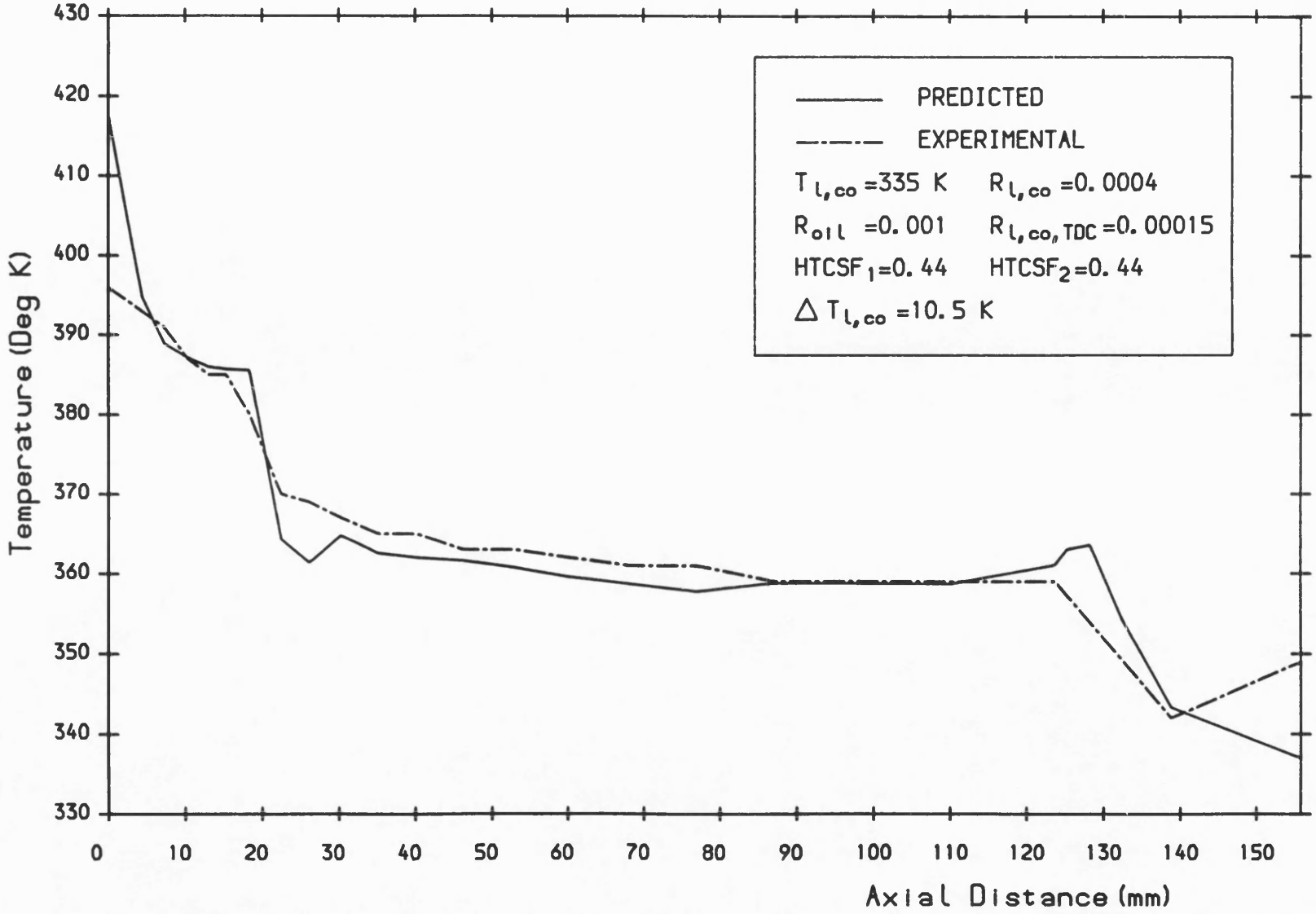

Fig. 5.22 Liner surface temperature distribution obtained with thermal resistances only in the radial direction.

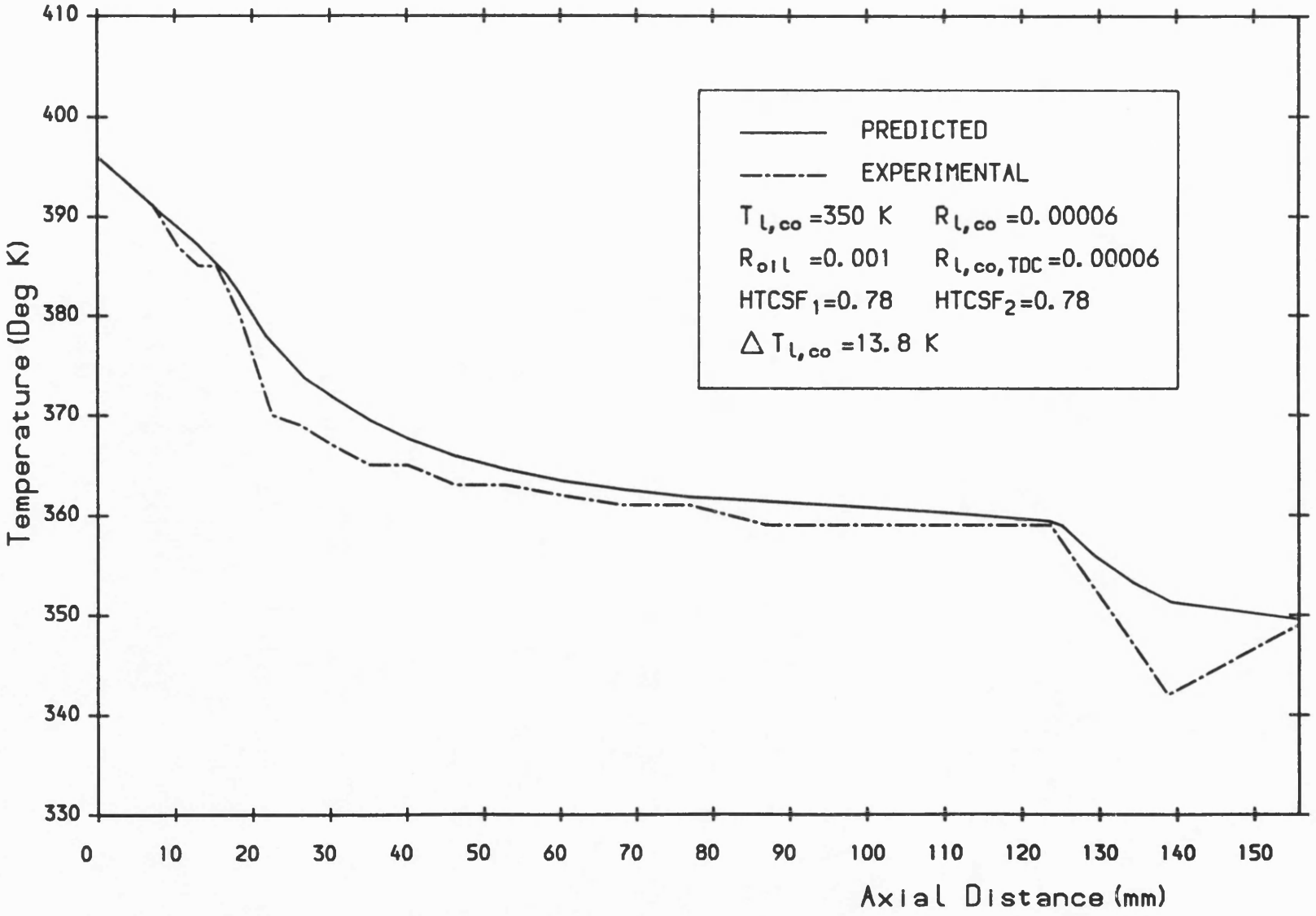

Fig. 5.23 Liner surface temperature distribution obtained by using high coolant htc and temperature.

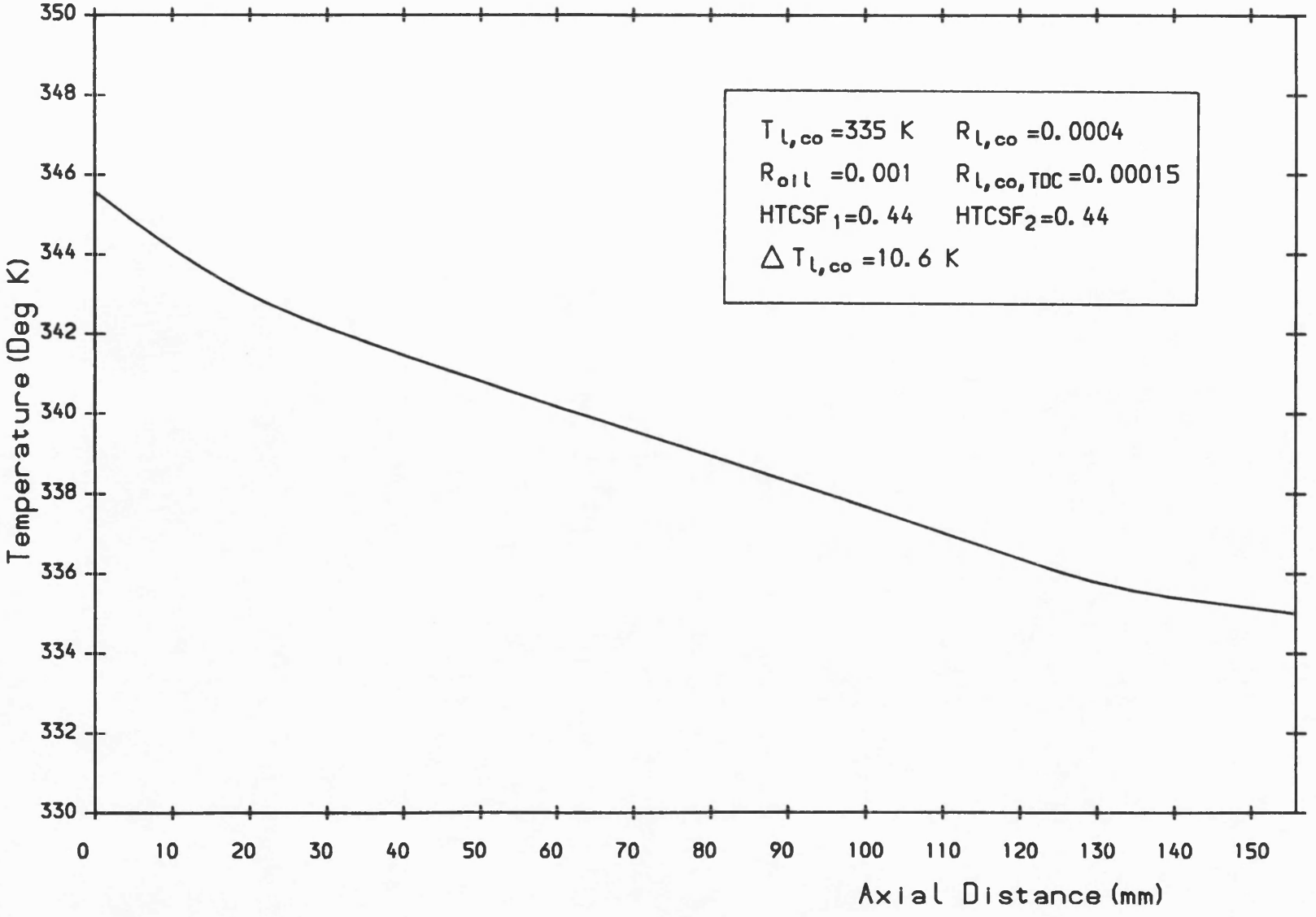

Fig. 5.24 Liner coolant temperature versus axial distance.

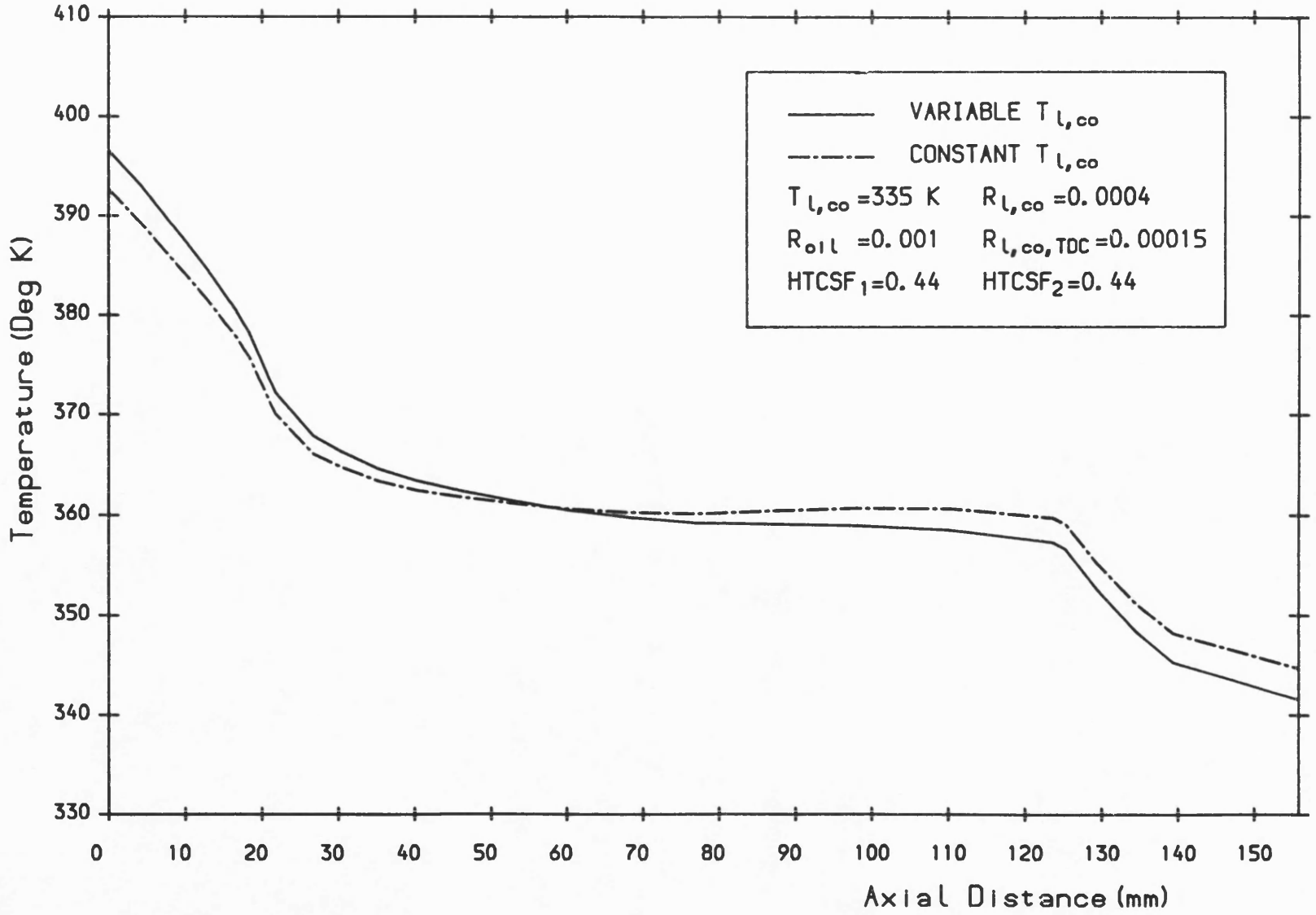

Fig. 5.25 Liner surface temperature distributions obtained with constant and variable coolant temperatures.

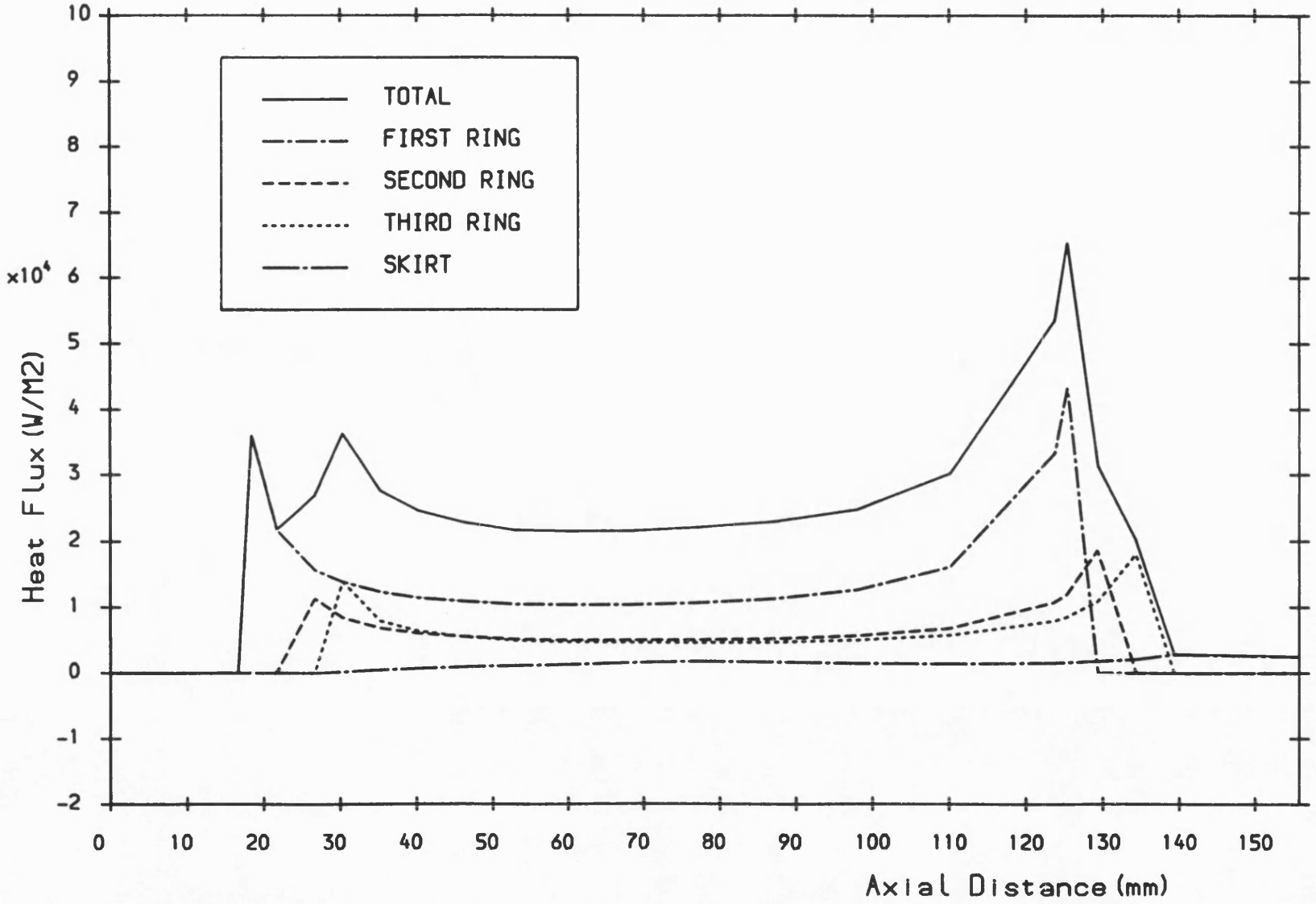

Fig. 5.26 Piston-liner mean cycle conduction heat flux and its components versus axial distance.

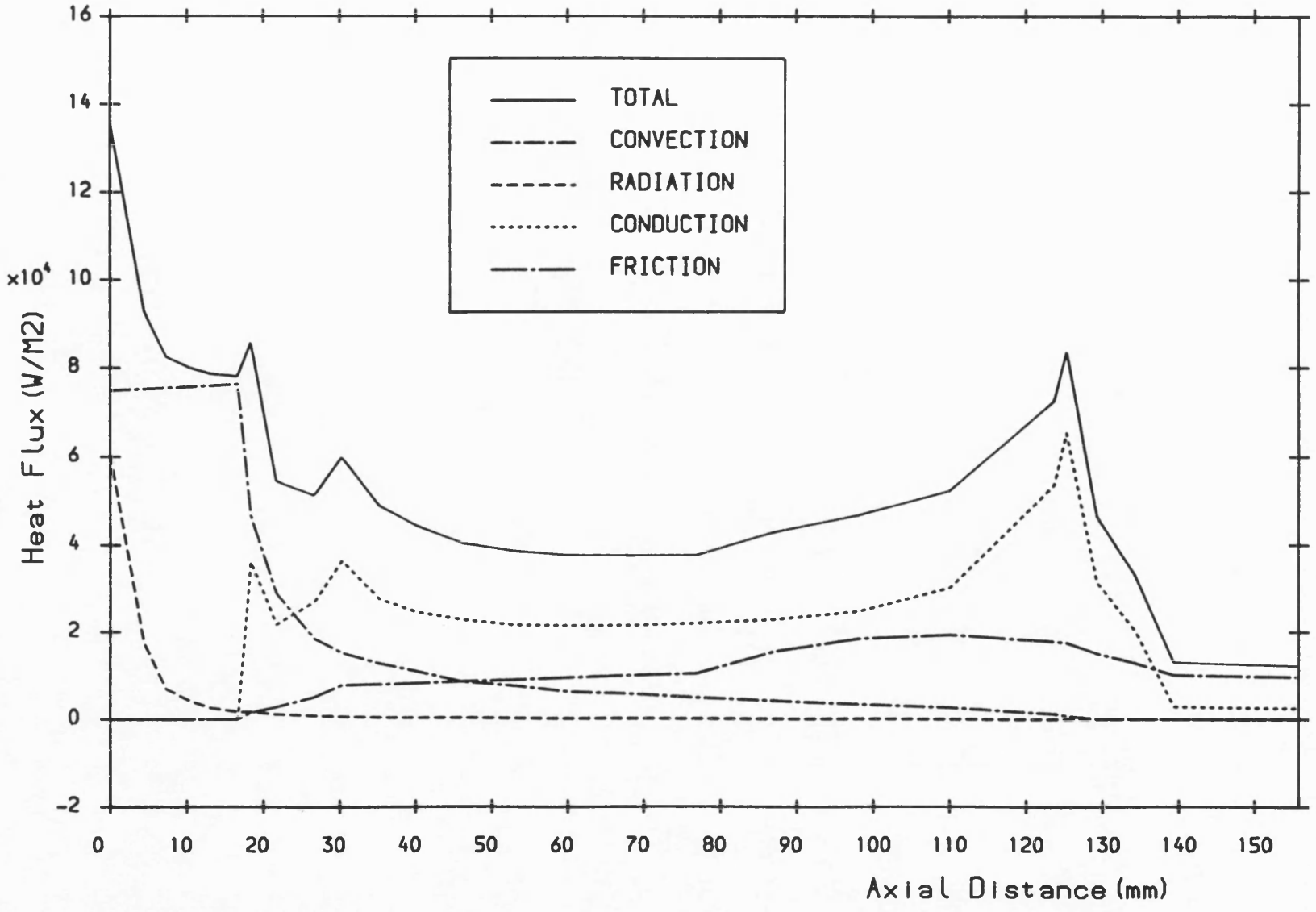

Fig. 5.27 Liner mean cycle heat flux and its components versus axial distance.

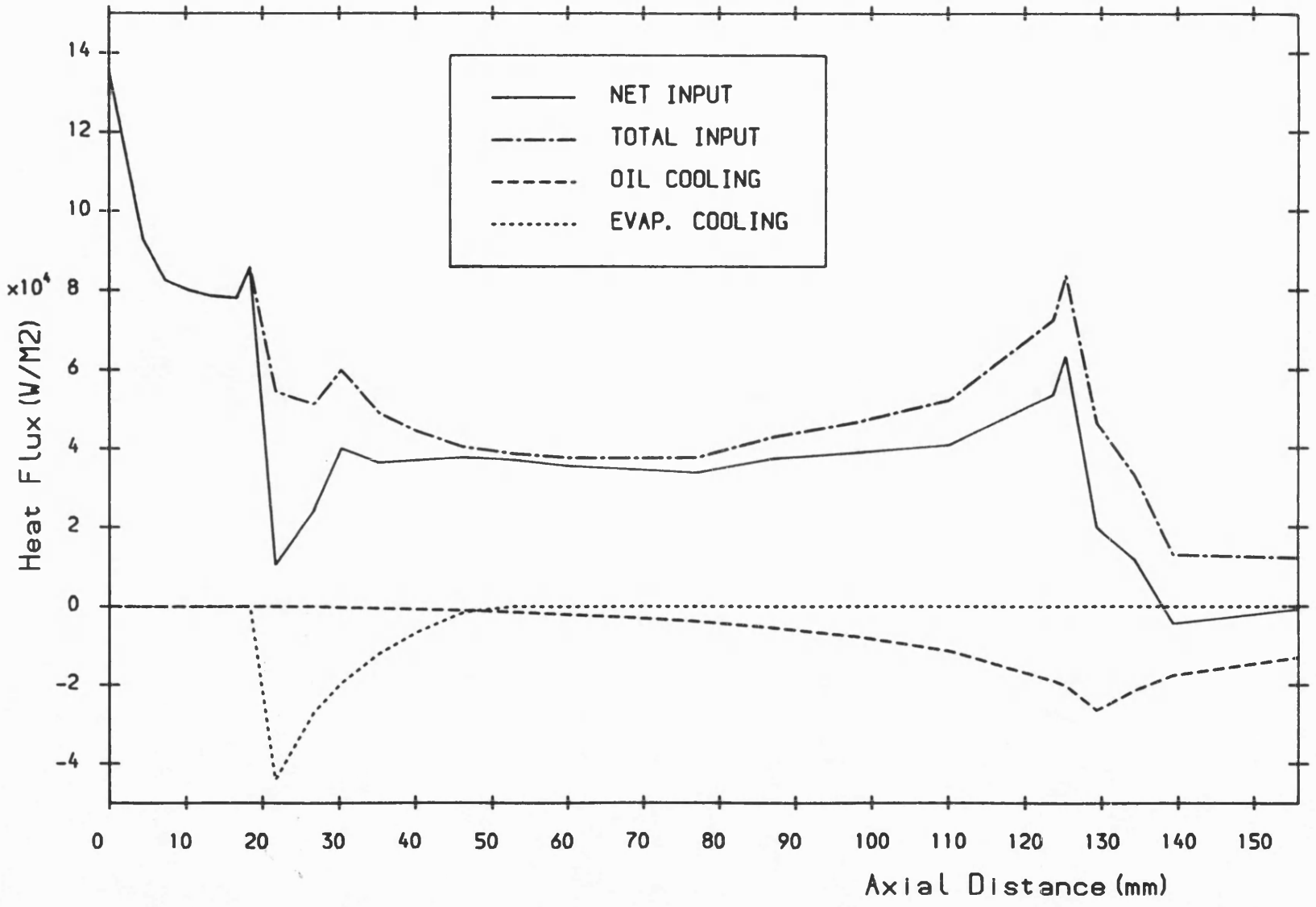

Fig. 5.28 Total, oil cooling, evaporative cooling and net heat flux conducted through the liner versus axial distance.

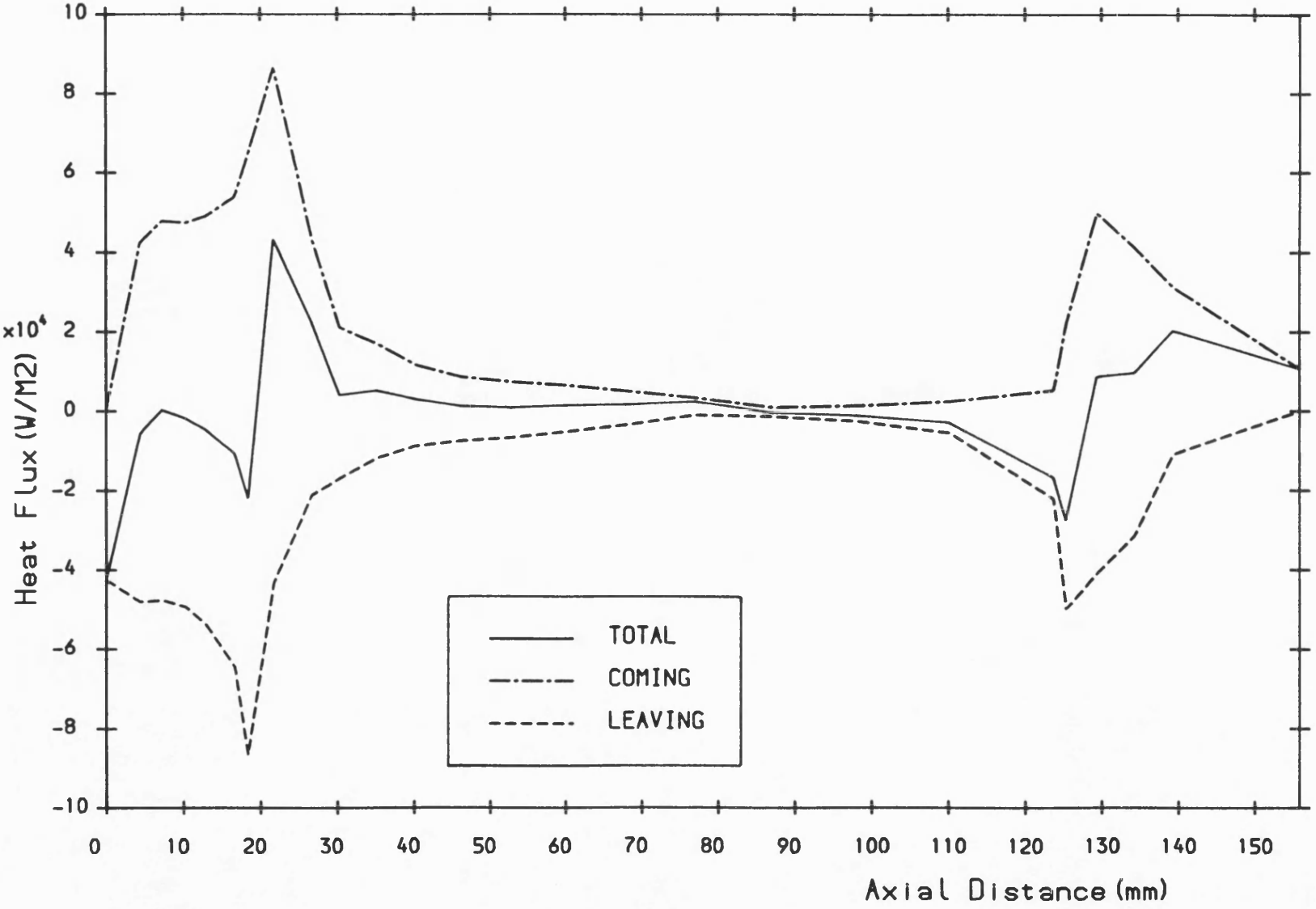

Fig. 5.29 The axial heat flux arriving at and leaving the liner nodes and their difference, which is conducted in radial direction.

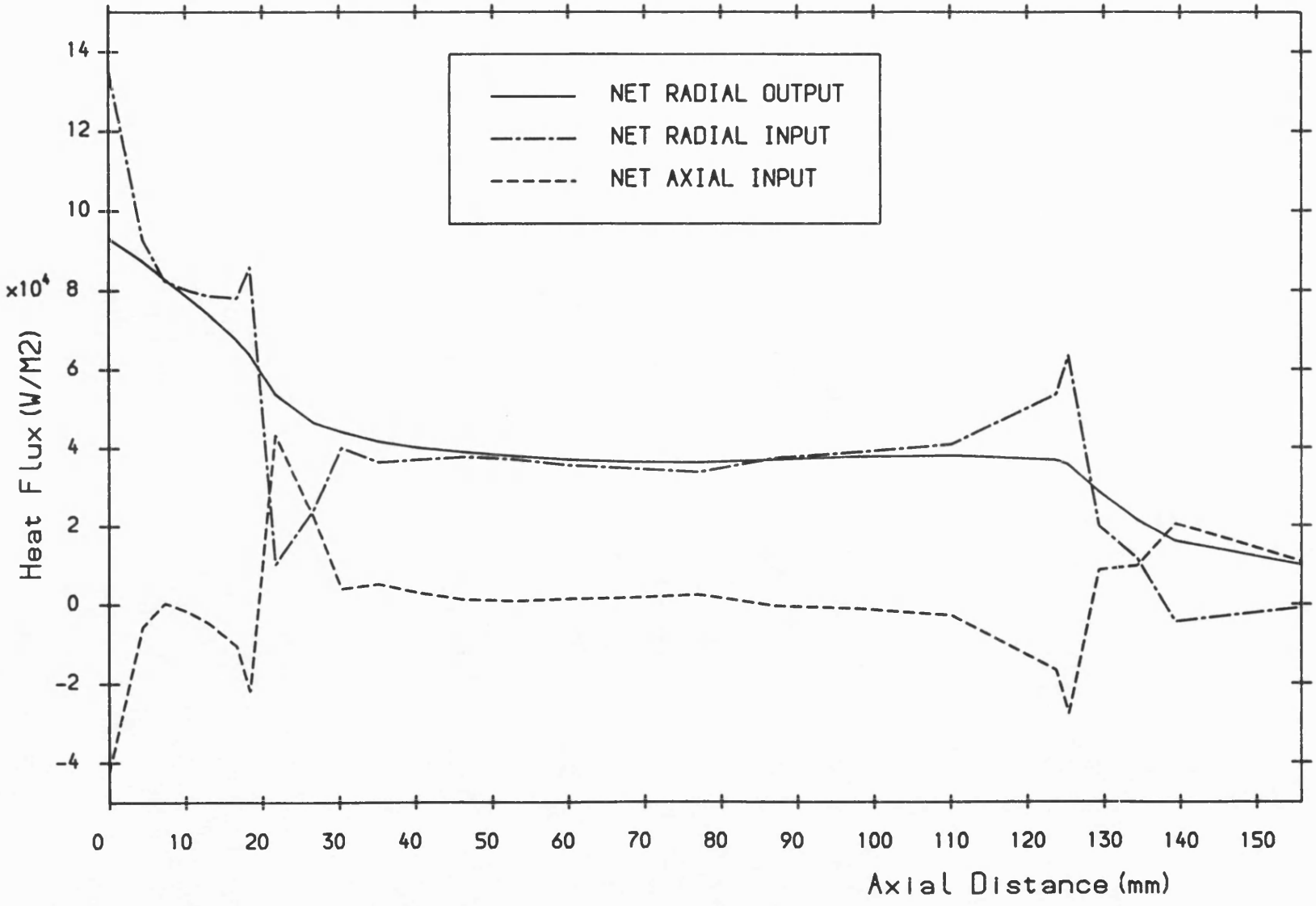

Fig. 5.30 The net radial and axial input heat fluxes at the liner nodes and their summation, which is conducted to the coolant.

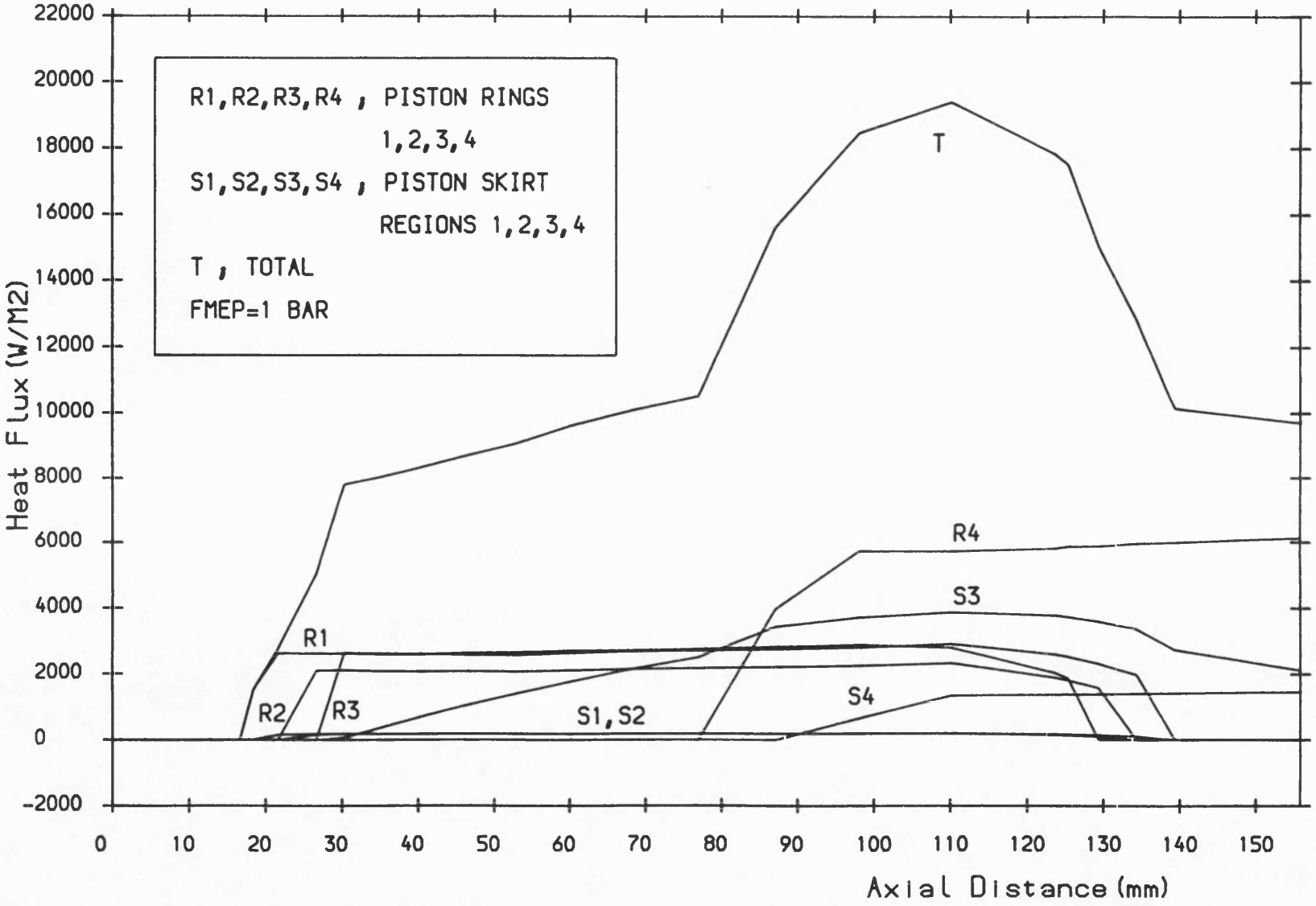

Fig. 5.31 Friction generated mean cycle heat flux and its components versus axial distance.

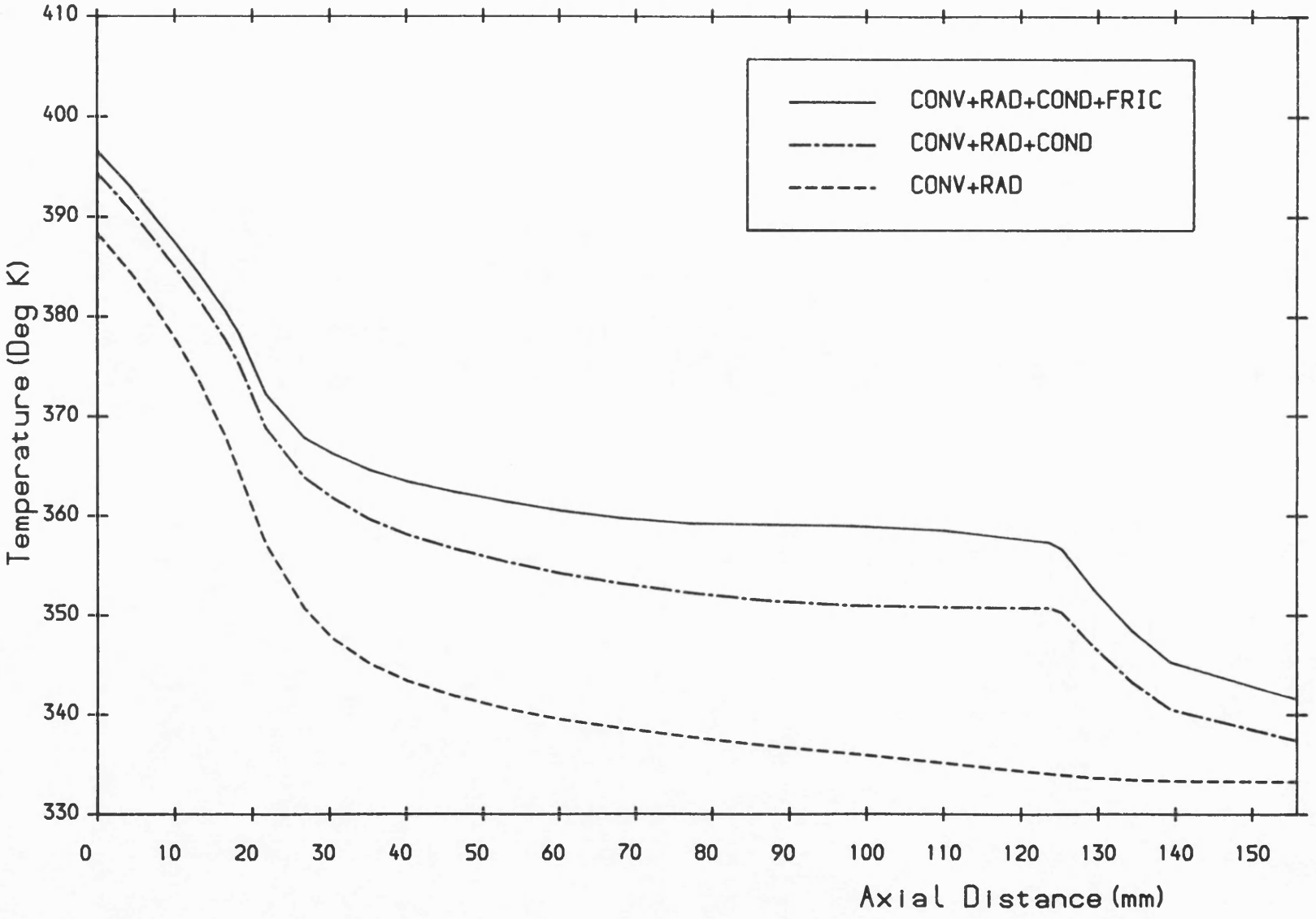

Fig. 5.32 Liner surface temperature versus axial distance with various gas side boundary conditions.

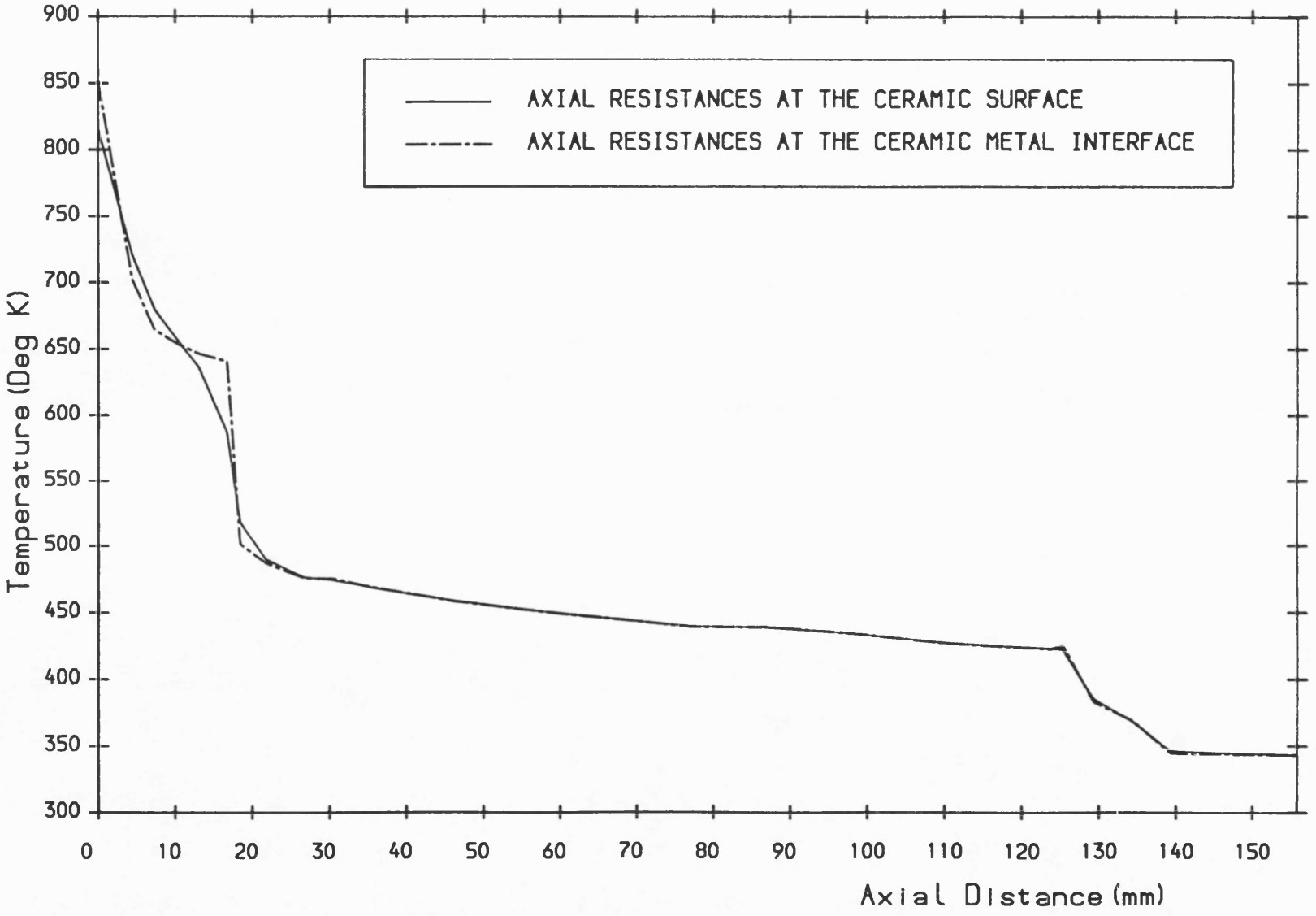

Fig. 5.33 The effect of axial resistance position on liner surface temperature distribution.

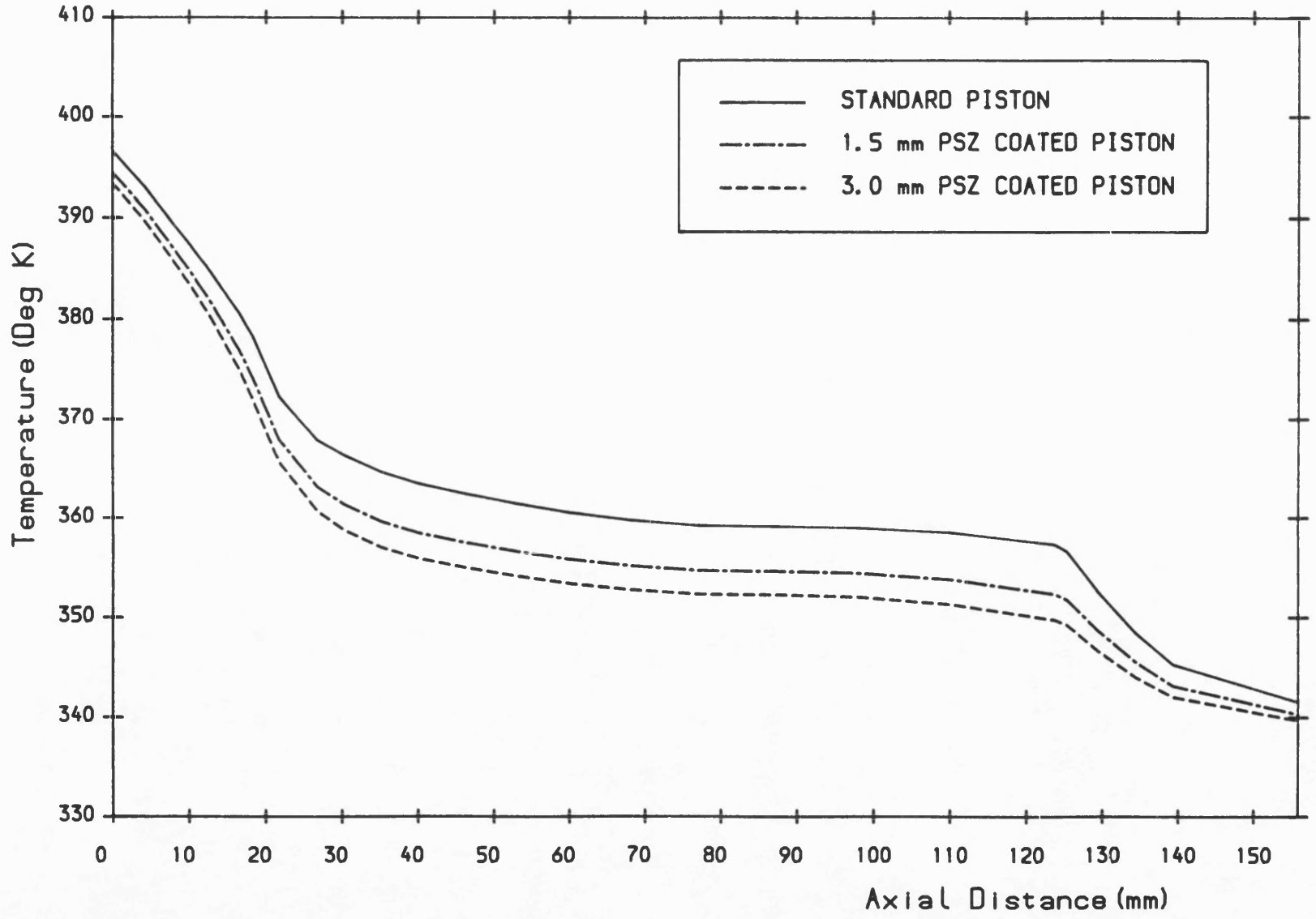

Fig. 5.34 The effect of piston insulation on liner surface temperature distribution.

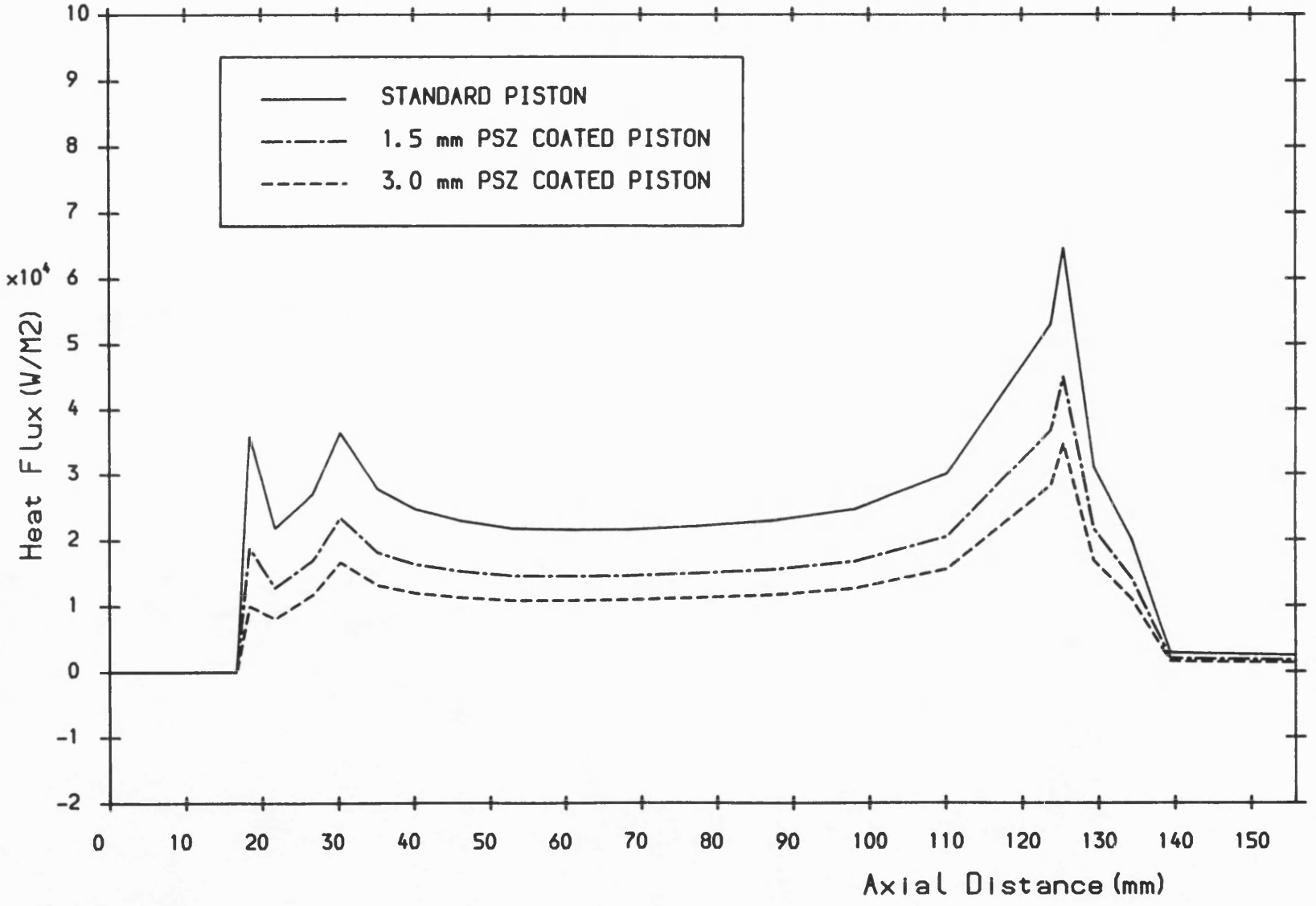

Fig. 5.35 The effect of piston insulation on piston-liner conduction heat flux.

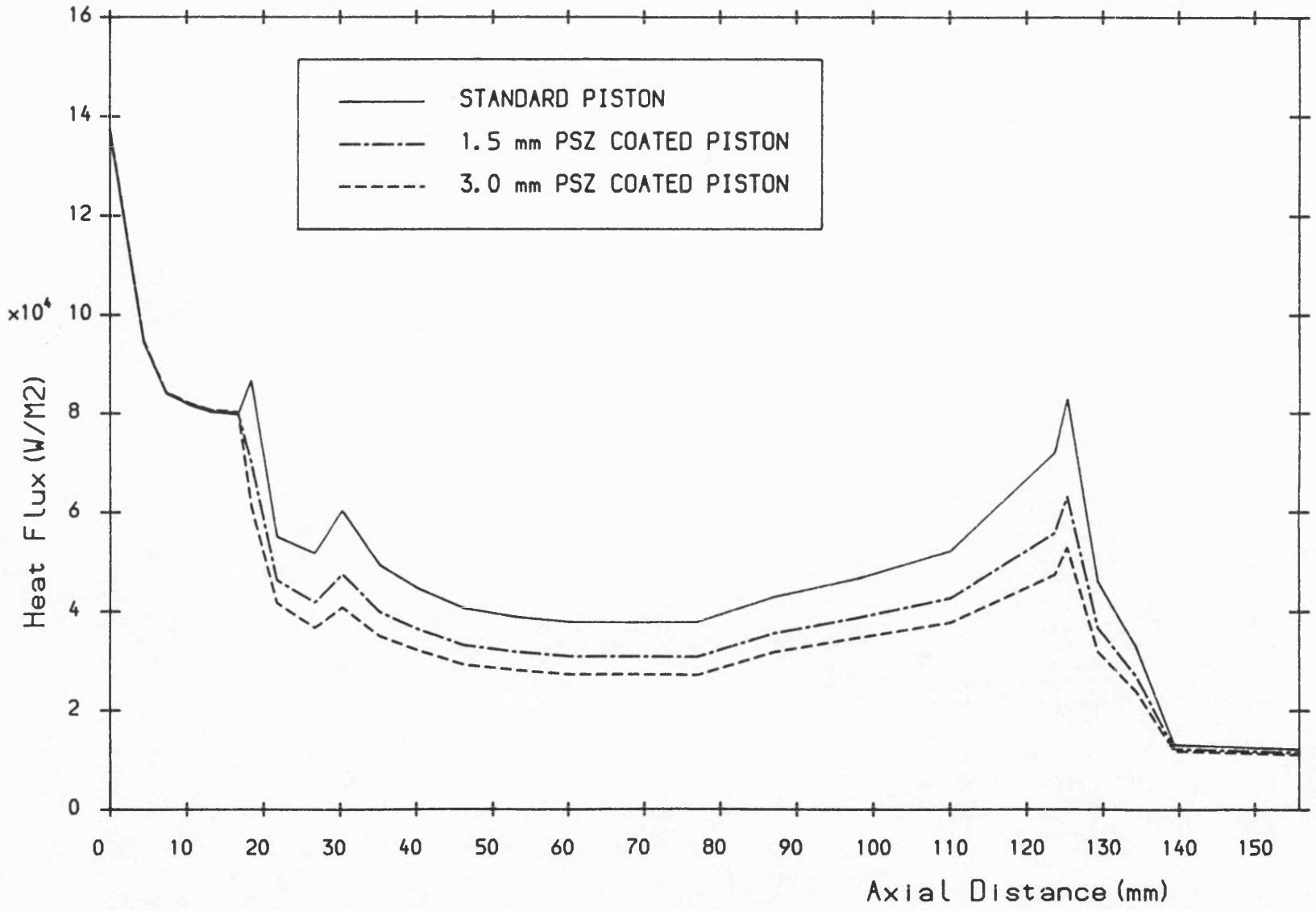

Fig. 5.36 The effect of piston insulation on the total liner heat flux distribution.

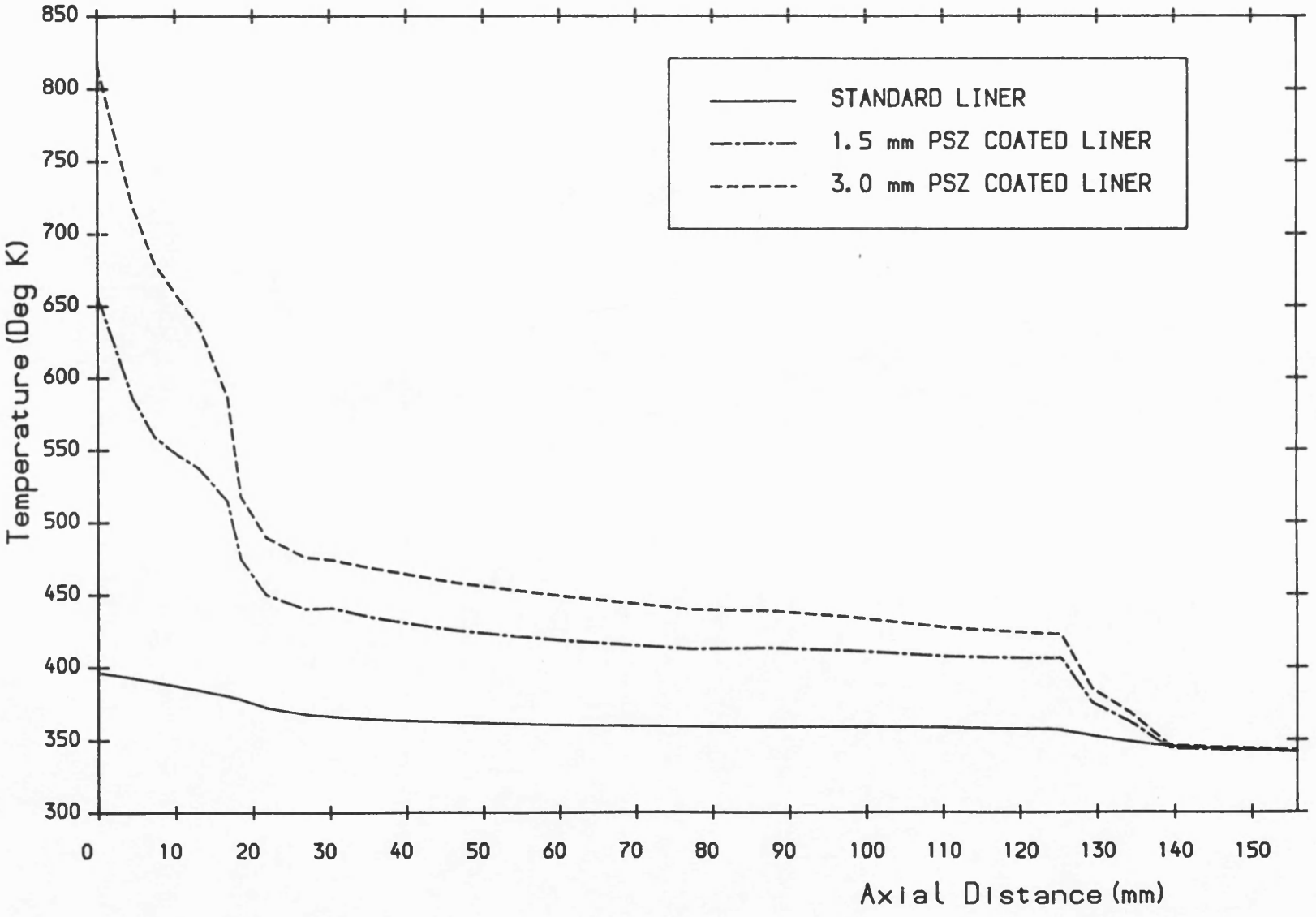

Fig. 5.37 The effect of liner insulation on liner surface temperature distribution.

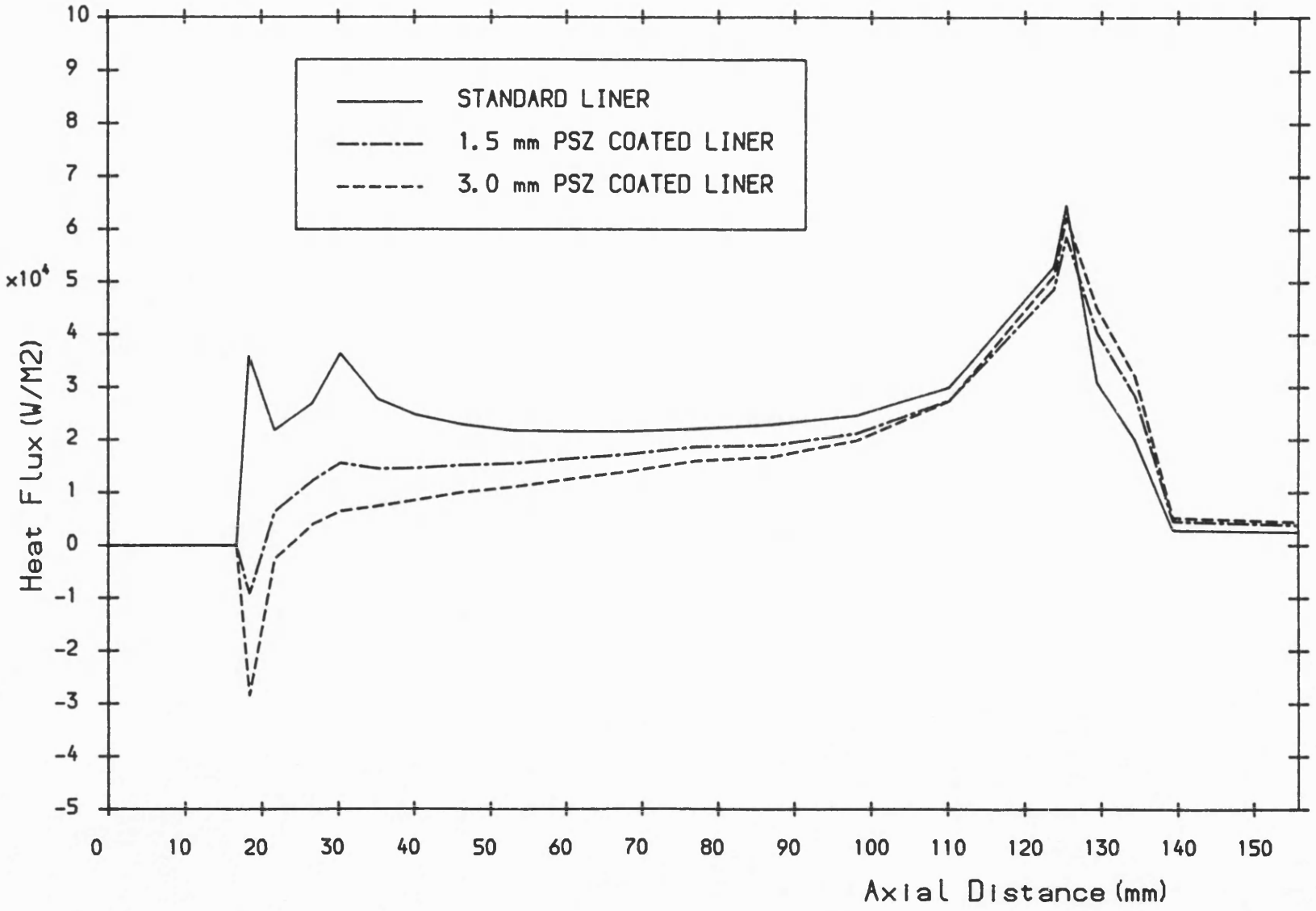

Fig. 5.38 The effect of liner insulation on piston-liner conduction heat flux distribution.

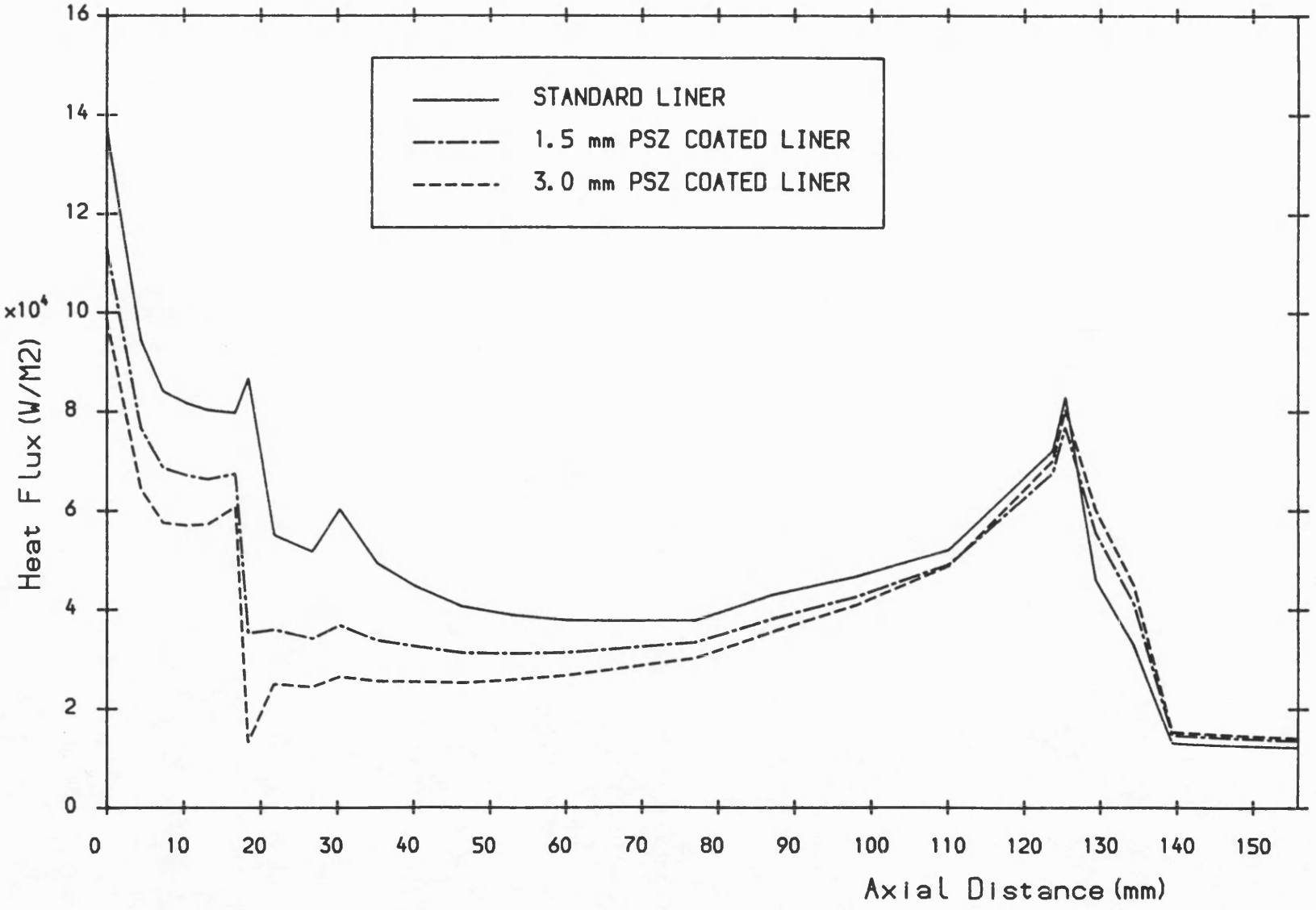

Fig. 5.39 The effect of liner insulation on total liner heat flux distribution.

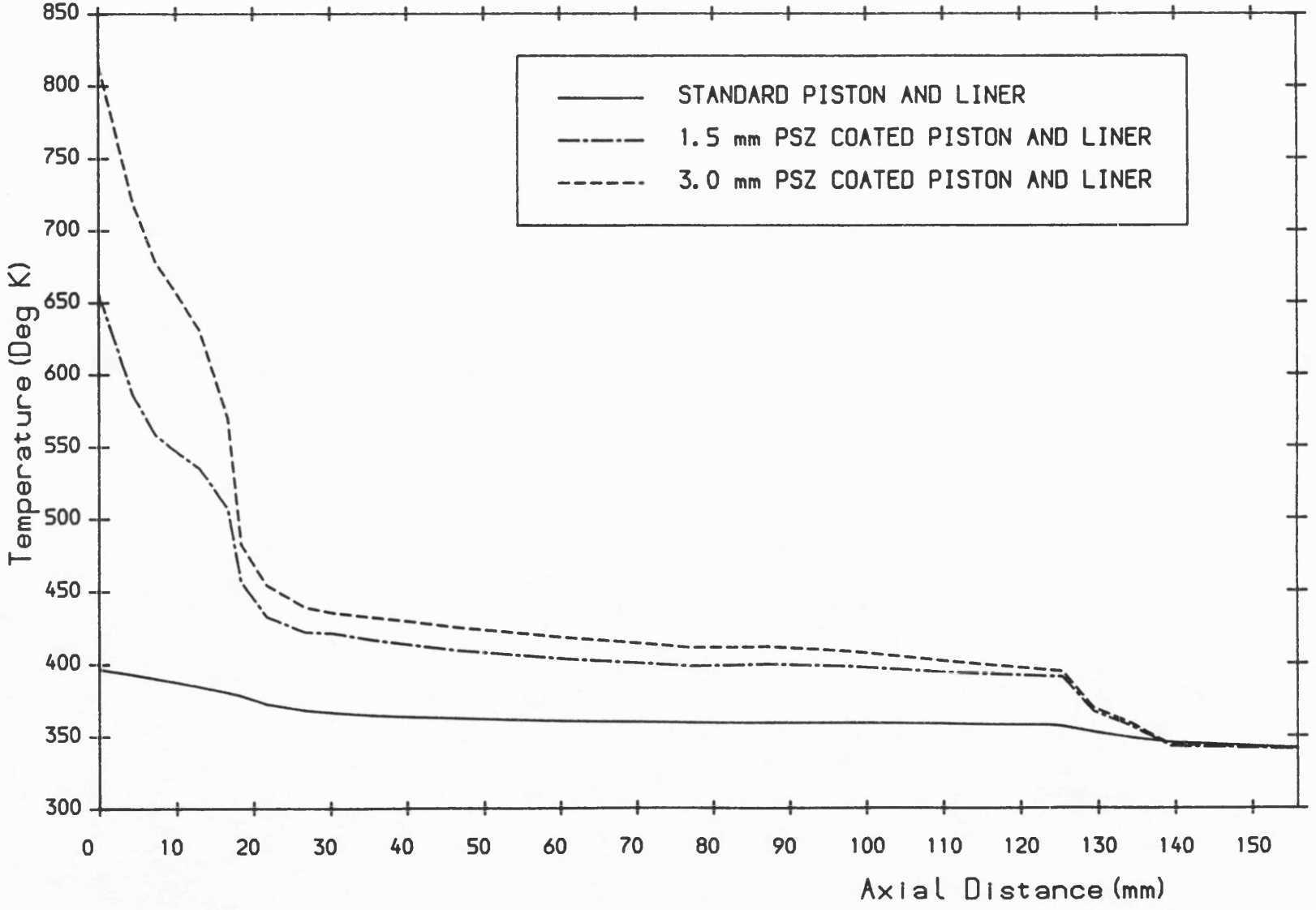

Fig. 5.40 The effect of piston and liner insulation on liner surface temperature distribution.

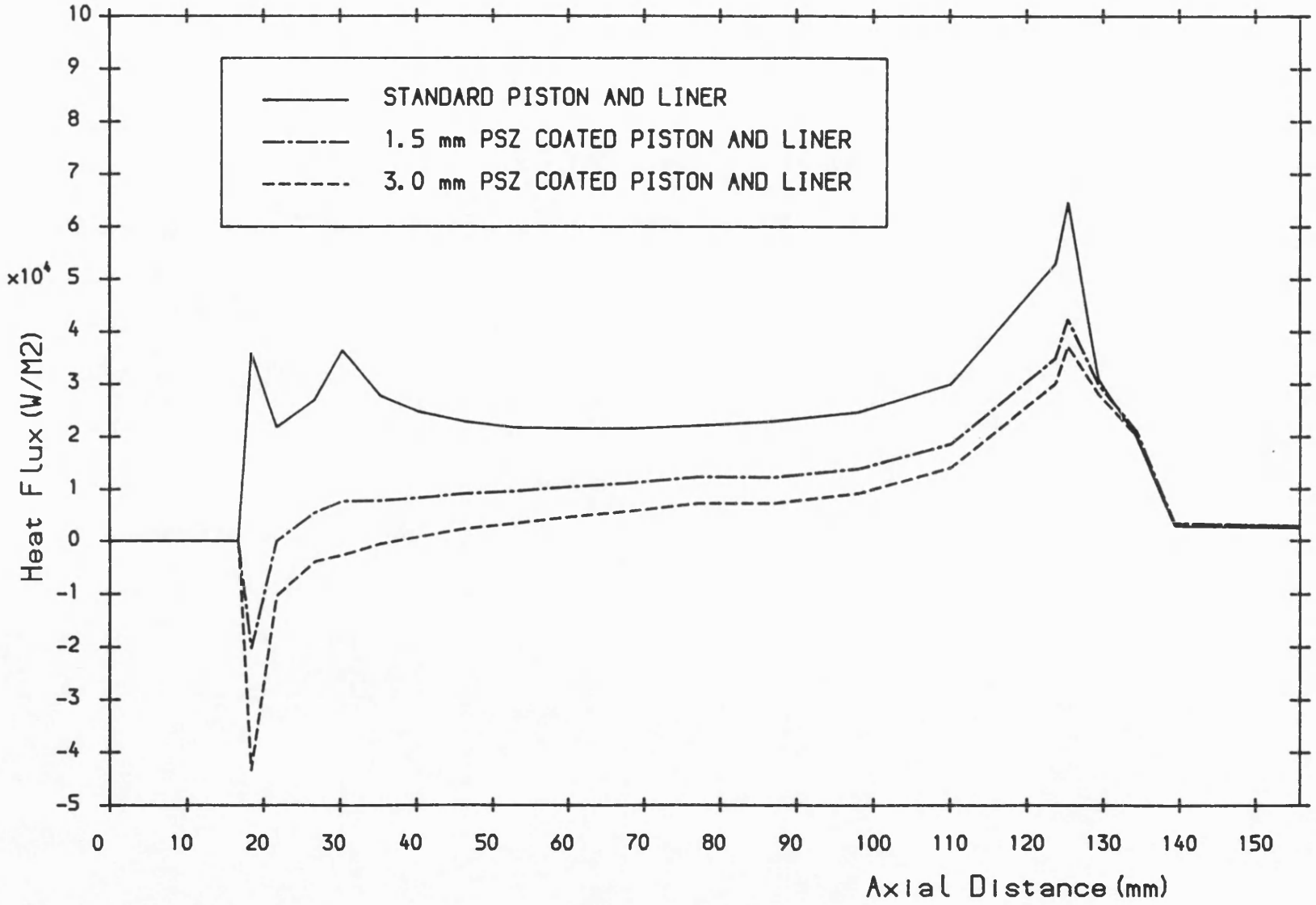

Fig. 5.41 The effect of piston and liner insulation on piston-liner conduction heat flux distribution.

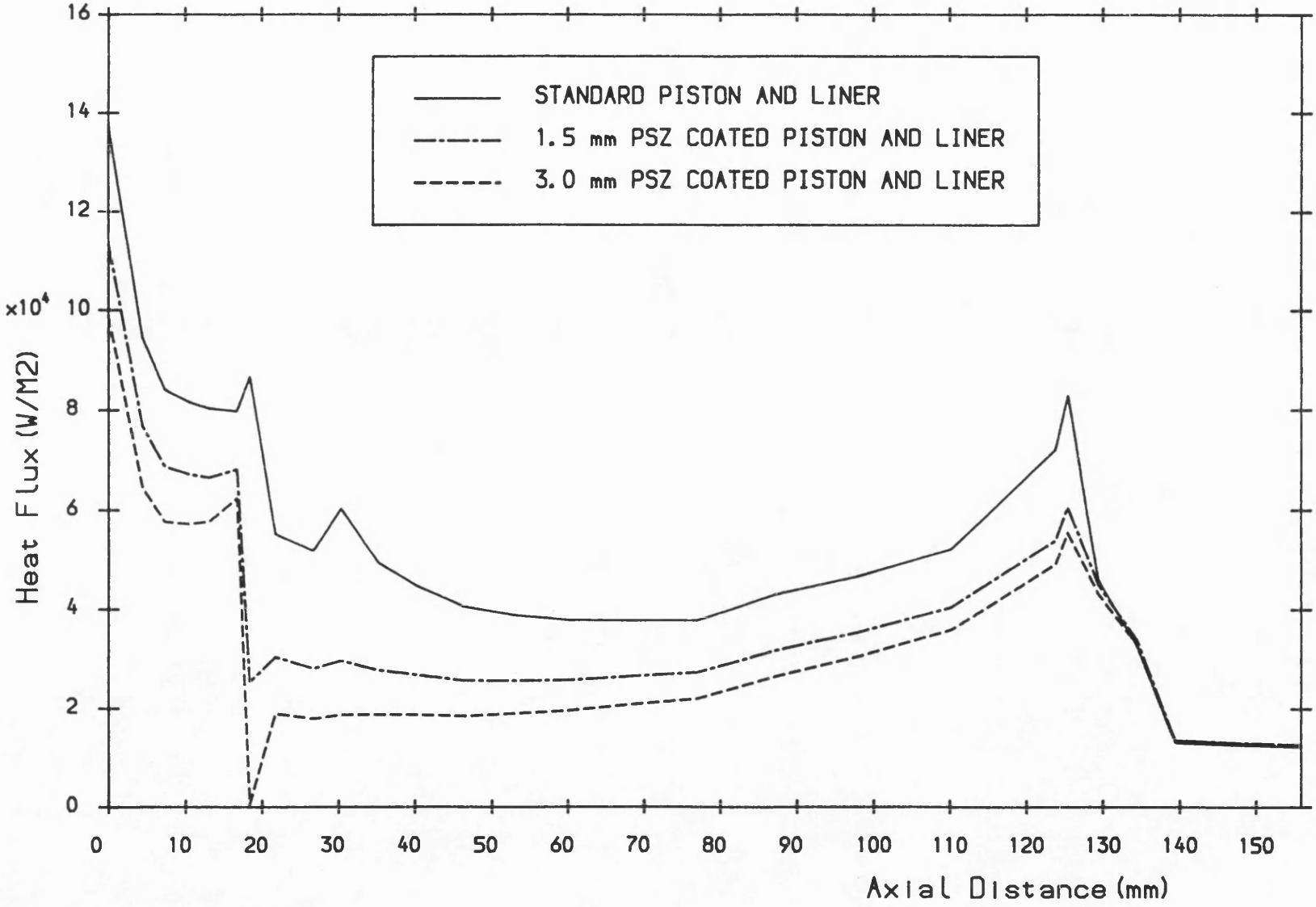

Fig. 5.42 The effect of piston and liner insulation on liner total heat flux distribution.

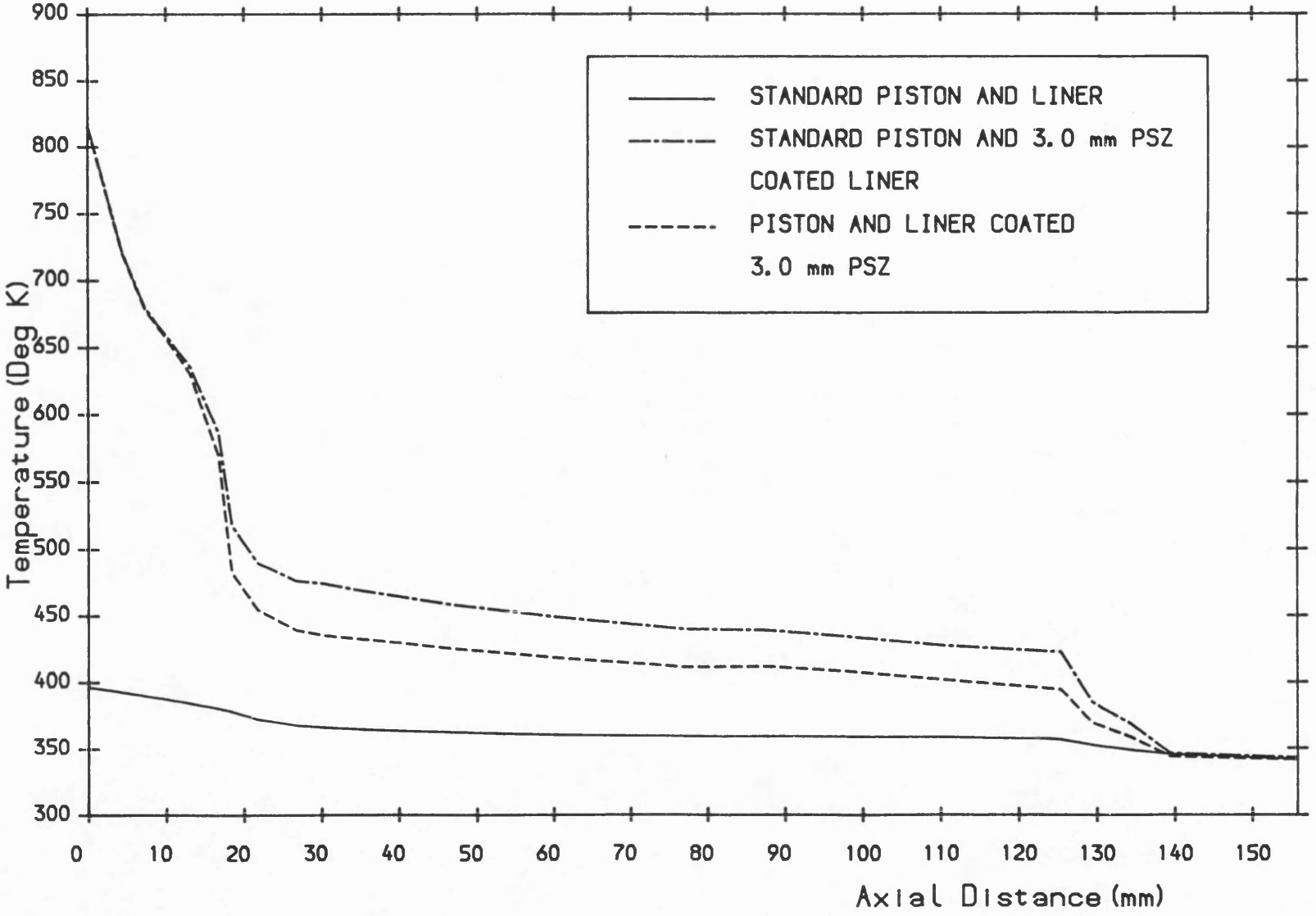

Fig. 5.43 The effect of liner and piston plus liner insulation on liner surface temperature distribution.

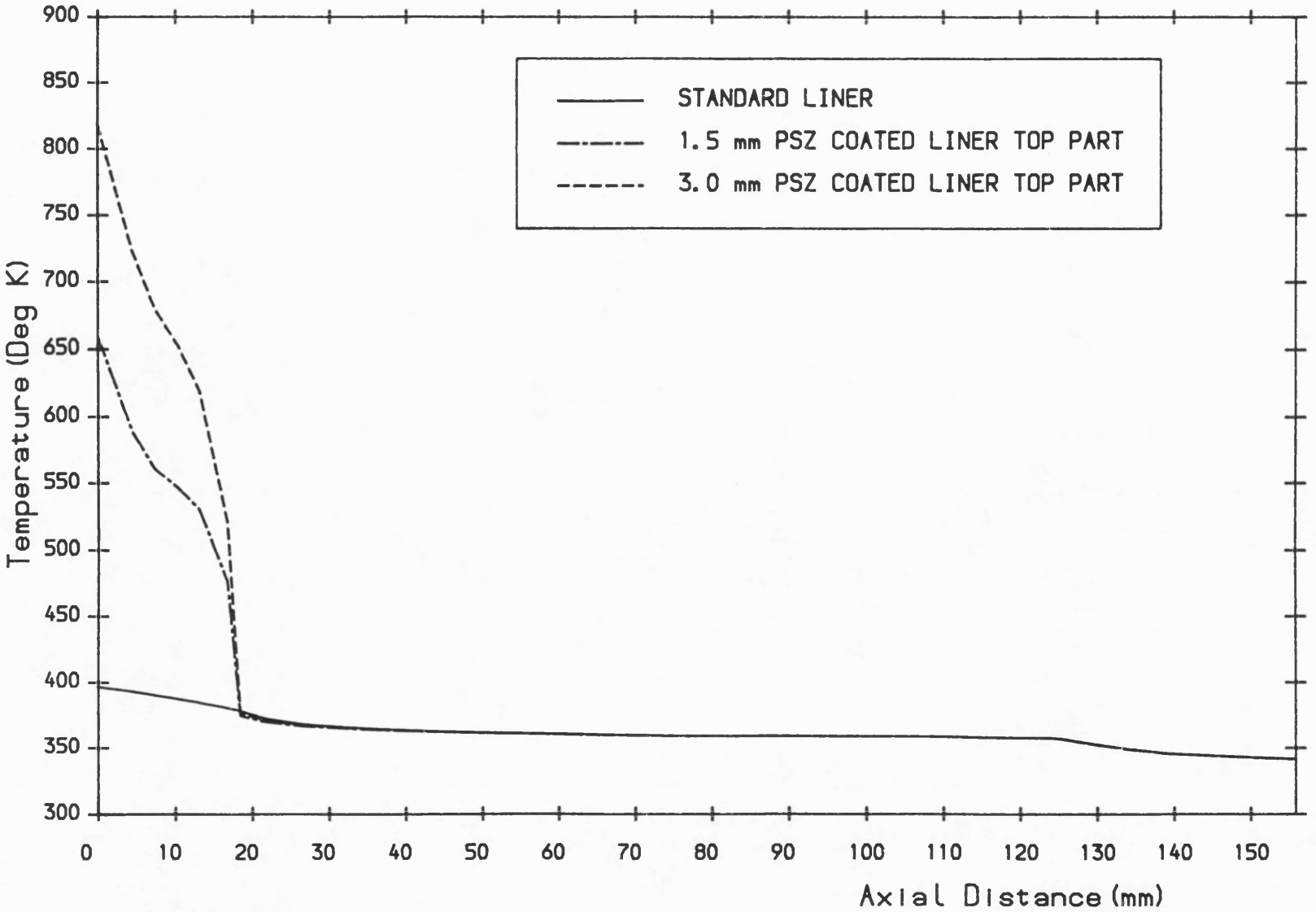

Fig. 5.44 The effect of liner top part insulation on liner surface temperature distribution.

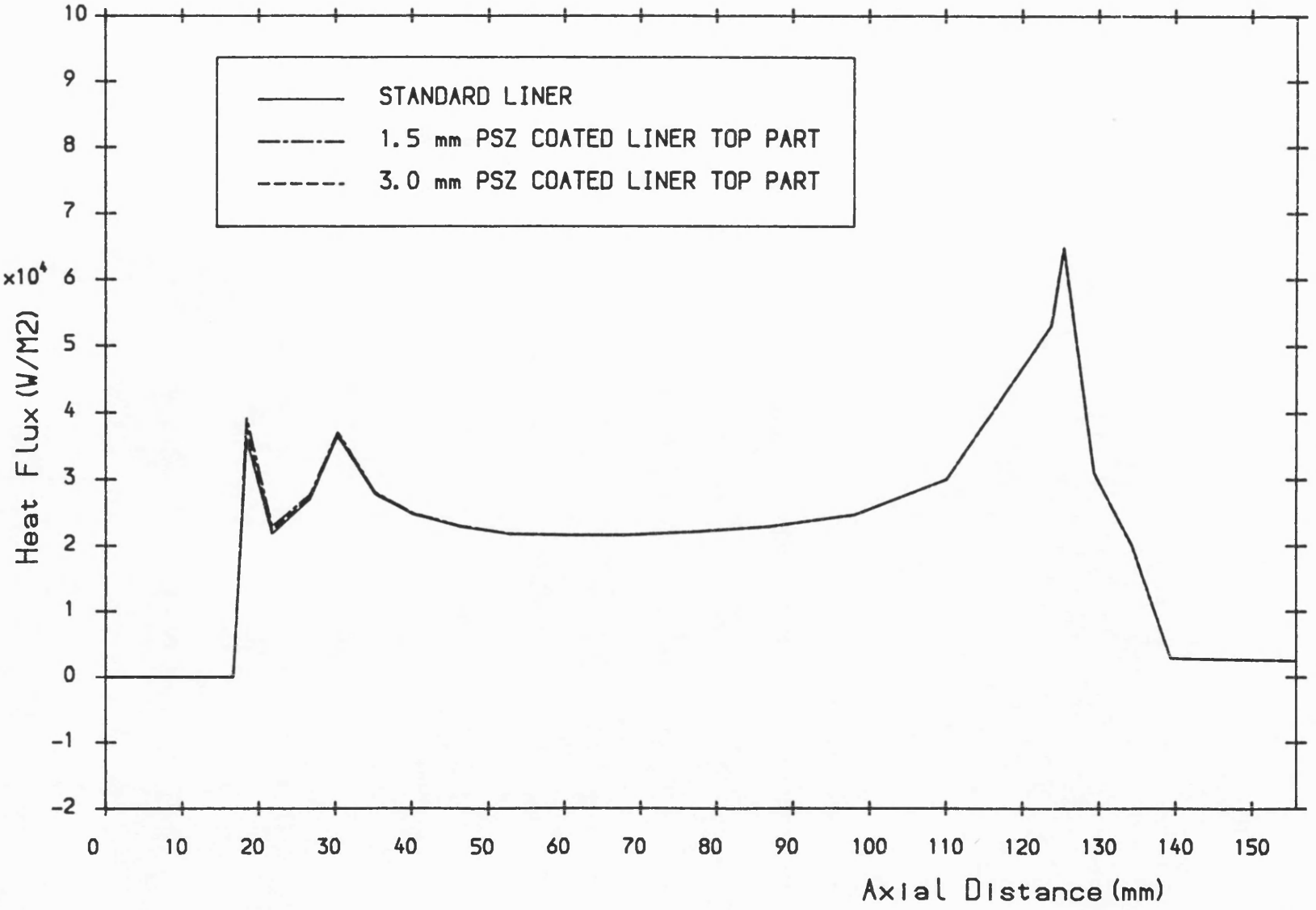

Fig. 5.45 The effect of liner top part insulation on piston-liner conduction heat flux distribution.

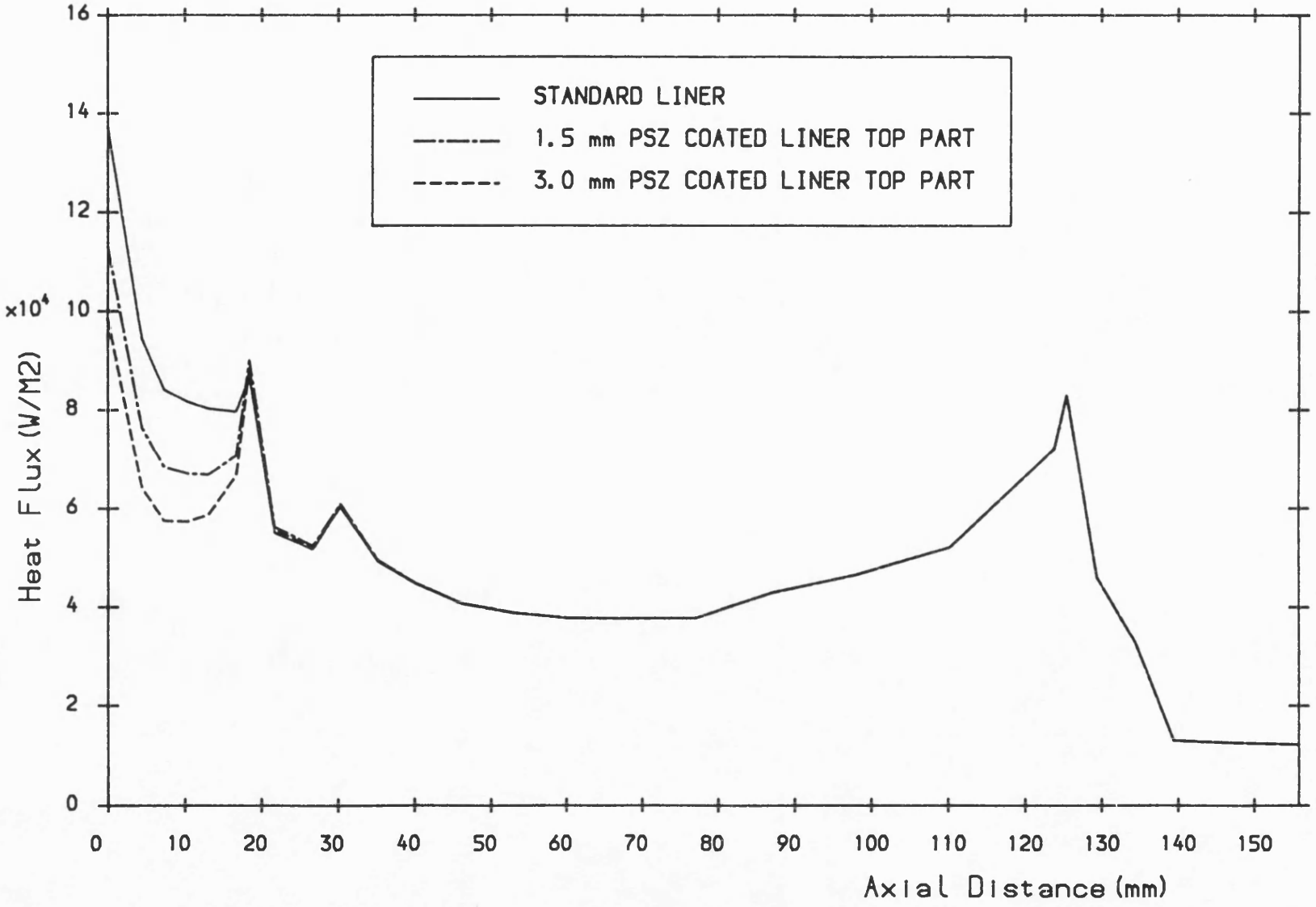

Fig. 5.46 The effect of liner top part insulation on liner total heat flux distribution.

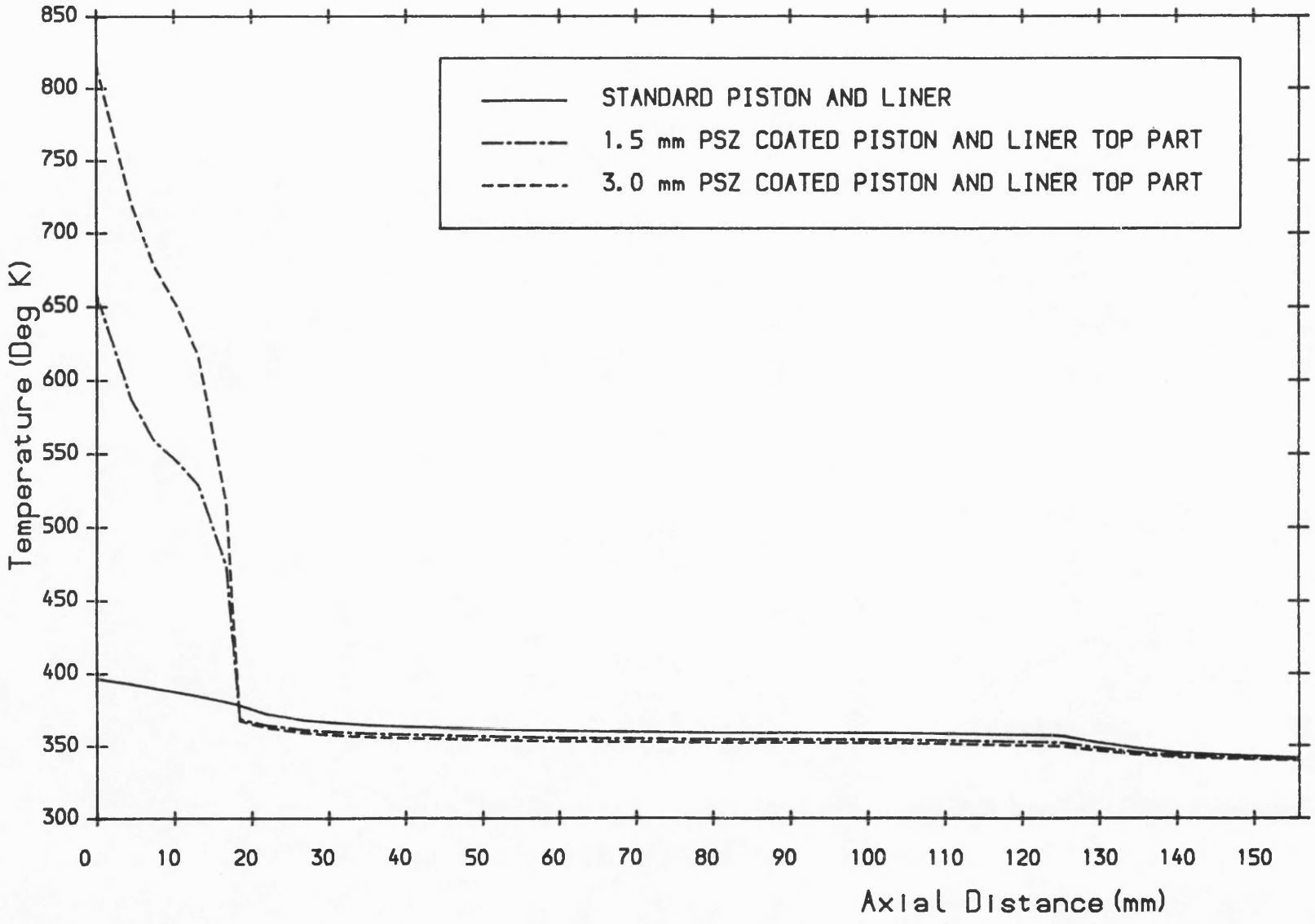

Fig. 5.47 The effect of piston and liner top part insulation on liner surface temperature distribution.

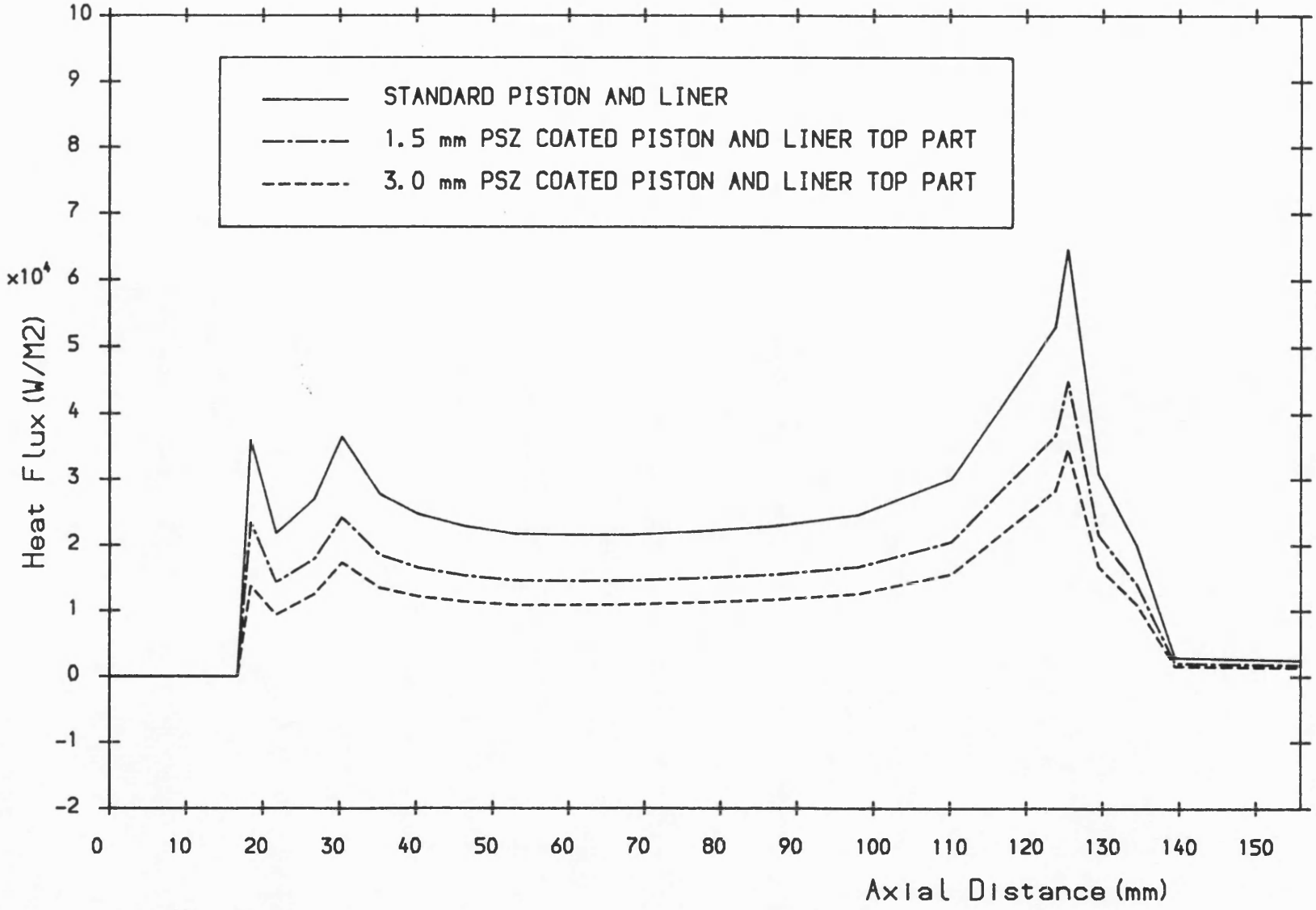

Fig. 5.48 The effect of piston and liner top part insulation on piston-liner conduction heat flux distribution.

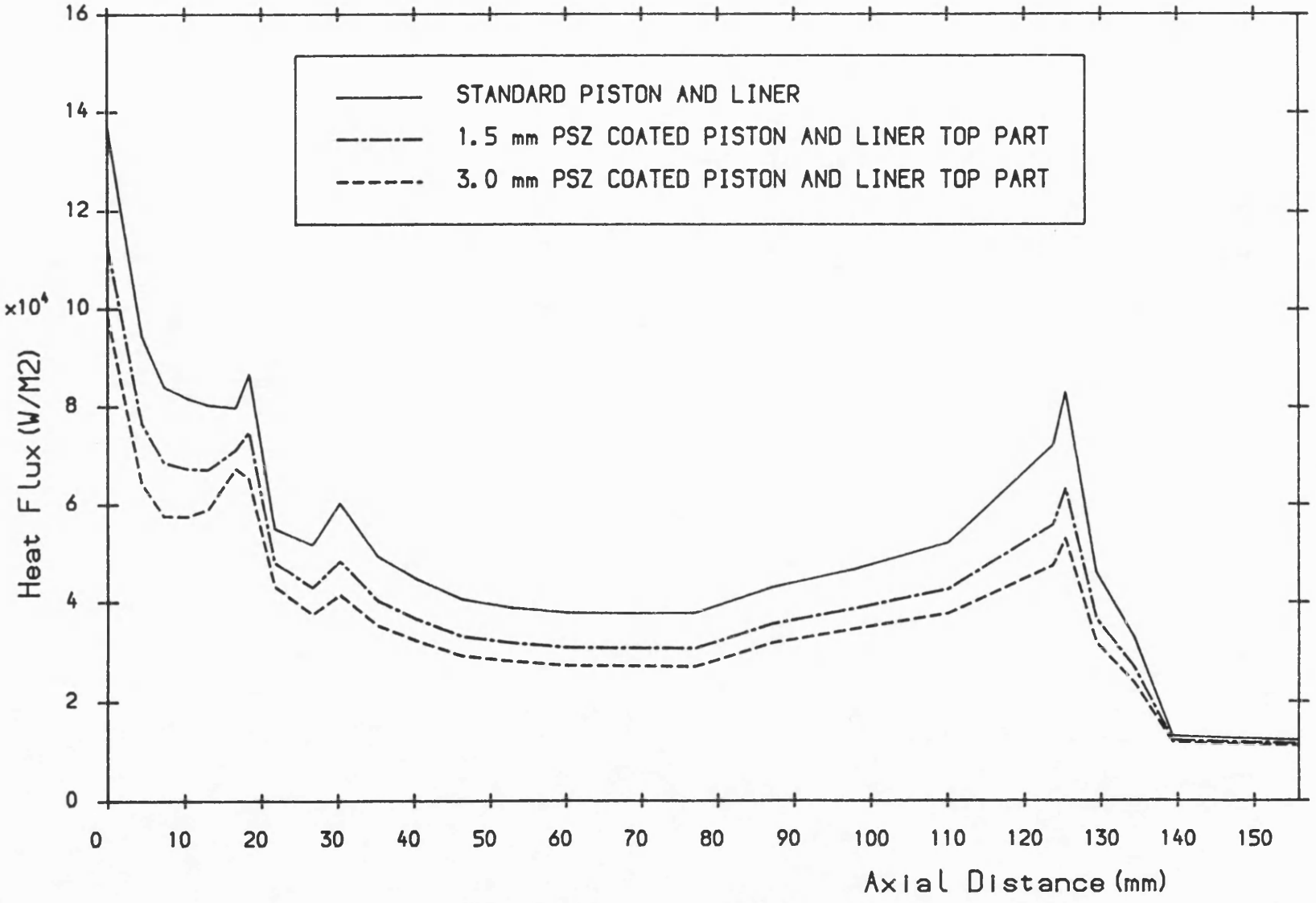

Fig. 5.49 The effect of piston and liner top part insulation on liner total heat flux distribution.

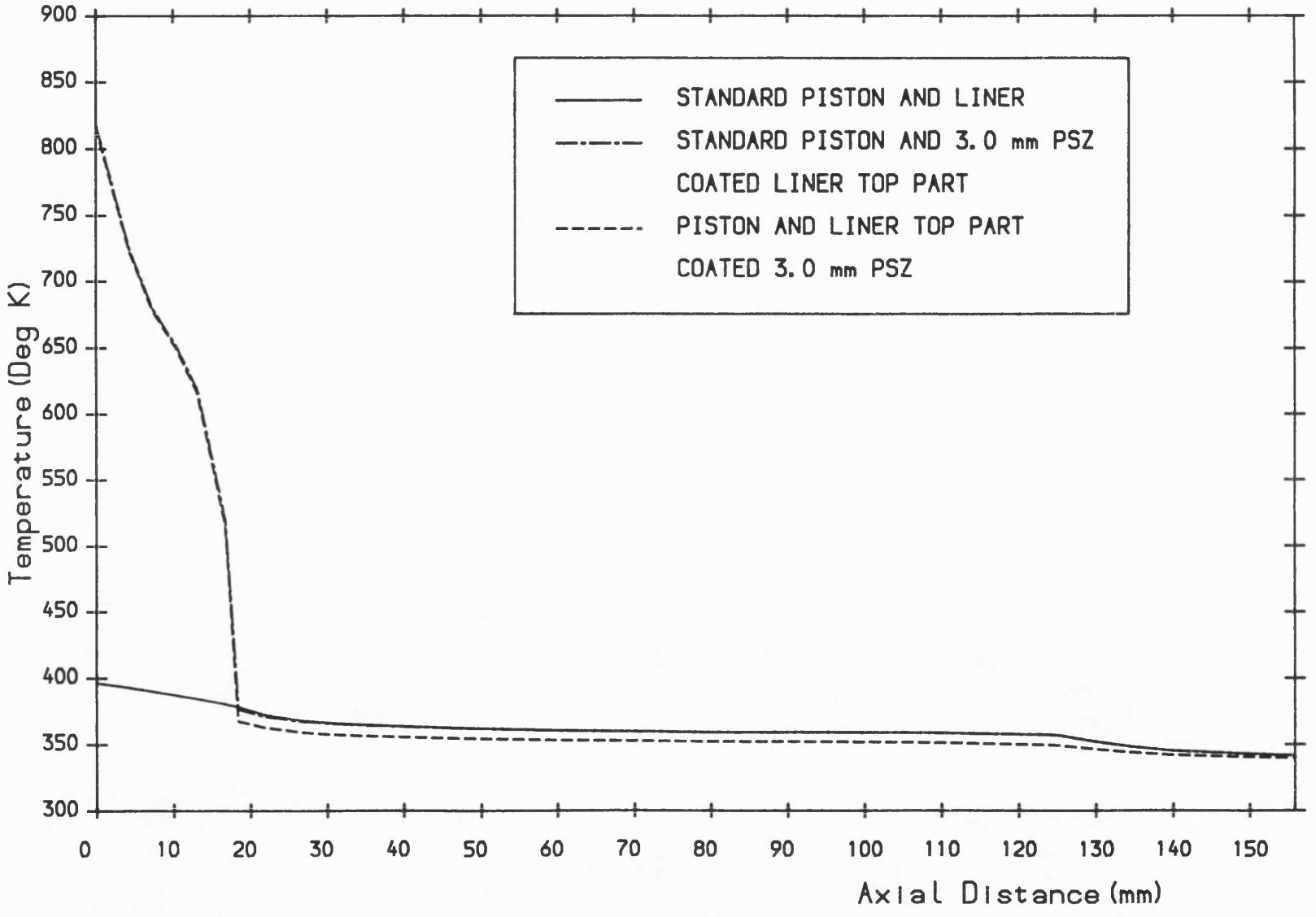

Fig. 5.50 The effect of liner top and piston plus liner top part insulation on liner surface temperature distribution.

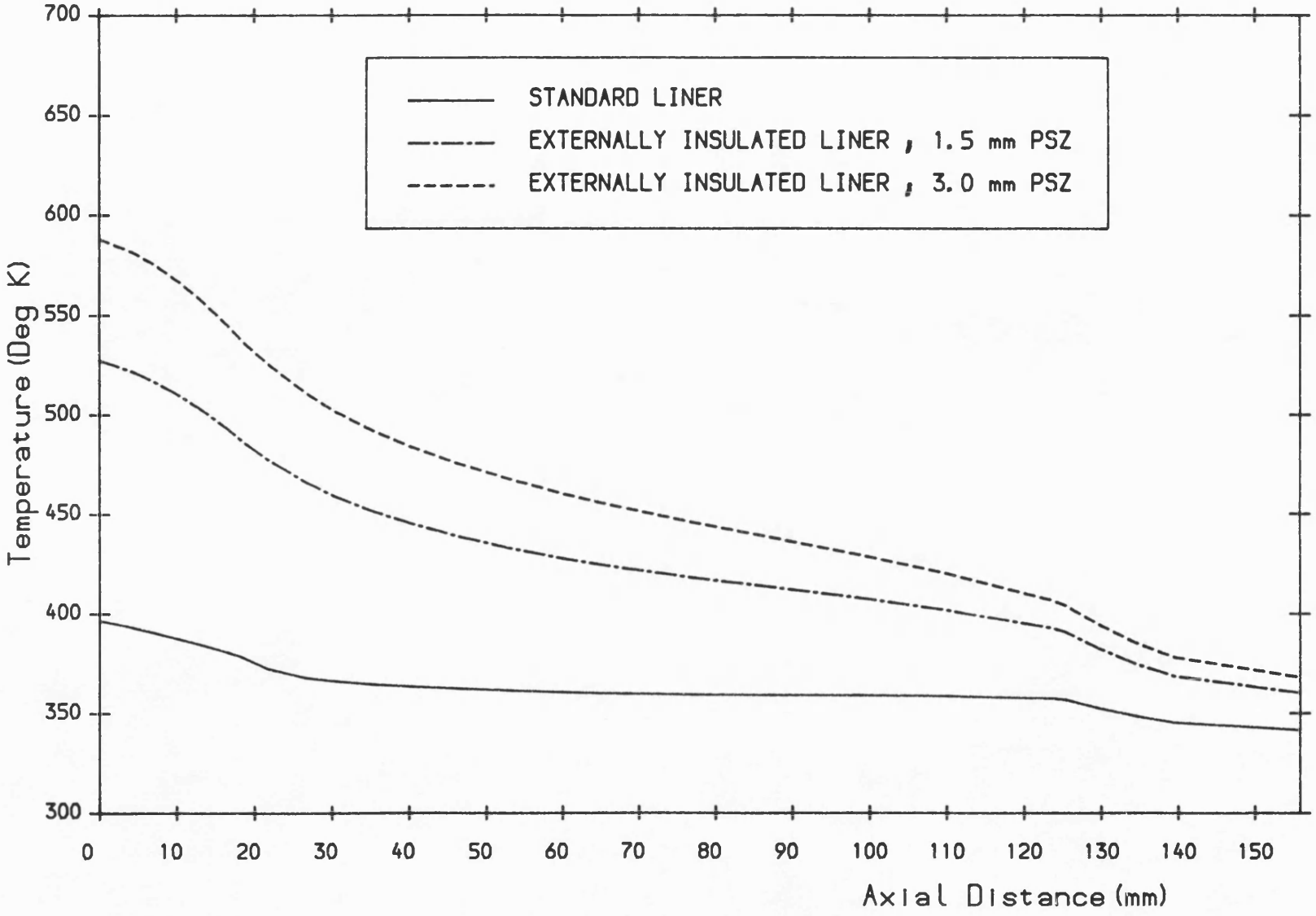

Fig. 5.51 The effect of external liner insulation on liner surface temperature distribution.

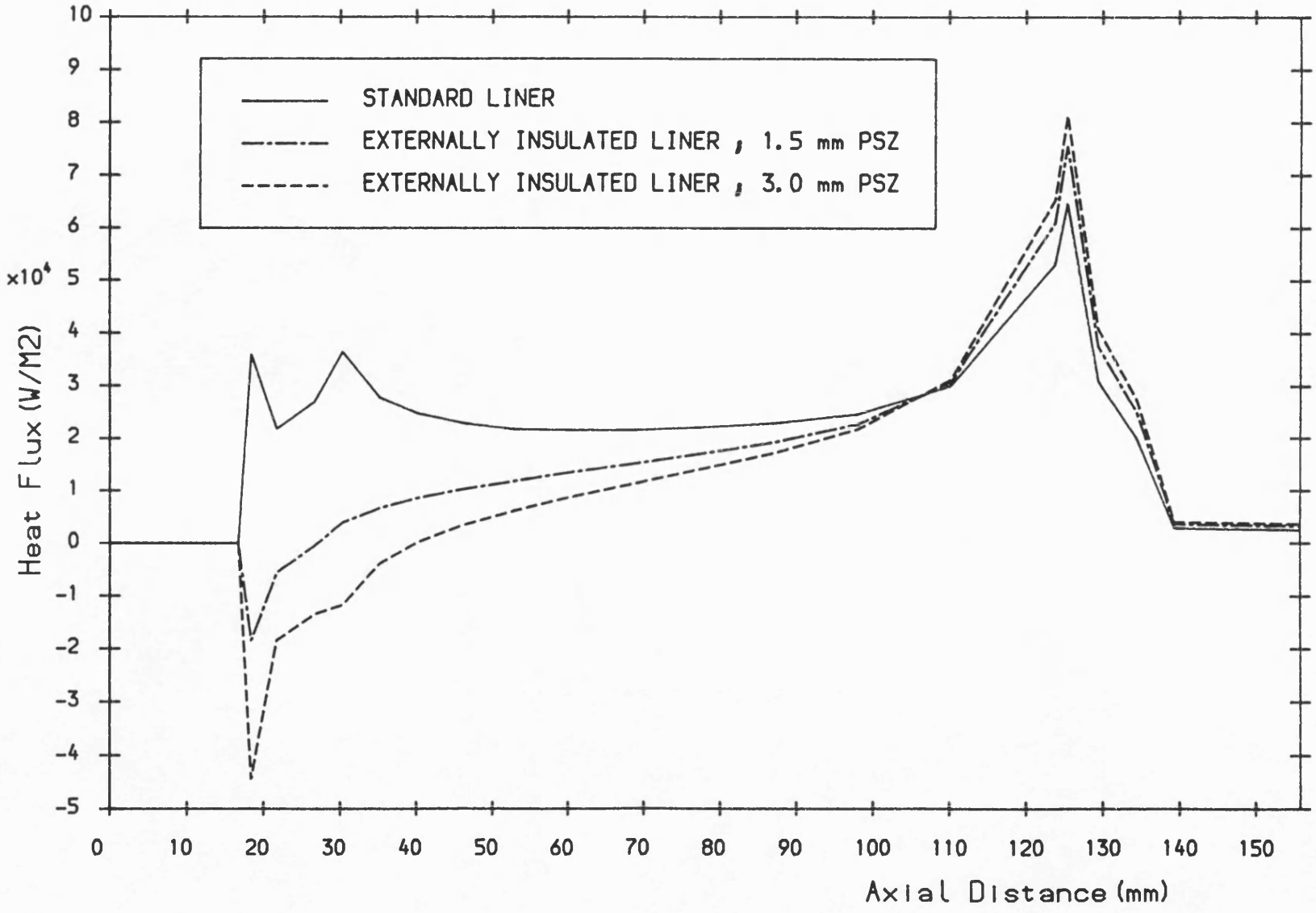

Fig. 5.52 The effect of external liner insulation on piston-liner conduction heat flux distribution.

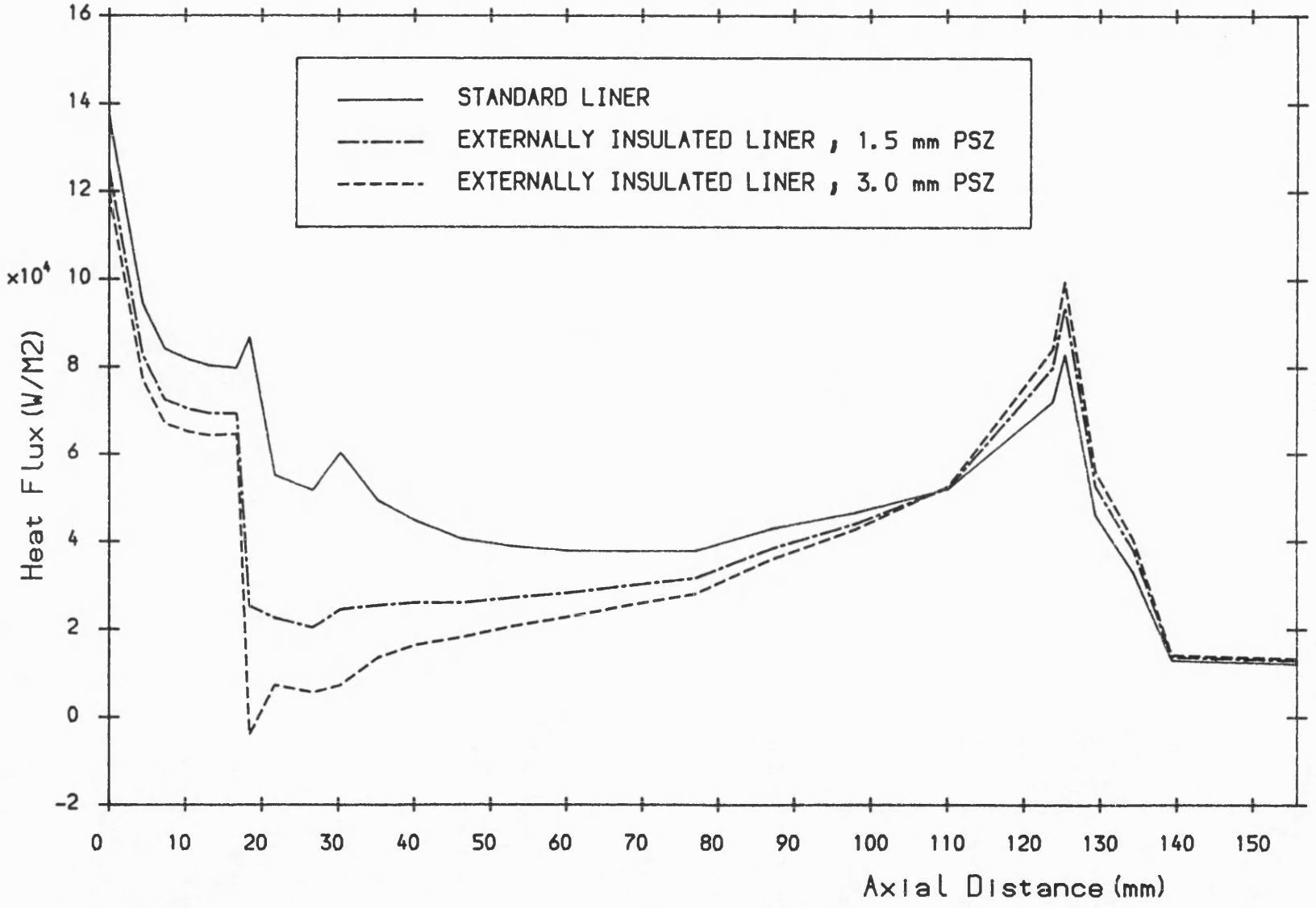

Fig. 5.53 The effect of external liner insulation on liner total heat flux distribution.

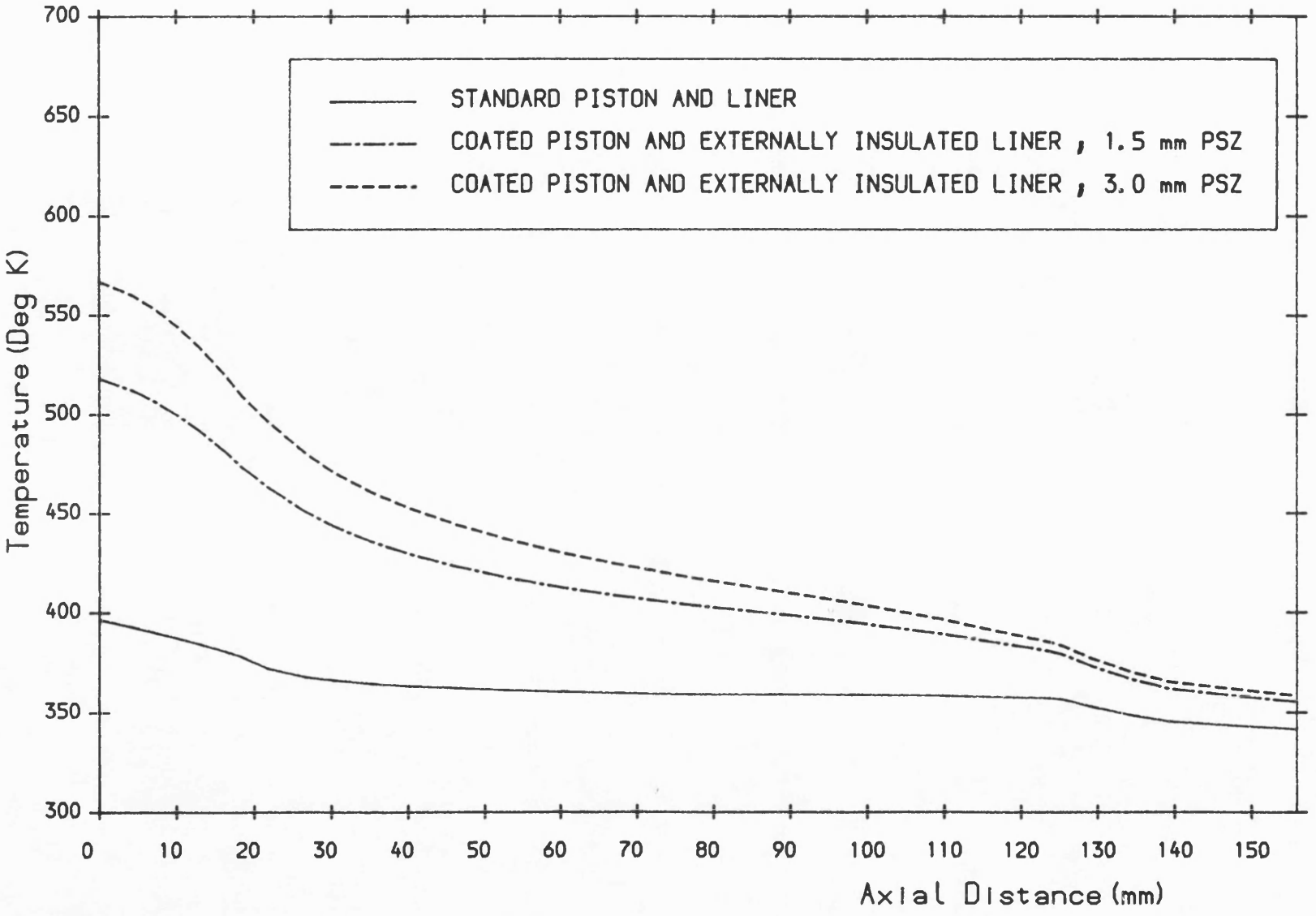

Fig. 5.54 The effect of piston and external liner insulation on liner surface temperature distribution.

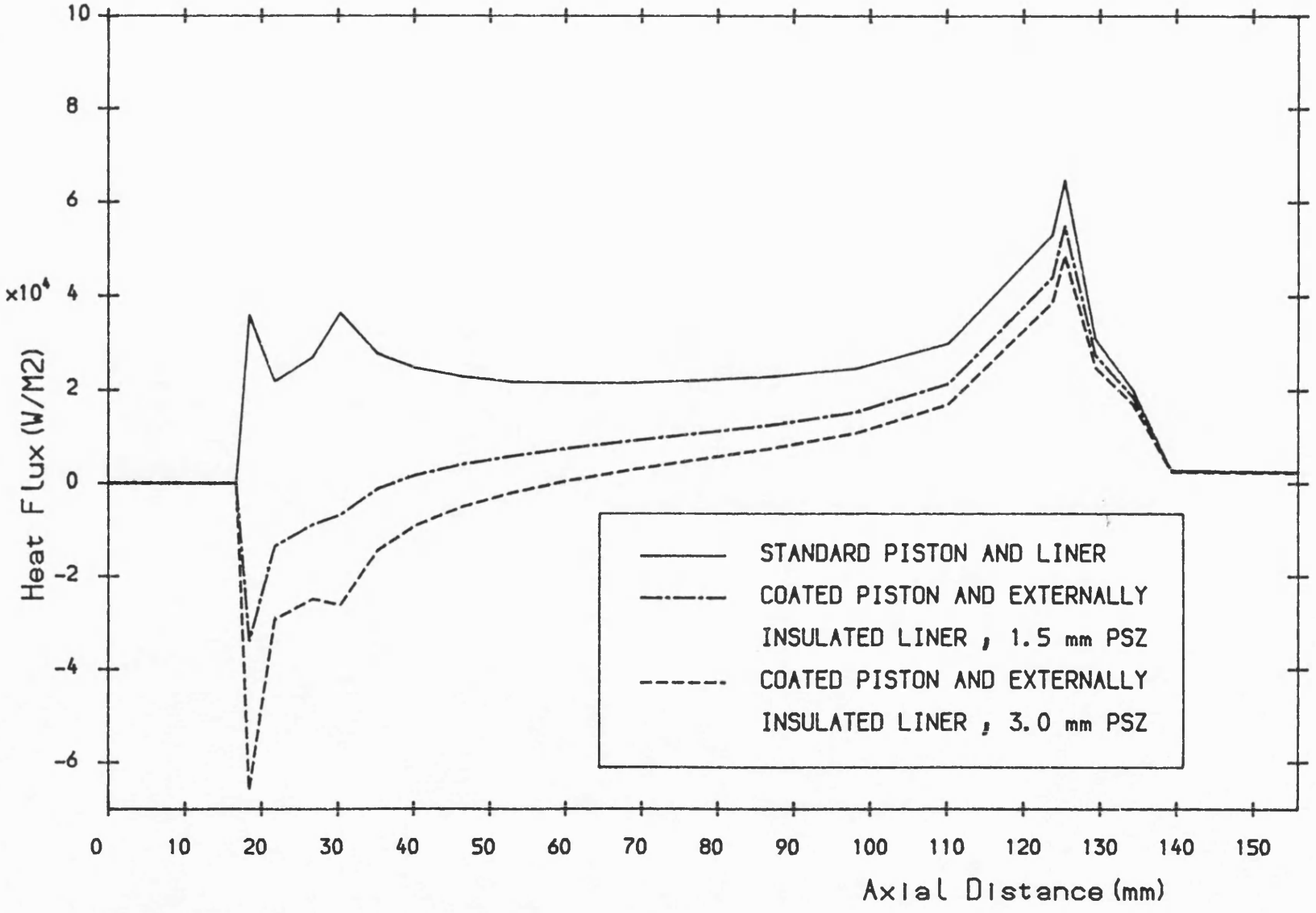

Fig. 5.55 The effect of piston and external liner insulation on piston-liner conduction heat flux distribution.

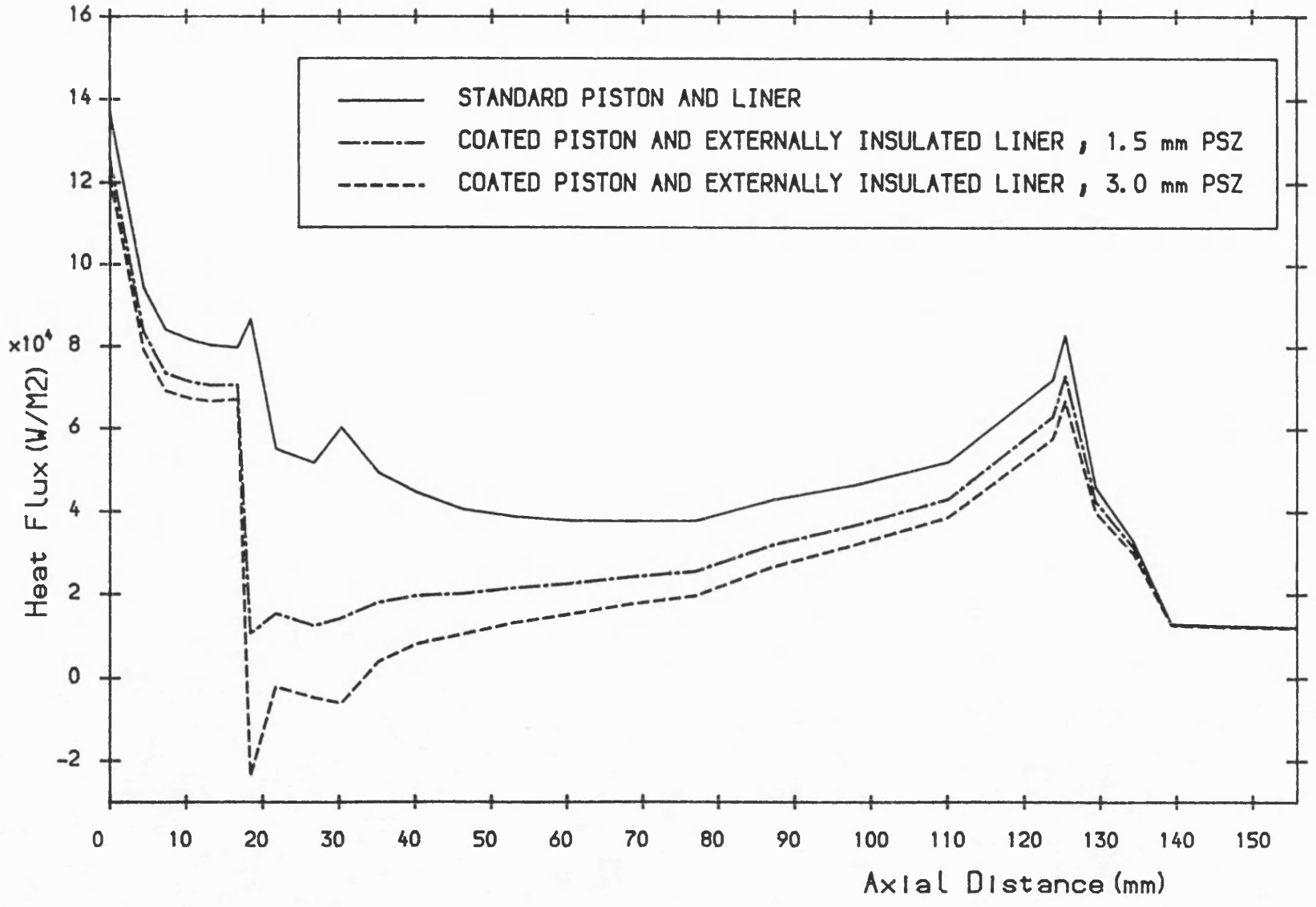

Fig. 5.56 The effect of piston and external liner insulation on liner total heat flux distribution.

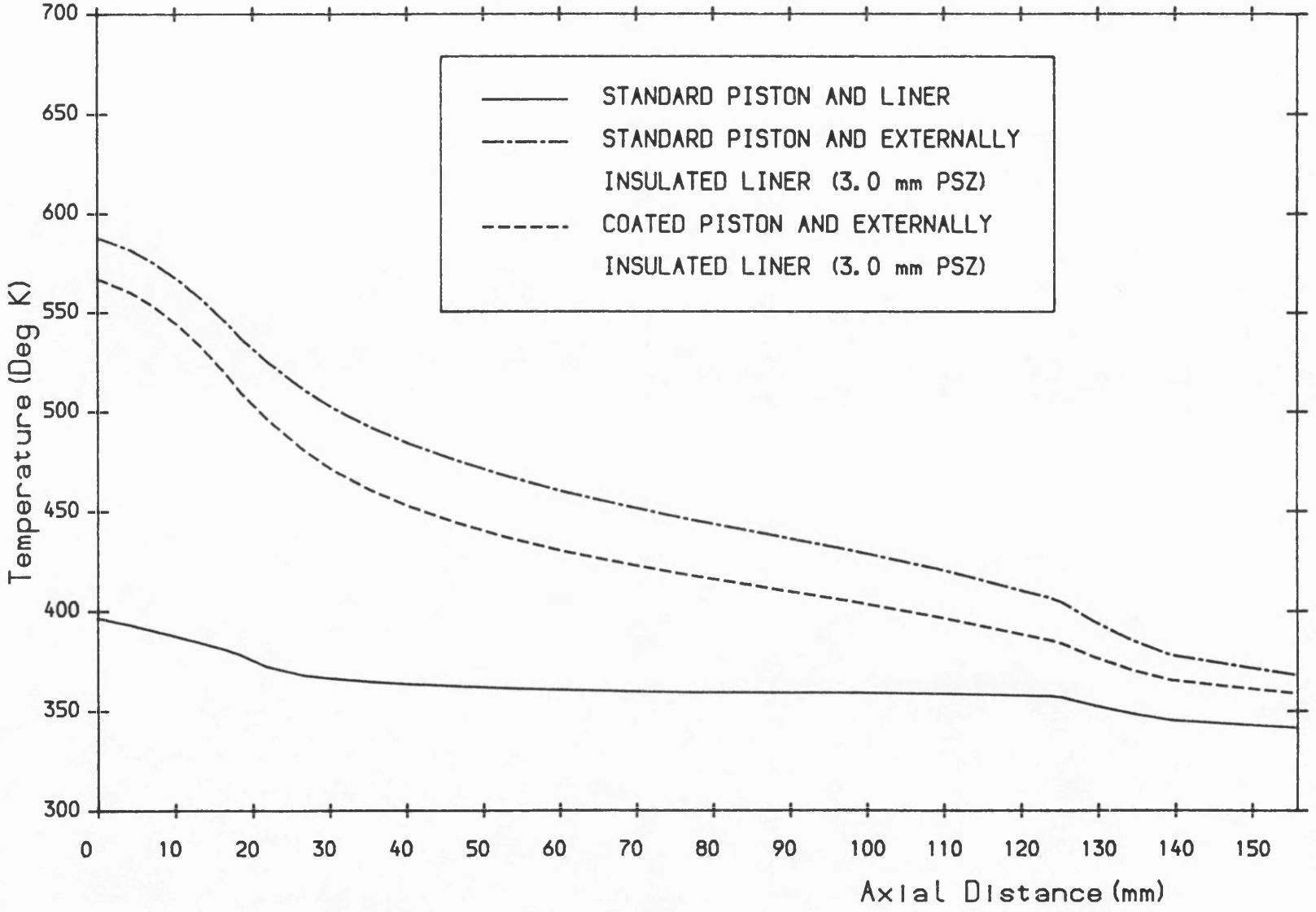

Fig. 5.57 The effect of external liner and piston plus external liner insulation on liner surface temperature distribution.

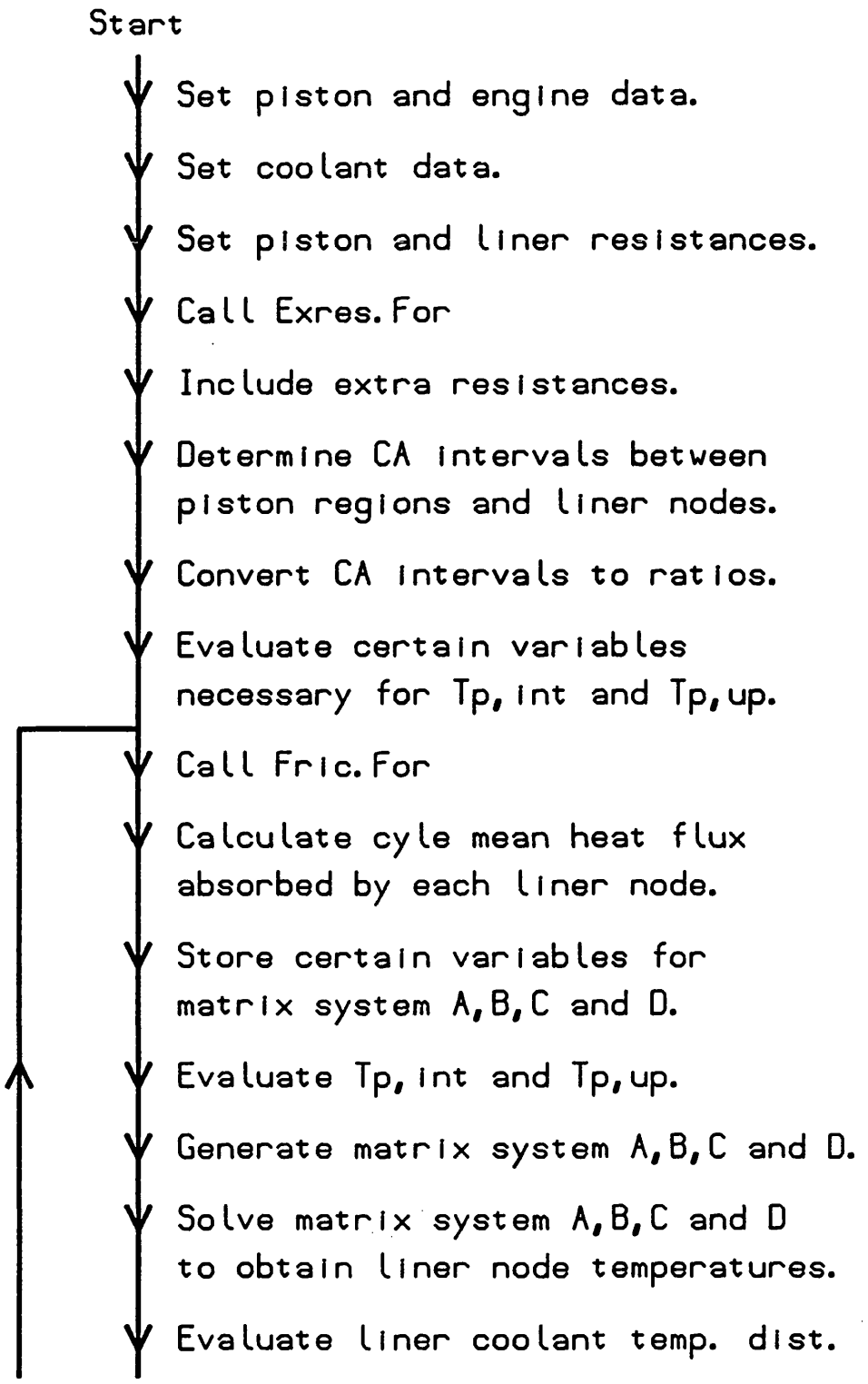

Fig. 5.58 The flowchart for Resist.For.

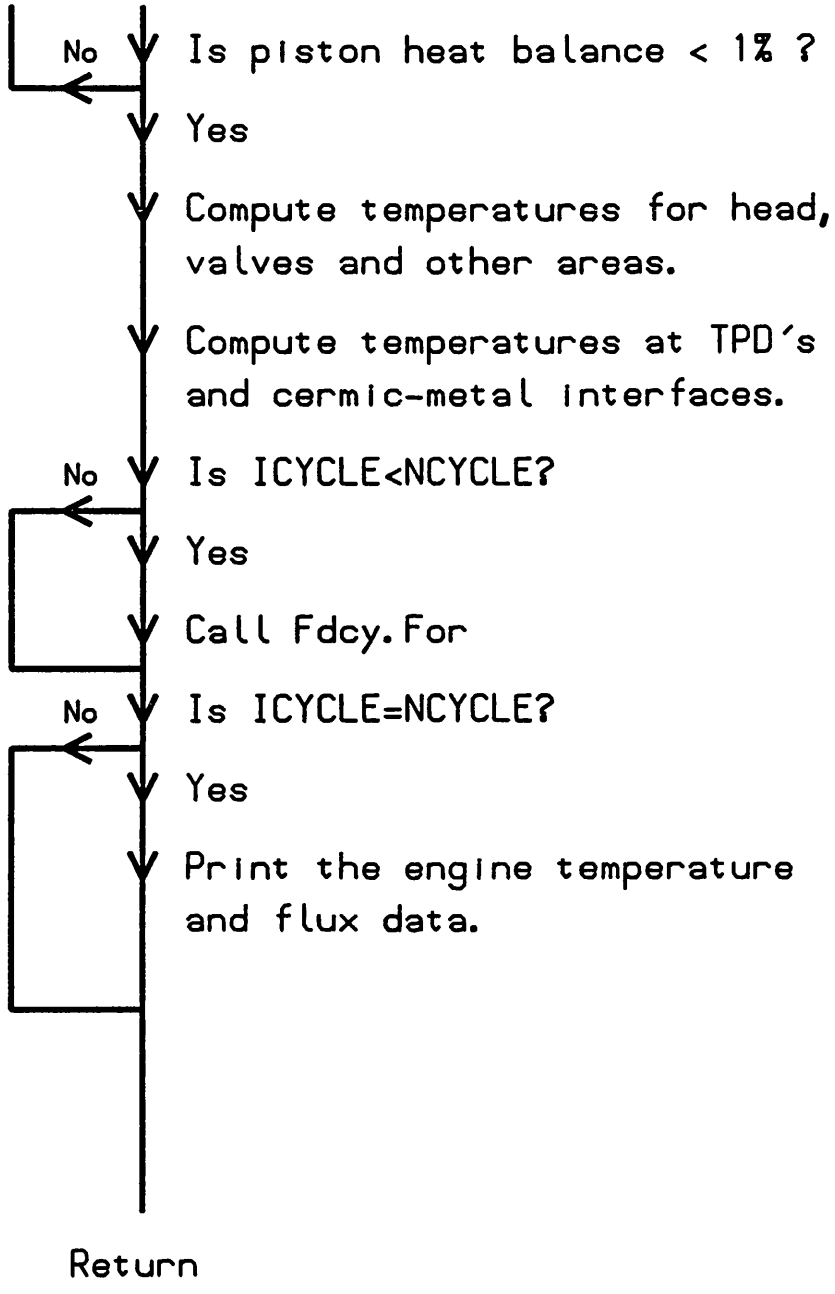

Fig. 5.58 Continued.

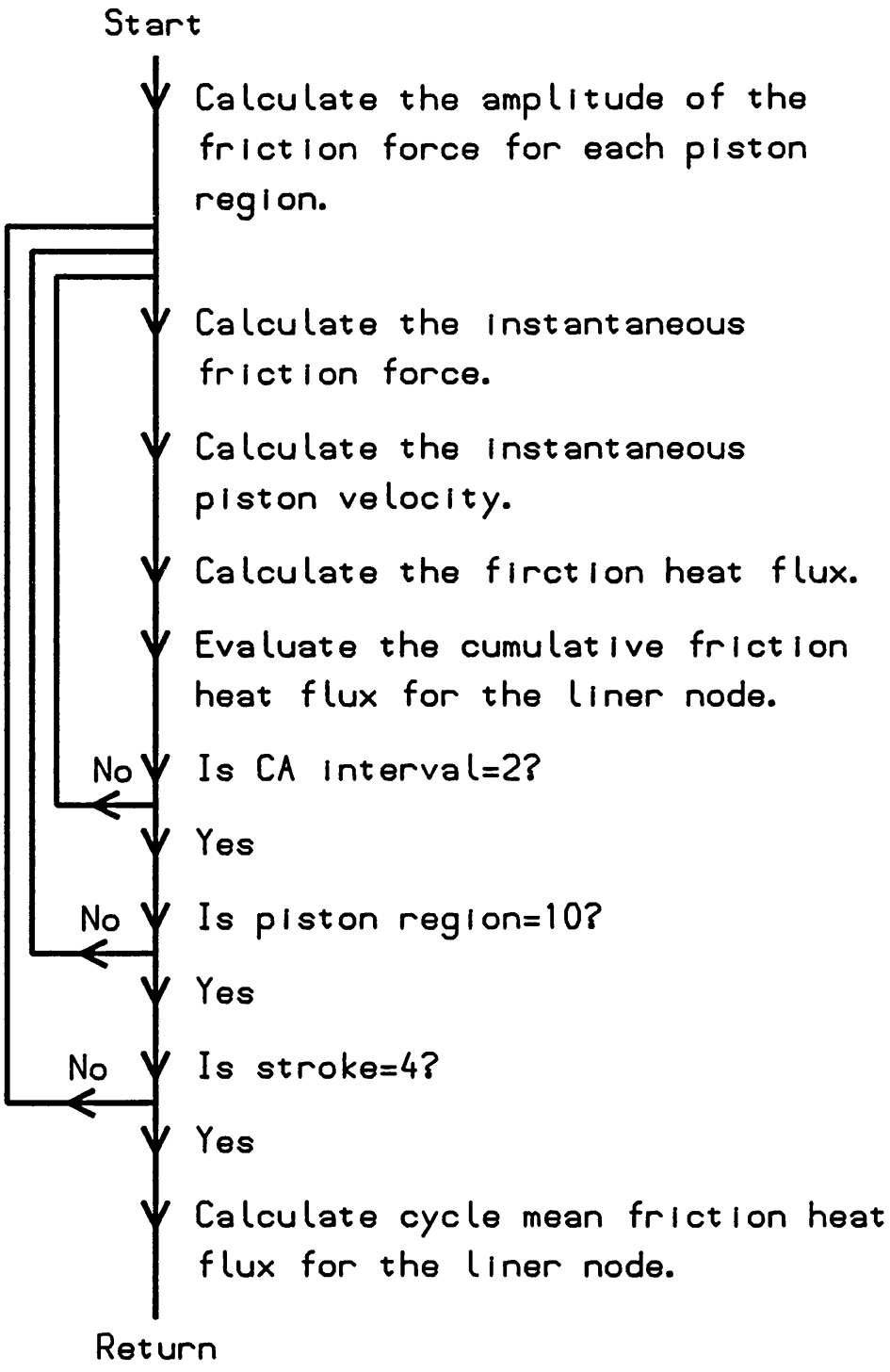

Fig. 5. 59 The flowchart for Fric. For.

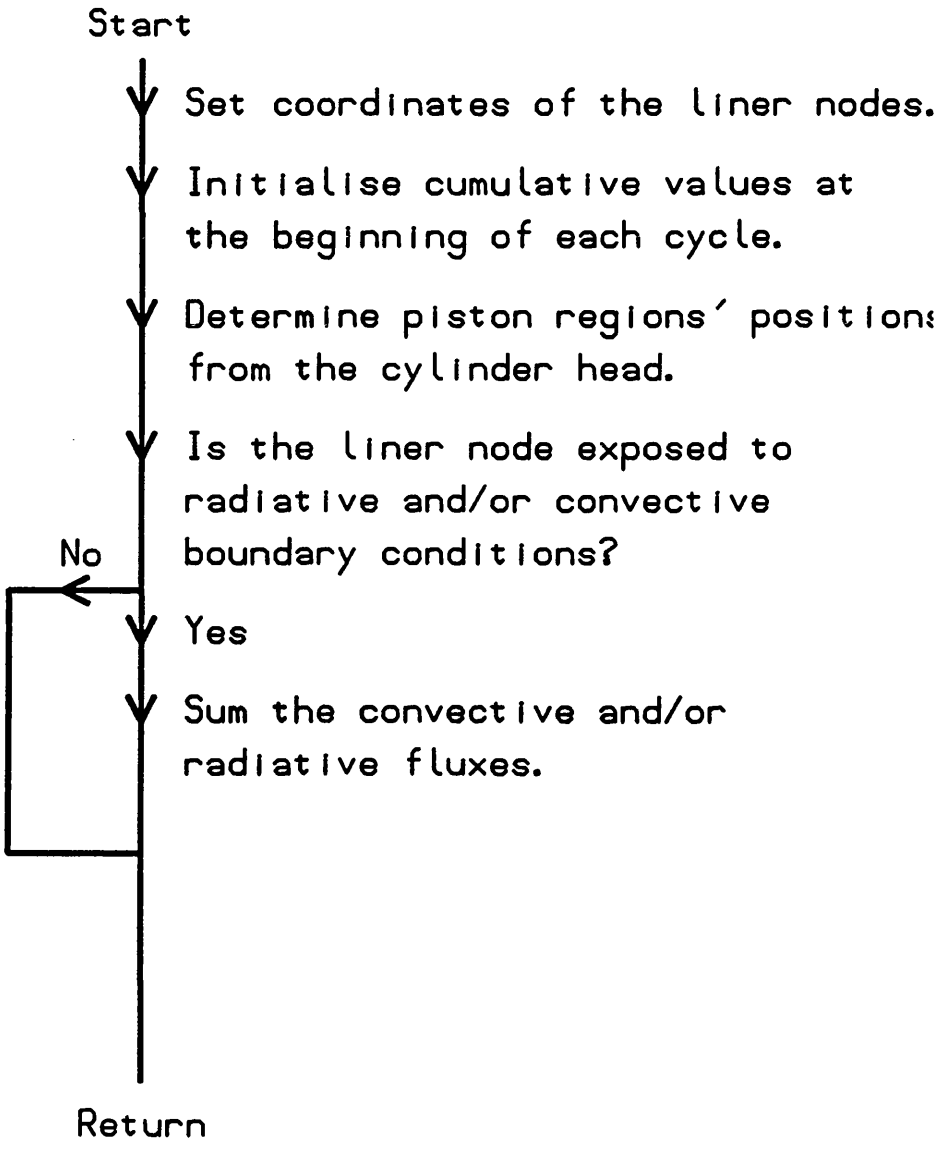

Fig. 5.60 The flowchart for Resdat.For.

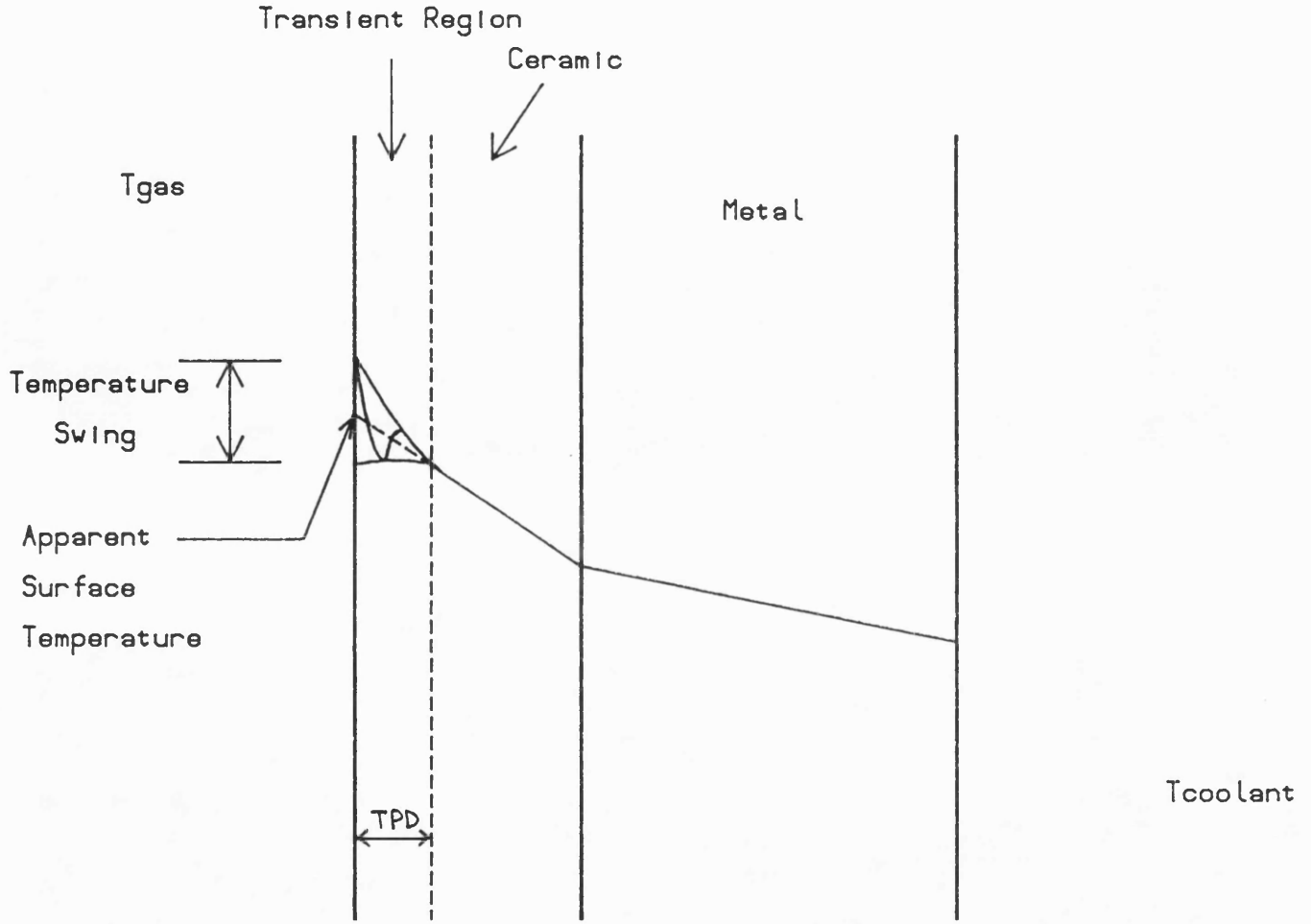

Fig. 6.1 Temperature profile in a combustion chamber wall.

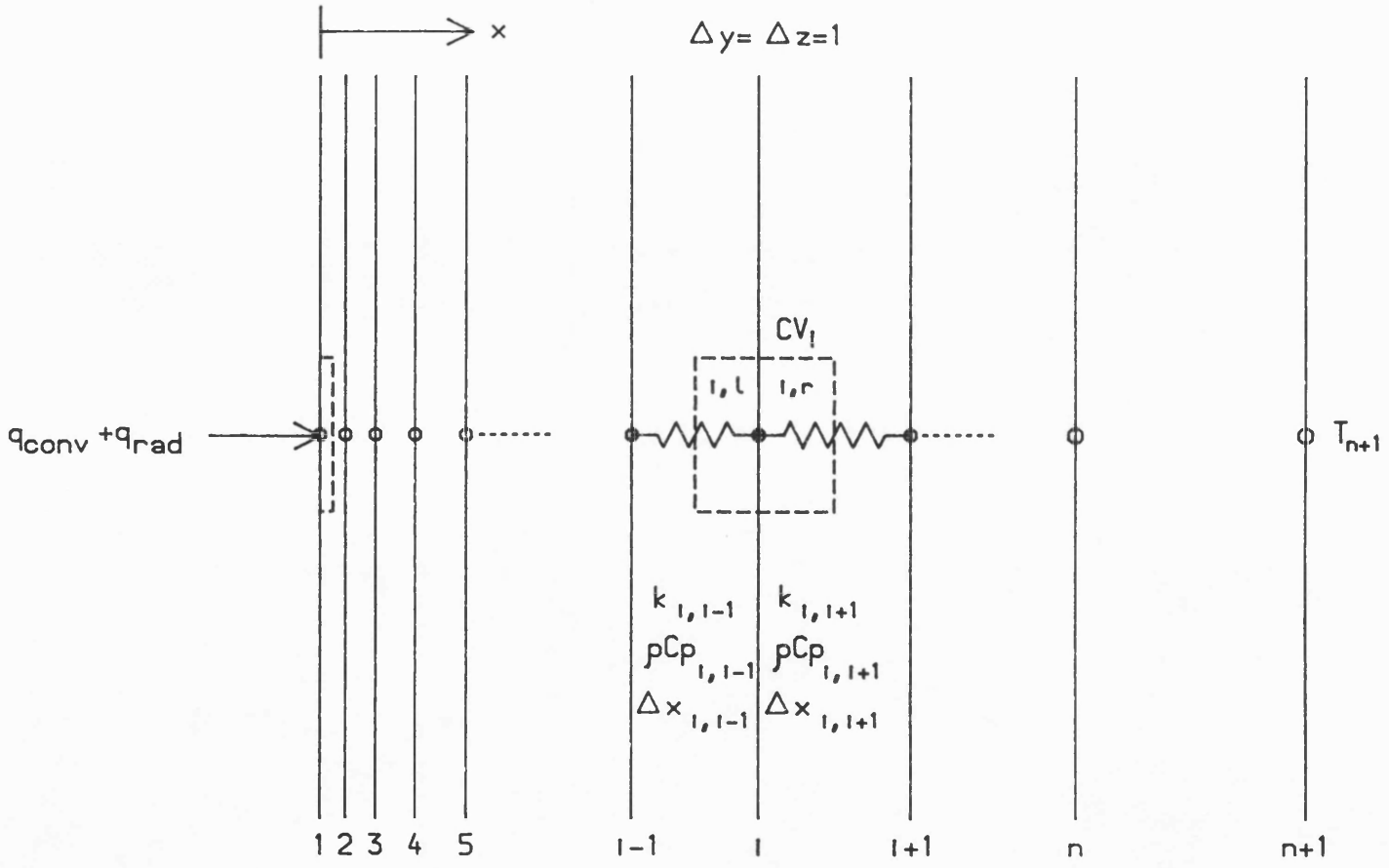

Fig. 6.2 Representation of the wall with FD nodes.

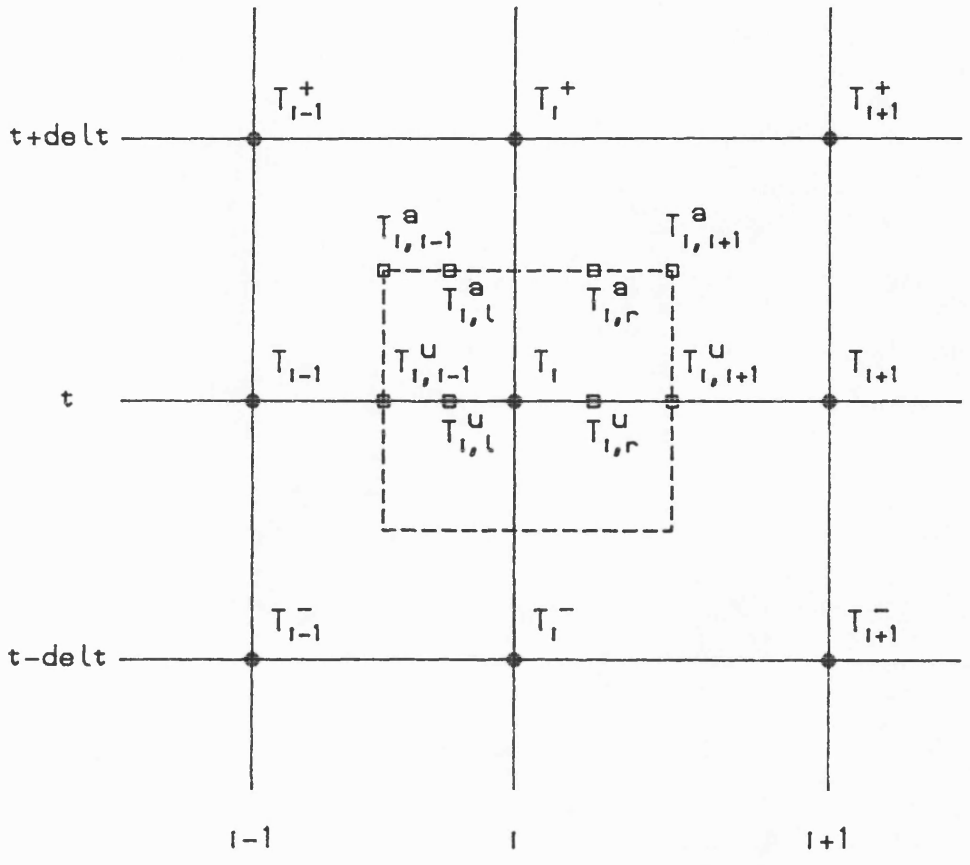

+ Denotes future values.
- Denotes past values
a Denotes actual mean values.
u Denotes used mean values.

Fig. 6.3 Actual and used mean temperatures in the temperature dependent properties.

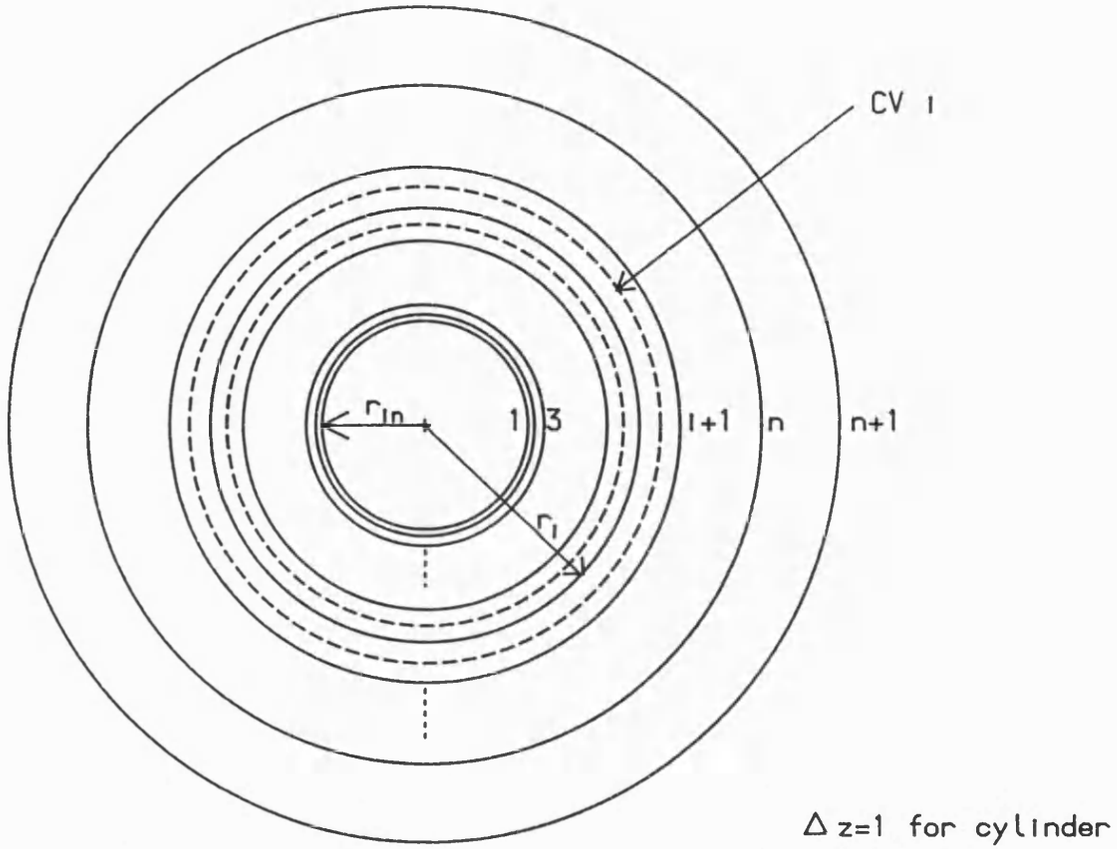

Fig. 6.4 Representation of a cylinder and sphere with FD surfaces.

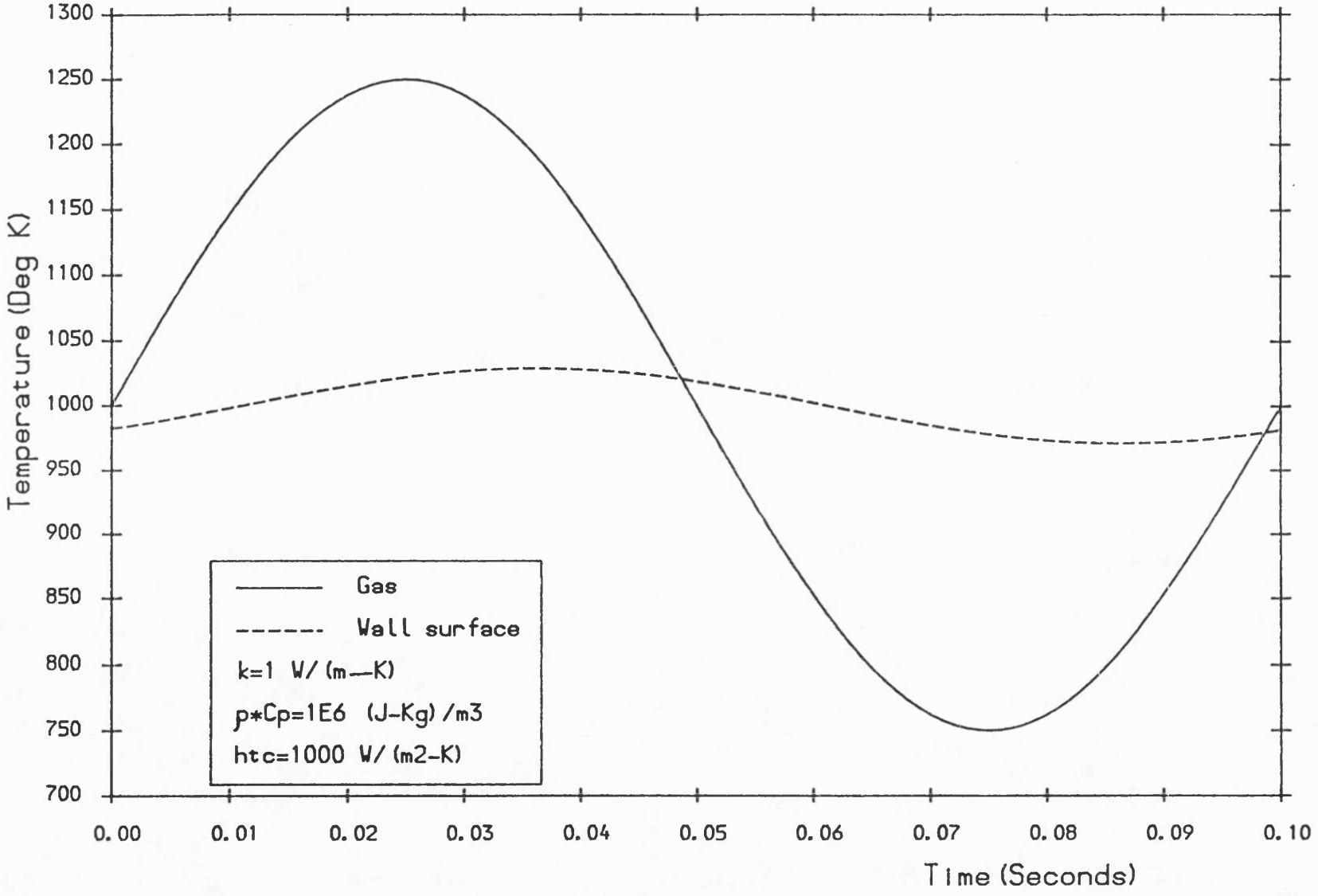

Fig. 6.5 Gas and wall surface temperature versus time with a phase difference of 0.011 seconds.

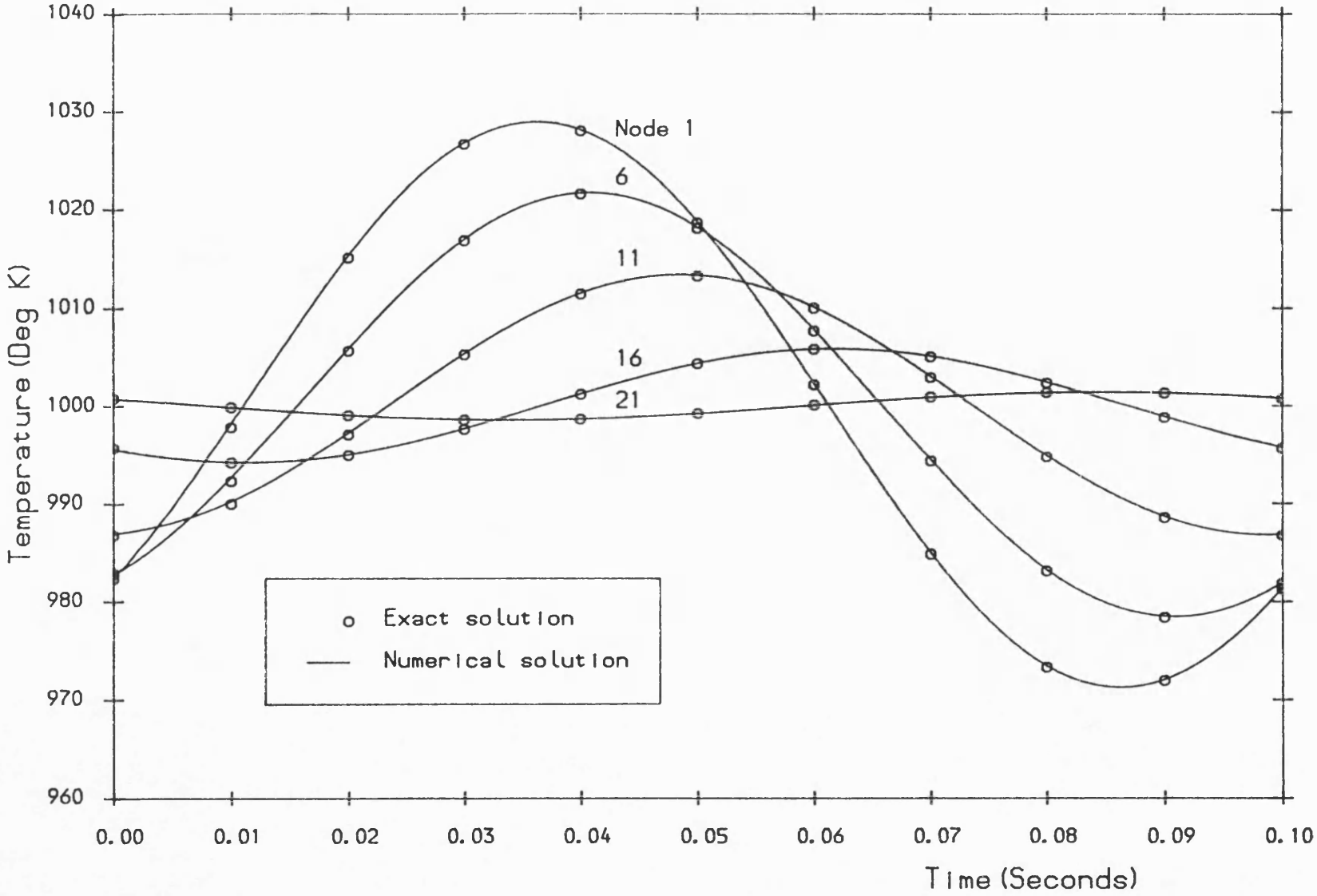

Fig. 6.6 The comparison of the exact and numerical solutions of the temperature wave at the specified nodes.

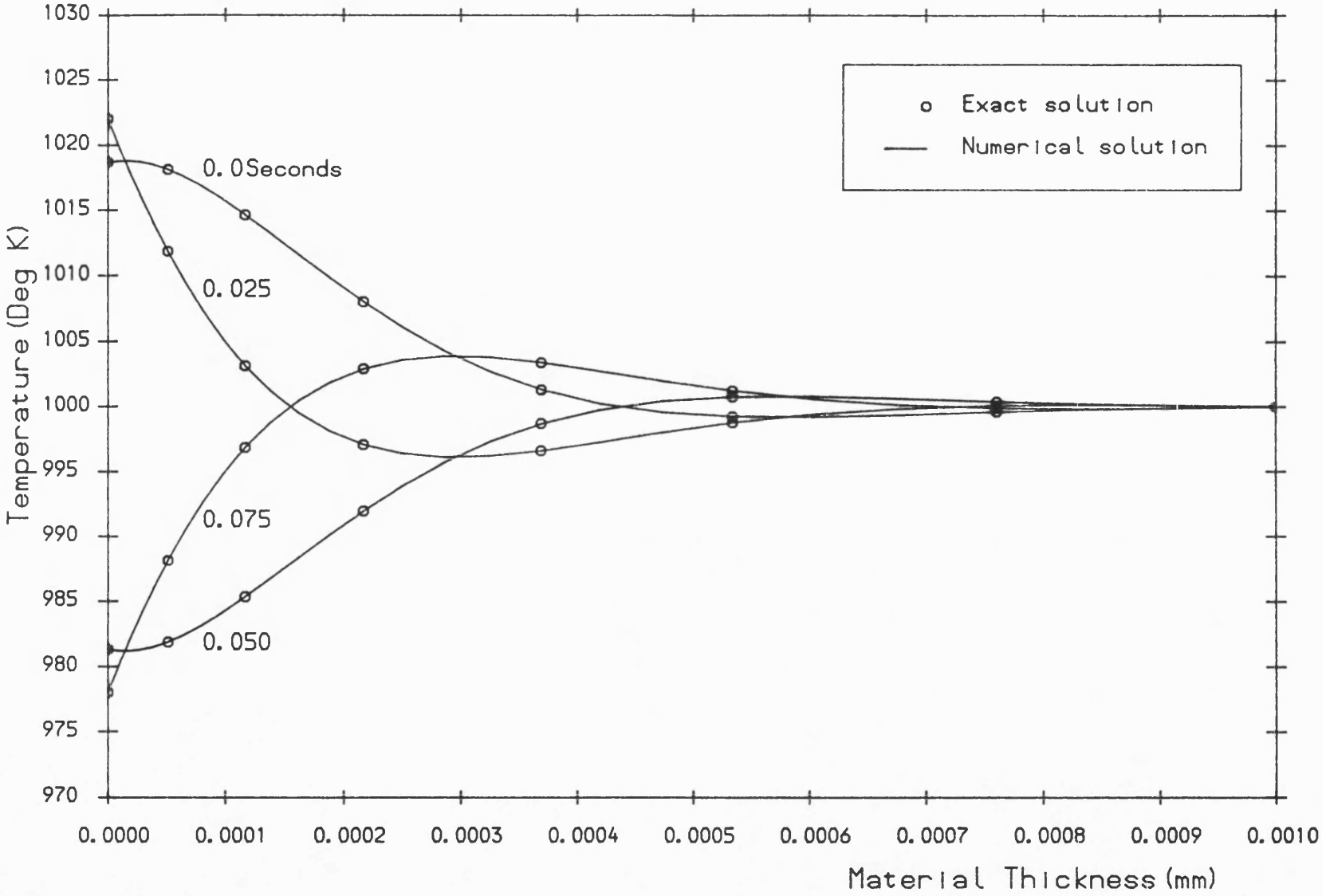

Fig. 6.7 The comparison of the exact and numerical solutions of the temperature wave through the material.

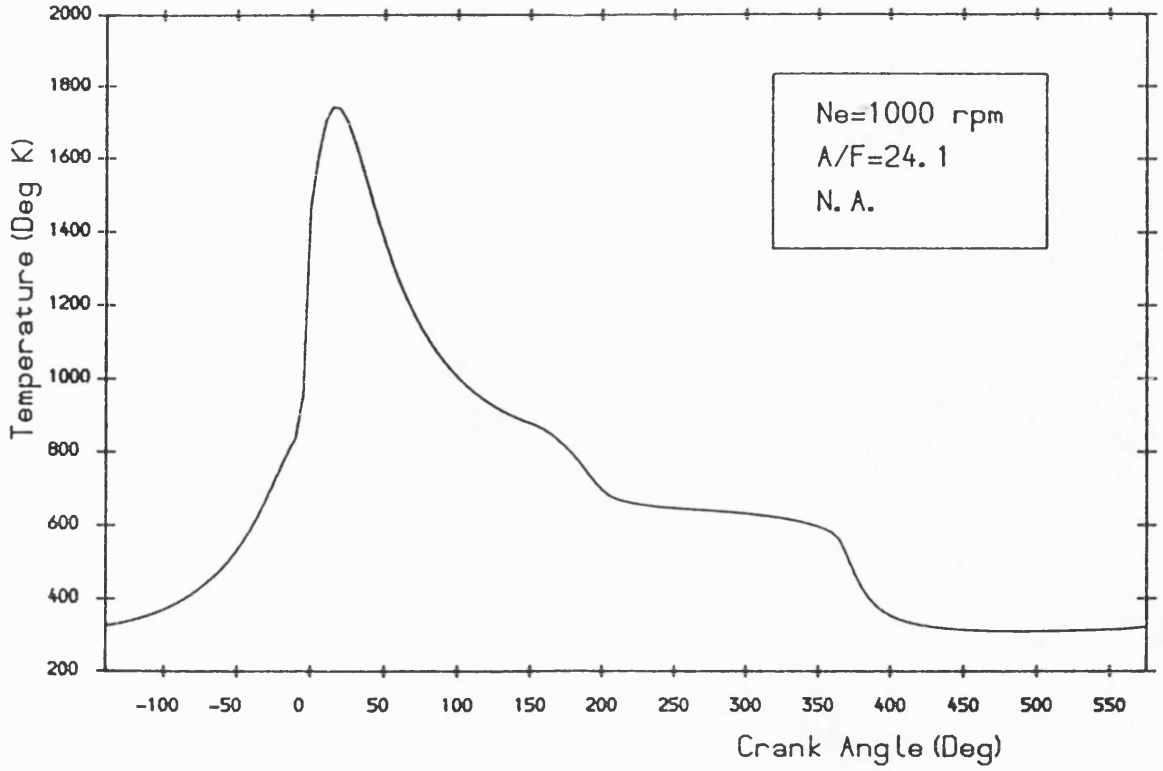

Fig. 6.8 Cylinder gas temperature versus crank angle.

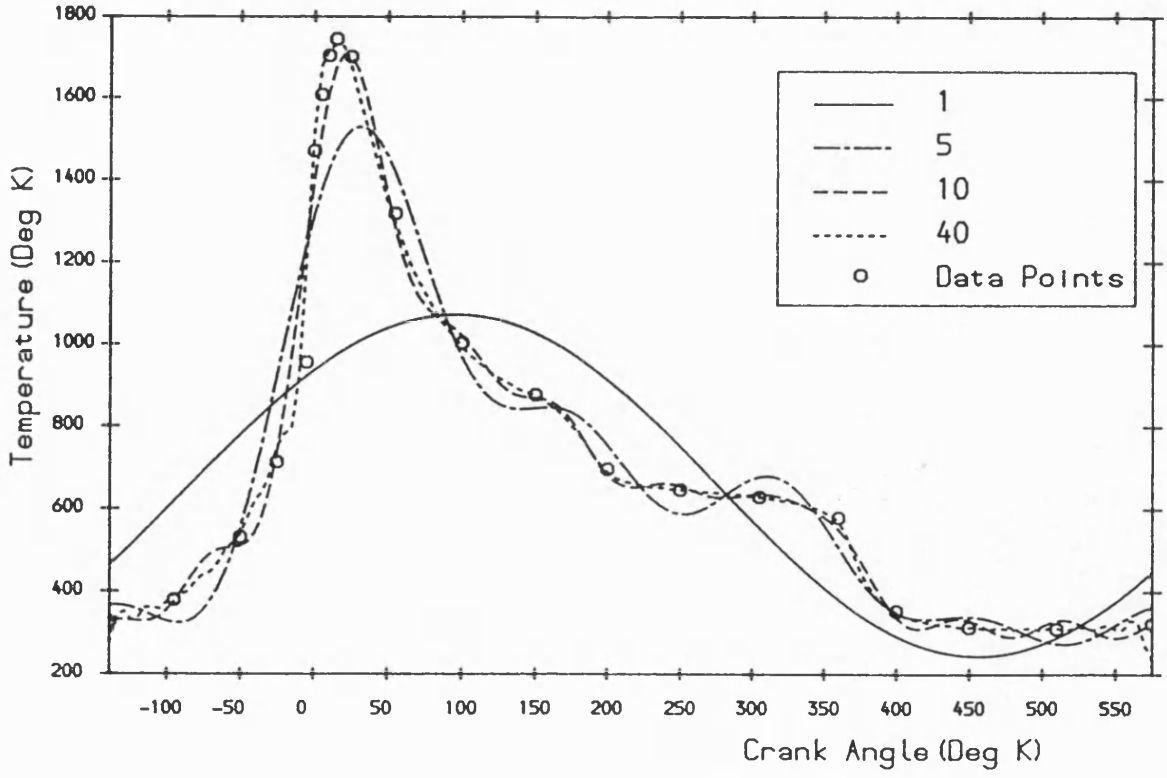

Fig. 6.9 Cylinder gas temperature represented by various numbers of Fourier harmonics.

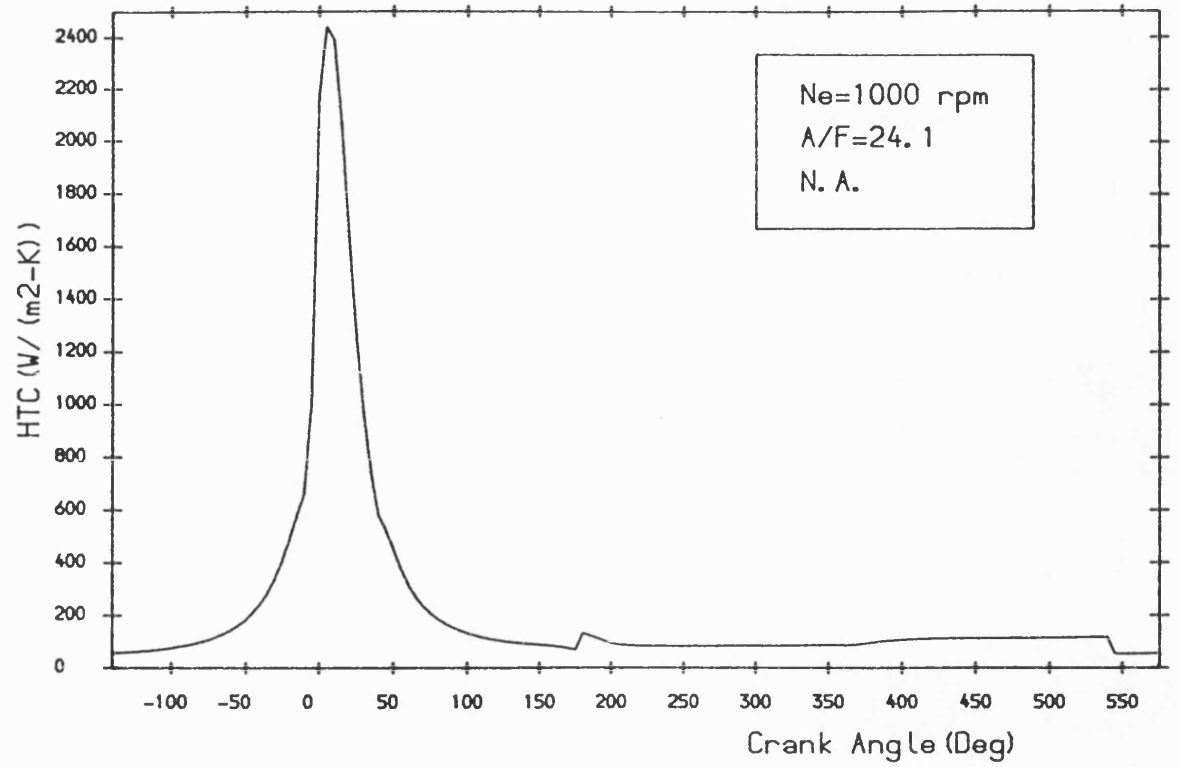

Fig. 6.10 Gas heat transfer coefficient versus crank angle.

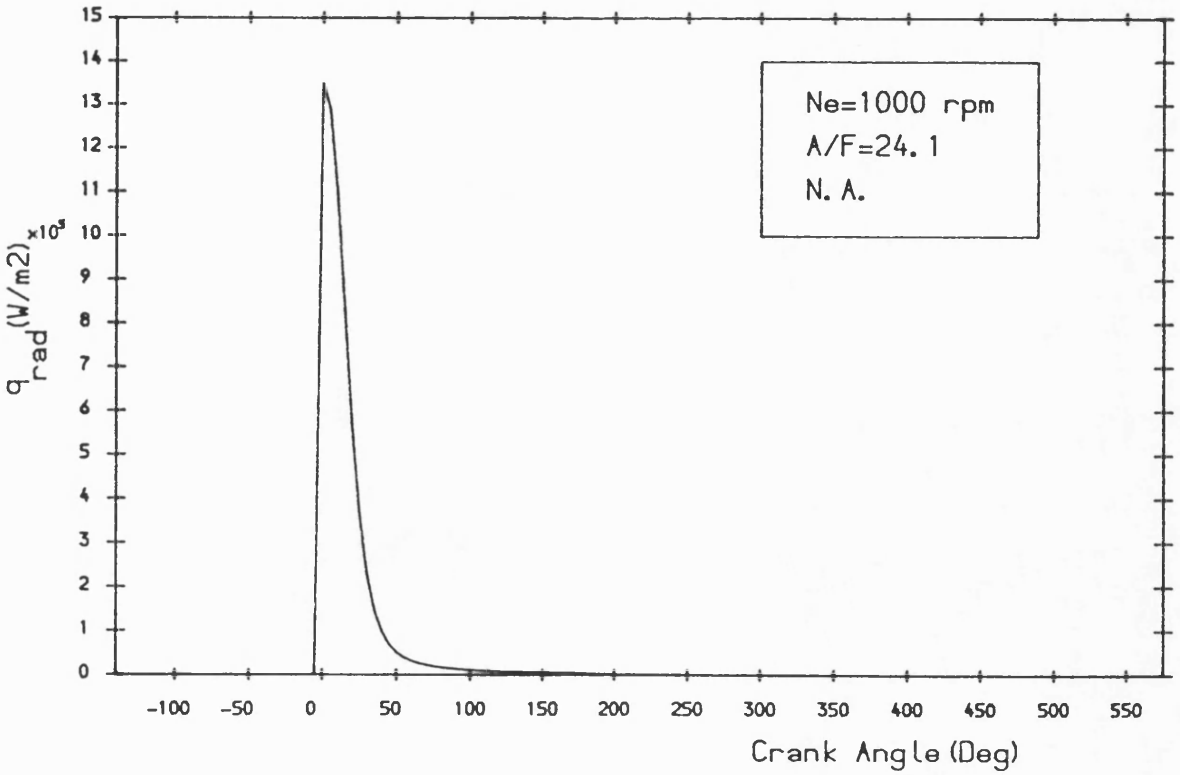

Fig. 6.11 Radiation heat flux versus crank angle.

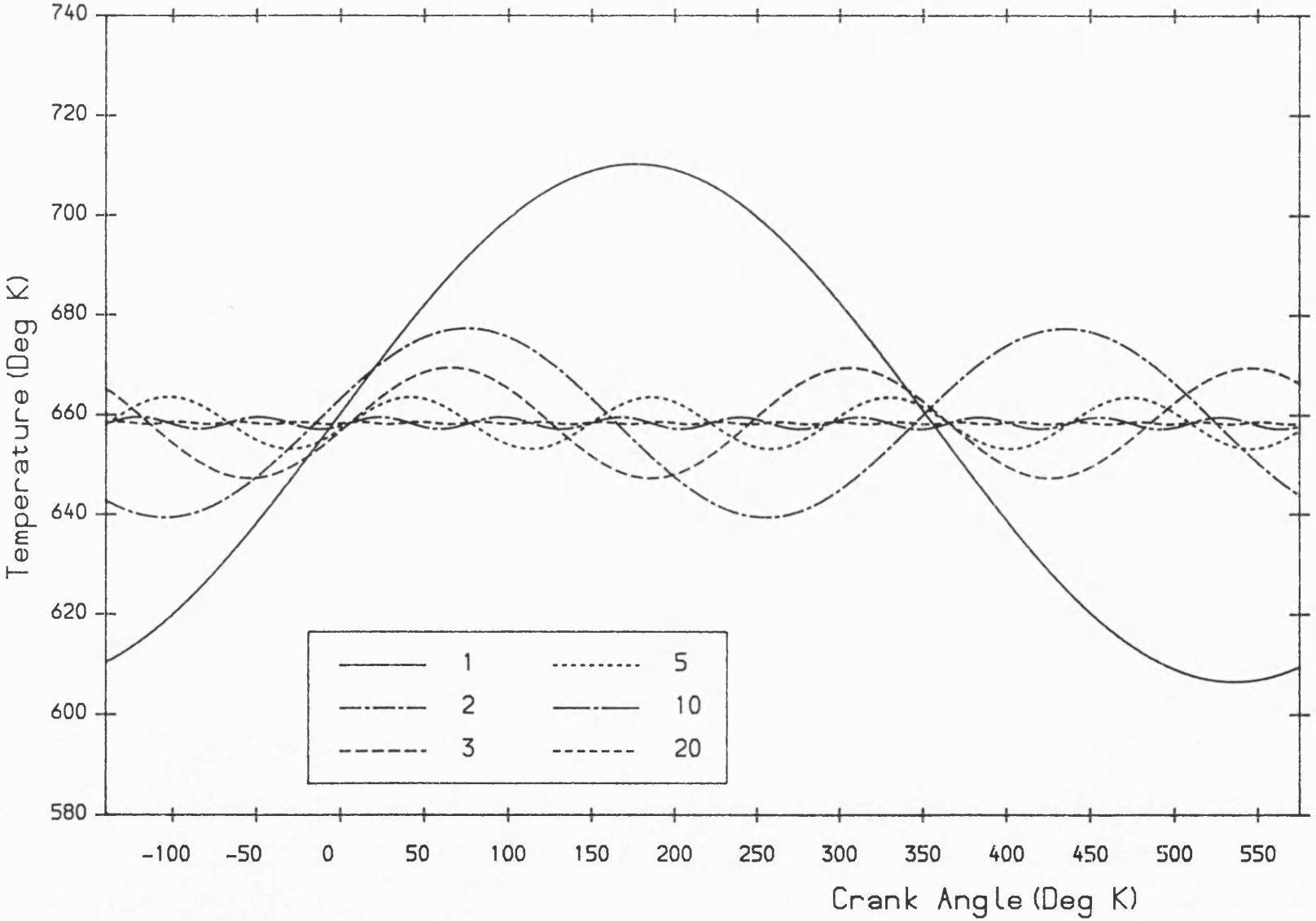

Fig. 6.12 The effect of various individual gas temperature harmonics on wall surface temperature swing.

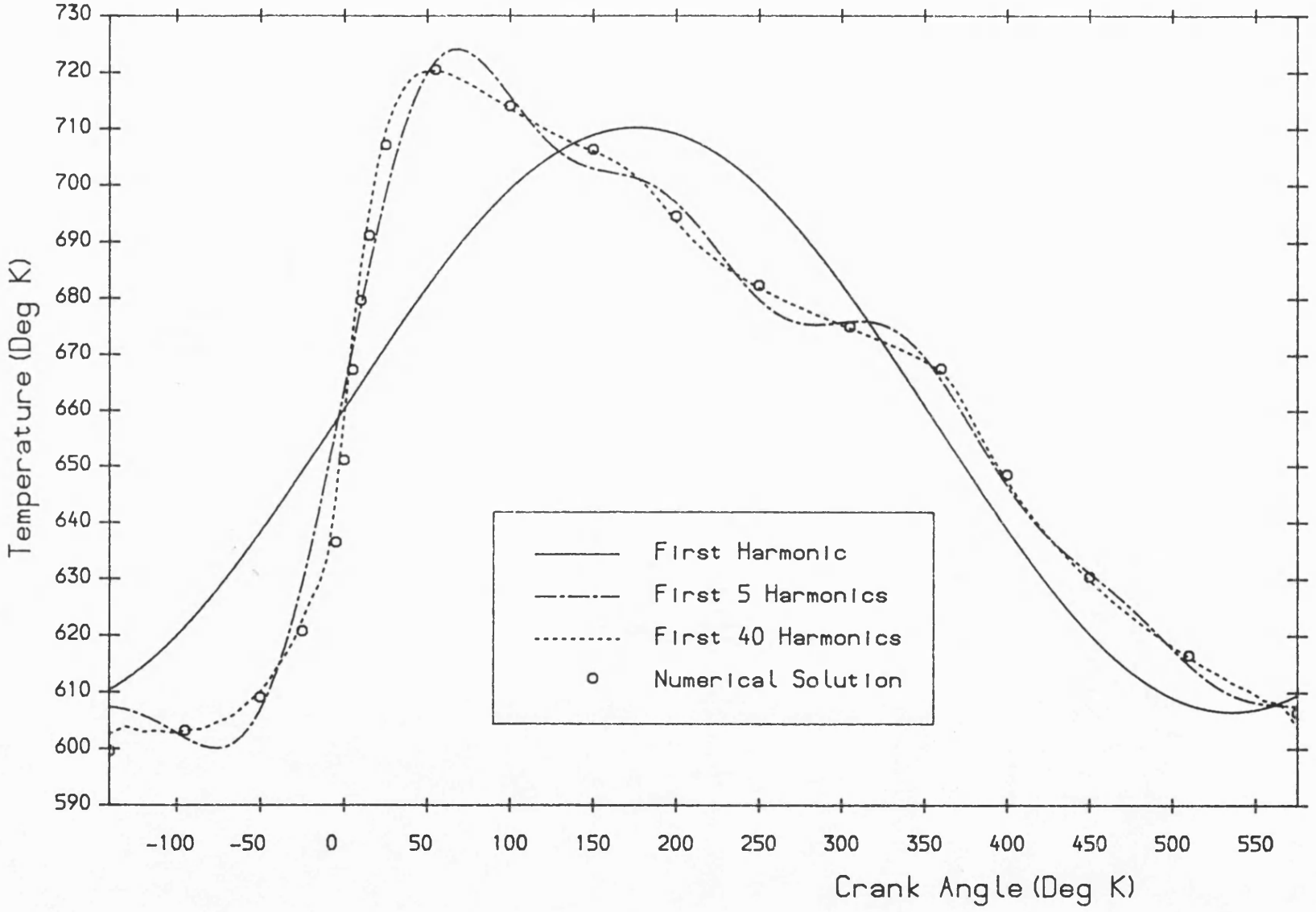

Fig. 6.13 Comparison of the numerical and exact solutions for different numbers of harmonics.

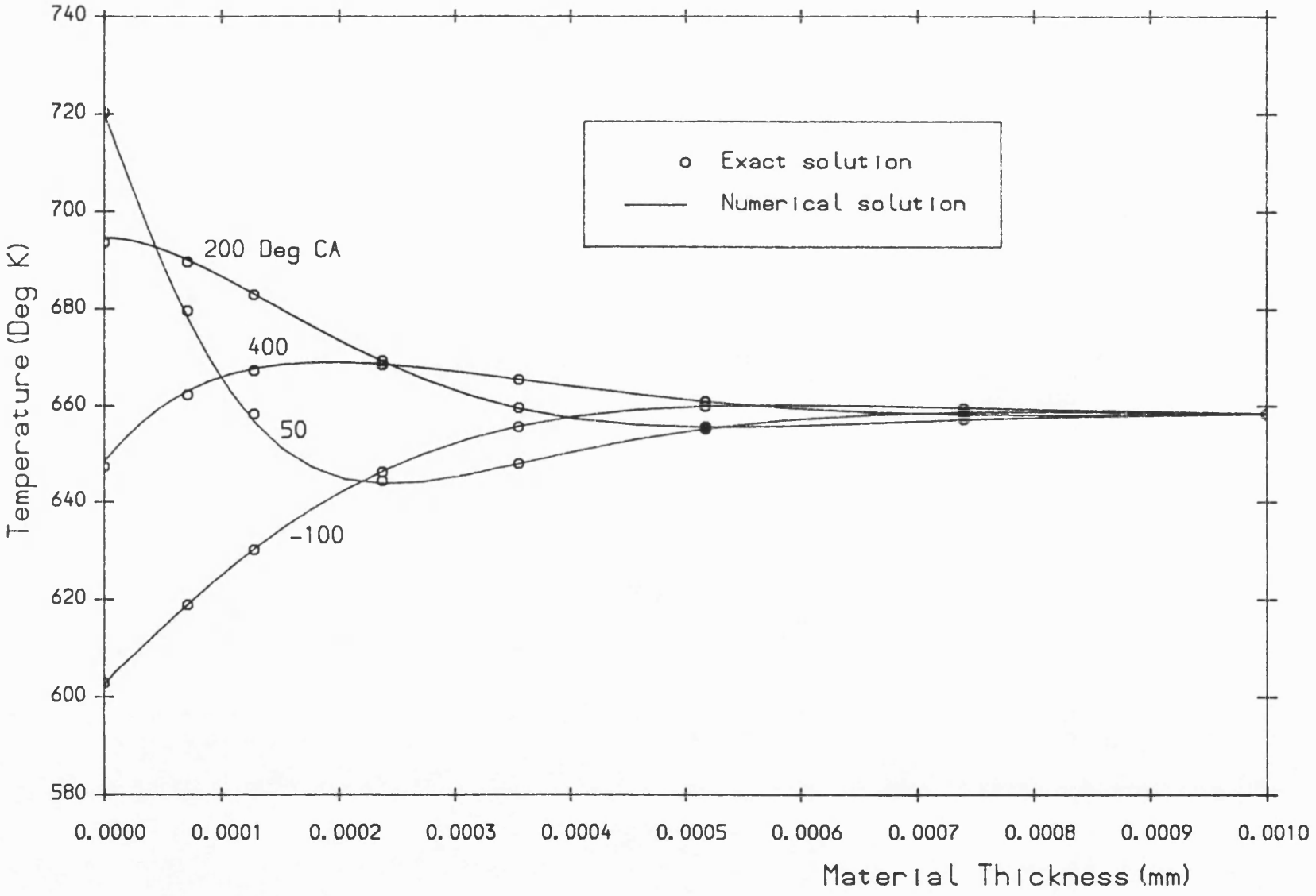

Fig. 6.14 The exact solution with 40 Fourier harmonics and numerical solution of the temperature wave through the material.

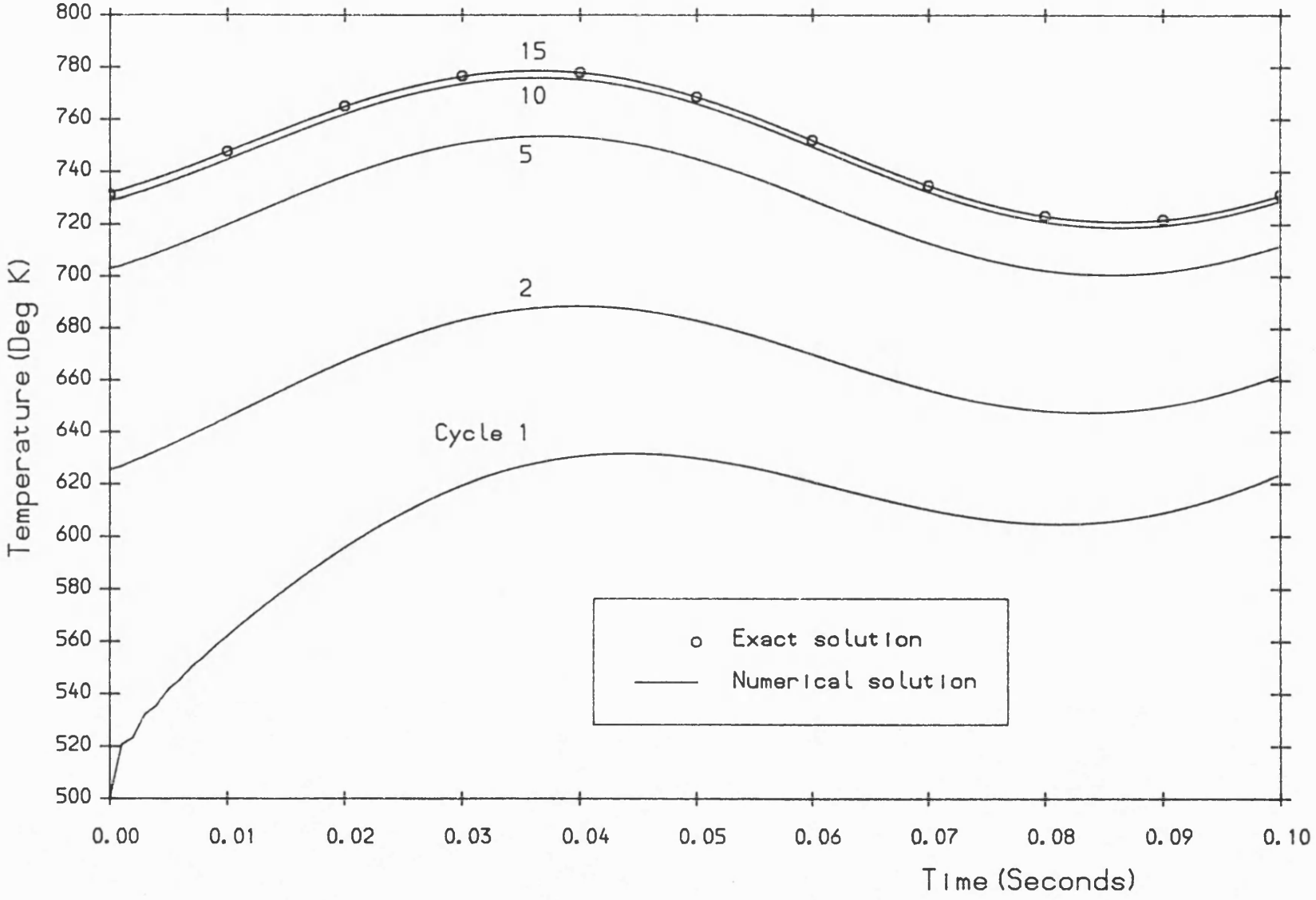

Fig. 6.15 The number of cycles necessary for the numerical solution to reach steady state.

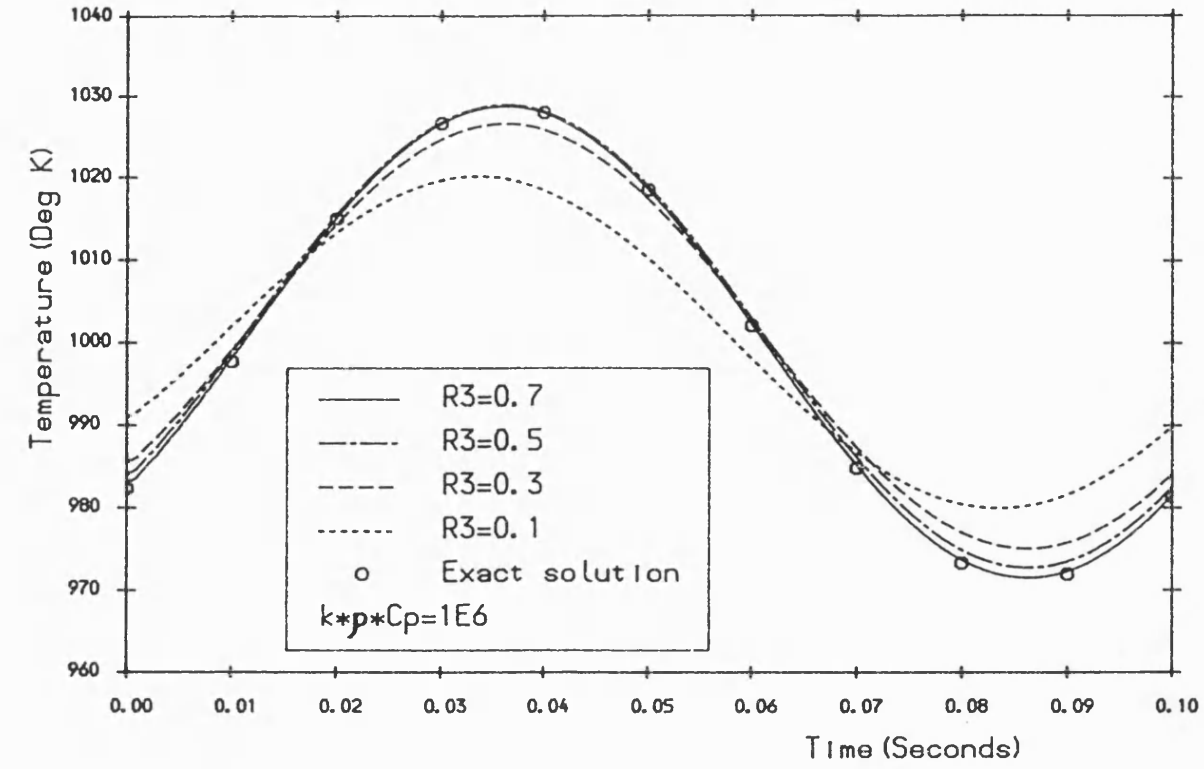

Fig. 6.16 The effect of the layer thickness ratio, R3, on ceramic wall surface temperature swing.

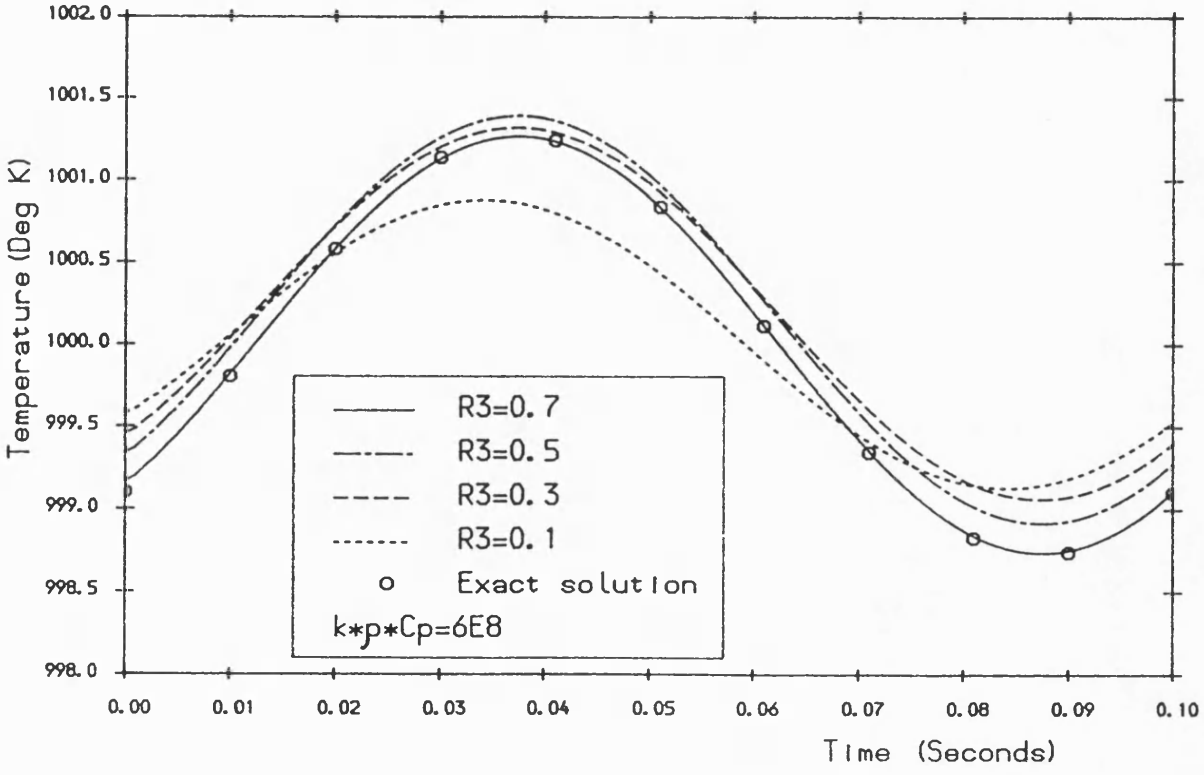

Fig. 6.17 The effect of the layer thickness ratio, R3, on aluminum wall surface temperature swing.

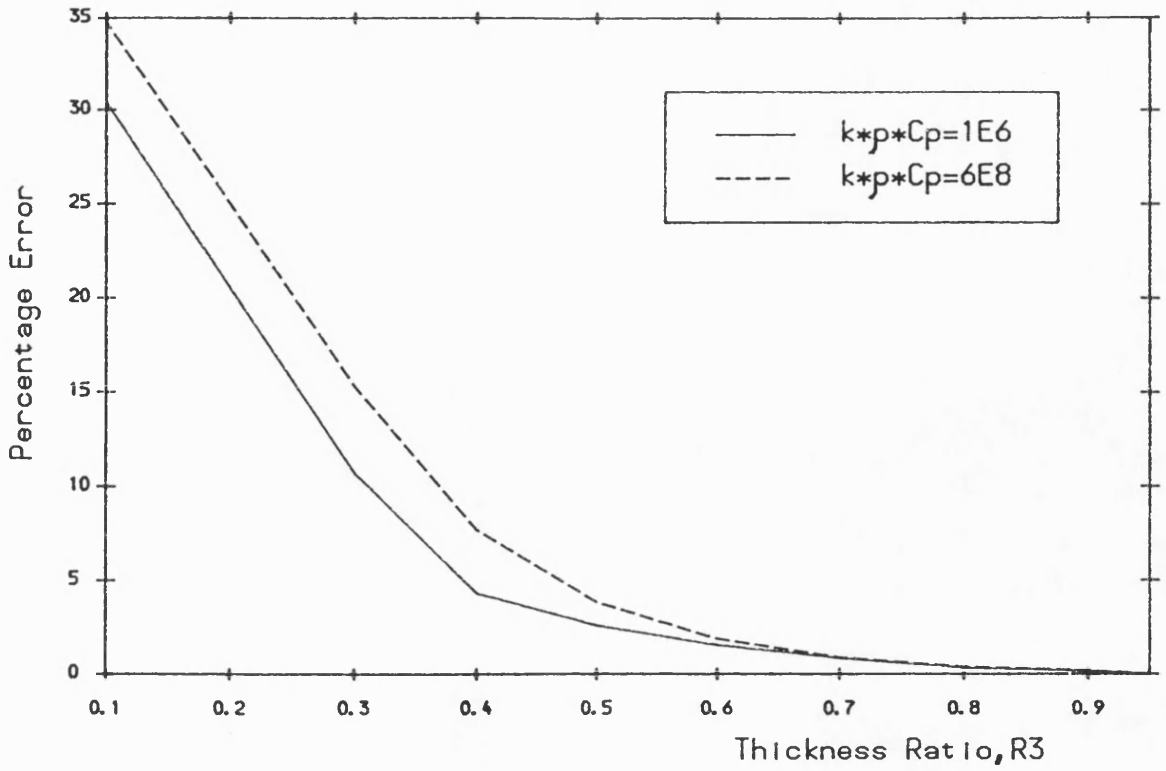

Fig. 6.18 The percentage error of wall surface temperature swing versus the layer thickness ratio, R3.

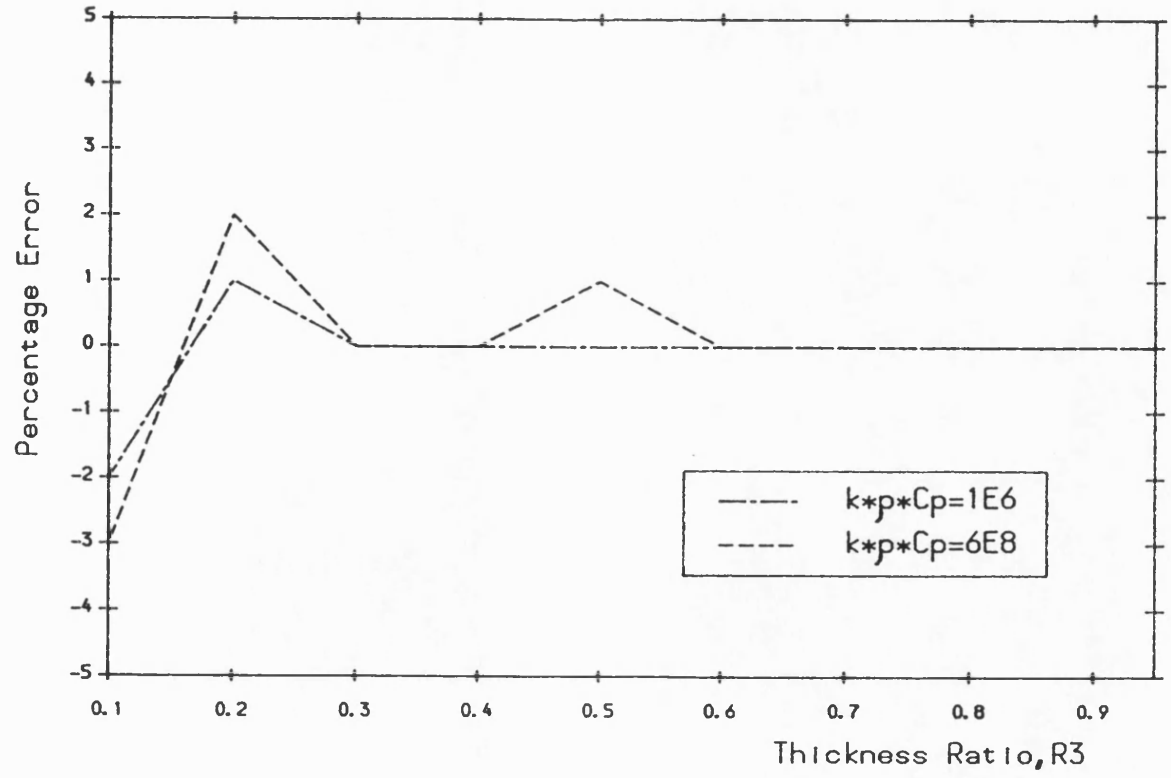

Fig. 6.19 The percentage error of phase angle versus the layer thickness ratio, R3.

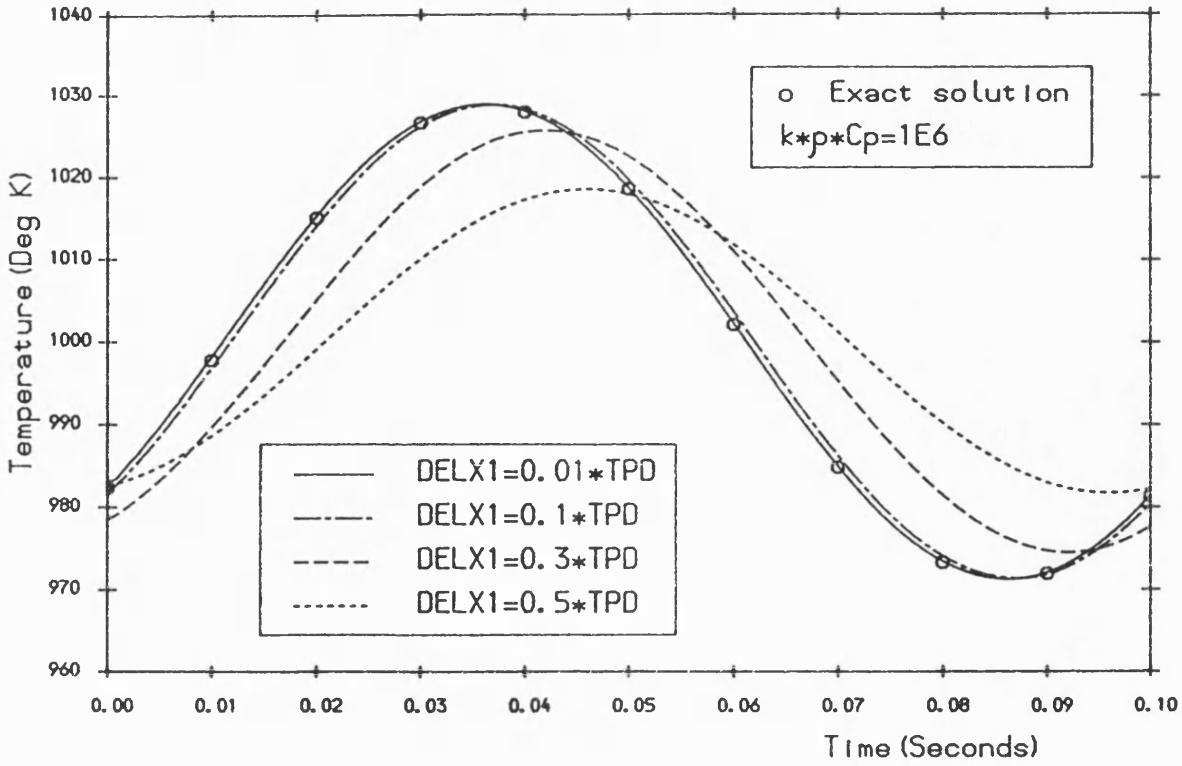

Fig. 6.20 The effect of first layer thickness on the ceramic wall surface temperature swing.

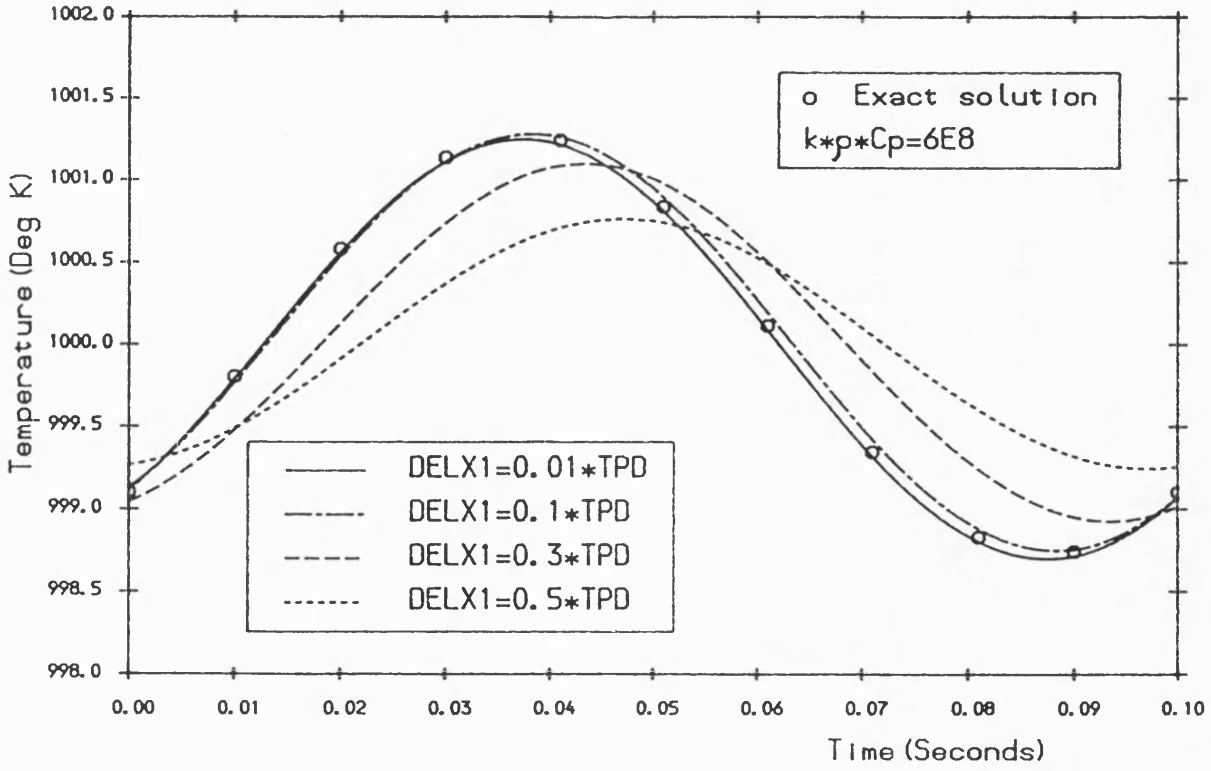

Fig. 6.21 The effect of first layer thickness on the aluminum wall surface temperature swing.

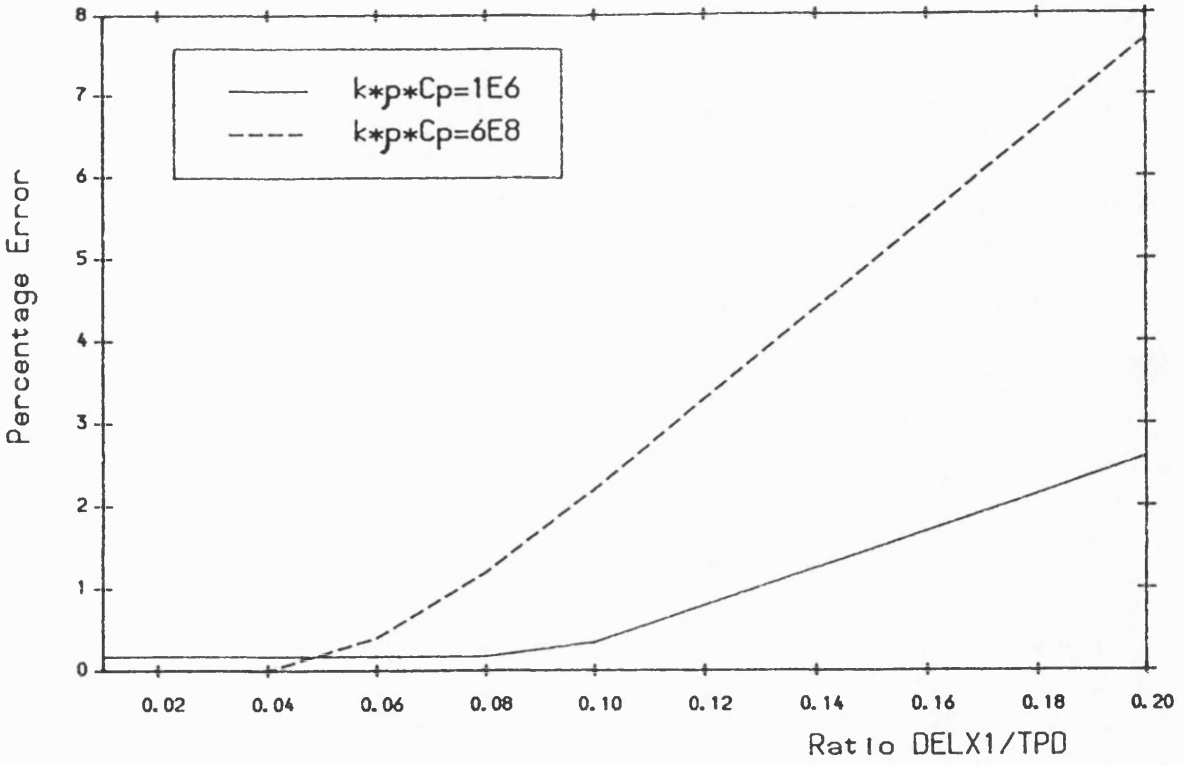

Fig. 6.22 Percentage error of wall surface temperature swing versus first layer thickness to thermal penetration depth ratio.

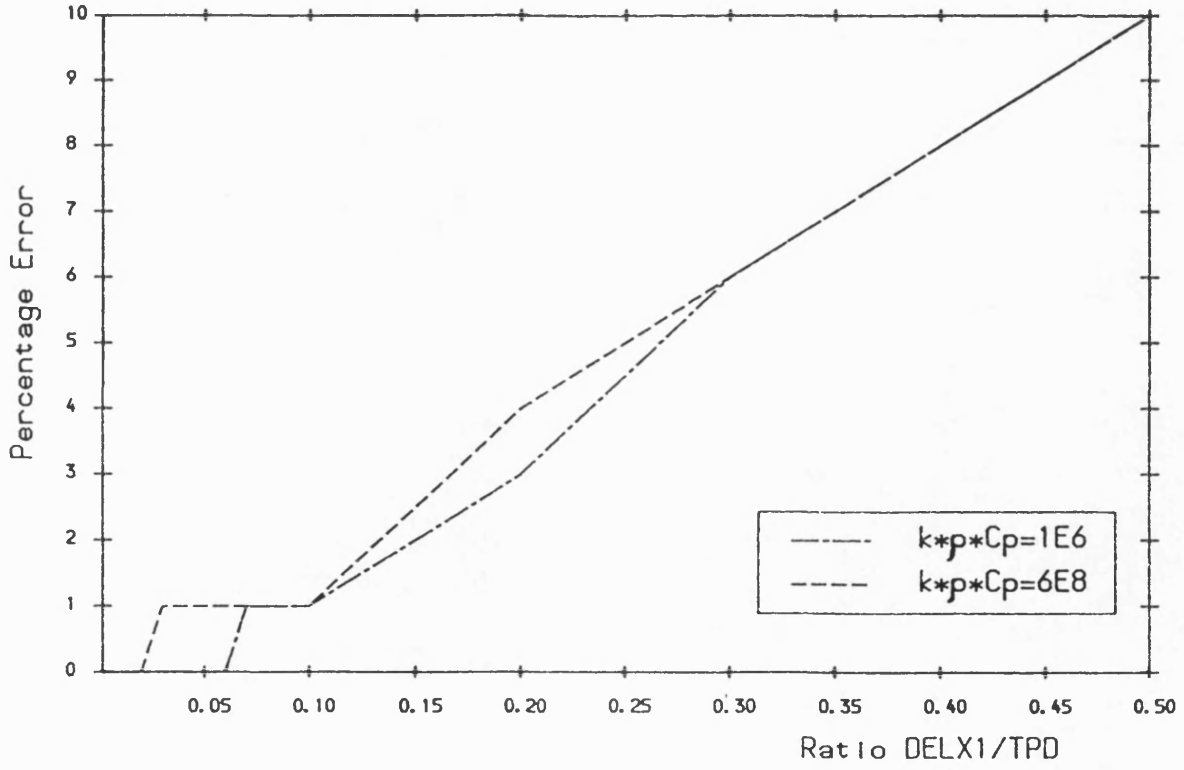

Fig. 6.23 Percentage error of phase angle versus first laye thickness to thermal penetration depth ratio.

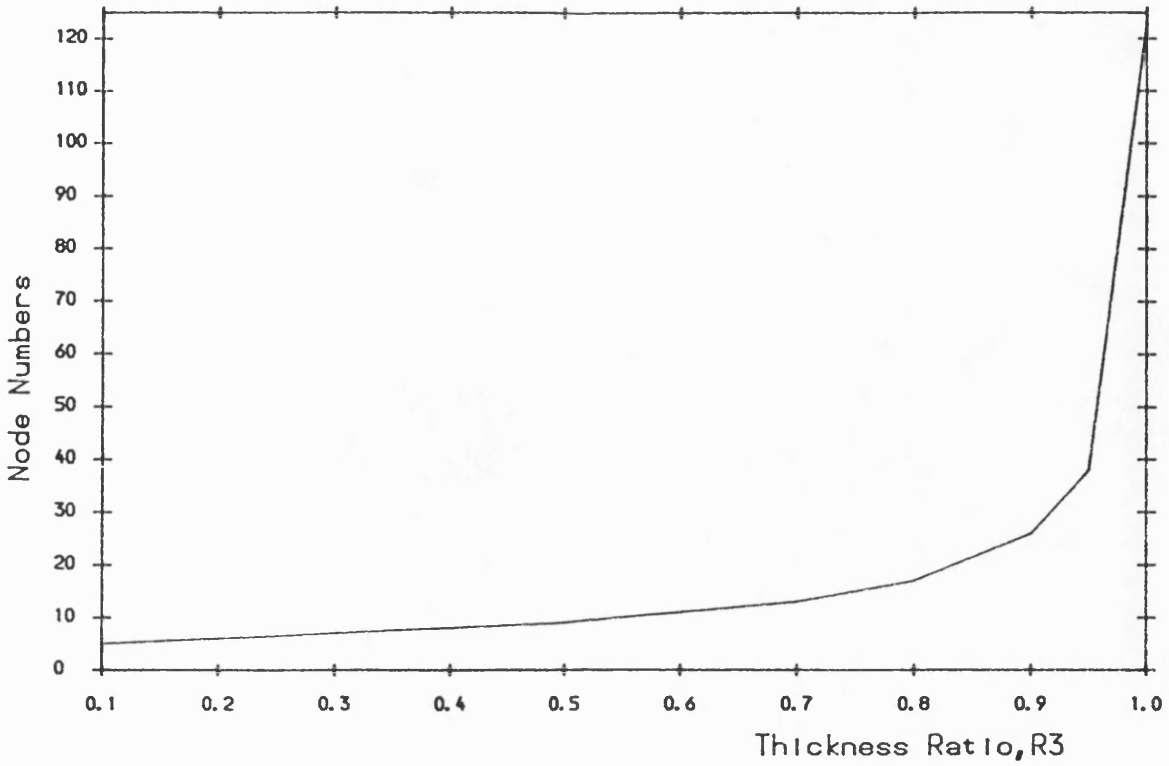

Fig. 6.24 The FD node numbers versus the layer thickness ratio, R3.

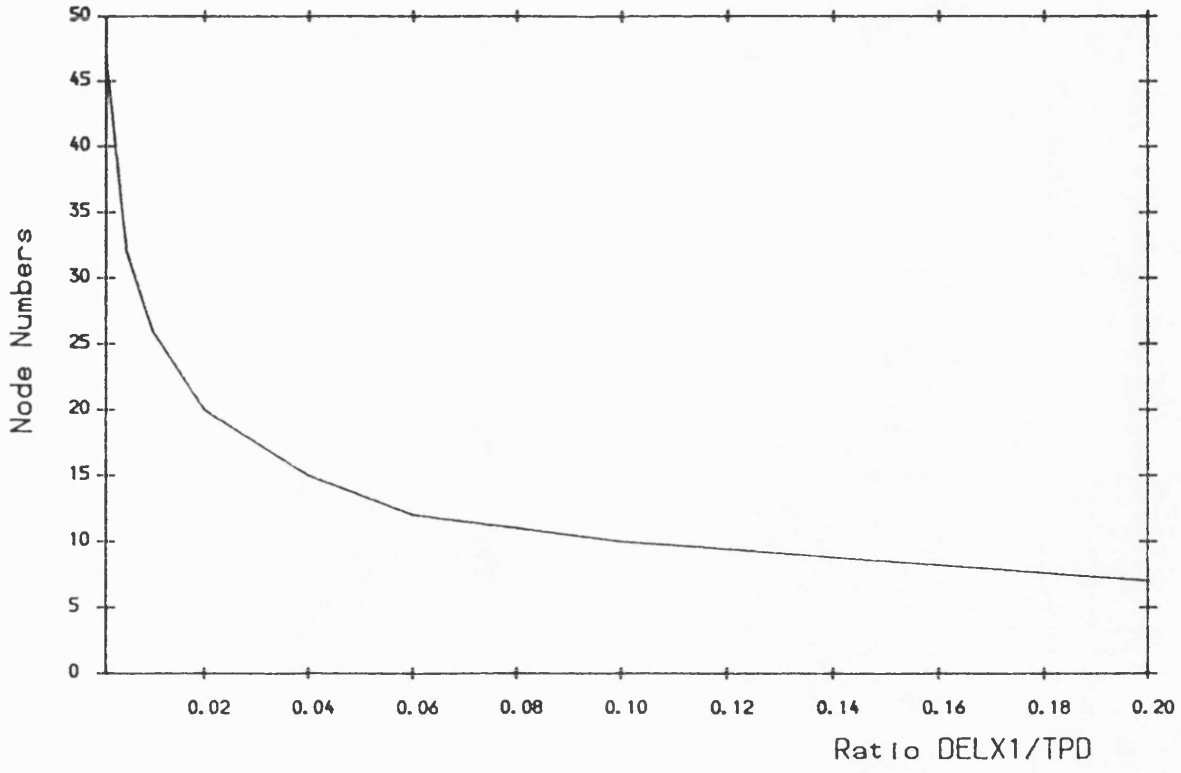

Fig. 6.25 The FD node numbers versus first layer thickness to thermal penetration depth ratio.

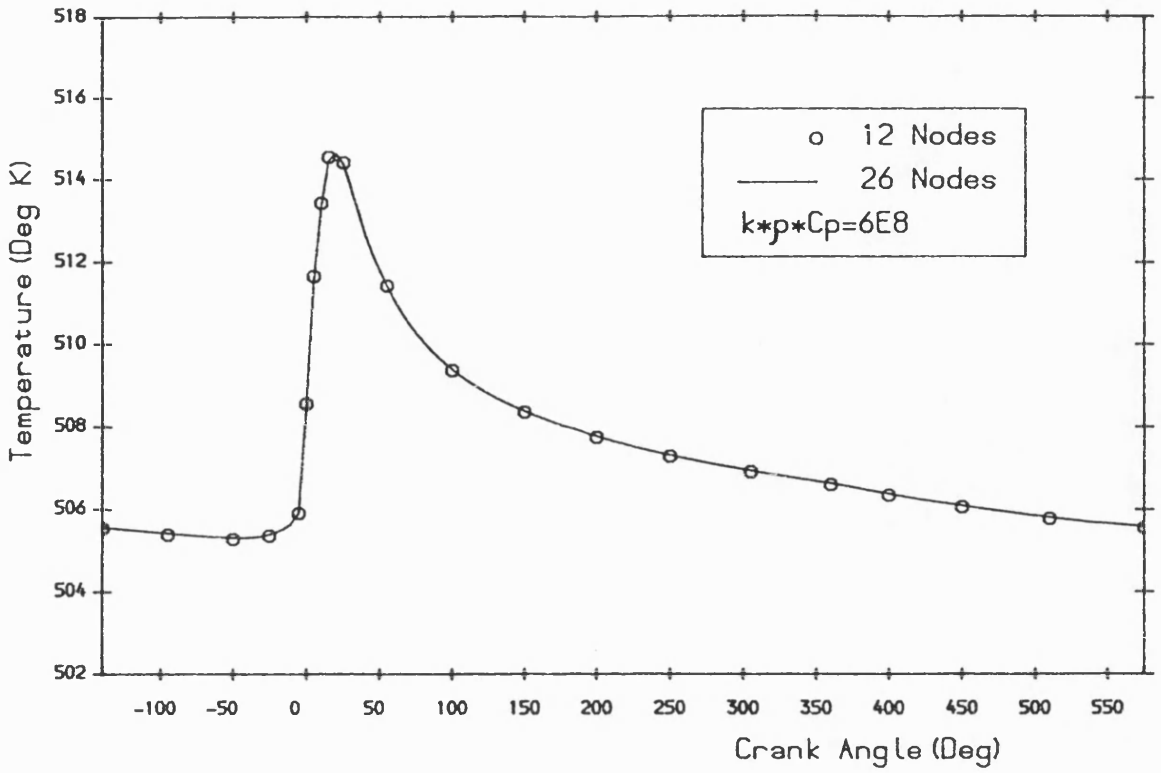

Fig. 6.26 Ceramic wall surface temperature versus crank angle for two different FD node numbers.

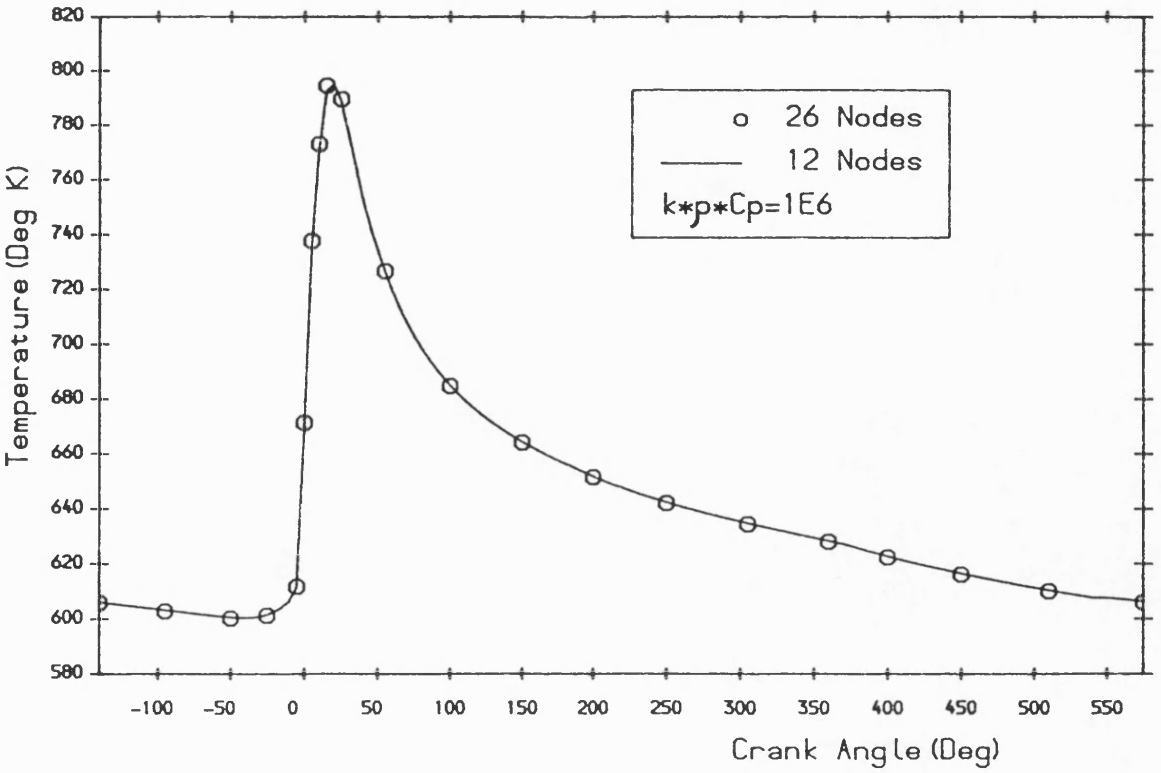

Fig. 6.27 Aluminum wall surface temperature versus crank angle for two different FD node numbers.

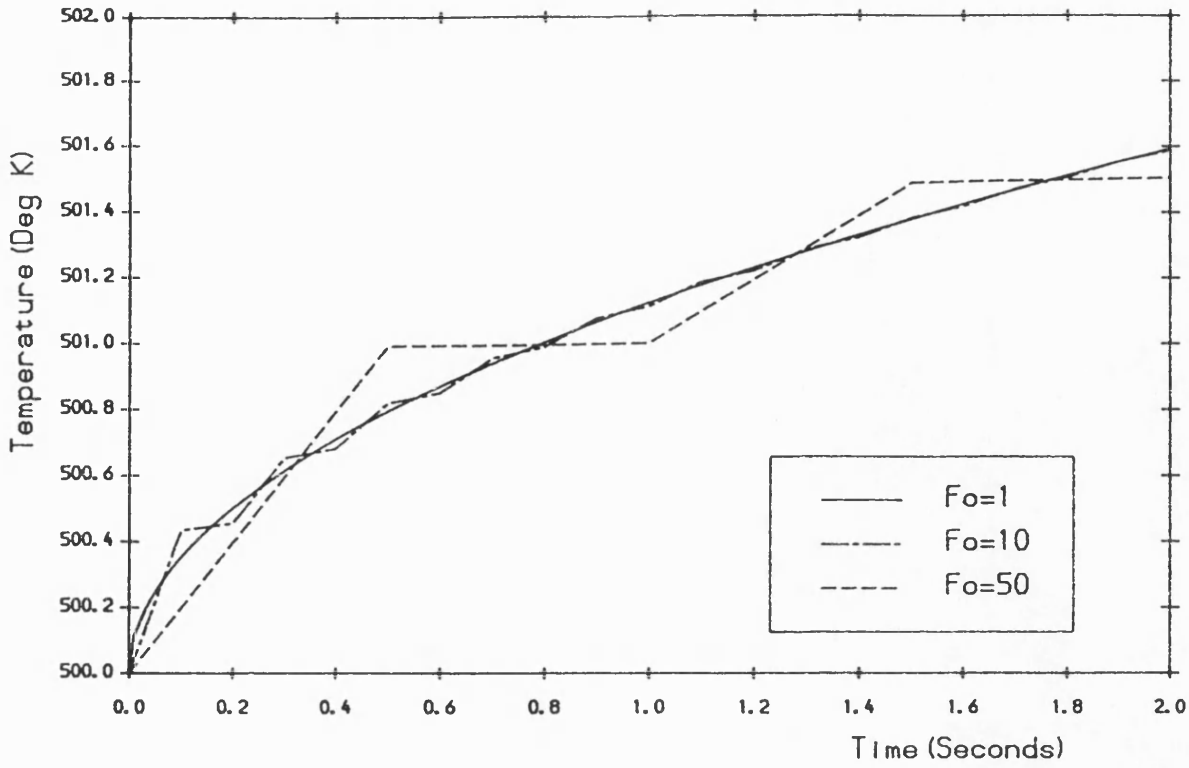

Fig. 6.28 The effect of Fourier number on the numerical solution.

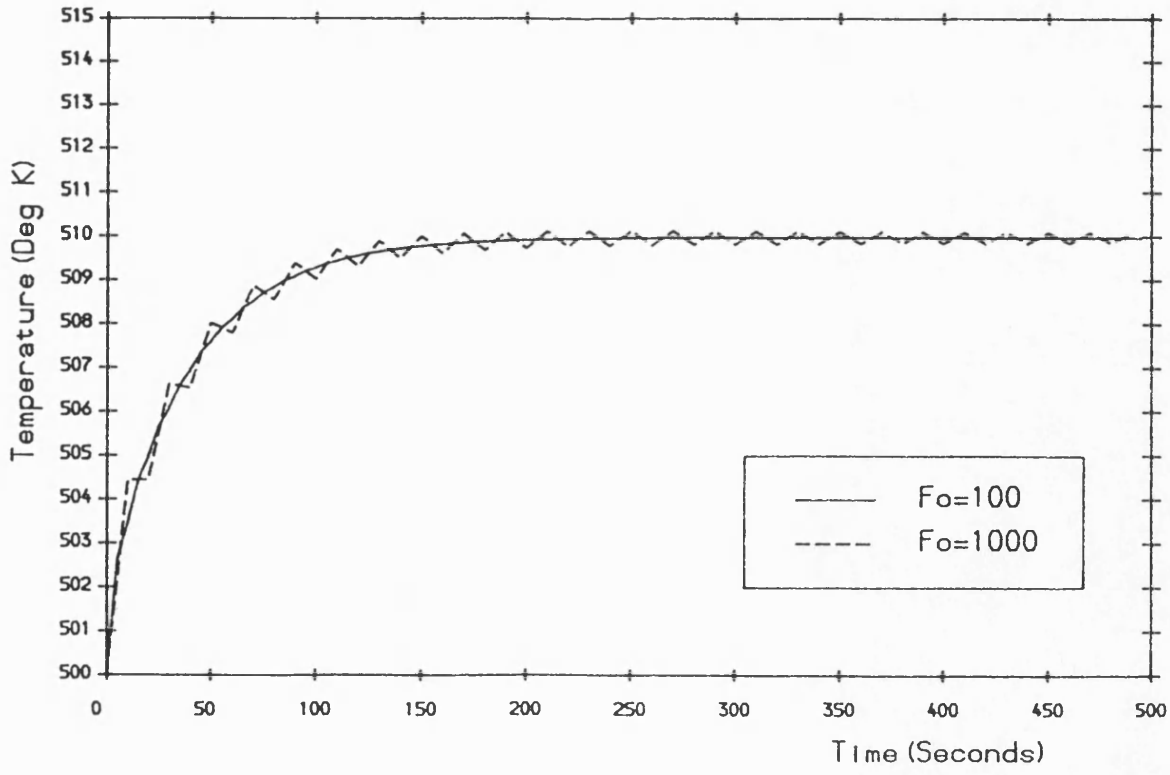

Fig. 6.29 The effect of Fourier number on the numerical solution.

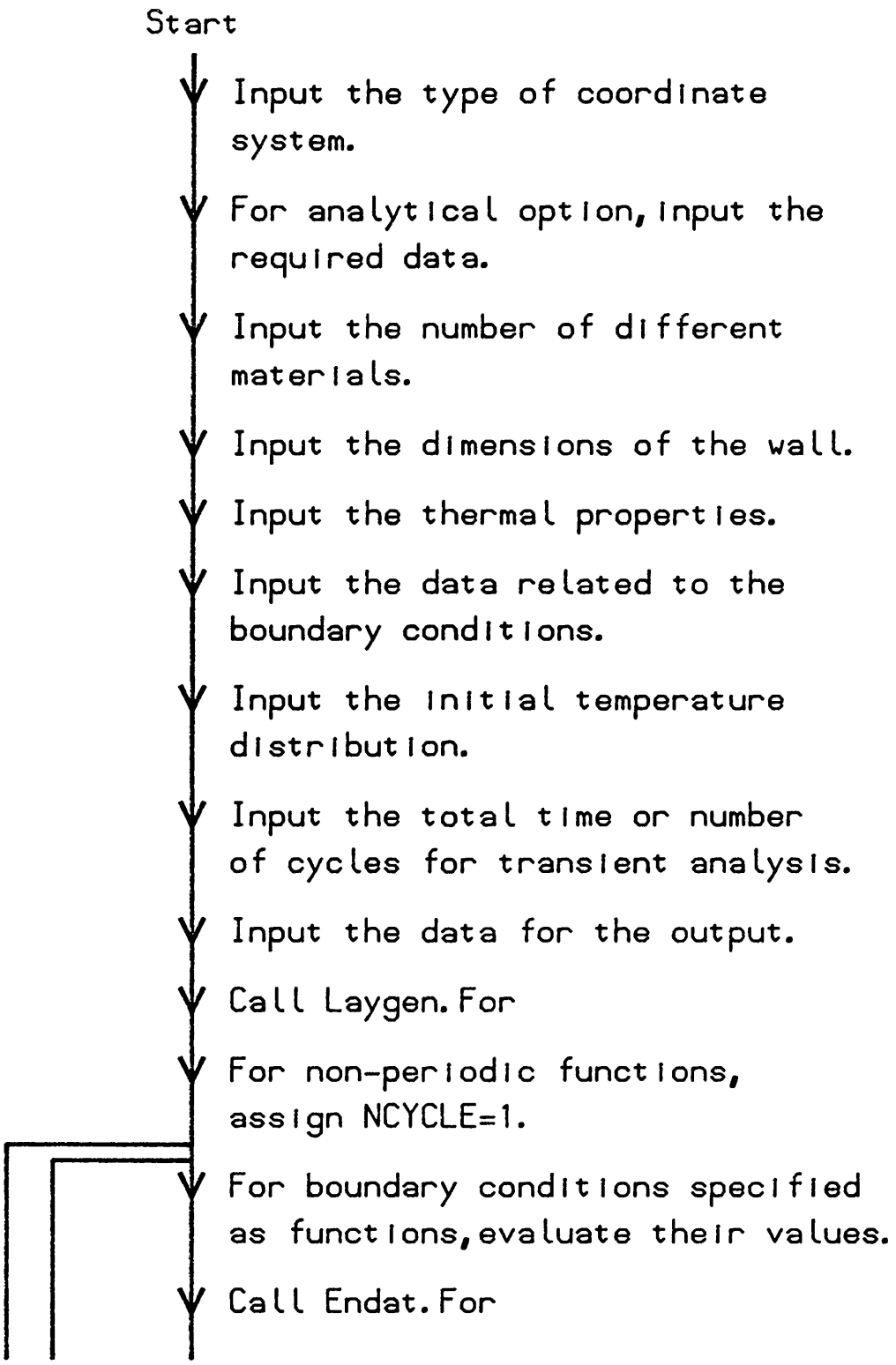

Fig. 6.30 The flowchart for Fd.For.

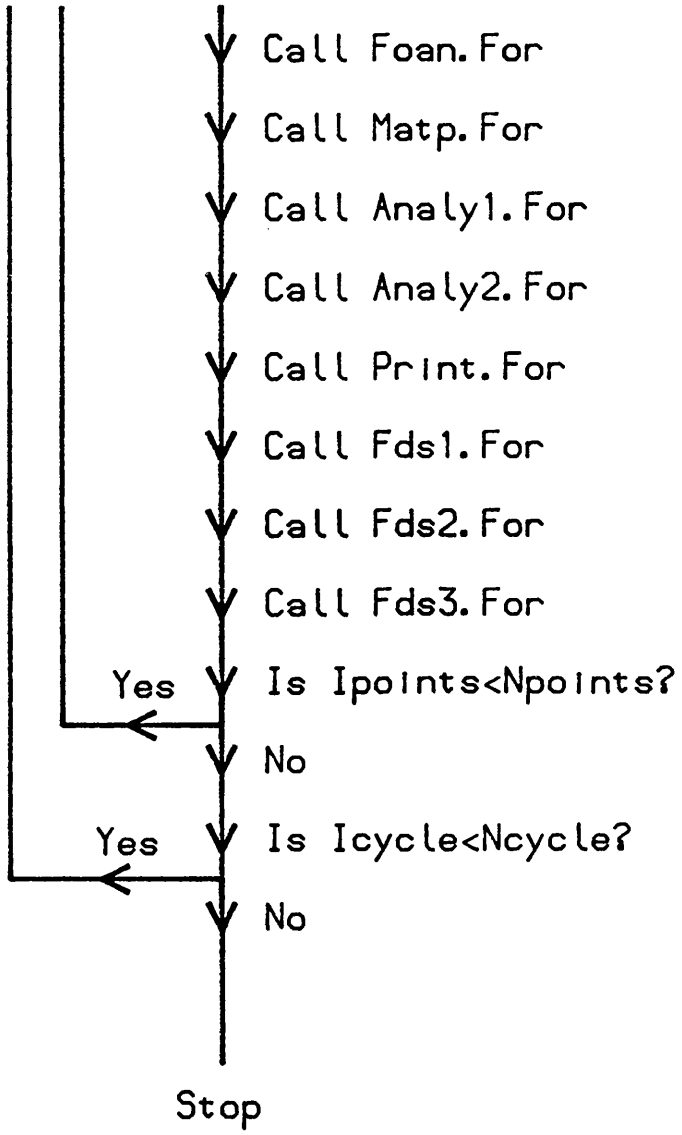

Fig. 6.30 Continued.

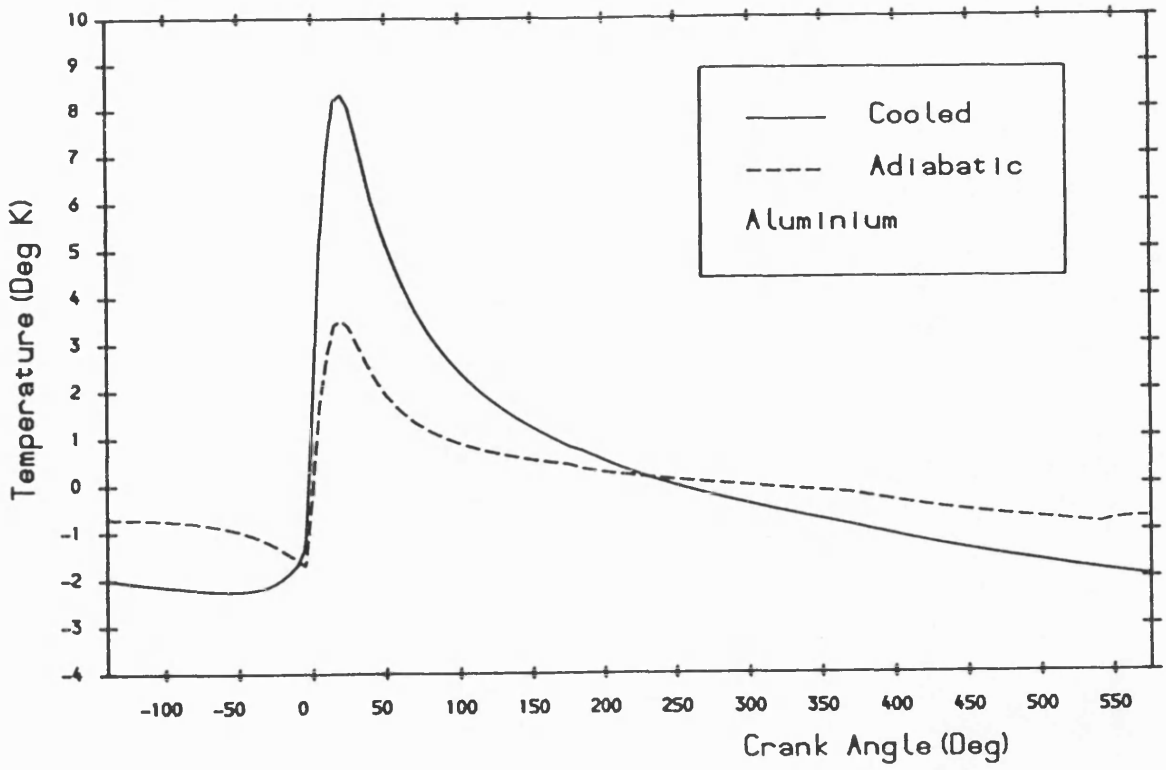

Fig. 6.31 Aluminium wall surface temperature swing at different coolant side boundary conditions.

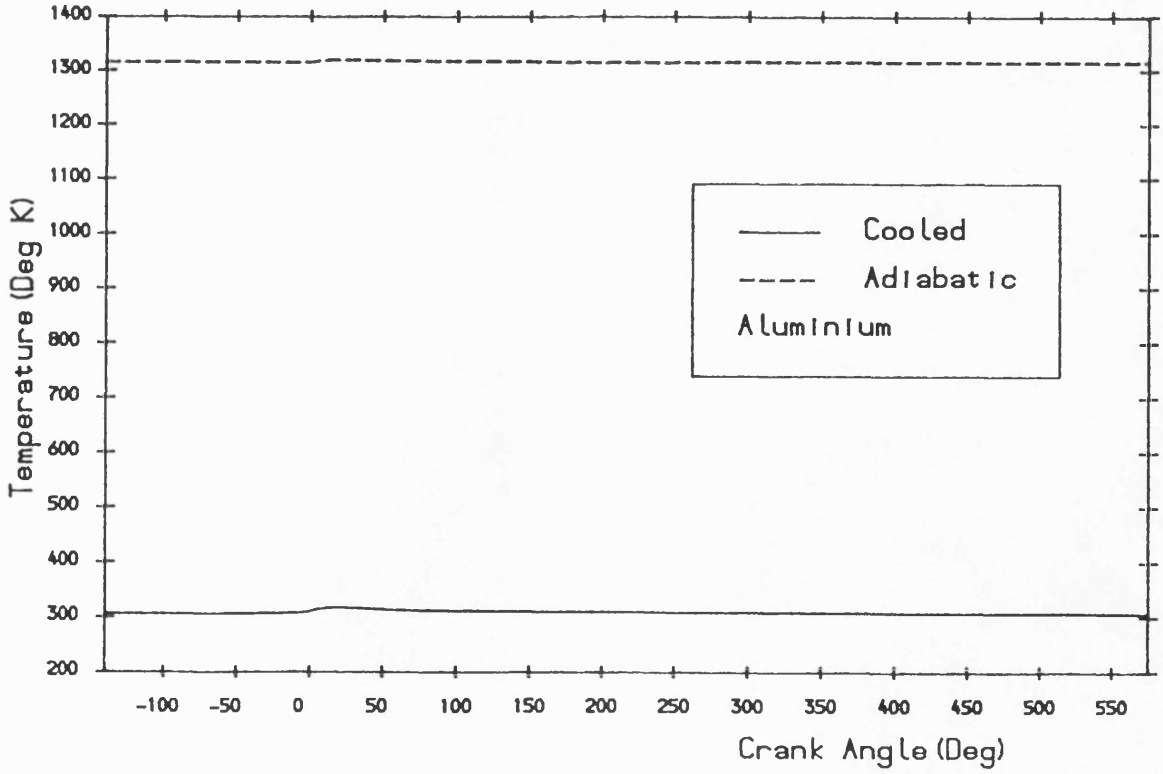

Fig. 6.32 Aluminium wall surface temperature versus crank angle at different coolant side boundary conditions.

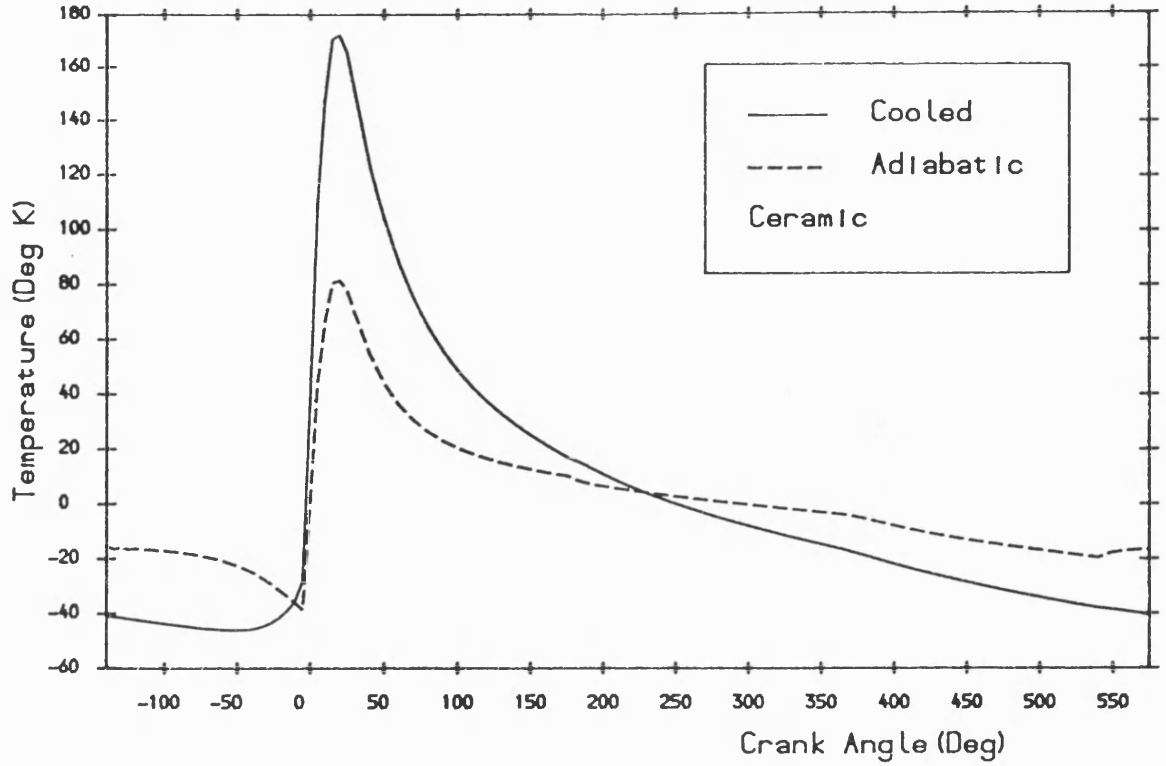

Fig. 6.33 Ceramic wall surface temperature swing at different coolant side boundary conditions.

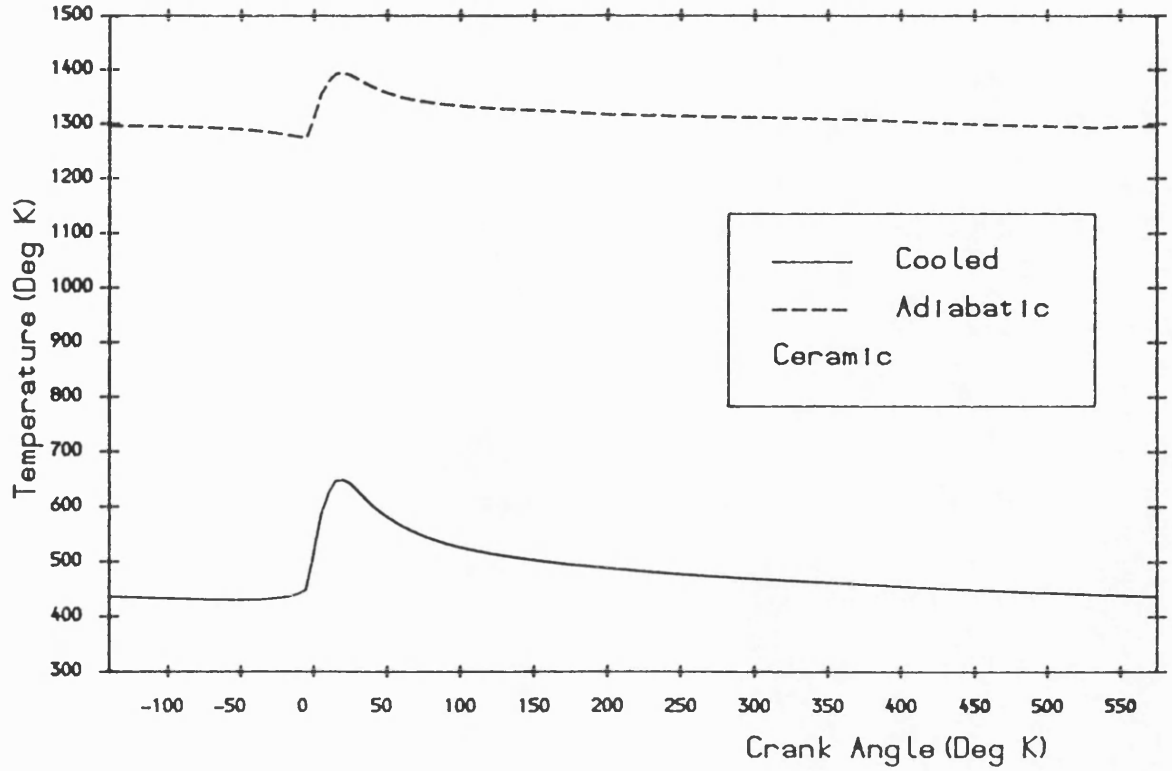

Fig. 6.34 Ceramic wall surface temperature versus crank angle at different coolant side boundary conditions.

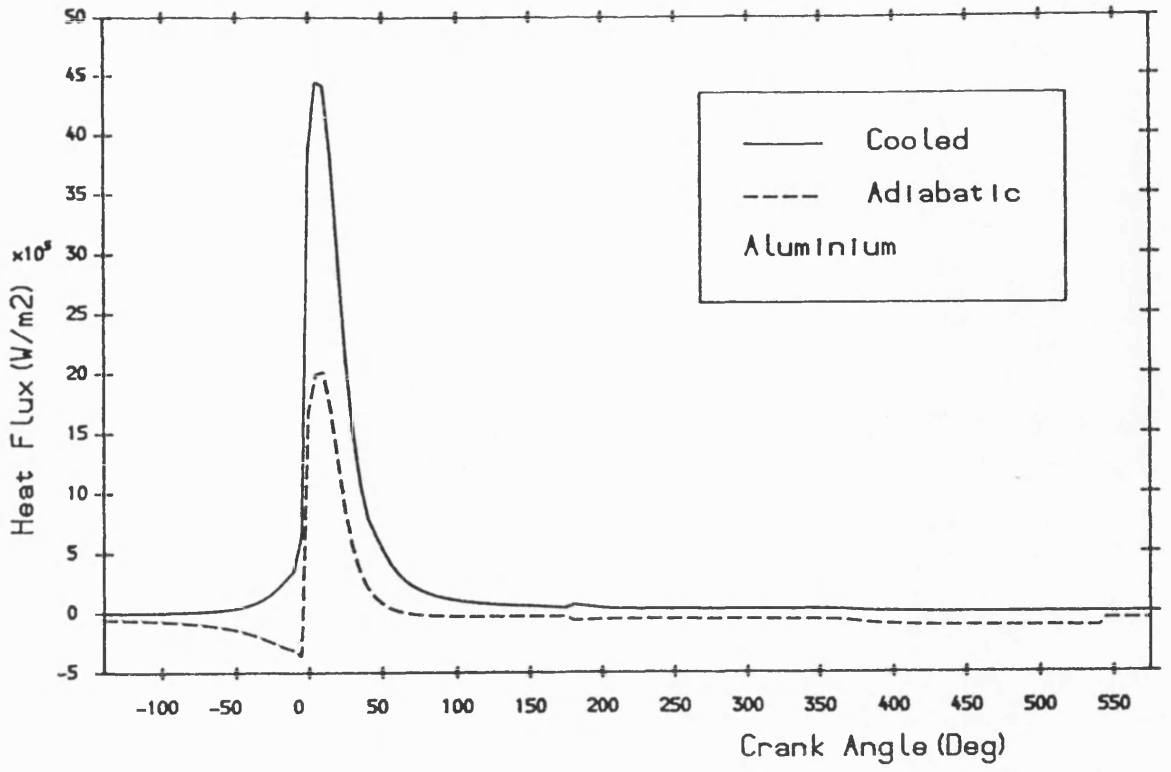

Fig. 6.35 Heat flux versus crank angle on aluminium wall at two coolant side boundary conditions.

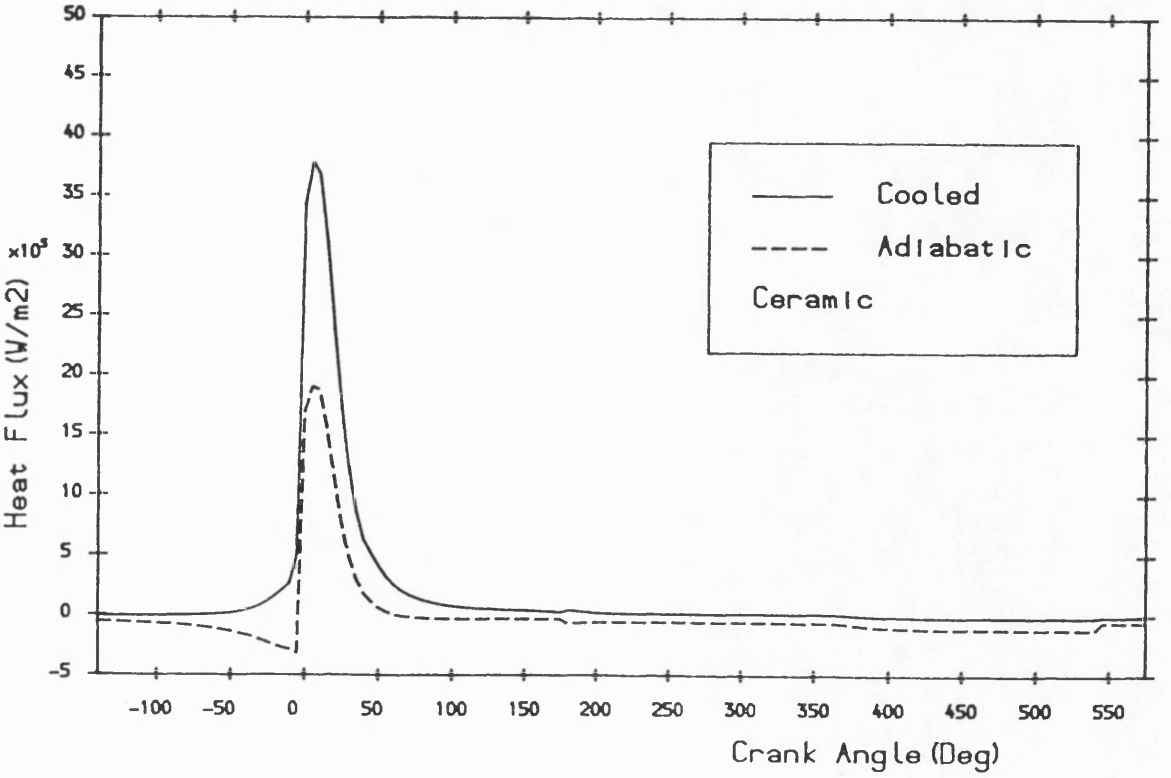

Fig. 6.36 Heat flux versus crank angle on ceramic wall at two coolant side boundary conditions.

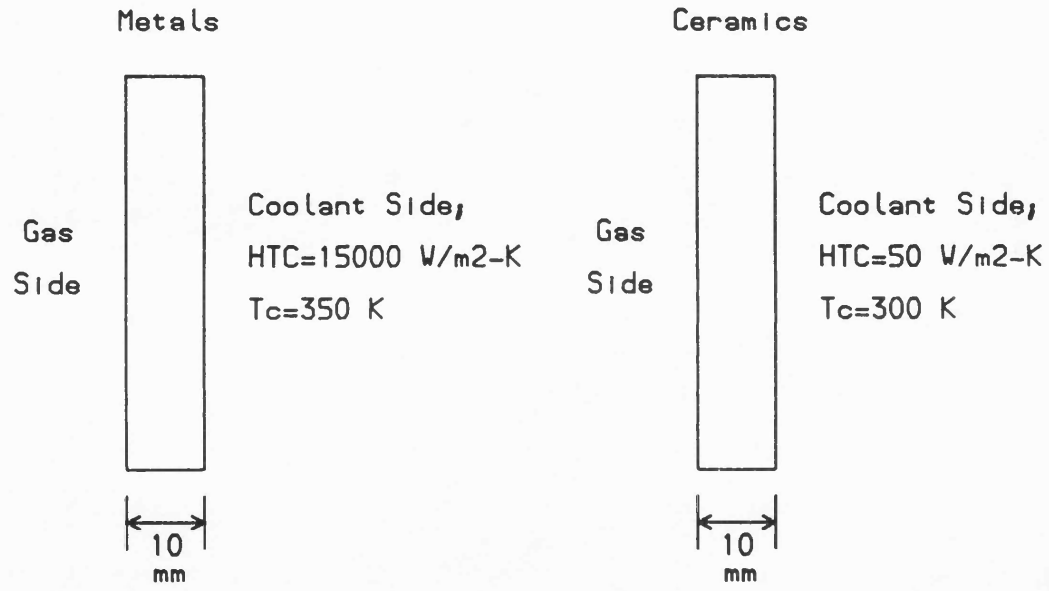

Fig. 6.37 Coolant side boundary conditions on metal and ceramic walls for figures 6.39-6.47.

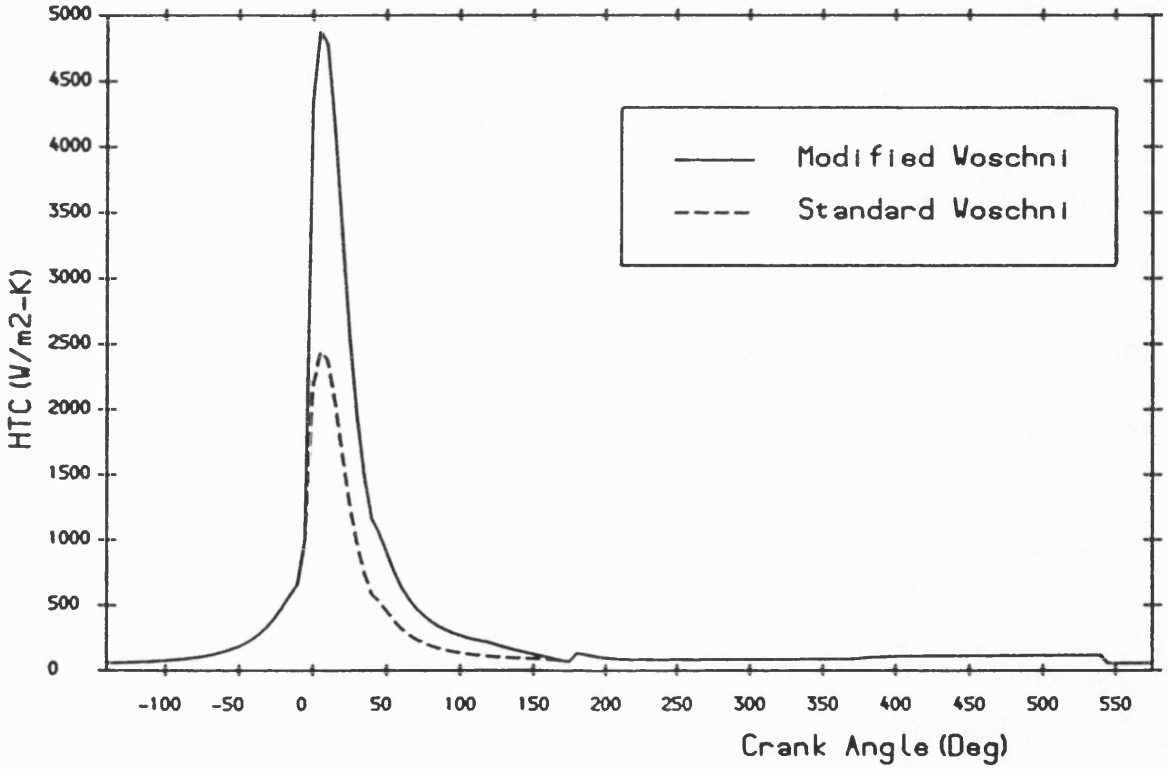

Fig. 6.38 Standard and modified Woschni heat transfer coefficient versus crank angle.

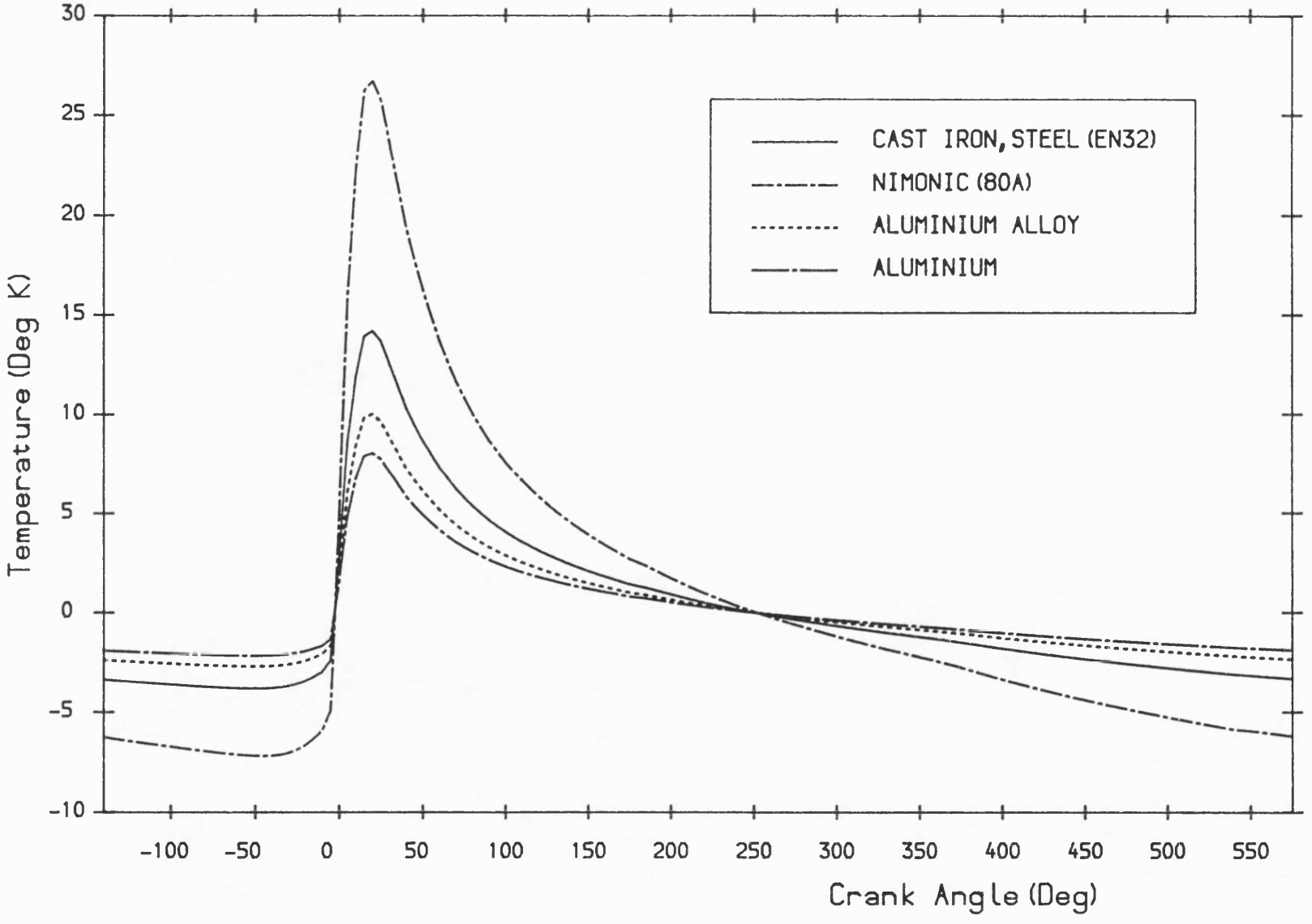

Fig. 6.39 Surface temperature swings for several metals.

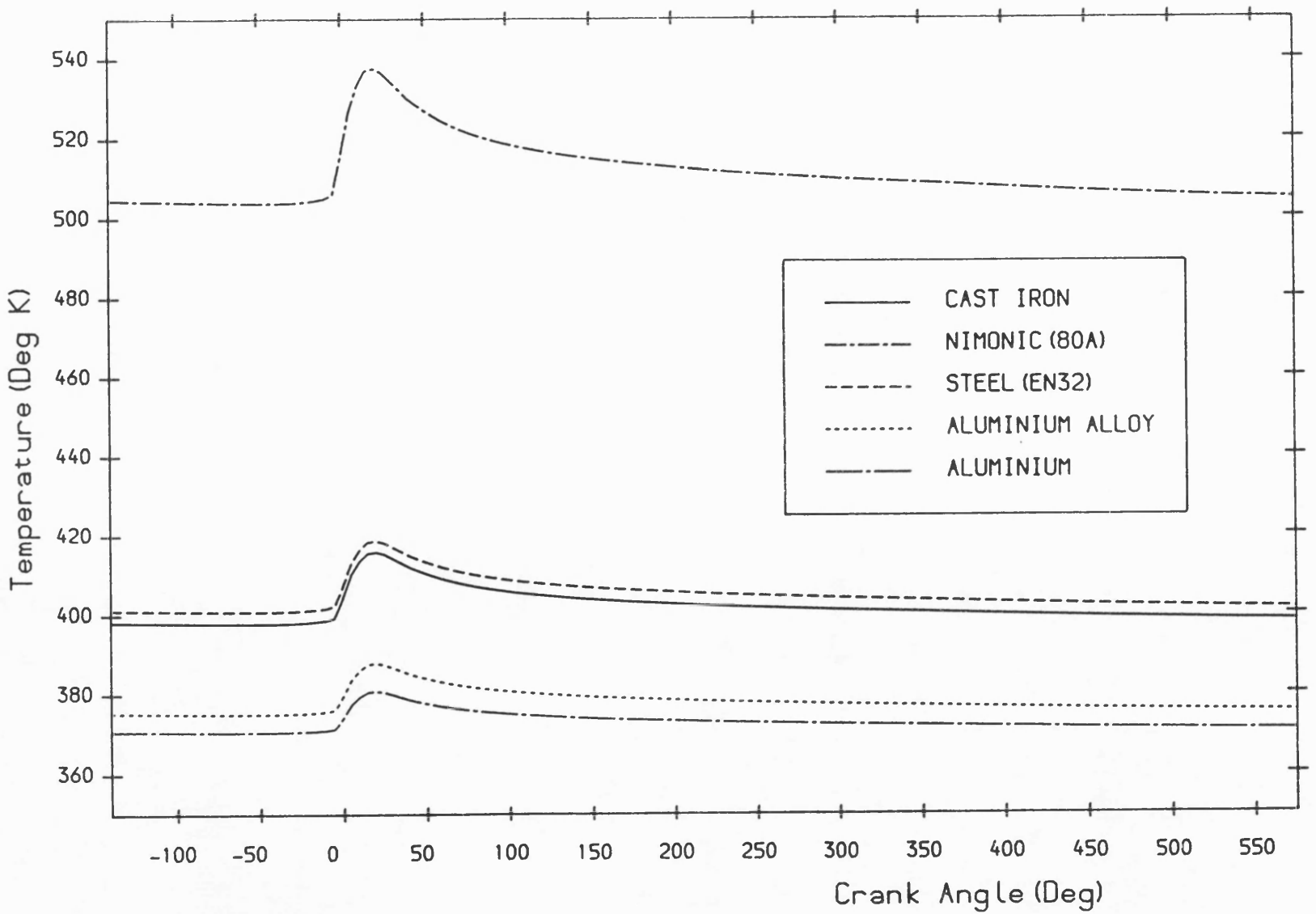

Fig. 6.40 Surface temperature versus crank angle for several metals.

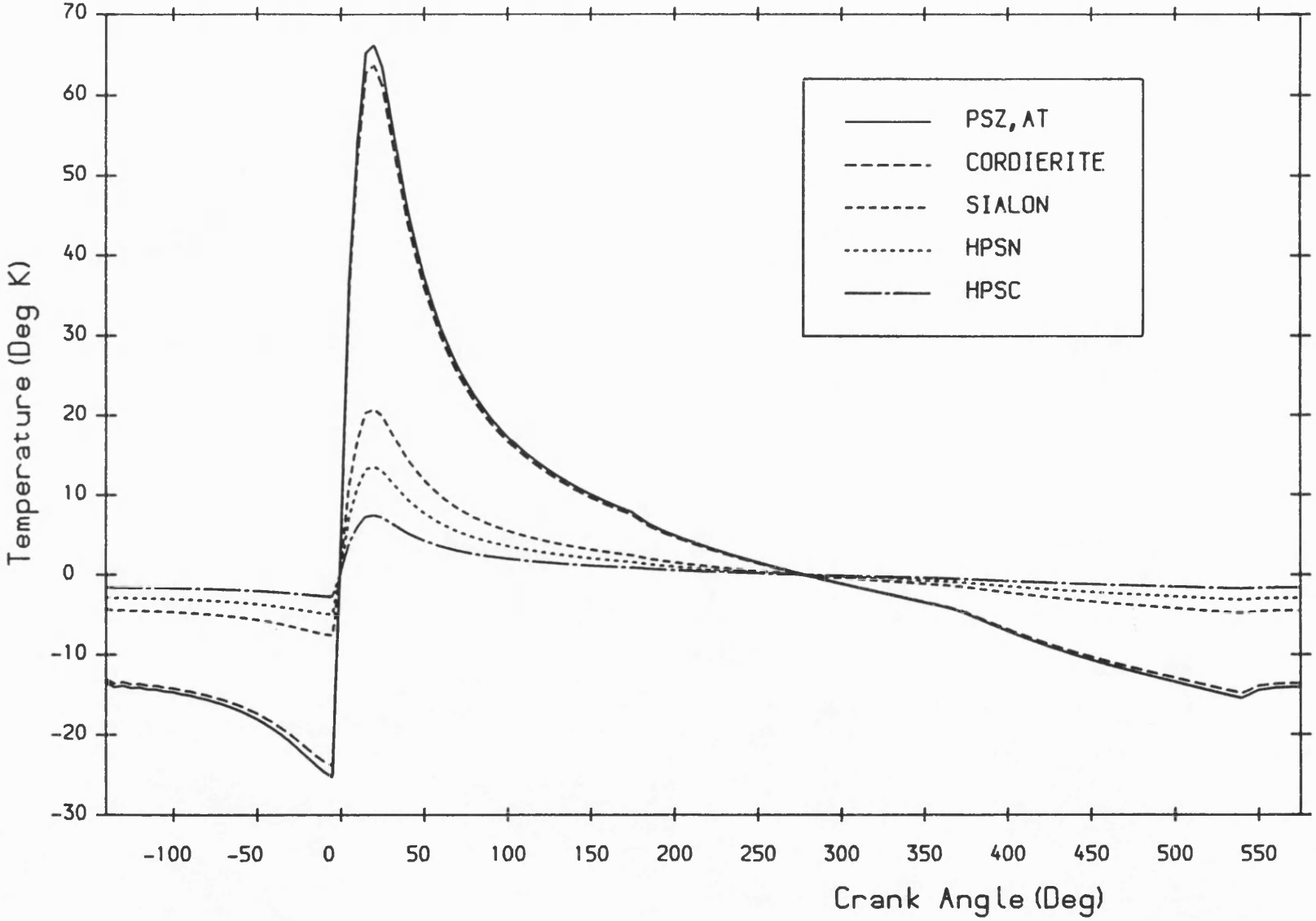

Fig. 6.41 Surface temperature swings for several ceramics.

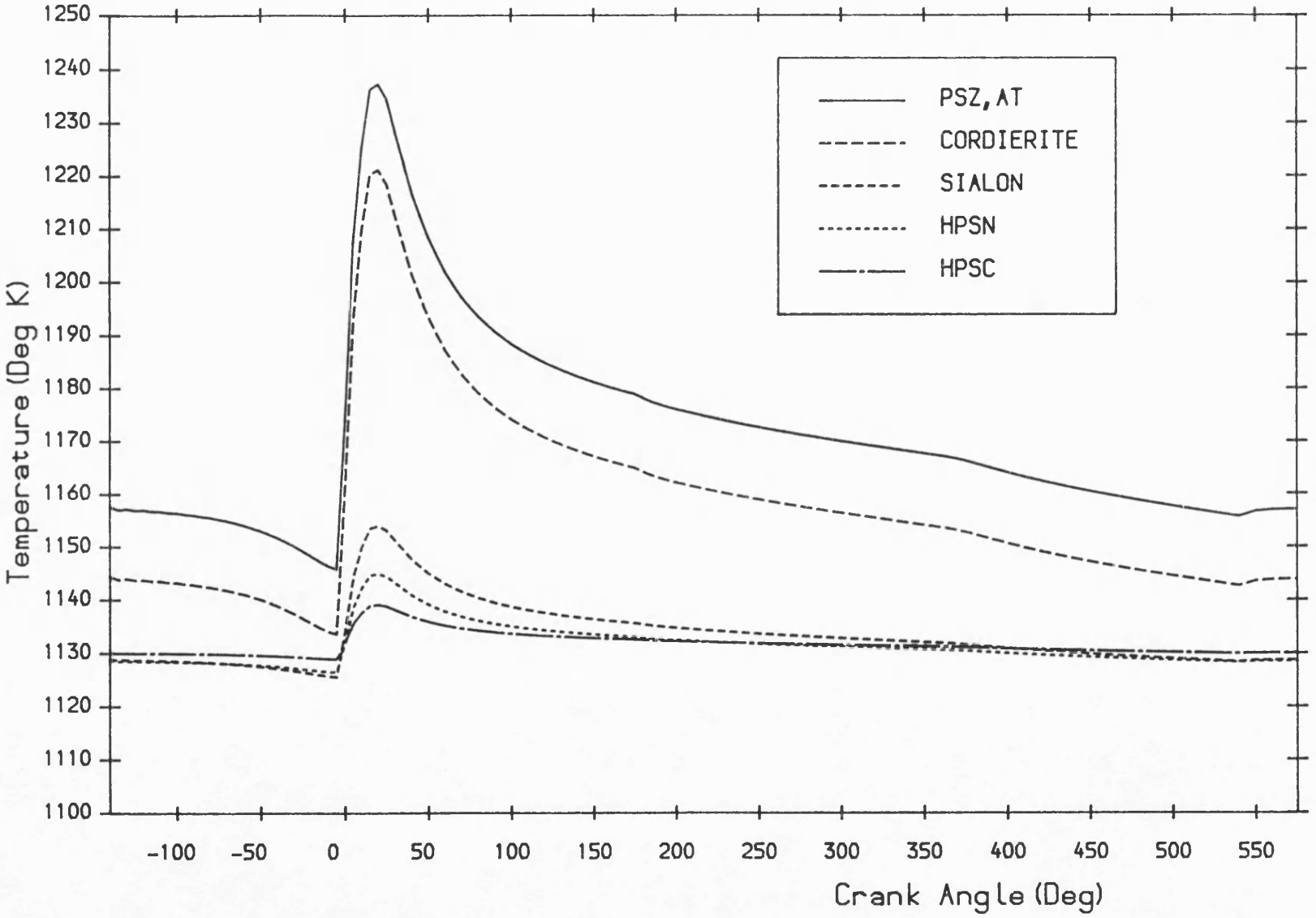

Fig. 6.42 Surface temperature versus crank angle for several ceramics.

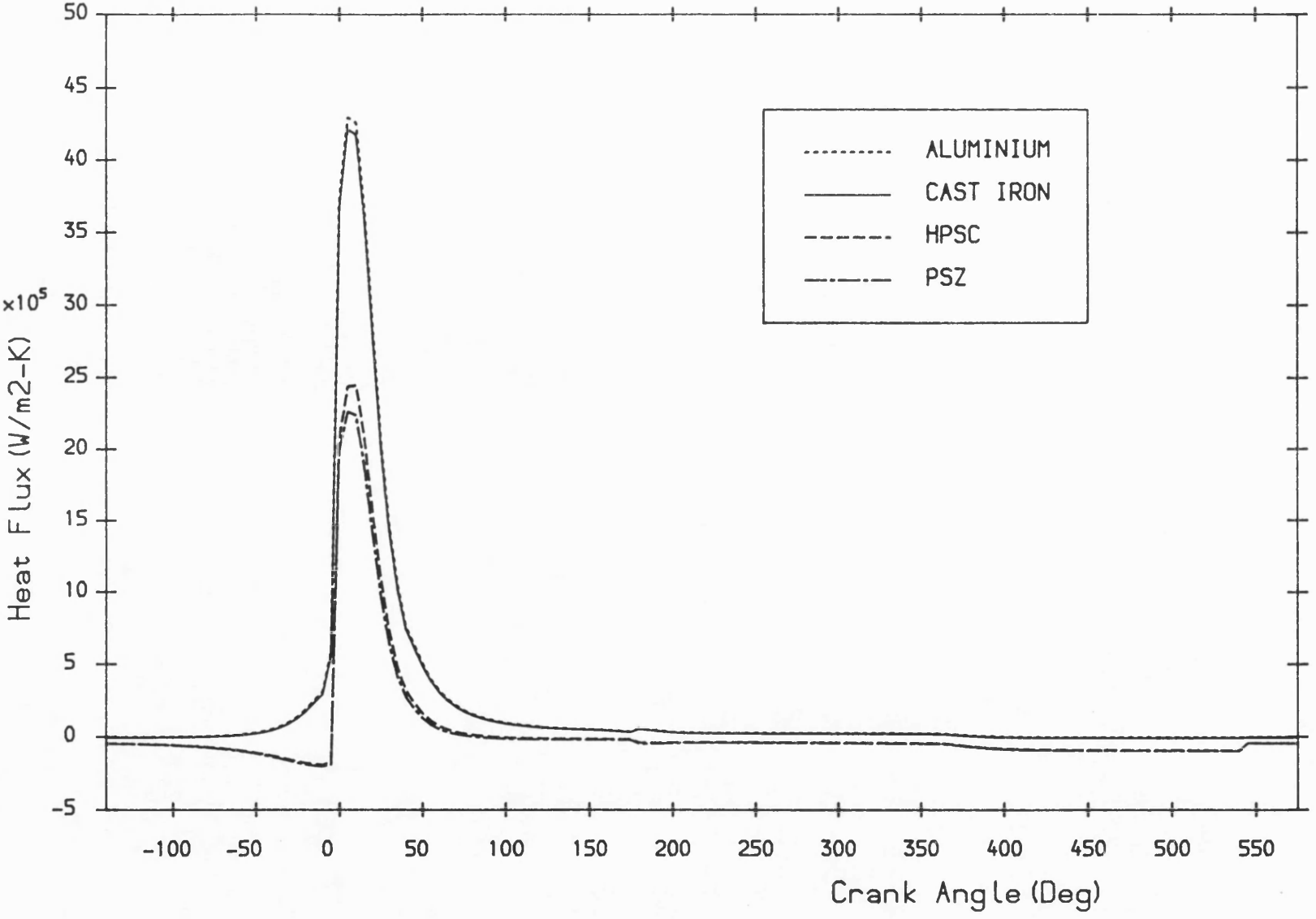

Fig. 6.43 Heat flux versus crank angle for several materials.

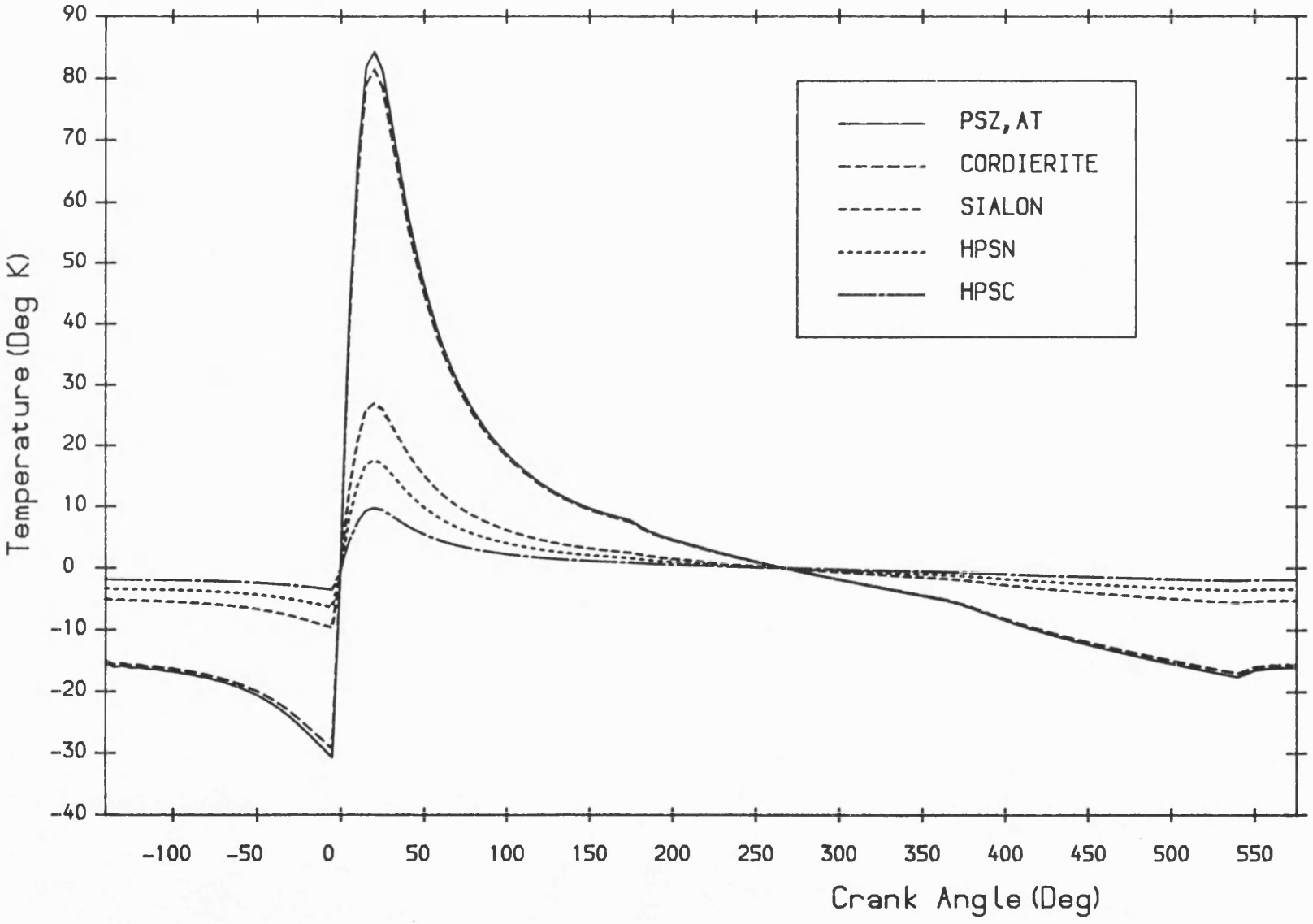

Fig. 6.44 Surface temperature swings for various ceramics with modified Woschni heat transfer coefficient.

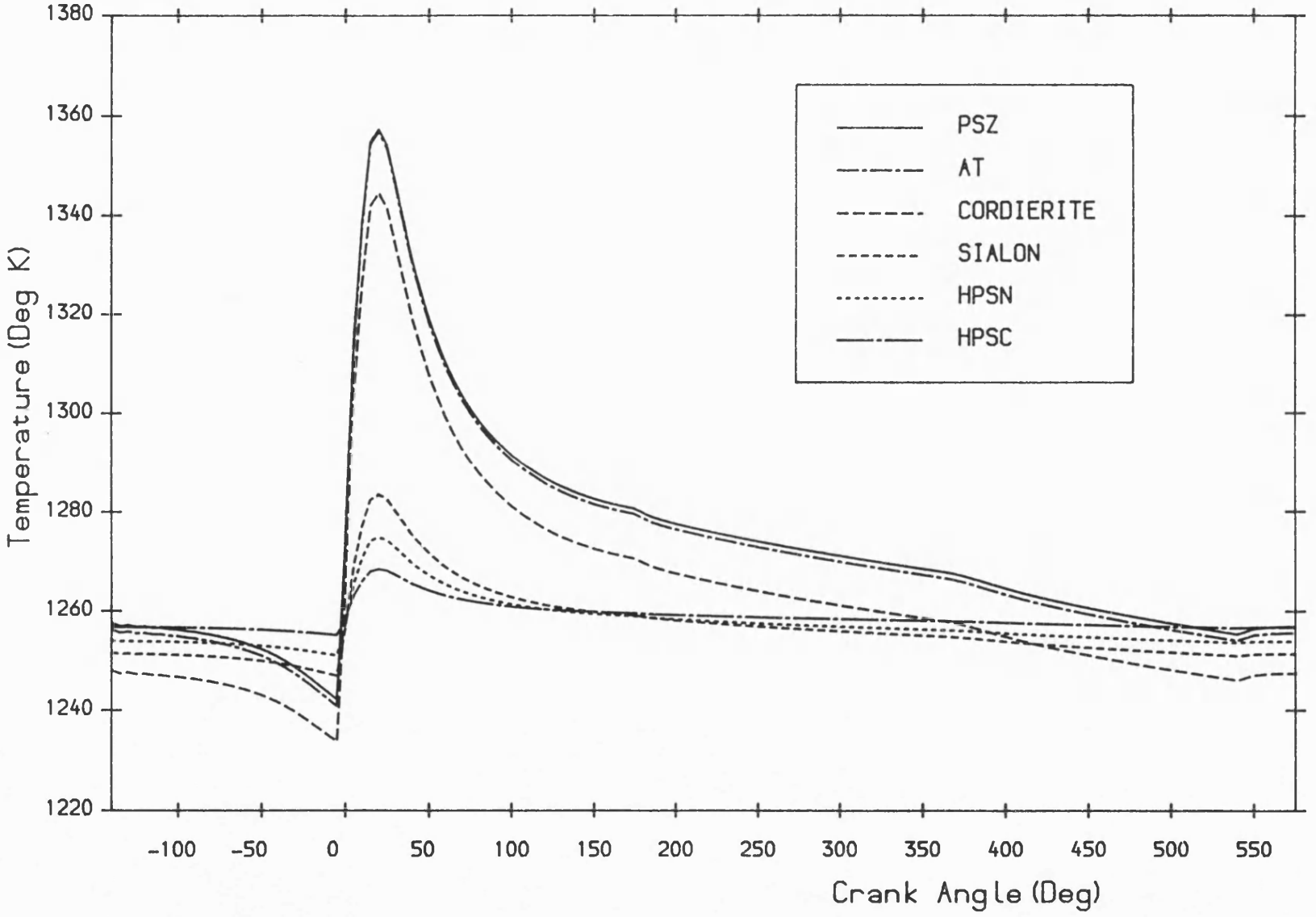

Fig. 6.45 Surface temperature versus crank angle for various ceramics with modified Woschni heat transfer coefficient.

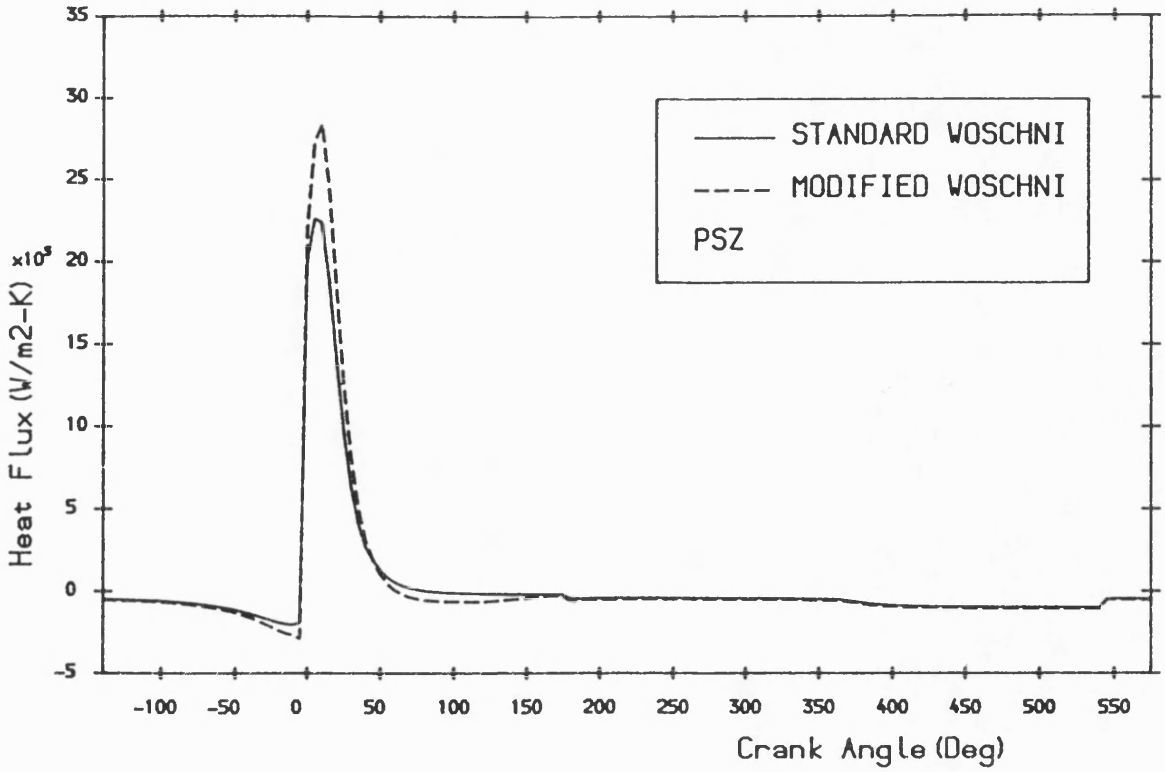

Fig. 6.46 Heat flux versus crank angle with standard and modified Woschni htc on a PSZ wall.

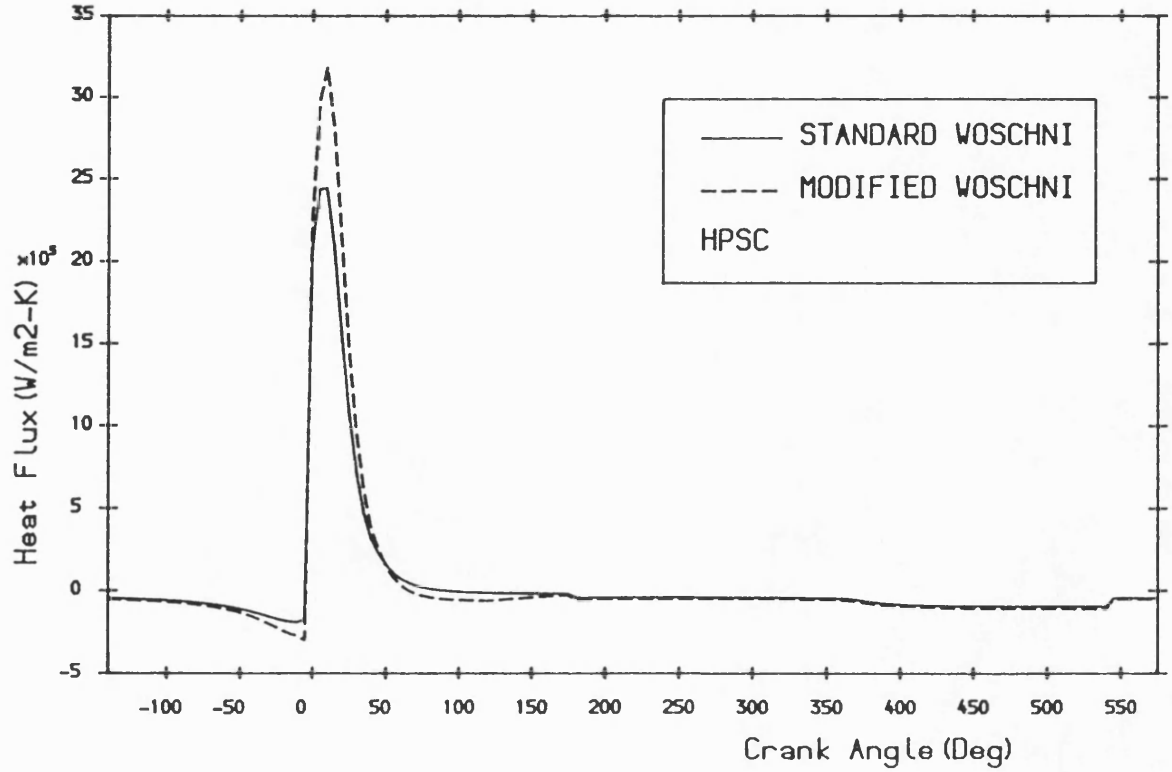

Fig. 6.47 Heat flux versus crank angle with standard and modified Woschni htc on a HPSC wall.

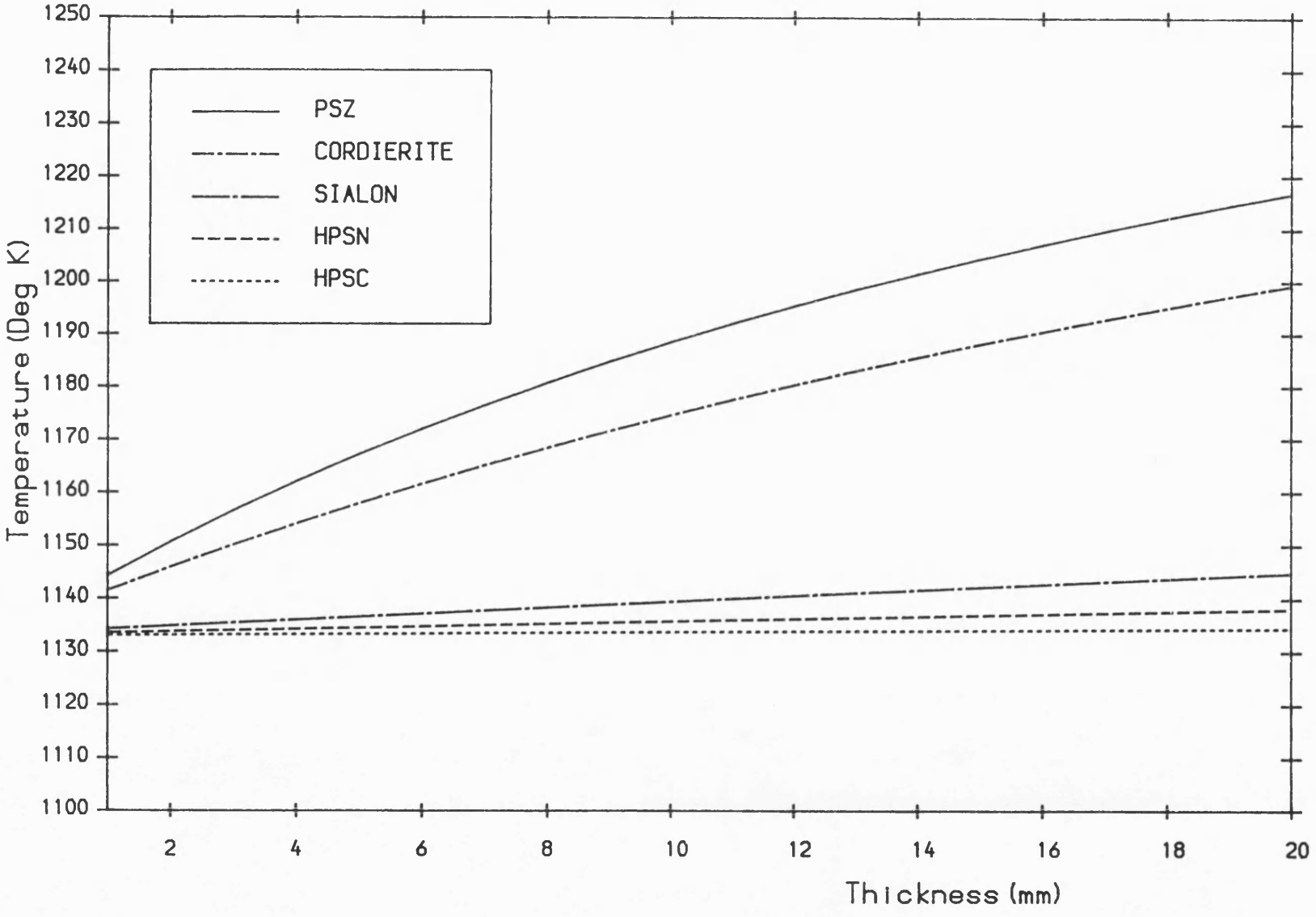

Fig. 6.48 Apparent wall surface temperature versus wall thickness.

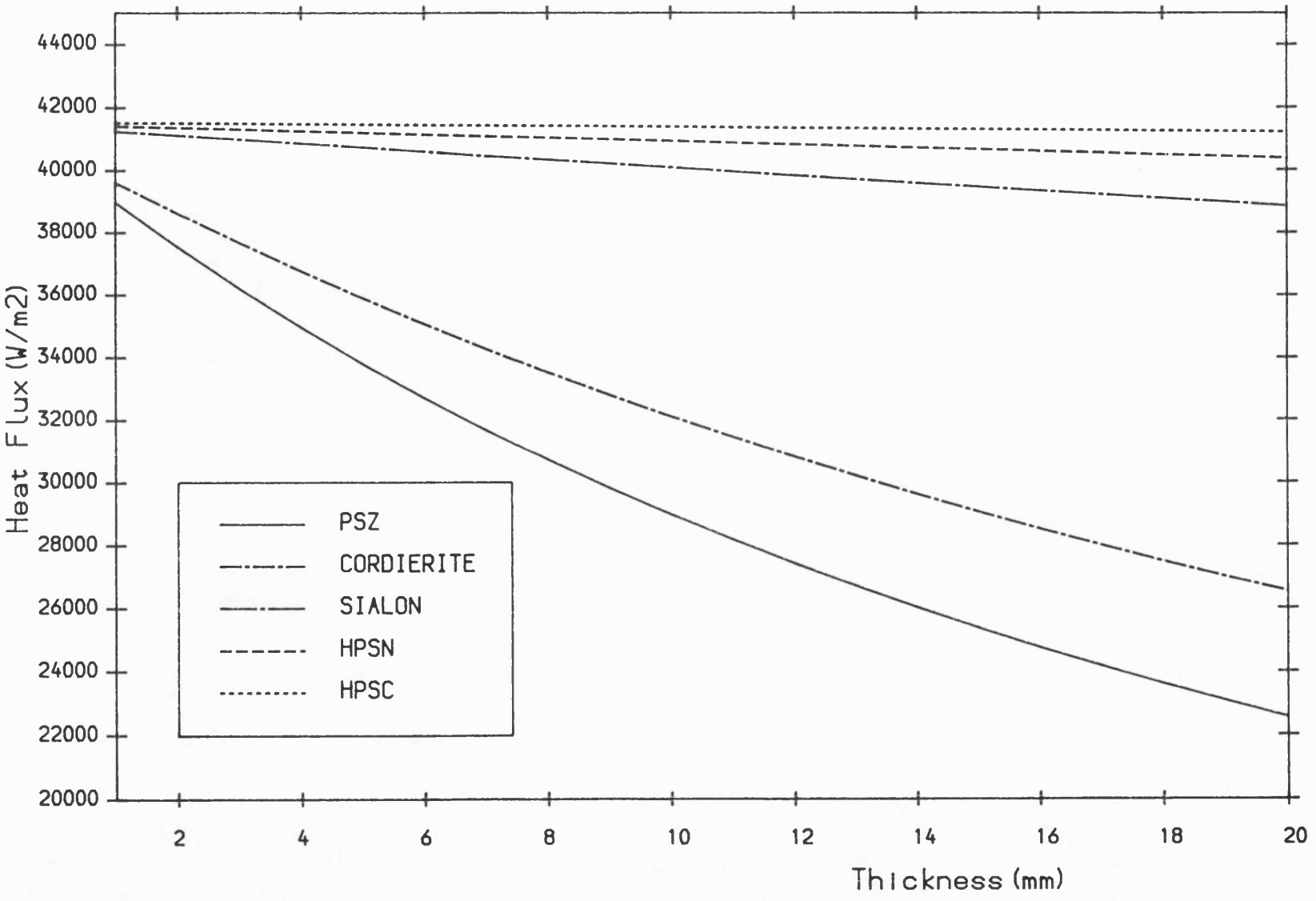

Fig. 6.49 Wall mean heat flux versus wall thickness.

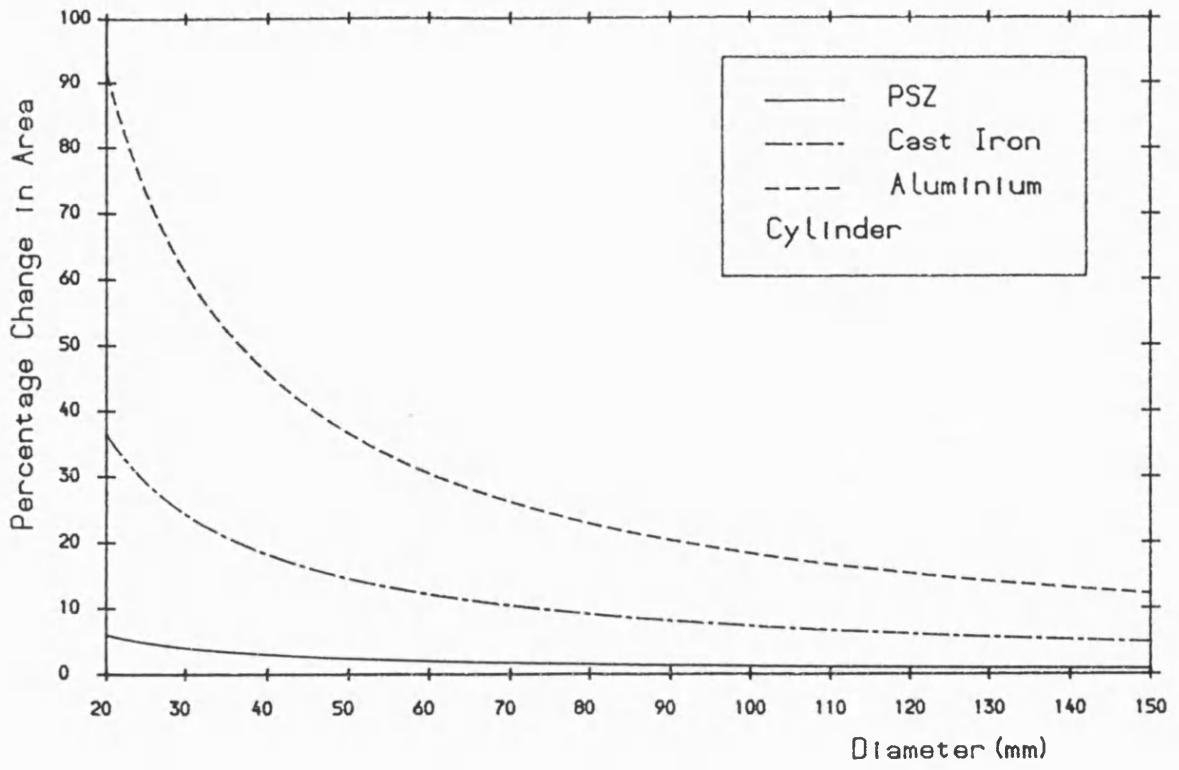

Fig. 6.50 Percentage change in the TPD cylinder surface area versus cylinder inner diameter.

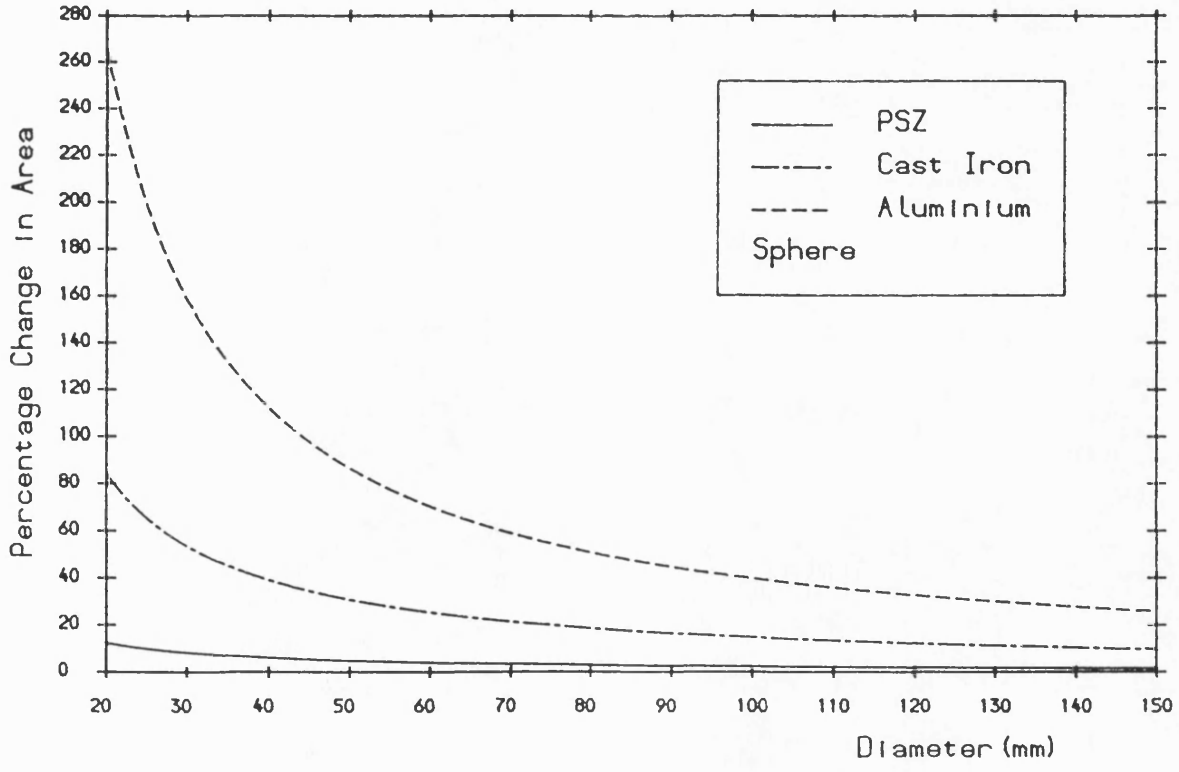

Fig. 6.51 Percentage change in the TPD sphere surface area versus sphere inner diameter.

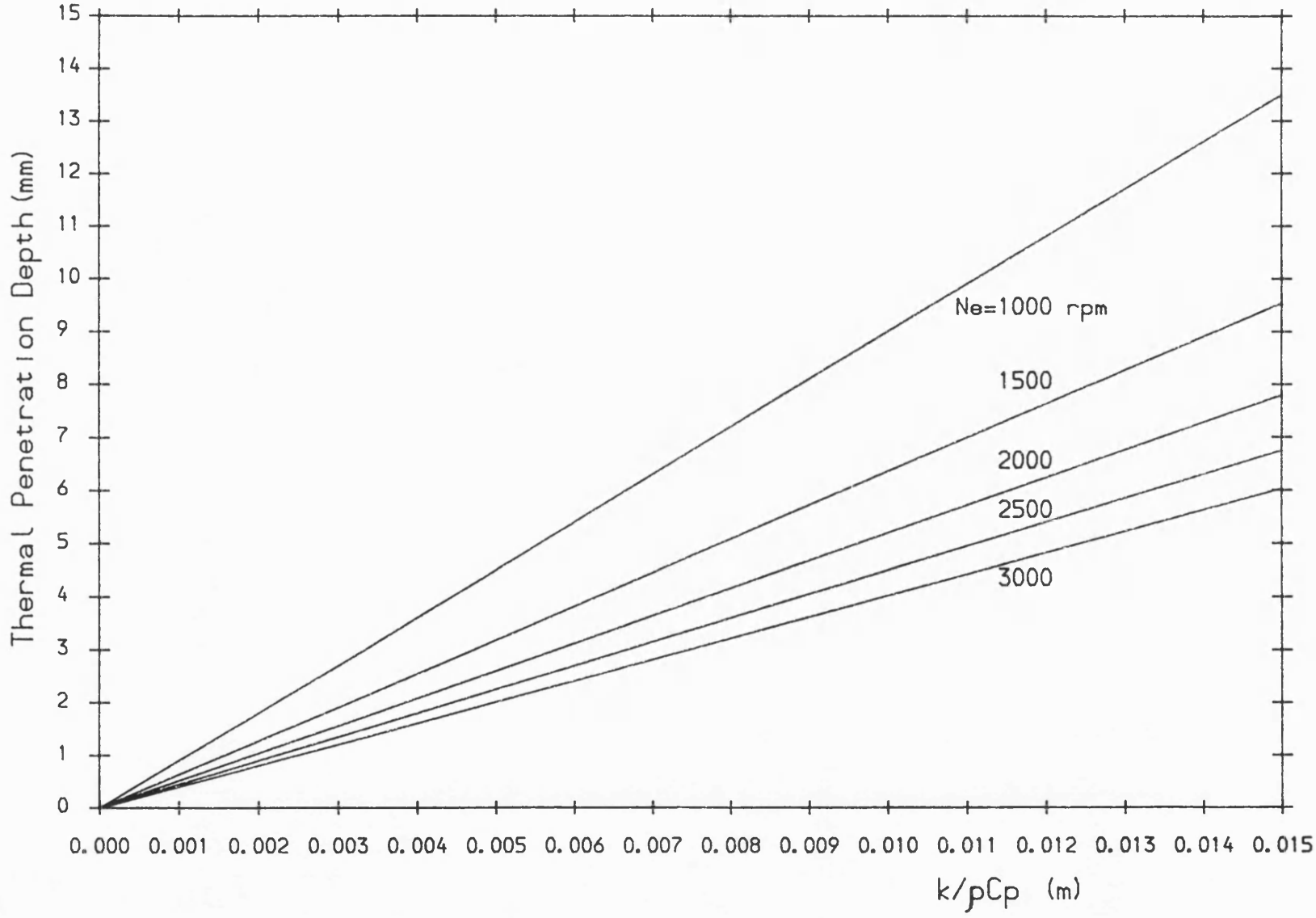

Fig. 6.52 The thermal penetration depth (TPD) versus material thermal properties at various engine speeds.

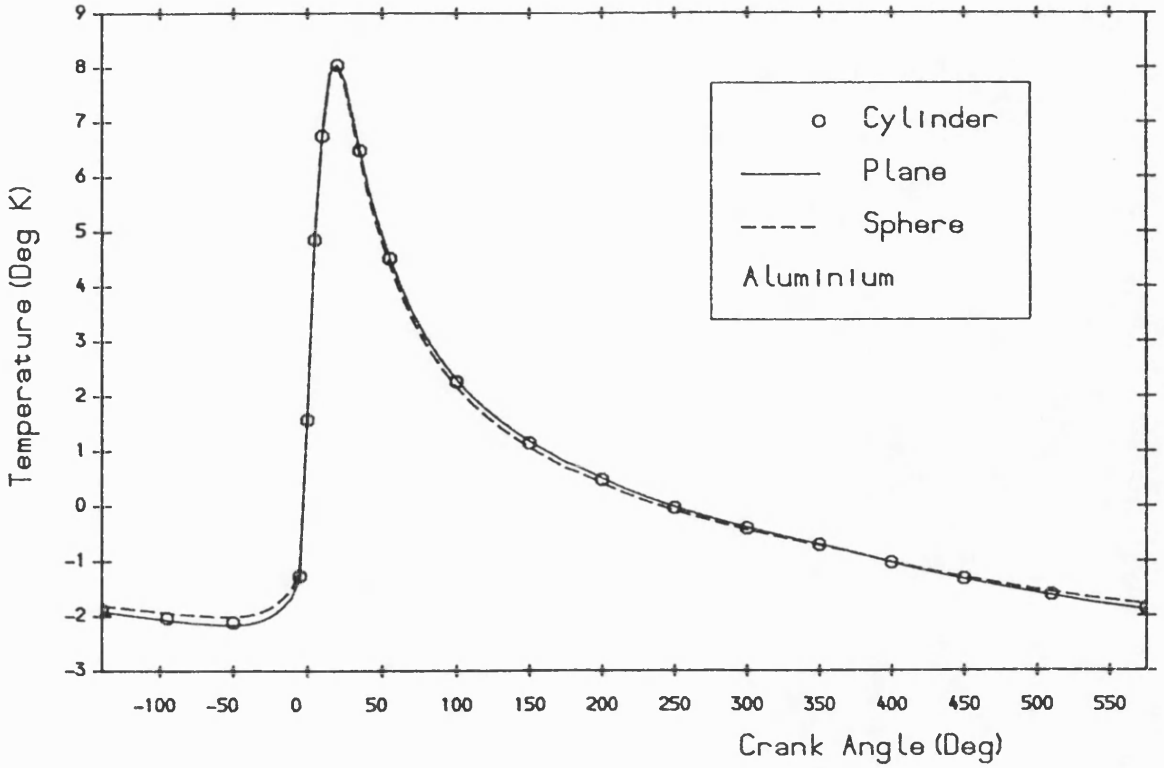

Fig. 6.53 Aluminium wall surface temperature swings at different geometries obtained by using temperature 364.2 K at 1.2*TPD.

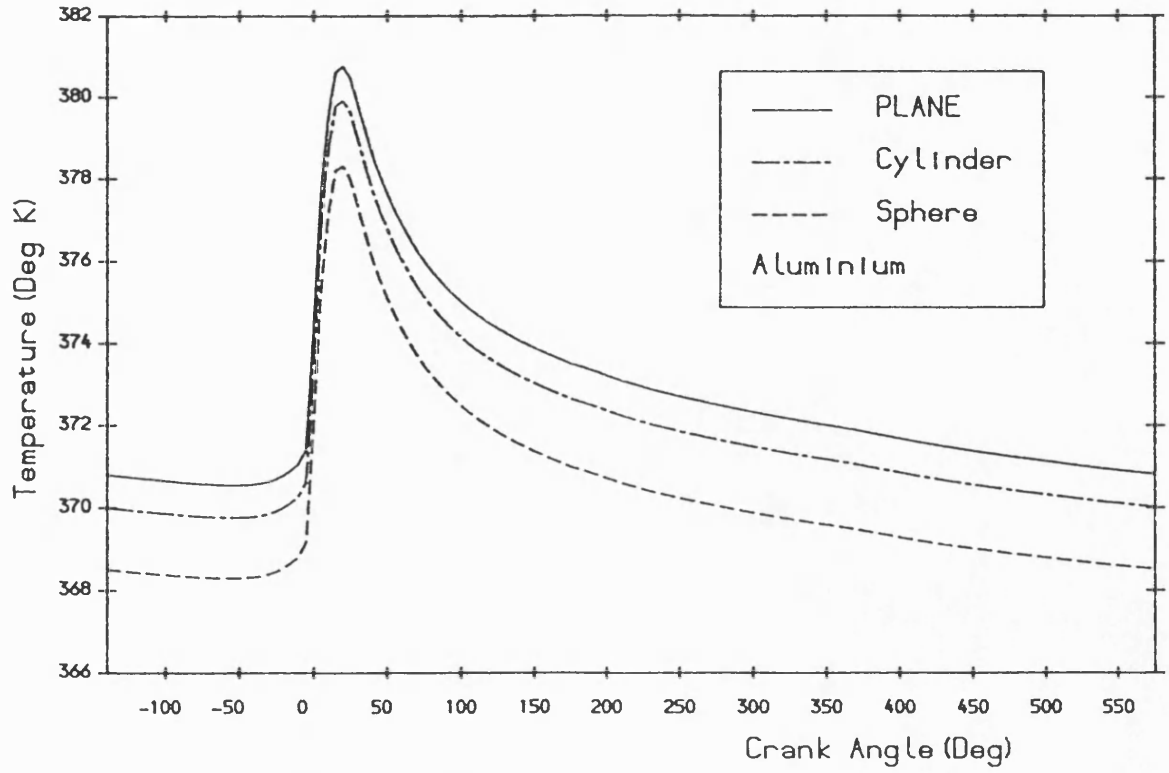

Fig. 6.54 Aluminium wall surface temperature versus crank angle at different geometries obtained by using temperature 364.2 K at 1.2*TPD.

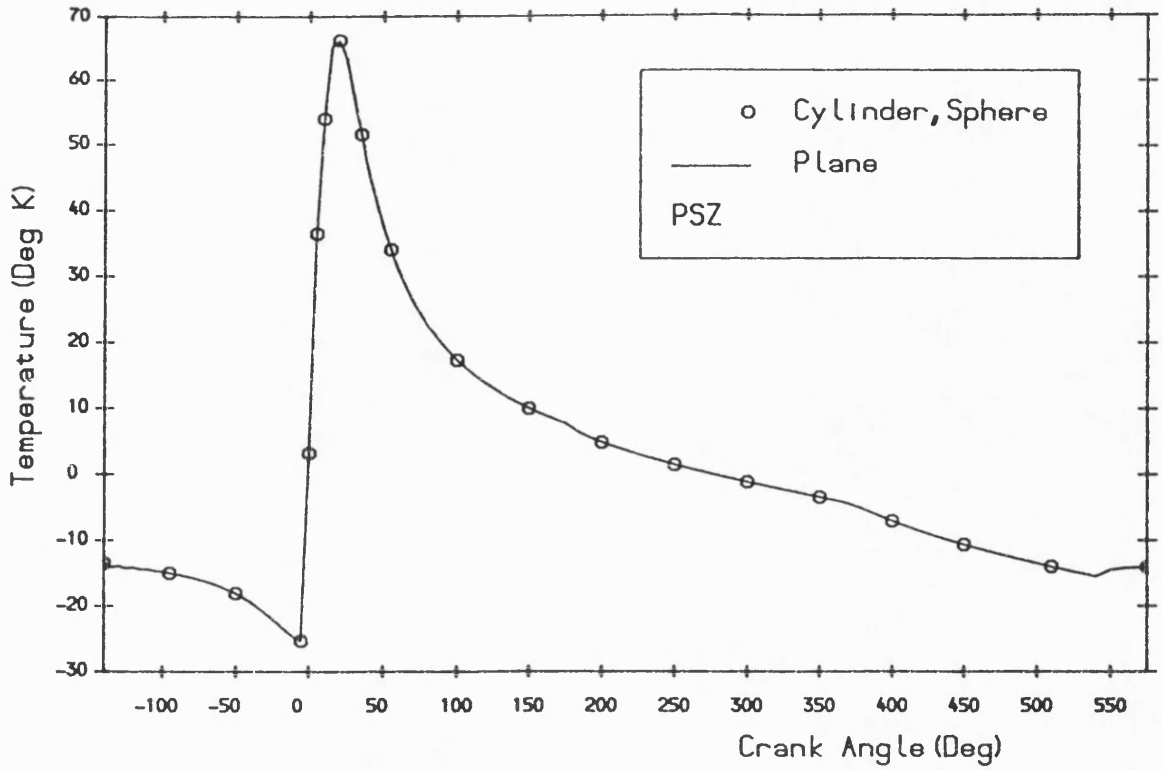

Fig. 6.55 PSZ wall surface temperature swings at different geometries obtained by using temperature 1150.9 K at 1.2*TPD.

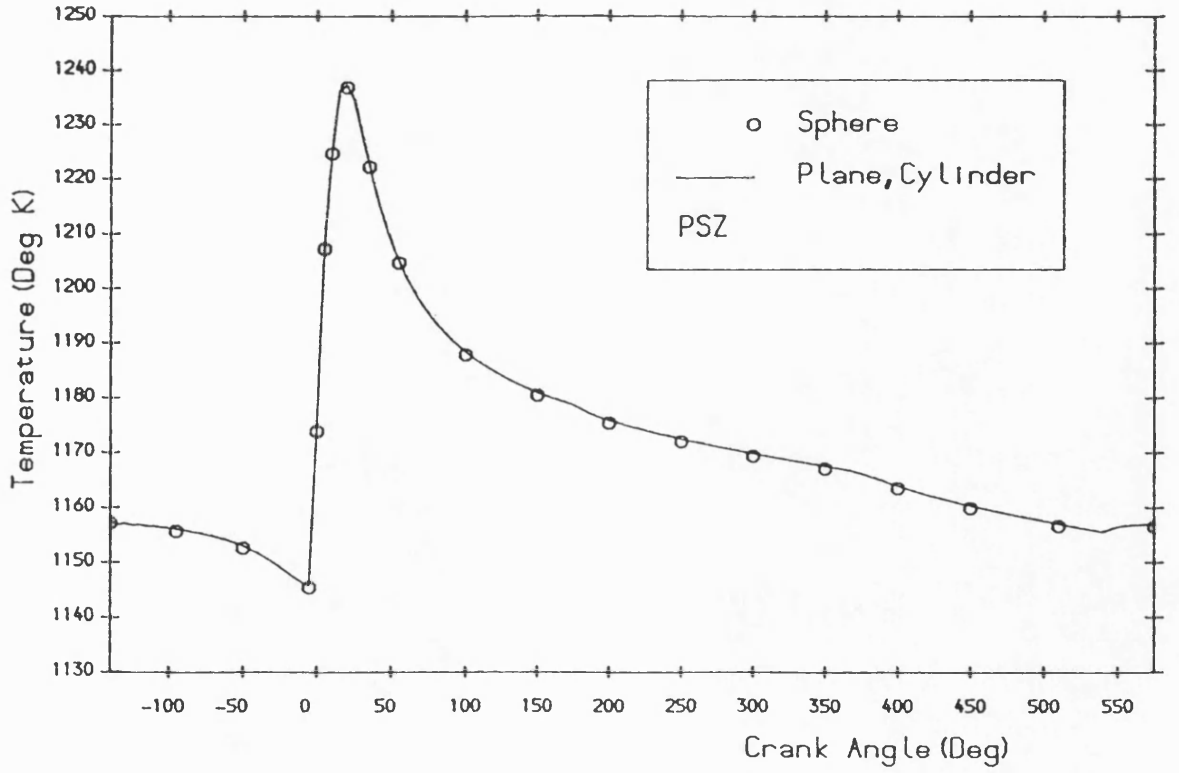

Fig. 6.56 PSZ wall surface temperature versus crank angle at different geometries obtained by using temperature 1150.9 K at 1.2*TPD.

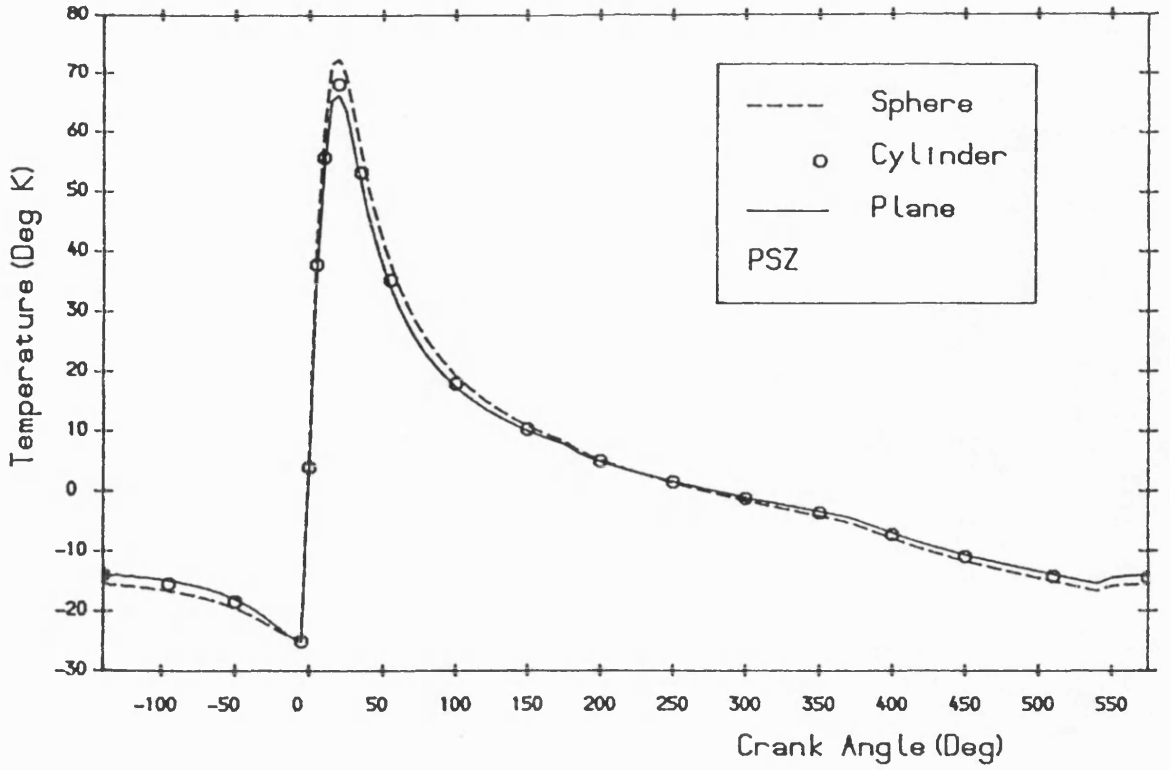

Fig. 6.57 PSZ wall surface temperature swings at different geometries obtained by using boundary conditions shown in Fig. 6.37.

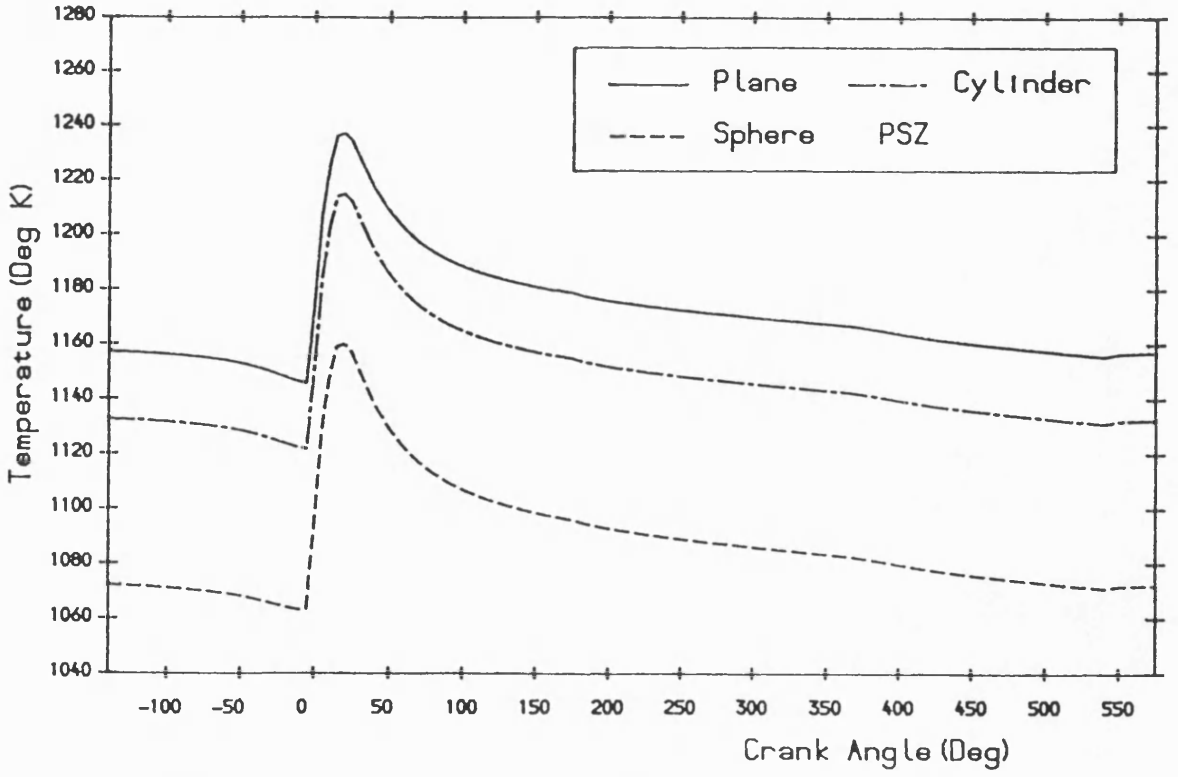

Fig. 6.58 PSZ wall surface temperature versus crank angle at different geometries obtained by using boundary conditions shown in Fig. 6.37

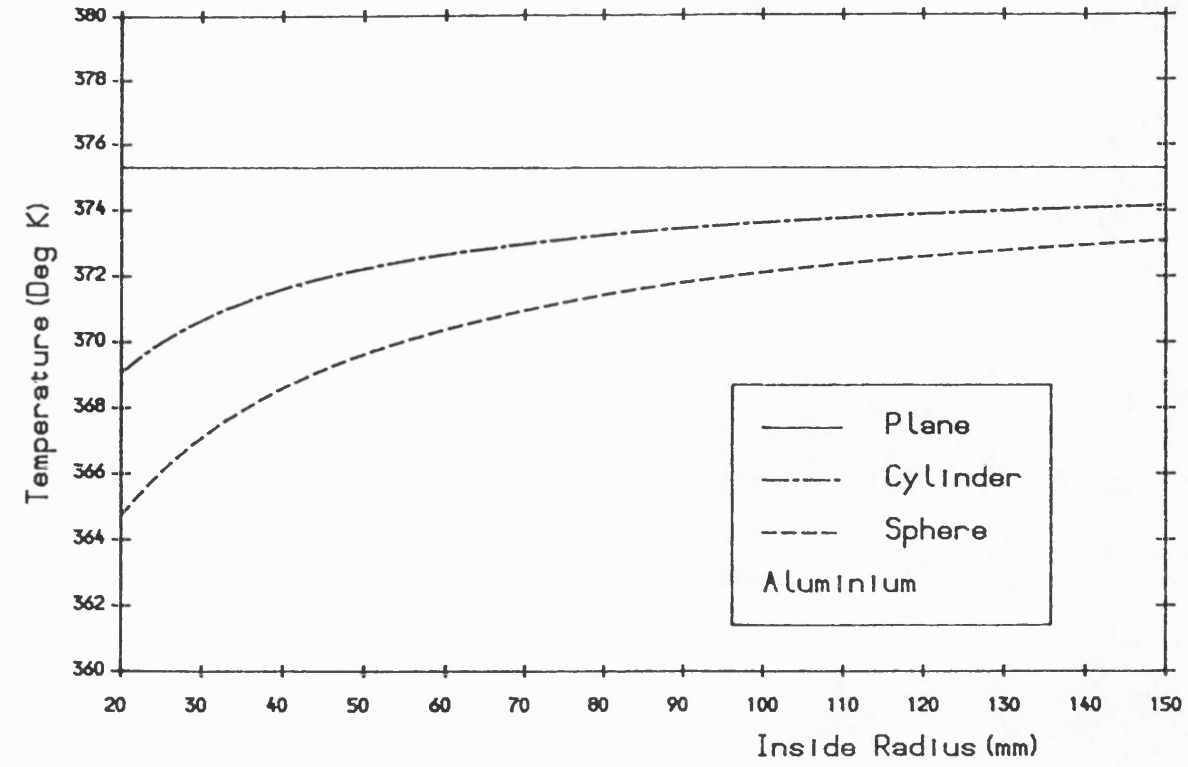

Fig. 6.59 The effect of cylinder or sphere inner radius on the aluminium apparent wall surface temperature.

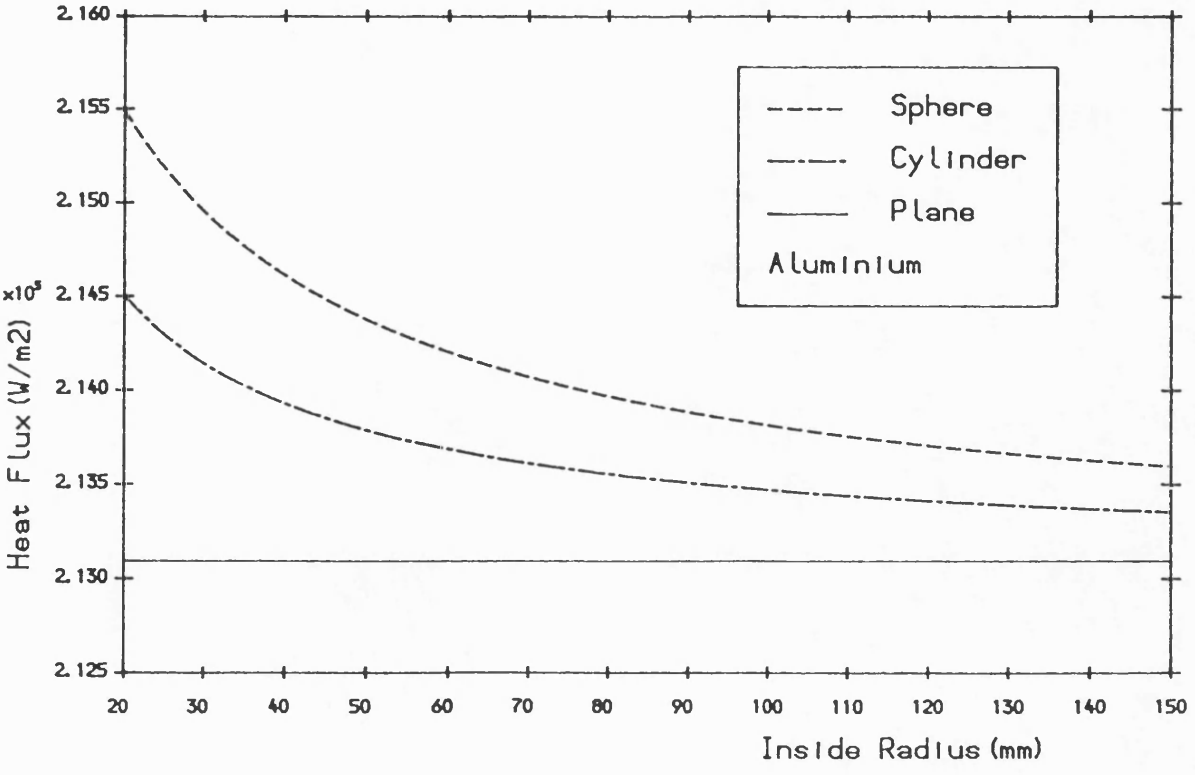

Fig. 6.60 The effect of cylinder or sphere inner radius on the mean heat flux through the aluminium wall.

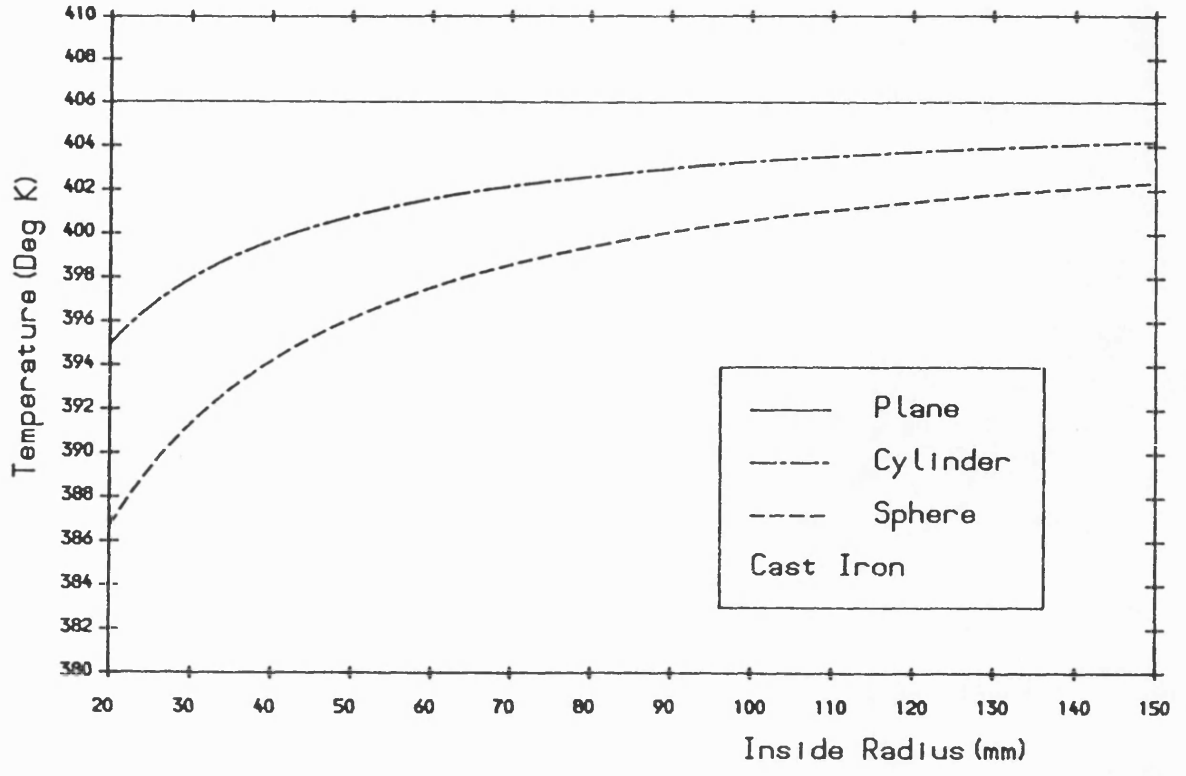

Fig. 6.61 The effect of cylinder or sphere inner radius on the cast iron apparent wall surface temperature.

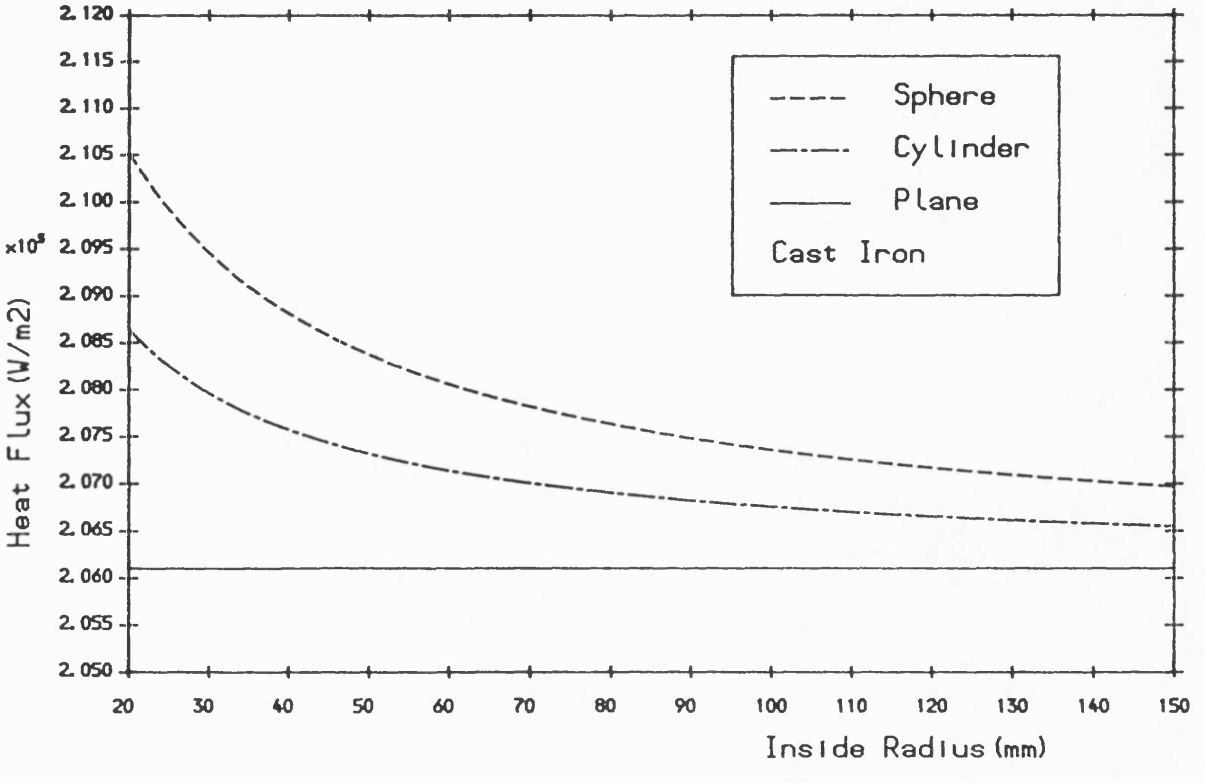

Fig. 6.62 The effect of cylinder or sphere inner radius on the mean heat flux through the cast iron wall.

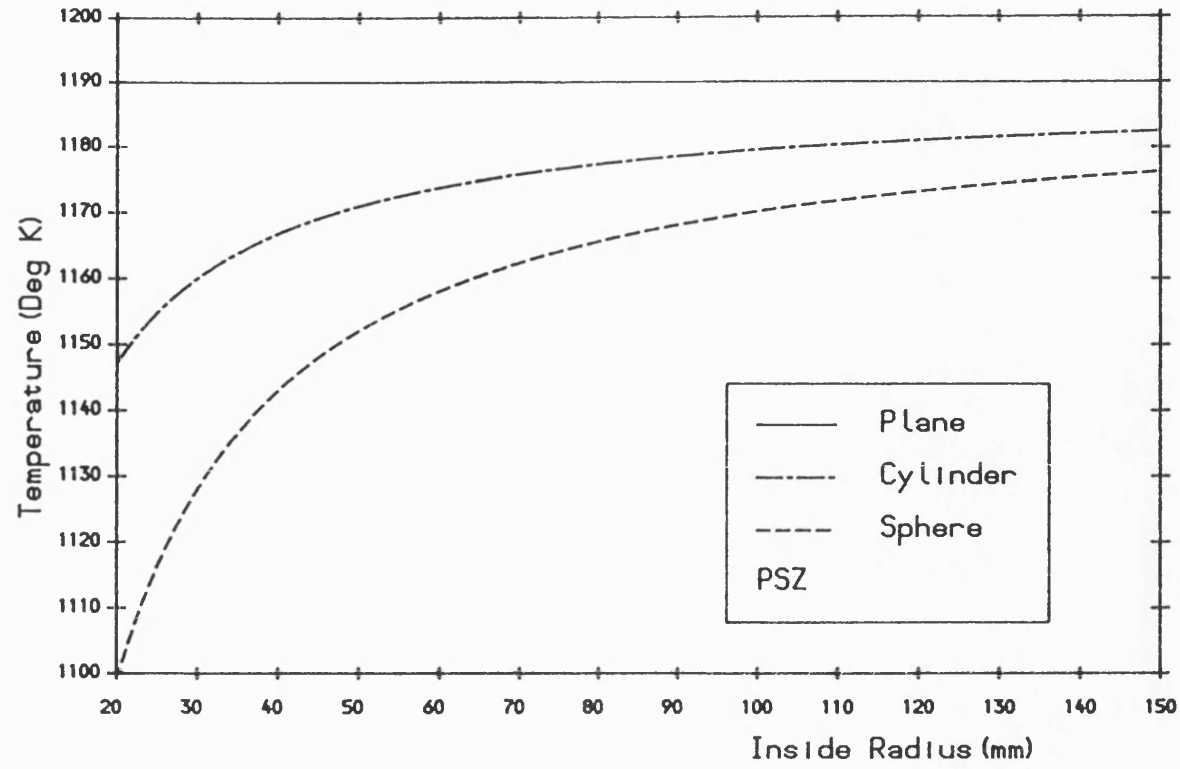

Fig. 6.63 The effect of cylinder or sphere inner radius on the PSZ apparent wall surface temperature.

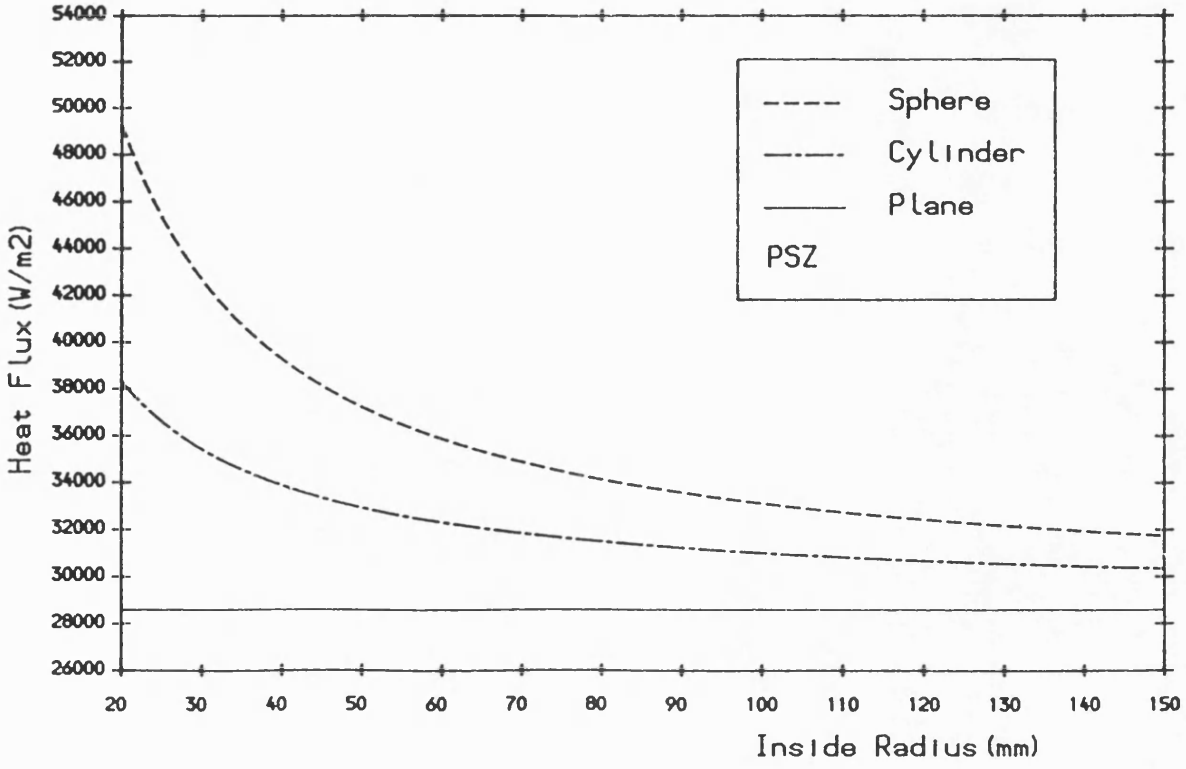

Fig. 6.64 The effect of cylinder or sphere inner radius on the mean heat flux through the PSZ wall.

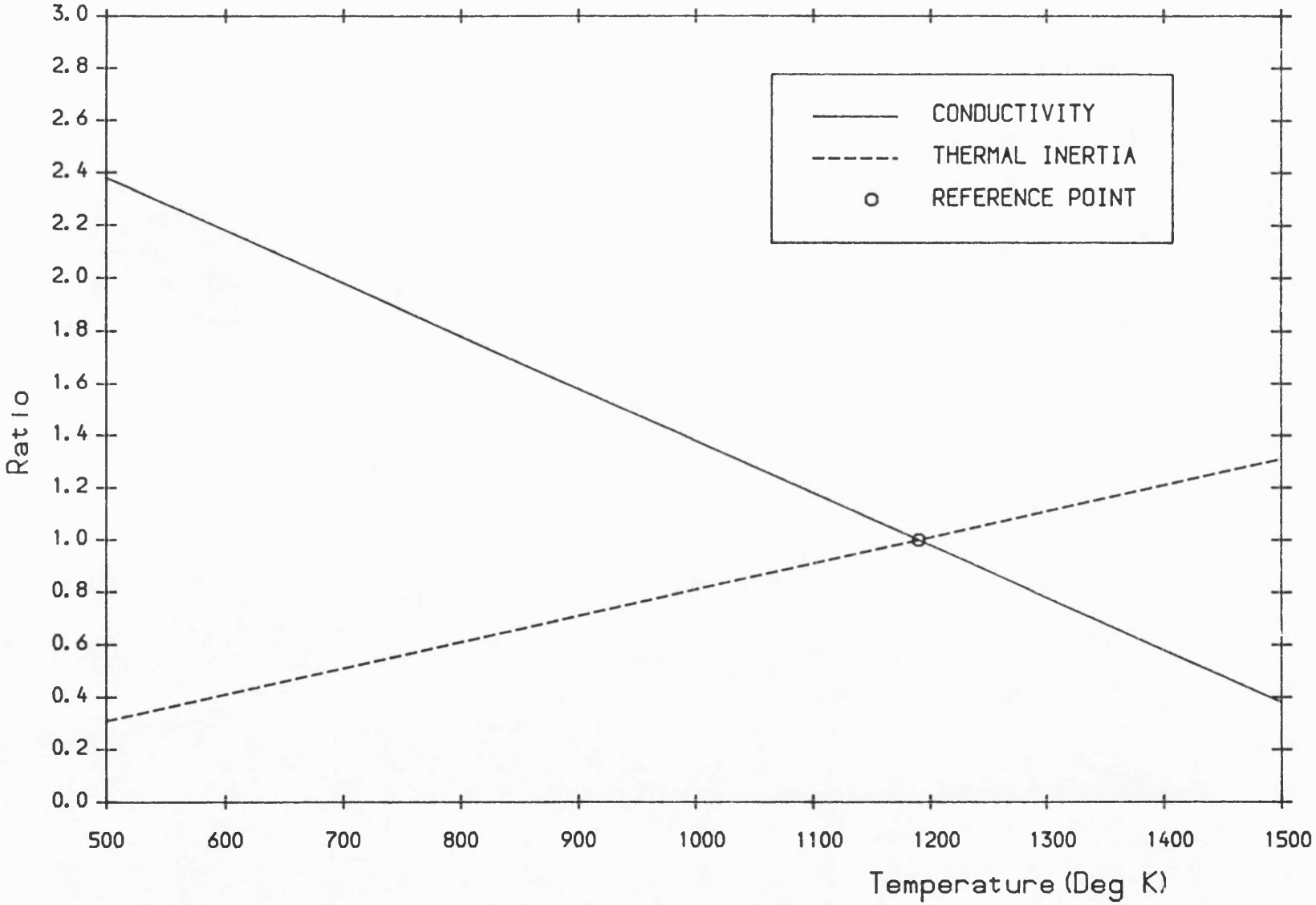

Fig. 6.65 Assumed thermal inertia and conductivity ratios versus temperature, referenced at apparent surface temperature.

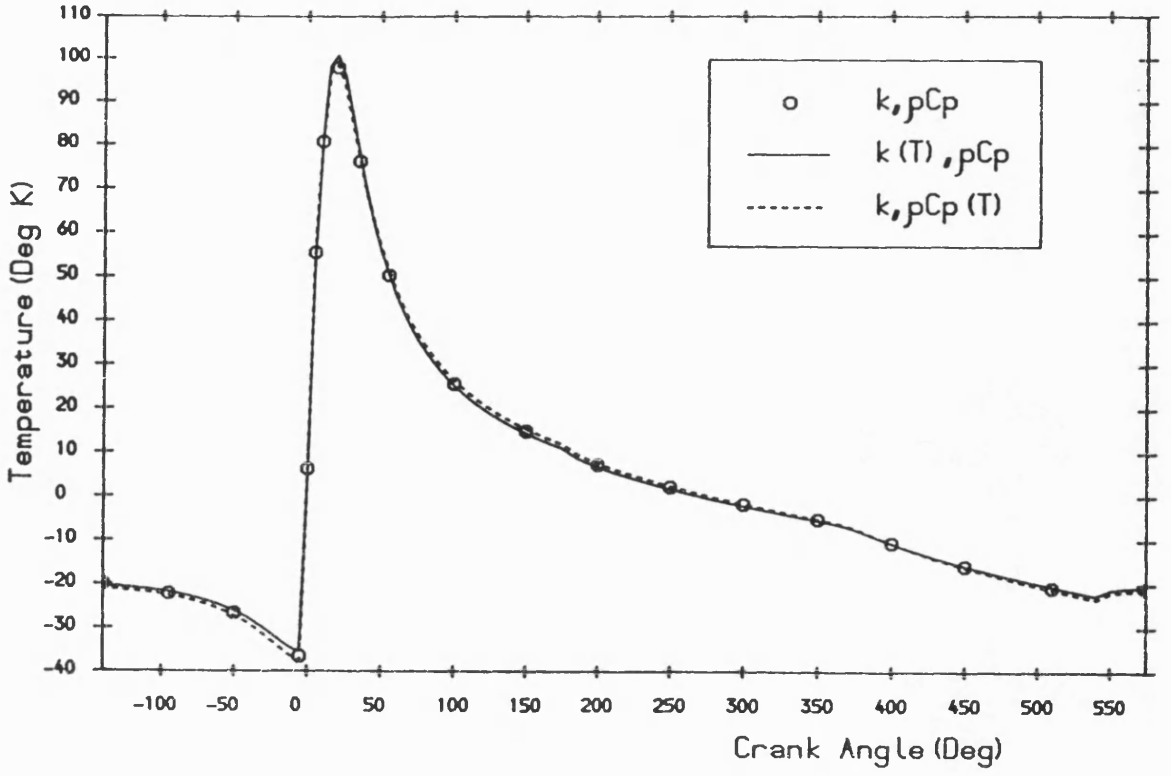

Fig. 6.66 Surface temperature swings for constant and temperature dependent properties.

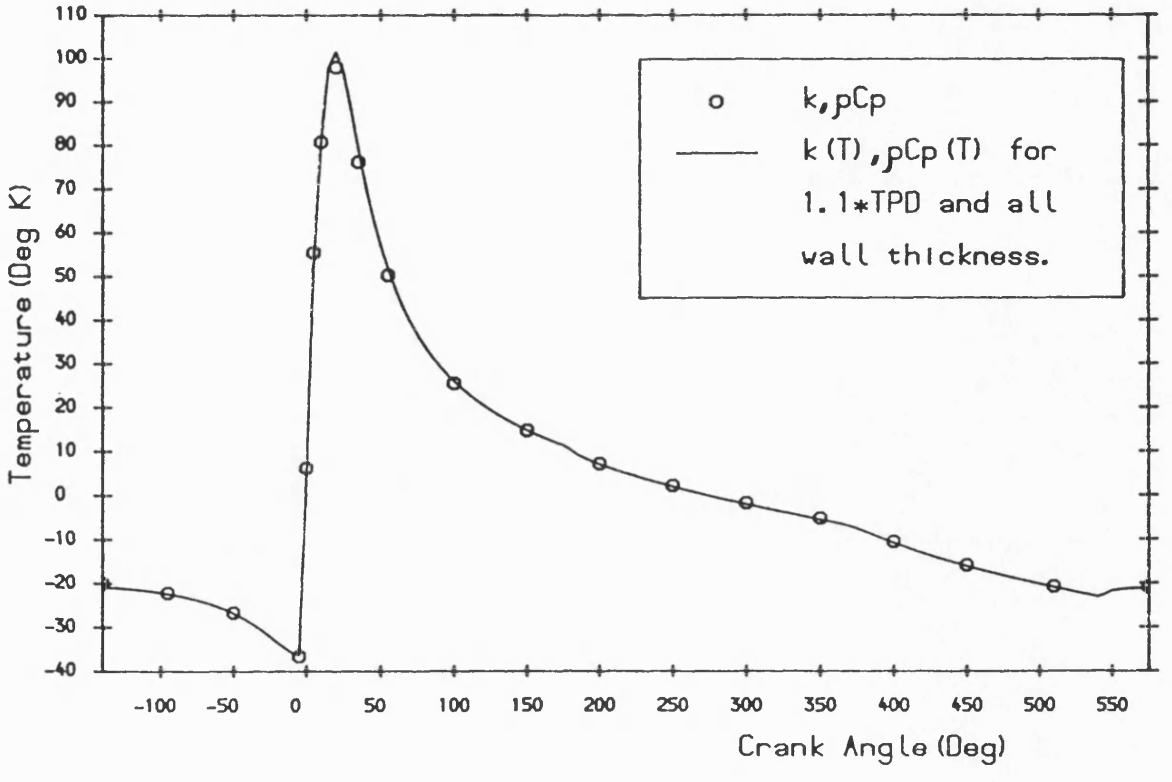

Fig. 6.67 Surface temperature swings for constant and temperature dependent properties.

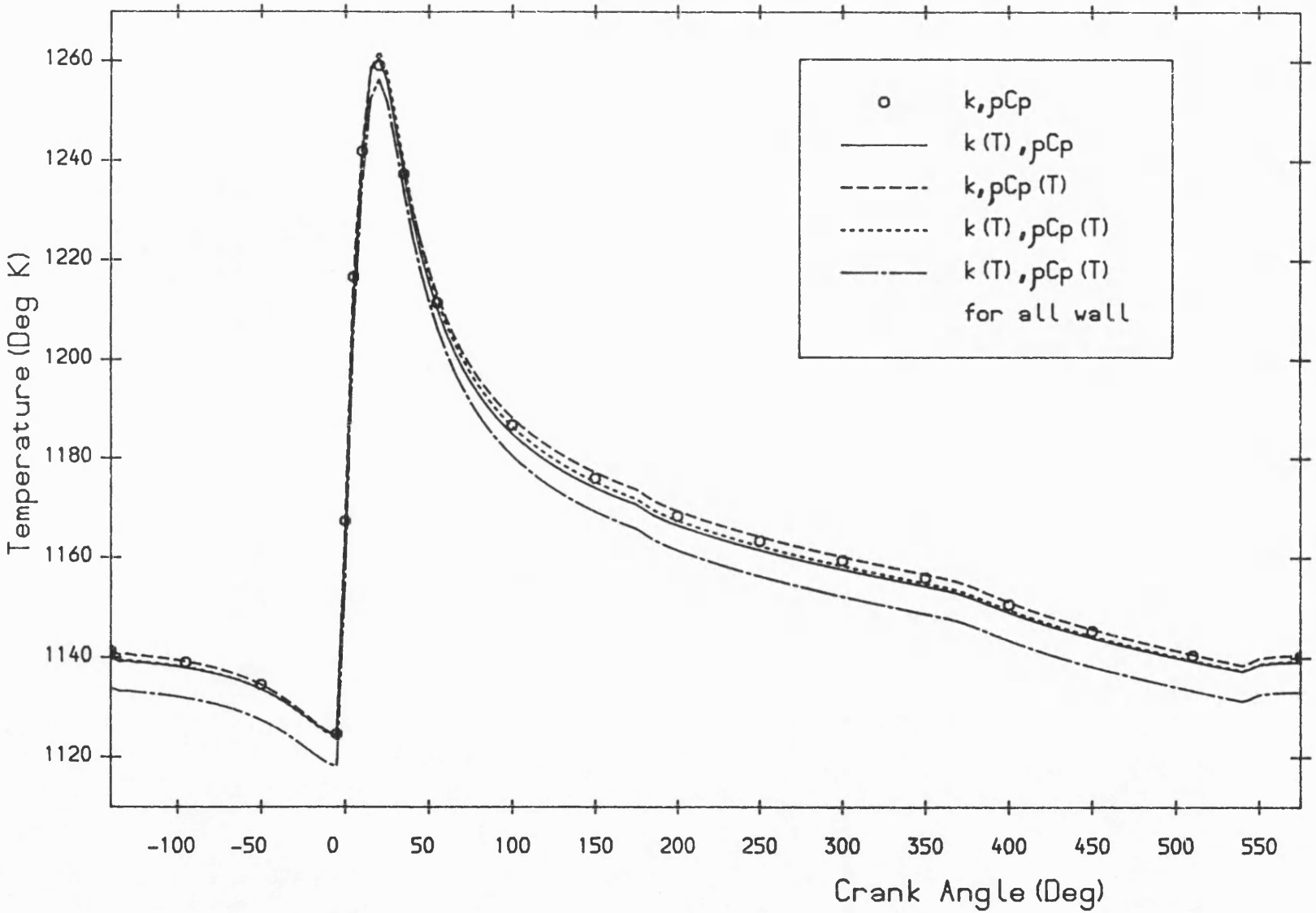

Fig. 6.68 Surface temperature versus crank angle with constant and temperature dependent thermal properties.

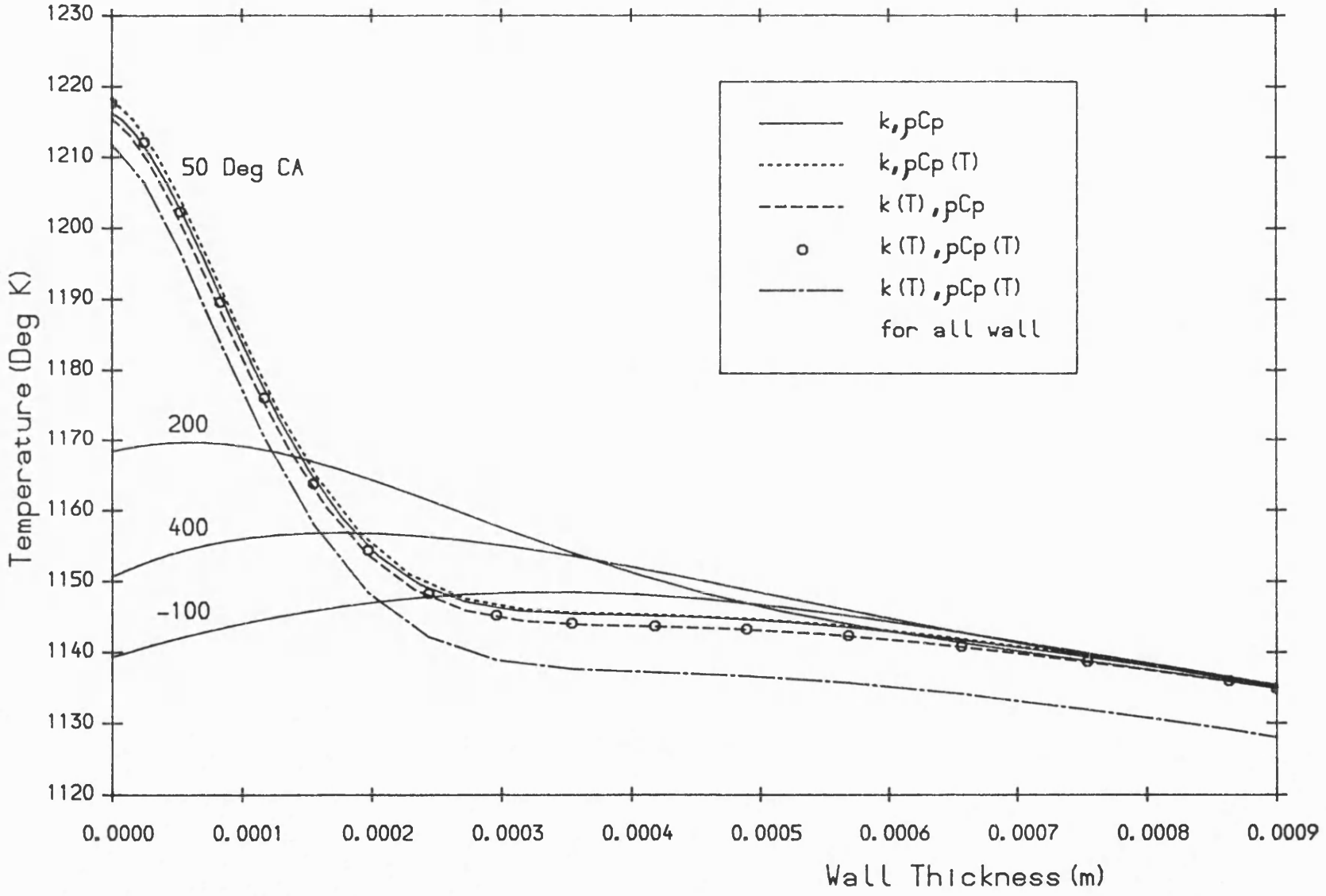

Fig. 6.69 Temperature wave through the wall for constant and temperature dependent material properties.

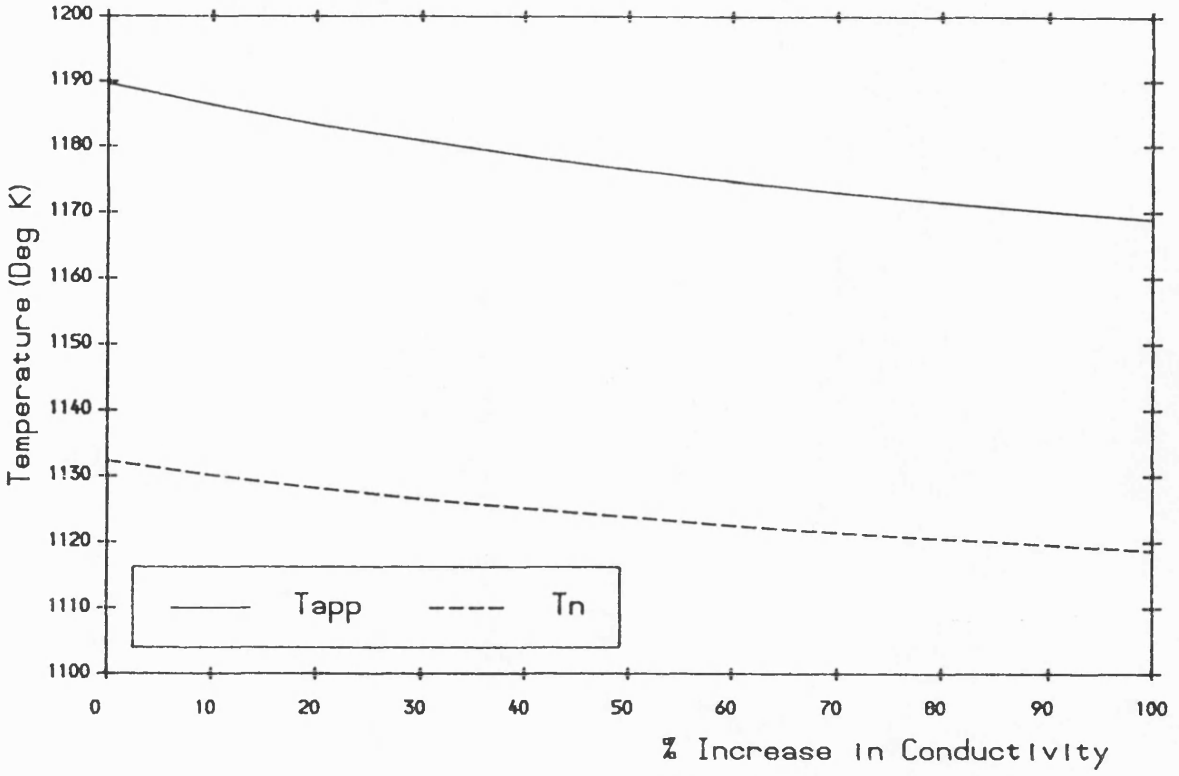

Fig. 6.70 Variation of apparent surface temperature Tapp, and temperature Tn at 1.1*TPD with percentage increase in conductivity.

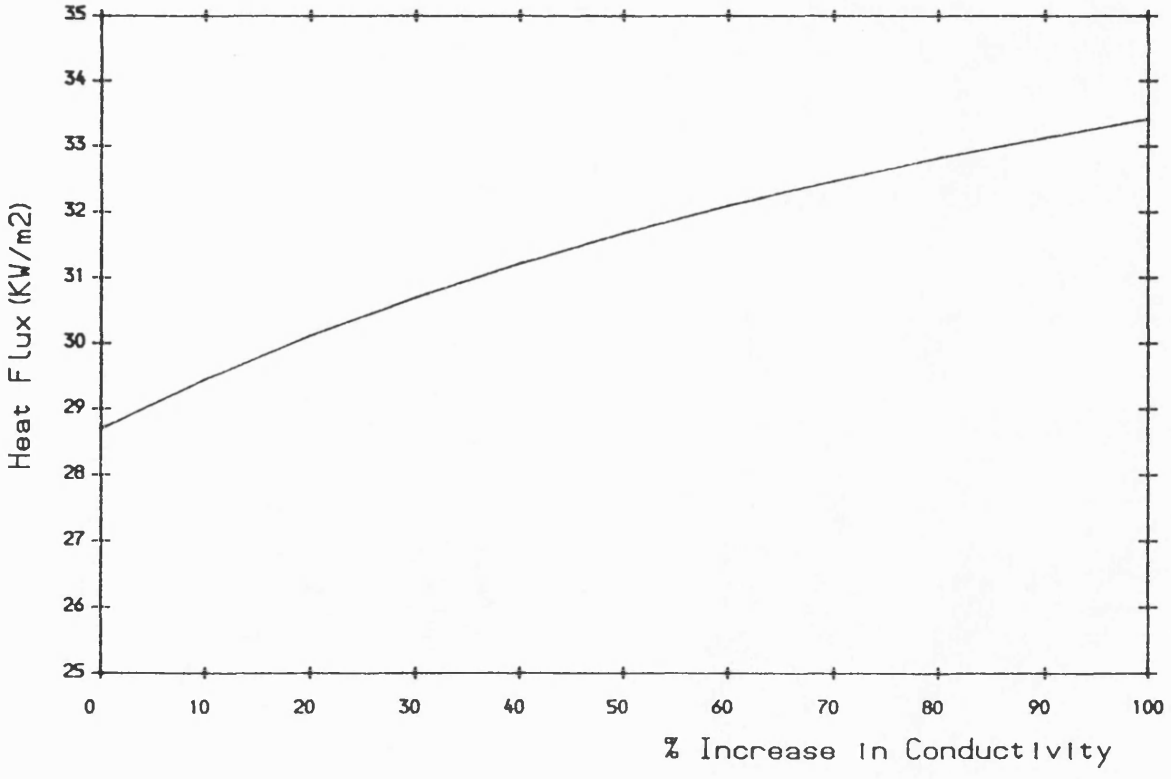

Fig. 6.71 Variation of mean heat flux with percentage increase in conductivity.

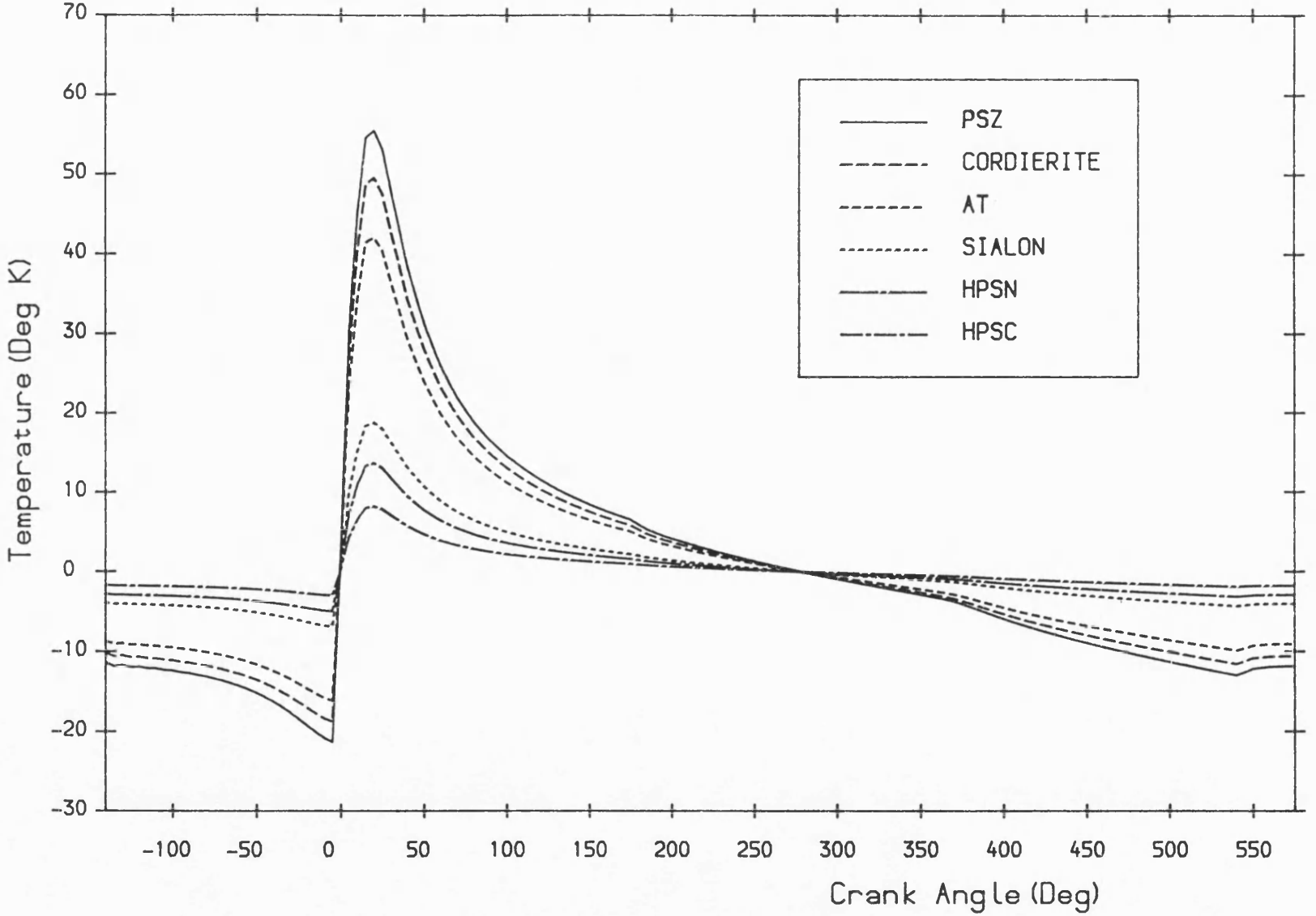

Fig. 6.72 Surface temperature swings for several ceramics with temperature dependent material properties.

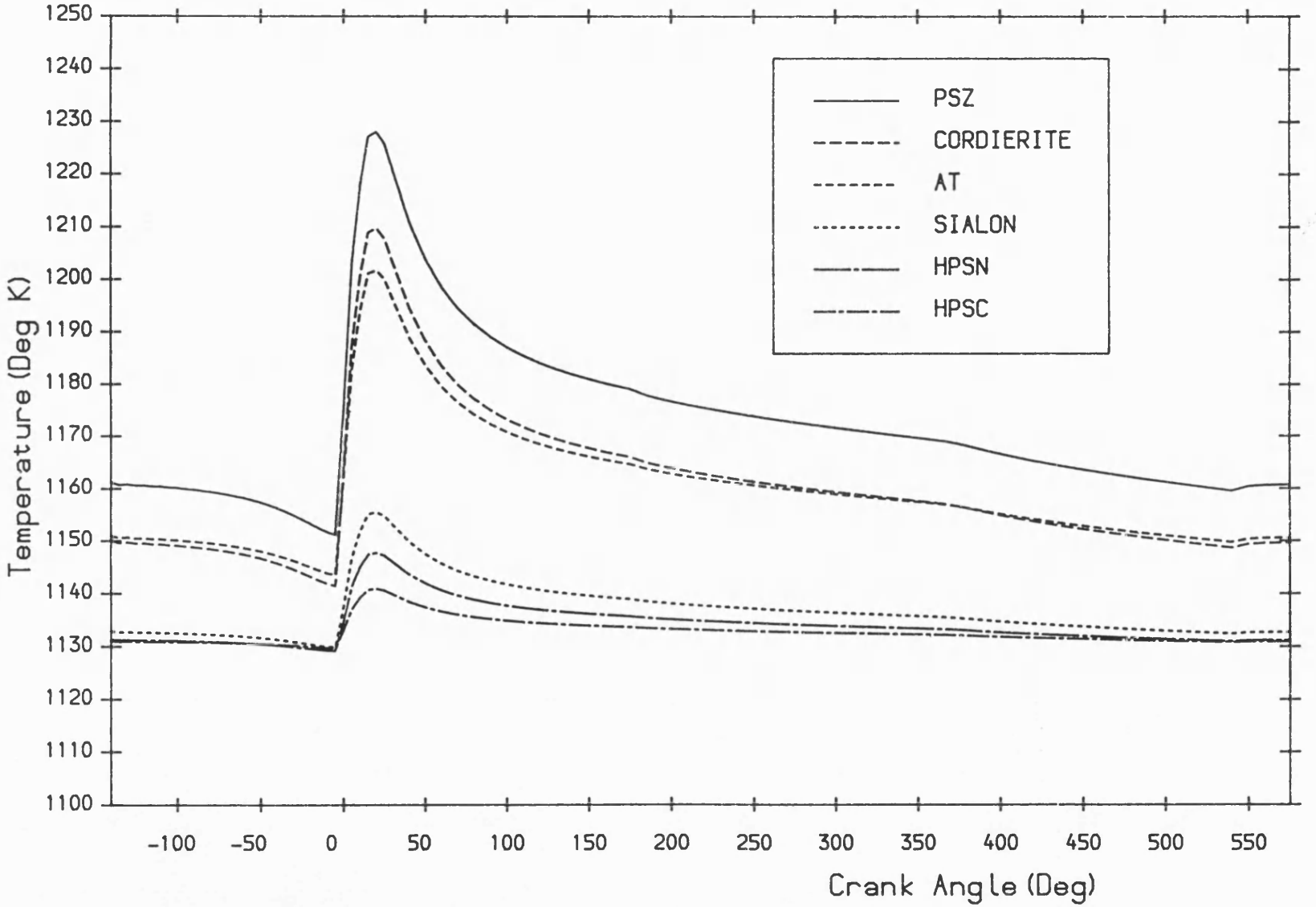

Fig. 6.73 Surface temperature versus crank angle for several ceramics with temperature dependent material properties.

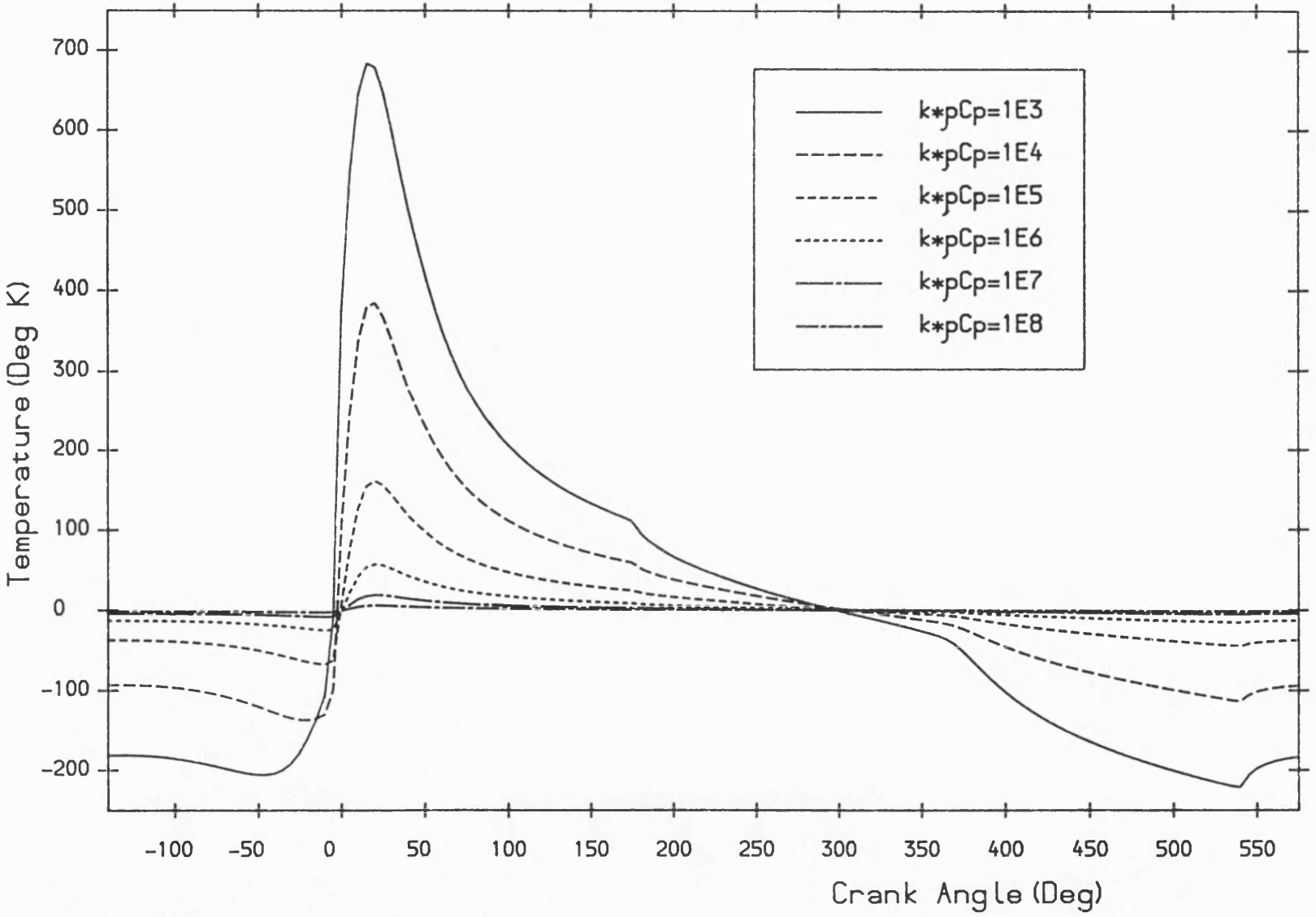

Fig. 6.74 Surface temperature swings for various k*pCp values with convection gas side boundary condition.

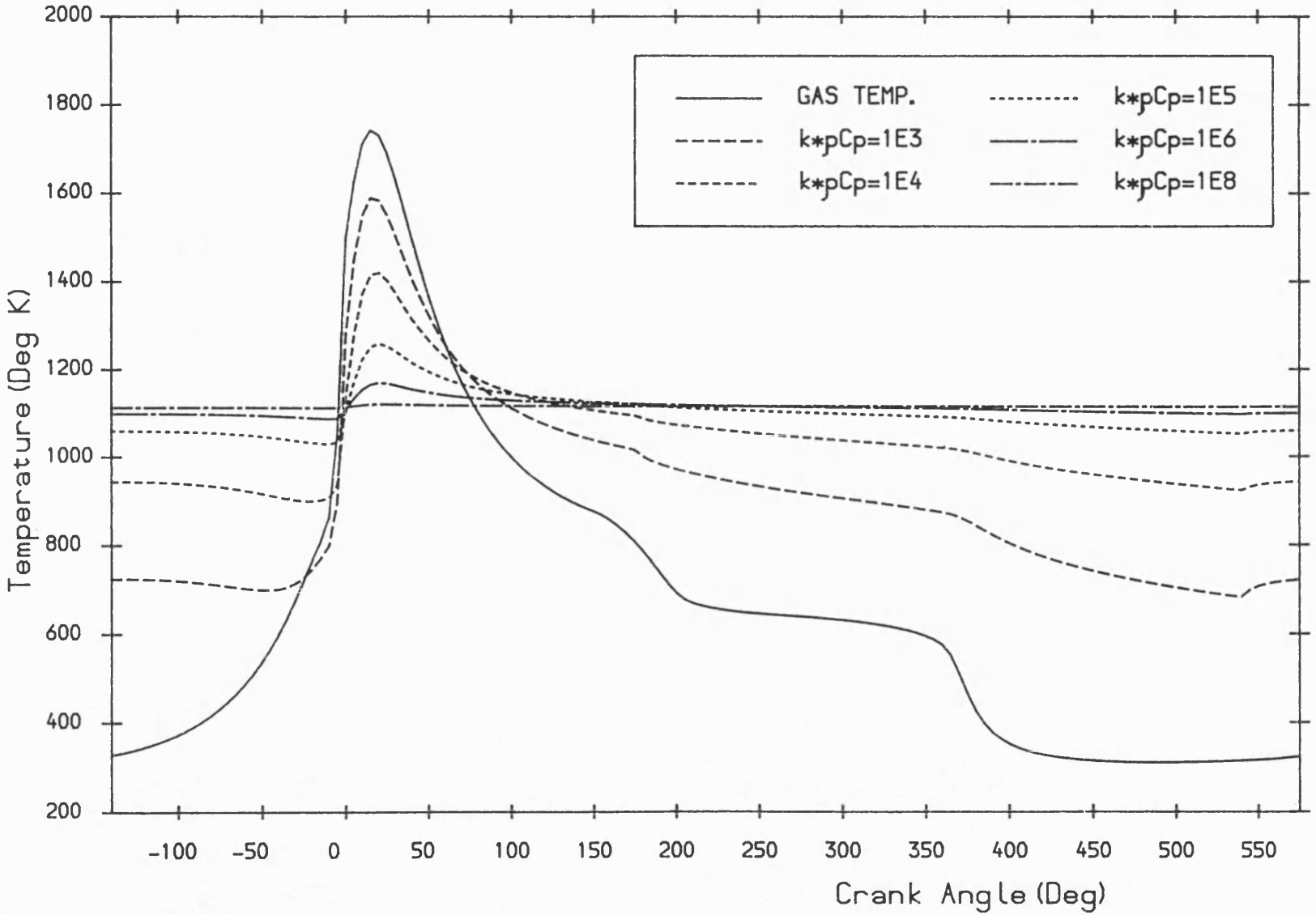

Fig. 6.75 Gas and wall surface temperatures versus crank angle for various k*pCp values with convective gas boundary condition.

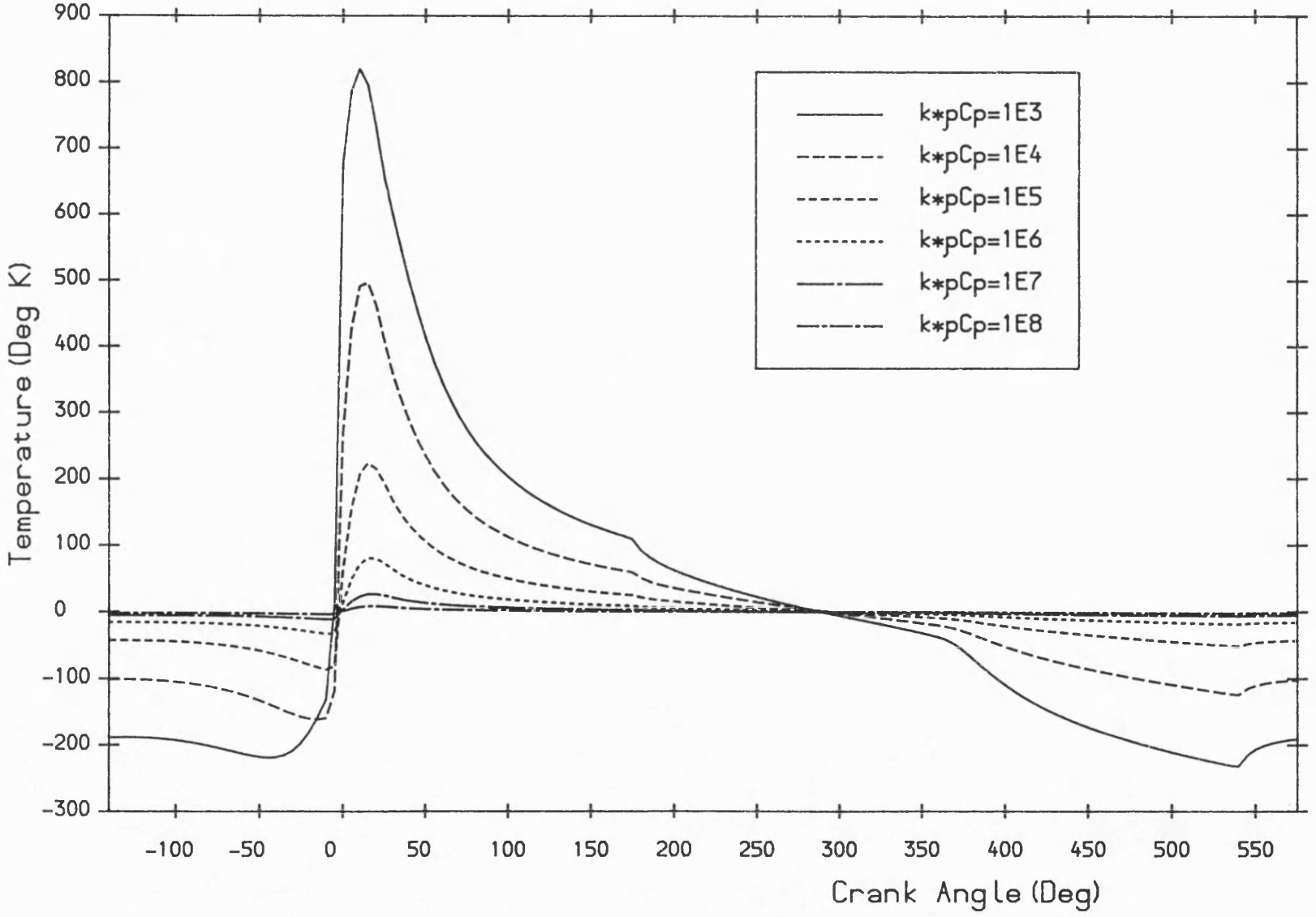

Fig. 6.76 Surface temperature swings for various k*pCp values with convective and radiative gas side boundary condition.

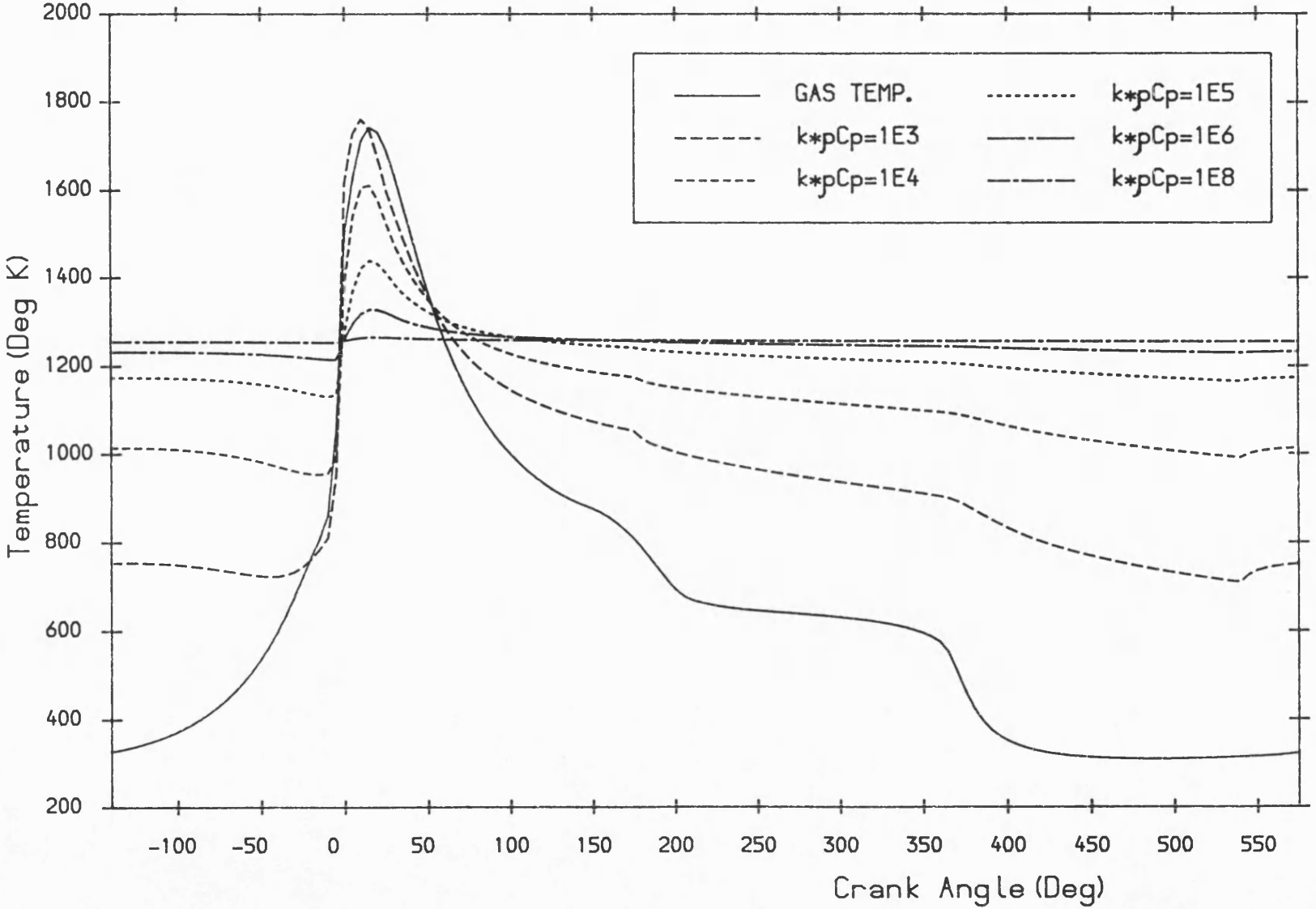

Fig. 6.77 Gas and wall surface temperatures at various k*pCp values with convective and radiative gas boundary condition.

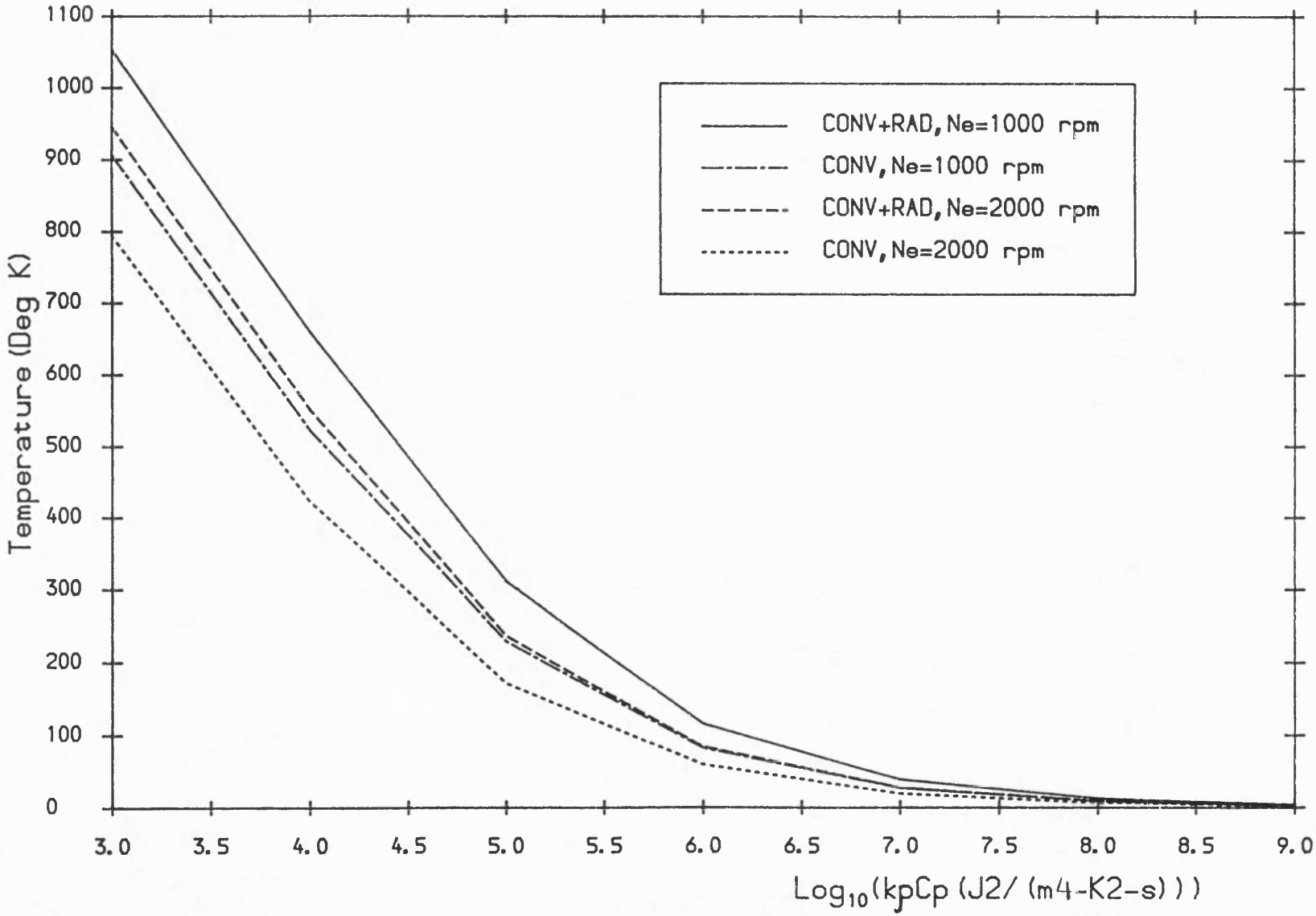

Fig. 6.78 Surface temperature swing versus $\log_{10}(kpCp)$ with different gas boundary conditions at 1000 and 2000 rpm engine speeds.

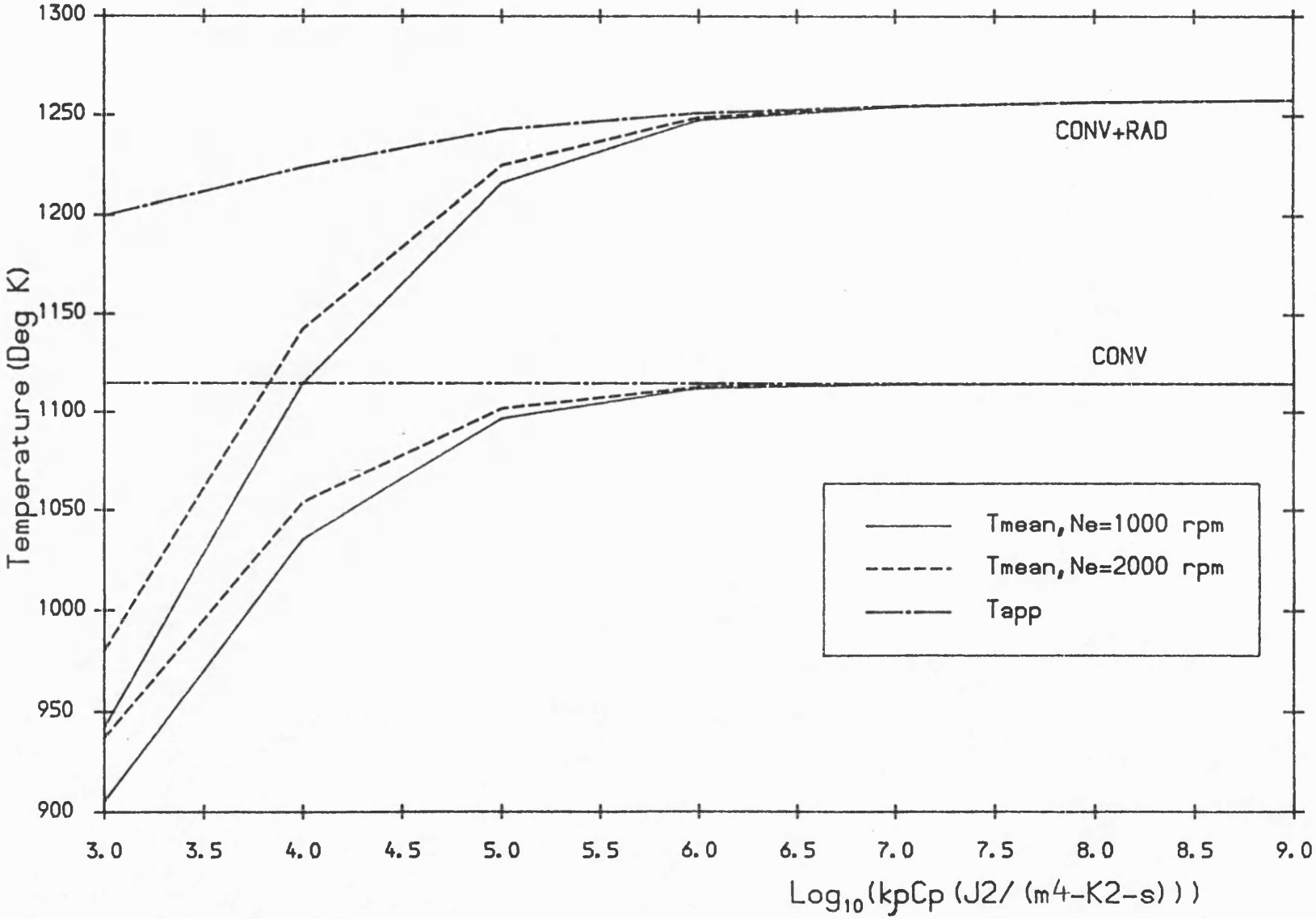

Fig. 6.79 Mean and apparent surface temperatures versus $\log_{10}(kpCp)$ at 1000 and 2000 rpm engine speeds.

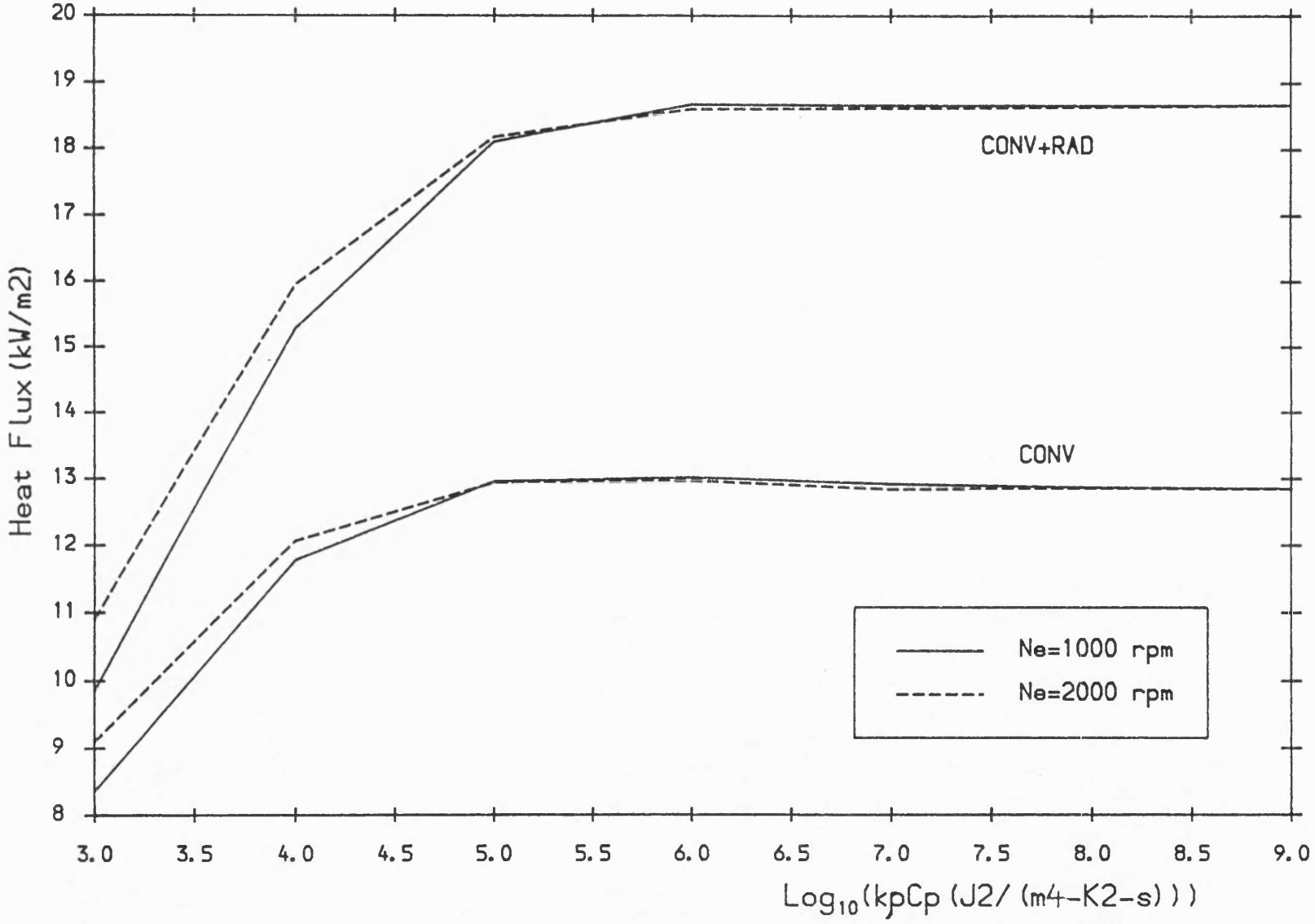

Fig. 6.80 Wall mean pumped heat flux versus $\log_{10}(kpCp)$ during exhaust stroke of the cycle at 1000 and 2000 rpm engine speeds.

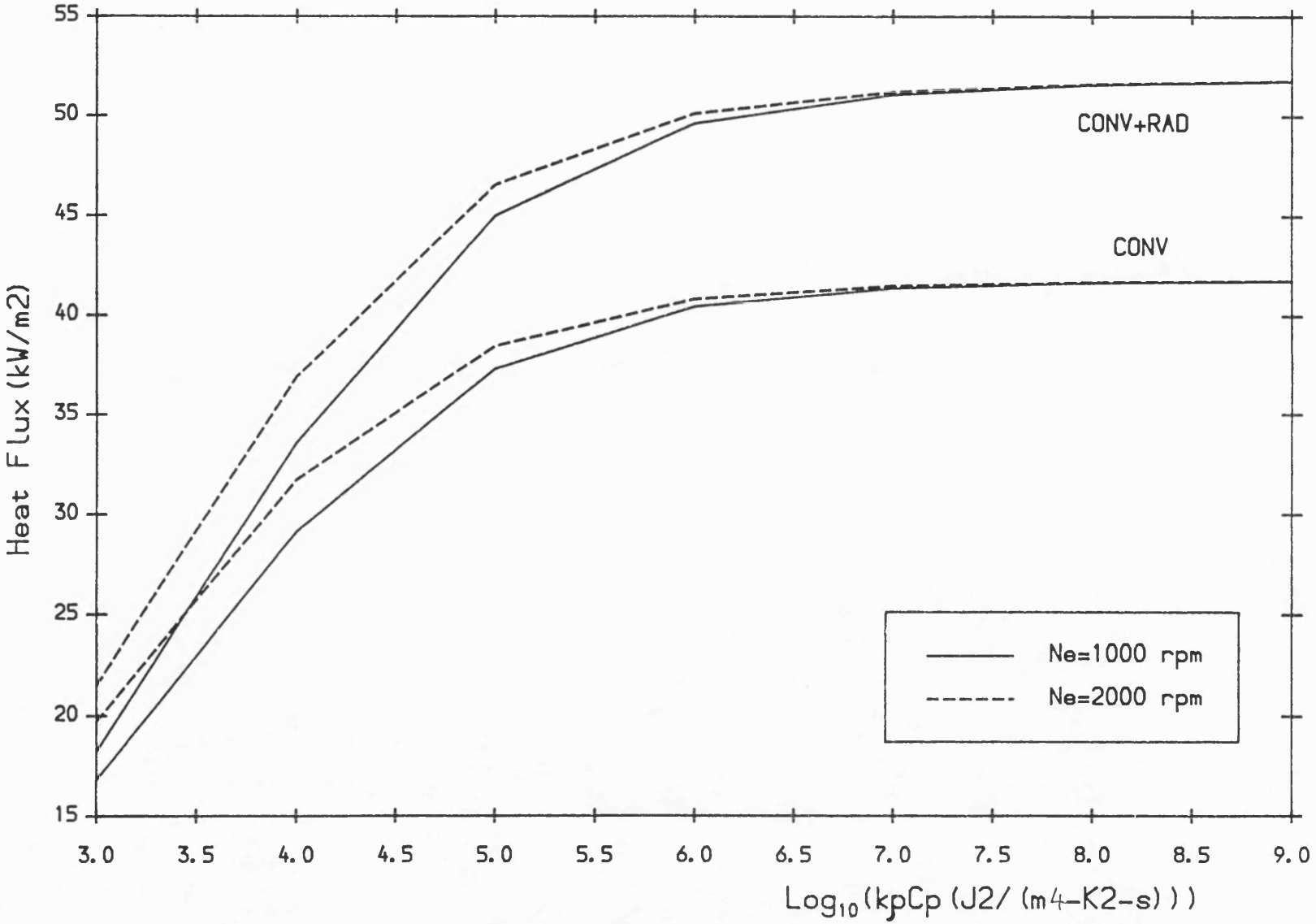

Fig. 6.81 Wall mean pumped heat flux versus $\log_{10}(k_pC_p)$ during intake stroke of the cycle at 1000 and 2000 rpm engine speeds.

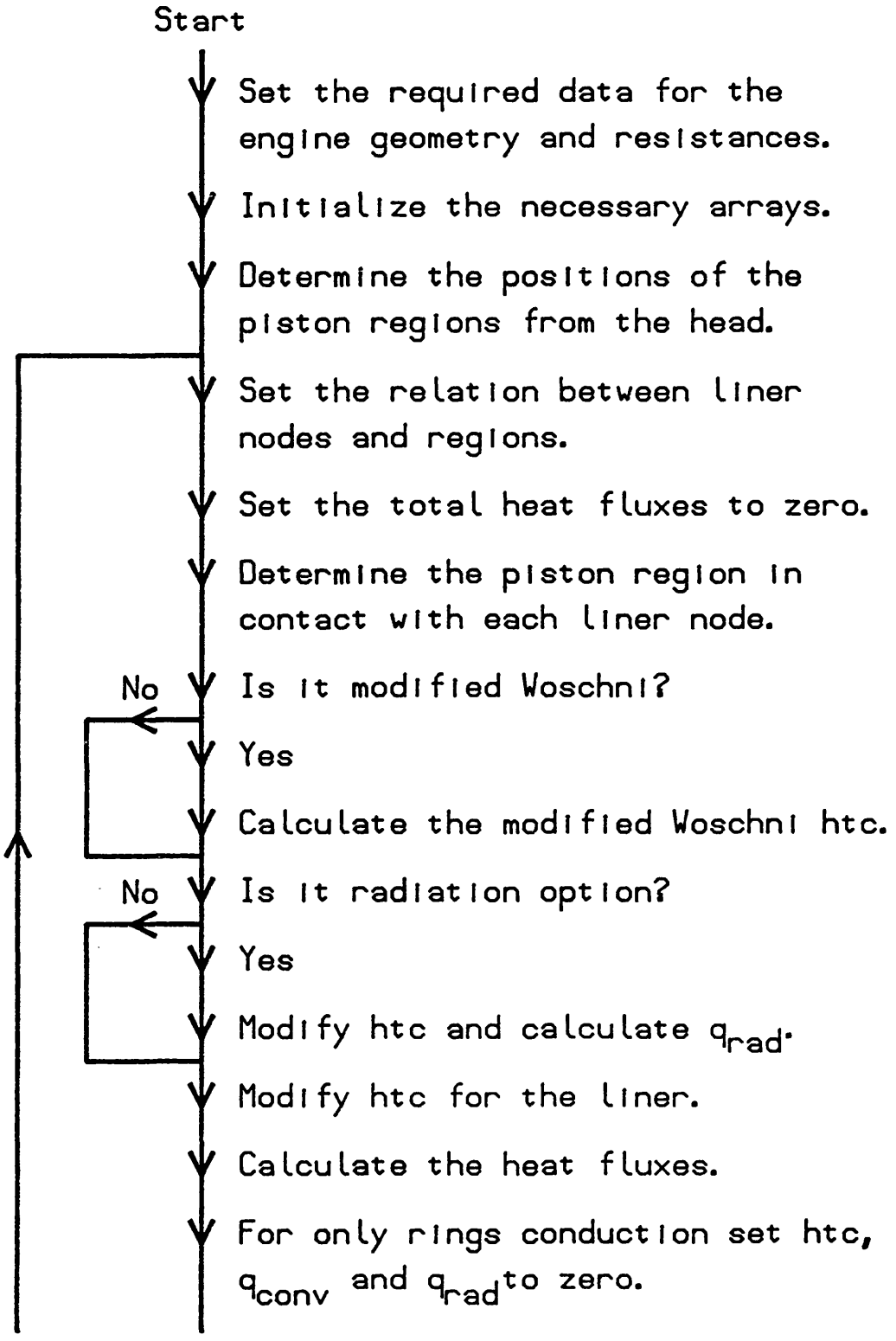

Fig. 6.82 The flowchart for Linat.For.

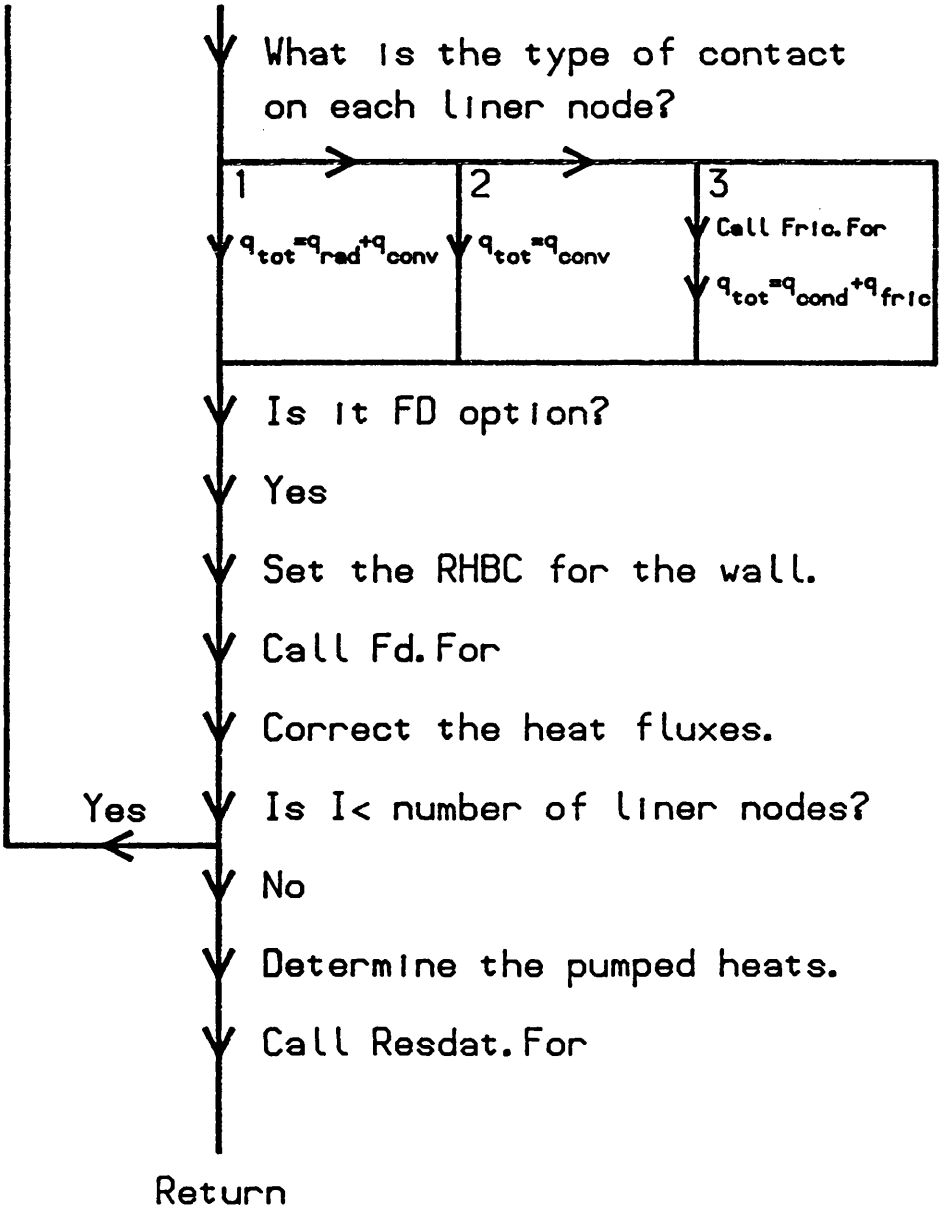

Fig. 6.82 Continued.

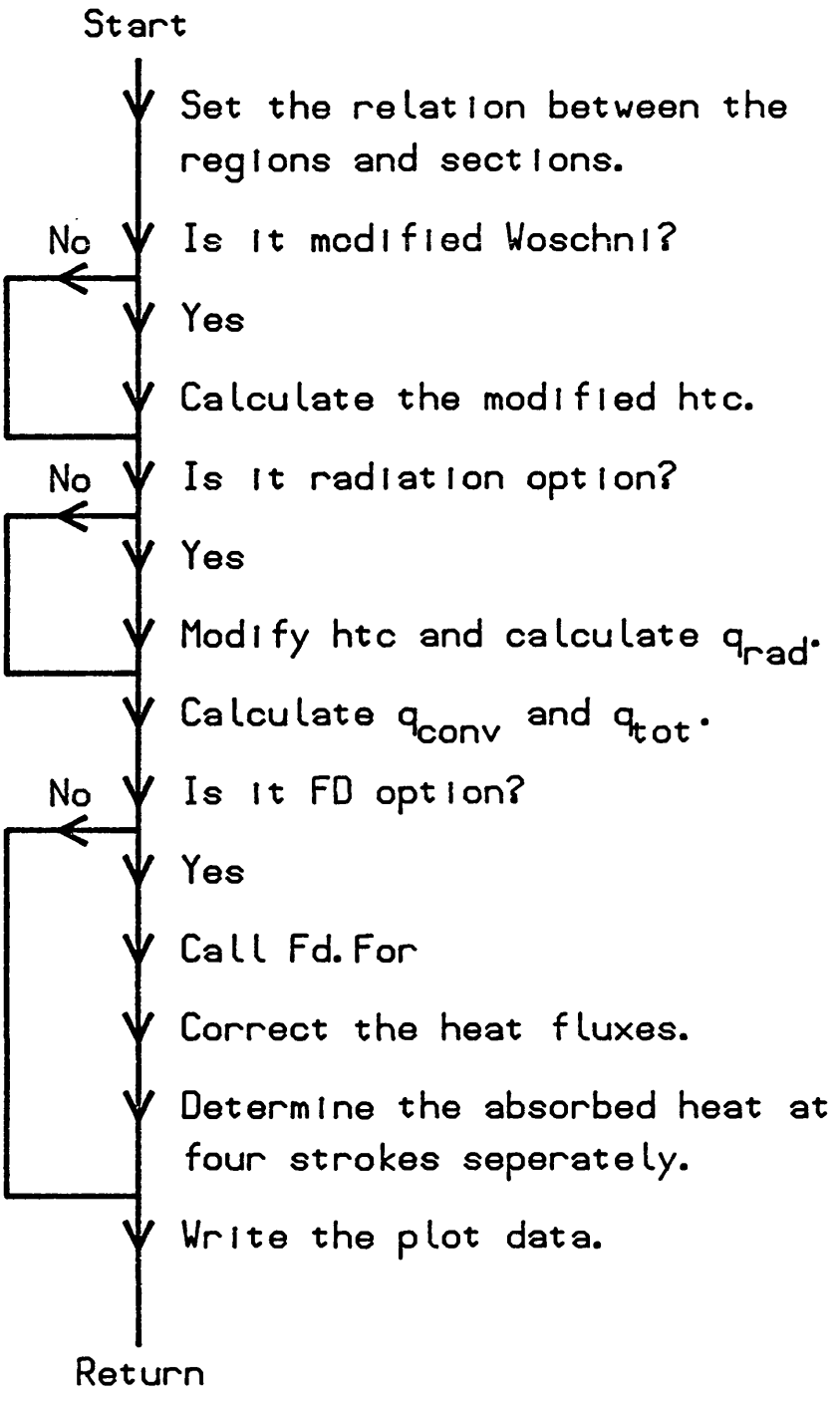

Fig. 6.83 The flowchart for Rest.For.

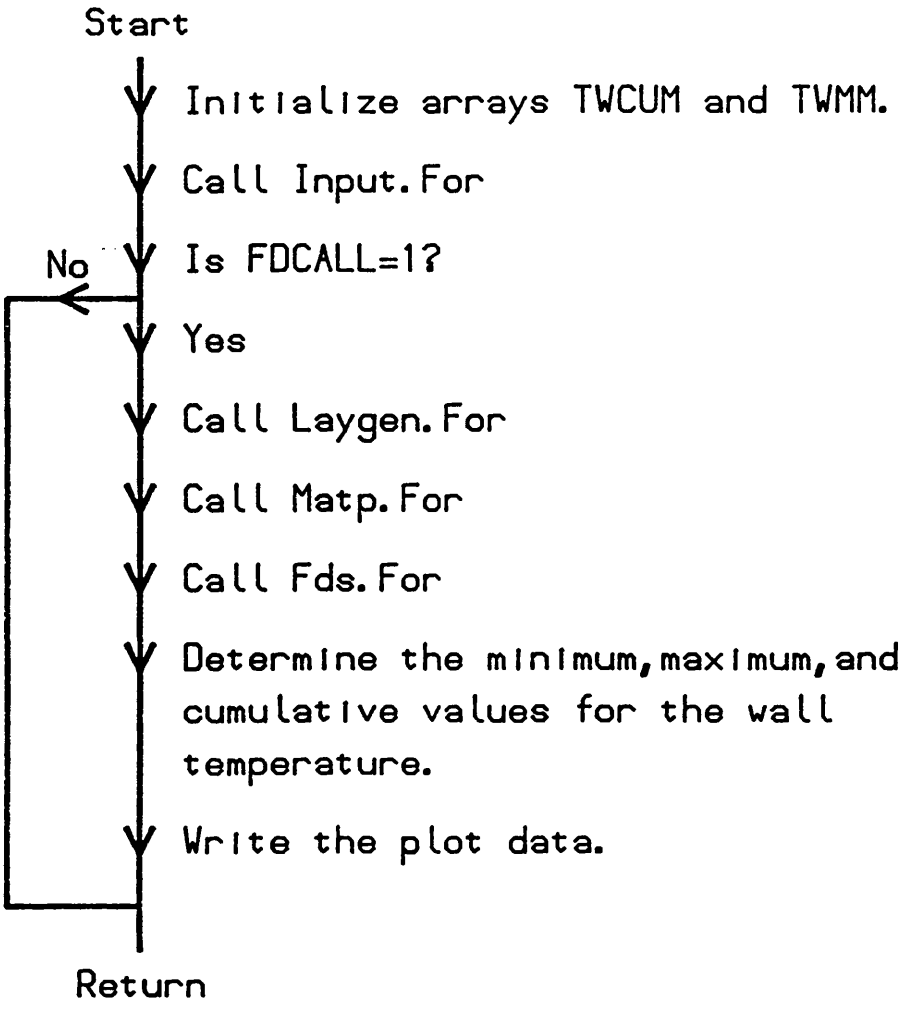

Fig. 6.84 The flowchart for Fd.For.

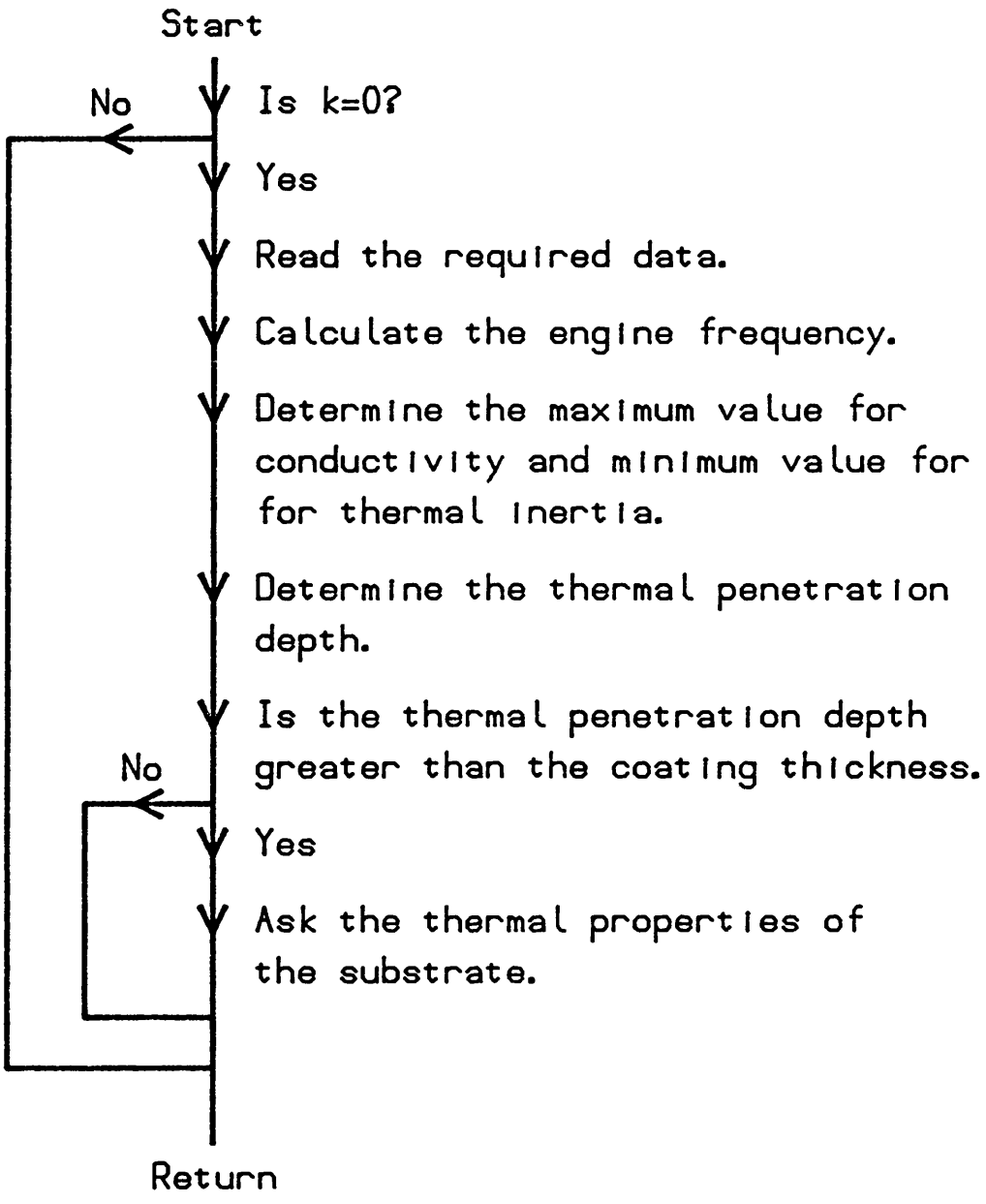

Fig. 6.85 The flowchart for Input.For.

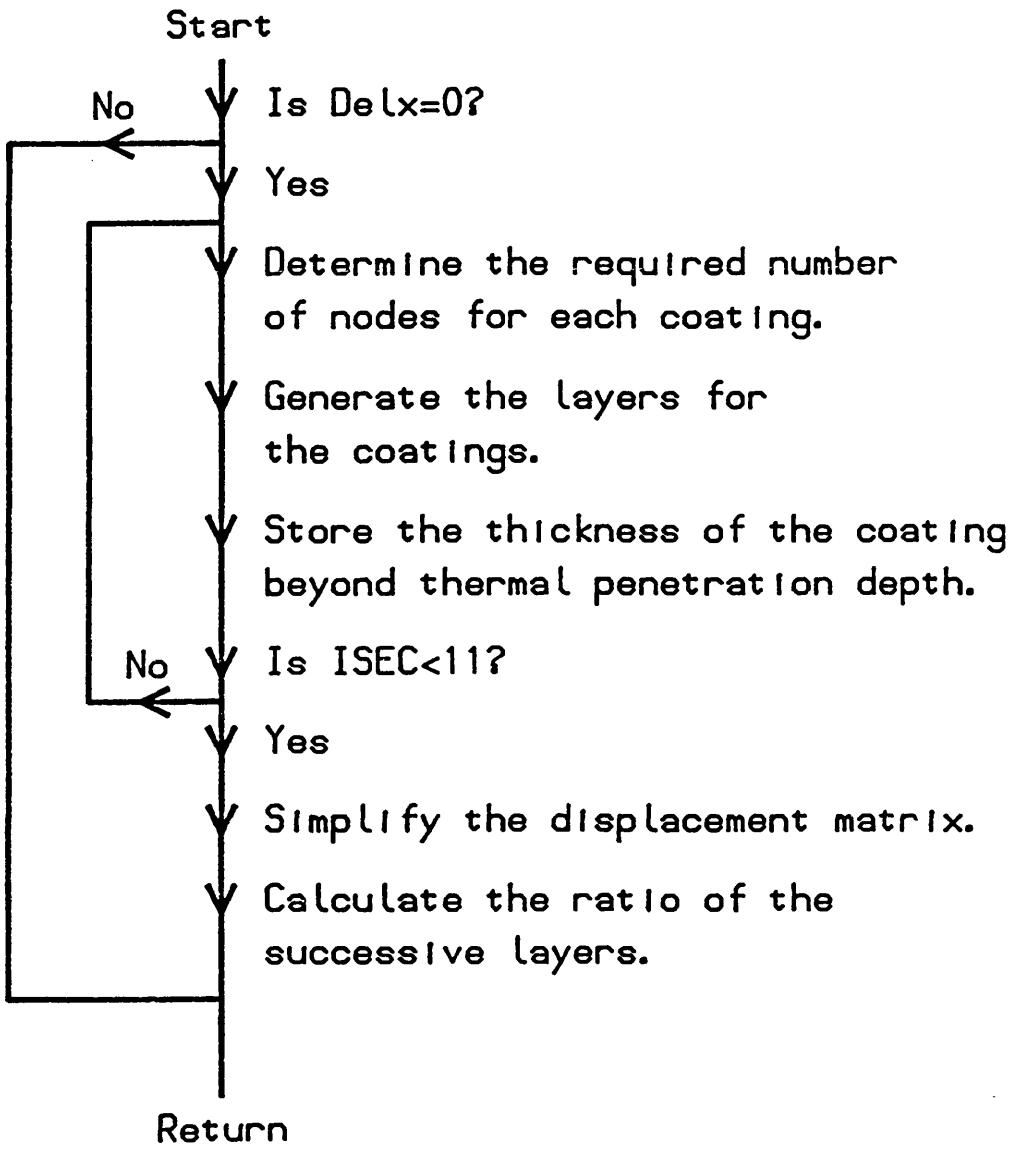

Fig. 6.86 The flowchart for Laygen.For.

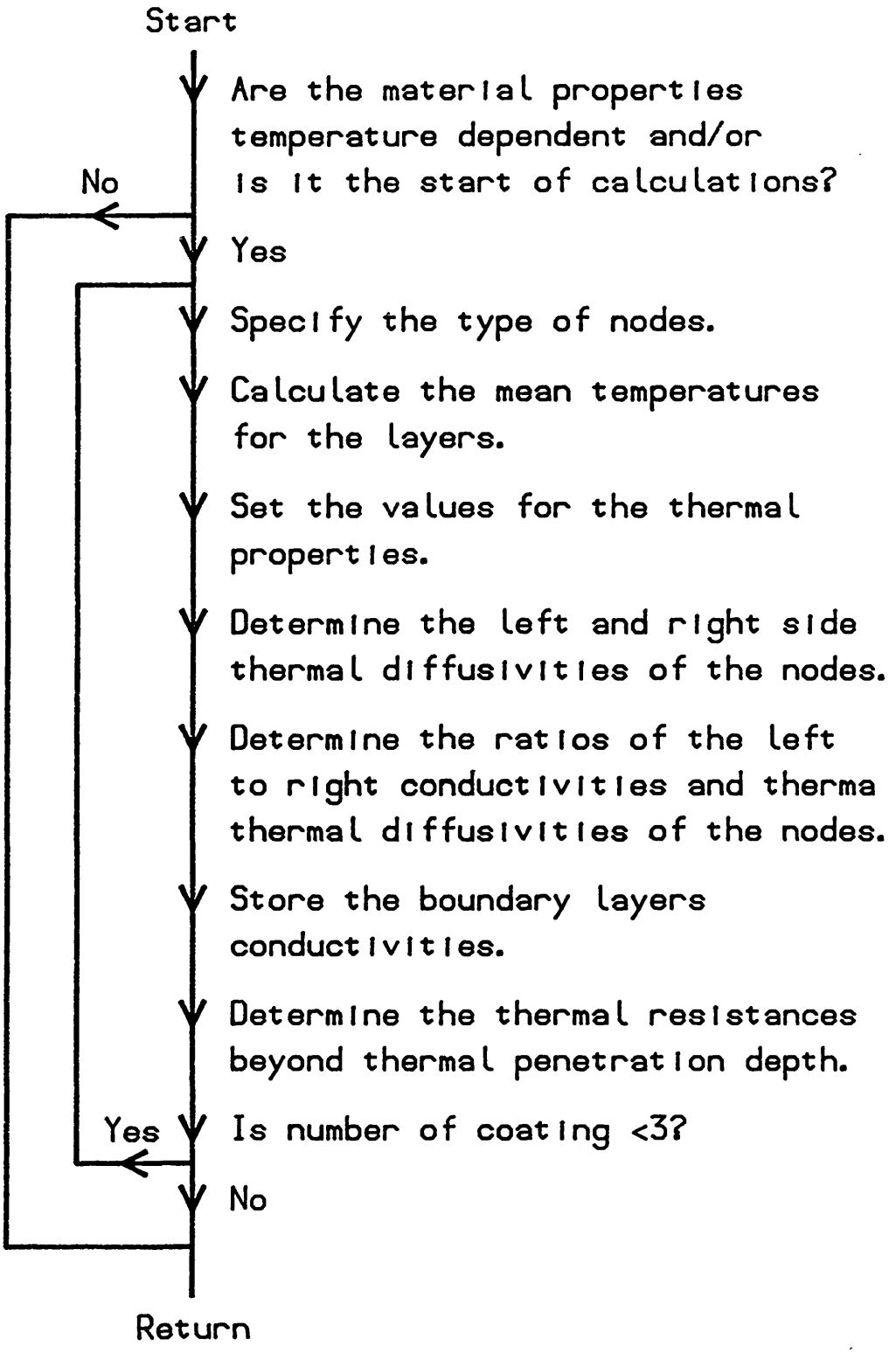

Fig. 6.87 The flowchart for Matp.For.

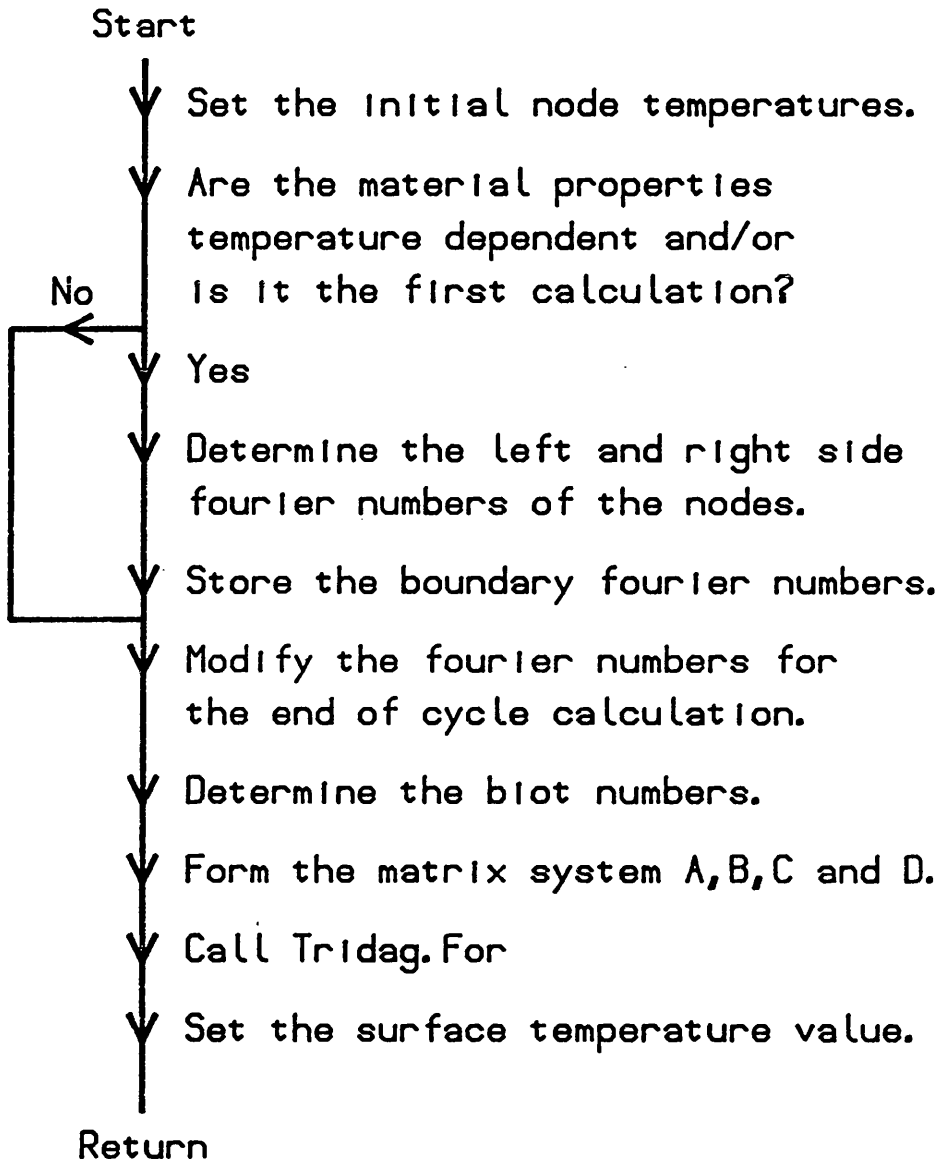

Fig. 6. 88 The flowchart for Fds. For.

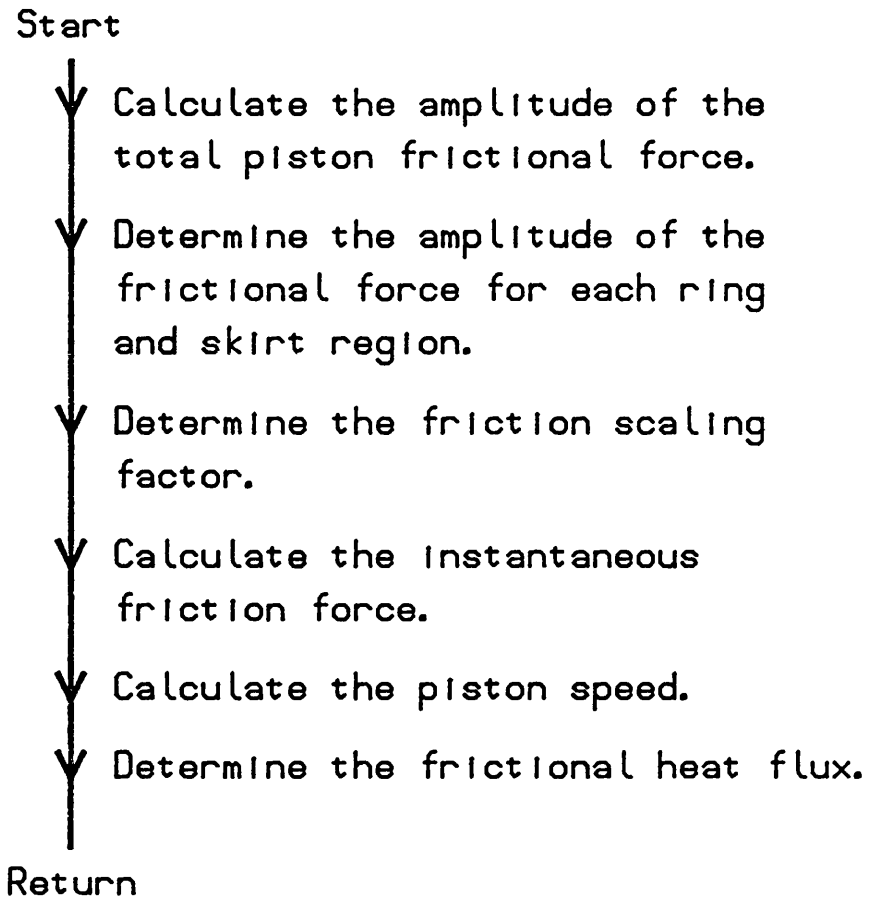

Fig. 6.89 The flowchart for Fricfd.For.

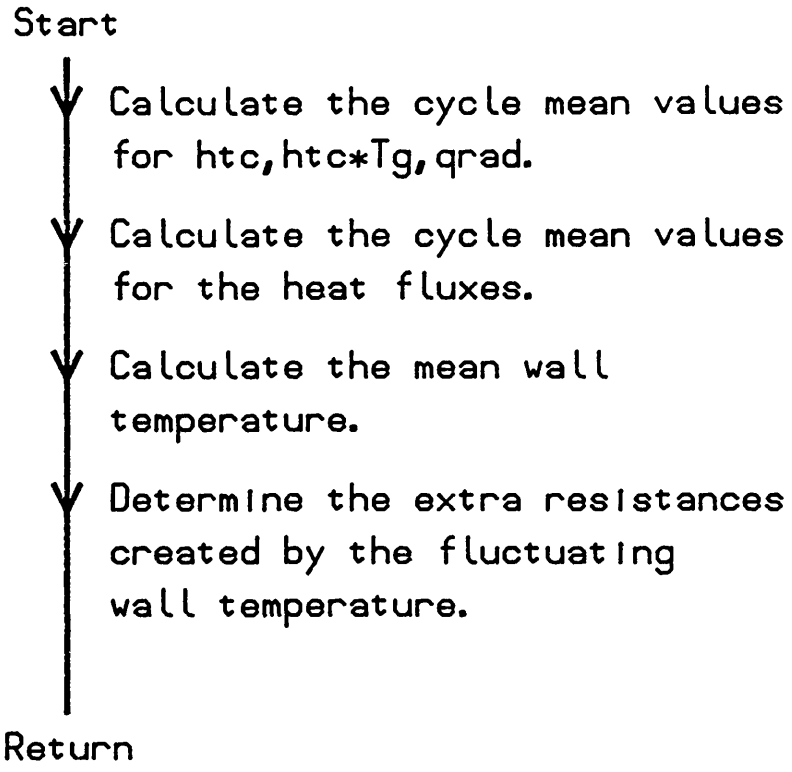

Fig. 6.90 The flowchart for Exres.For.

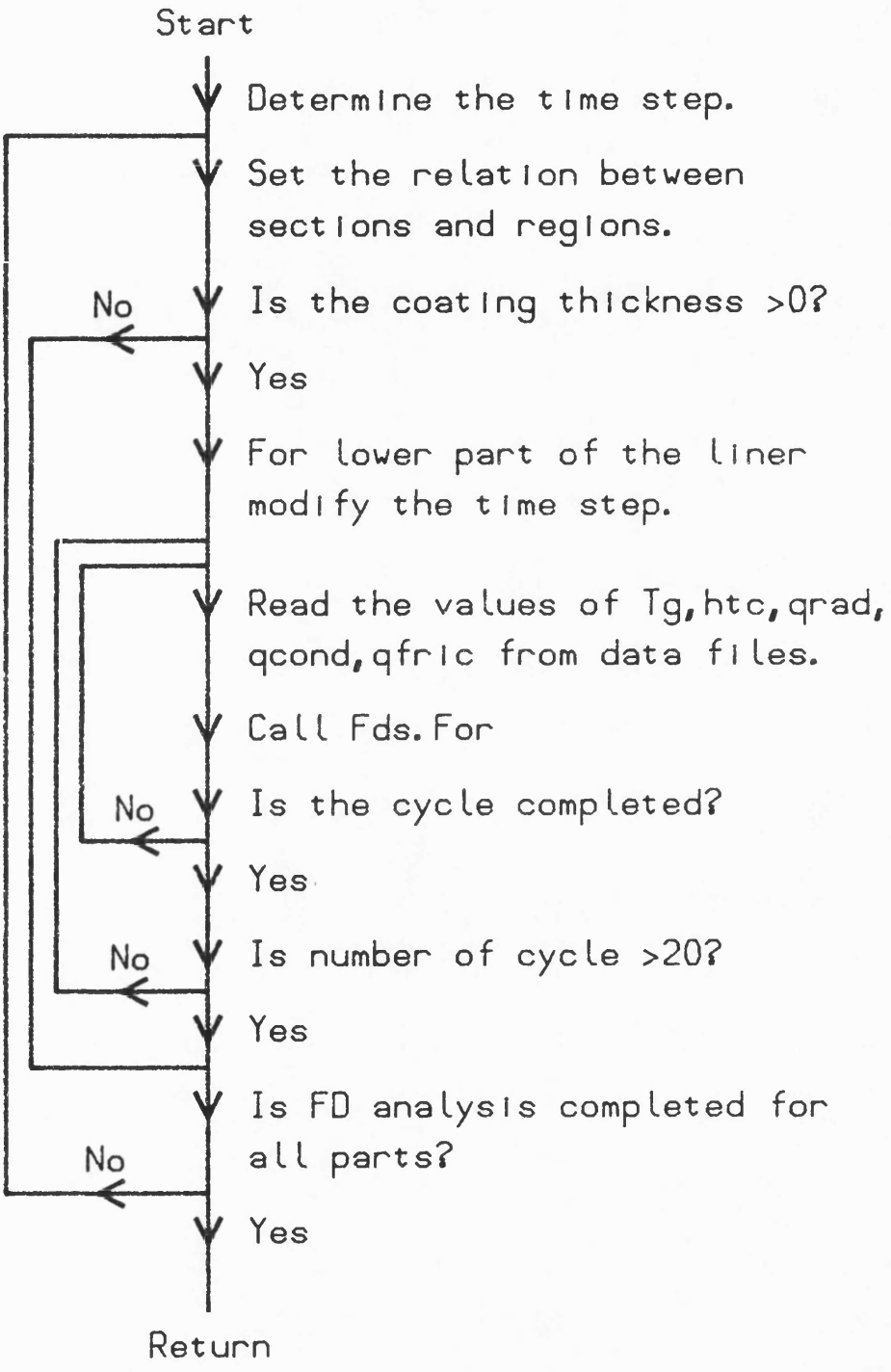

Fig. 6.91 The flowchart for Fdcy.For.

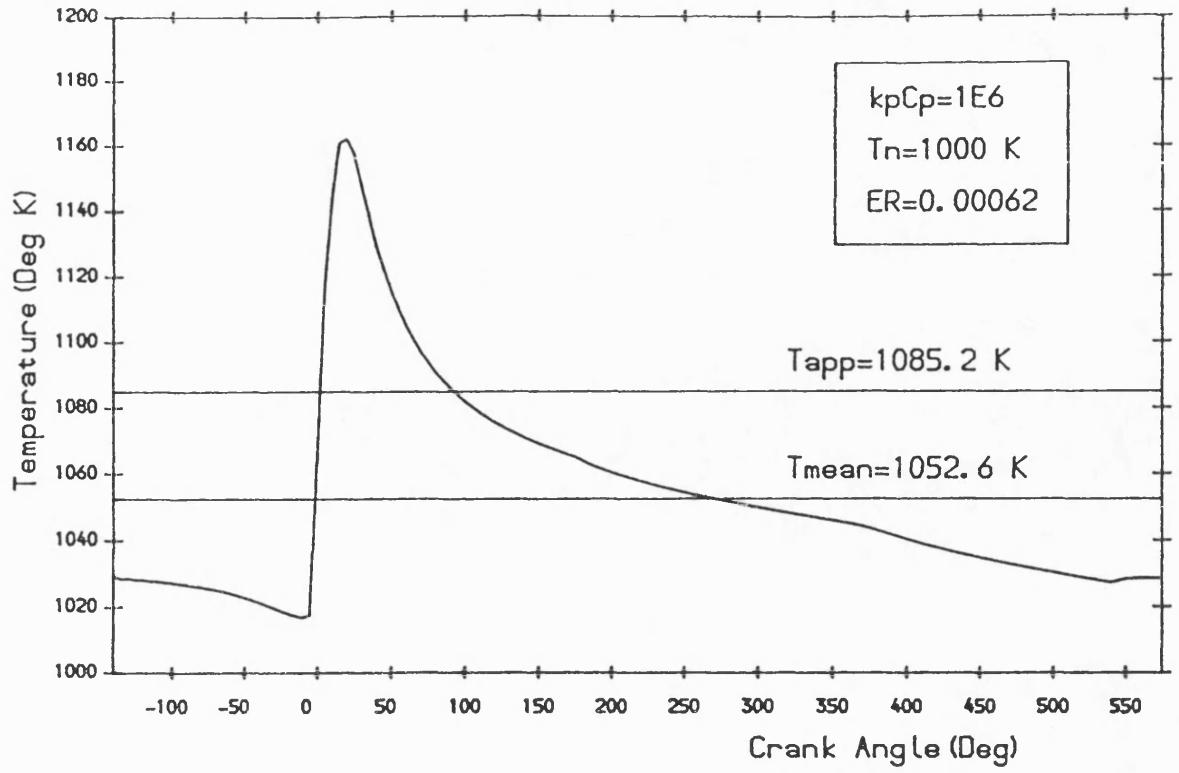

Fig. 6.92 Mean, apparent and transient surface temperatures of a ceramic with thermal properties kpCp=1E6.

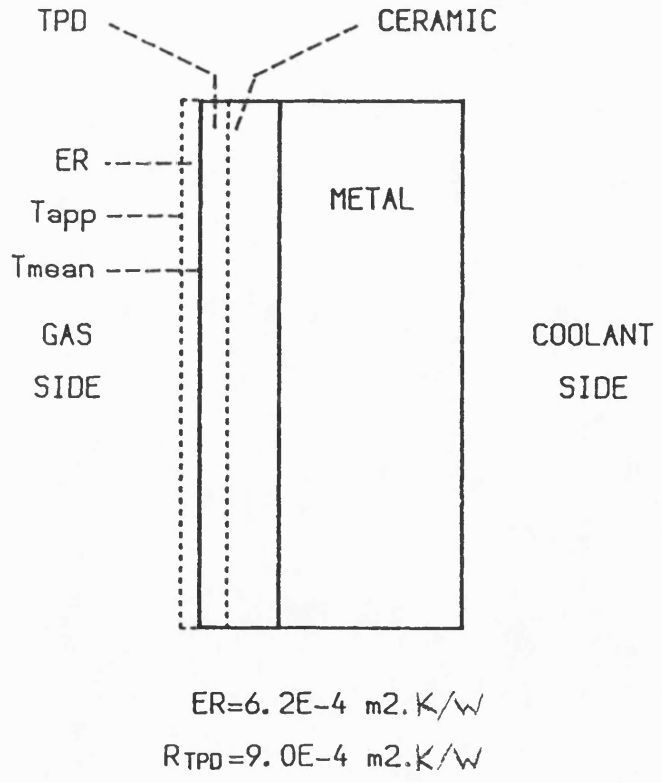

Fig. 6.93 Representation of the wall with extra resistance term ER.

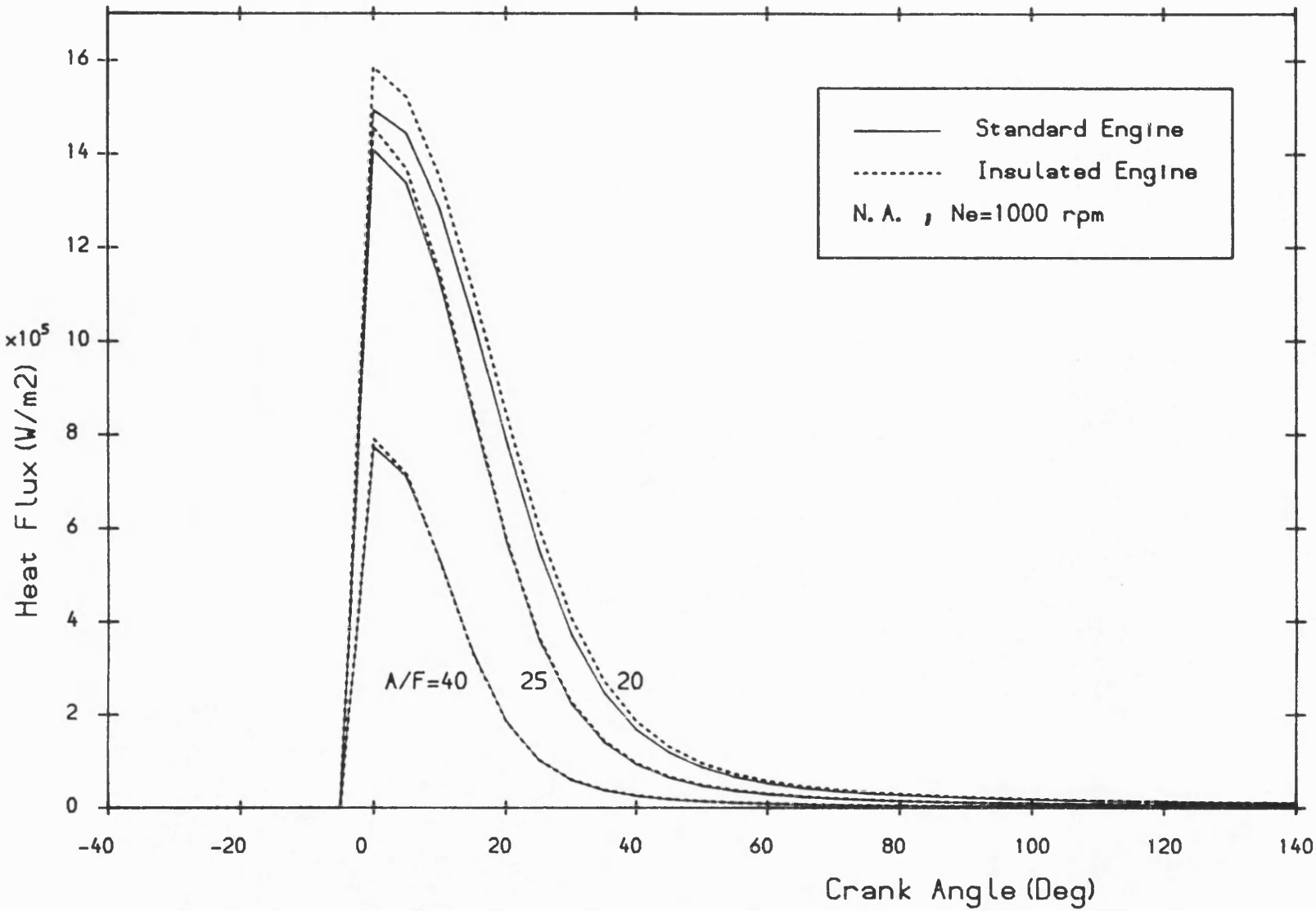

Fig. 7.1 Radiative heat flux versus crank angle at various air-fuel ratios for standard and insulated engines.

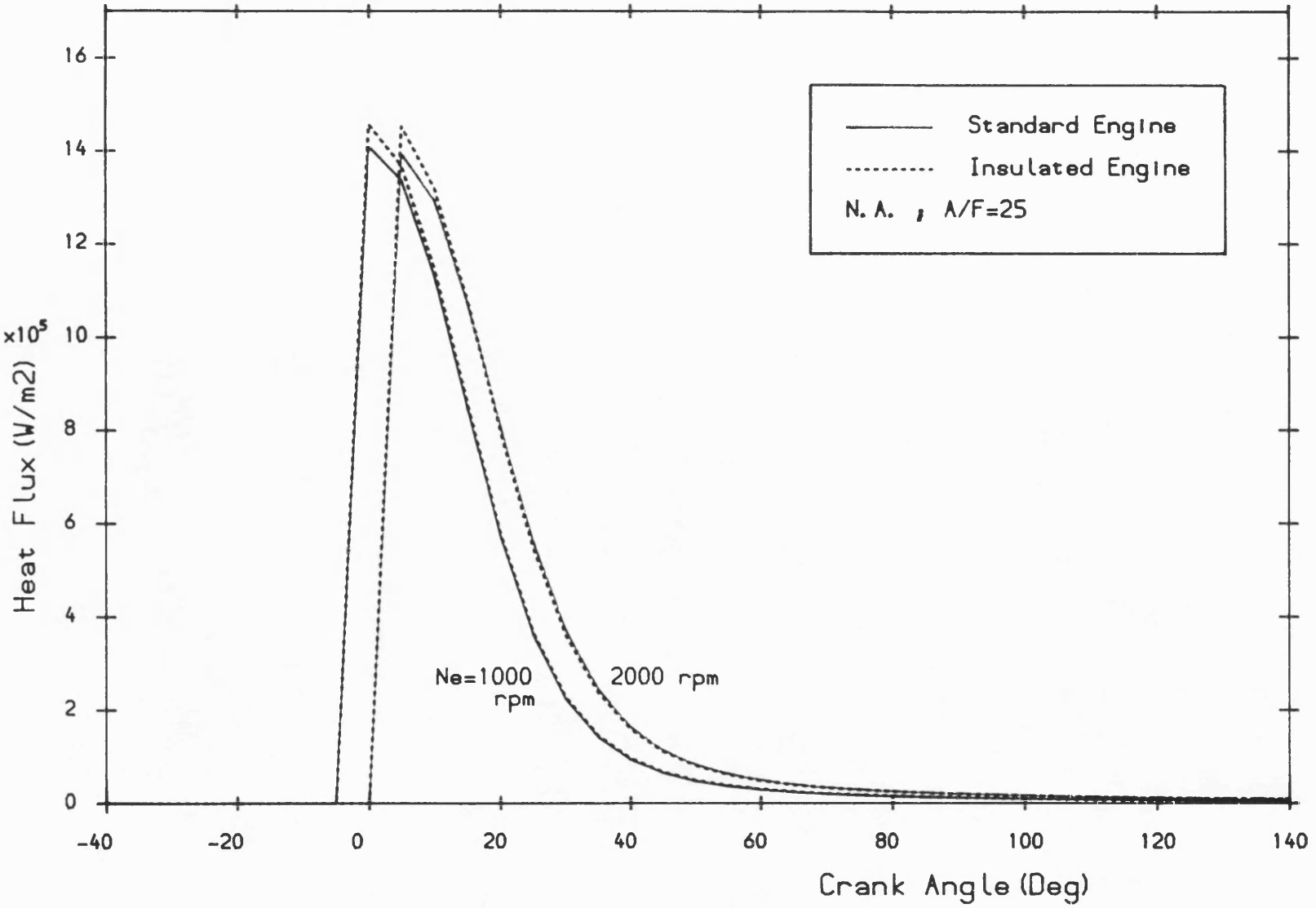

Fig. 7.2 Radiative heat flux versus crank angle at 2 different engine speeds for standard and insulated engines.

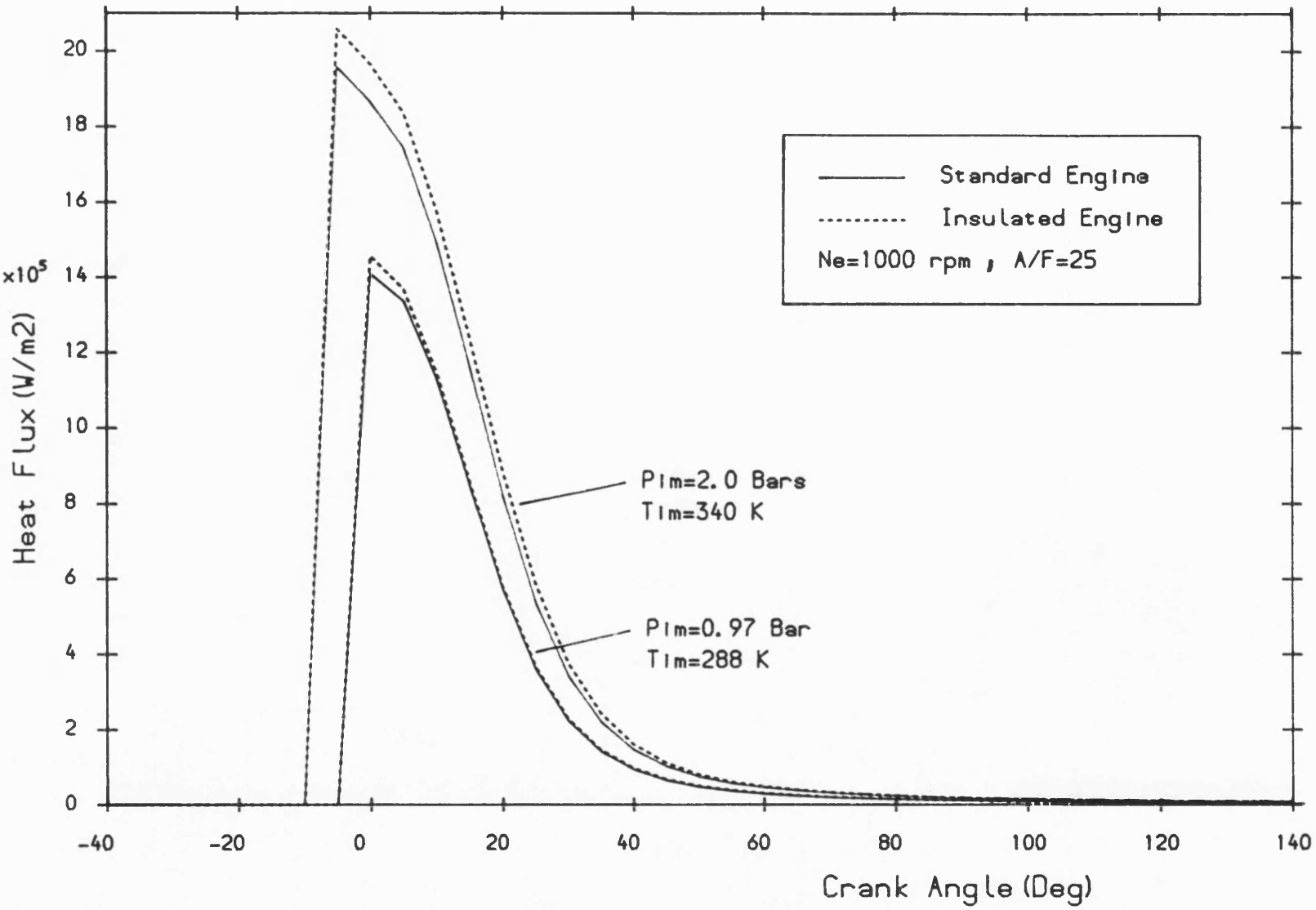

Fig. 7.3 Radiative heat flux versus crank angle at 2 different inlet manifold conditions for standard and insulated engines.

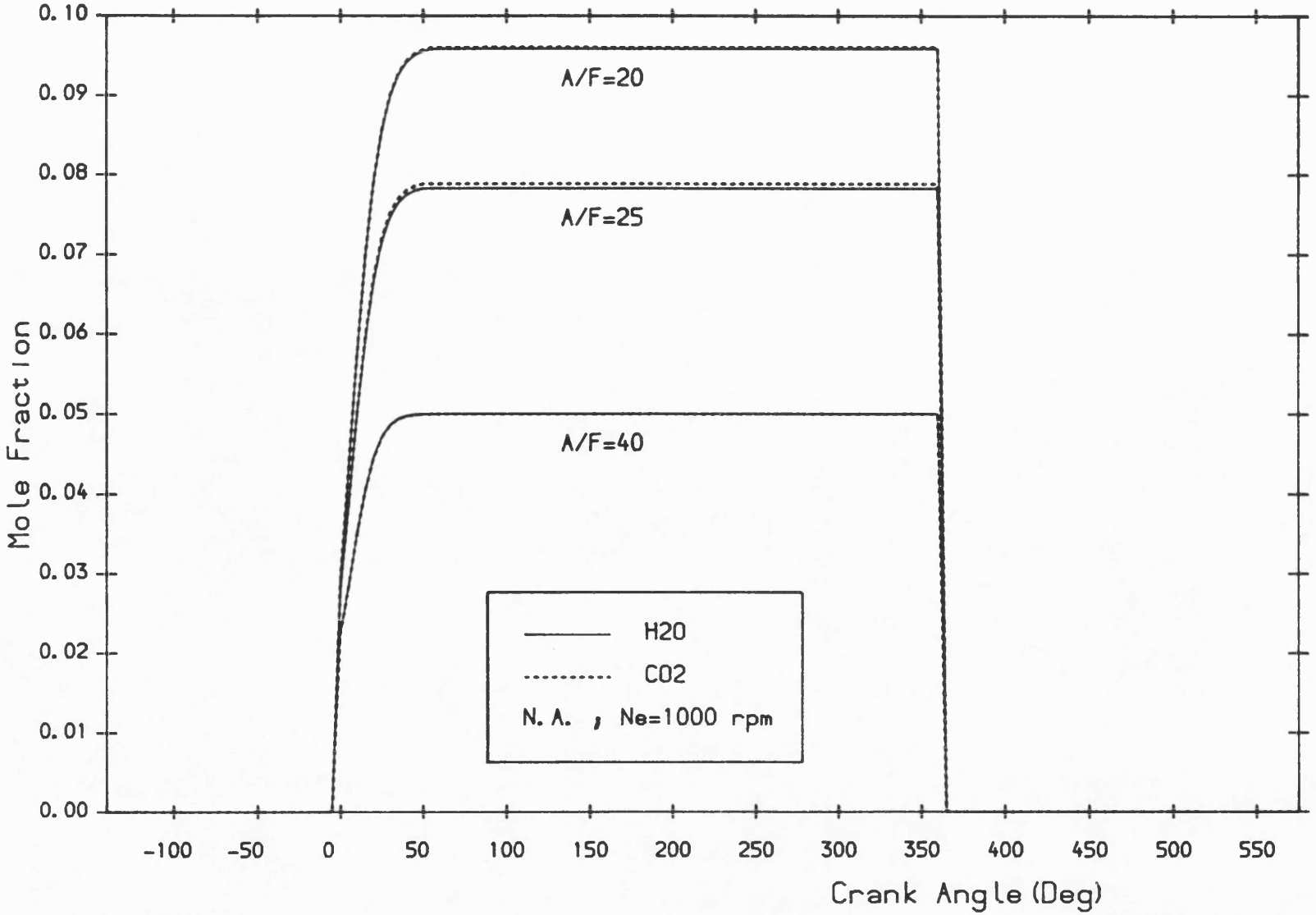

Fig. 7.4 Mole fractions of water-vapour and carbon-dioxide versus crank angle at various air-fuel ratios.

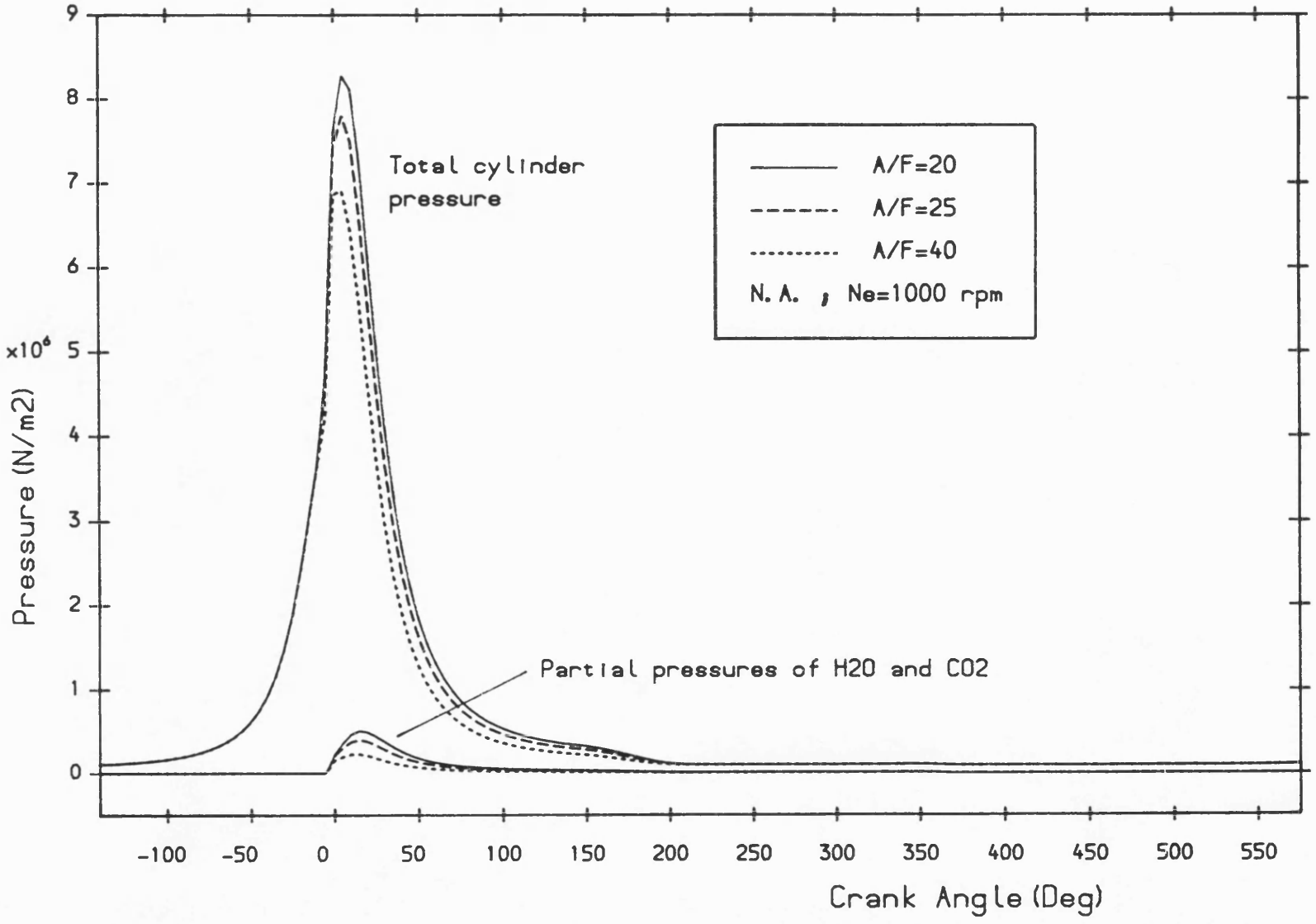

Fig. 7.5 Total cylinder pressure and partial pressures of H20 and C02 versus crank angle at varios air-fuel ratios.

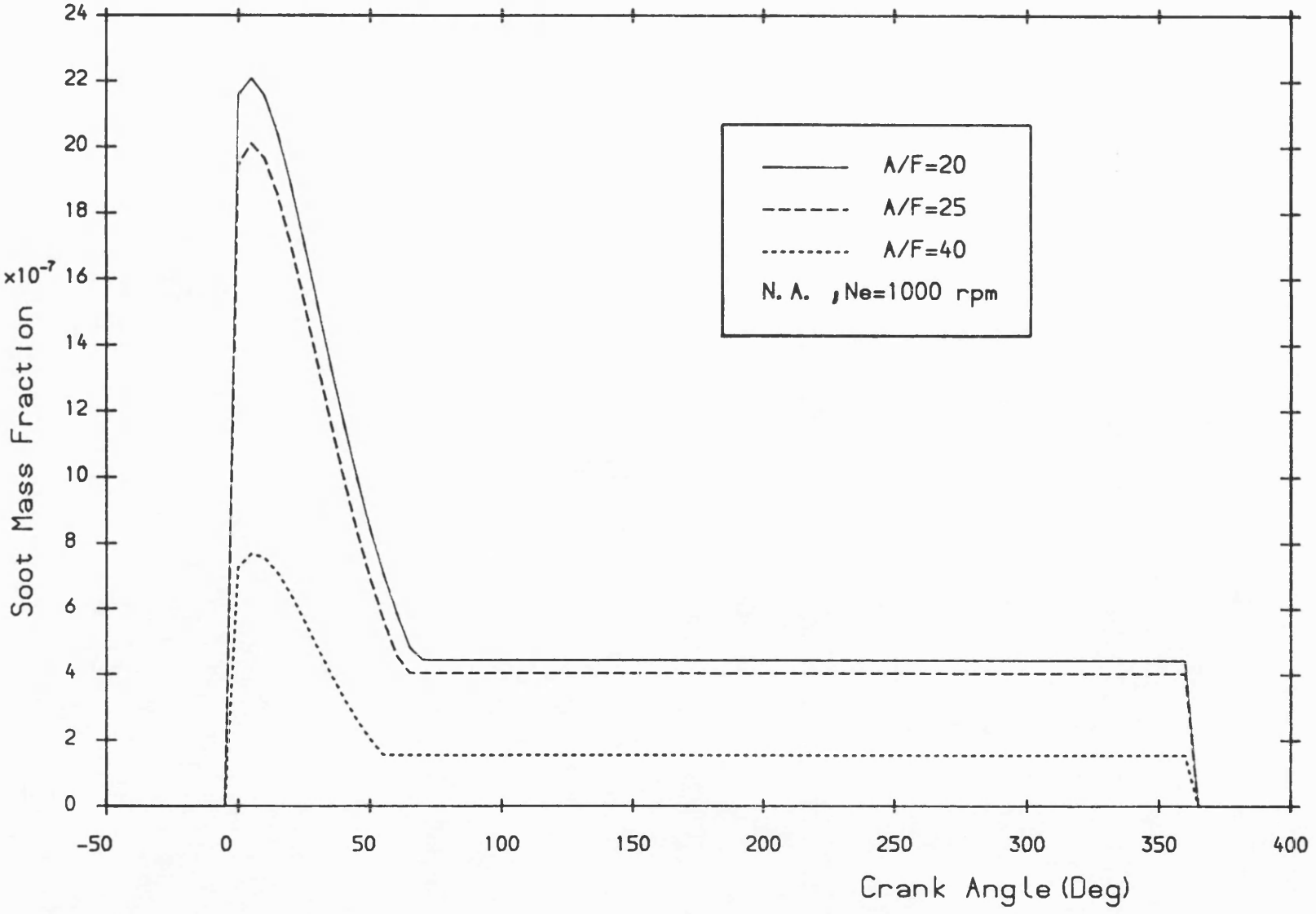

Fig. 7.6 Soot mass fraction versus crank angle at various air-fuel ratios.

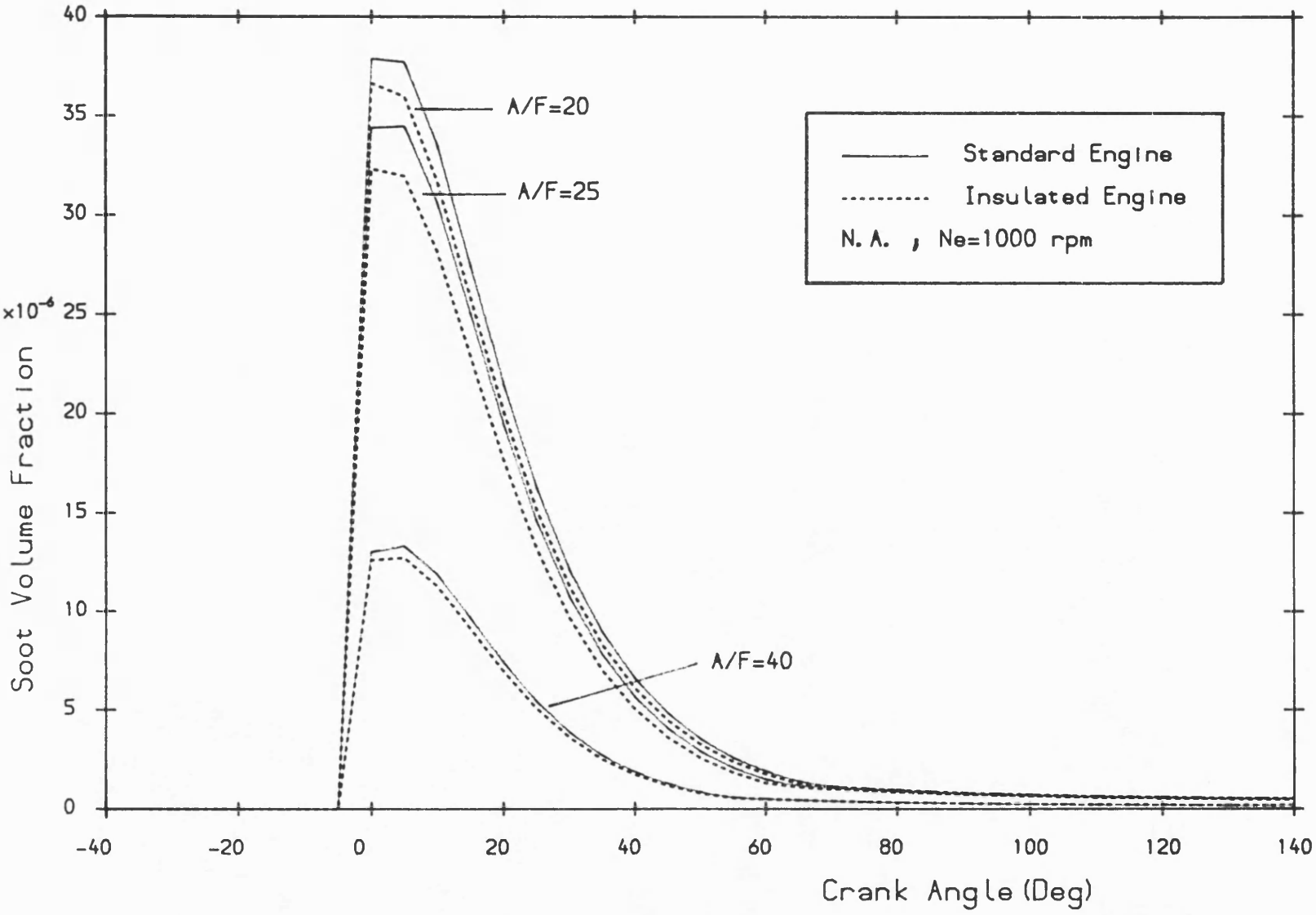

Fig. 7.7 Soot volume fraction versus crank angle at various air-fuel ratios for standard and insulated engines.

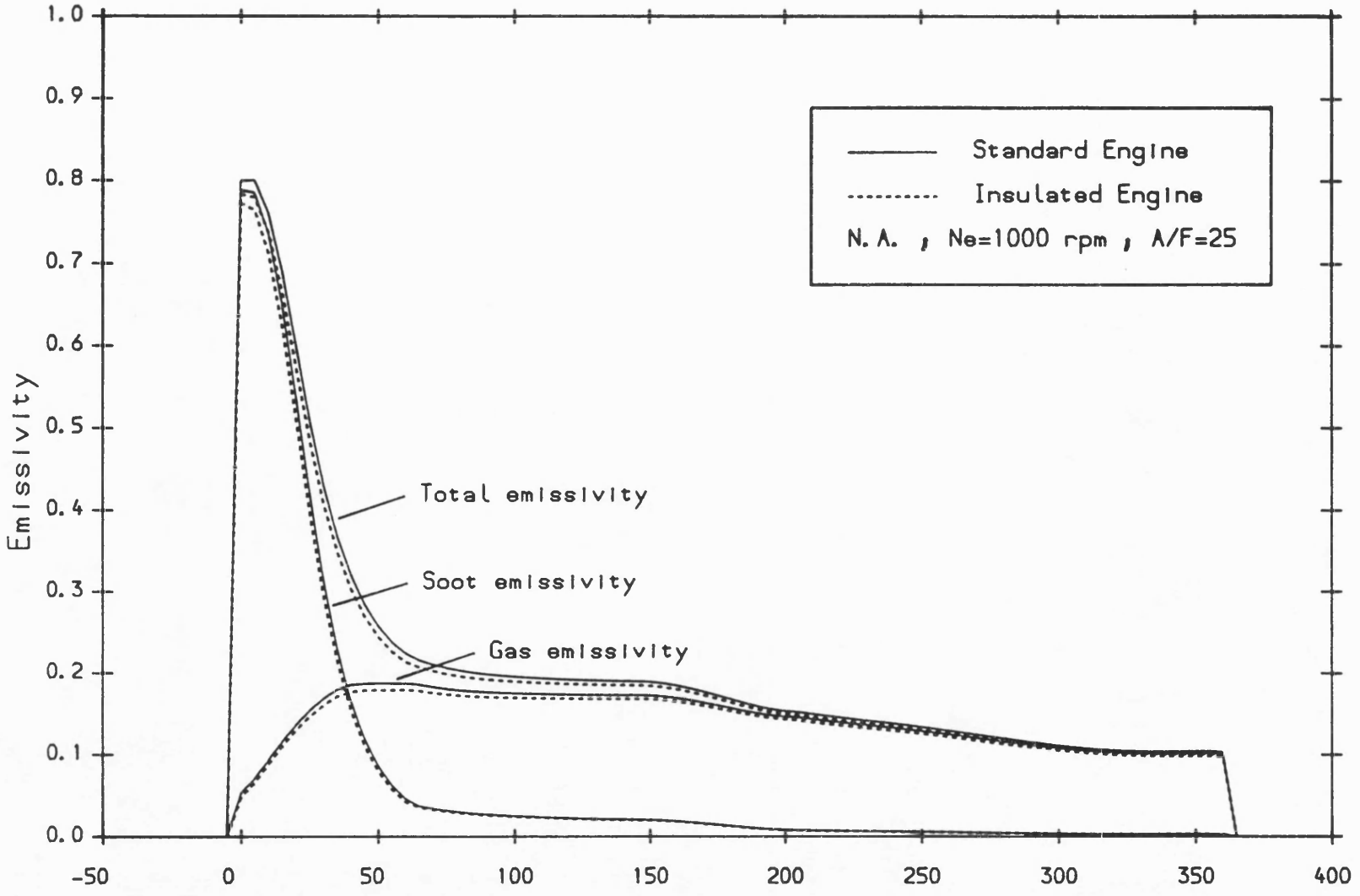

Fig. 7.8 Soot, gas and total emissivities versus crank angle observed at piston surface for standard and insulated engines.

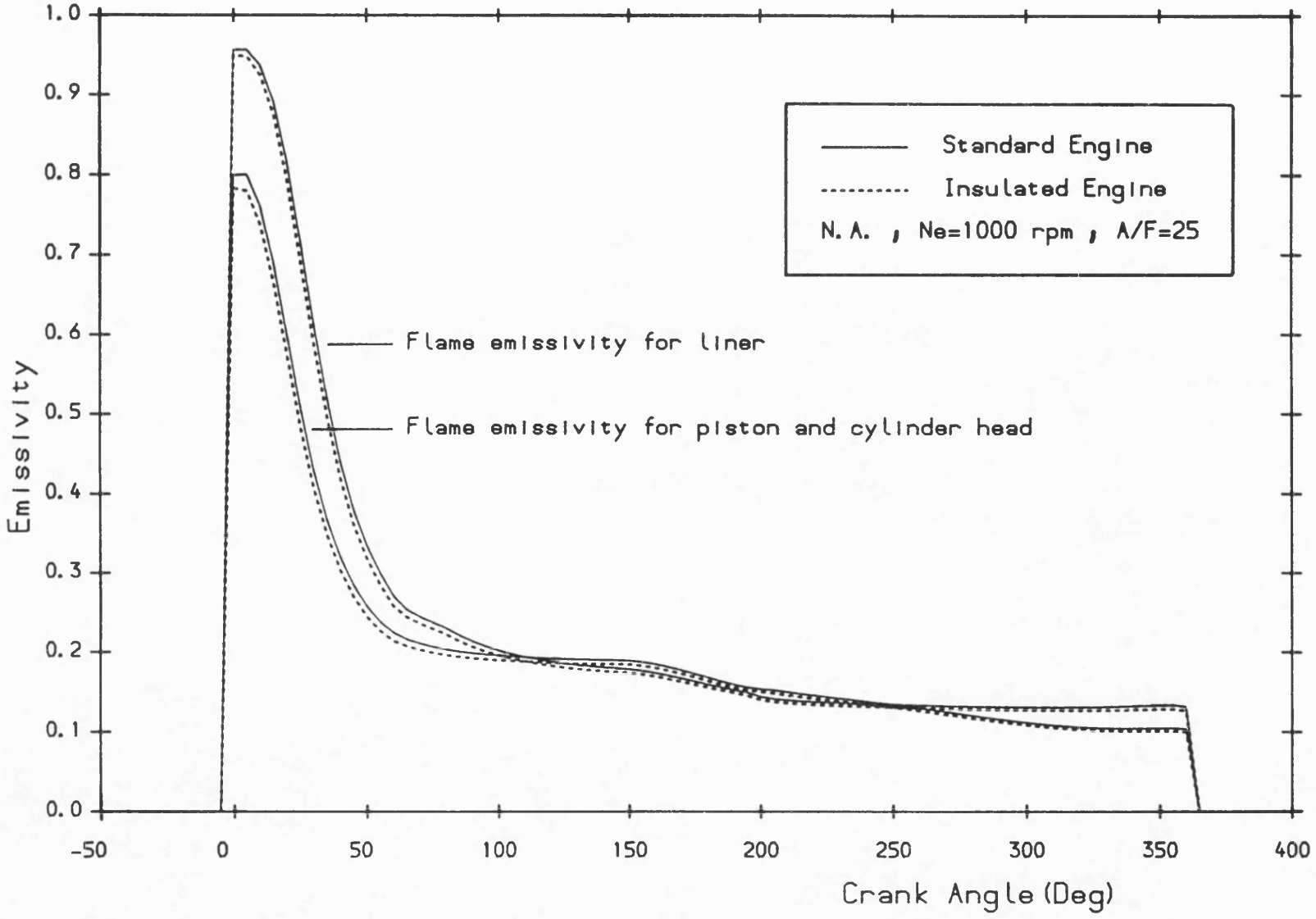

Fig. 7.9 Total flame emissivity versus crank angle observed at piston, cylinder head and liner for standard and insulated engines.

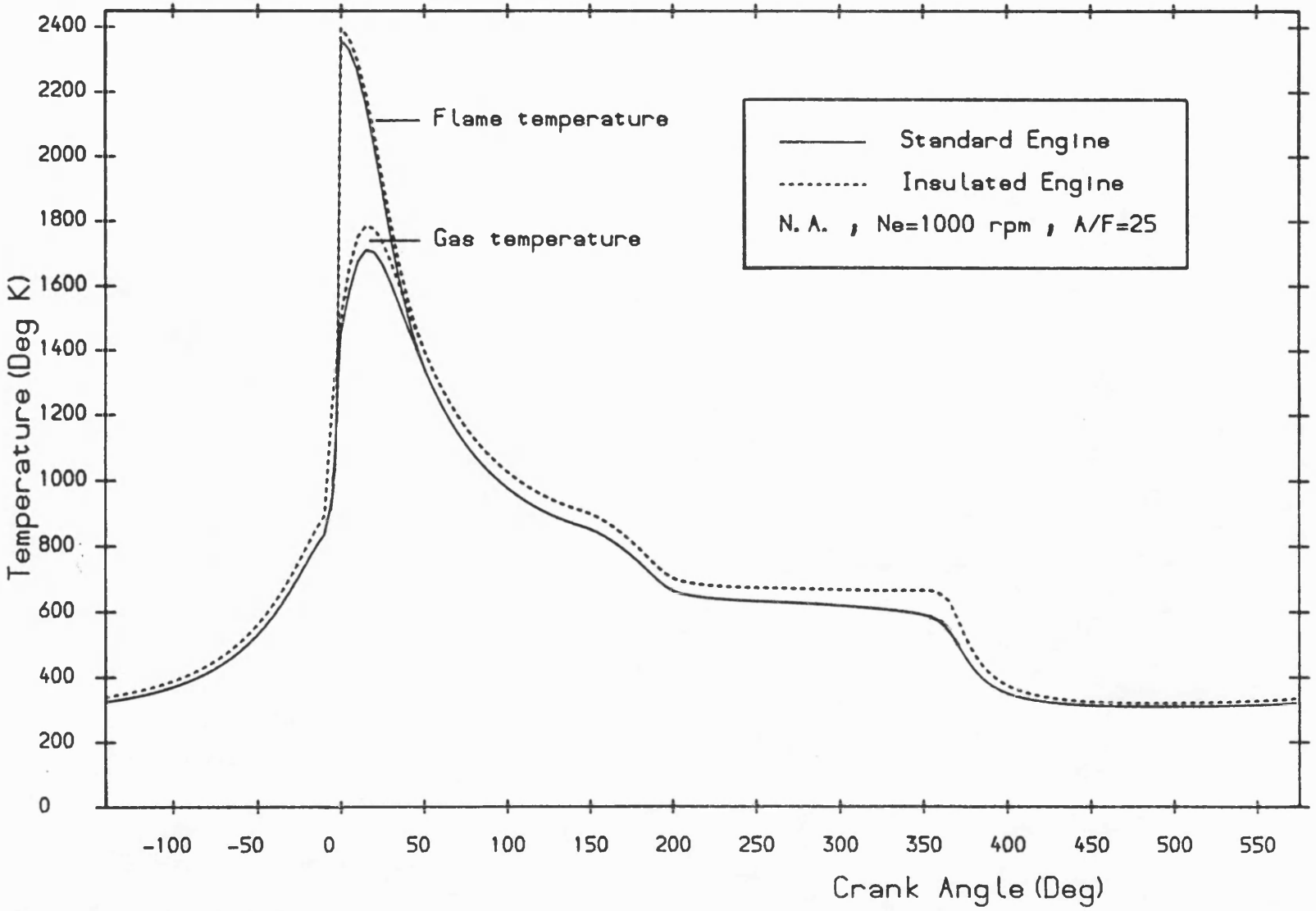

Fig. 7.10 Cylinder gas and flame temperatures versus crank angle for standard and insulated engines.

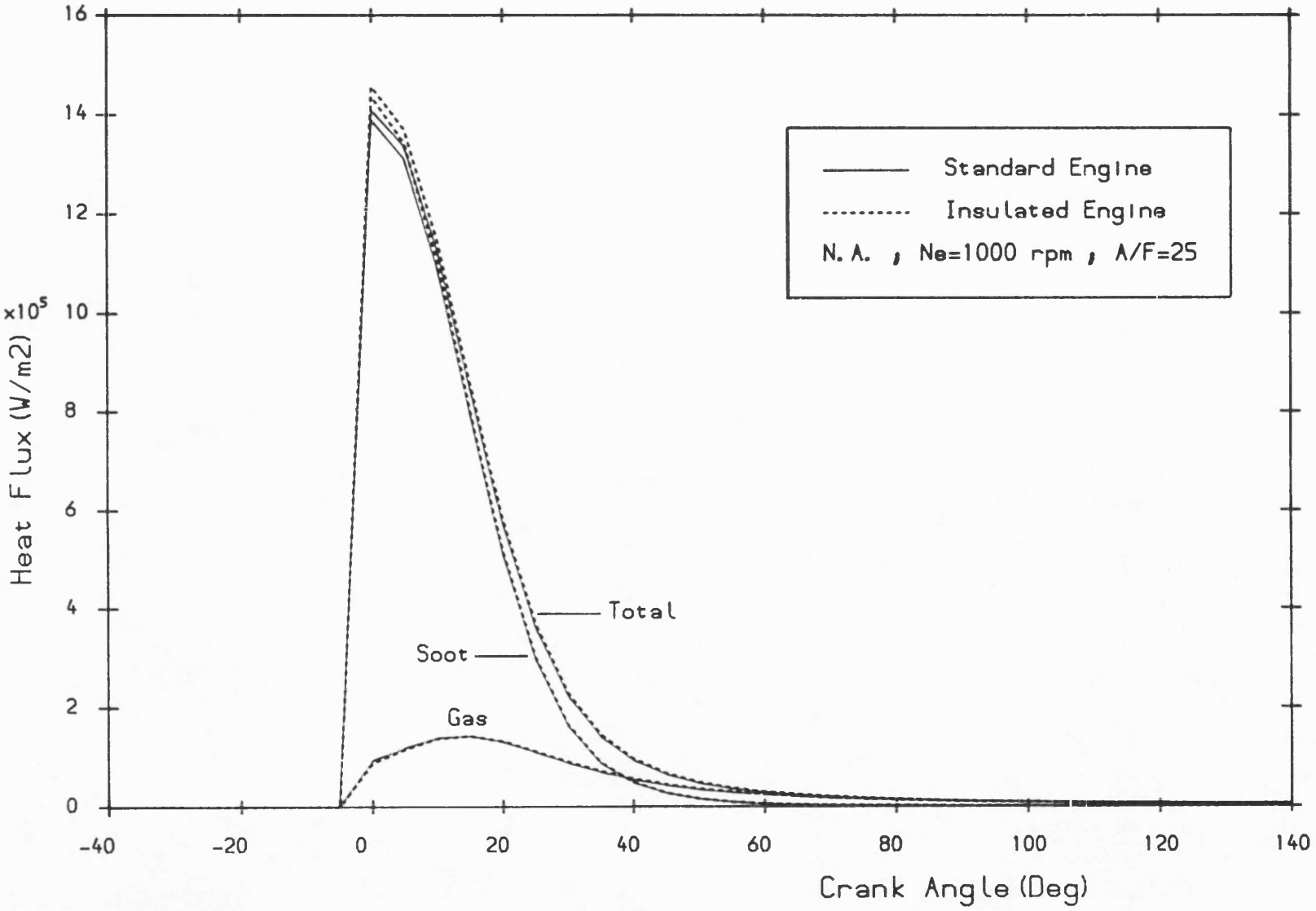

Fig. 7.11 Soot, gas and total radiative heat fluxes at piston surface versus crank angle for standard and insulated engines.

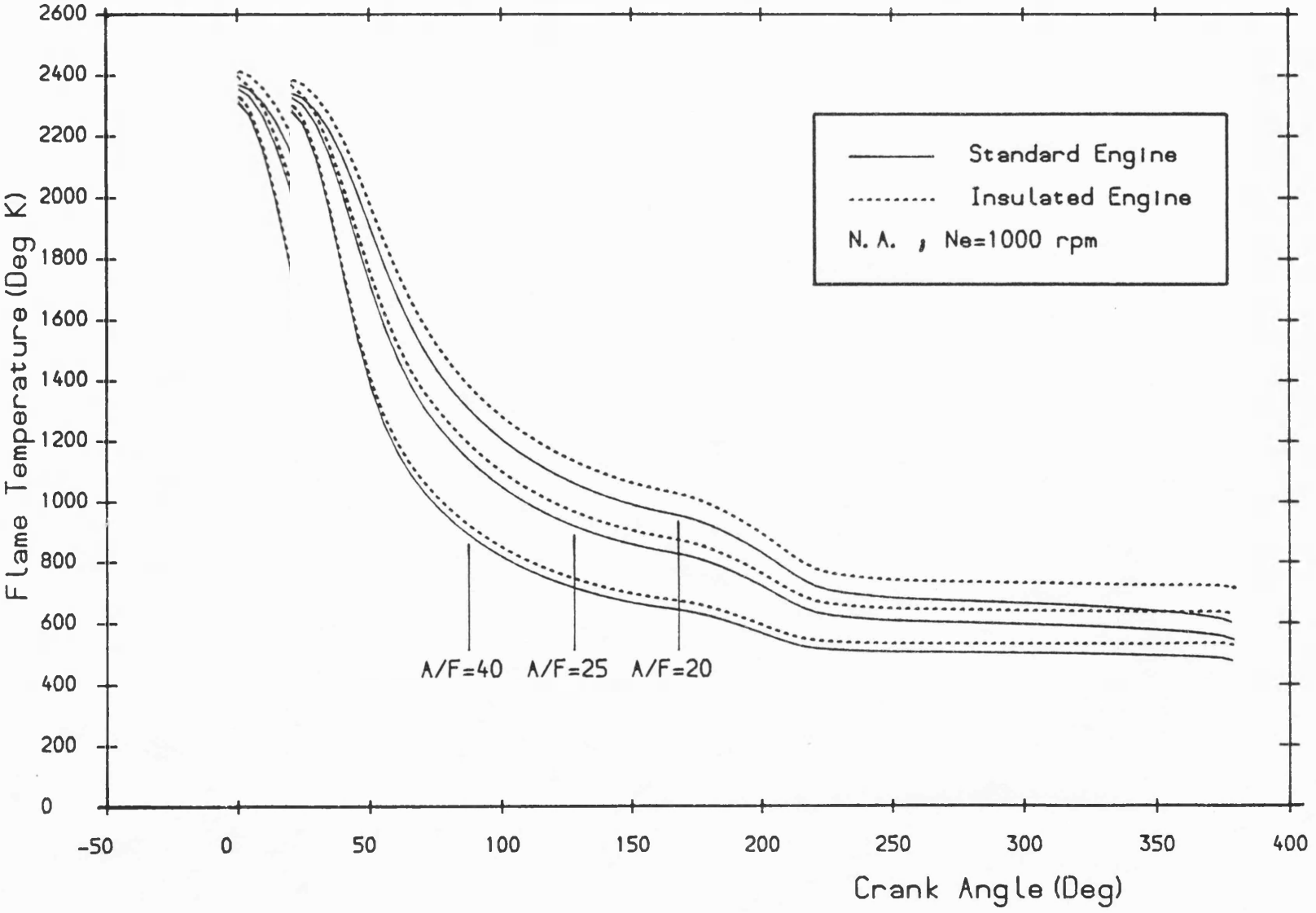

Fig. 7. 12 Flame temperature versus crank angle at various air-fuel ratios for standard and insulated engines.

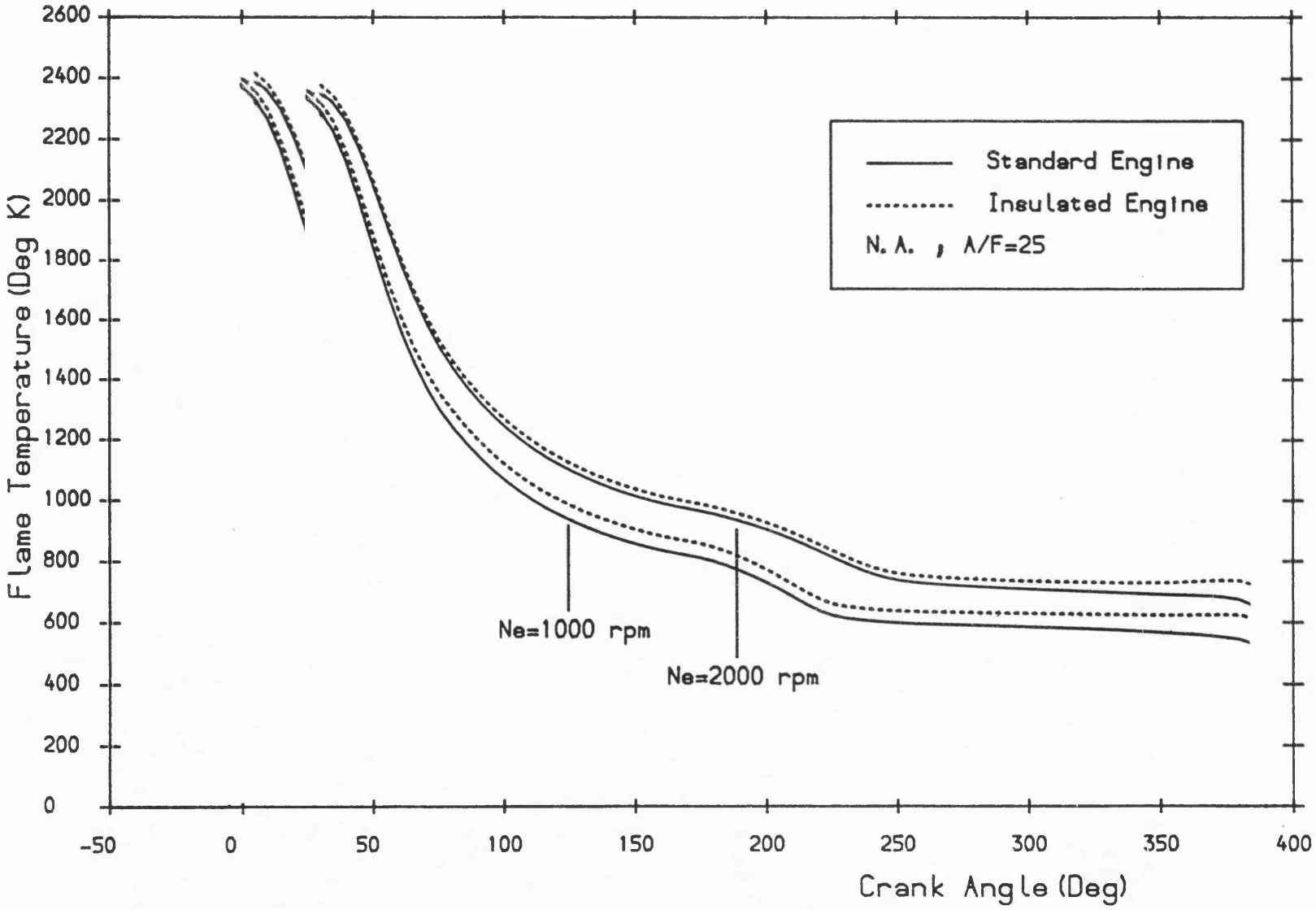

Fig. 7.13 Flame temperature versus crank angle at 2 different engine speeds for standard and insulated engines.

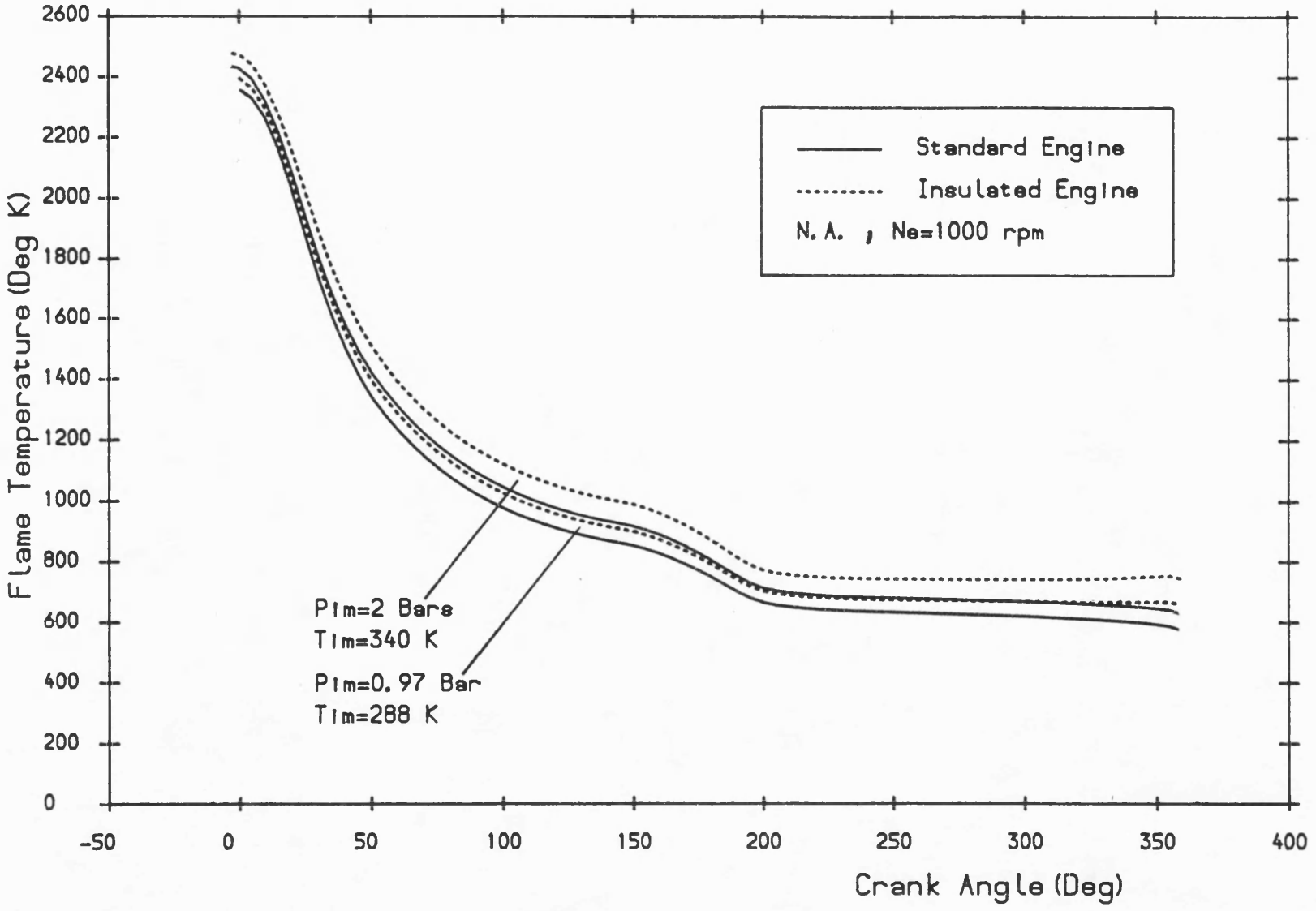

Fig. 7.14 Flame temperature versus crank angle at 2 different inlet manifold conditions for standard and insulated engines.

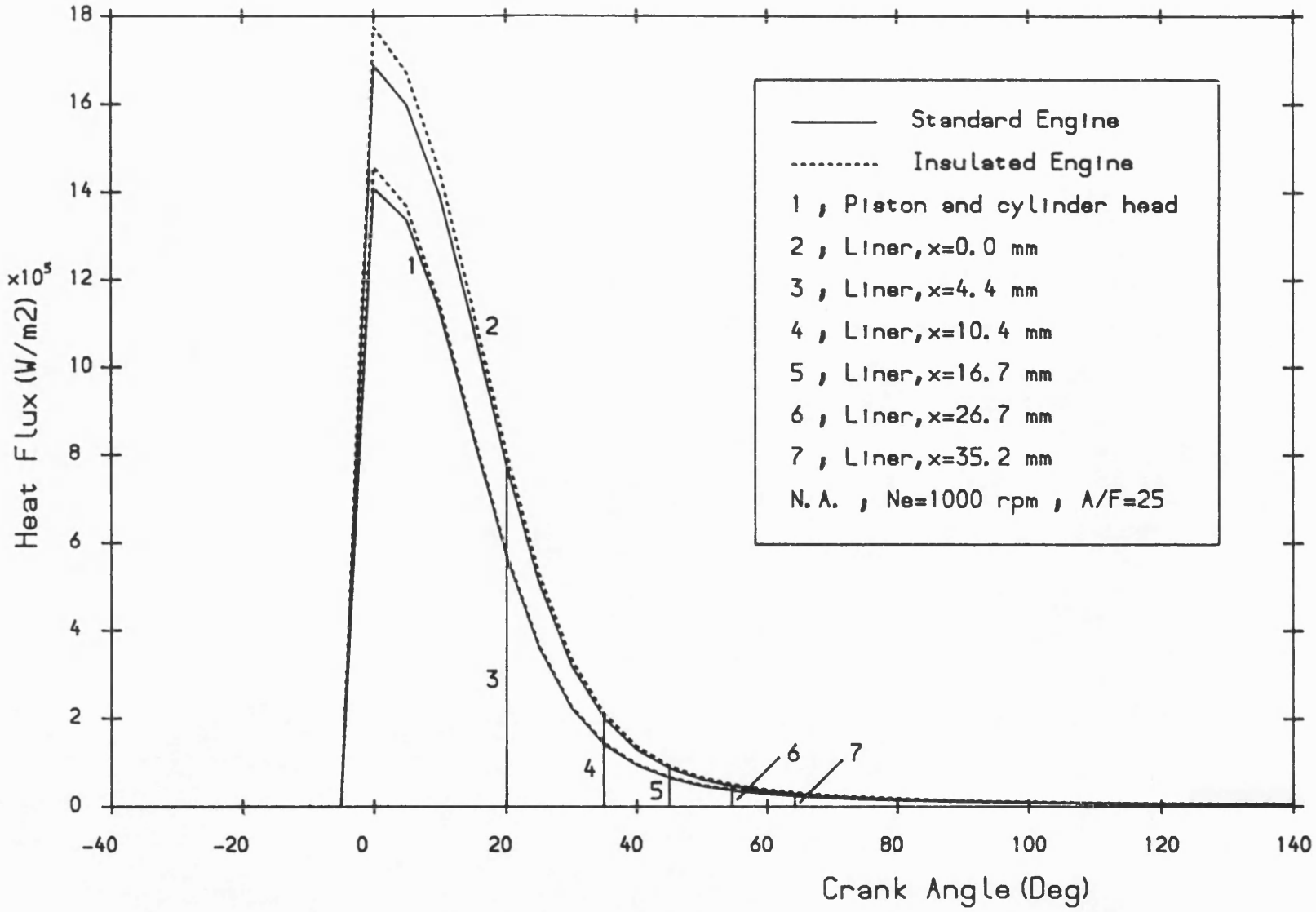

Fig. 7.15 Radiative heat flux versus crank angle at various parts of the combustion chamber.

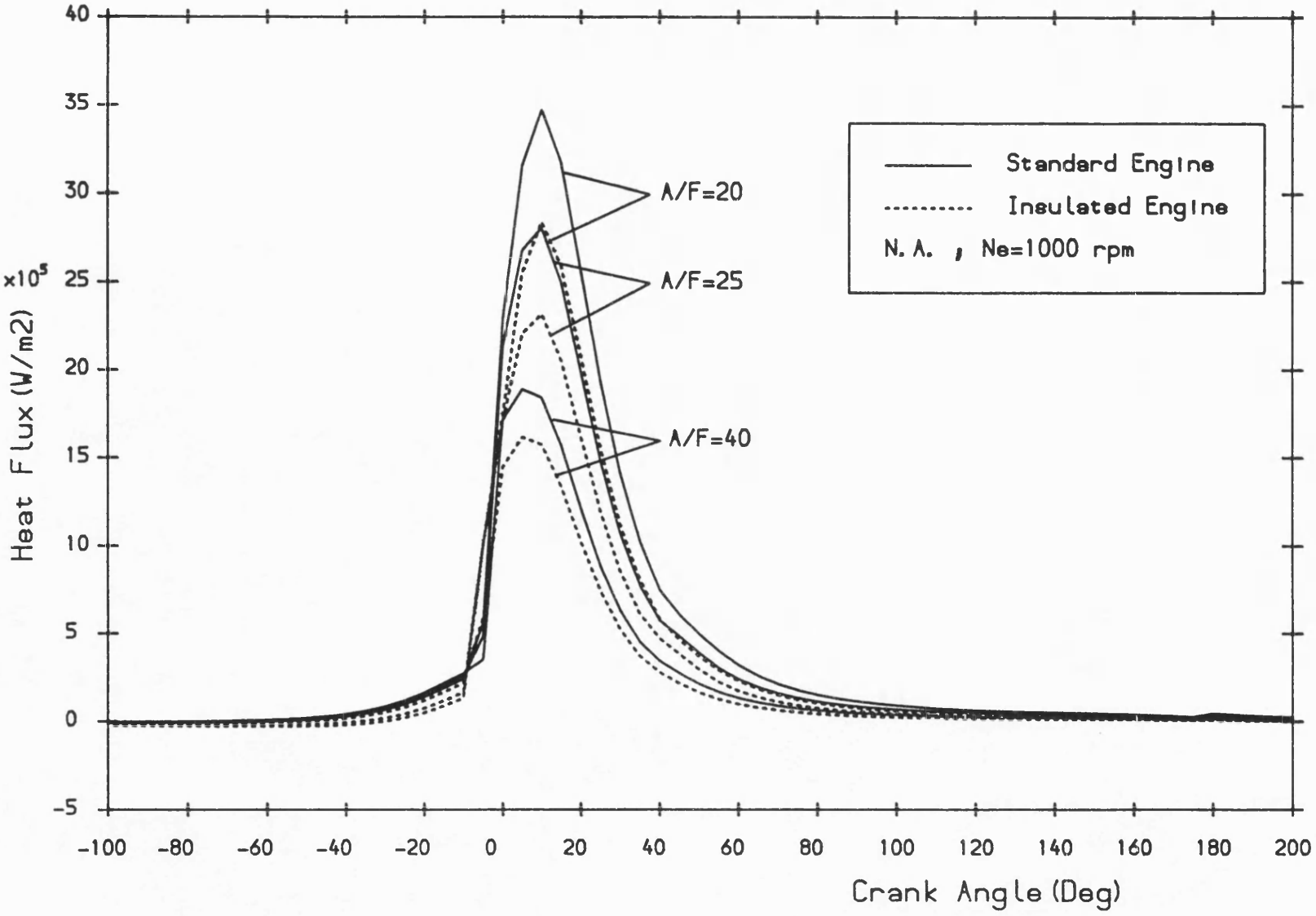

Fig. 7.16 Convective heat flux versus crank angle at various air-fuel ratios for standard and insulated engines.

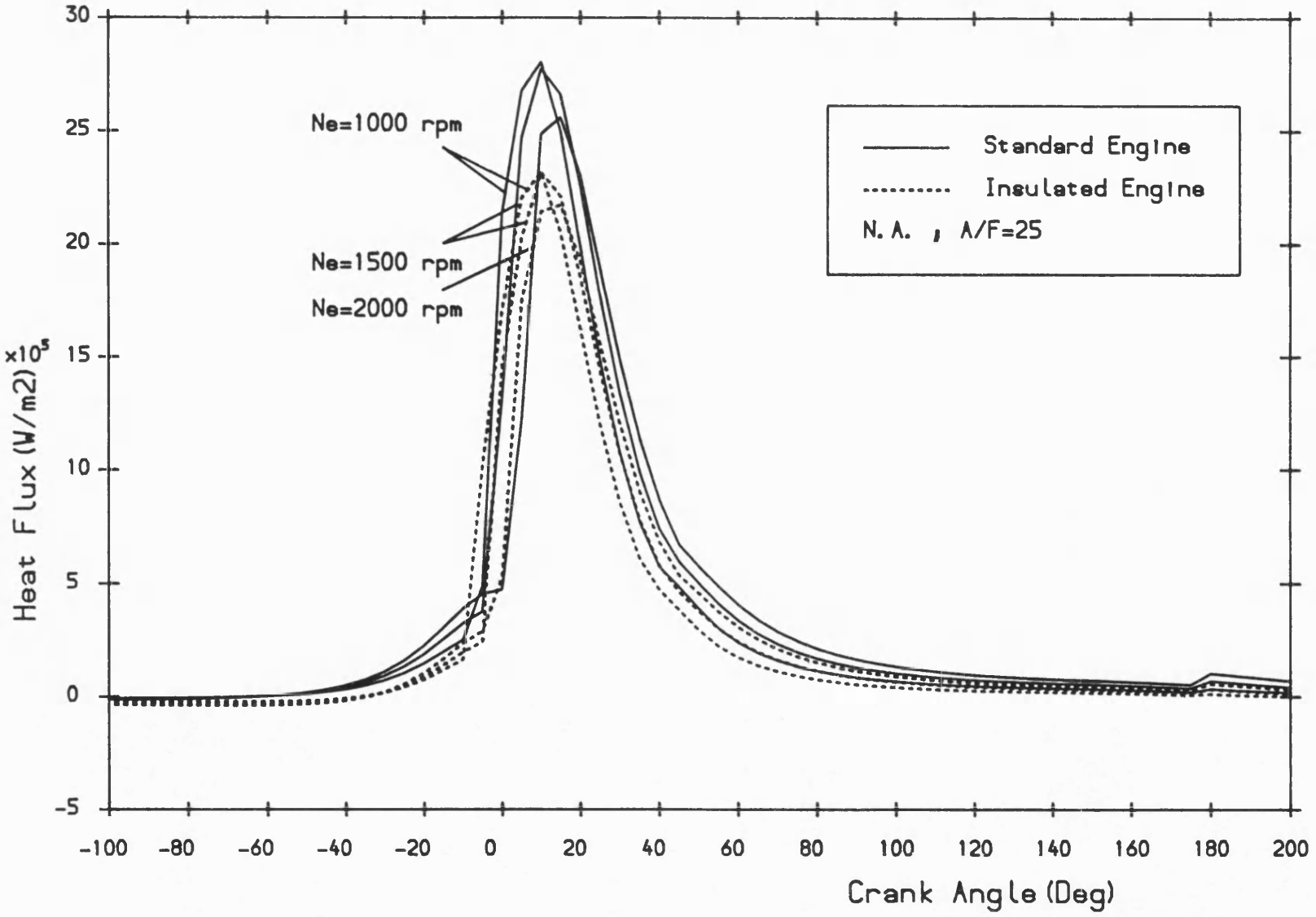

Fig. 7.17 Convective heat flux versus crank angle at various engine speeds for standard and insulated engines.

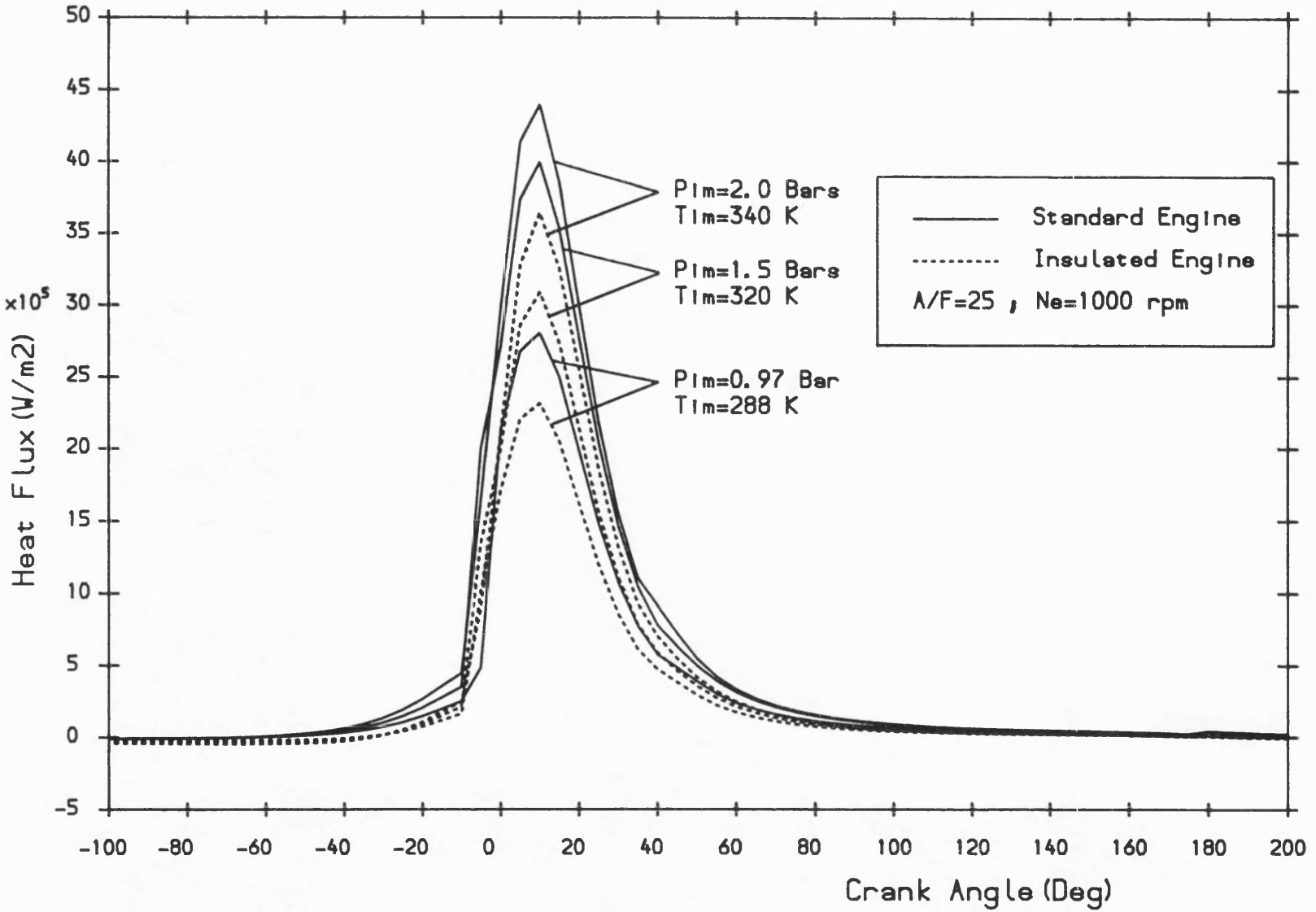

Fig. 7.18 Convective heat flux versus crank angle at various boost conditions for standard and insulated engines.

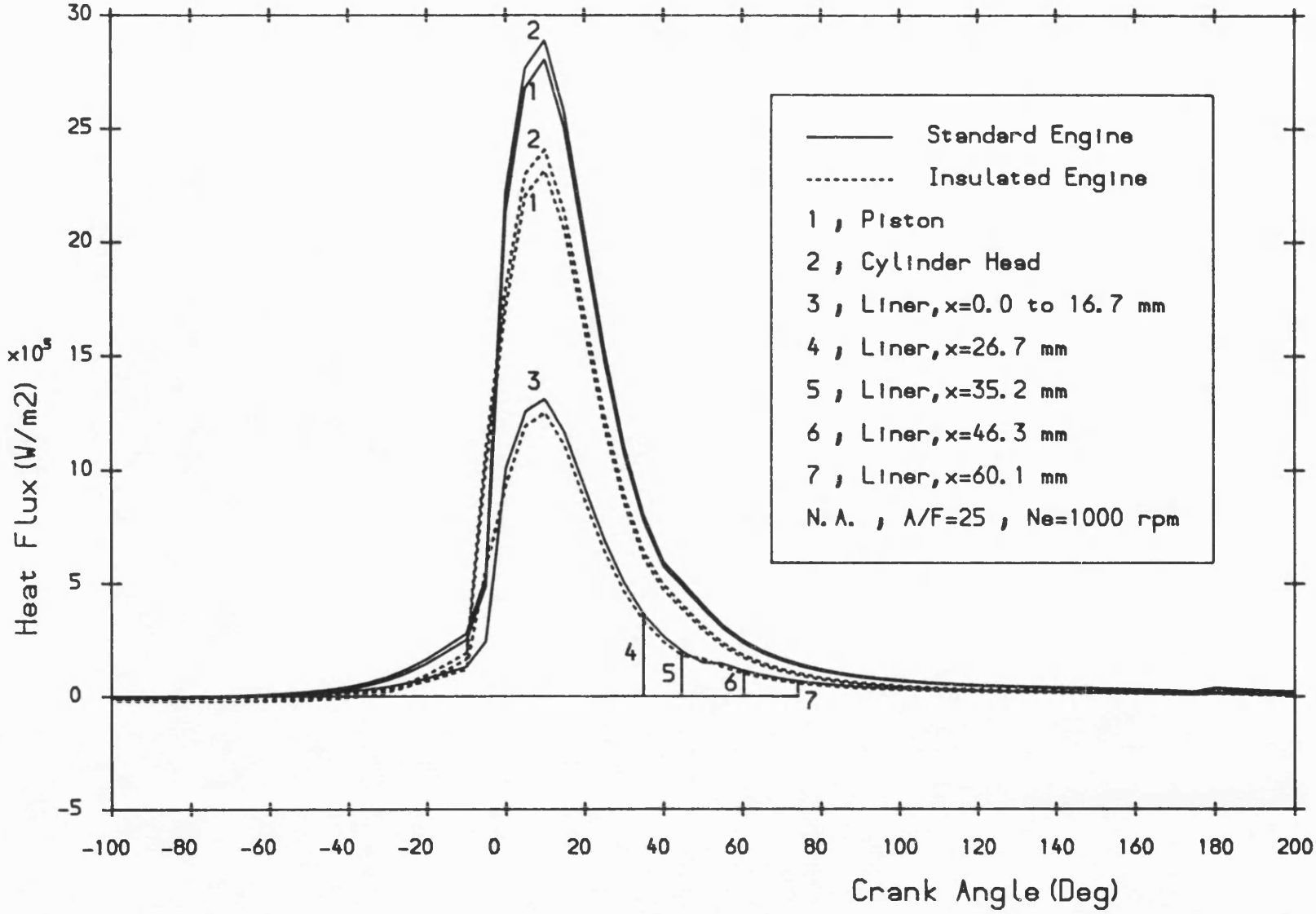

Fig. 7.19 Convective heat flux versus crank angle at various parts of the combustion chamber for standard and insulated engines.

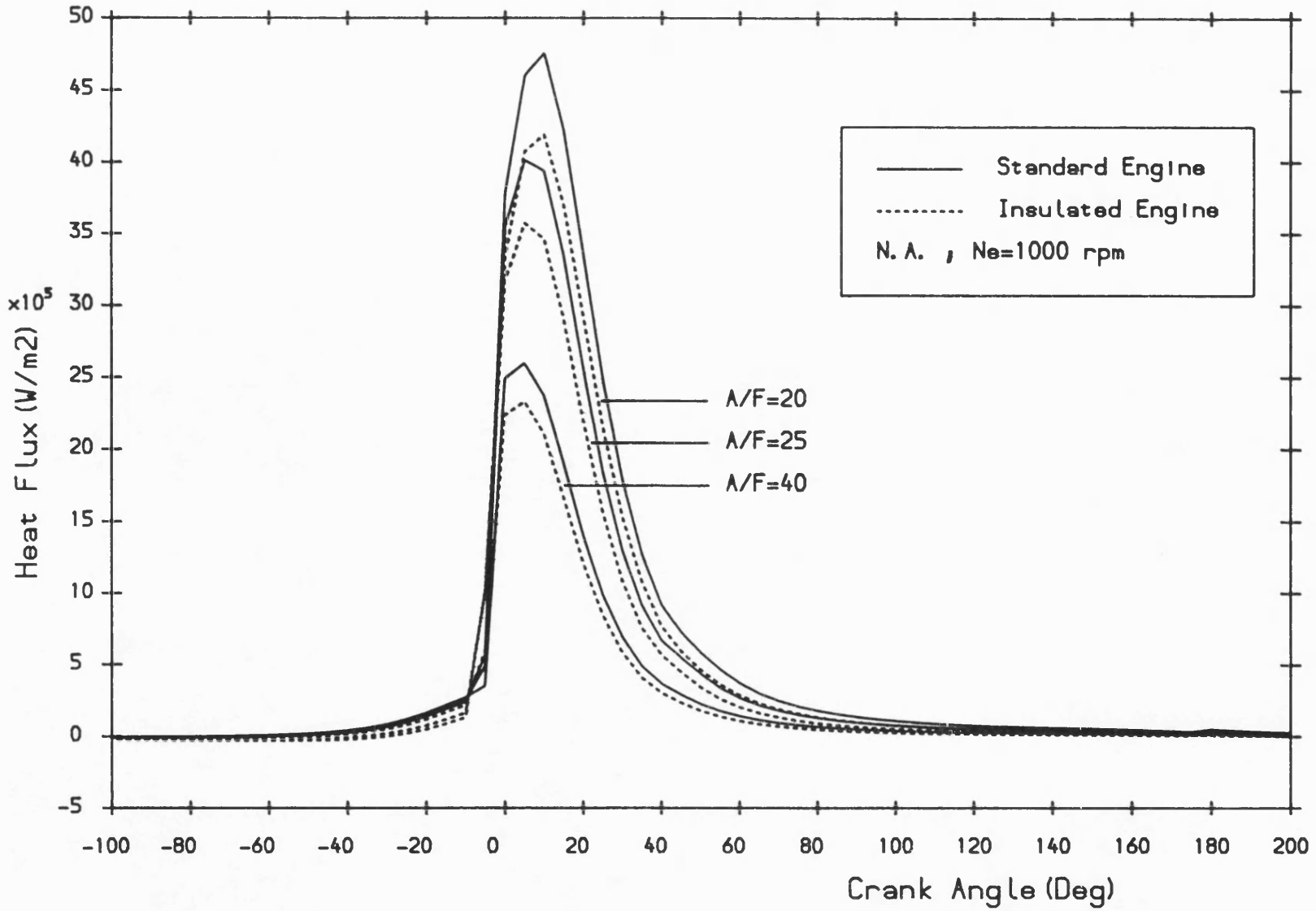

Fig. 7.20 Total gas heat flux versus crank angle at various air-fuel ratios for standard and insulated engines.

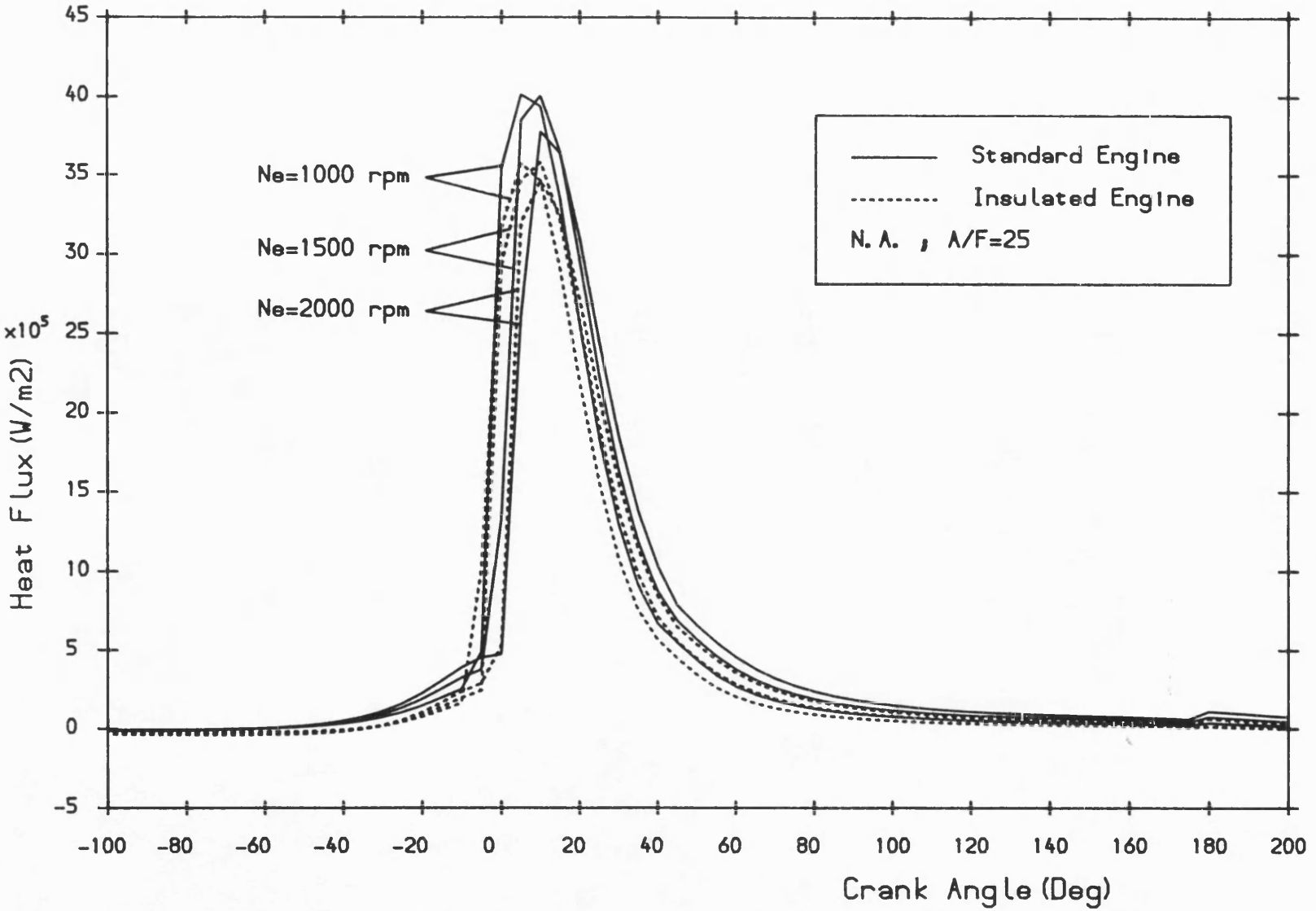

Fig. 7.21 Total gas heat flux versus crank angle at various engine speeds for standard and insulated engines.

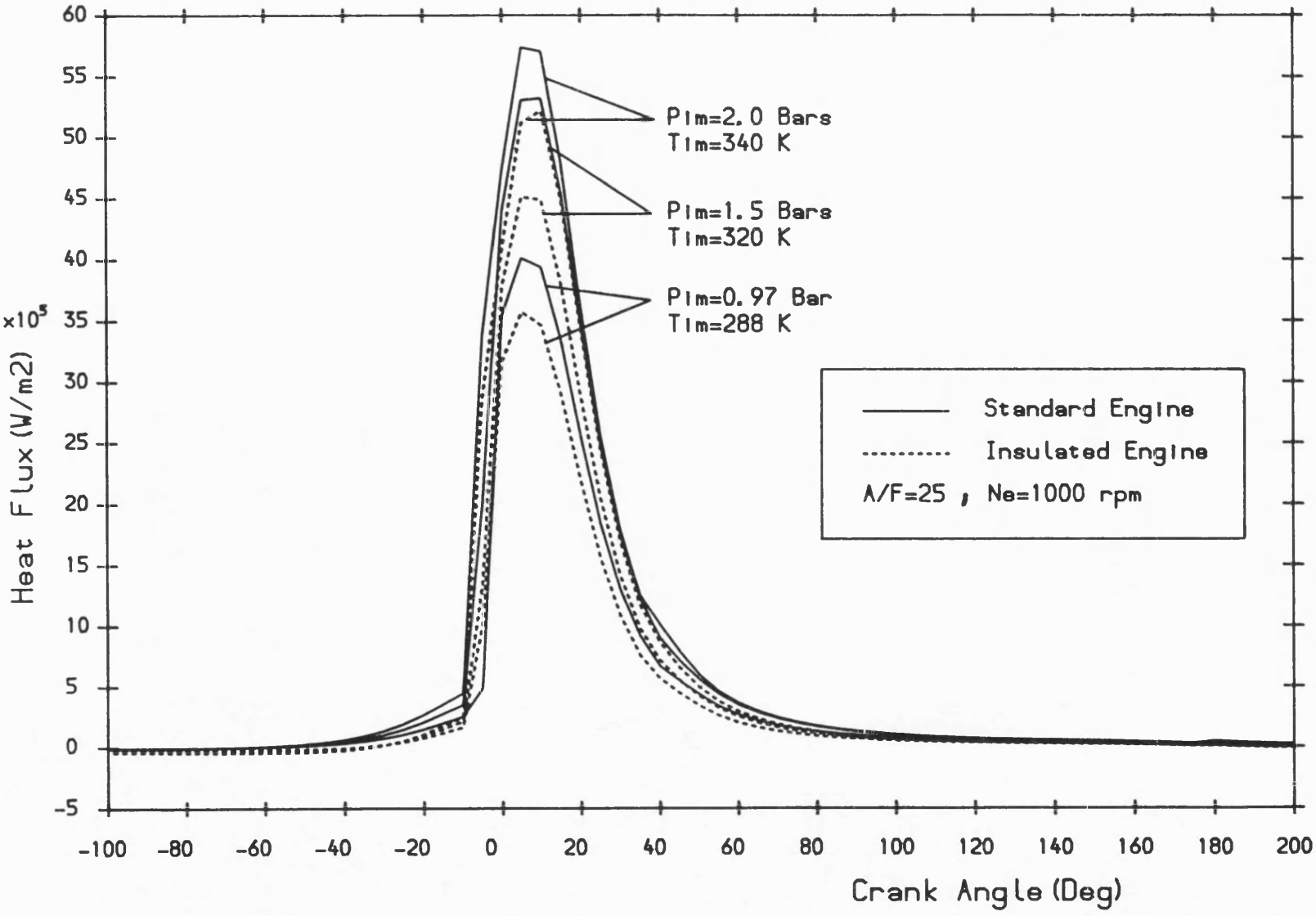

Fig. 7.22 Total gas heat flux versus crank angle at various boost conditions for standard and insulated engines.

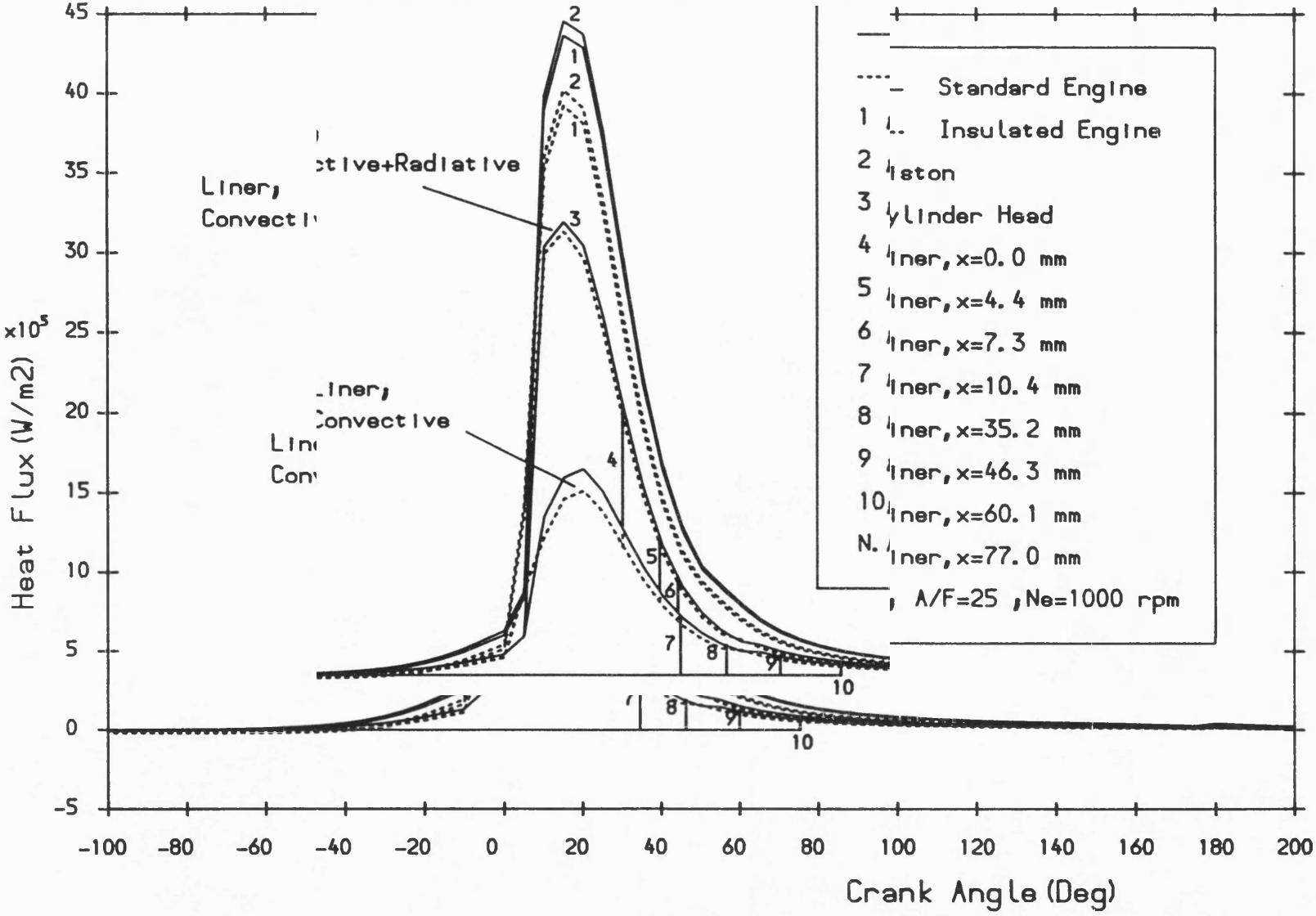

Fig. 7.23 Total gas heat flux versus crank angle at various parts of the combustion chamber for standard and insulated engines.

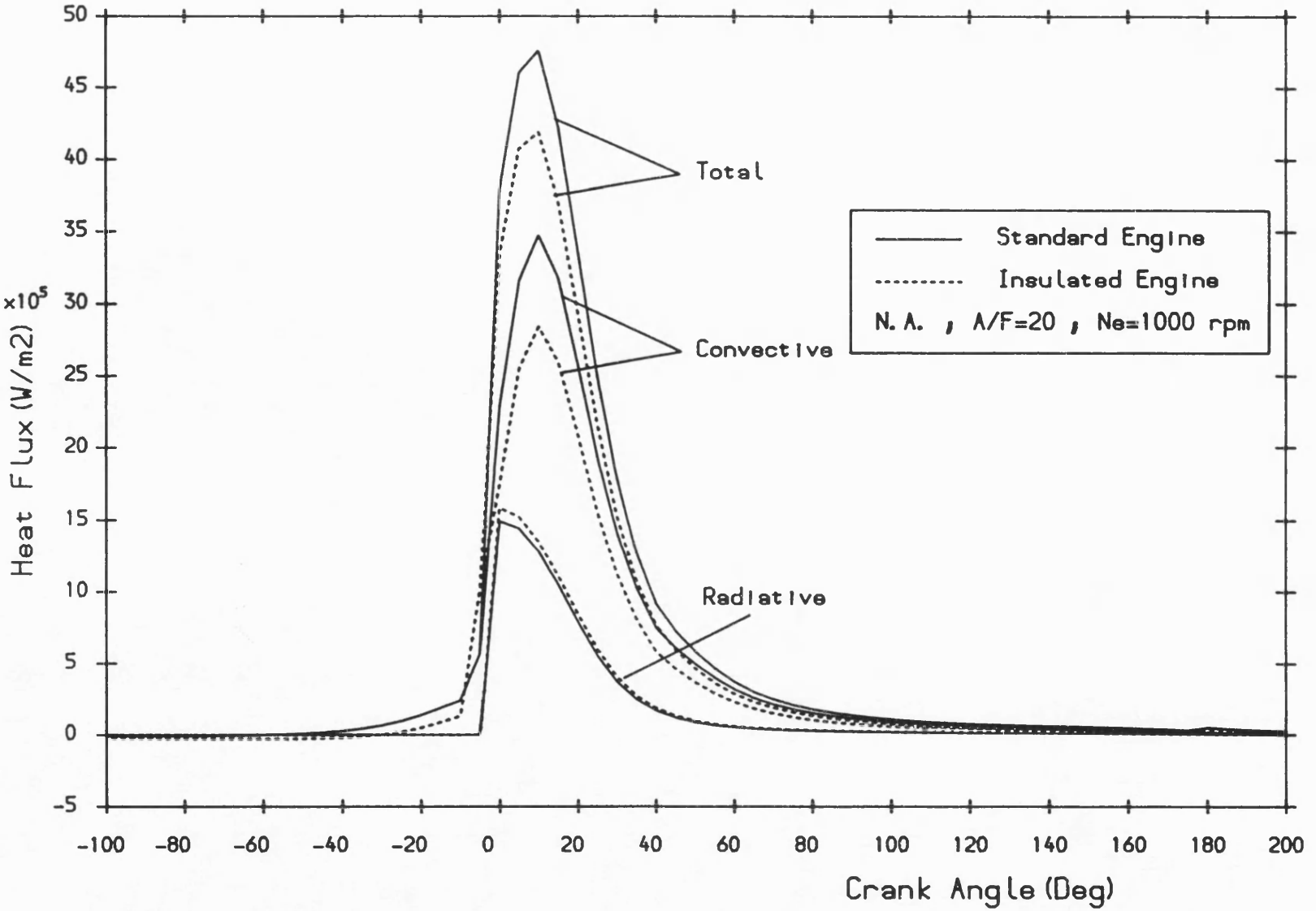

Fig. 7.24 Radiative, convective and total heat flux versus crank angle for standard and insulated engines.

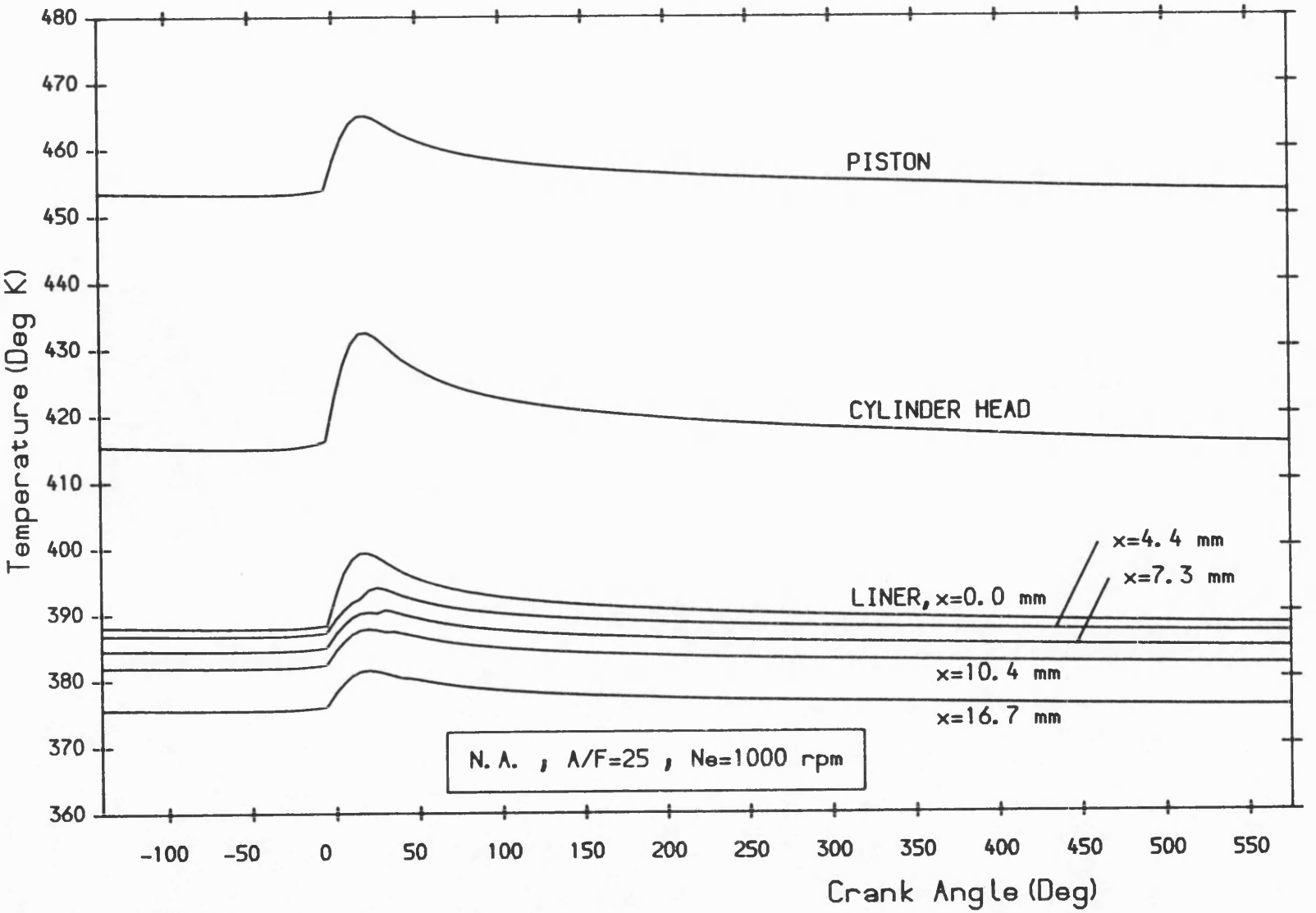

Fig. 7.25 Surface temperature versus crank angle at various parts of the metallic combustion chamber.

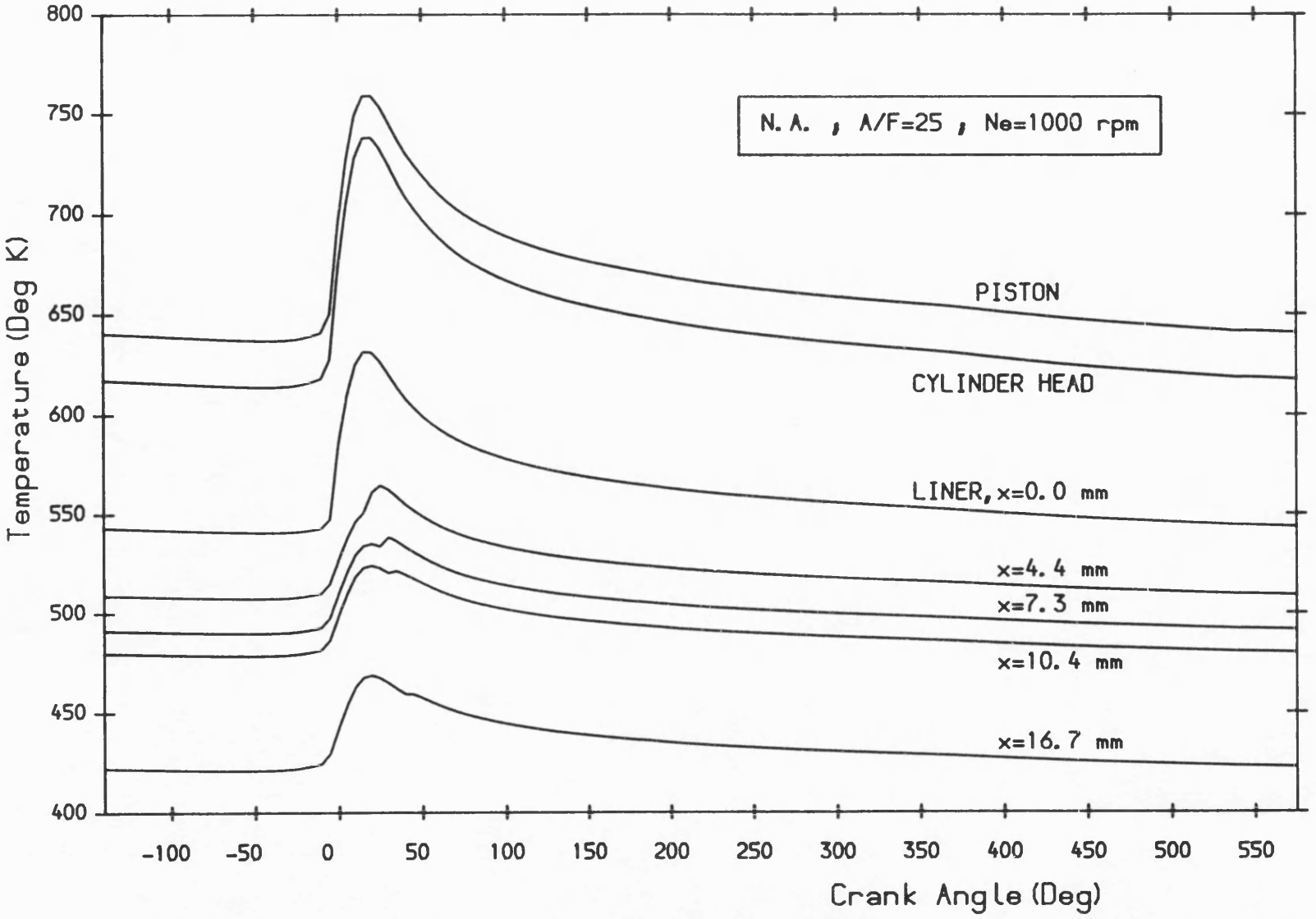

Fig. 7.26 Surface temperature versus crank angle at various parts of the 1.5 mm PSZ coated combustion chamber.

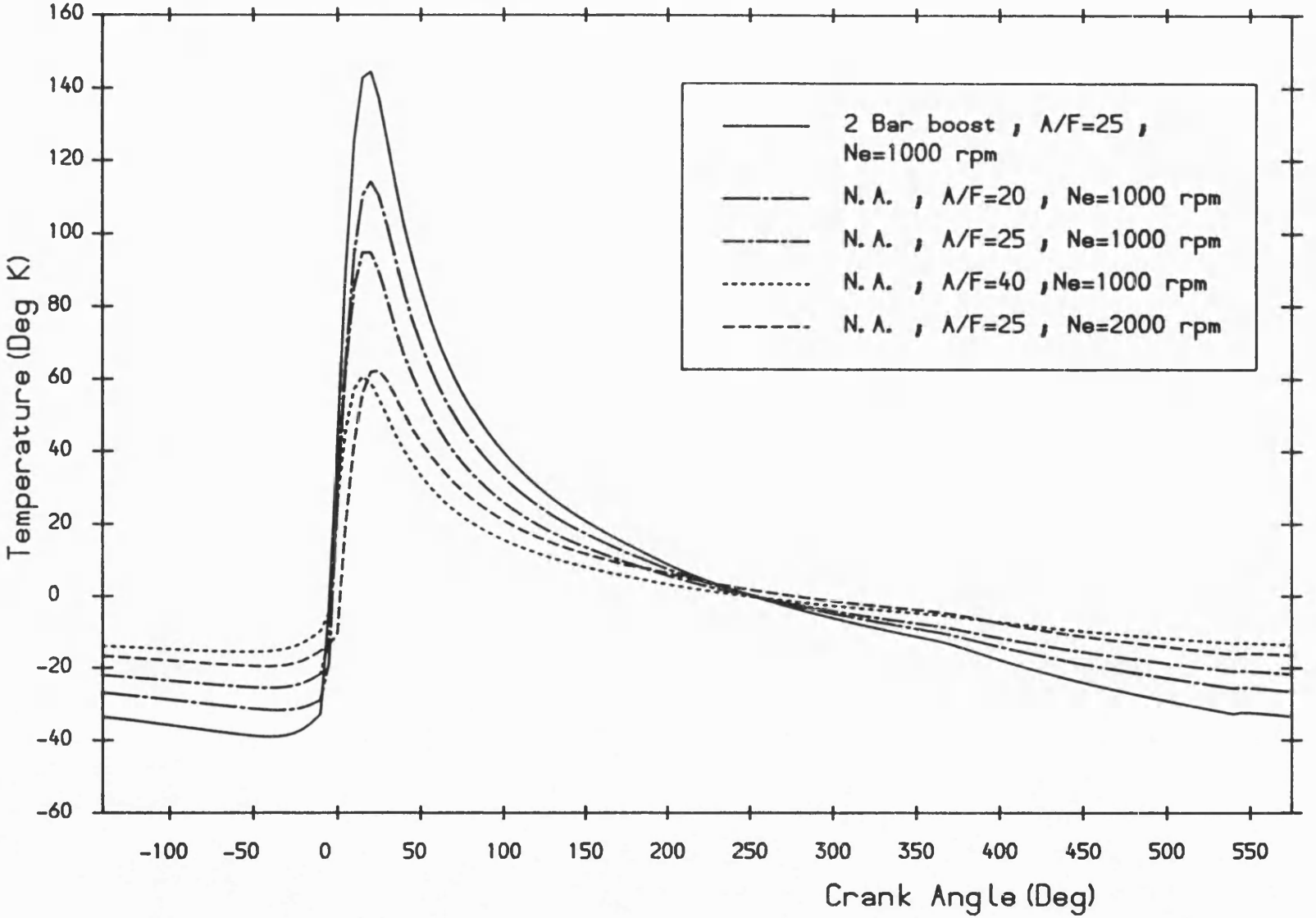

Fig. 7.27 The effect of engine operating condition on piston surface temperature fluctuation of insulated engine.

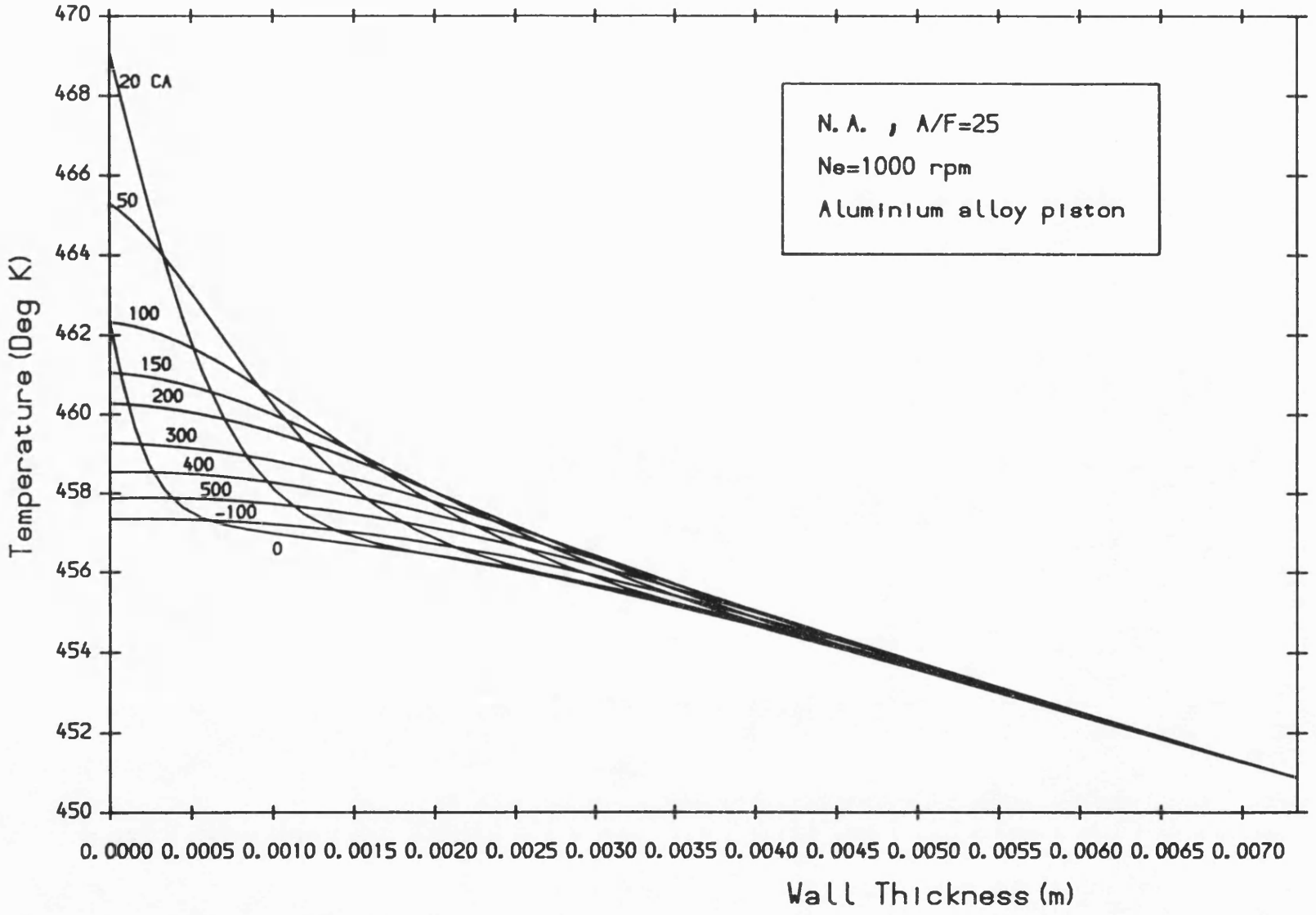

Fig. 7. 28 Propagation of temperature wave through the aluminium alloy piston.

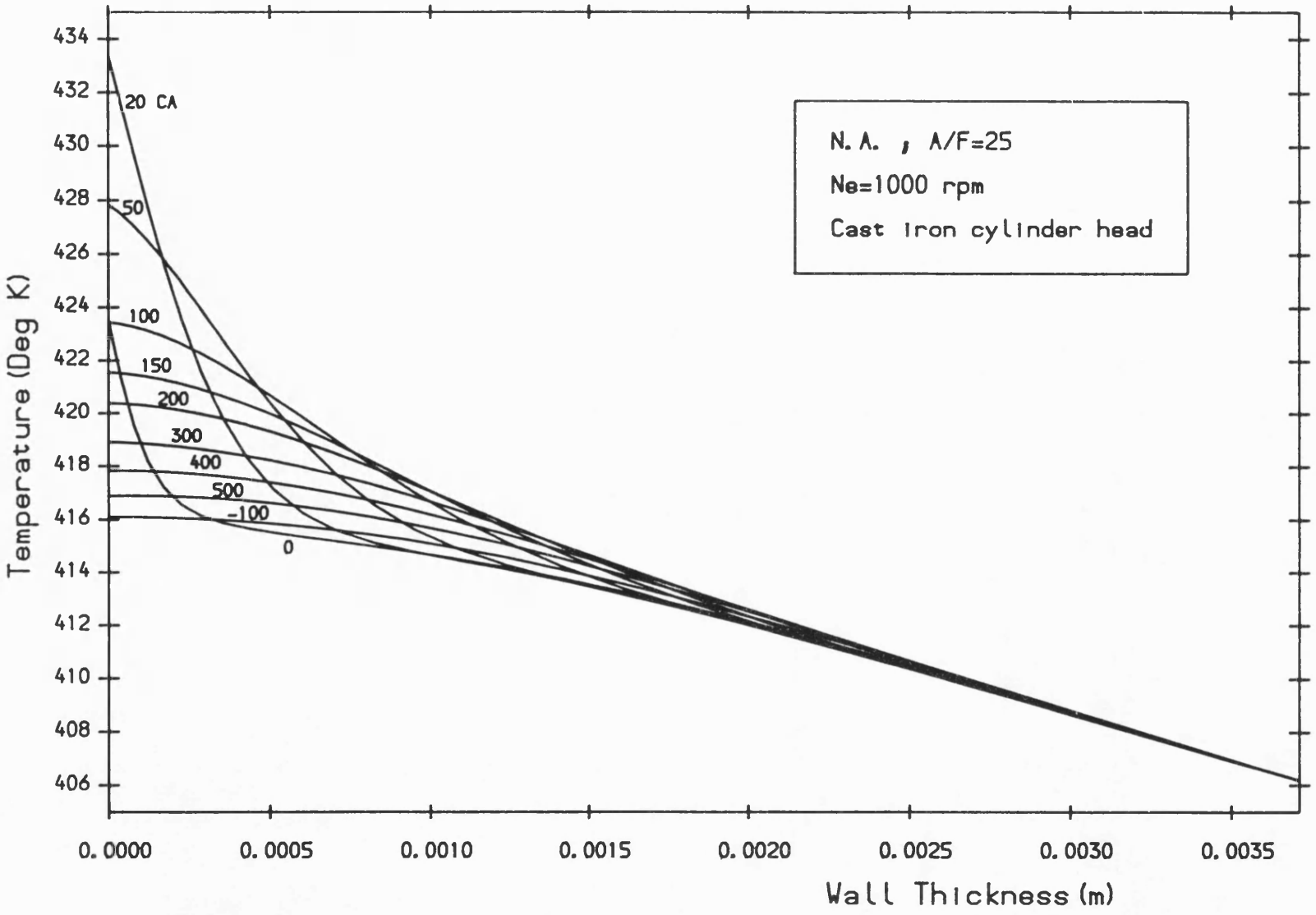

Fig. 7. 29 Propagation of temperature wave through the cast iron cylinder head.

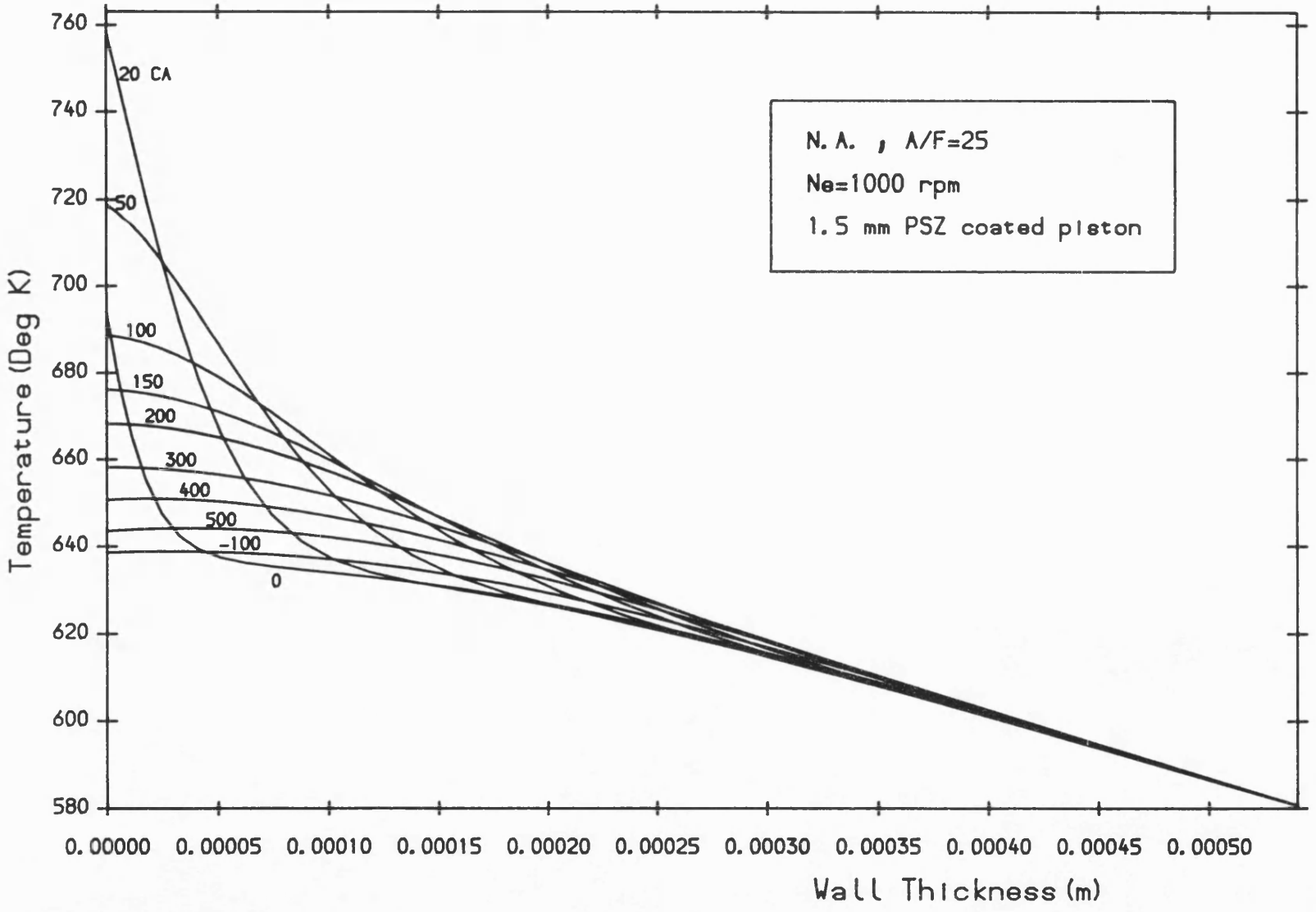

Fig. 7.30 Propagation of temperature wave through the PSZ coating at piston surface.

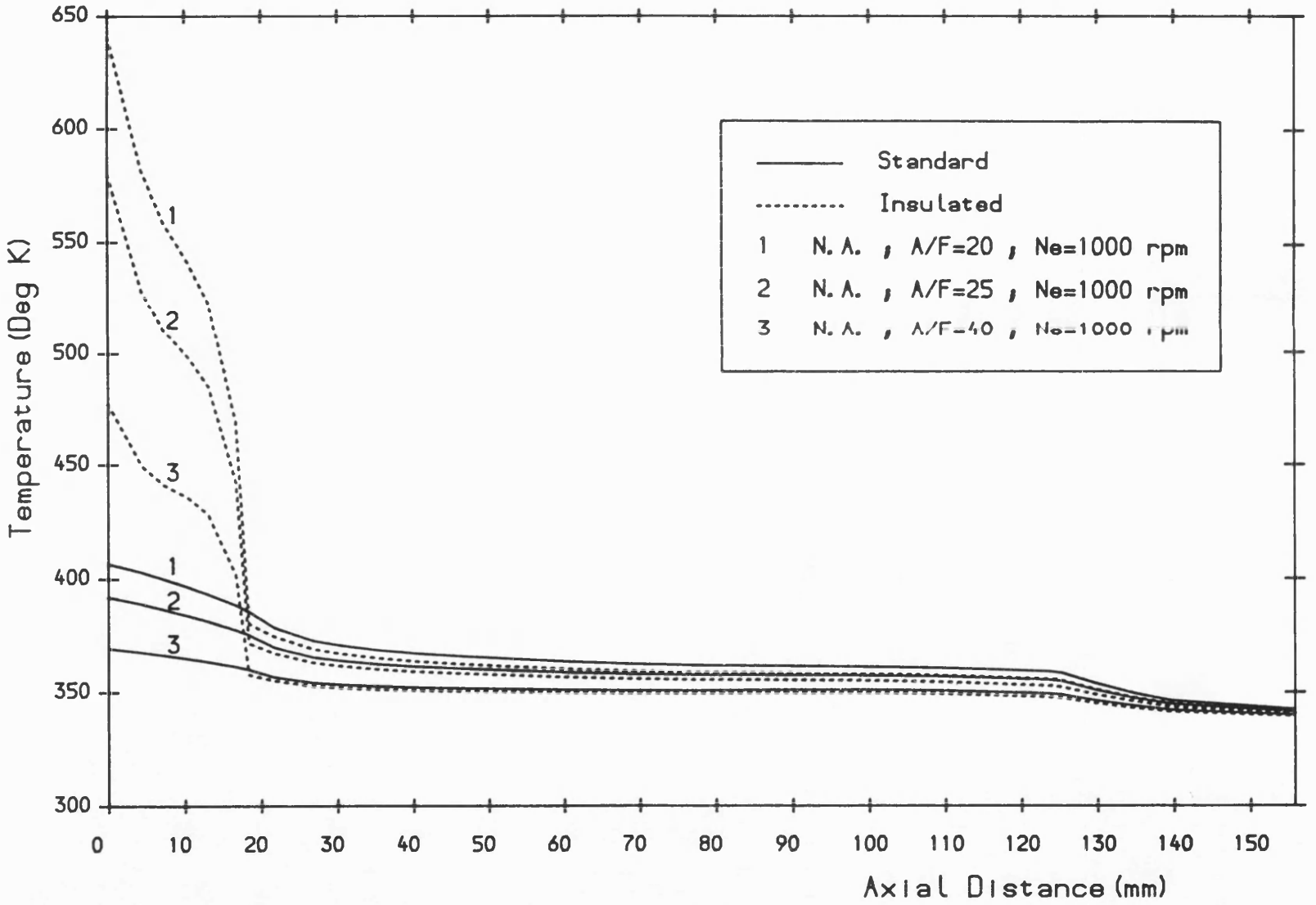

Fig. 7.31 Liner mean cycle surface temperature versus axial distance at various air-fuel ratios for standard and insulated engines.

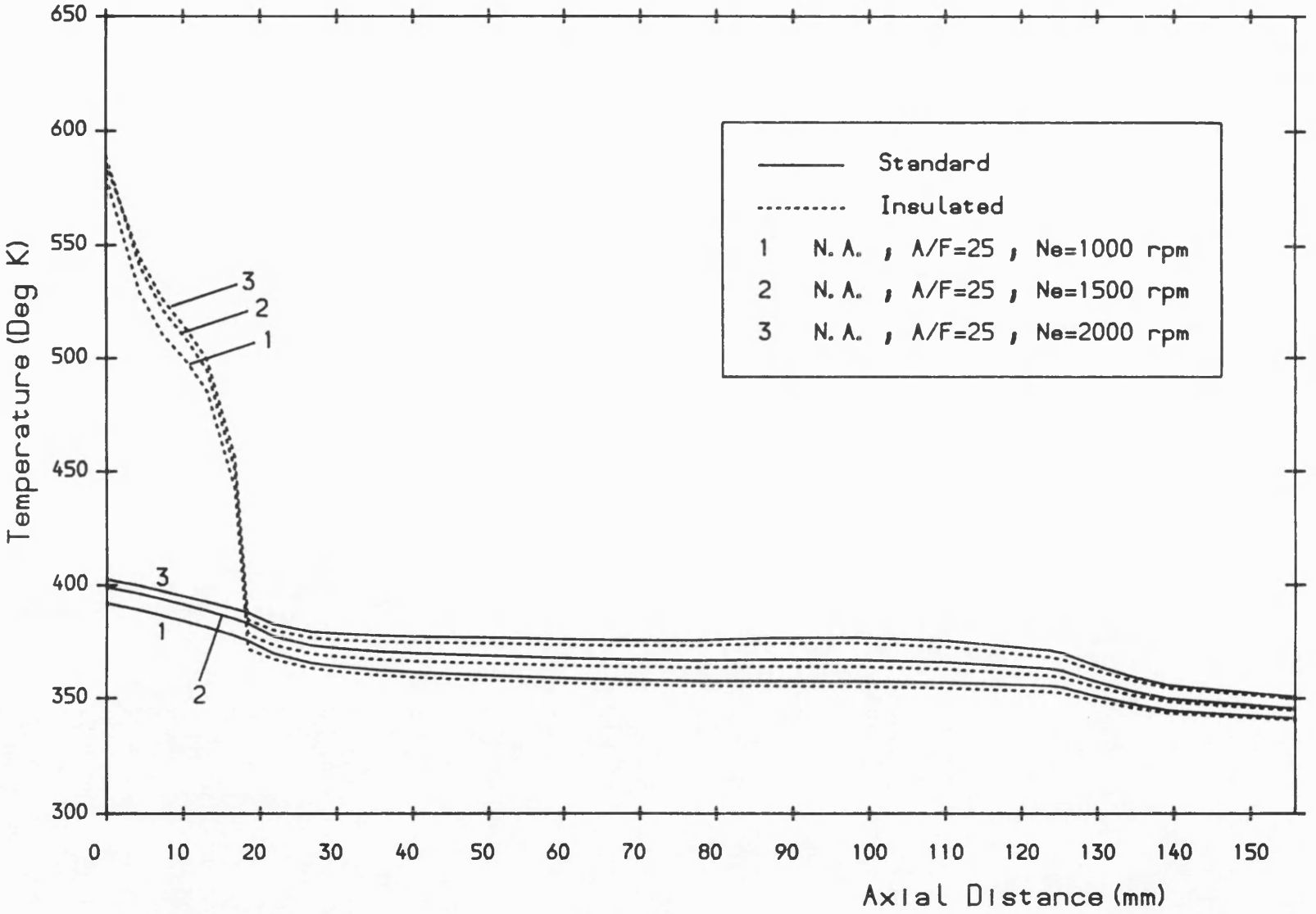

Fig. 7.32 Liner mean cycle surface temperature versus axial distance at various engine speeds for standard and insulated engines.

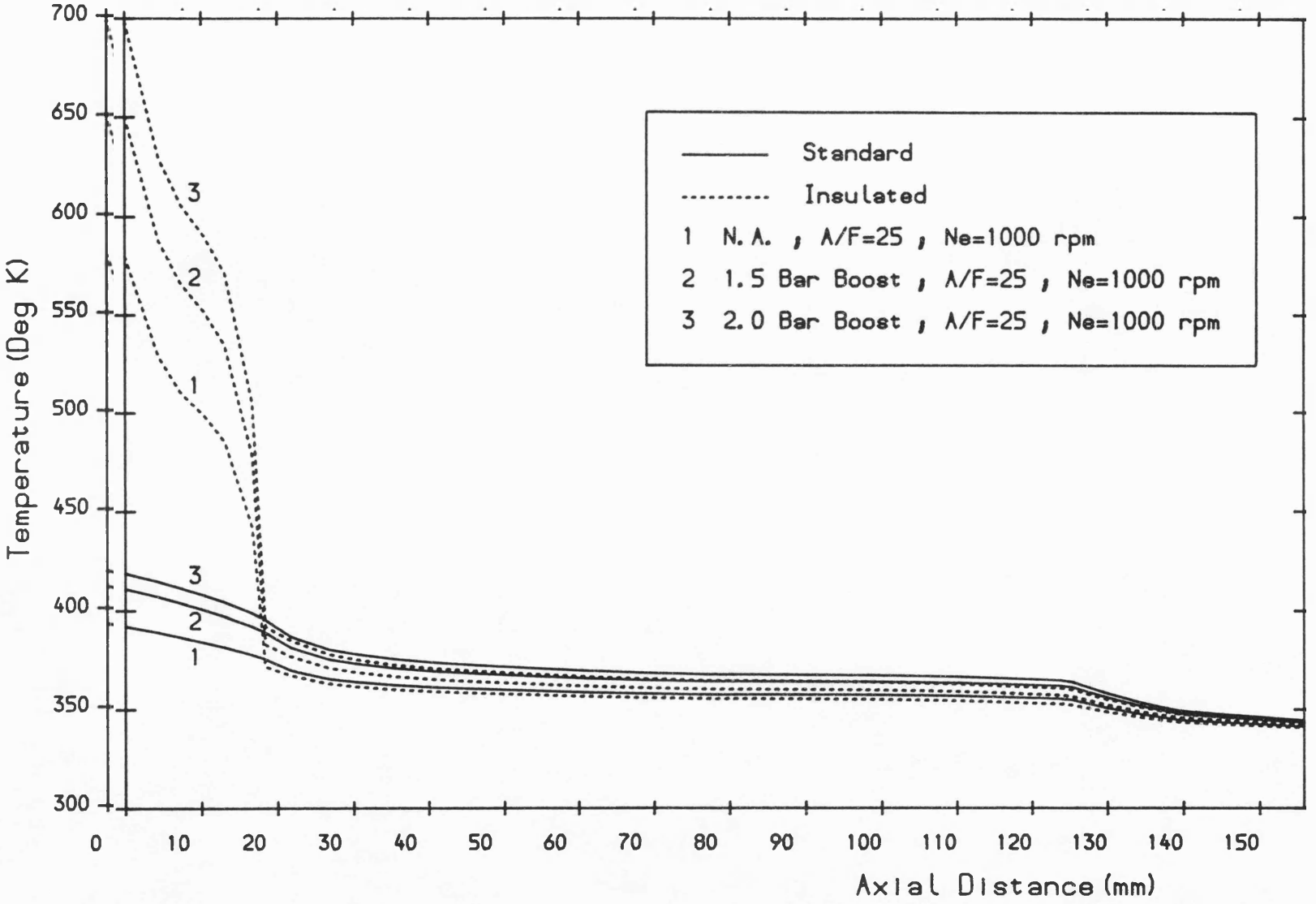

Fig. 7.33 Liner mean cycle surface temperature versus axial distance at various boost conditions for standard and insulated engines.

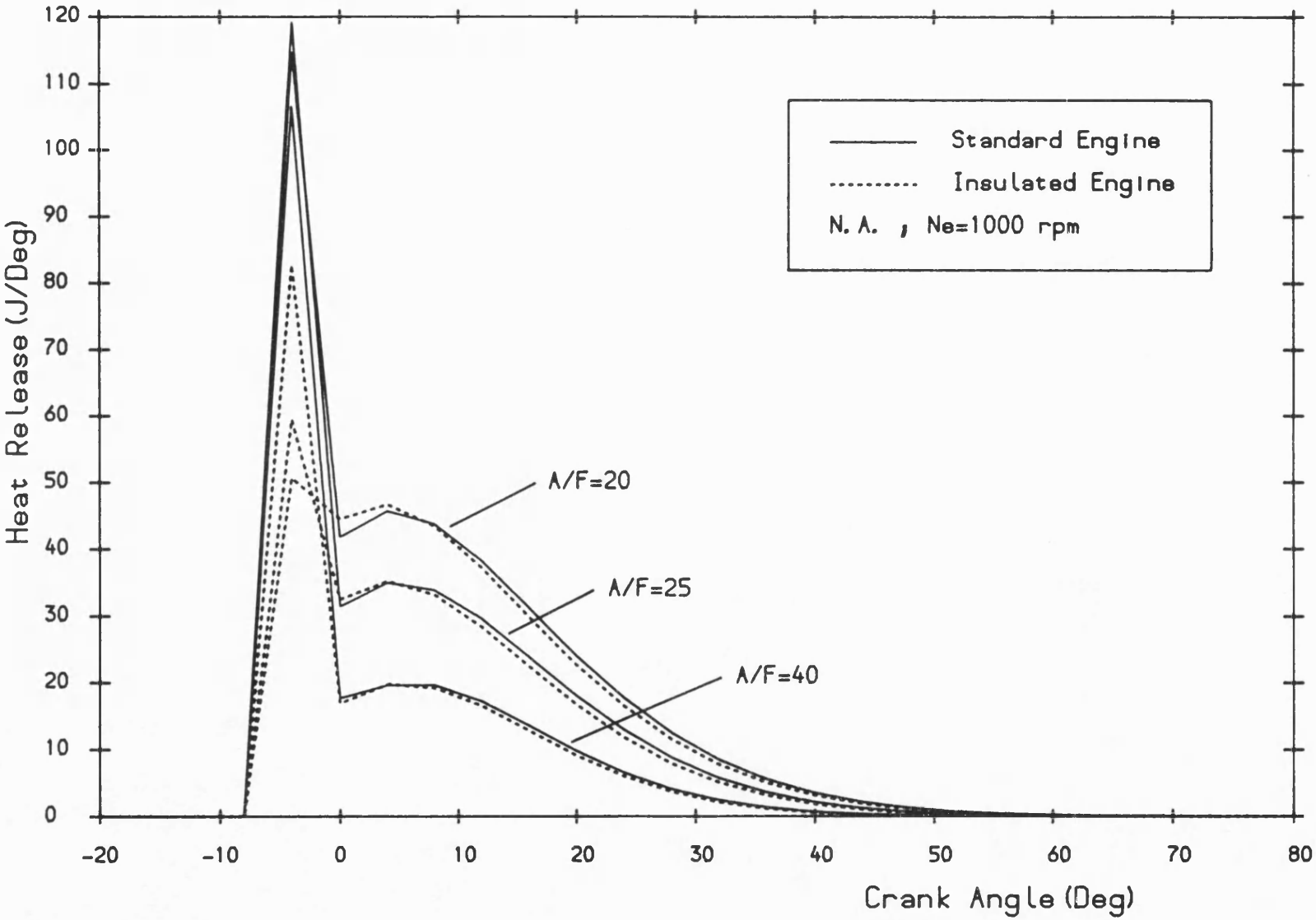

Fig. 7.34 Heat release curves at various air-fuel ratios for standard and insulated engines.

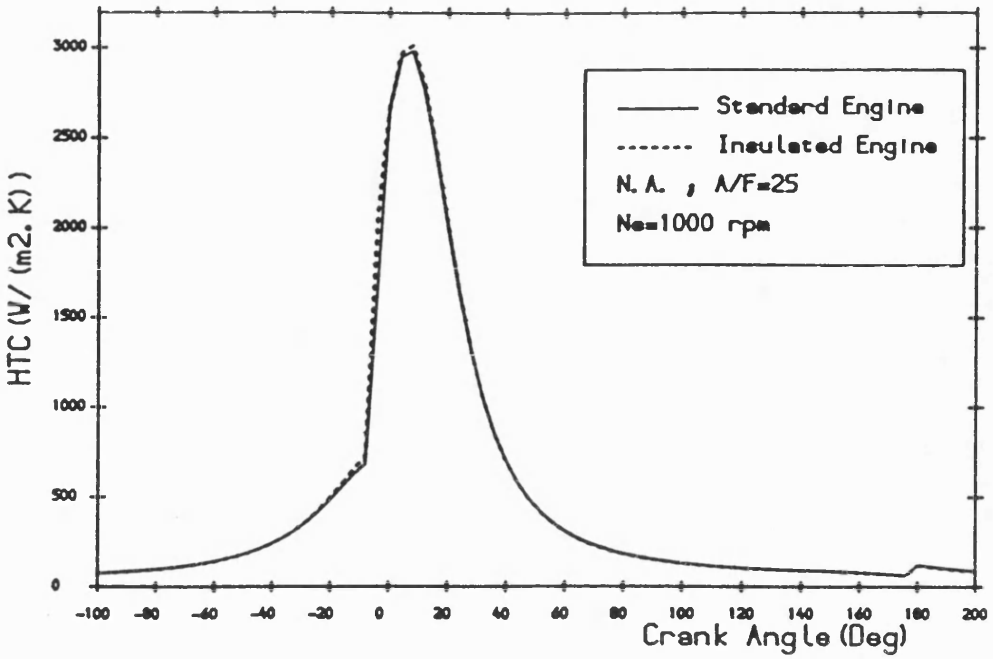

Fig. 7. 35 The effect of engine insulation on gas htc.

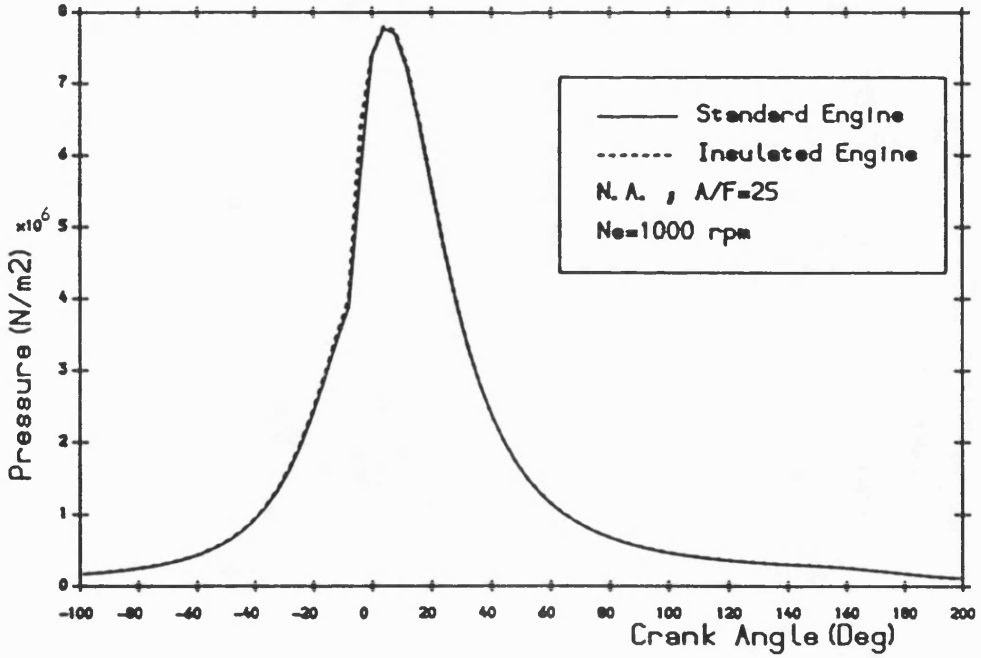

Fig. 7. 36 The effect of engine insulation on cylinder pressure.

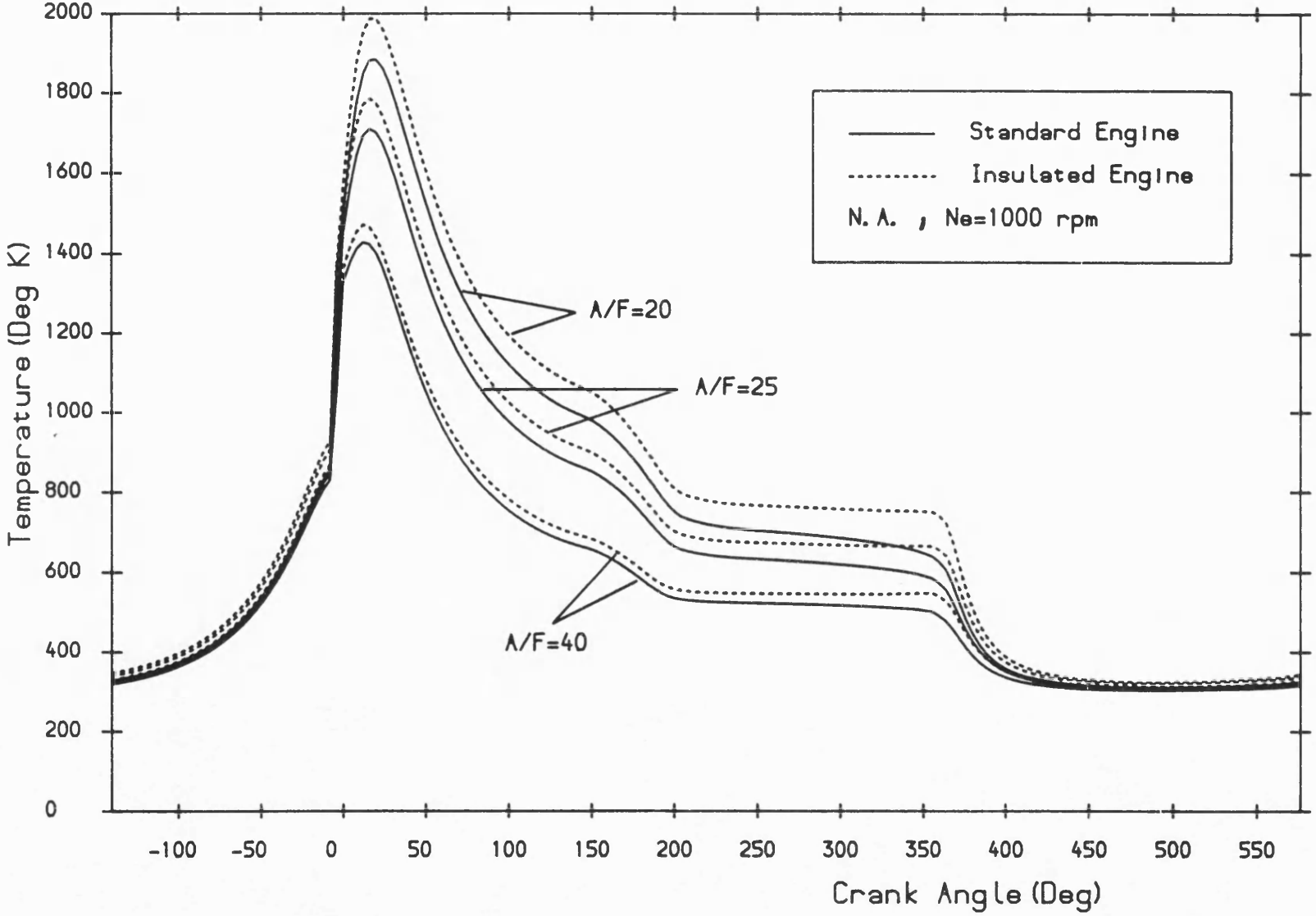

Fig. 7.37 The effect of engine insulation on cylinder gas temperature at various air-fuel ratios.

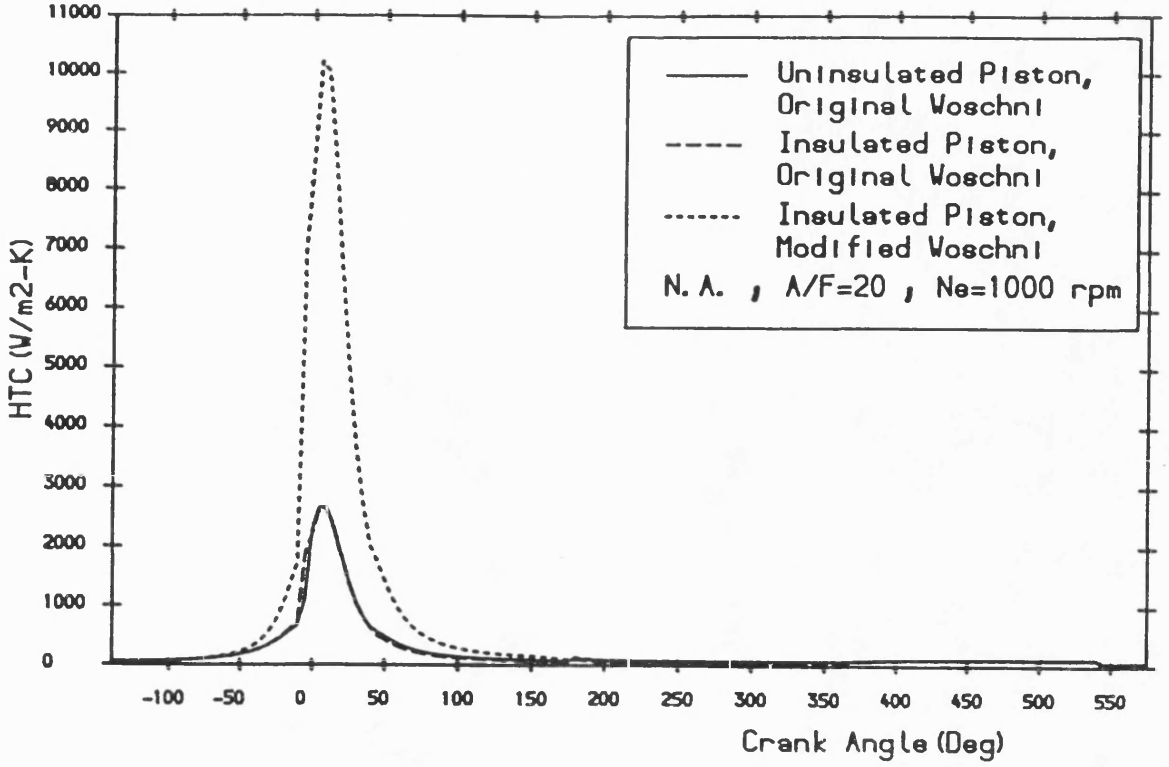

Fig. 7.38 Gas htc versus crank angle for standard and insulated piston engines obtained with both types of Woschni htc correlation.

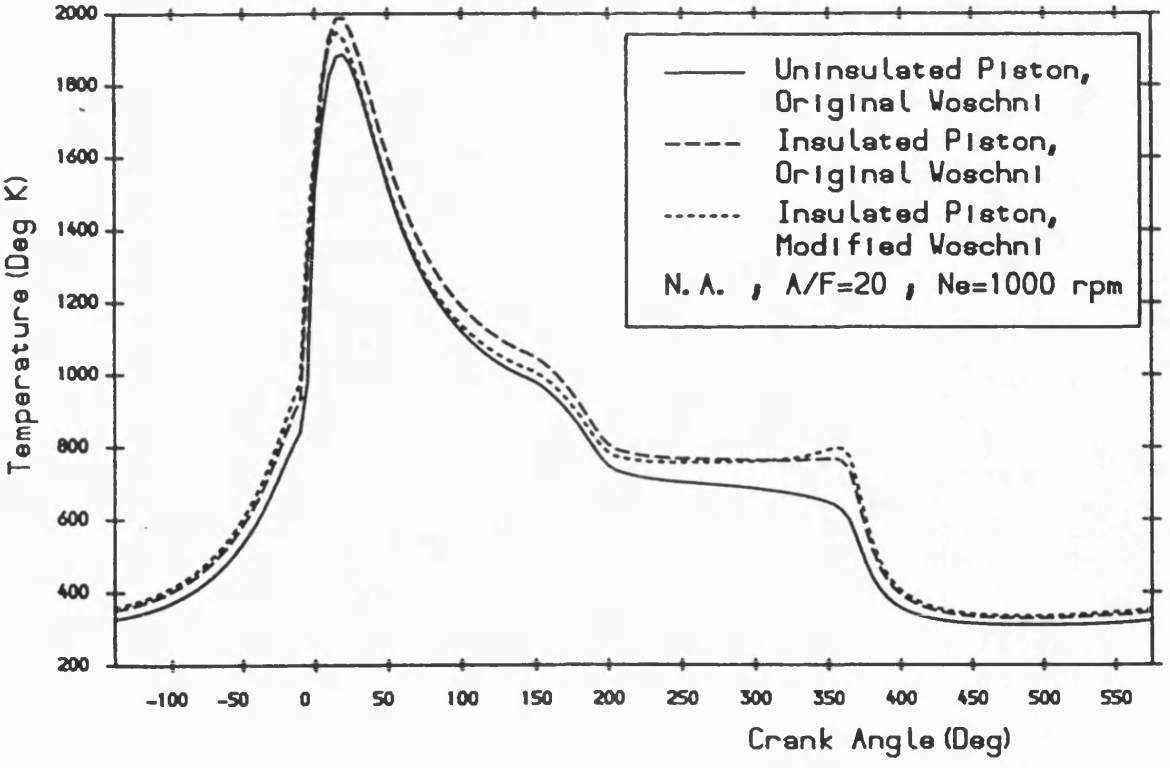

Fig. 7.39 Gas temperature versus crank angle for standard and insulated piston engines obtained with both types of Woschni htc correlation.

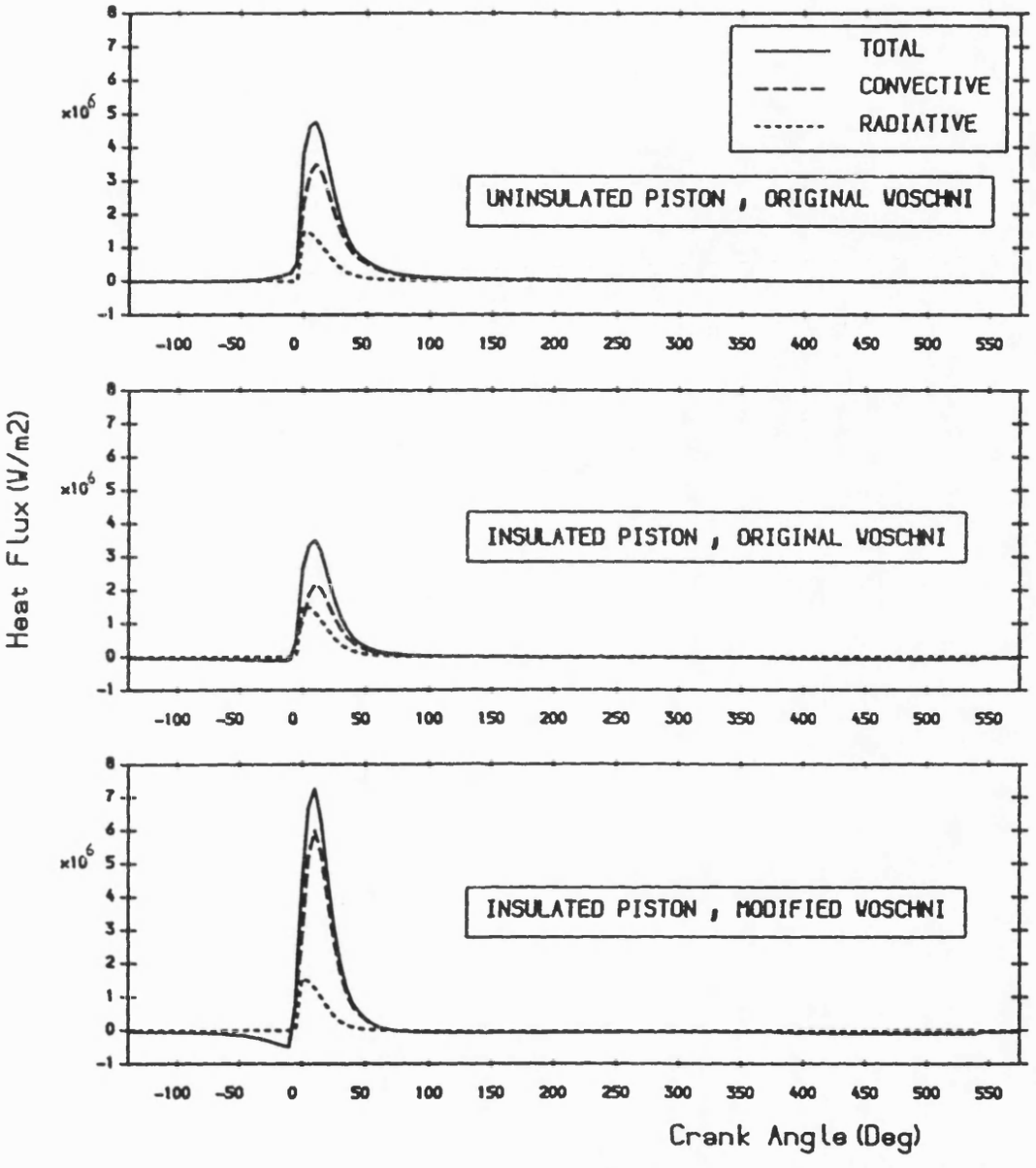

Fig. 7.40 Radiative, convective and total heat fluxes at piston surface for standard and insulated piston engines obtained with both types of Woschni htc correlation.

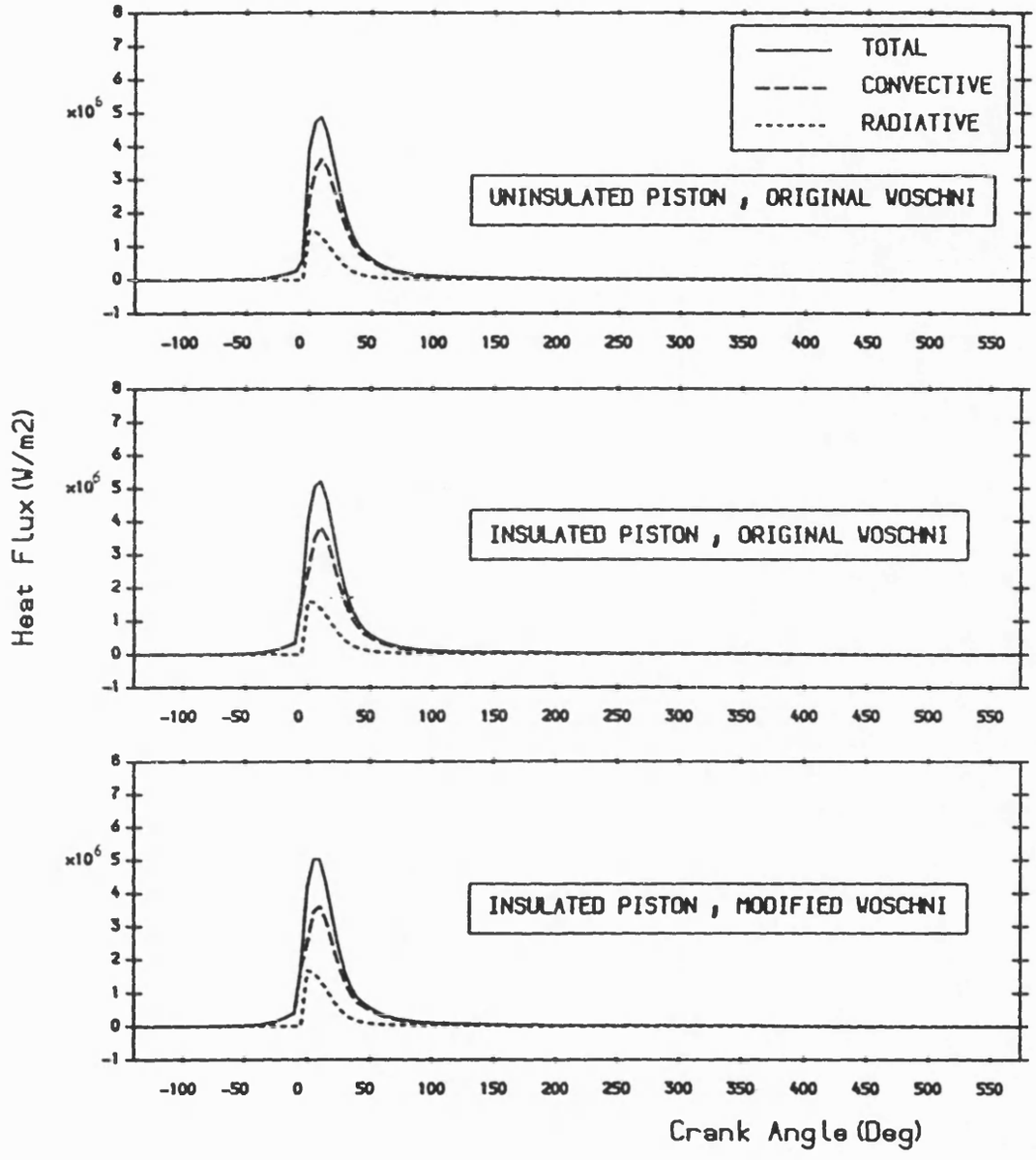

Fig. 7.41 Radiative, convective and total heat fluxes at cylinder head surface for standard and insulated piston engines obtained with both types of Woschni htc correlation.

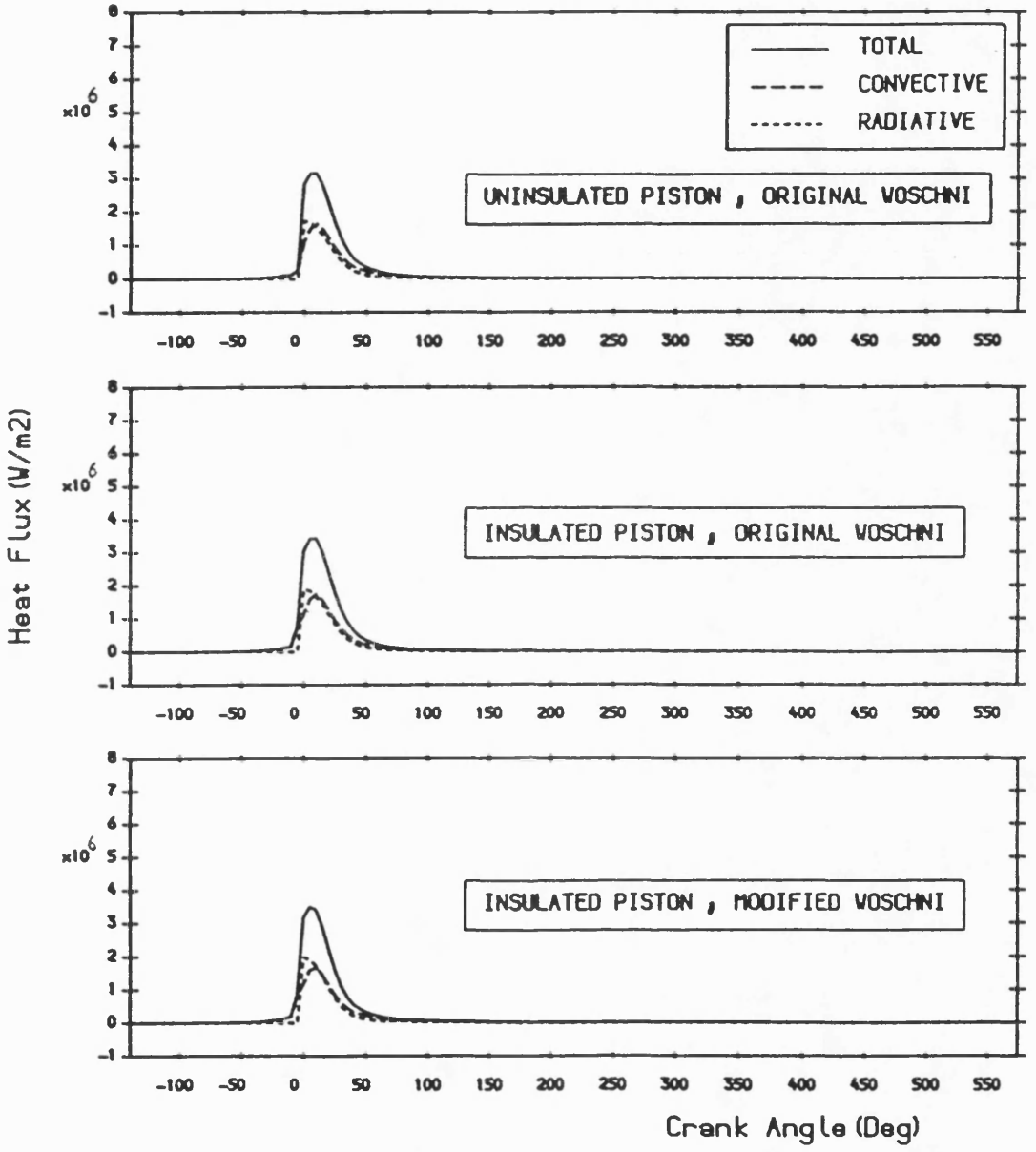

Fig. 7.42 Radiative, convective and total heat fluxes at liner surface, x=0.0 mm, for standard and insulated piston engines obtained with both types of Woschni htc correlation.

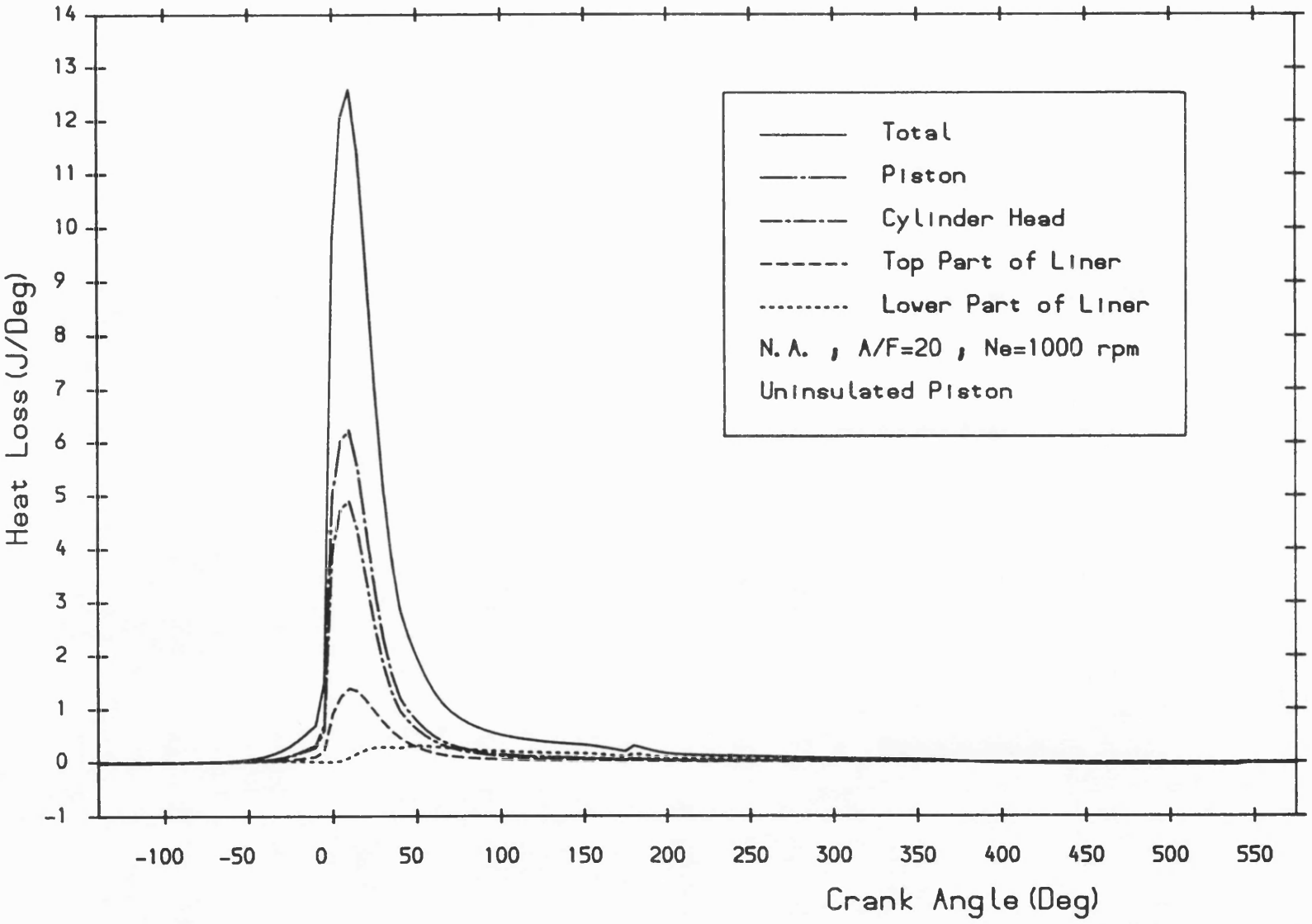

Fig. 7.43 Total gas heat loss and its distribution to different parts of the combustion chamber for the standard engine.

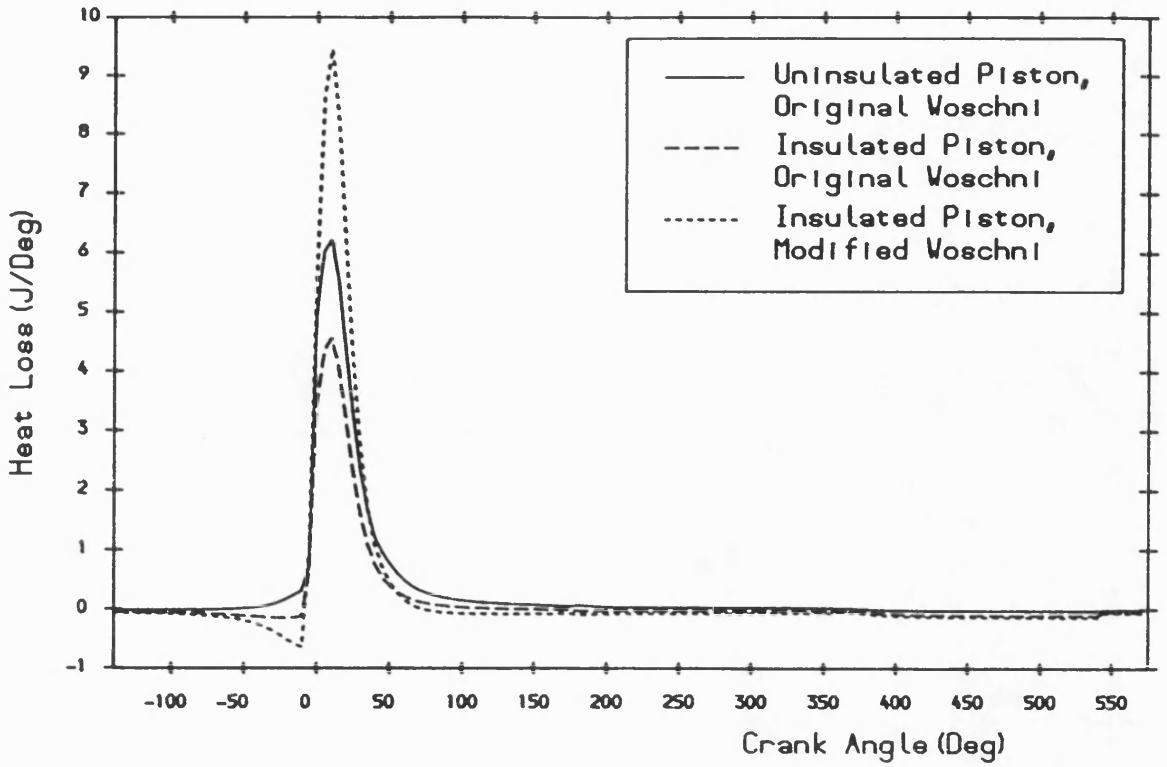

Fig. 7.44 Instantaneous gas to piston heat transfer for standard and insulated piston engines obtained with both types of Woschni htc correlation.

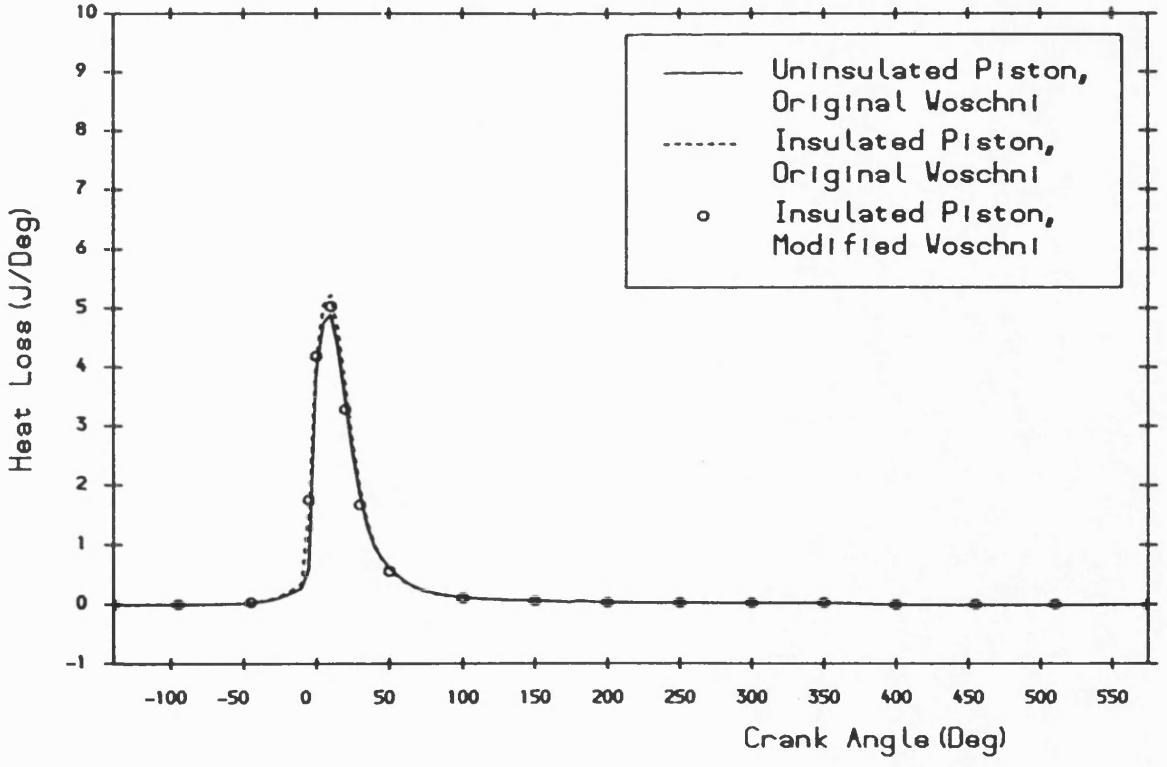

Fig. 7.45 Instantaneous gas to cylinder head heat transfer for standard and insulated piston engines obtained with both types of Woschni htc correlation.

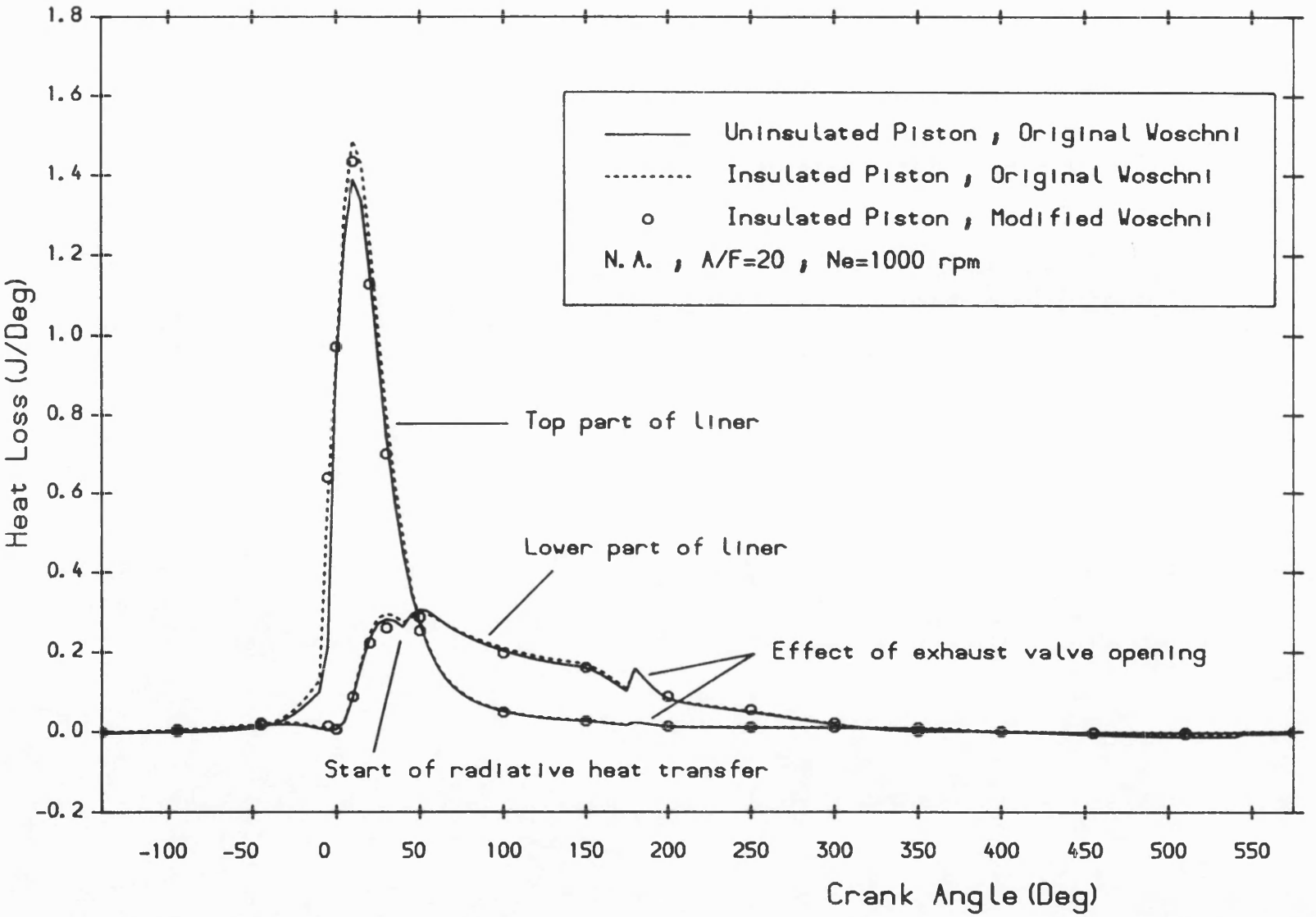

Fig. 7.46 The effect of piston insulation on heat loss from gas to the top and bottom parts of the liner.

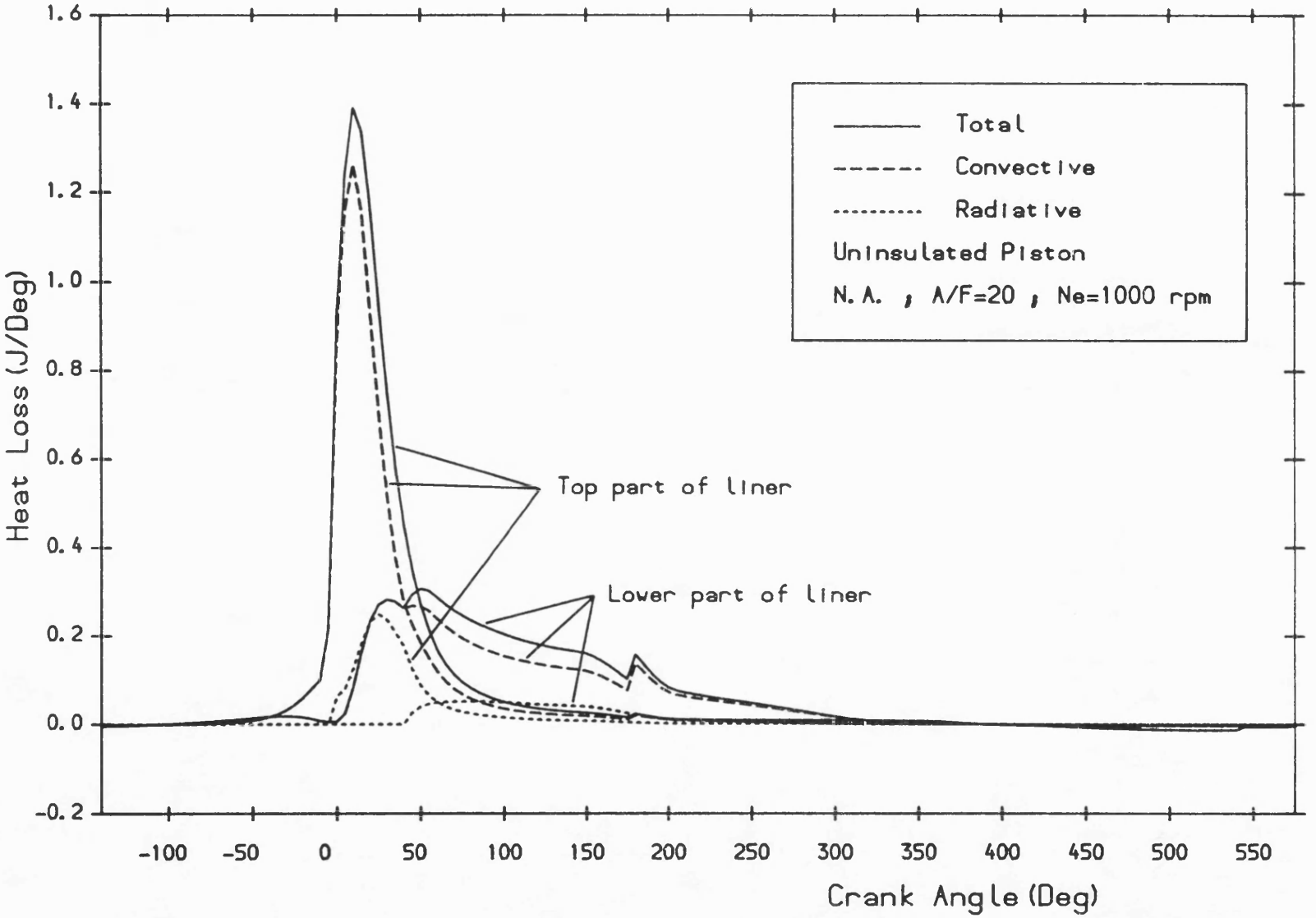

Fig.7.47 Radiative, convective and total heat transfer versus crank angle at the top and lower parts of the liner.

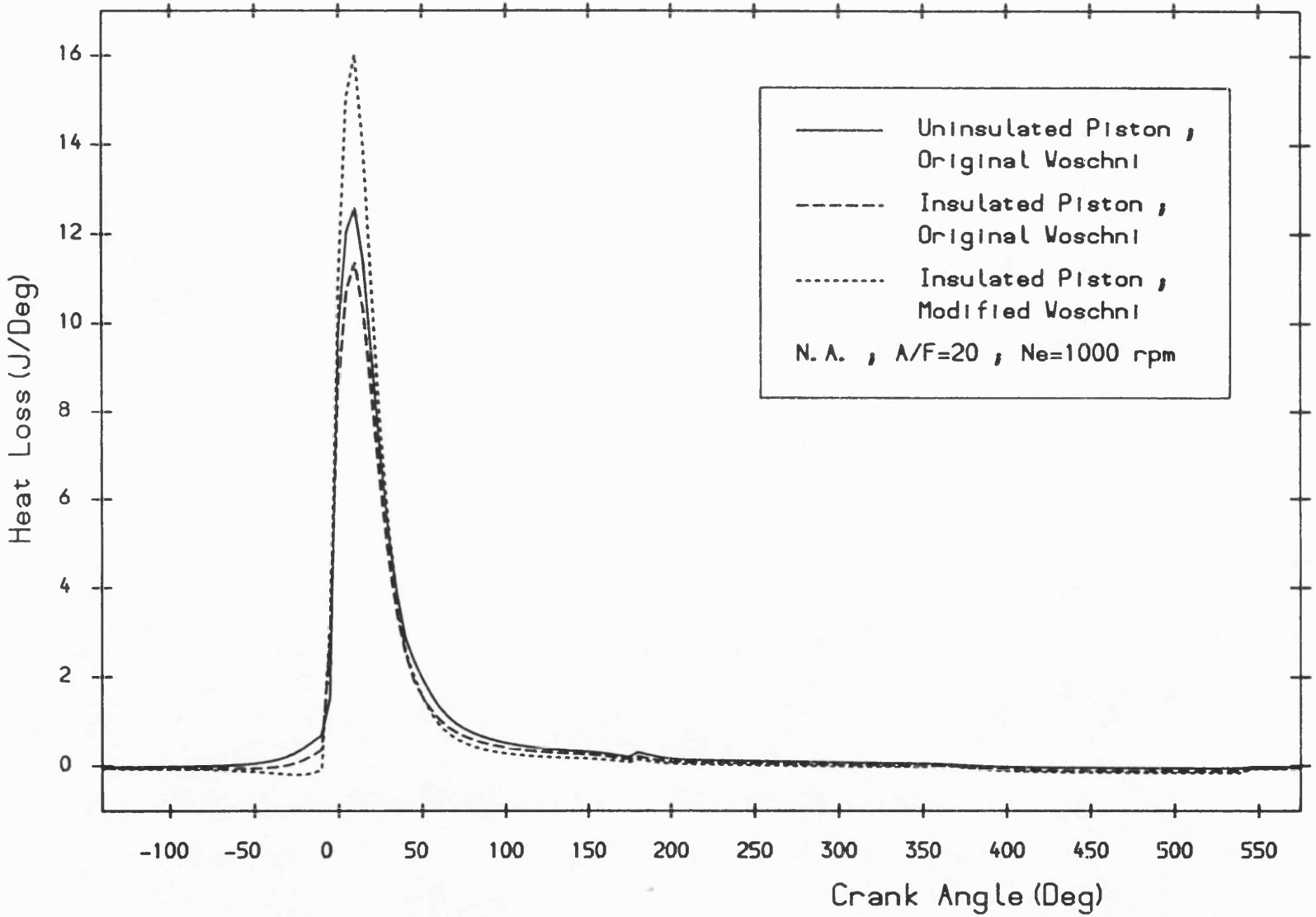

Fig. 7.48 Instantaneous total gas to wall heat transfer for standard and insulated piston engines obtained with both types of Woschni htc correlation.

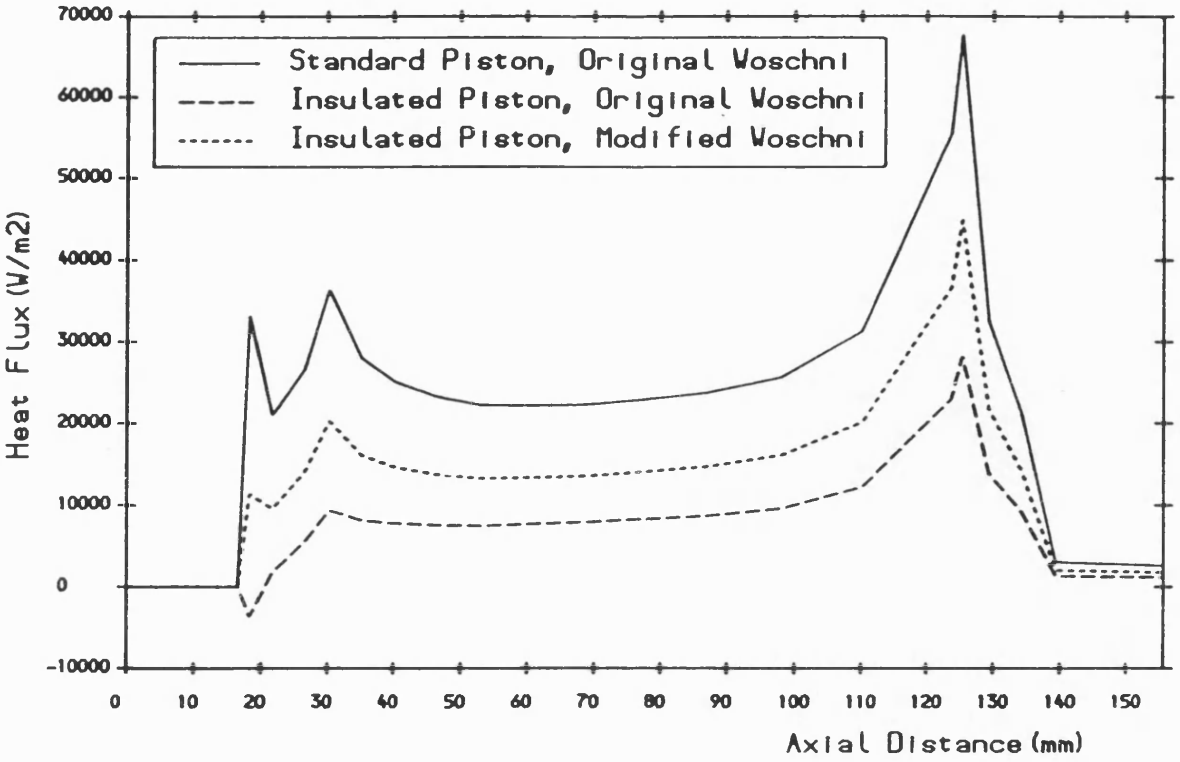

Fig. 7.49 The effect of piston insulation on piston to liner conduction heat flux.

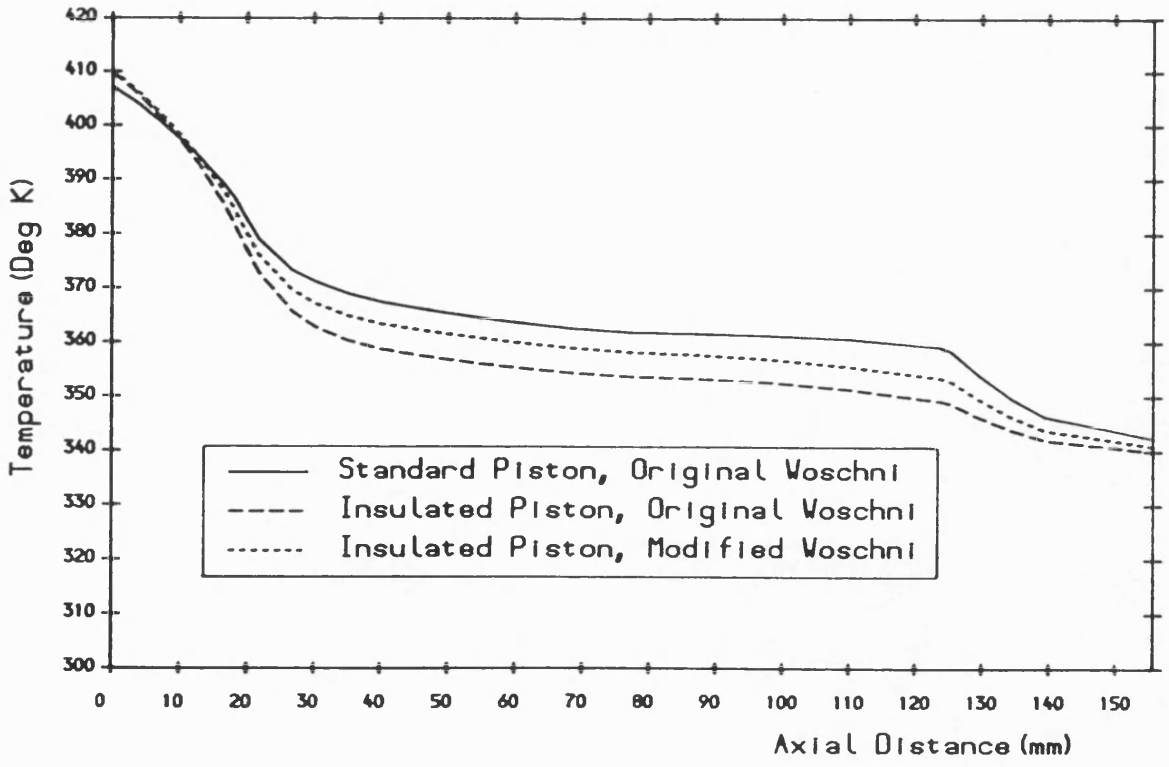

Fig. 7.50 The effect of piston insulation on liner temperature distribution.

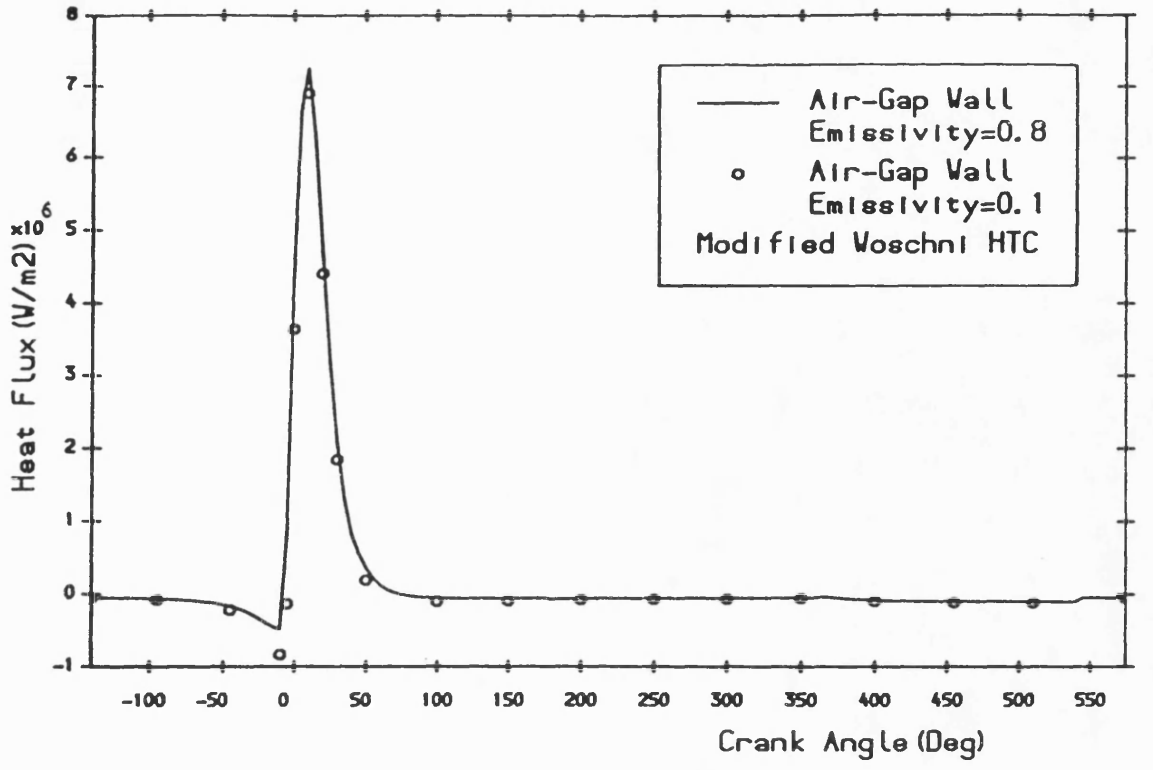

Fig. 7.51 The effect of air-gap wall emissivity on piston surface heat flux.

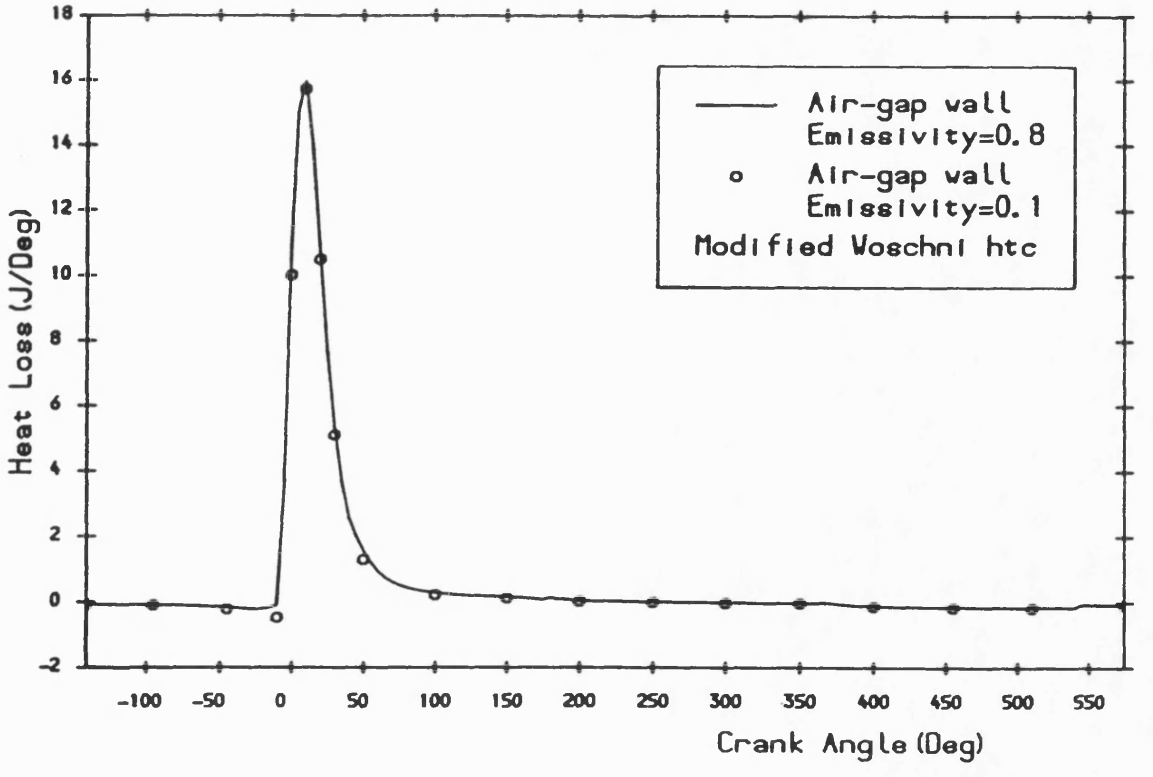

Fig. 7.52 The effect of air-gap wall emissivity on total gas to wall heat transfer.

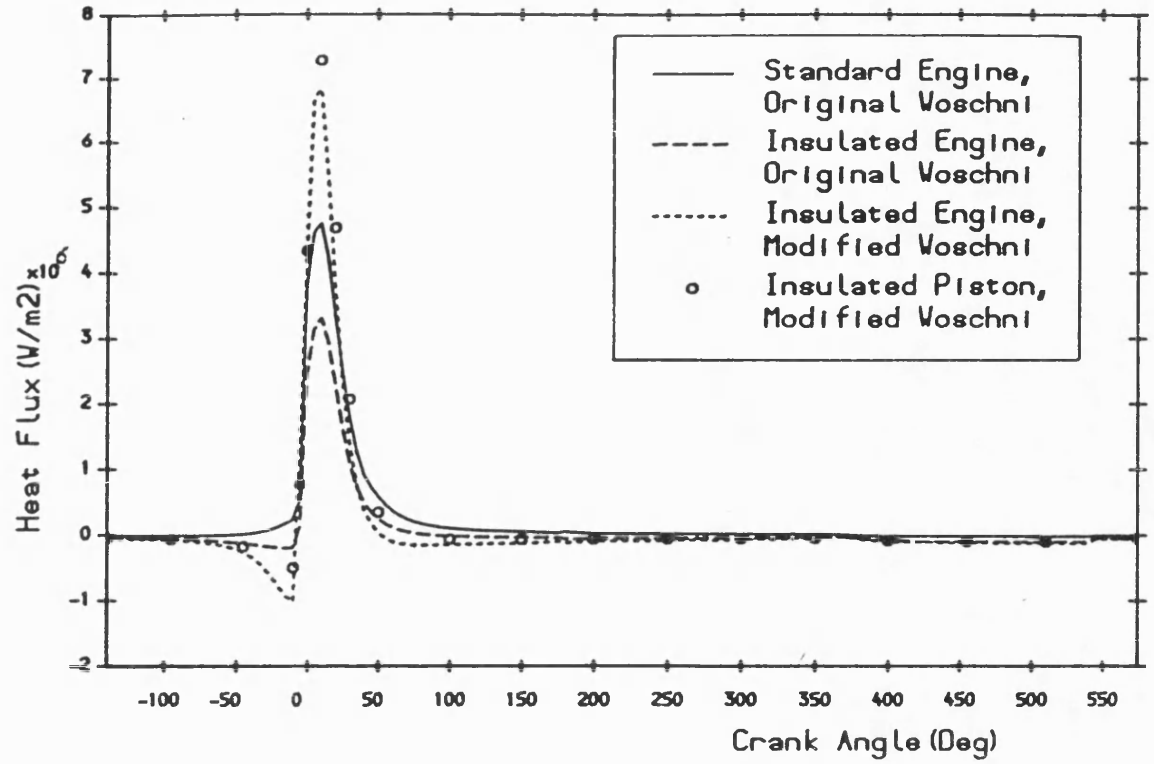

Fig. 7.53 The effect of total engine insulation on piston surface heat flux.

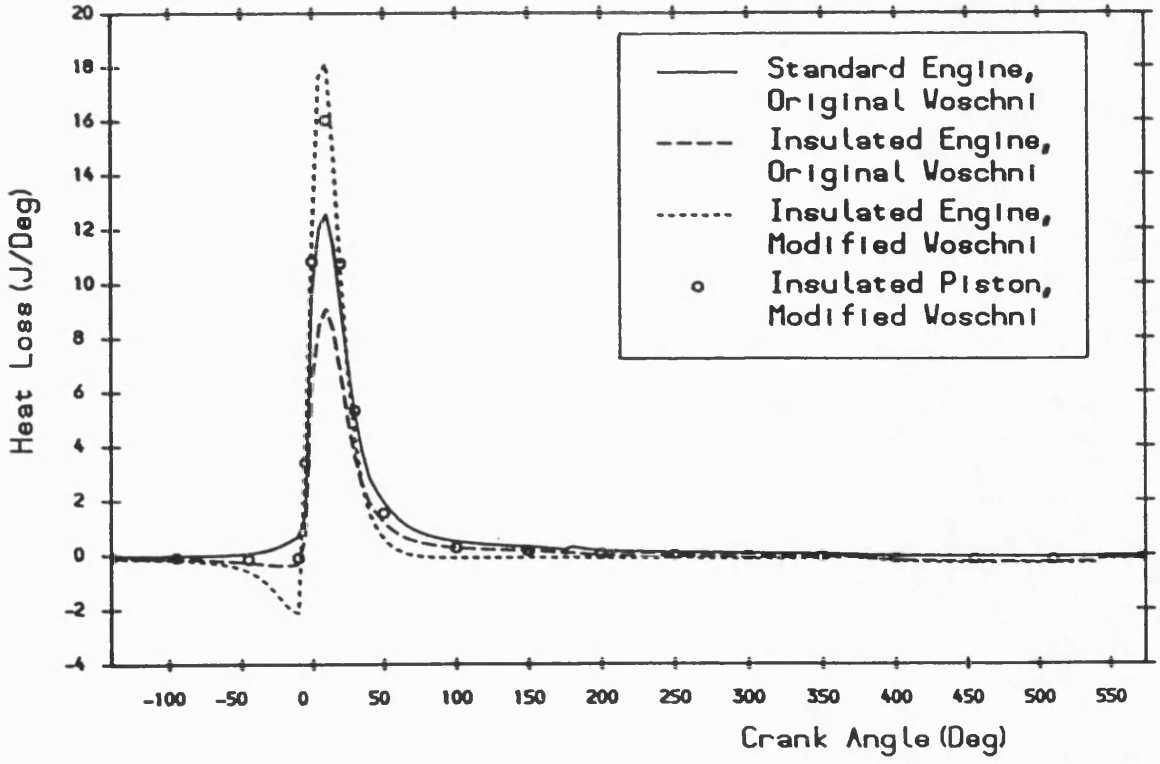

Fig. 7.54 The effect of total engine insulation on total gas to wall heat transfer.

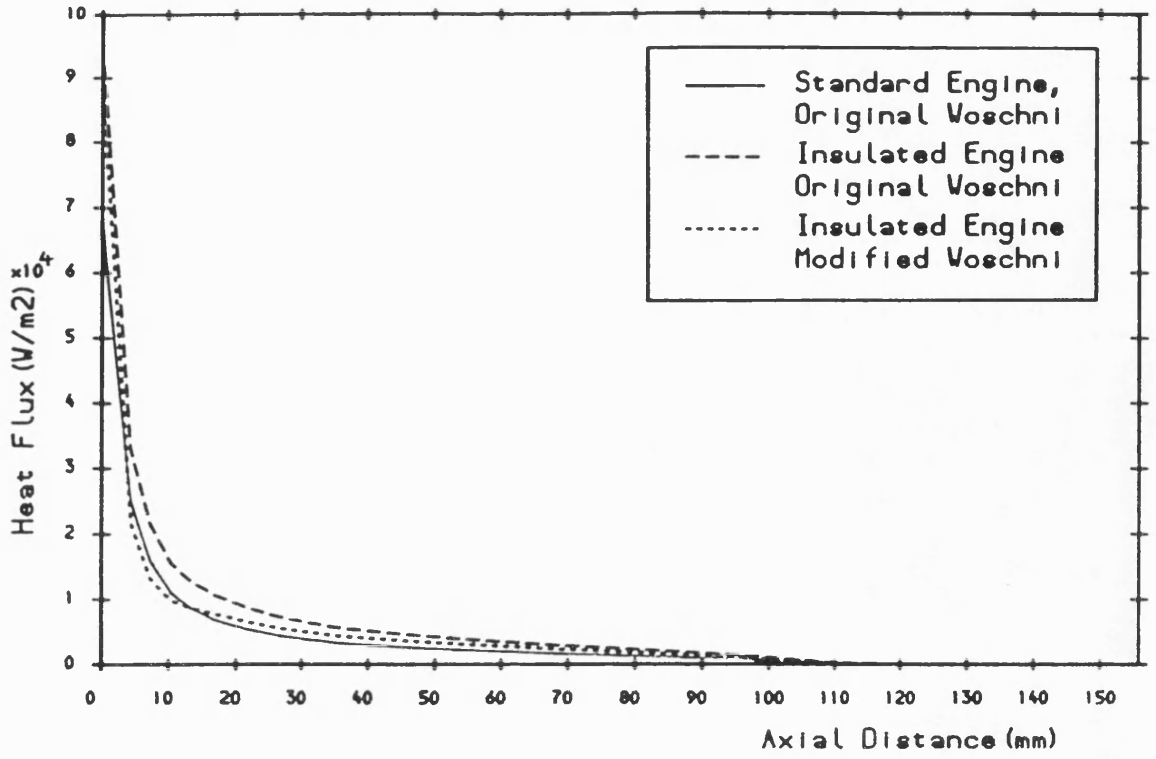

Fig. 7.55 The effect of total engine insulation on cycle mean flame radiative heat flux distribution at liner surface.

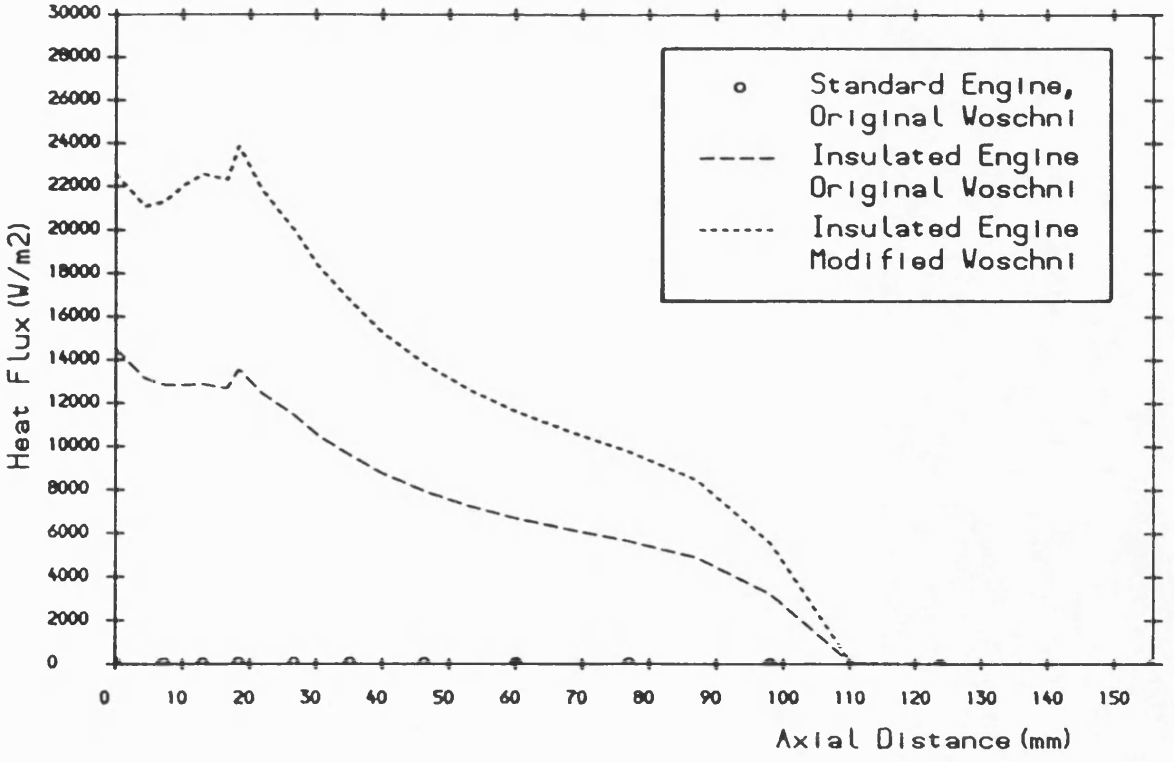

Fig. 7.56 The effect of total engine insulation on cycle mean wall radiative heat flux distribution at liner surface.

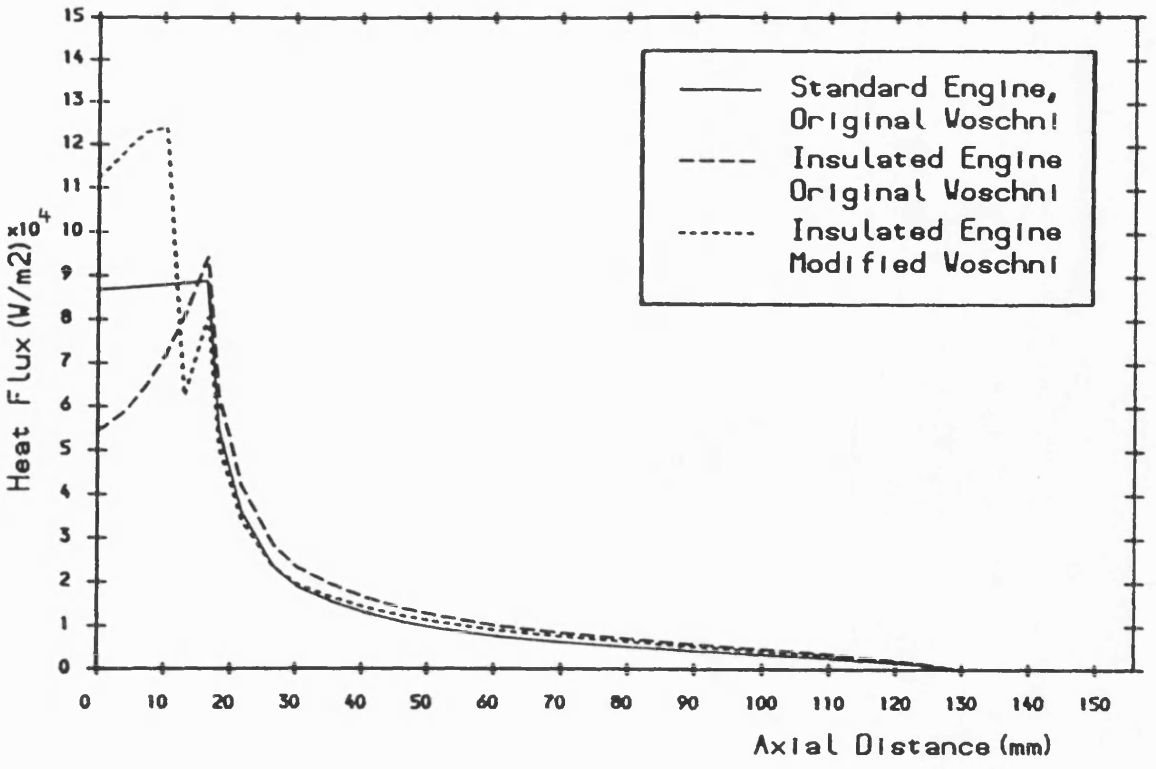

Fig. 7.57 The effect of total engine insulation on cycle mean convective heat flux distribution at liner surface.

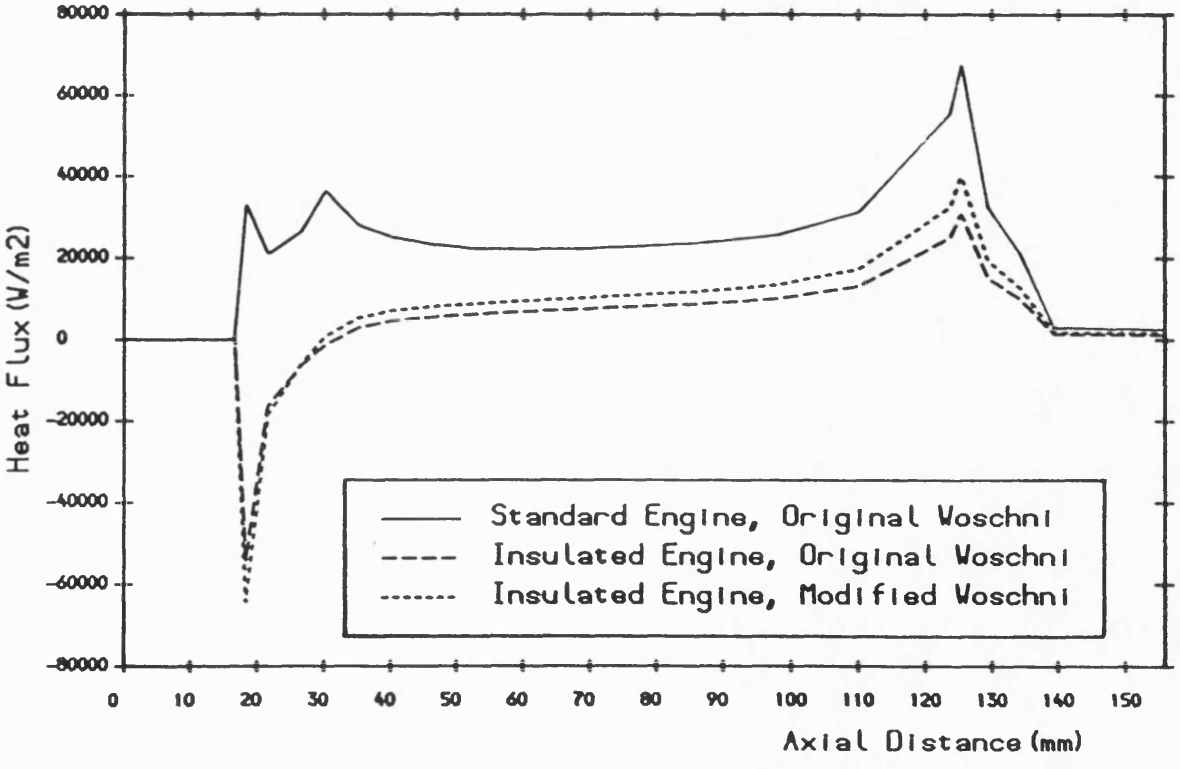

Fig. 7.58 The effect of total engine insulation on cycle mean conductive heat flux distribution at liner surface.

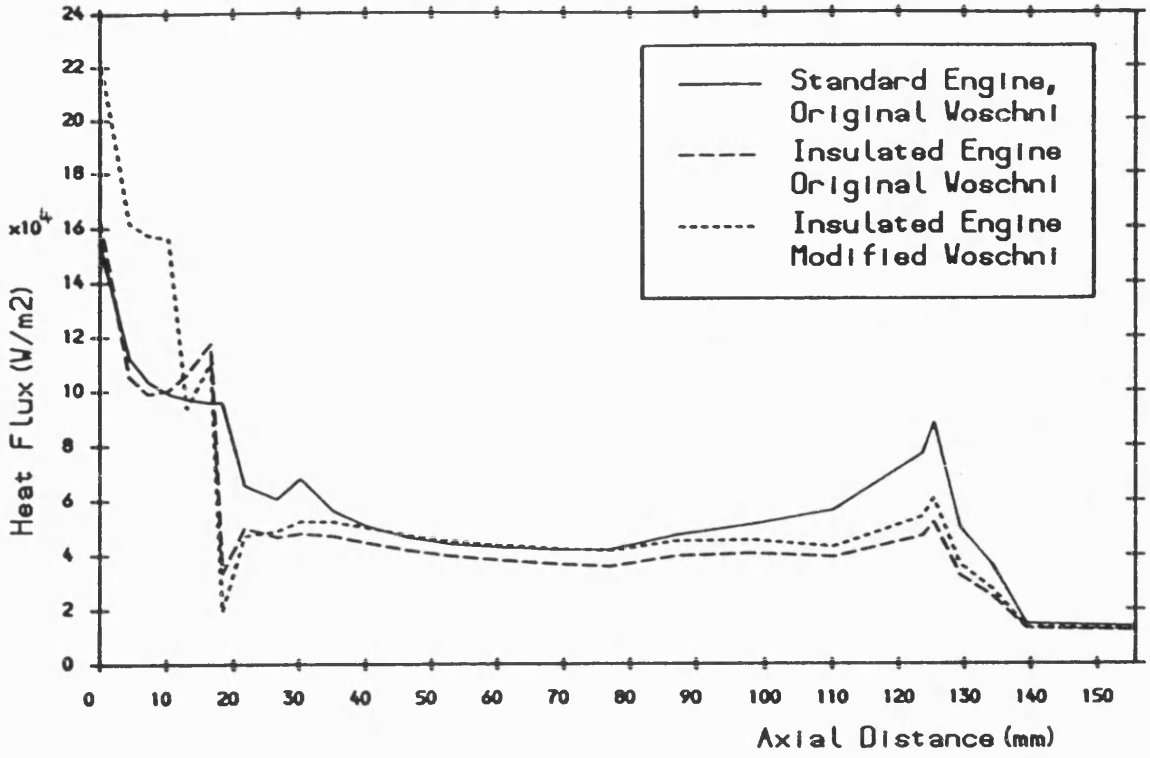

Fig. 7.59 The effect of total engine insulation on cycle mean total heat flux distribution at liner surface.

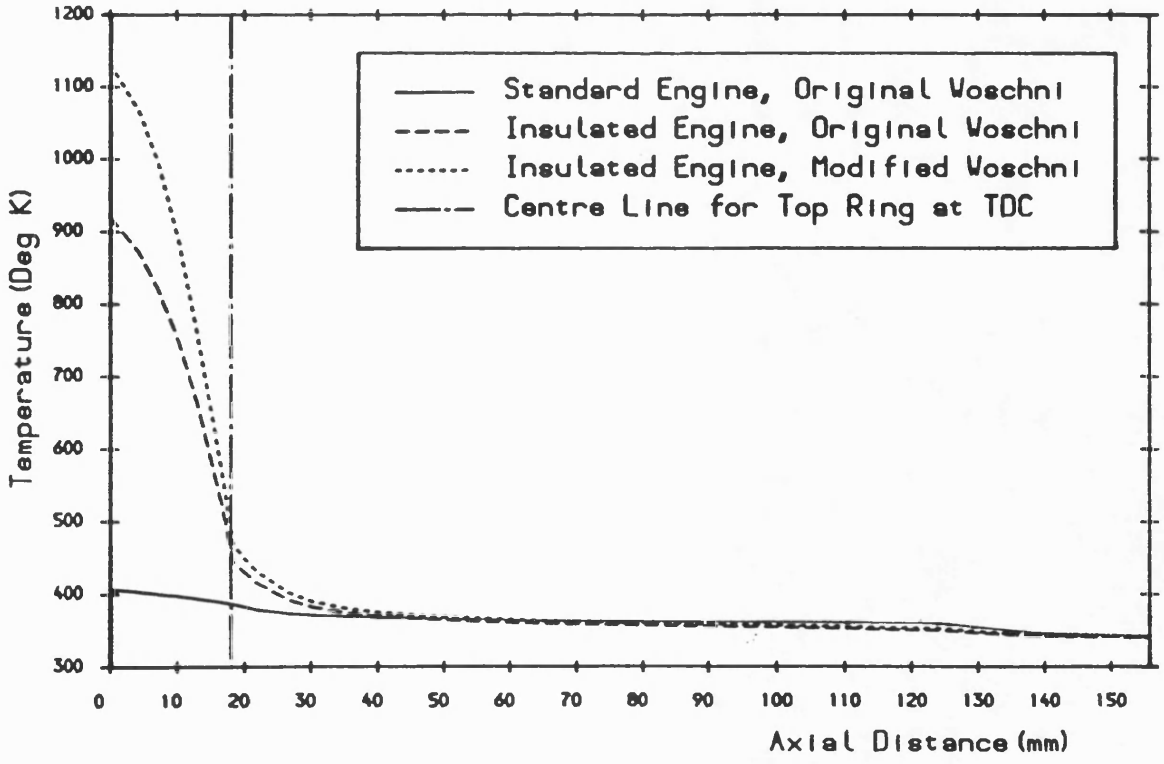

Fig. 7.60 The effect of total engine insulation on cycle mean liner surface temperature distribution.

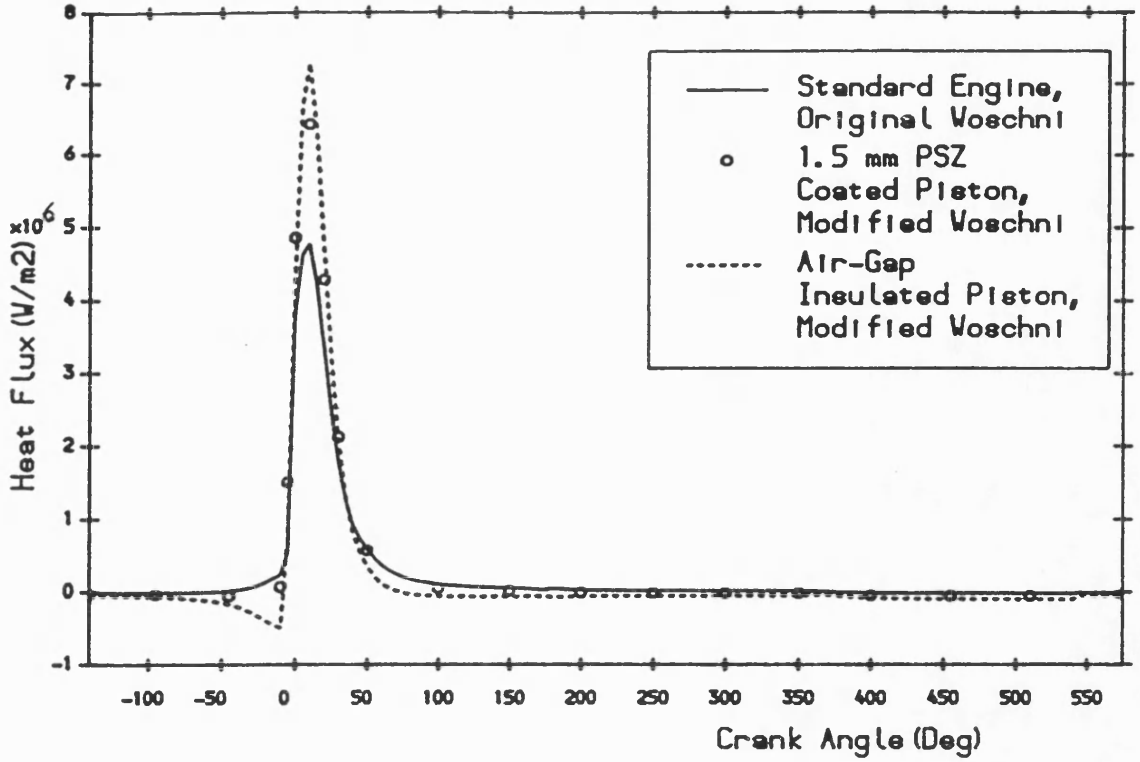

Fig. 7.61 The effect of insulation level on piston surface heat flux with modified Woschni htc correlation.

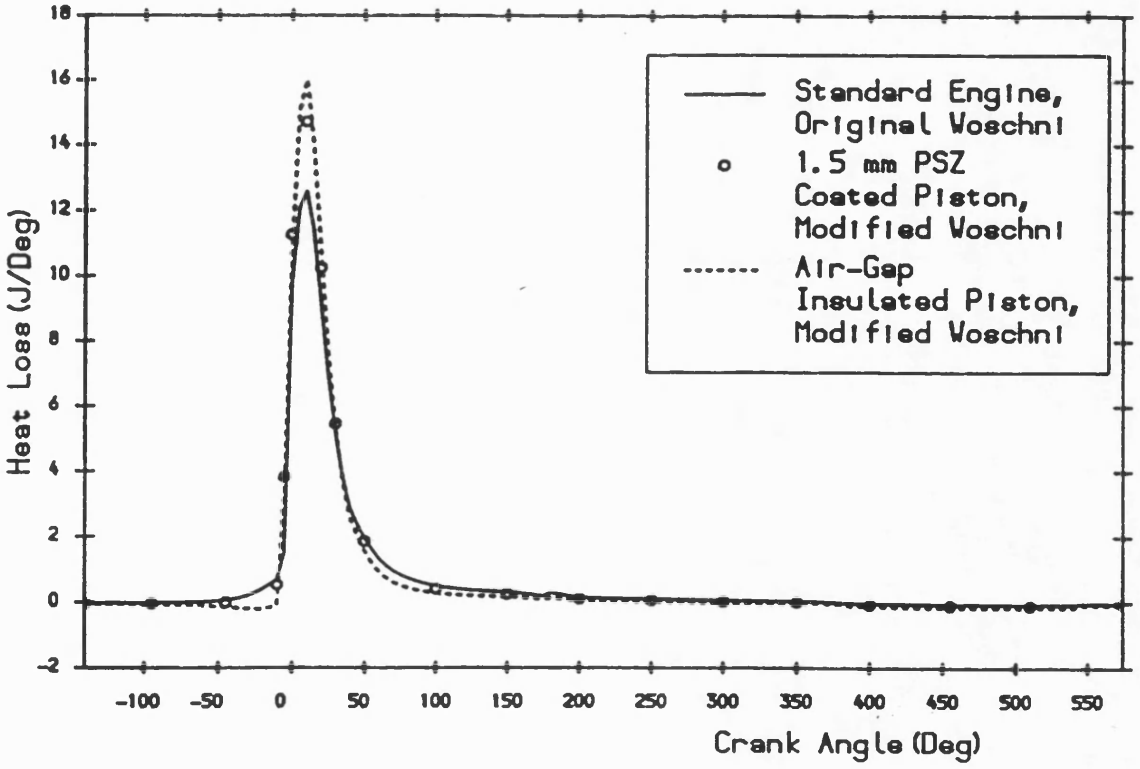

Fig. 7.62 The effect of piston insulation level on total gas to wall heat transfer with modified Woschni htc correlation.

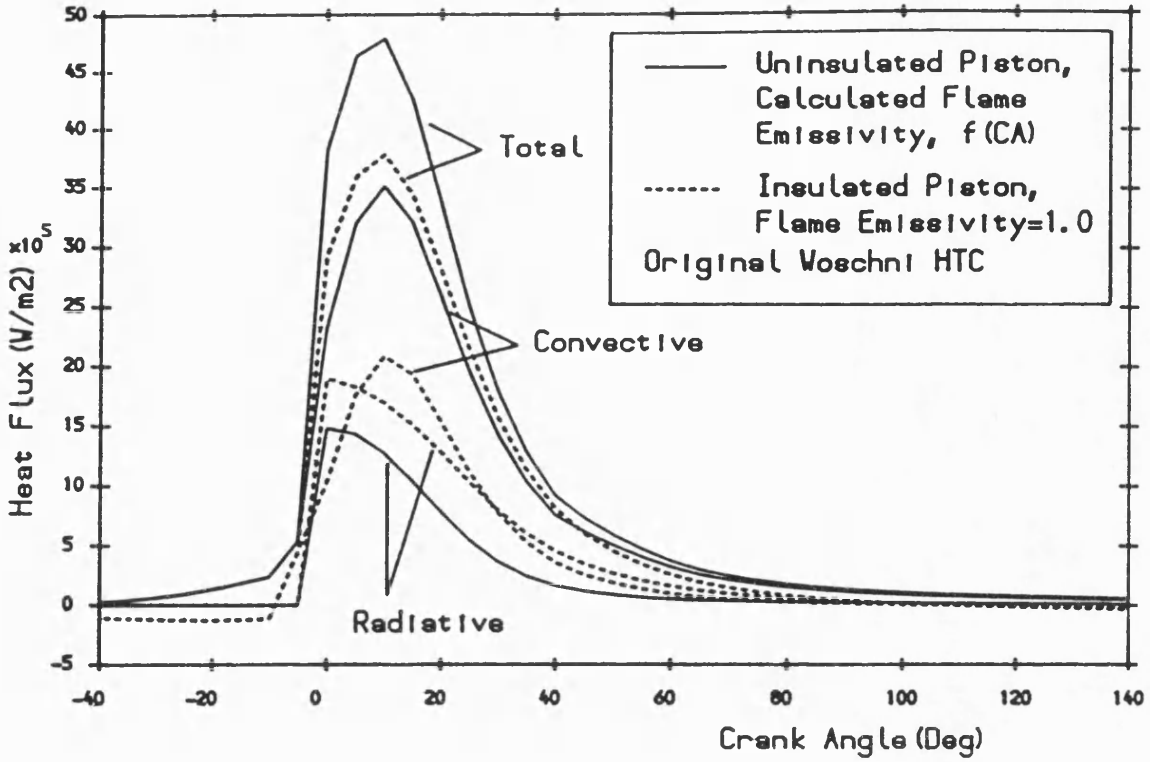

Fig. 7.63 The effect of flame emissivity on piston surface heat flux in the insulated piston engine.

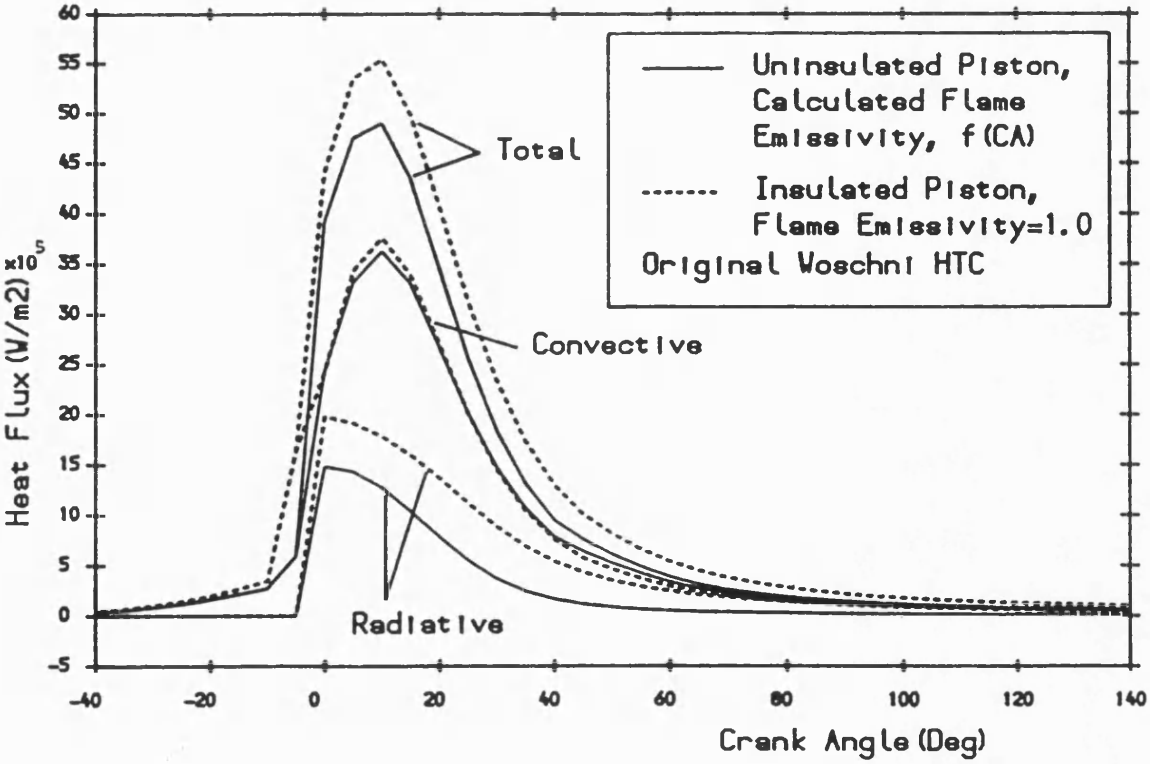

Fig. 7.64 The effect of flame emissivity on cylinder head surface heat flux in the insulated piston engine.

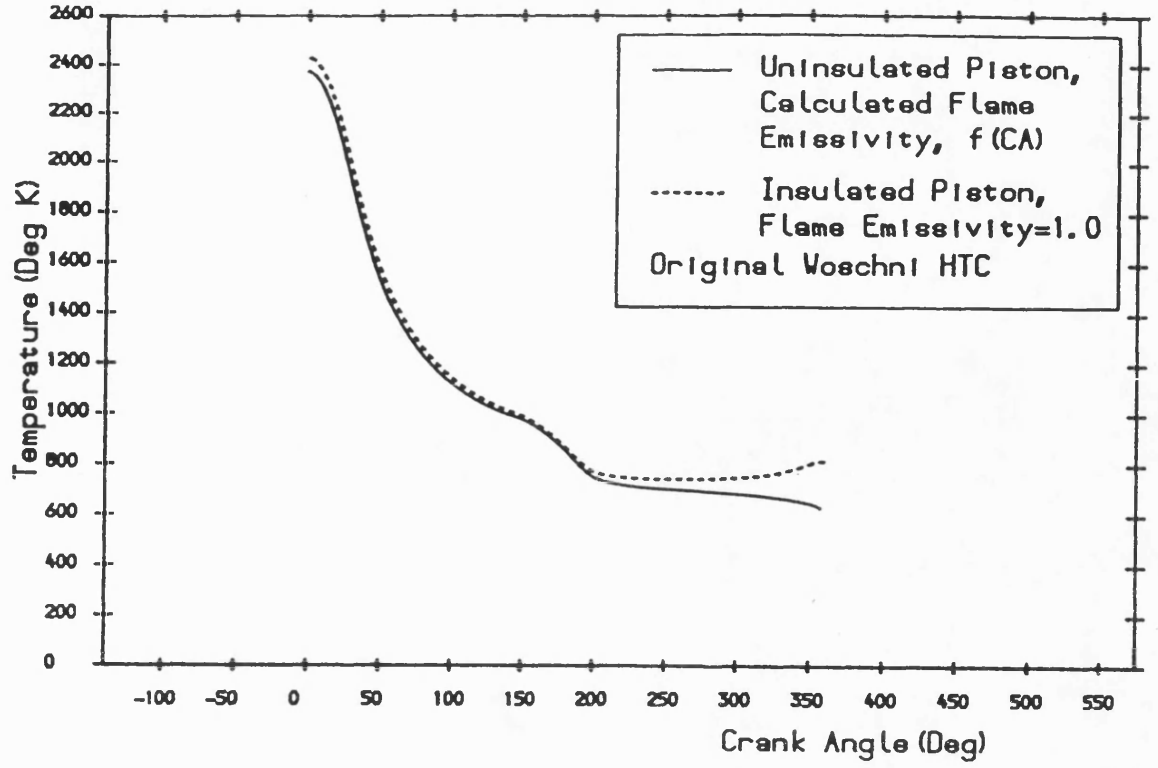

Fig. 7.65 The flame temperature in standard and insulated piston engines.

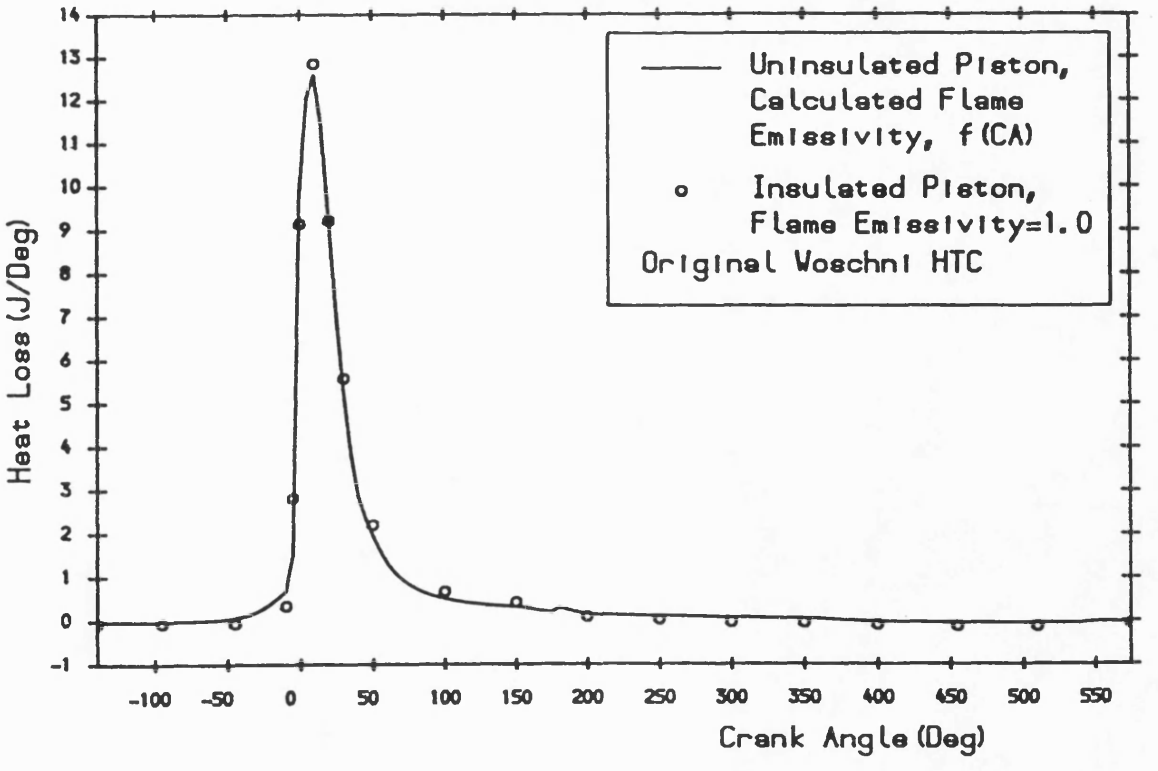

Fig. 7.66 The effect of flame emissivity on total gas to wall heat loss in the insulated piston engine.

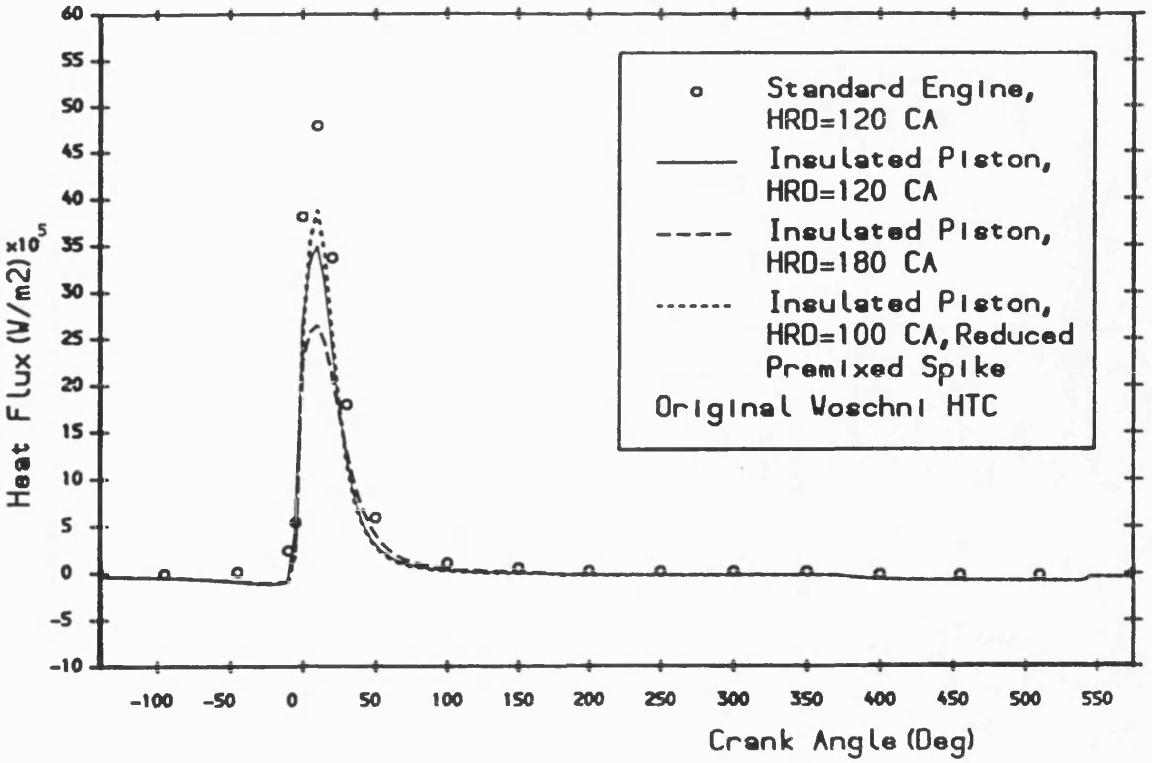

Fig. 7.67 The effect of heat release on piston surface heat flux in the insulated piston engine.

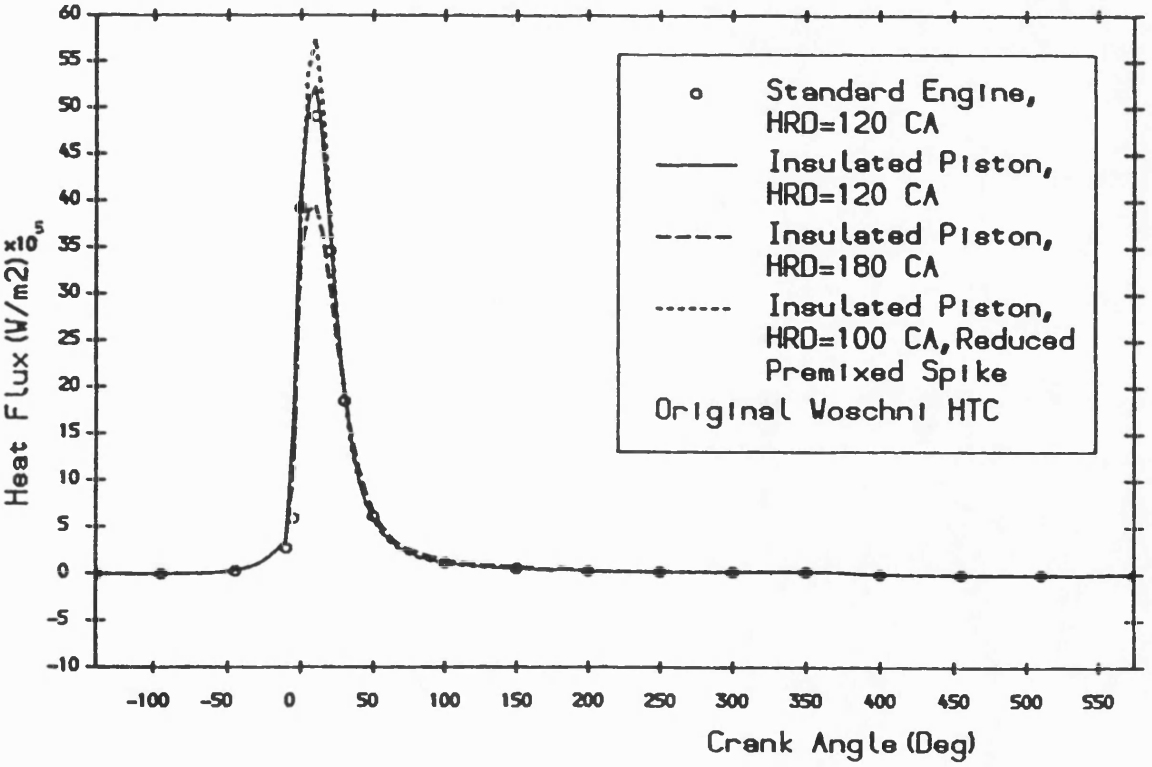

Fig. 7.68 The effect of heat release on cylinder head surface heat flux in the insulated piston engine.

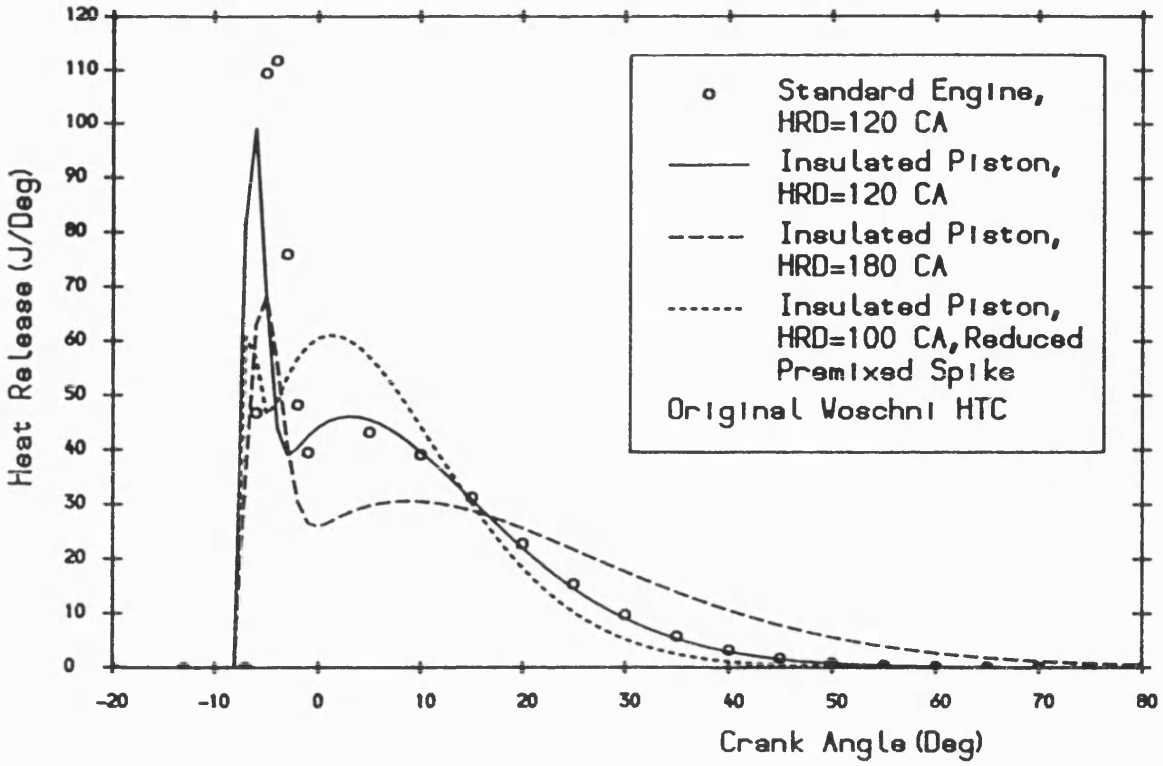

Fig. 7.69 The effect of heat release duration (HRD) on heat release curves in the insulated piston engine.

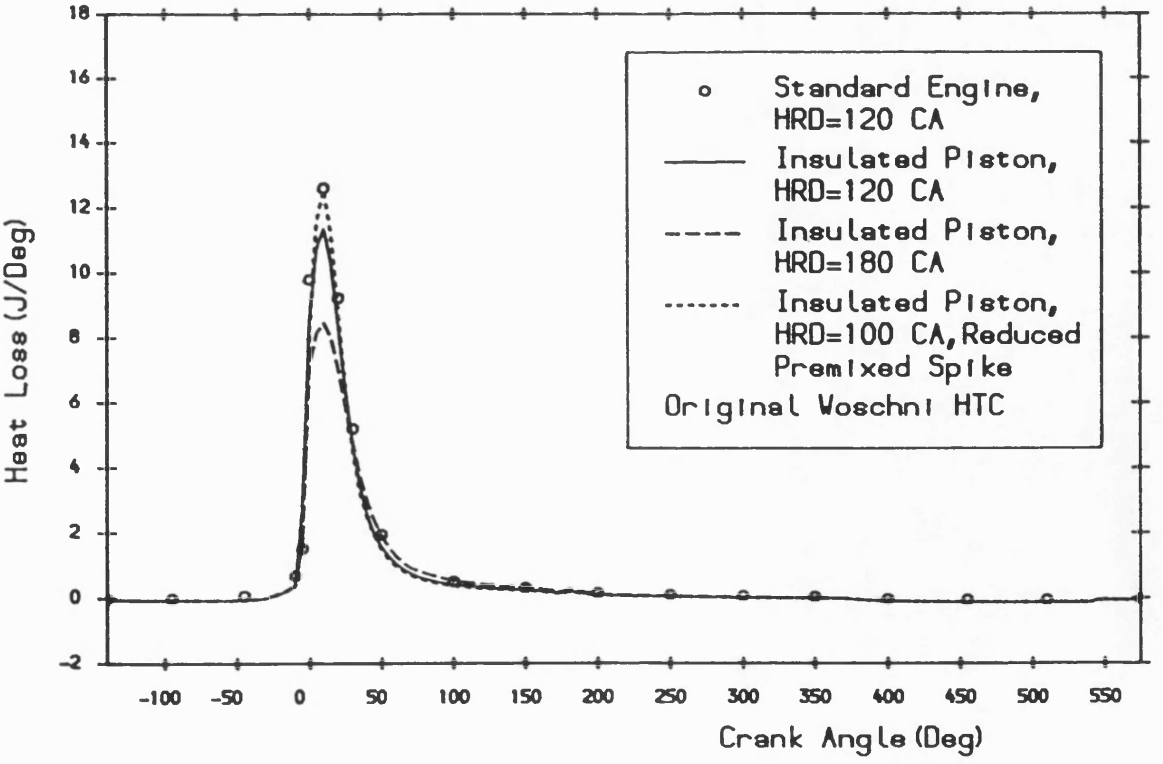

Fig. 7.70 The effect of heat release on total gas to wall heat transfer in the insulated piston engine.

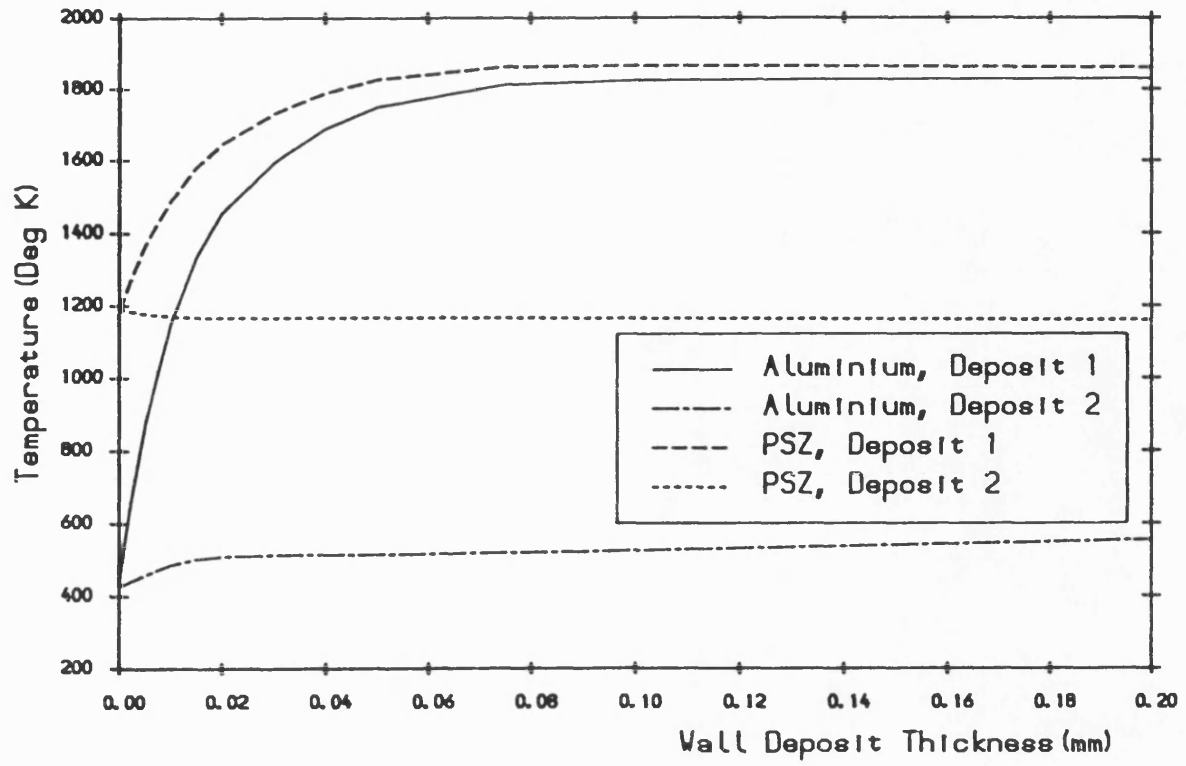

Fig. 7.71 The maximum wall deposit surface temperature versus wall deposit thickness at aluminium and PSZ walls for 2 different deposit types.

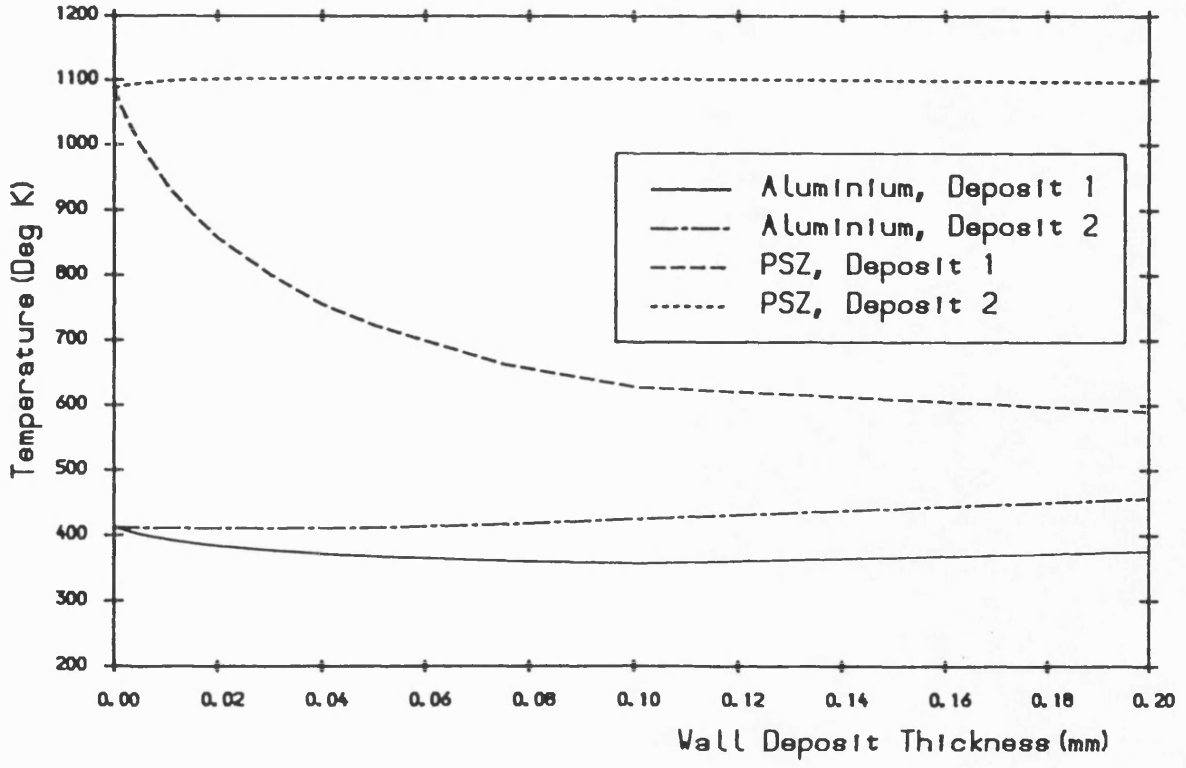

Fig. 7.72 The minimum wall deposit surface temperature versus wall deposit thickness at aluminium and PSZ walls for 2 different deposit types.

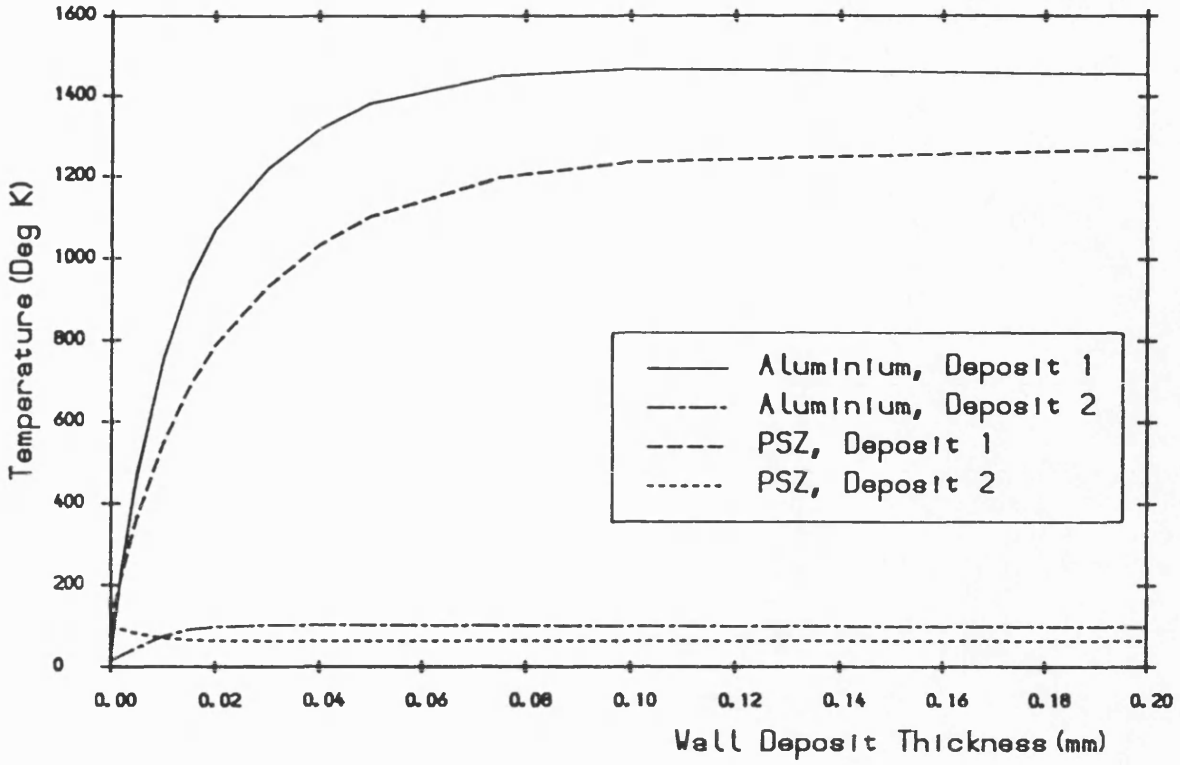

Fig. 7.73 The wall deposit surface temperature swing versus deposit thickness at aluminium and PSZ walls for 2 different deposit types.

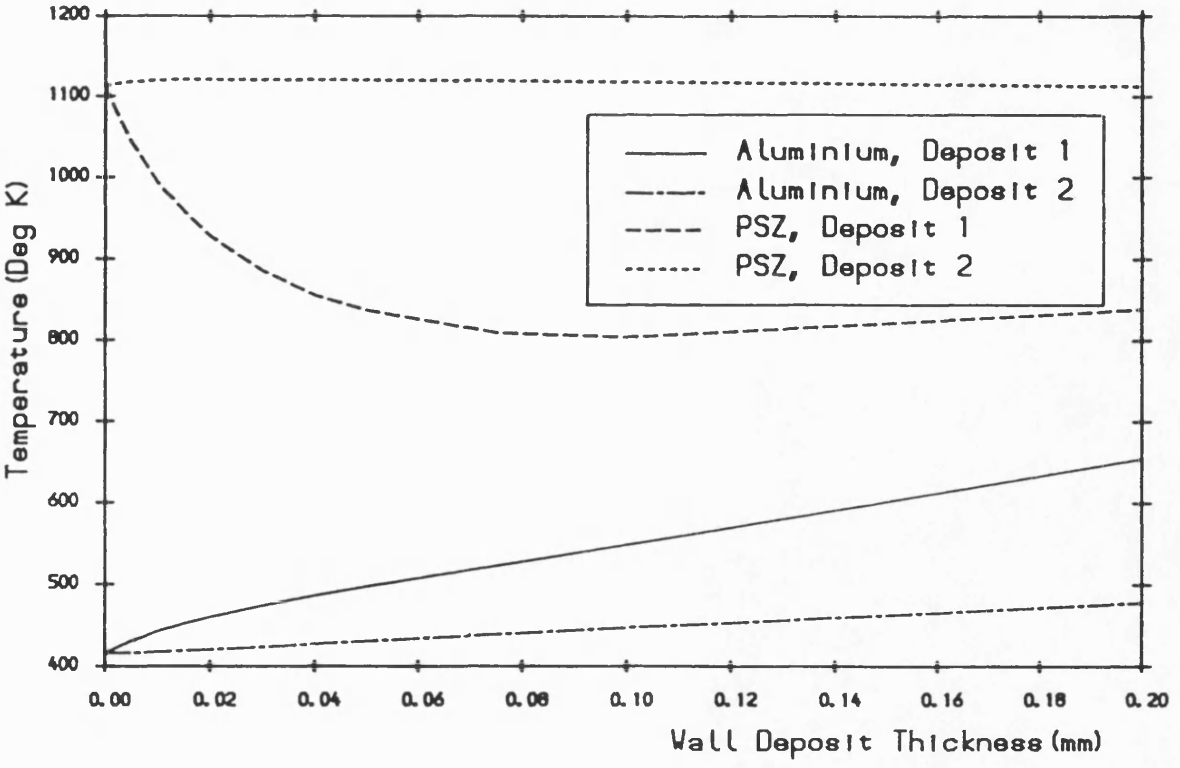

Fig. 7.74 The mean wall deposit surface temperature versus deposit thickness at aluminium and PSZ walls for 2 different deposit types.

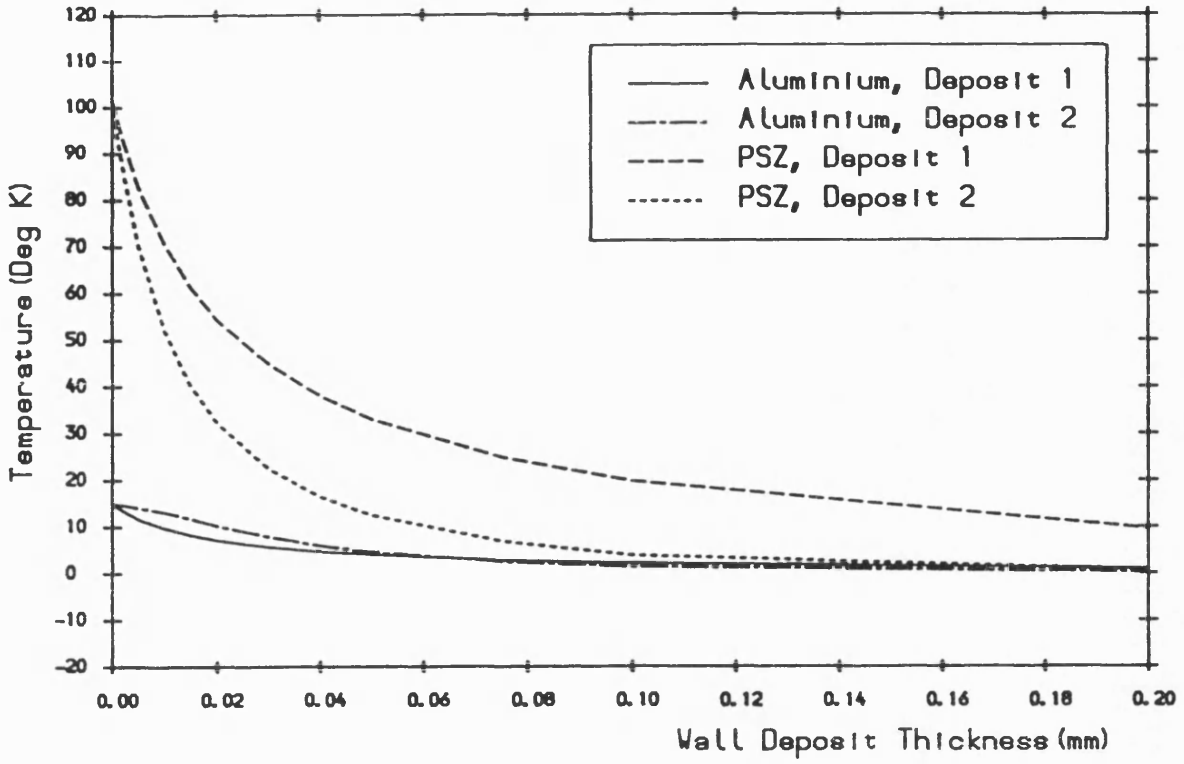

Fig. 7.75 The deposit-wall interface temperature swing versus deposit thickness at aluminium and PSZ walls for 2 different deposit types.

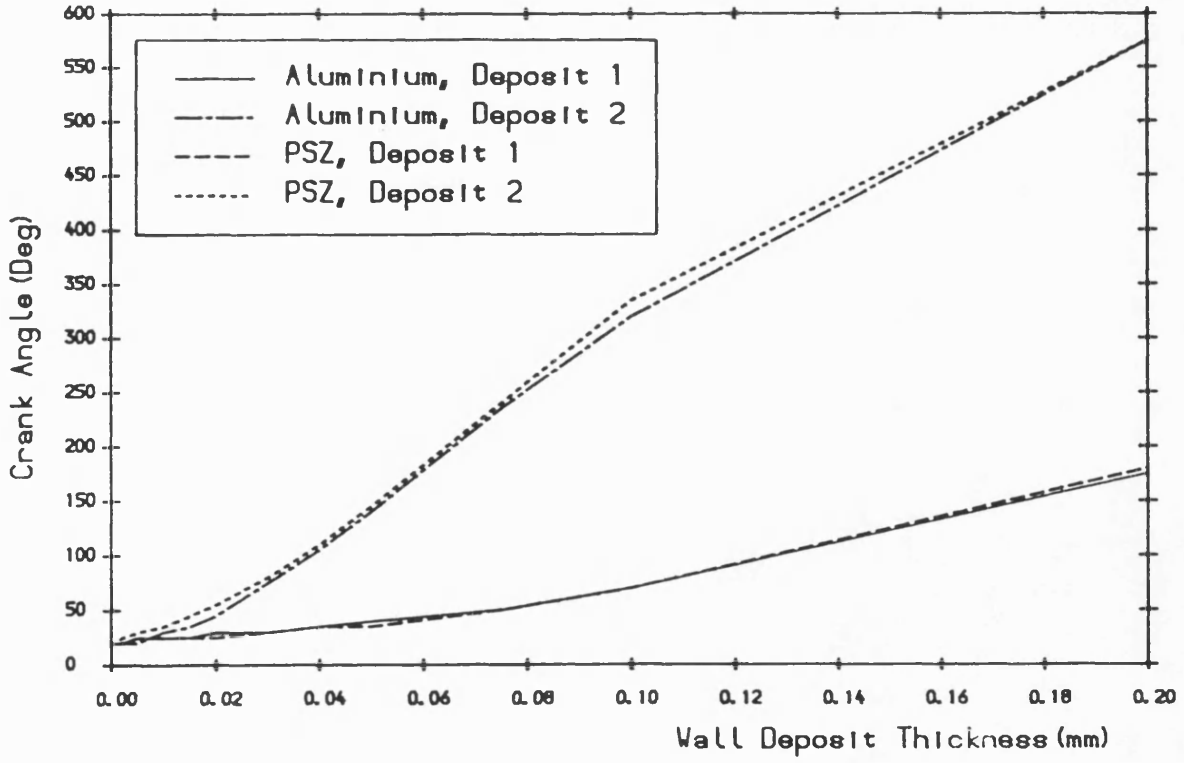

Fig. 7.76 The deposit-wall interface peak temperature timing versus deposit thickness at aluminium and PSZ walls for 2 different deposit types.

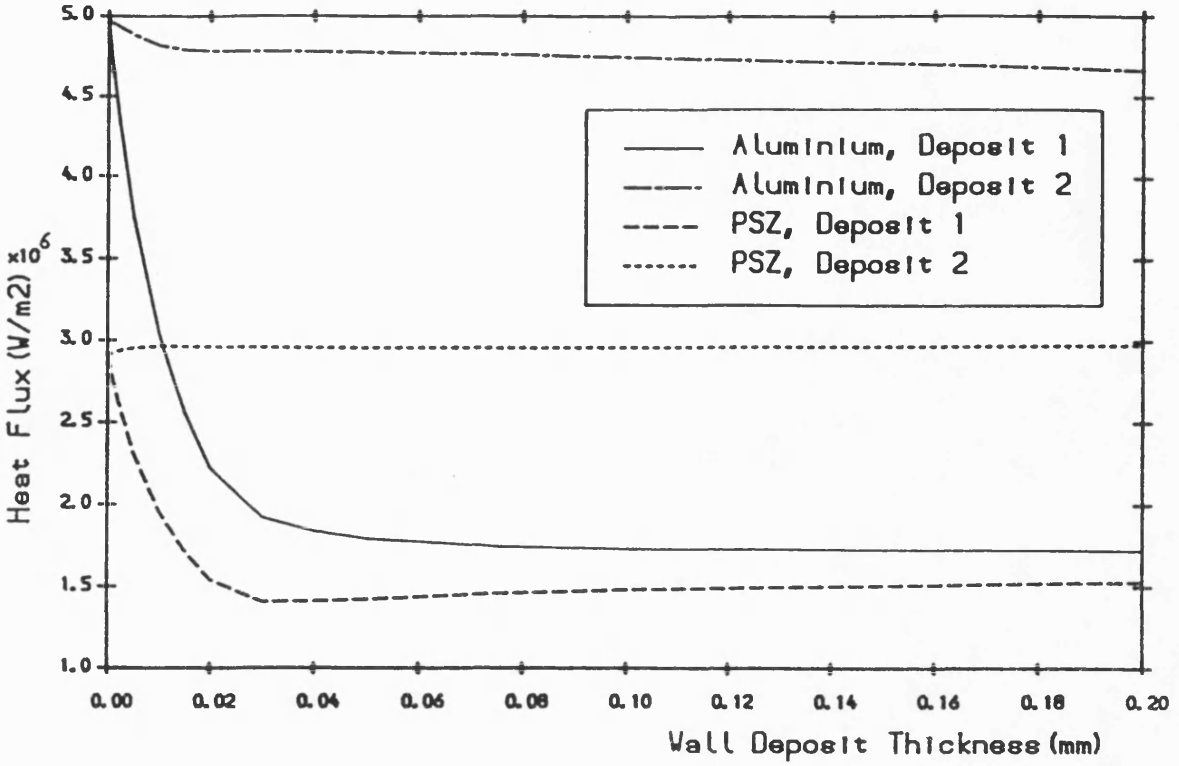

Fig. 7.77 The peak wall deposit surface heat flux versus deposit thickness at aluminium and PSZ walls for 2 different deposit types.

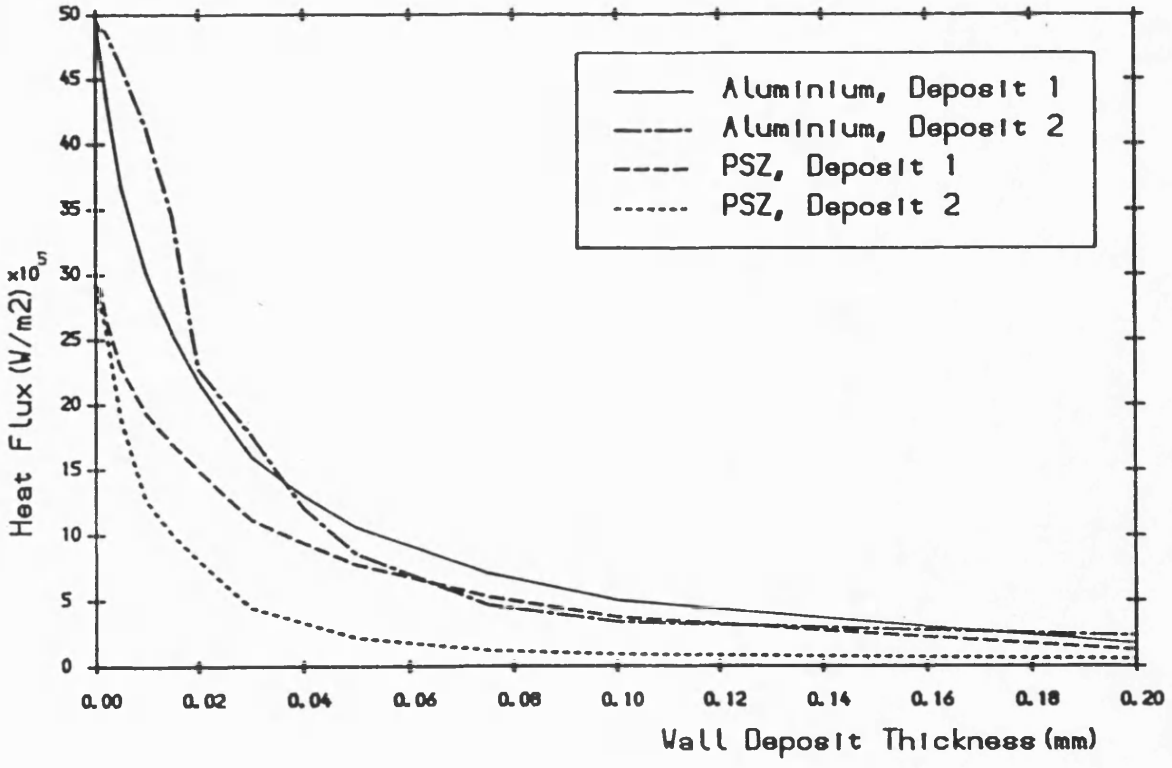

Fig. 7.78 The peak deposit-wall interface heat flux versus deposit thickness at aluminium and PSZ walls for 2 different deposit types.

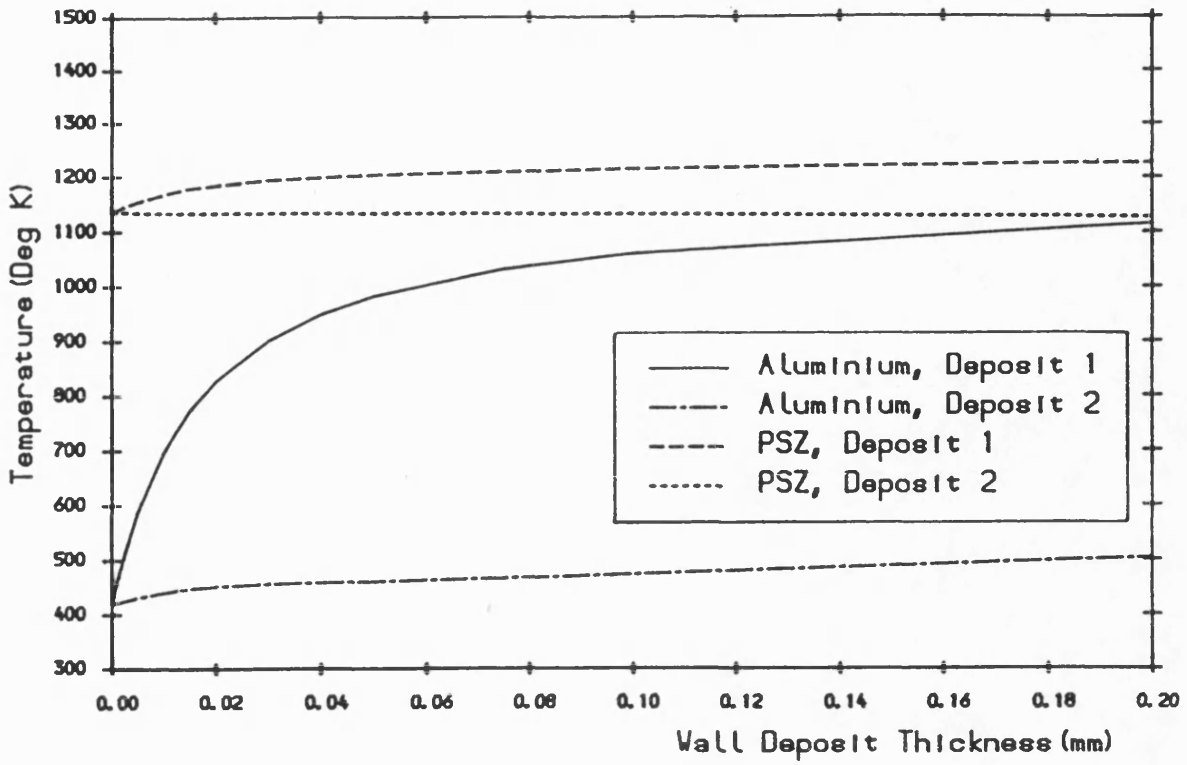

Fig. 7.79 The apparent wall deposit surface temperature versus deposit thickness at aluminium and PSZ walls for 2 different deposit types.

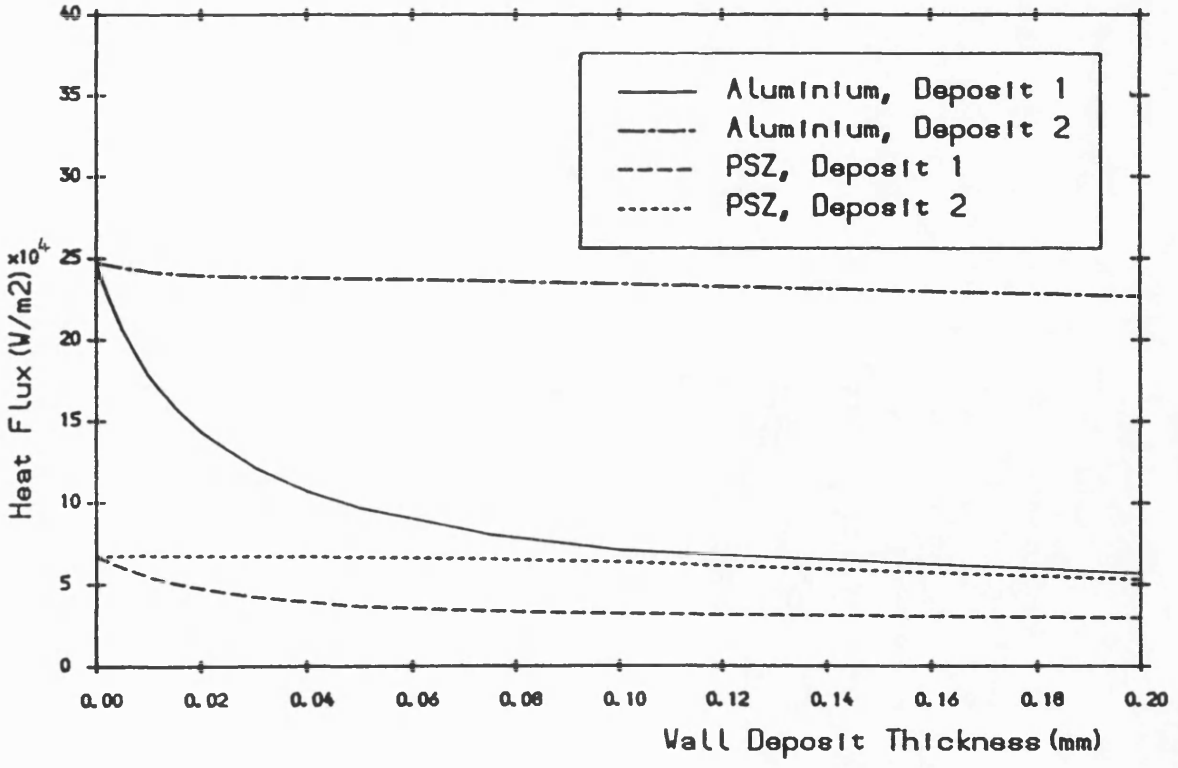

Fig. 7.80 The cycle mean heat flux versus deposit thickness at aluminium and PSZ walls for 2 different deposit types.

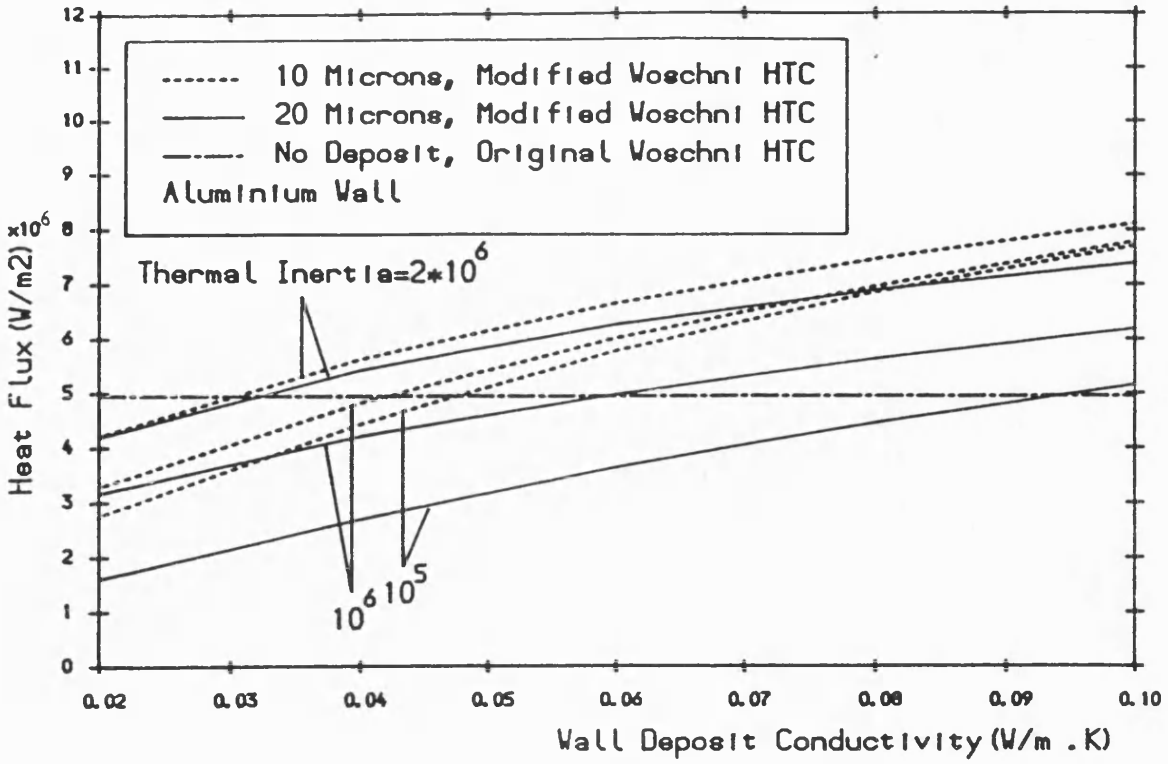

Fig. 7.81 The peak wall deposit surface heat flux versus deposit conductivity at various thermal inertias for 2 different deposit thicknesses.

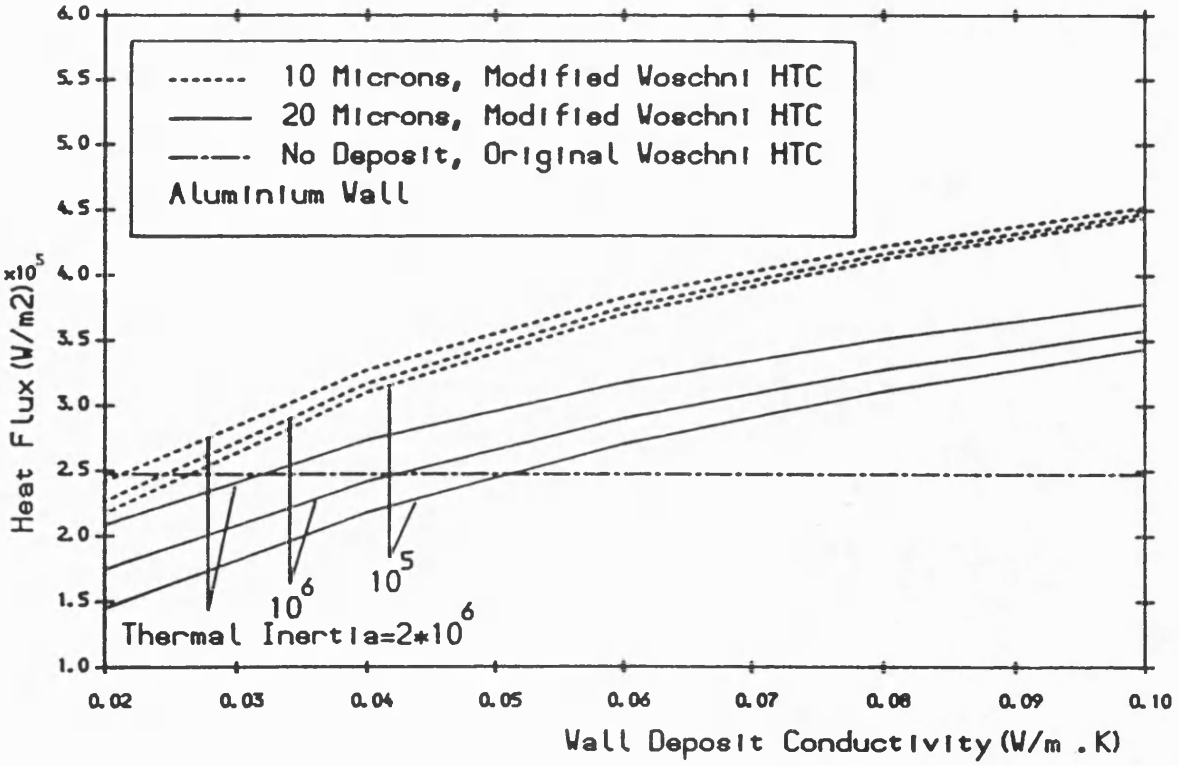

Fig. 7.82 The cycle mean heat flux versus deposit conductivity at various thermal inertias for 2 different deposit thicknesses.

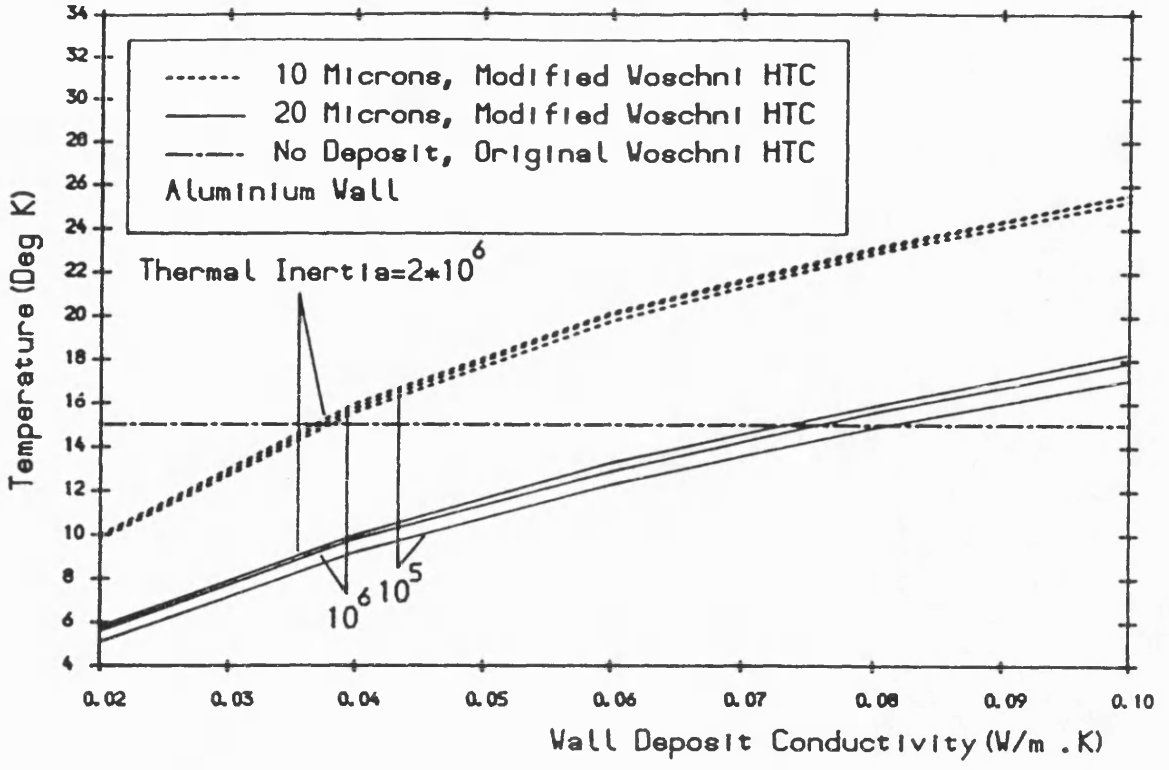

Fig. 7.83 The deposit-wall interface temperature swing versus deposit conductivity at various thermal inertias for 2 different deposit thicknesses.

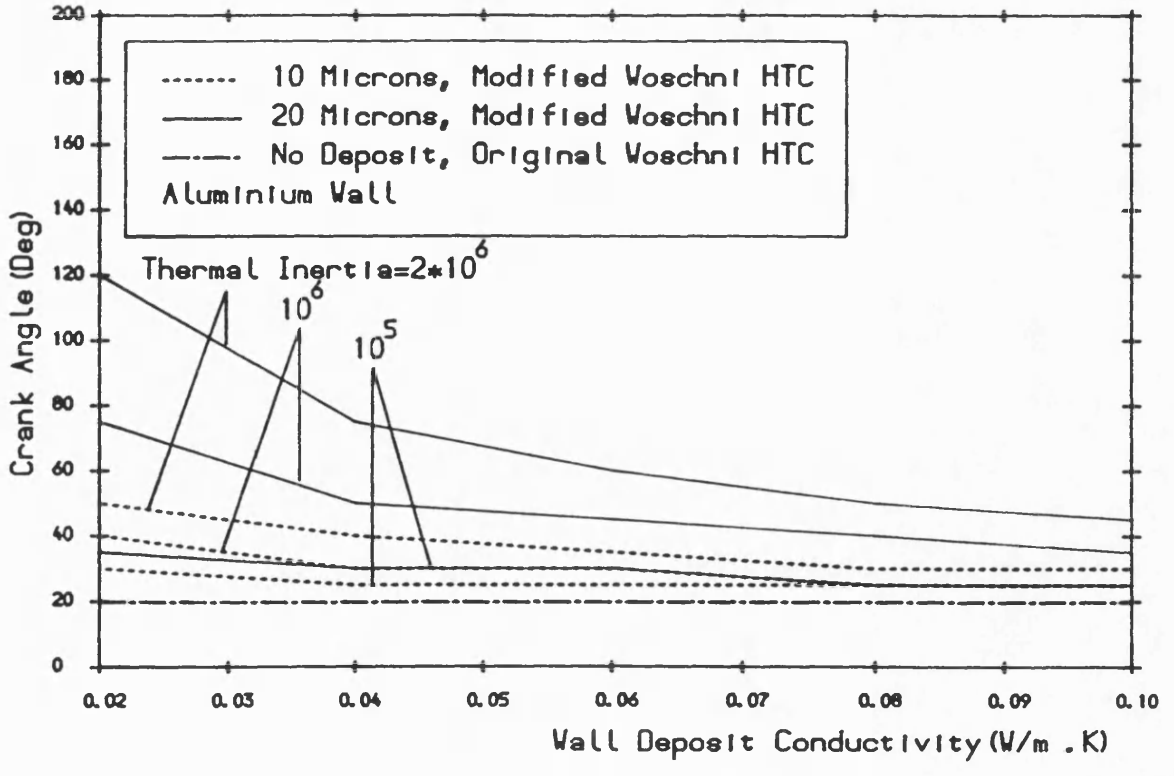

Fig. 7.84 The deposit-wall interface peak temperature timing versus deposit conductivity at various thermal inertias for 2 different deposit thicknesses.

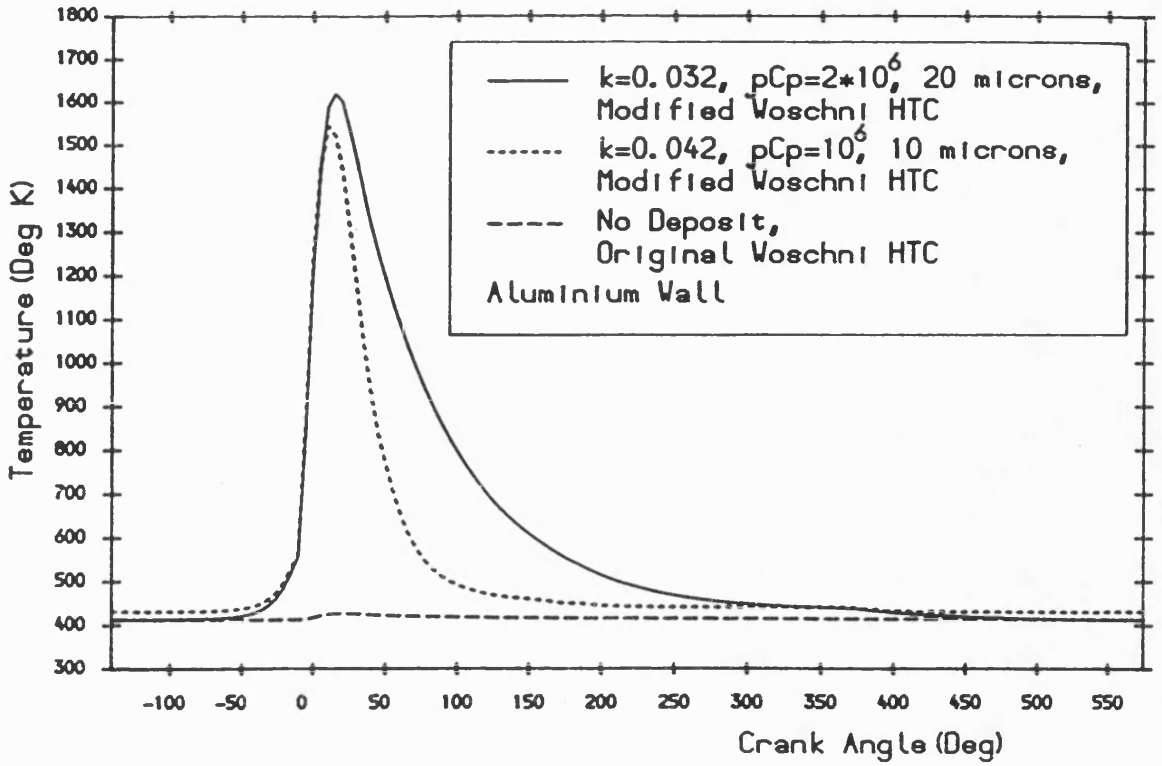

Fig. 7.85 The surface temperature versus crank angle for the specified wall deposits.

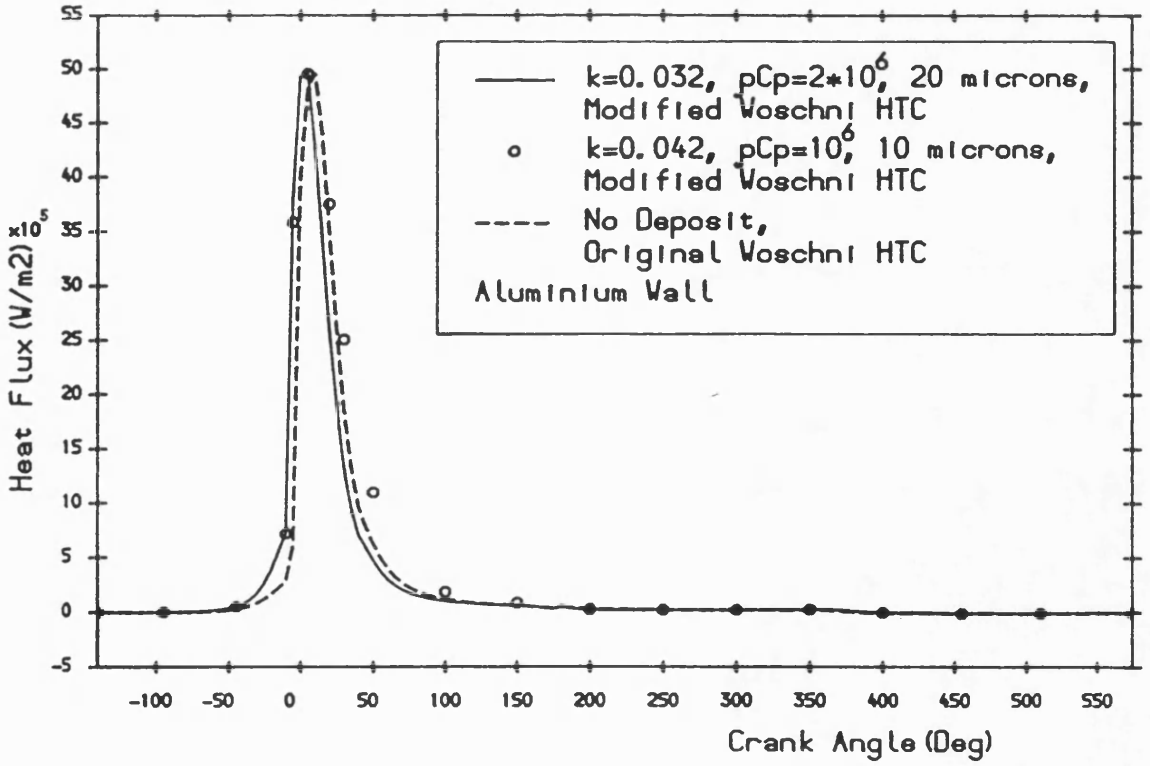

Fig. 7.86 The surface heat flux versus crank angle for the specified wall deposits.

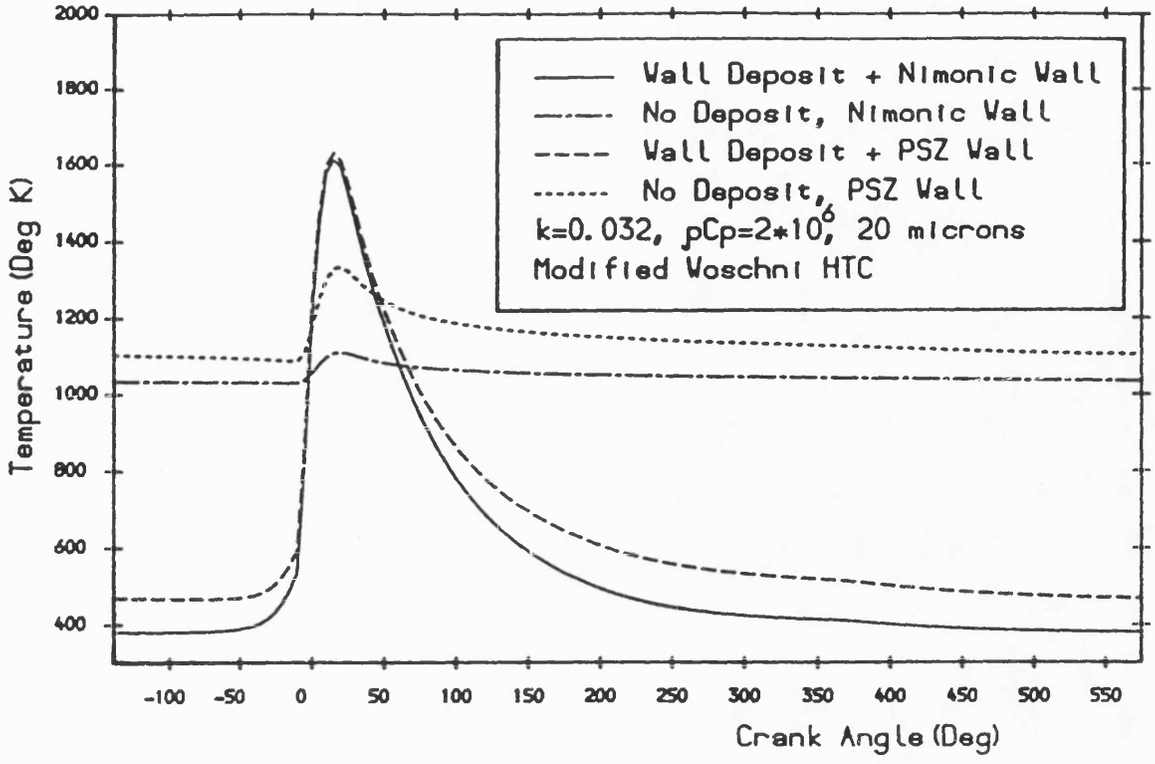

Fig. 7.87 The surface temperature versus crank angle for cold and hot Nimonic and PSZ walls with wall deposit effects.

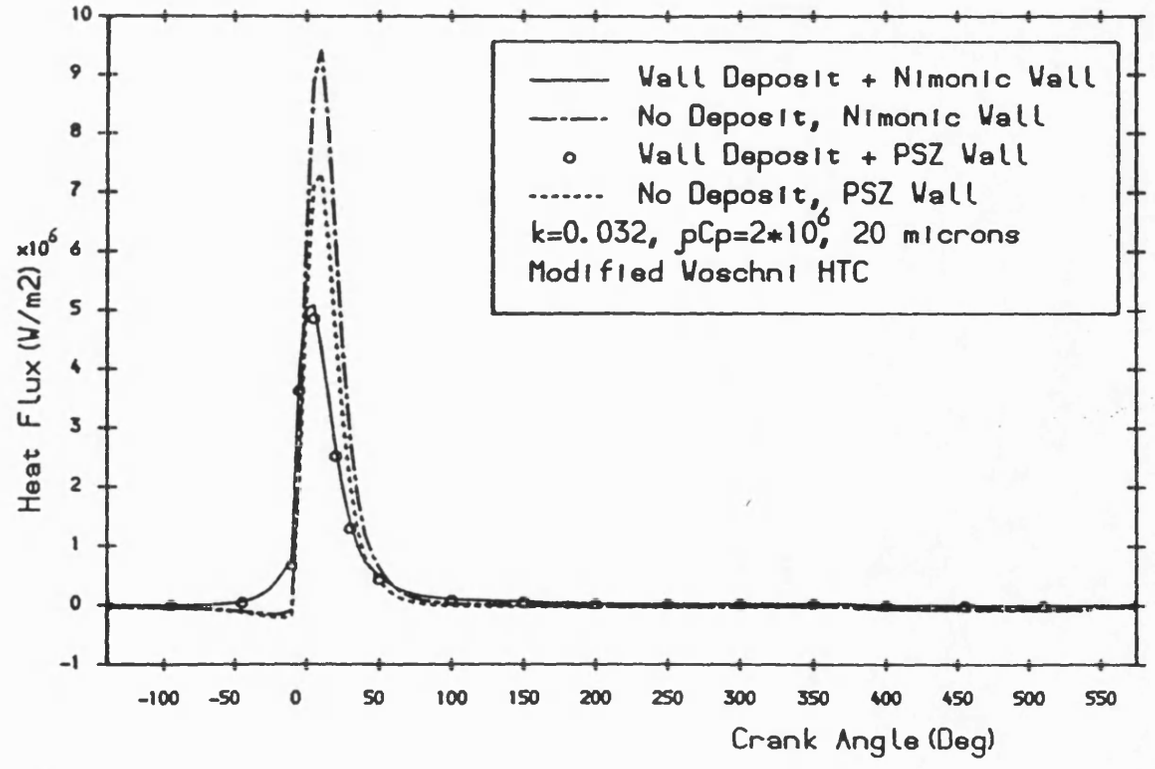

Fig. 7.88 The surface heat flux versus crank angle for cold and hot Nimonic and PSZ walls with wall deposit effects.

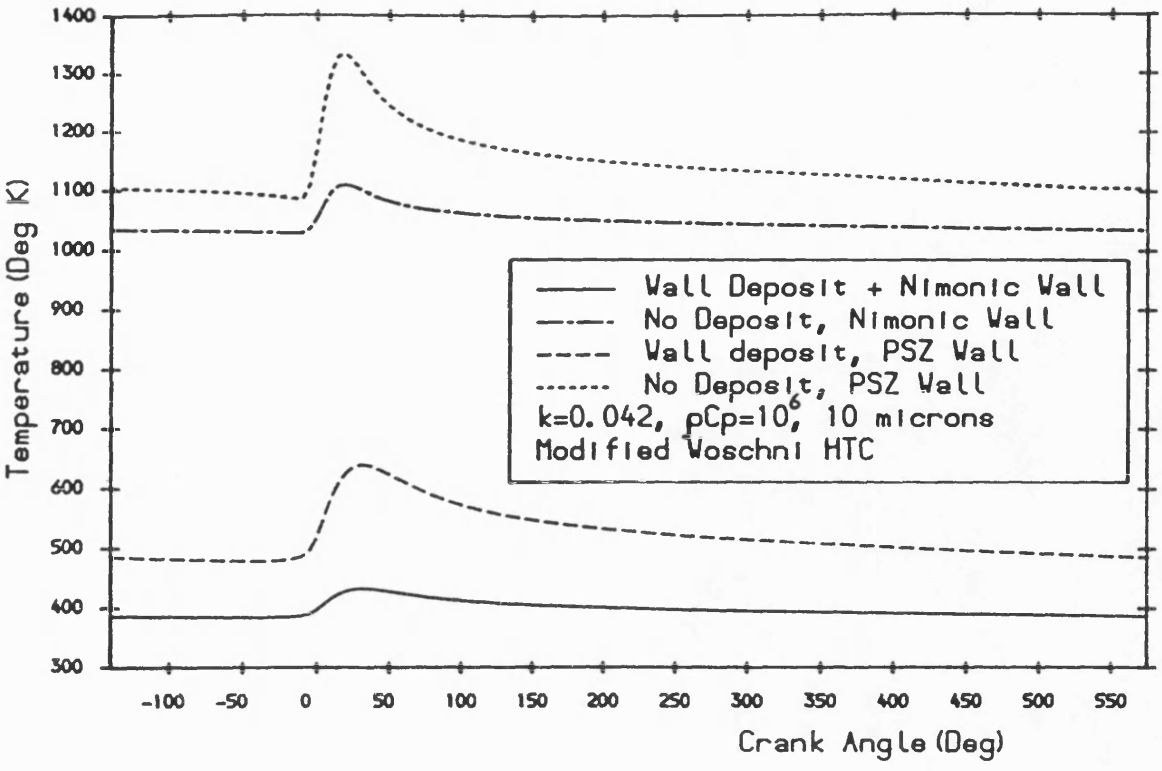

Fig. 7.89 The deposit-wall interface temperature versus crank angle for cold and hot Nimonic and PSZ walls with wall deposit effects.

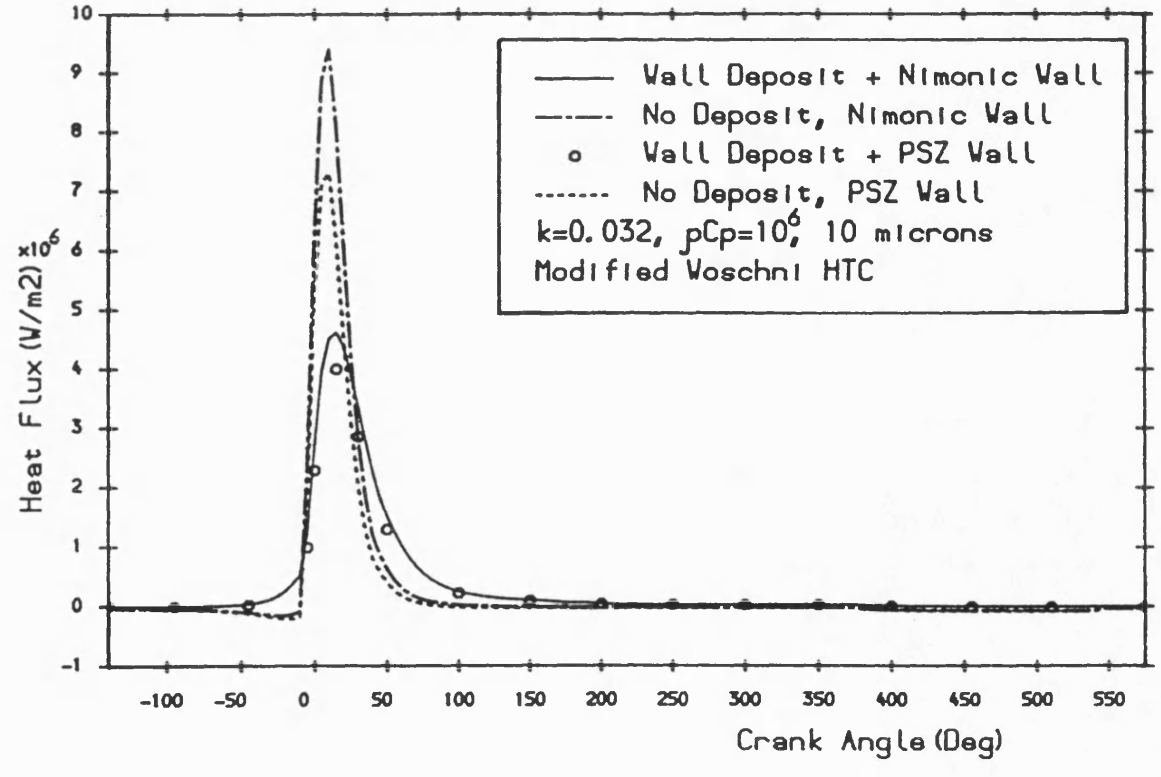

Fig. 7.90 The deposit-wall interface heat flux versus crank angle for cold and hot Nimonic and PSZ walls with wall deposit effects.

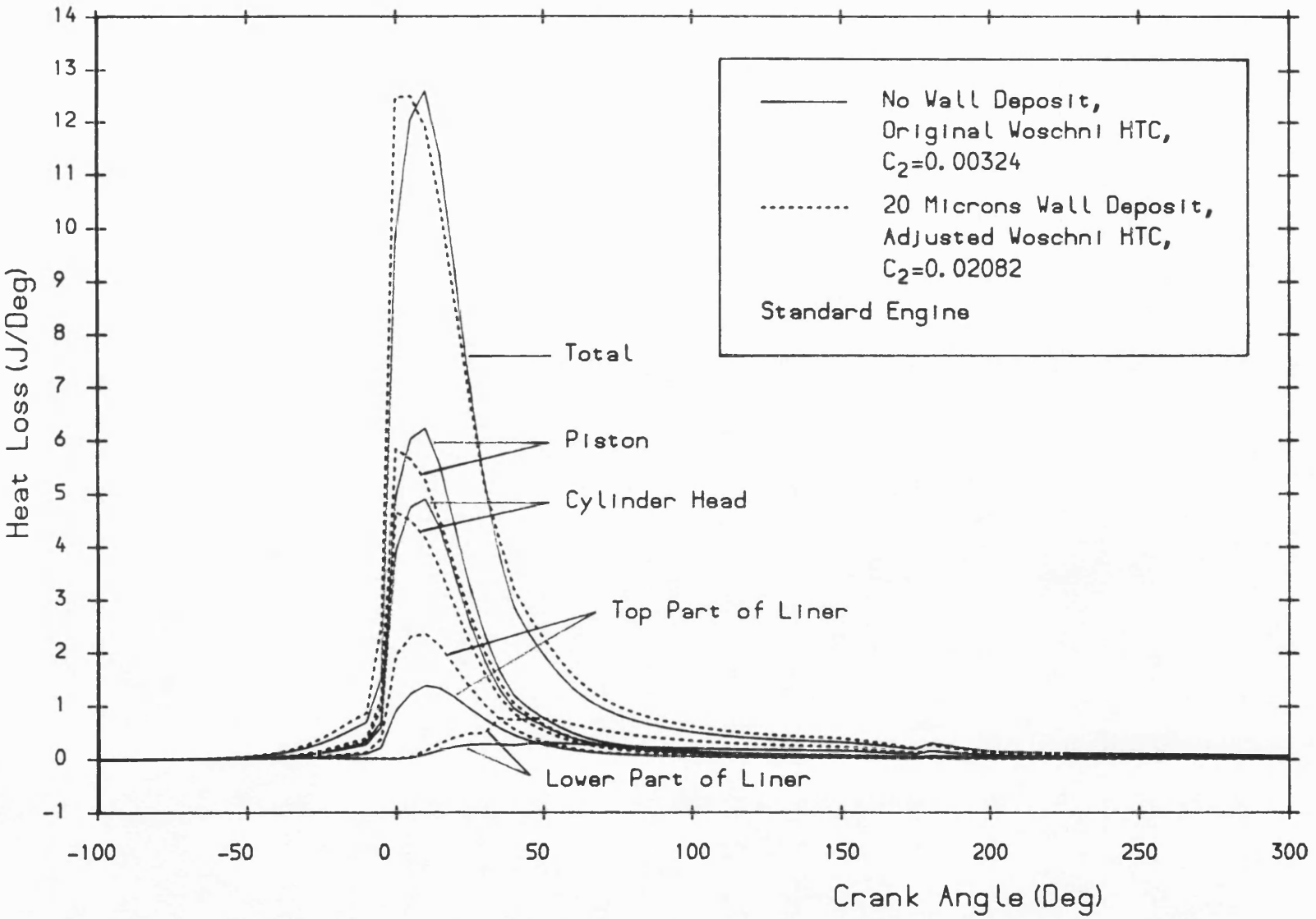

Fig. 7.91 Gas heat loss versus crank angle for clean and deposit covered walls with original and adjusted Woschni htc correlations.

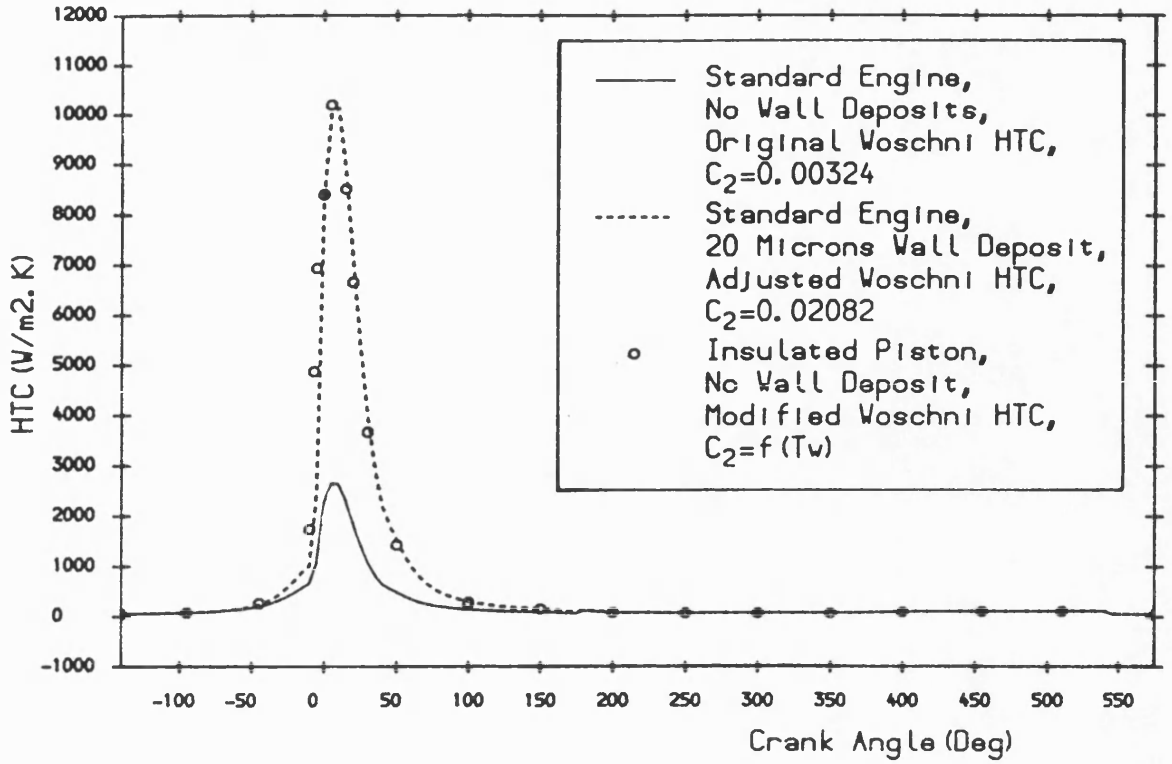

Fig. 7.92 Adjusted gas htc versus crank angle for the wall deposit application.

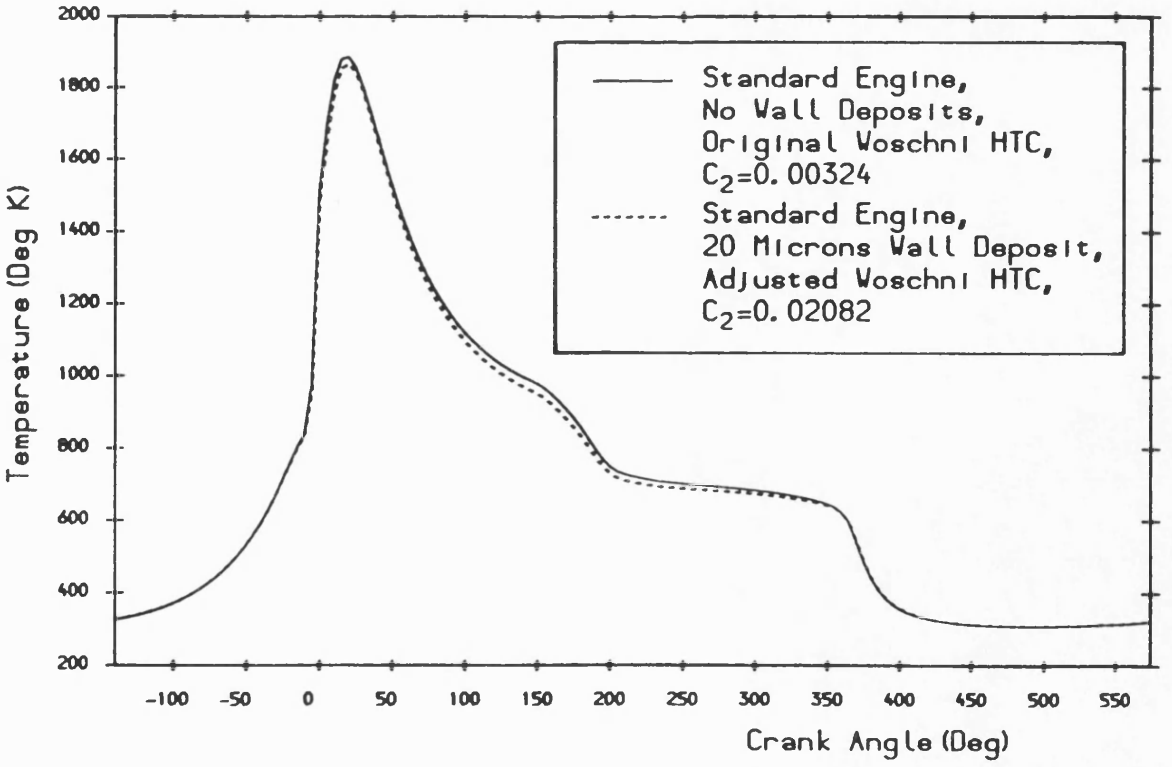

Fig. 7.93 Cylinder gas temperature versus crank angle for clean and deposit covered wall cases.

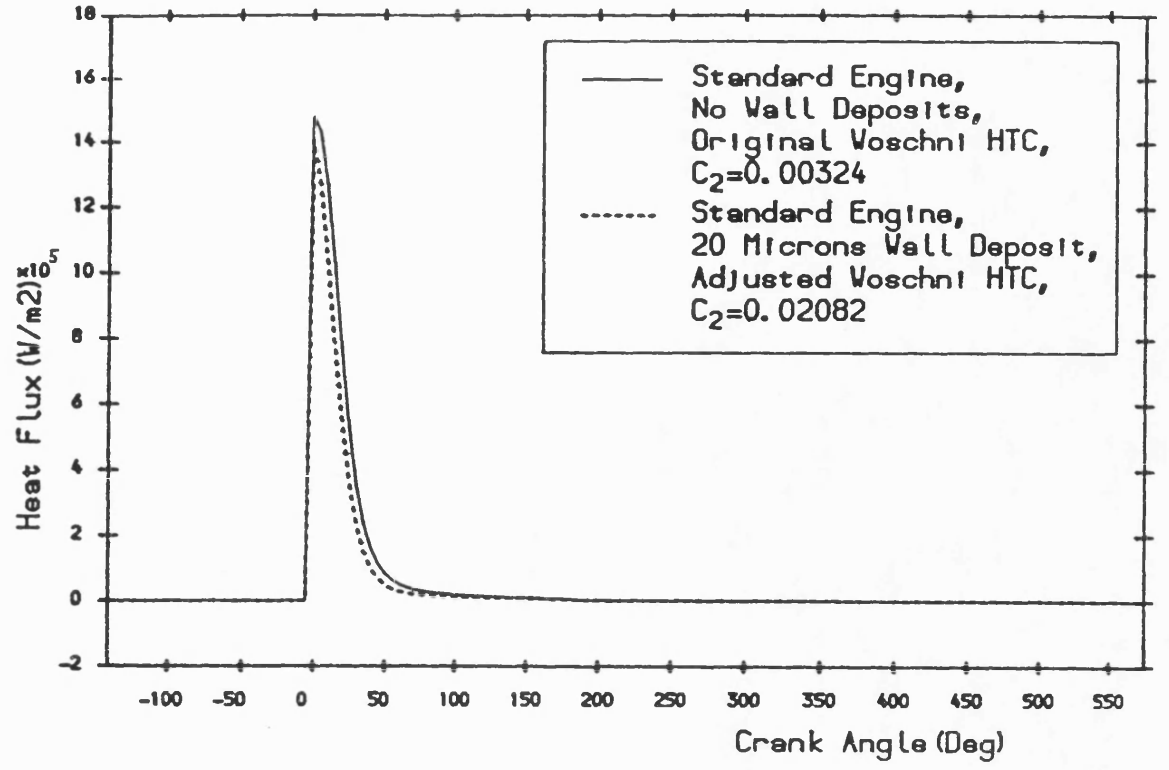

Fig. 7.94 Radiative heat flux versus crank angle for clean and deposit covered wall cases.

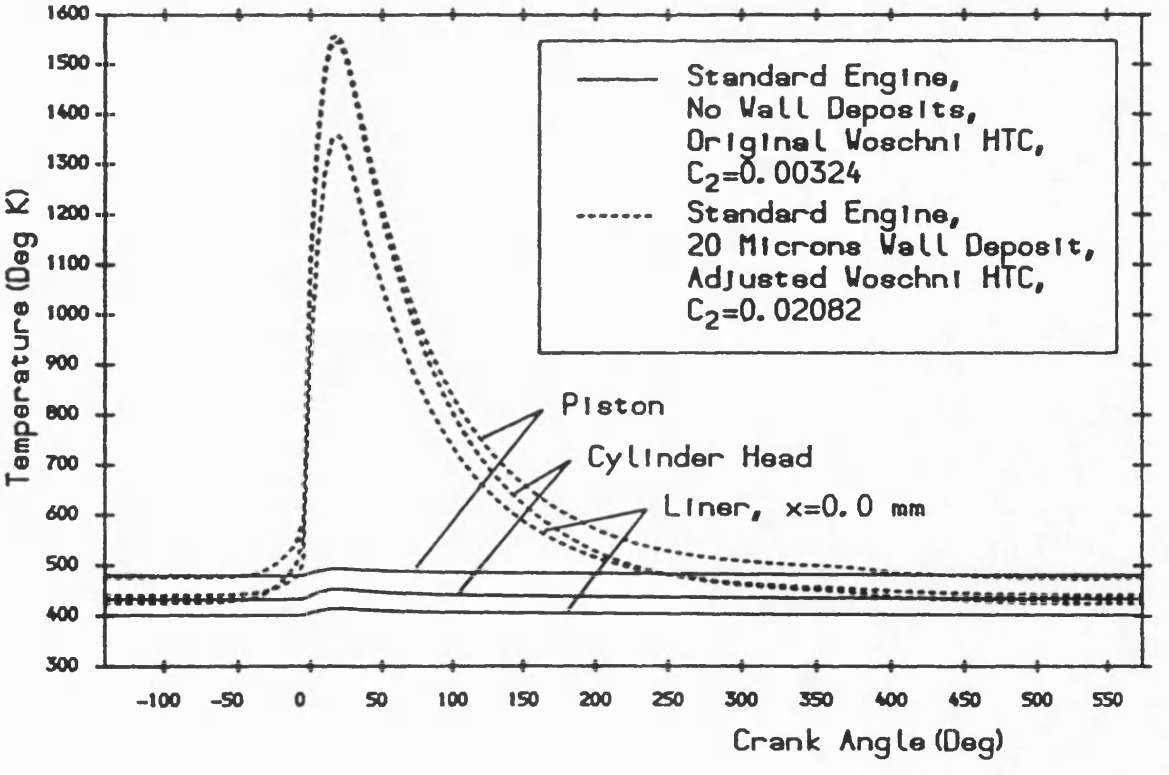

Fig. 7.95 Surface temperature versus crank angle at various parts of the combustion chamber for clean and deposit covered wall cases.

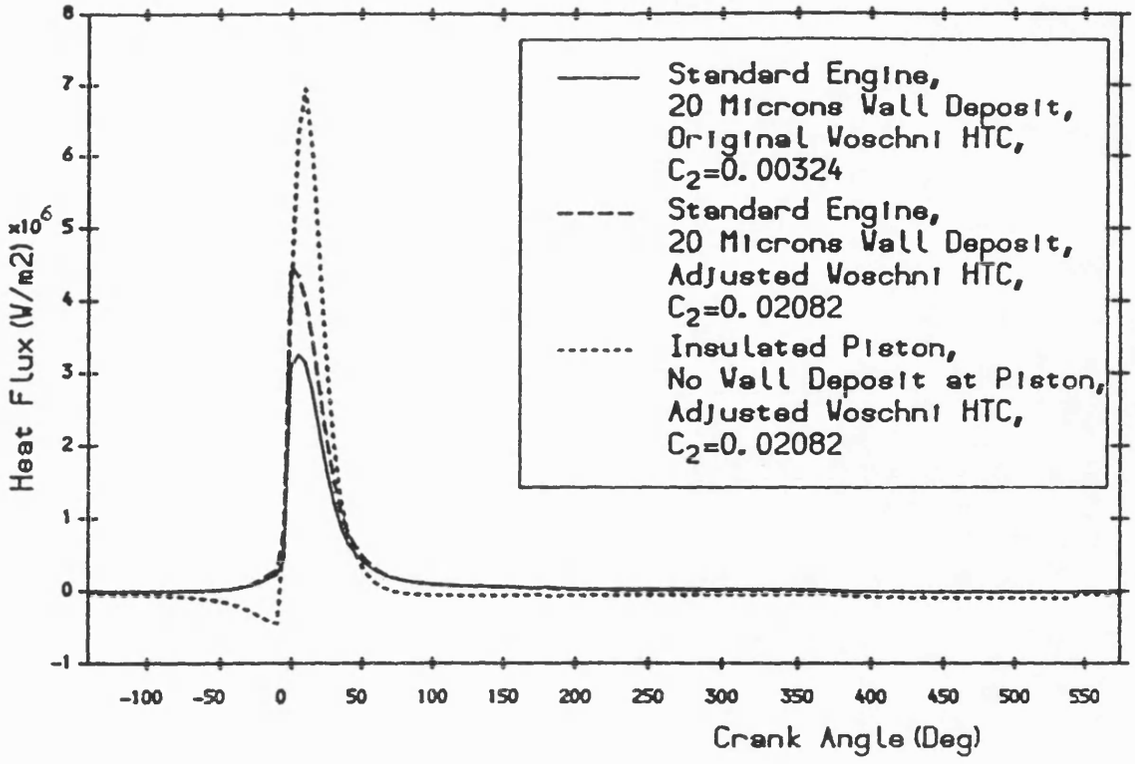

Fig. 7.96 The effect on piston surface heat flux with piston deposits eliminated by insulating.

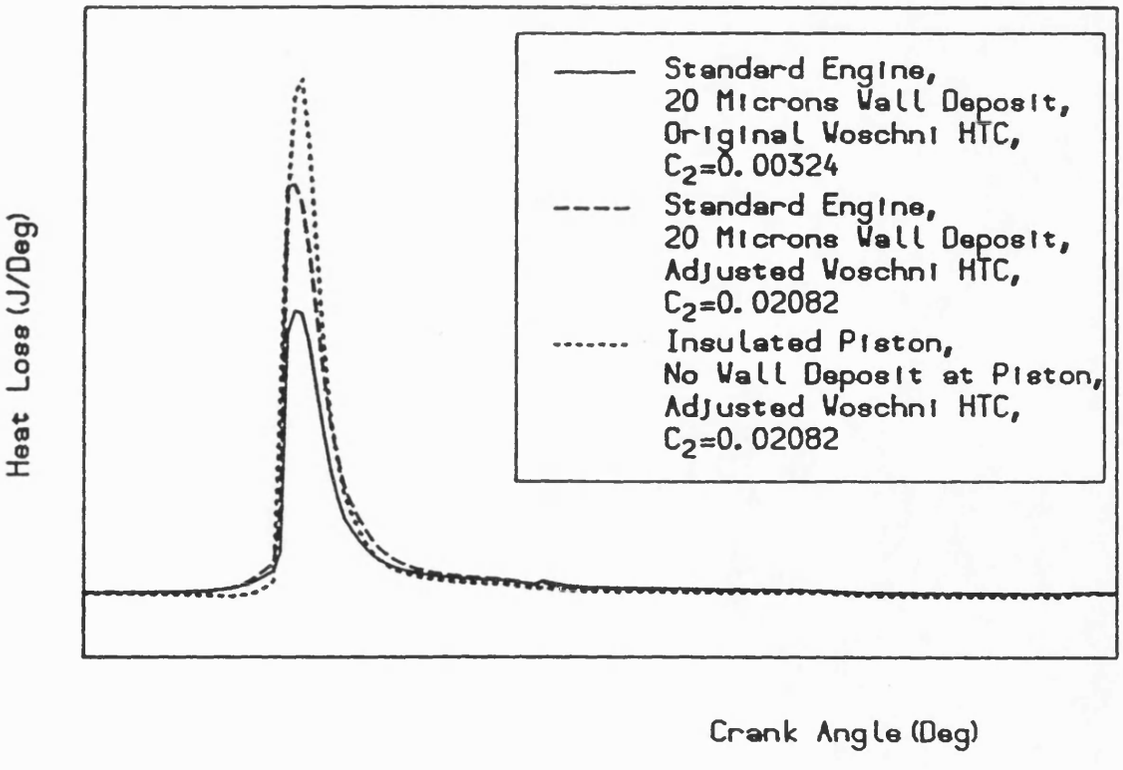

Fig. 7.97 The effect on gas to wall heat loss with piston deposits eliminated by insulating.

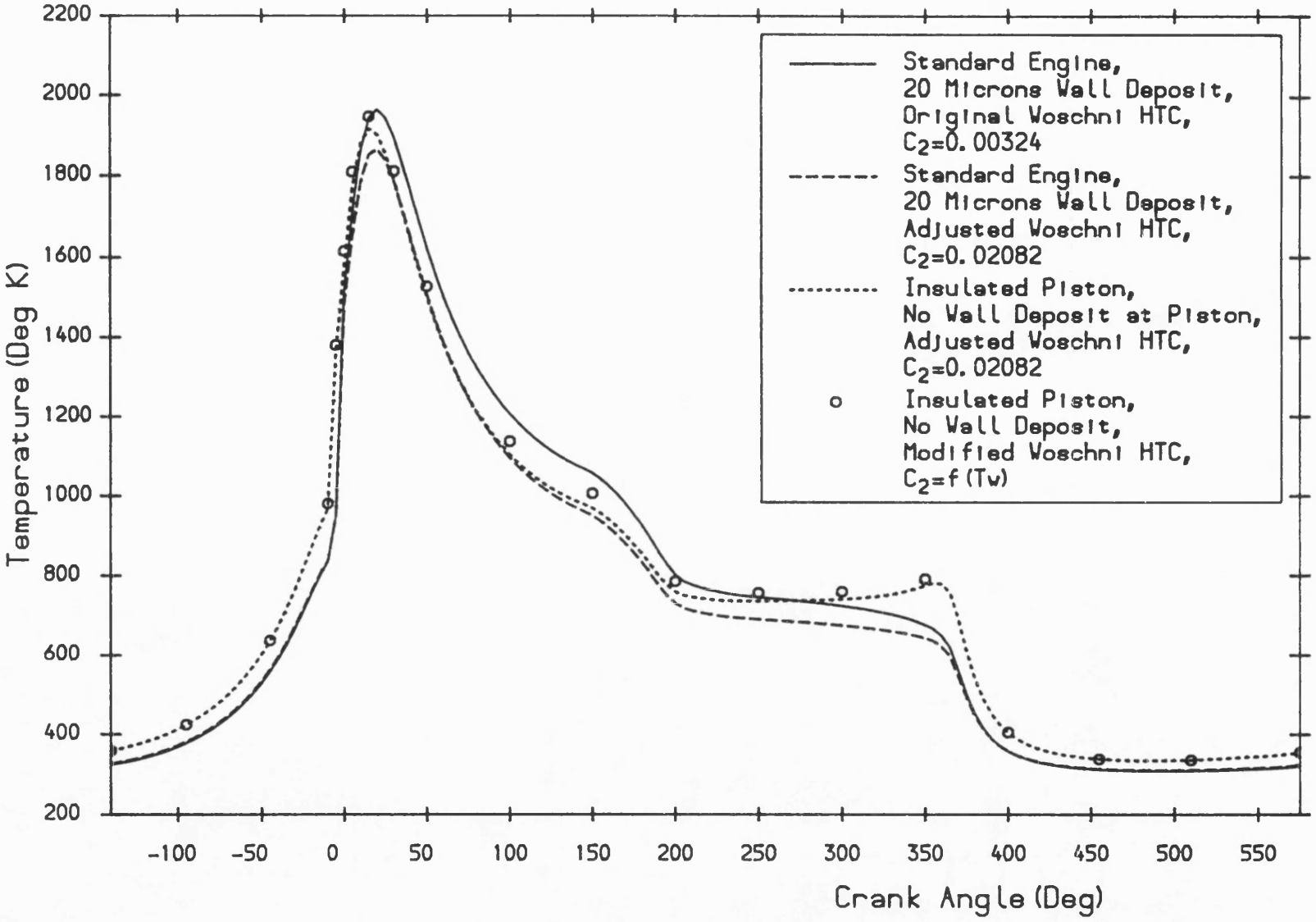

Fig. 7.98 The effect on cylinder gas temperature with piston deposits eliminated by insulating.

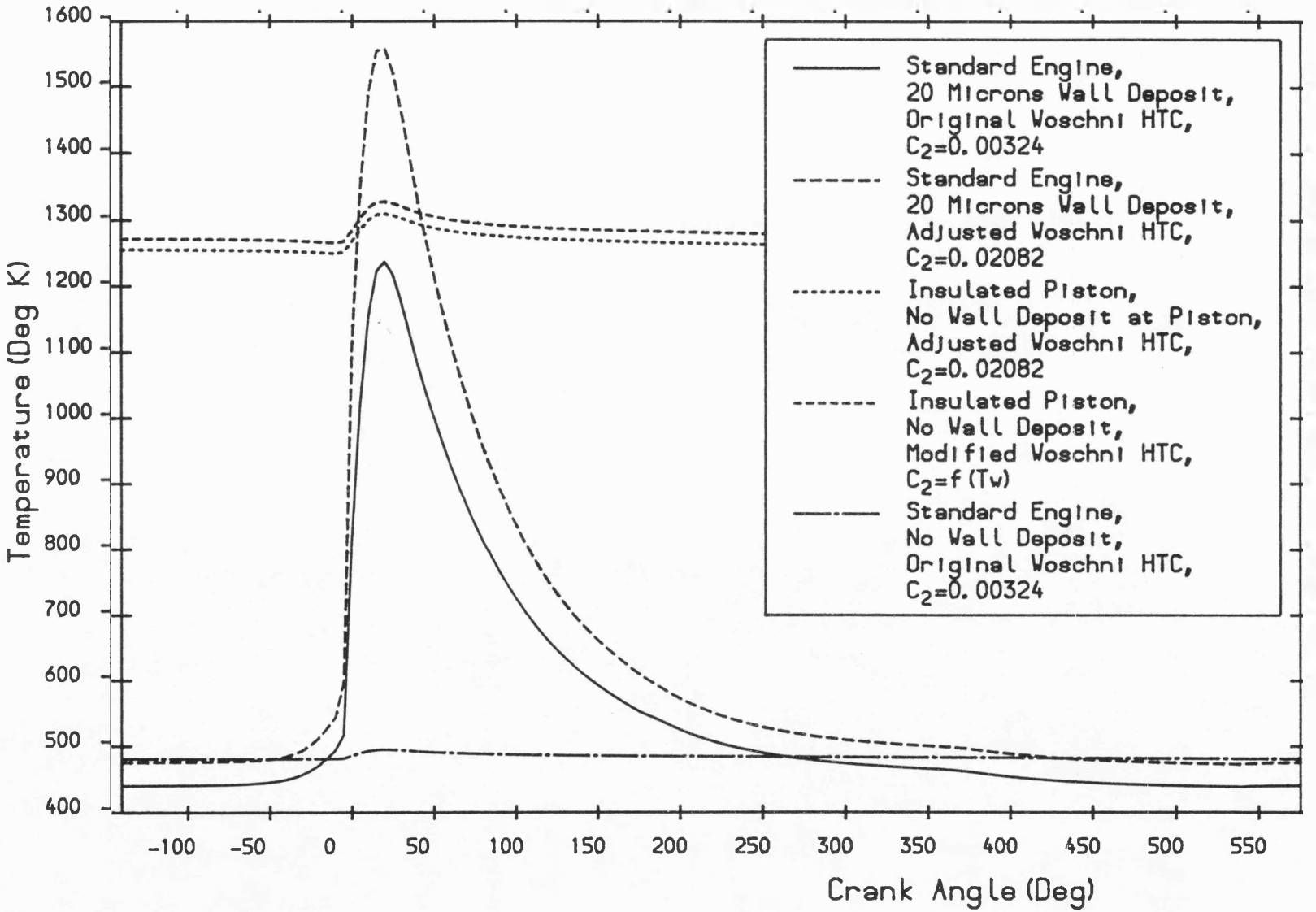

Fig. 7.99 Piston surface temperature versus crank angle with and without wall deposits, for various types of Woschni htc correlations.

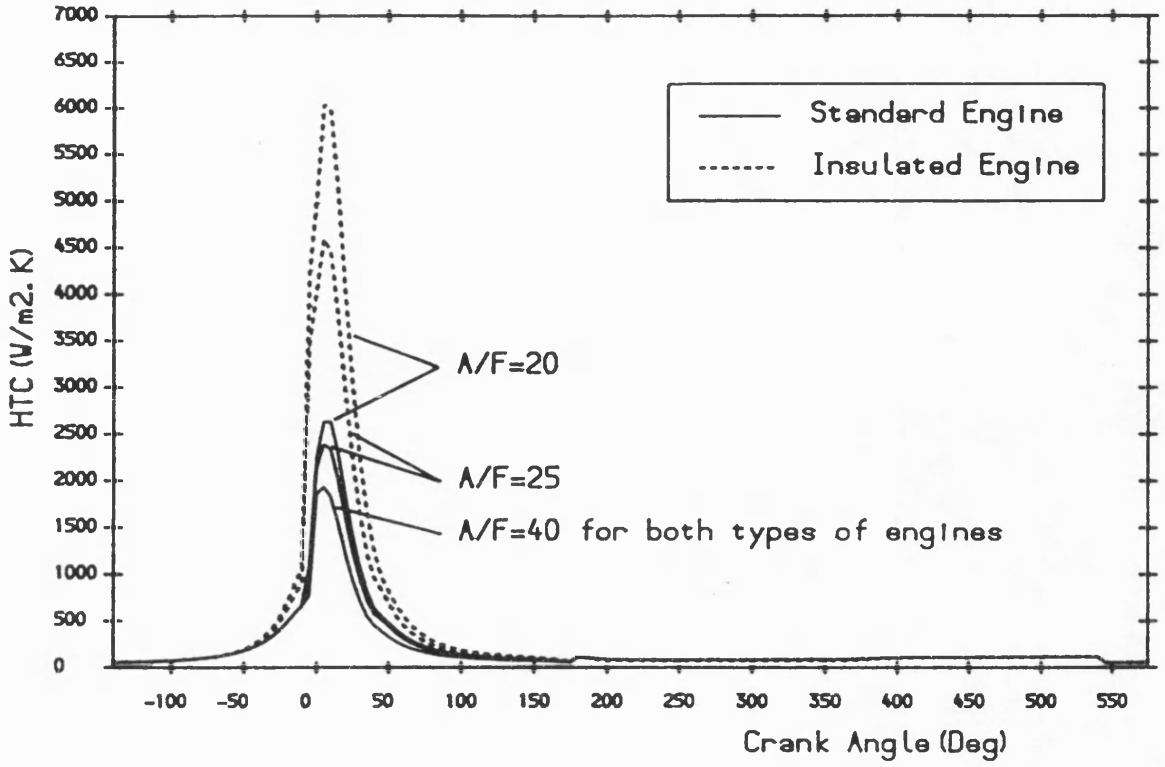

Fig. 7.100 Piston gas htc versus crank angle for standard and 1.5 mm PSZ coated engines at various air-fuel ratios obtained with the modified Woschni htc correlation.

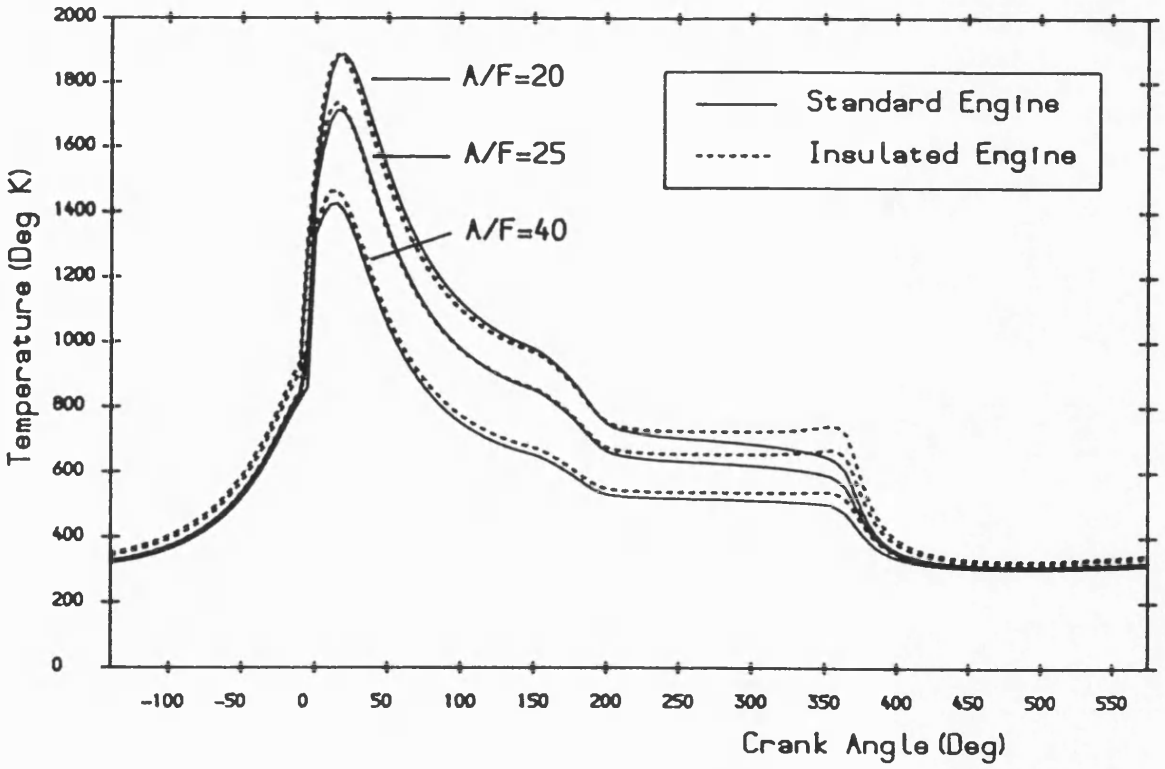

Fig. 7.101 Gas temperature versus crank angle for standard and 1.5 mm PSZ coated engines at various air-fuel ratios obtained with the modified Woschni htc correlation.

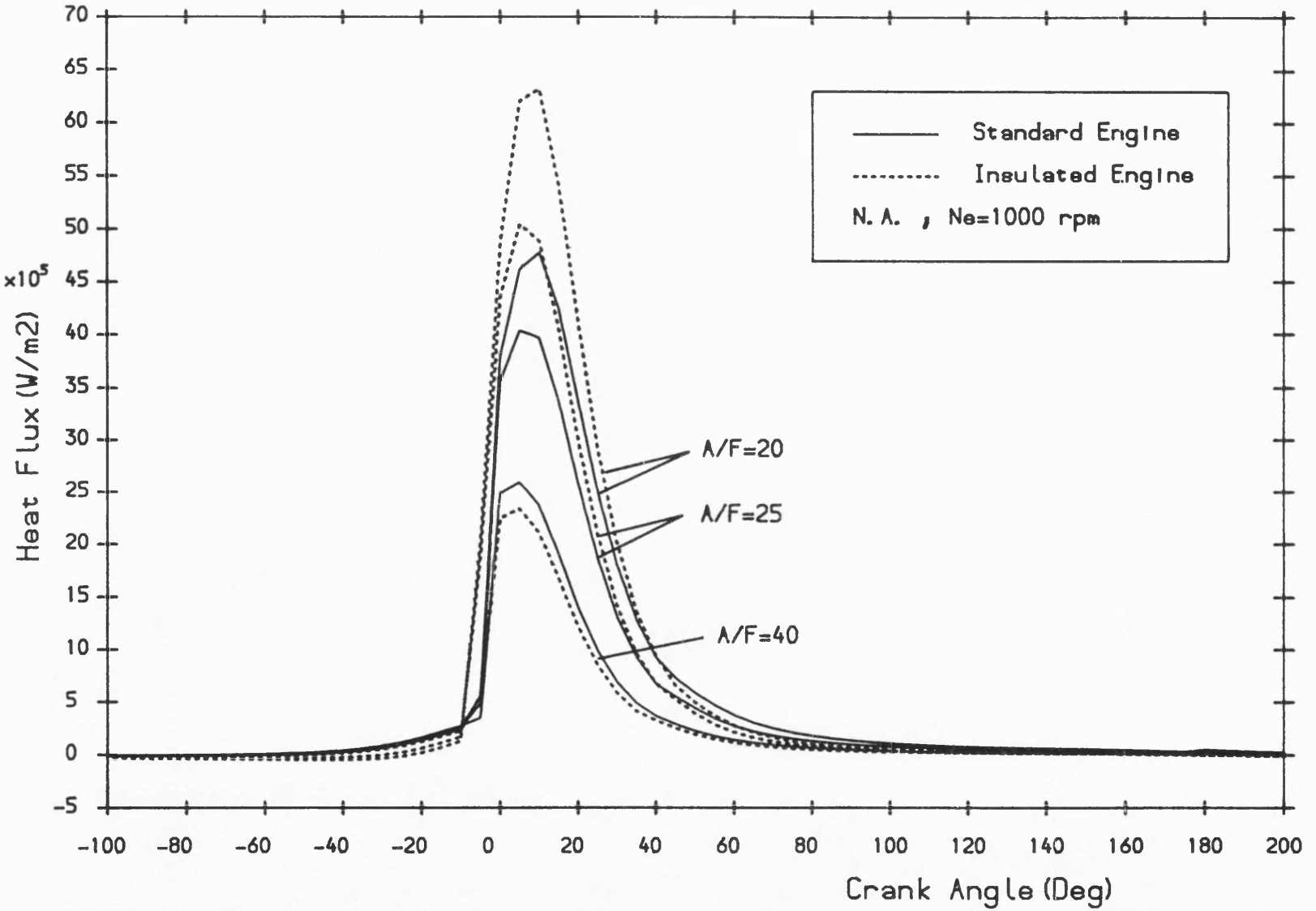

Fig. 7.102 Piston surface heat flux versus crank angle at various air-fuel ratios for standard and 1.5 mm PSZ coated engines obtained with the modified Woschni htc correlation.

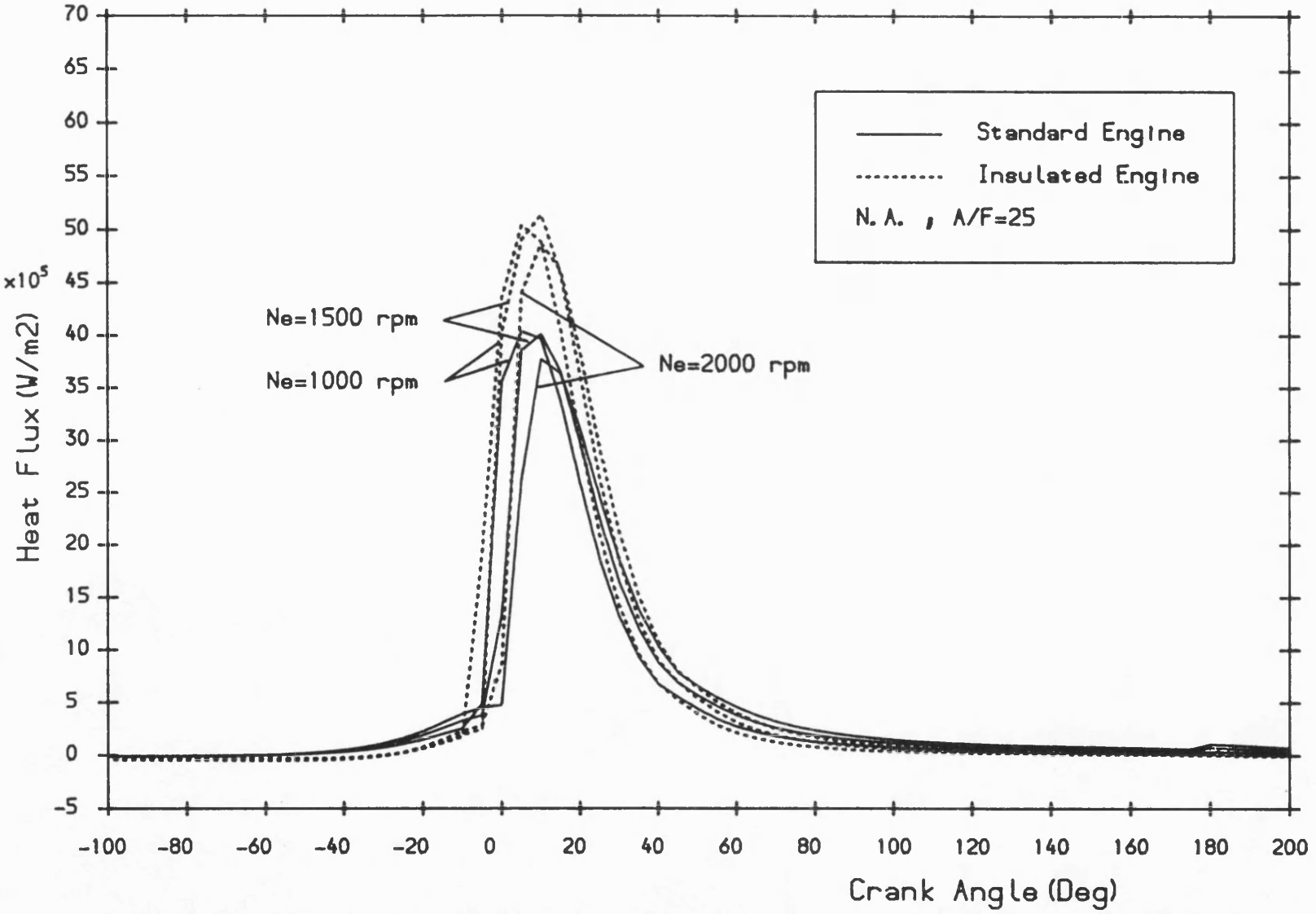

Fig. 7.103 Piston surface heat flux versus crank angle at various engine speeds for standard and 1.5 mm PSZ coated engines obtained with the modified Woschni htc correlation.

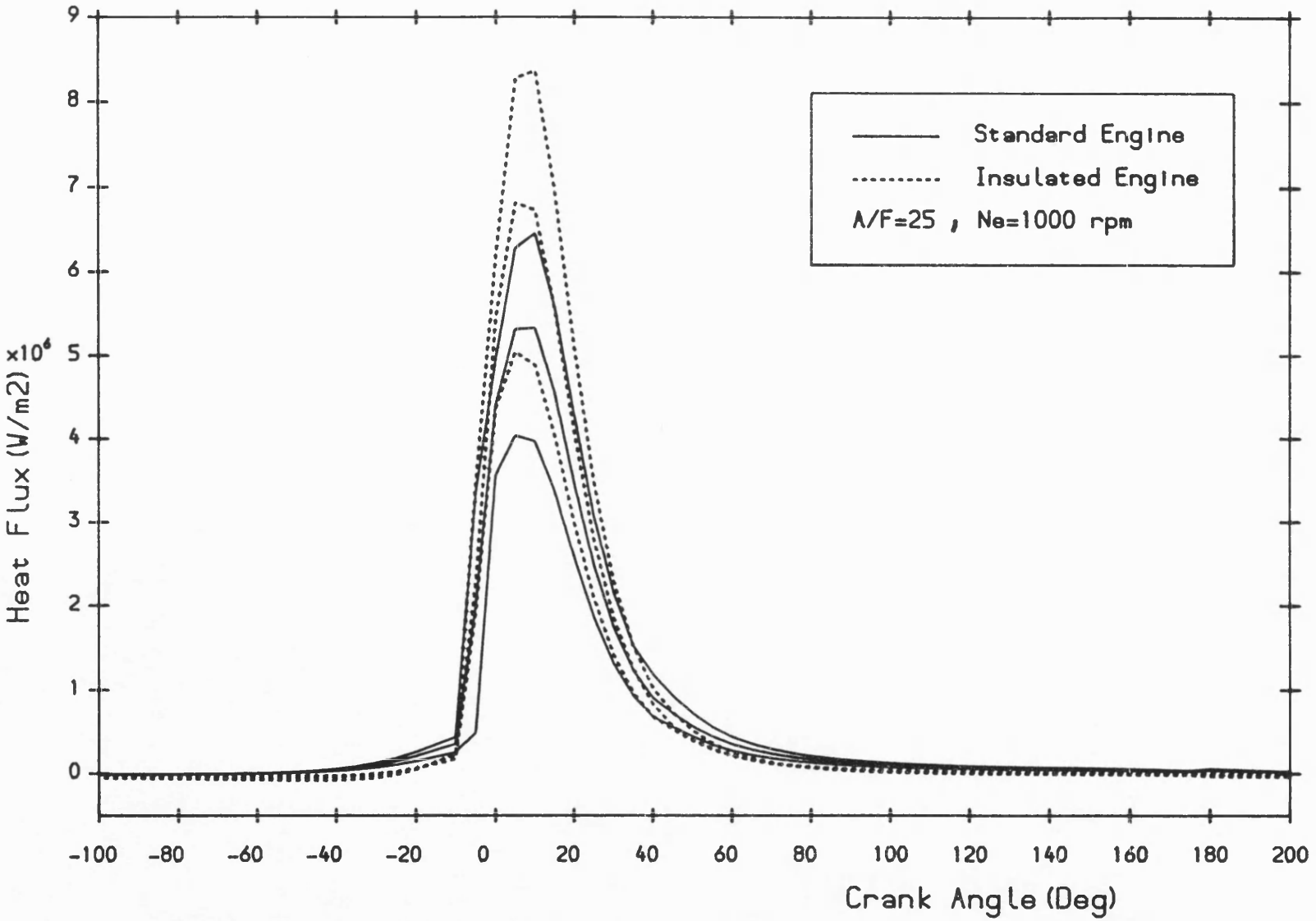

Fig. 7.104 Piston surface heat flux versus crank angle at various boost levels for standard and 1.5 mm PSZ coated engines obtained with the modified Woschni htc correlation.

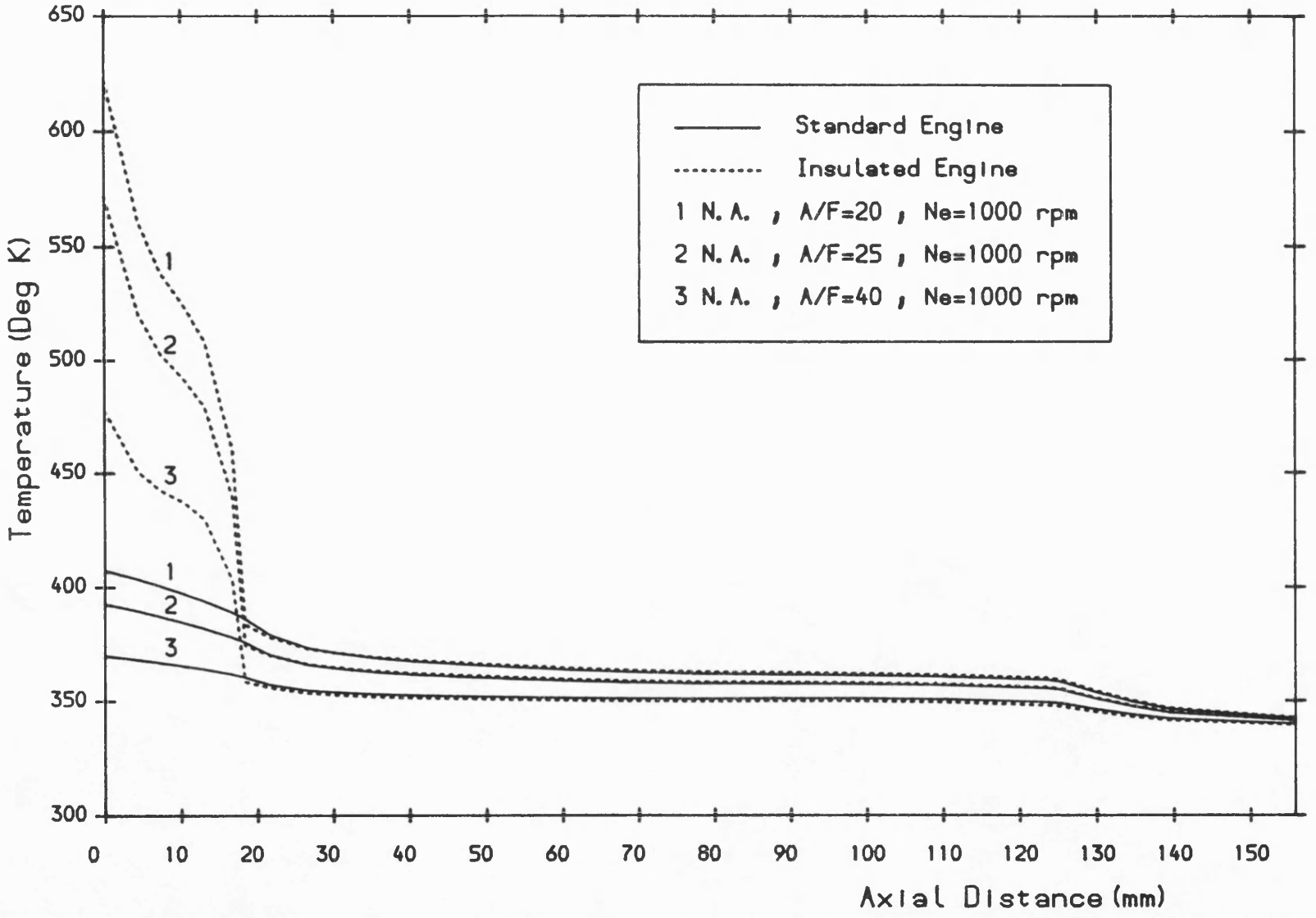

Fig. 7.105 Liner surface temperature versus axial distance at various air-fuel ratios for standard and 1.5 mm PSZ coated engines obtained with the modified Woschni htc correlation.

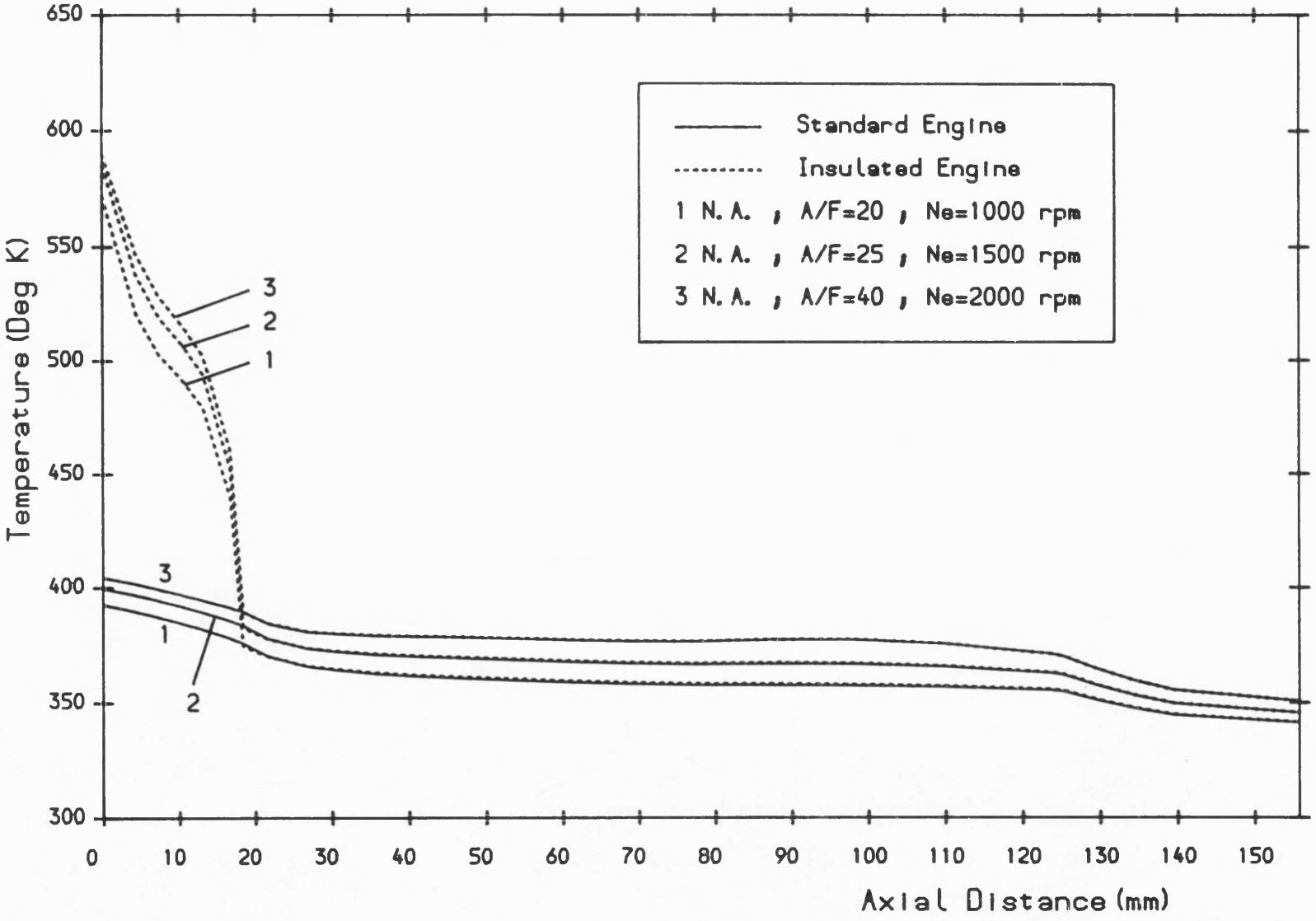

Fig. 7.106 Liner surface temperature versus axial distance at various engine speeds for standard and 1.5 mm PSZ coated engines obtained with the modified Woschni htc correlation.

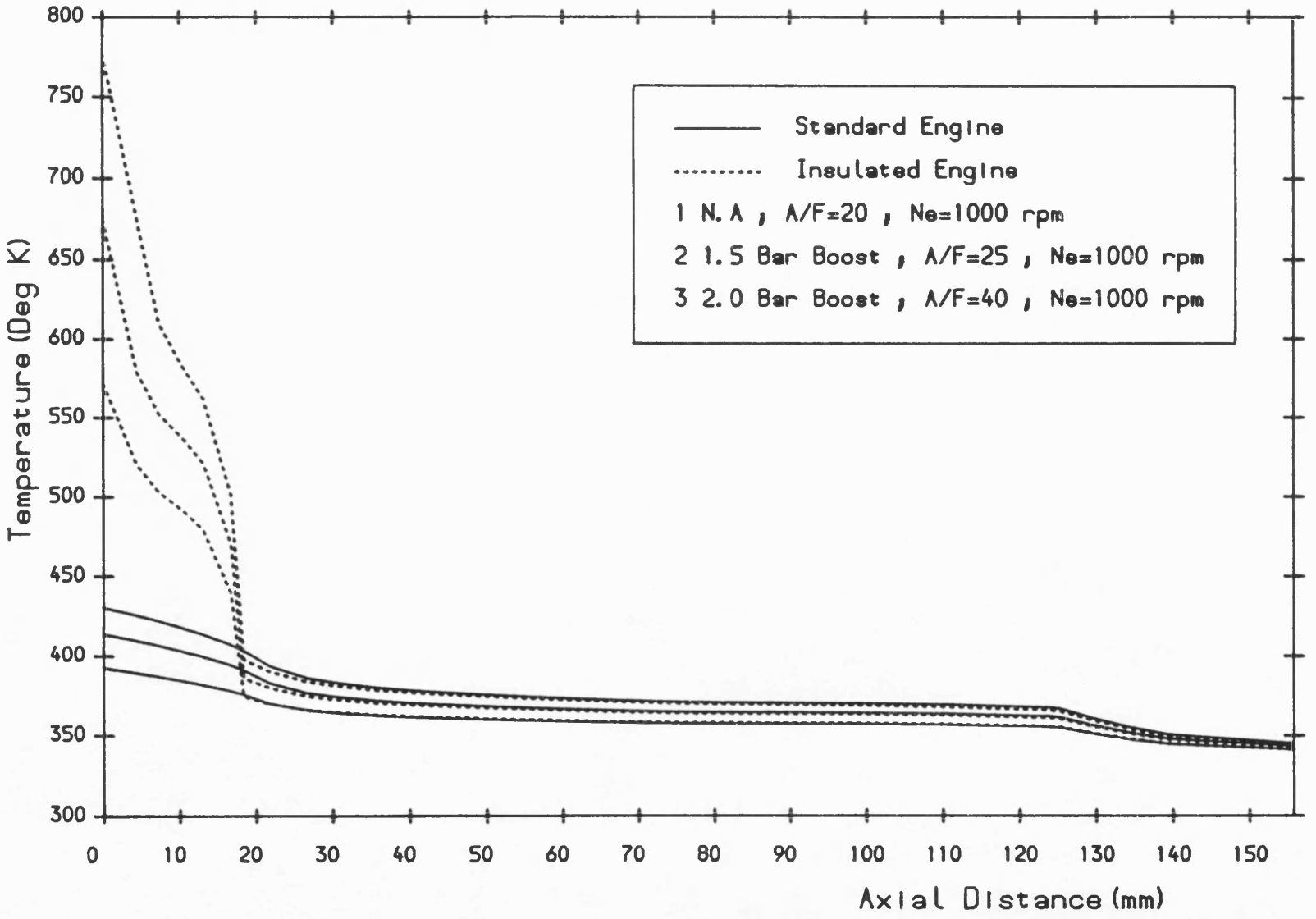

Fig. 7.107 Liner surface temperature versus axial distance at various boost levels for standard and 1.5 mm PSZ coated engines obtained with the modified Woschni htc correlation.

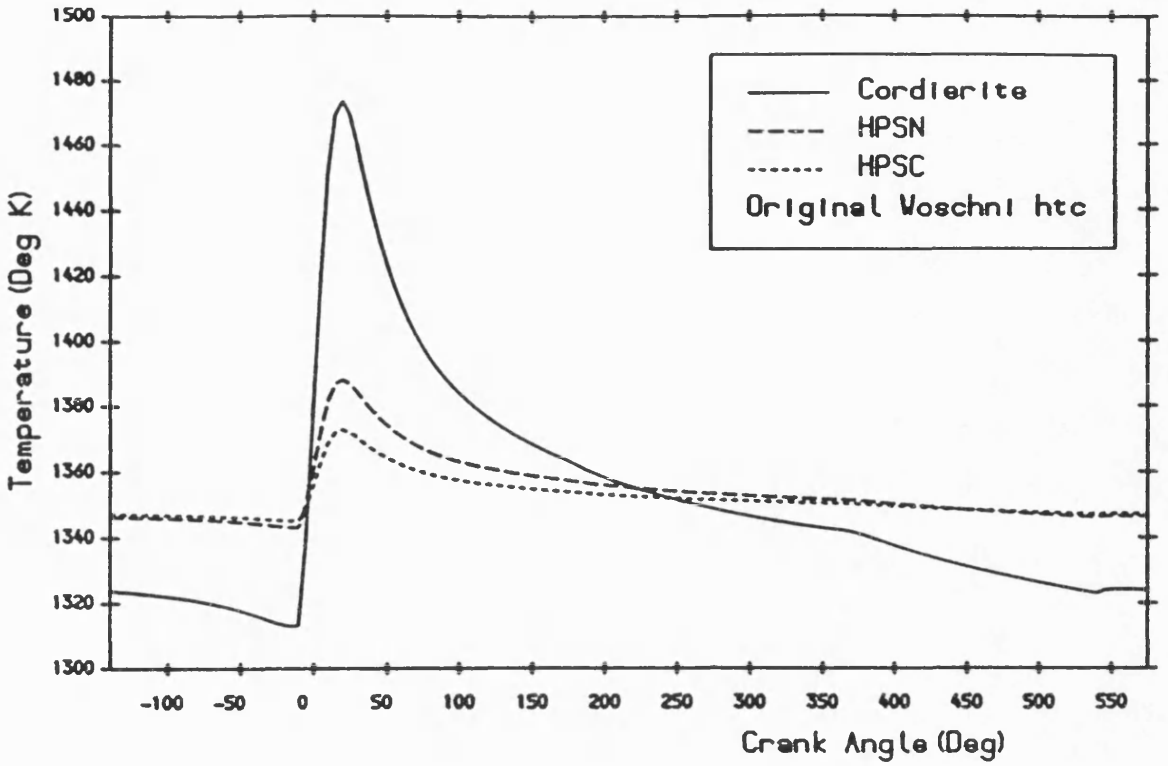

Fig. 7.108 Surface temperature versus crank angle for various ceramic pistons obtained with the original Woschni htc correlation in Sec. 7.5.

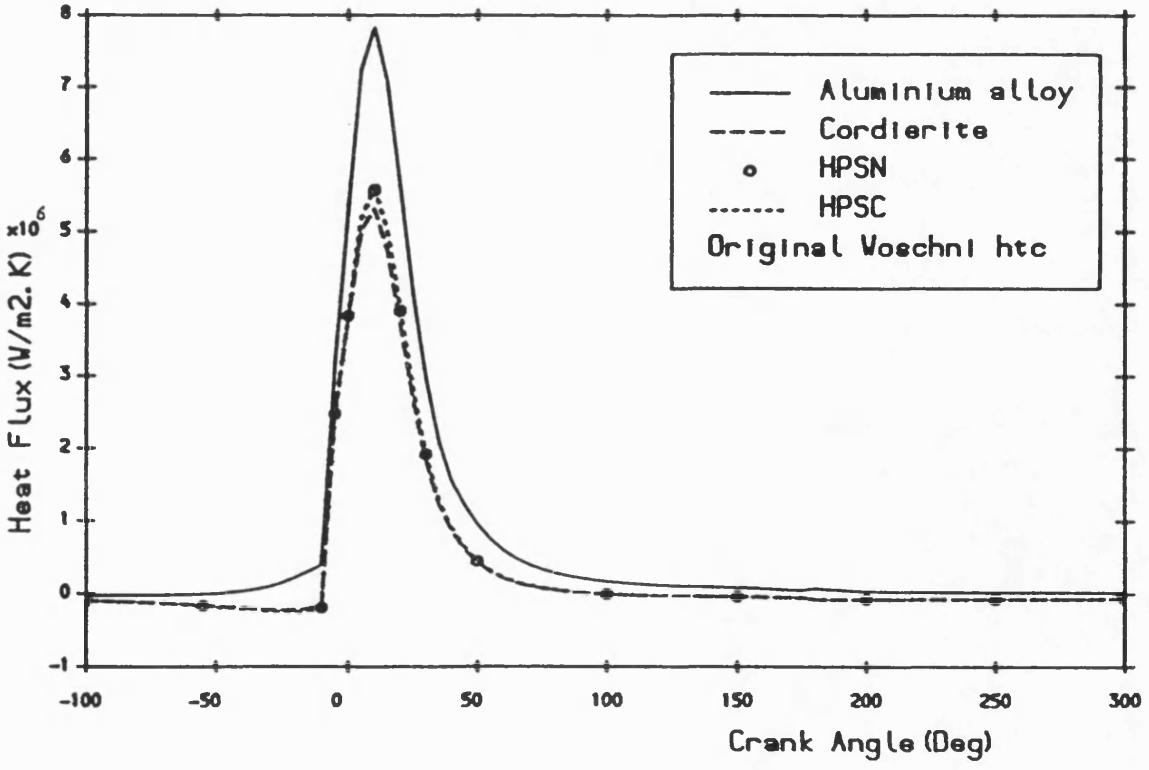

Fig. 7.109 Surface heat flux versus crank angle for various ceramic pistons obtained with the original Woschni htc correlation in Sec. 7.5.

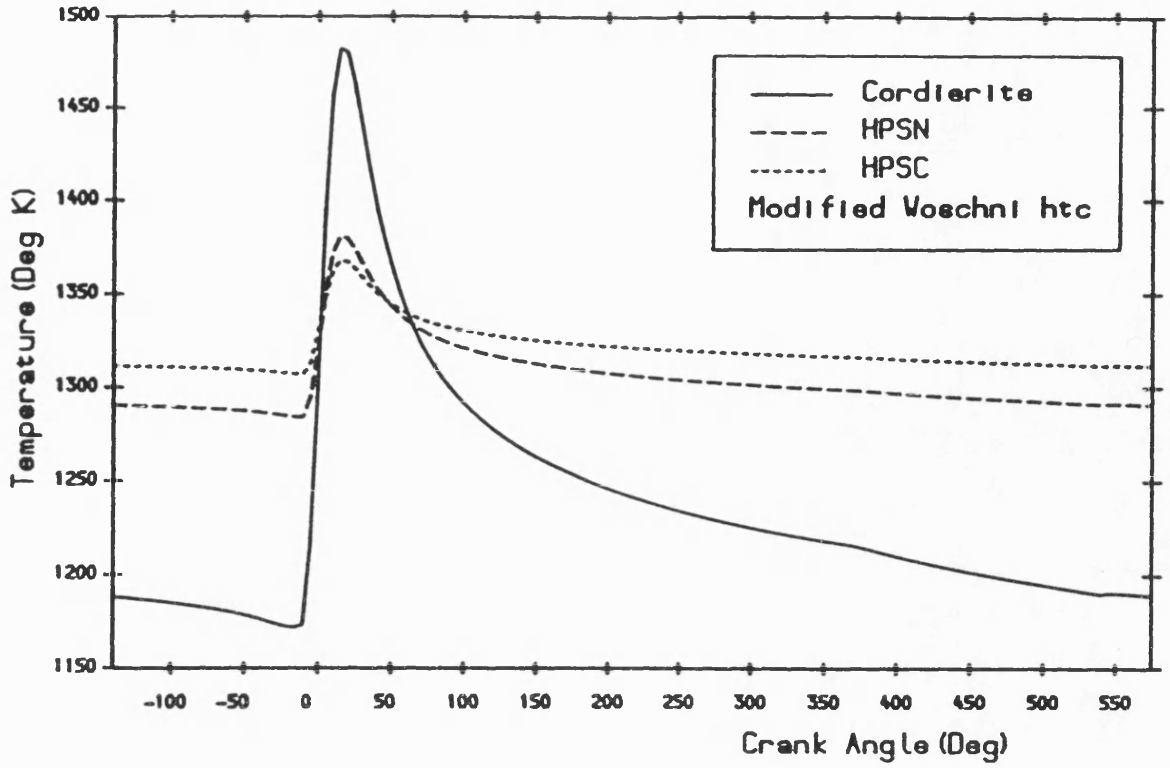

Fig. 7.110 Surface temperature versus crank angle for various ceramic pistons obtained with the modified Woschni htc correlation in Sec. 7.5.

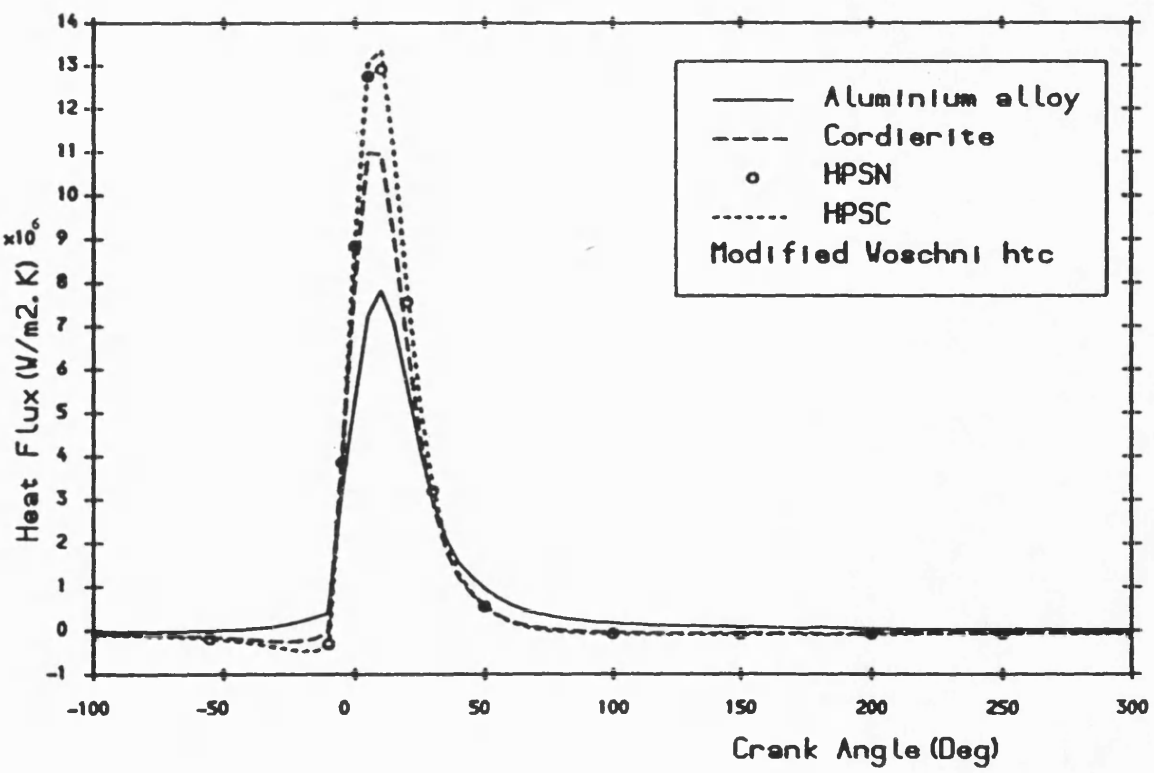

Fig. 7.111 Surface heat flux versus crank angle for various ceramic pistons obtained with the modified Woschni htc correlation in Sec. 7.5.

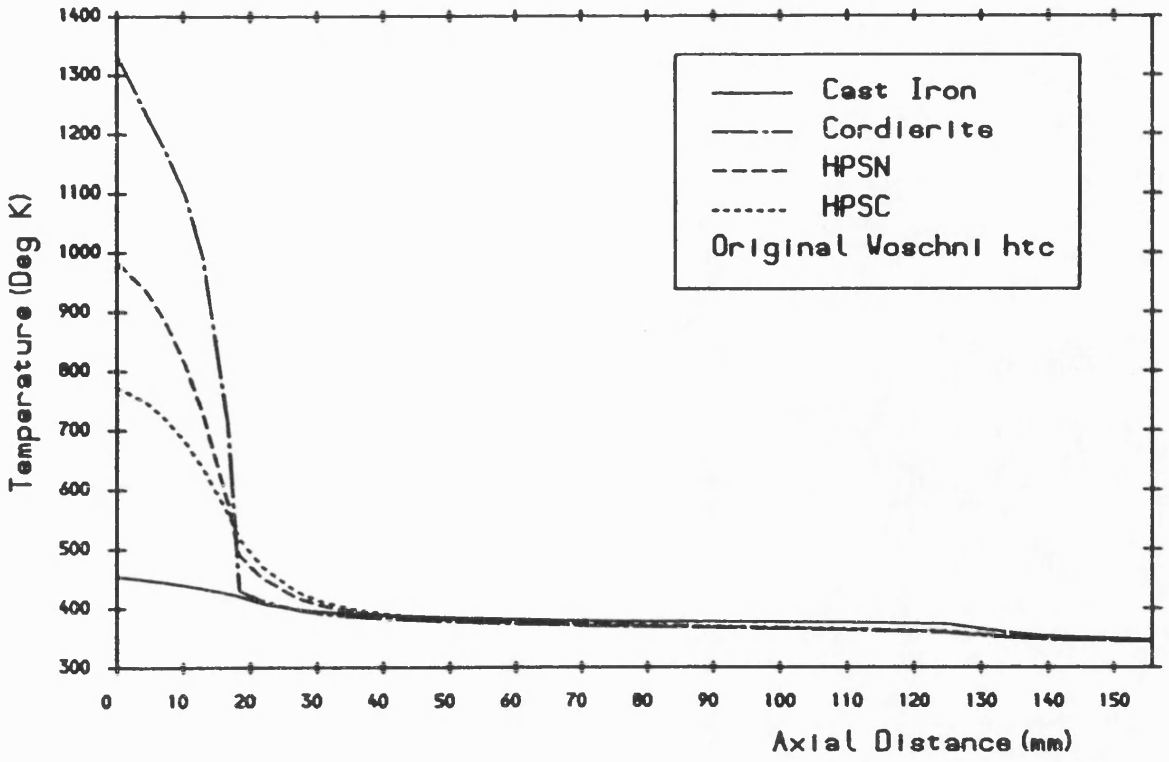

Fig. 7.112 Liner temperature versus axial distance for various ceramic engines obtained with the original Woschni htc correlation in Sec. 7.5.

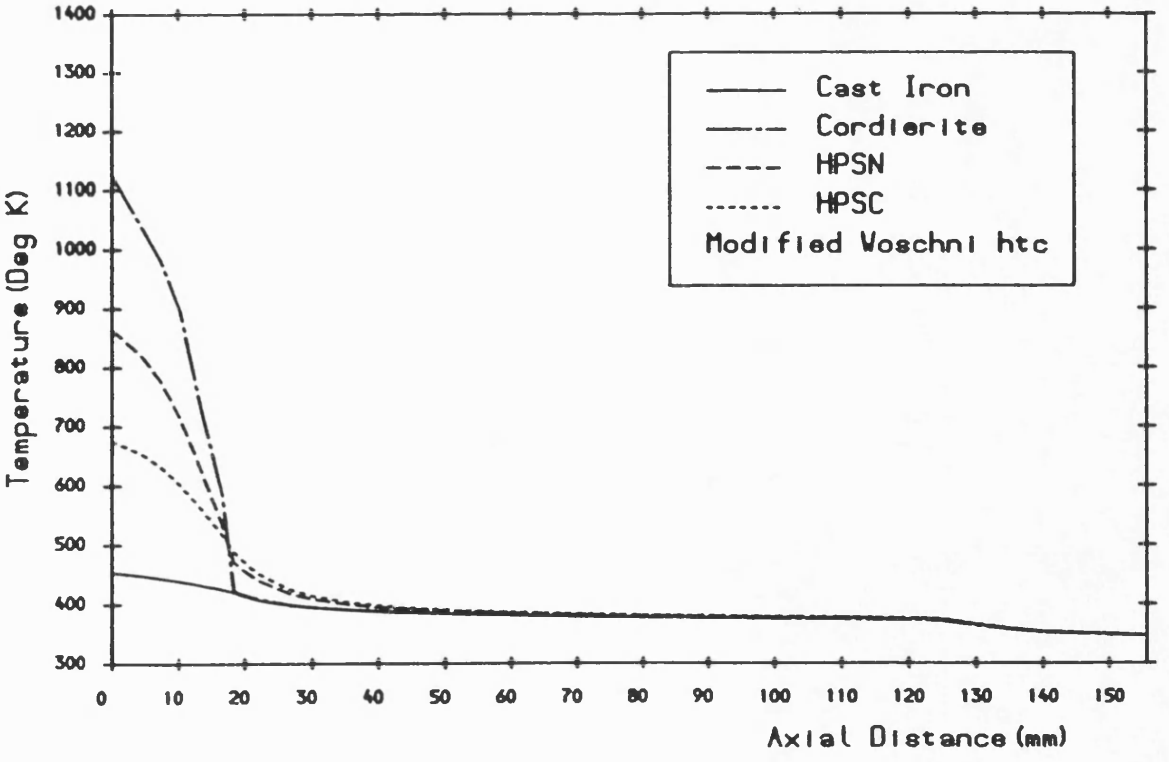

Fig. 7.113 Liner temperature versus axial distance for various ceramic engines obtained with the modified Woschni htc correlation in Sec. 7.5.

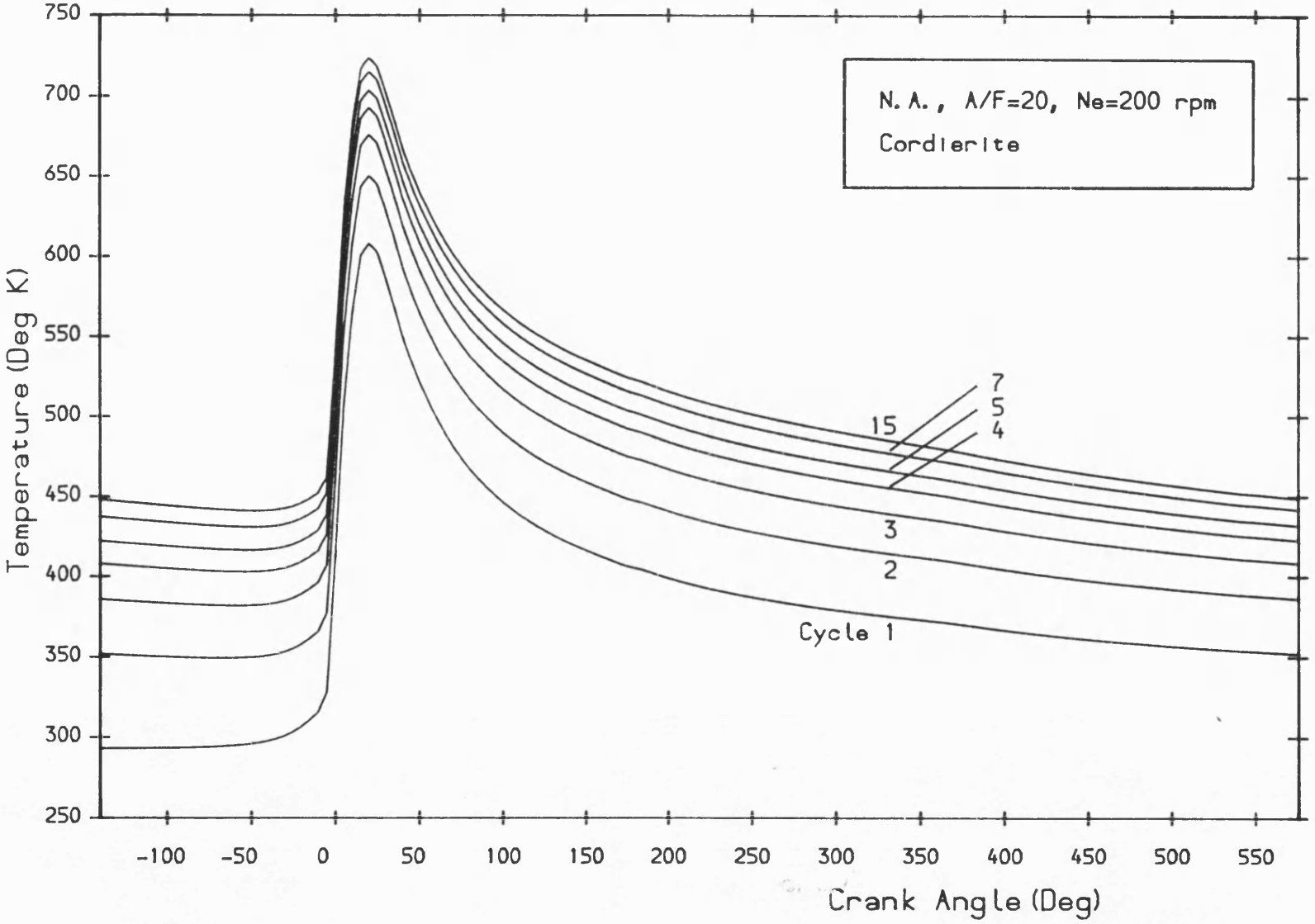

Fig. 7.114 Surface temperature versus crank angle at various successive cycles during engine start-up period.

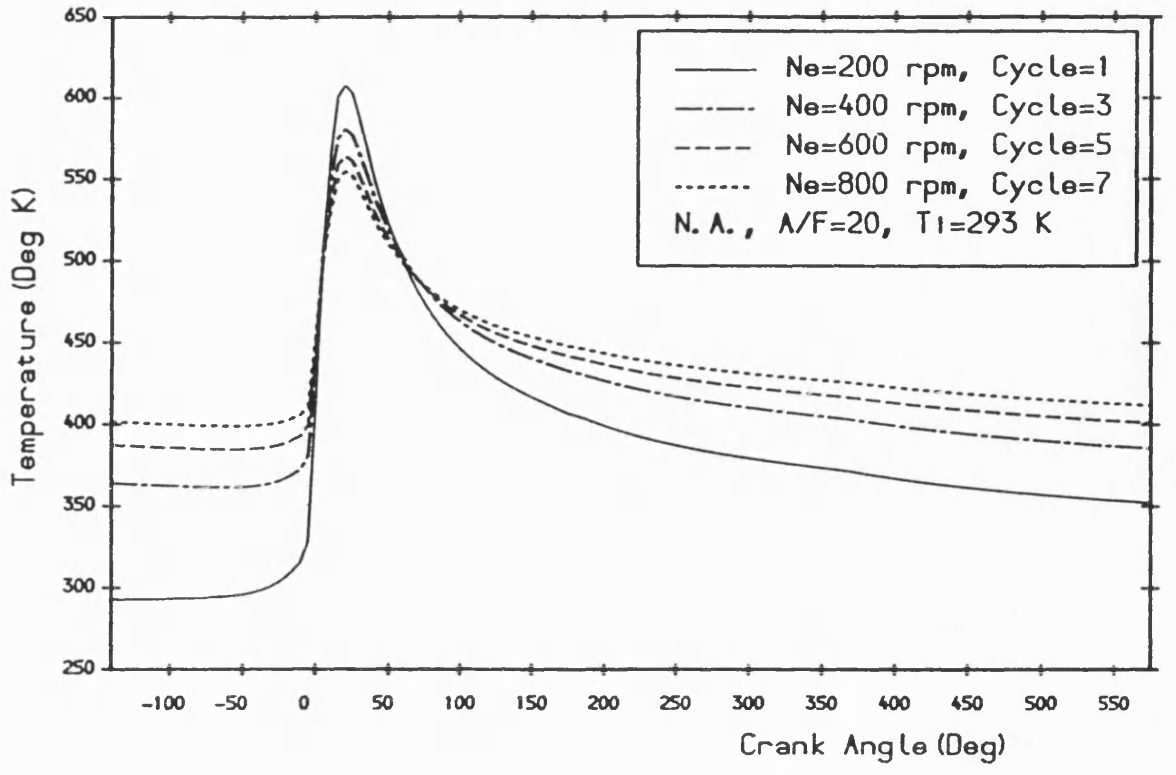

Fig. 7.115 Surface temperature versus crank angle during engine start-up period with A/F ratio of 20.

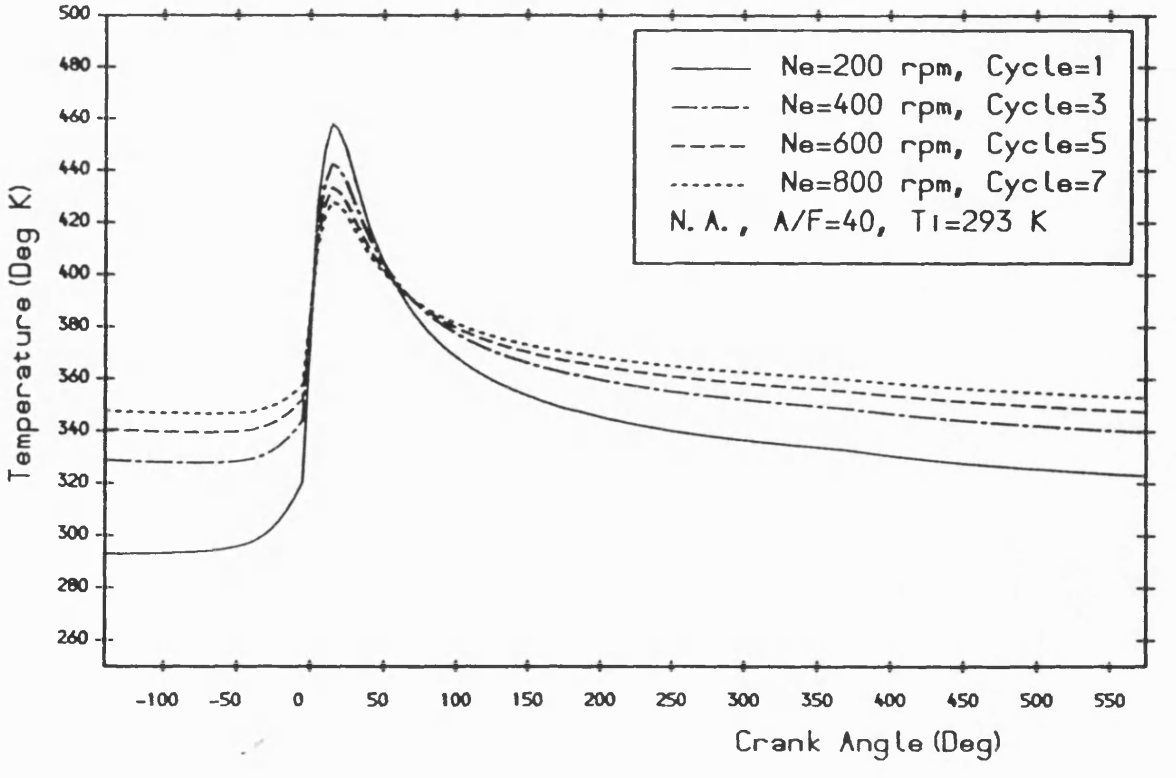

Fig. 7.116 Surface temperature versus crank angle during engine start-up period with A/F ratio of 40.

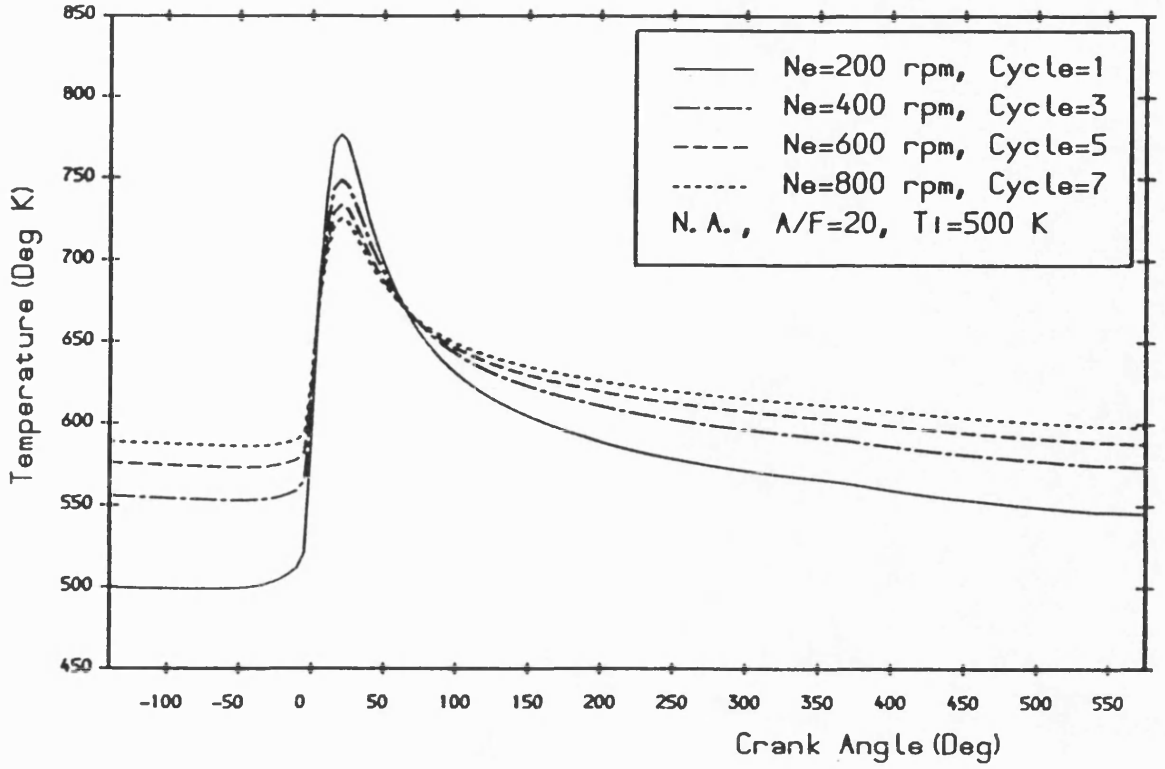

Fig. 7.117 Surface temperature versus crank angle during engine start-up period for initial wall temperature distribution of 500 K.

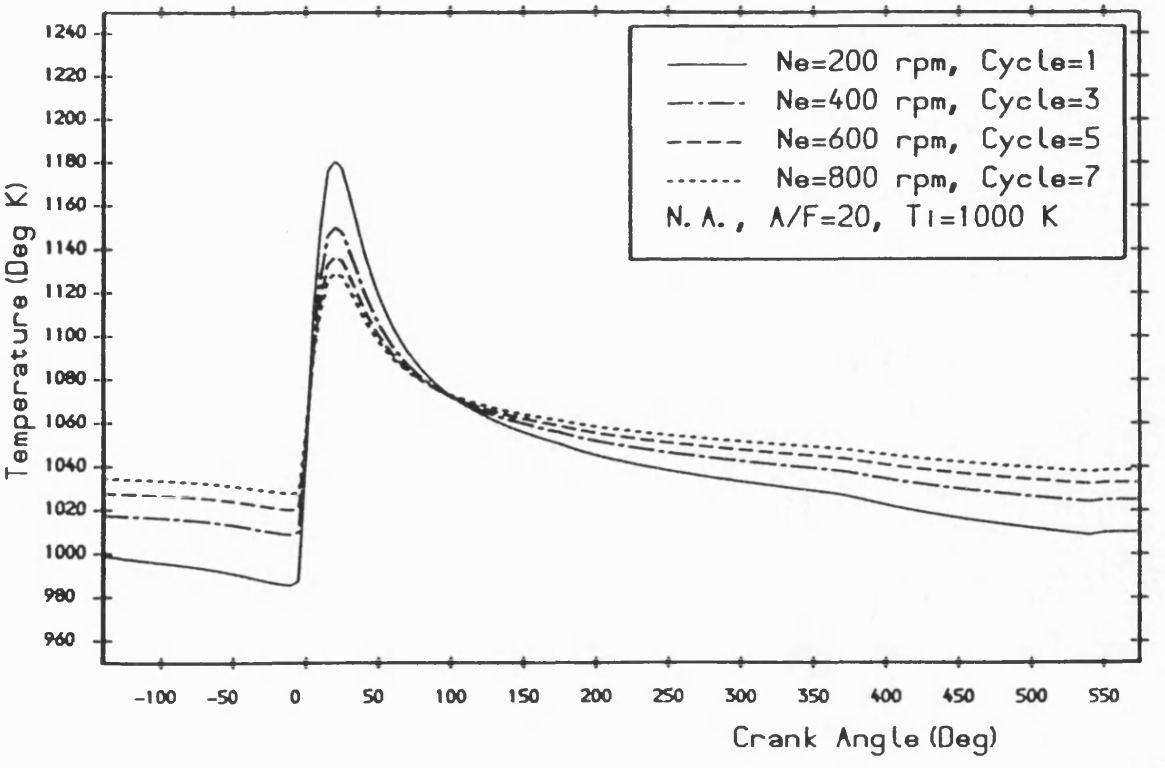

Fig. 7.118 Surface temperature versus crank angle during engine start-up period for initial wall temperature distribution of 1000 K.

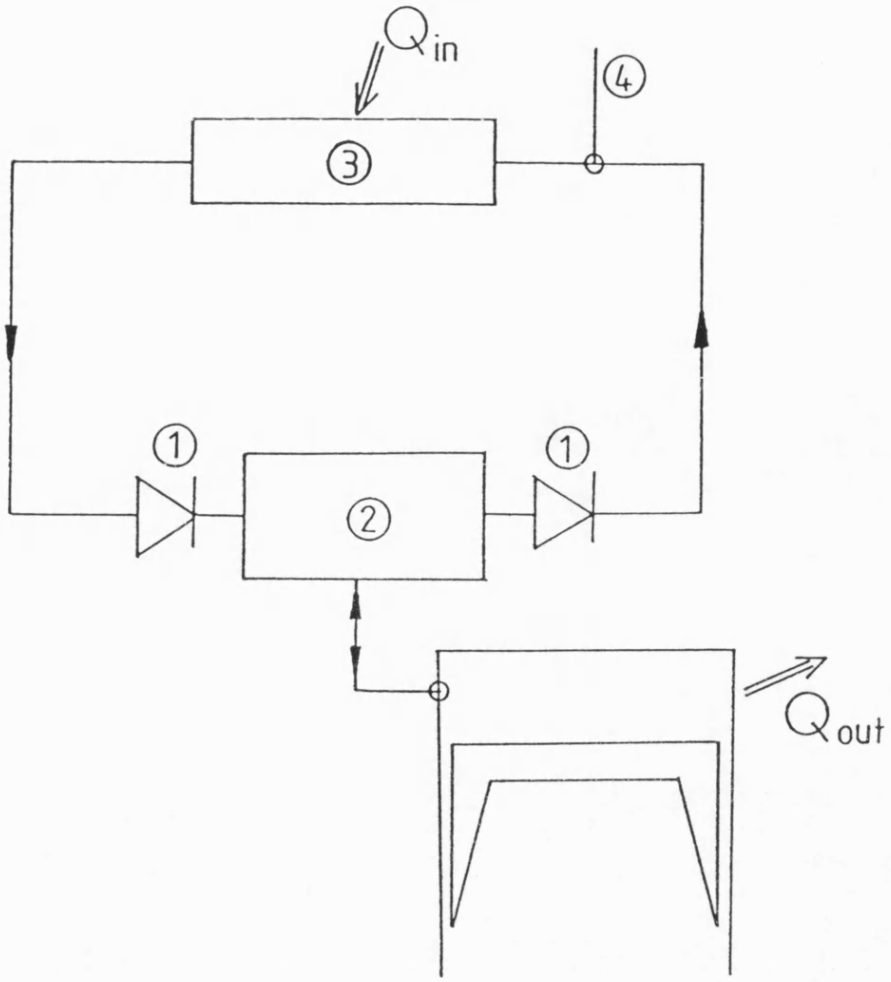

1 REED VALVES

2 POPPET VALVE

3 AIR HEATER

4 PRESSURISED AIR TOP UP

Fig. 8.1 Schematic layout of simulation rig.

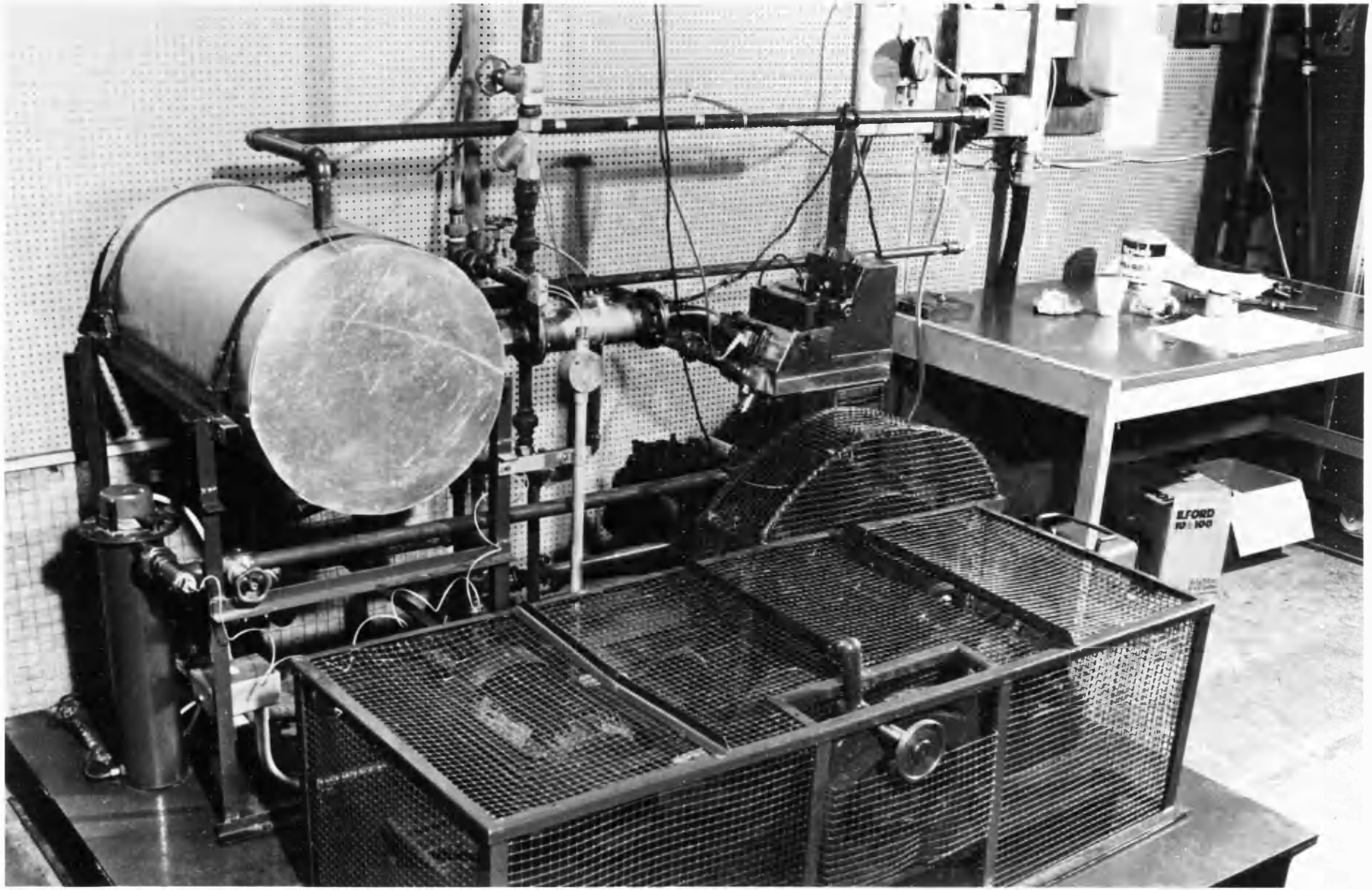

Fig. 8.2 Simulation test rig.

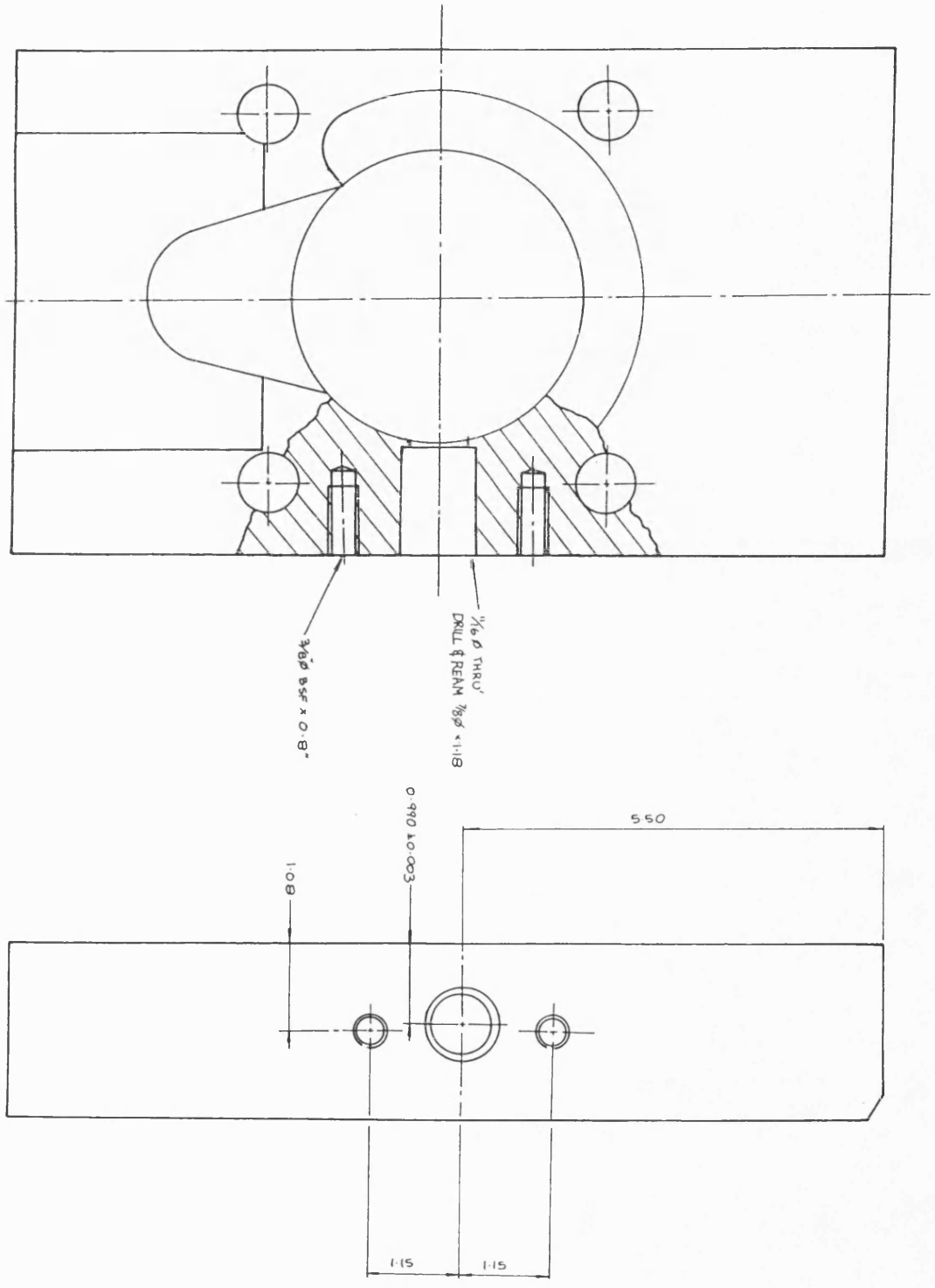

Fig. 8.3 Cylinder head of simulation rig.

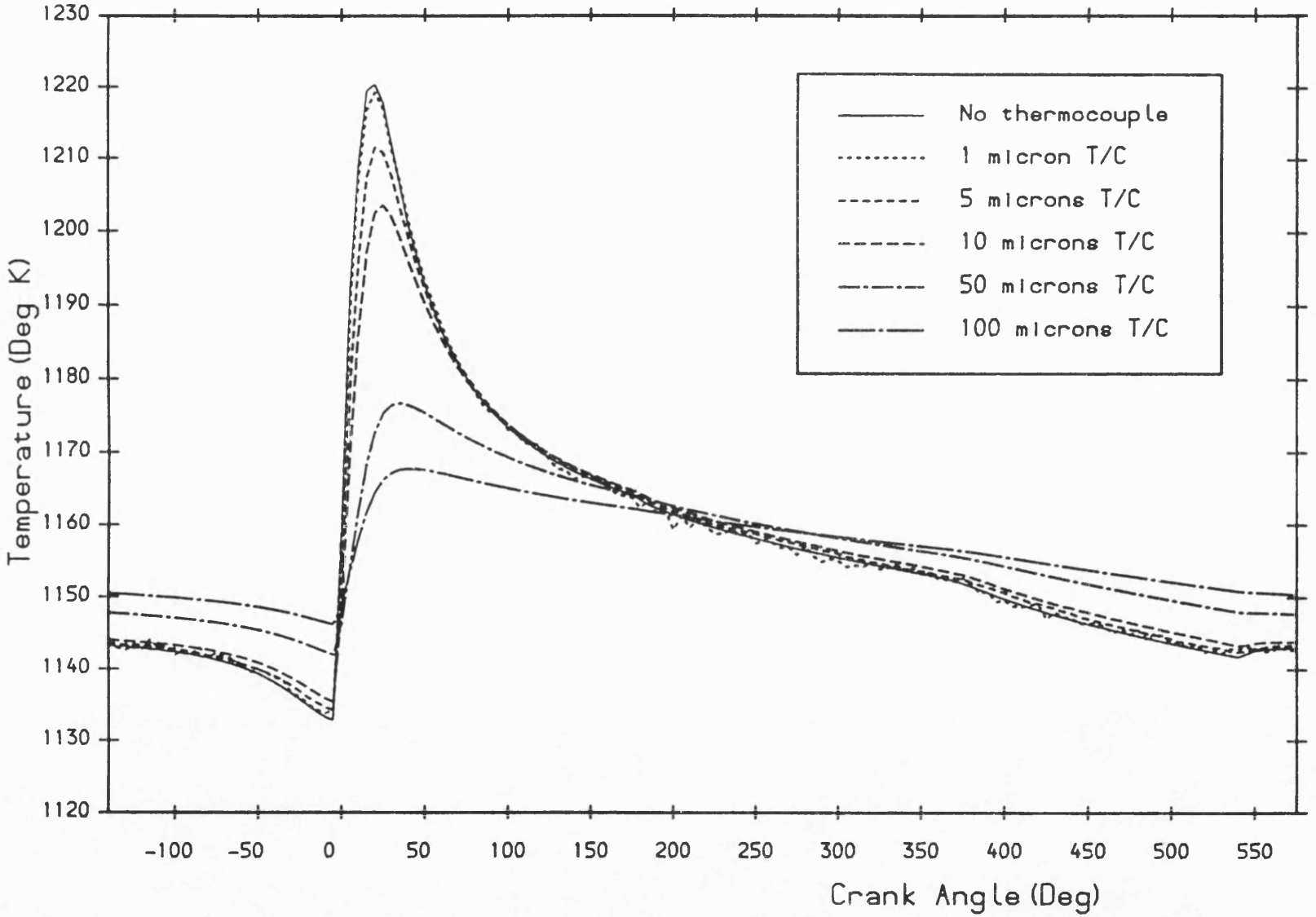

Fig. 8.4 The predicted effect of gold-platinium thermocouple thickness on the transient temperature reading at the cordierite surface.

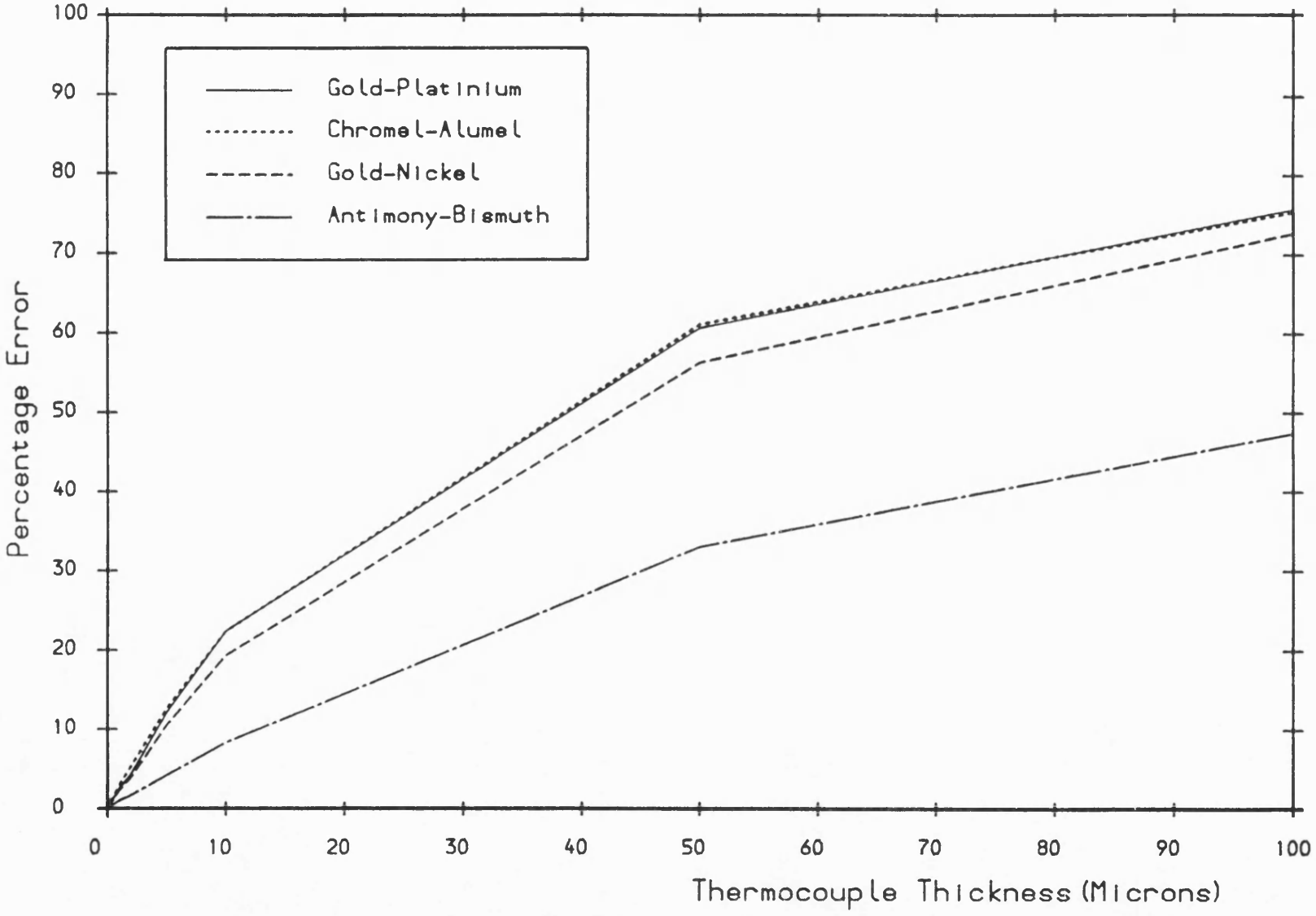

Fig. 8.5 Percentage error in surface temperature fluctuation versus thermocouple junction thickness for various thermocouples.

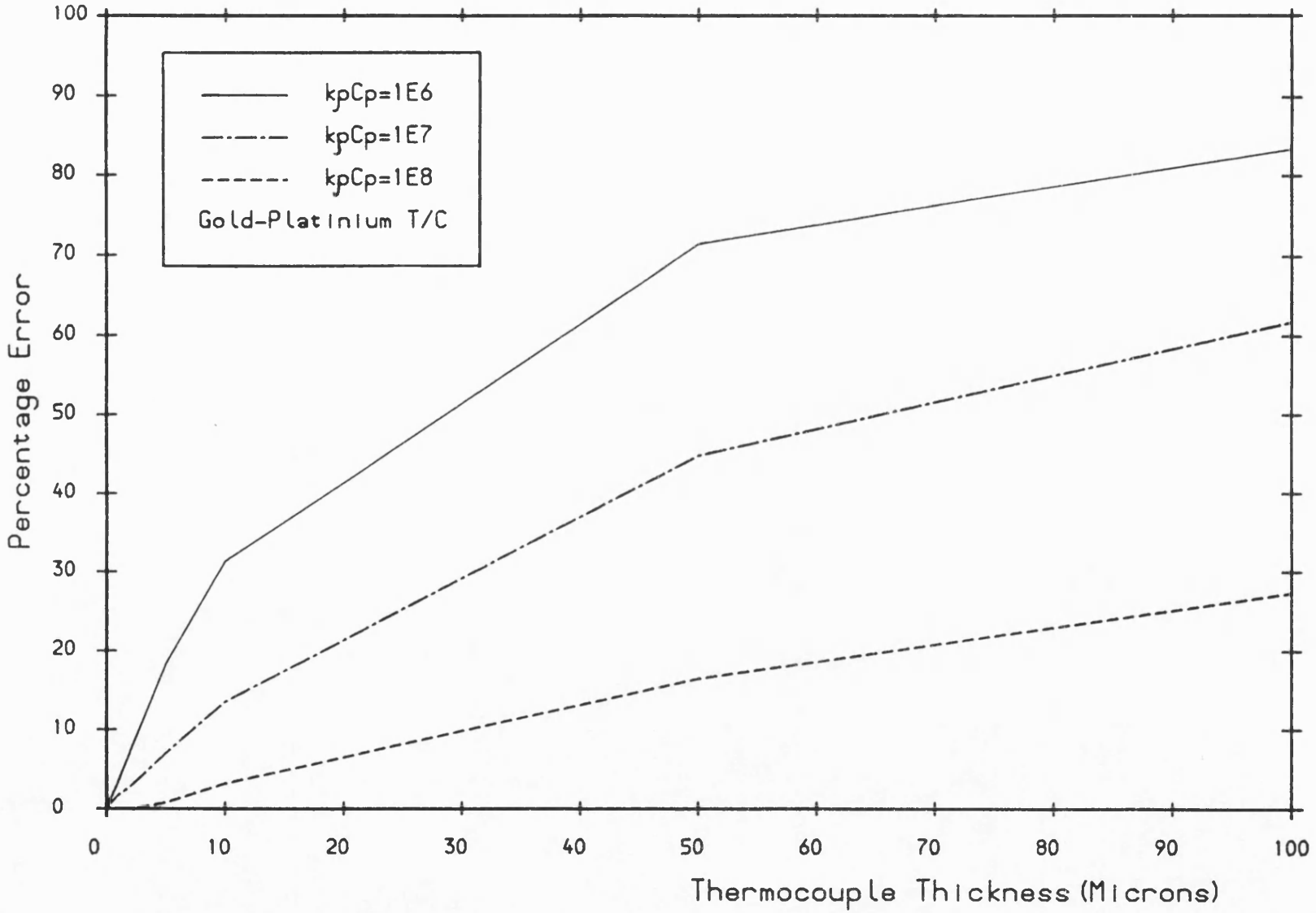

Fig. 8.6 Percentage error in surface temperature fluctuation versus thermocouple junction thickness for various ceramic substrates.

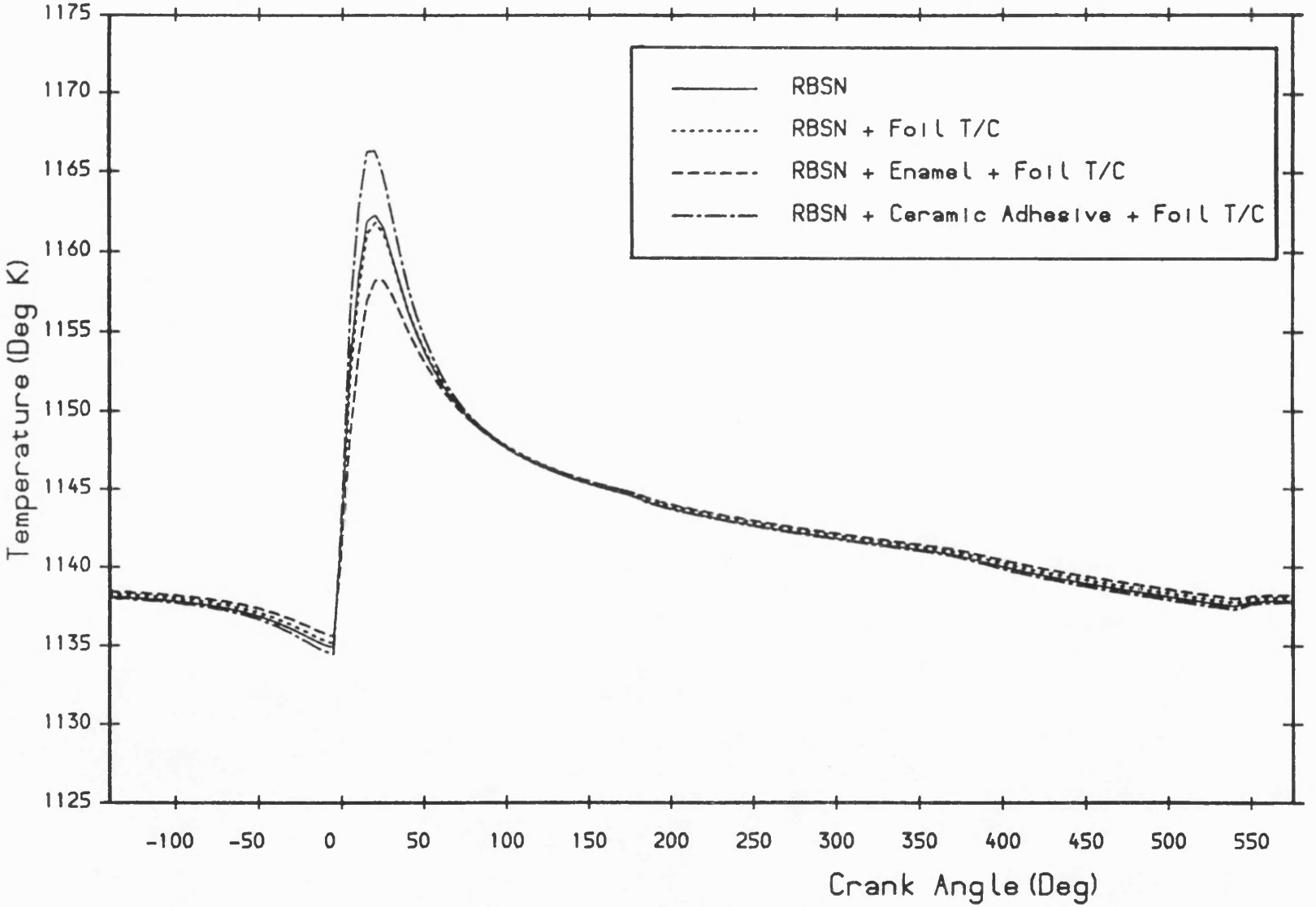

Fig. 8.7 The effect of 30 microns adhesive layer on chromel-alumel foil thermocouple reading at RBSN surface.

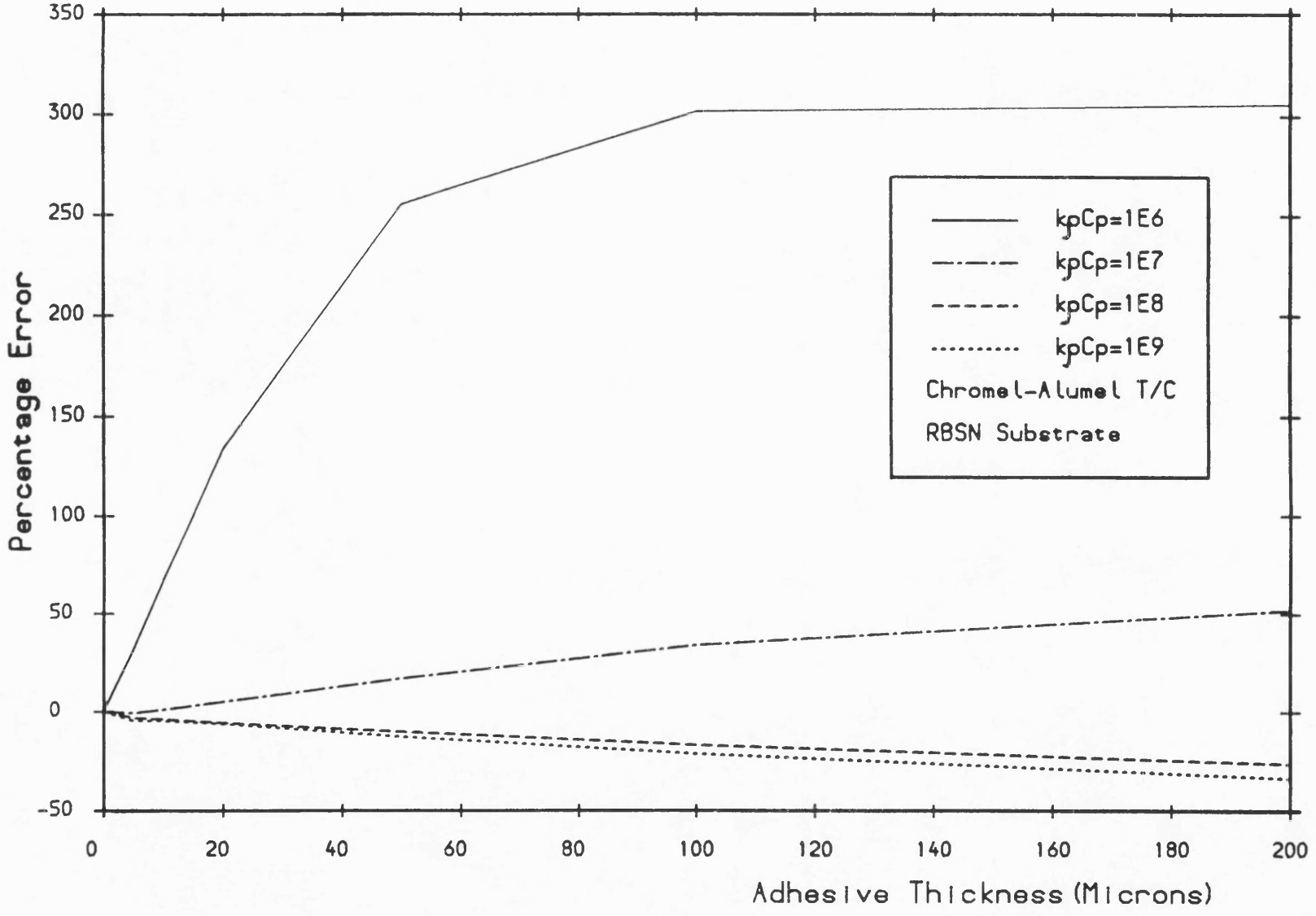

Fig. 8.8 Percentage error in surface temperature fluctuation versus adhesive thickness for various adhesive thermal properties.

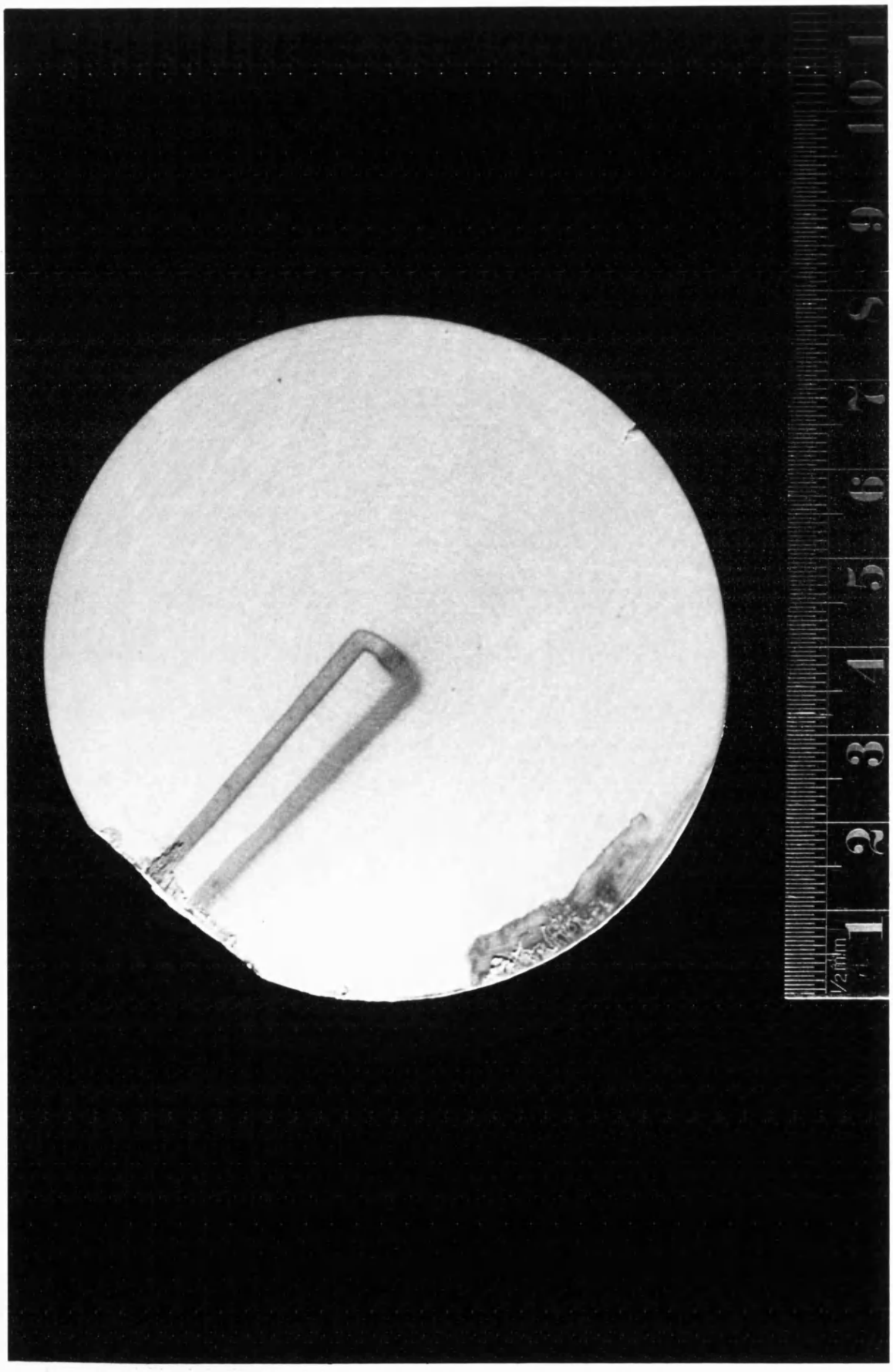

Fig. 8.9 Sputtered gold-platinium thermocouple at the cordierite surface.

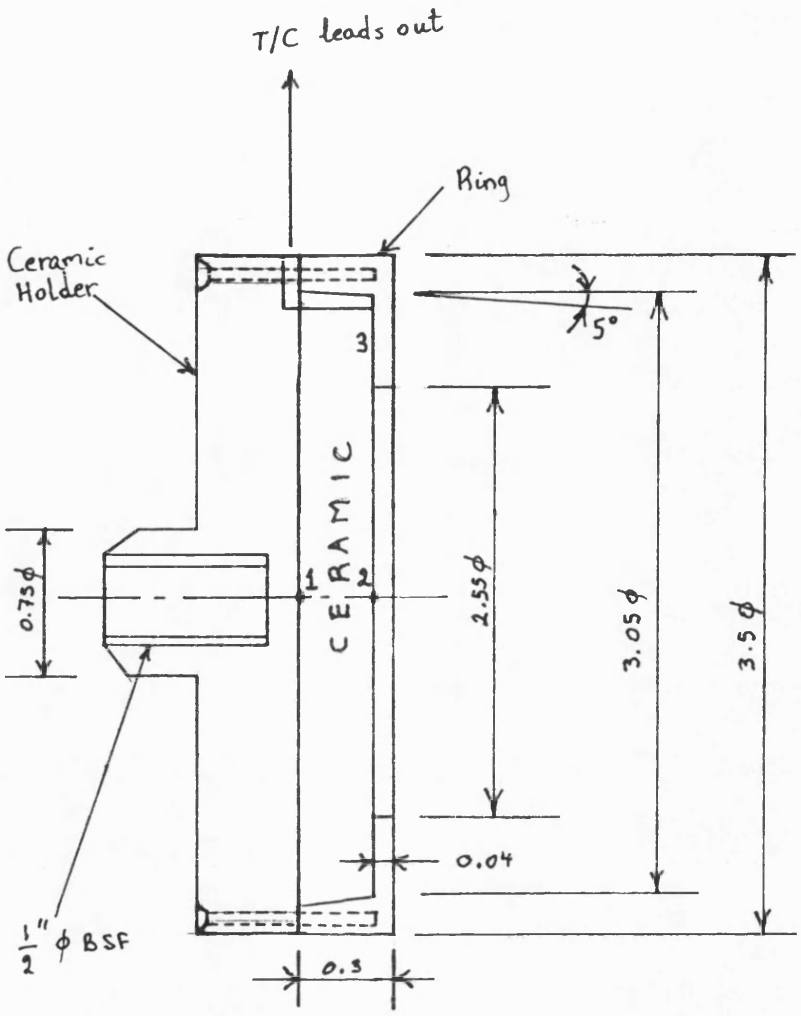

1 Backface T/C

2 Frontface T/C

3 Contact between T/C legs and wires.

Fig. 8.10 Ceramic specimen holder.

Fig. 8.11 High-speed data acquisition system.

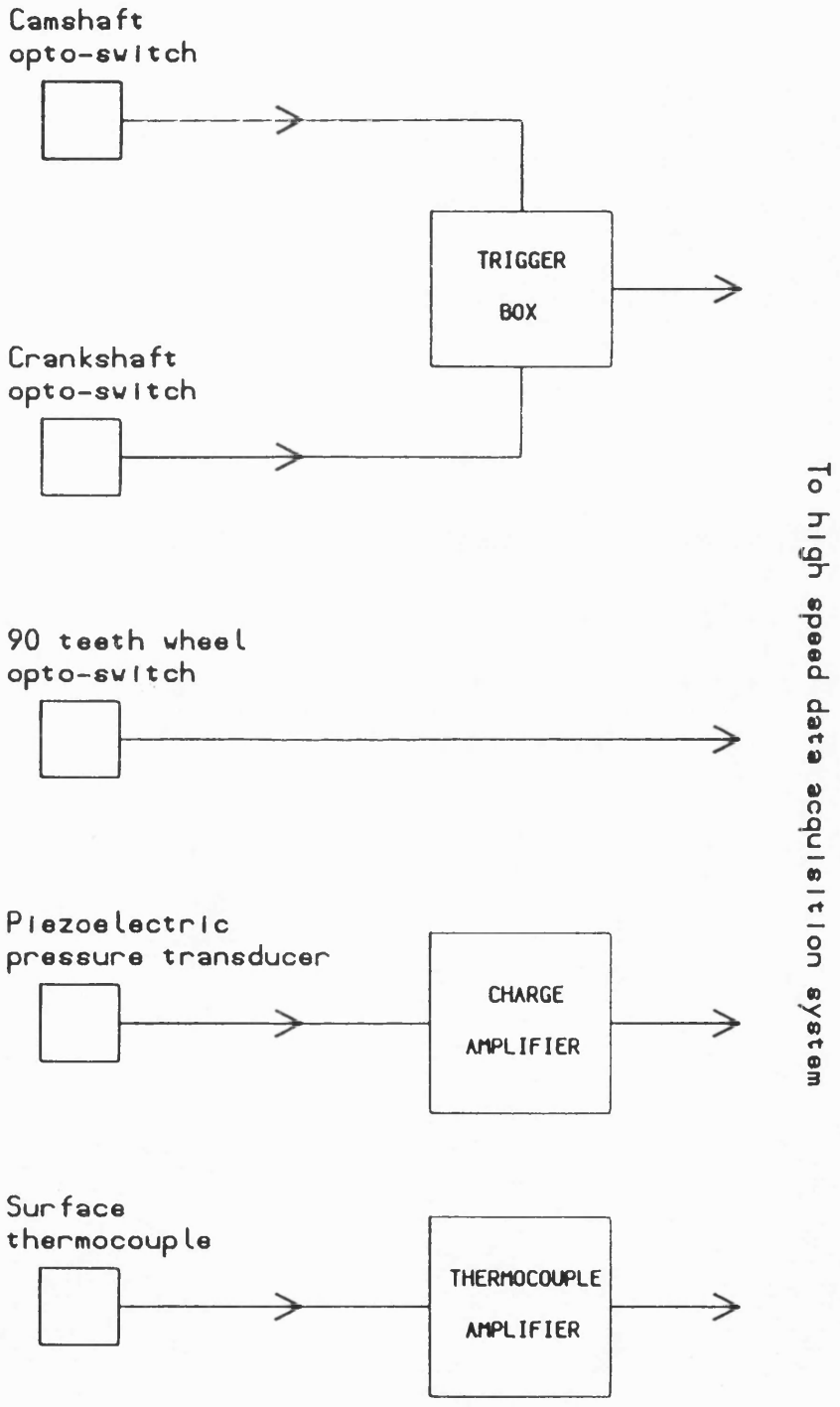

Fig. 8.12 Schematic instrumentation diagram of simulation rig.

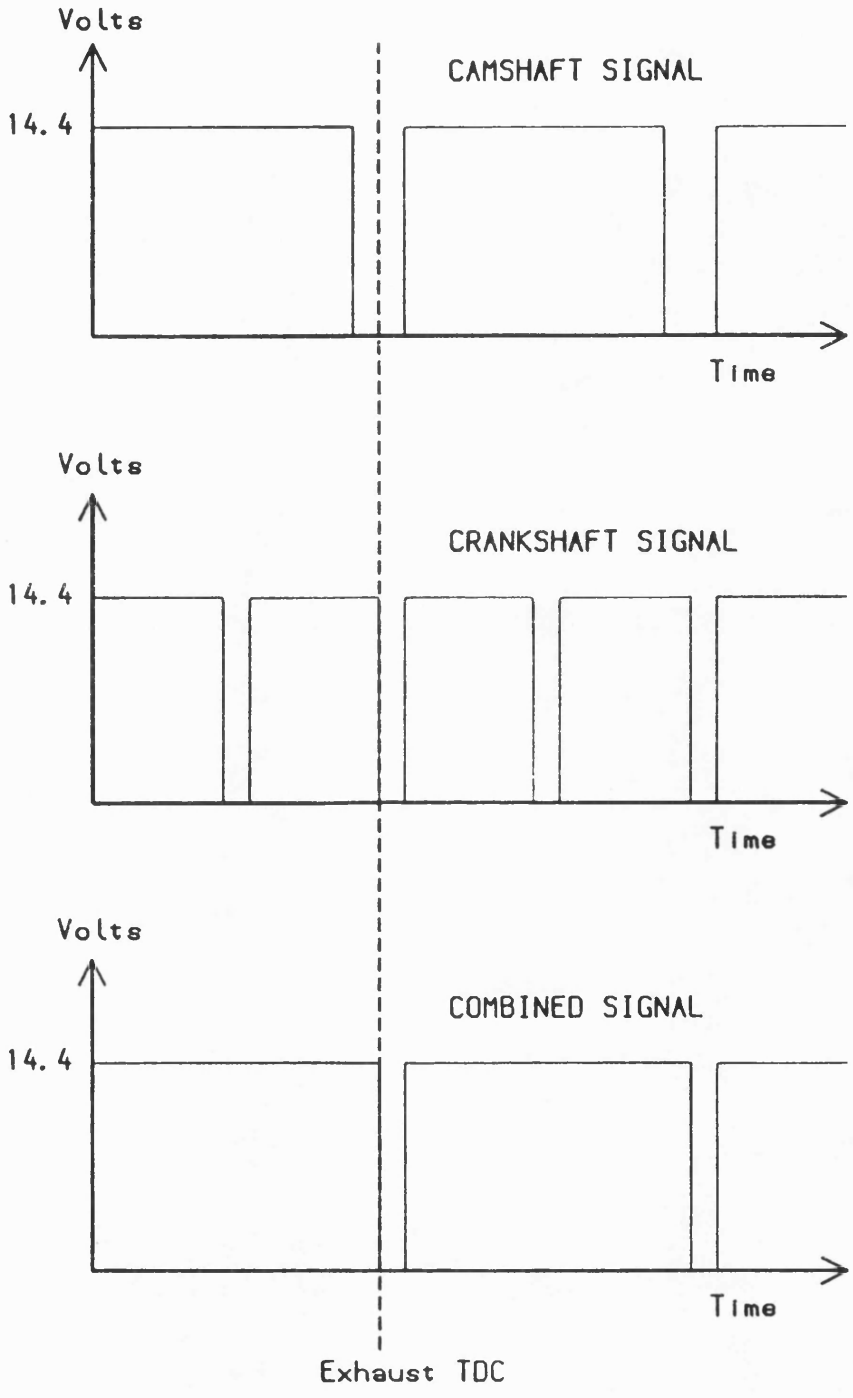

Fig. 8.13 Opto-switches timing diagrams for the simulation rig.

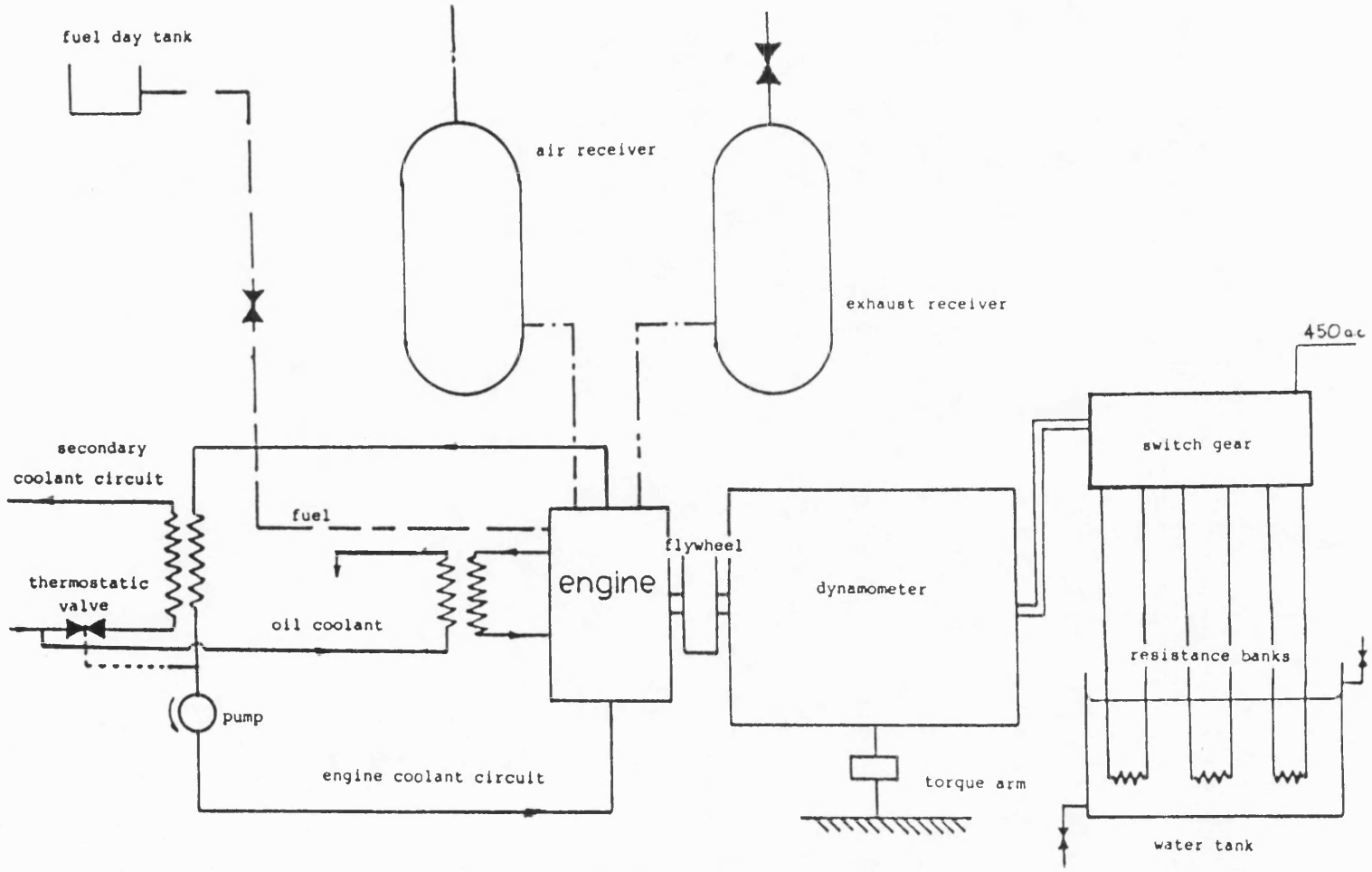

Fig. 8.14 Schematic diagram of firing rig.

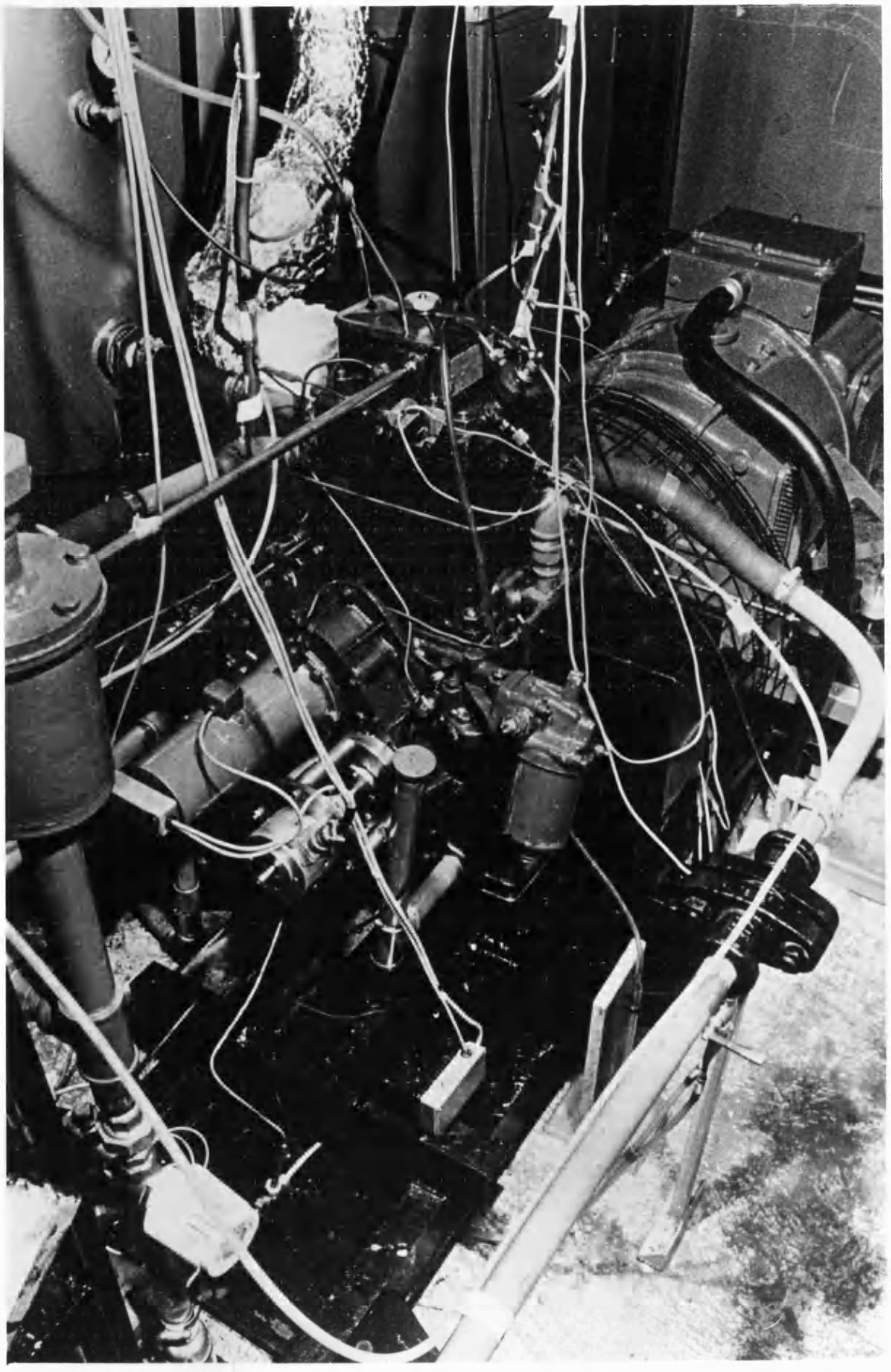

Fig. 8. 15 Firing test rig.

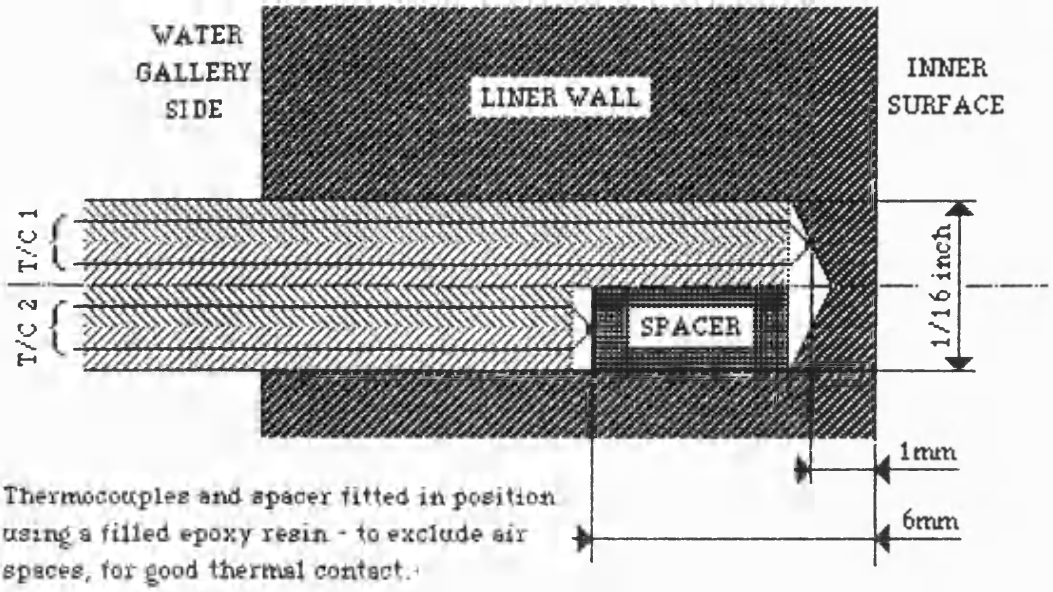

Fig. 8.16a Radial positions of the liner thermocouples.

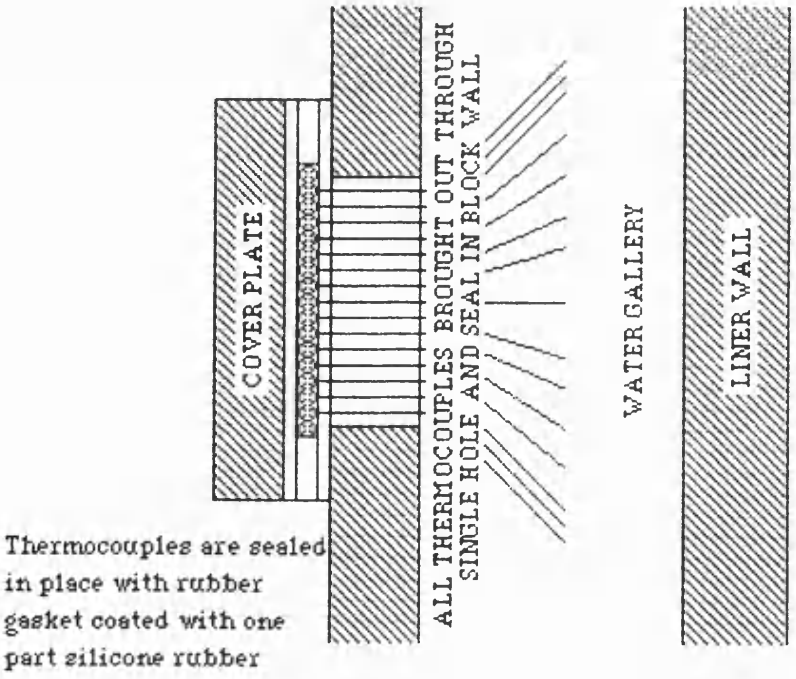

Fig. 8.16b Liner thermocouples installation.

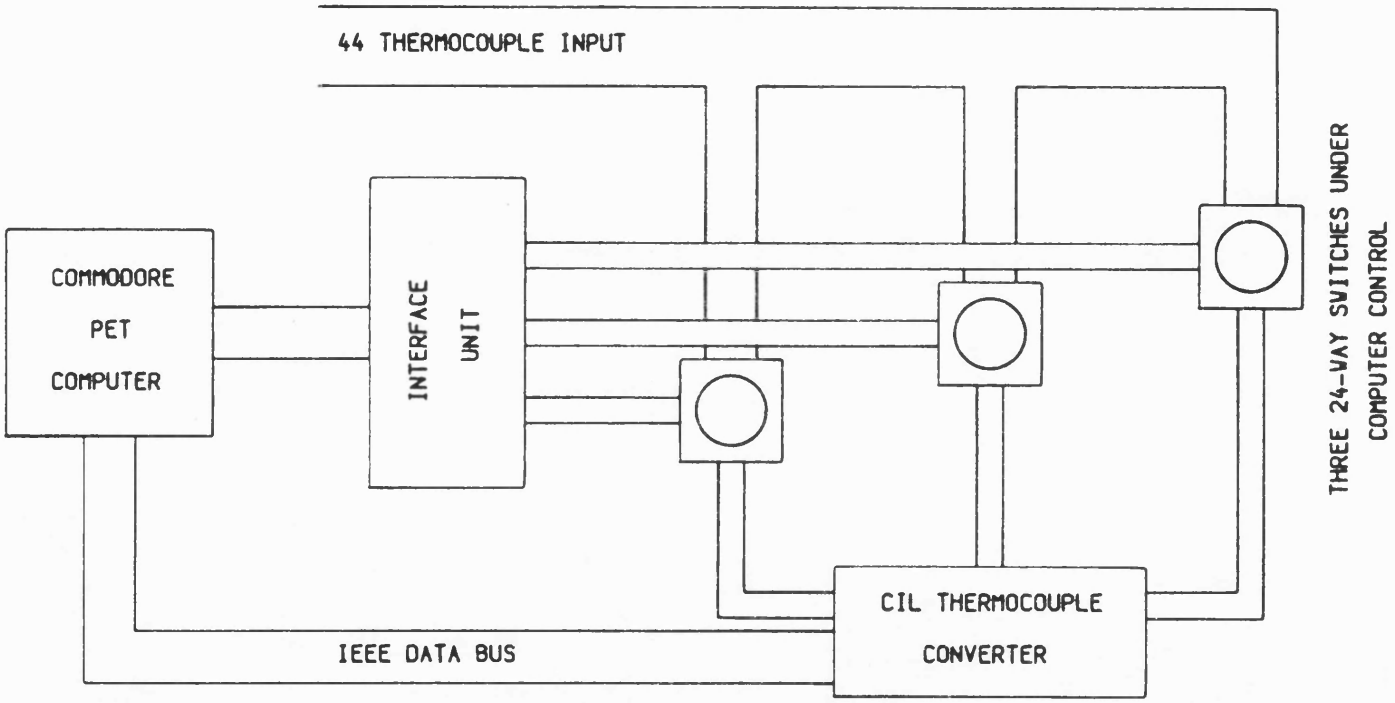

Fig. 8.17 Slow speed data acquisition system.

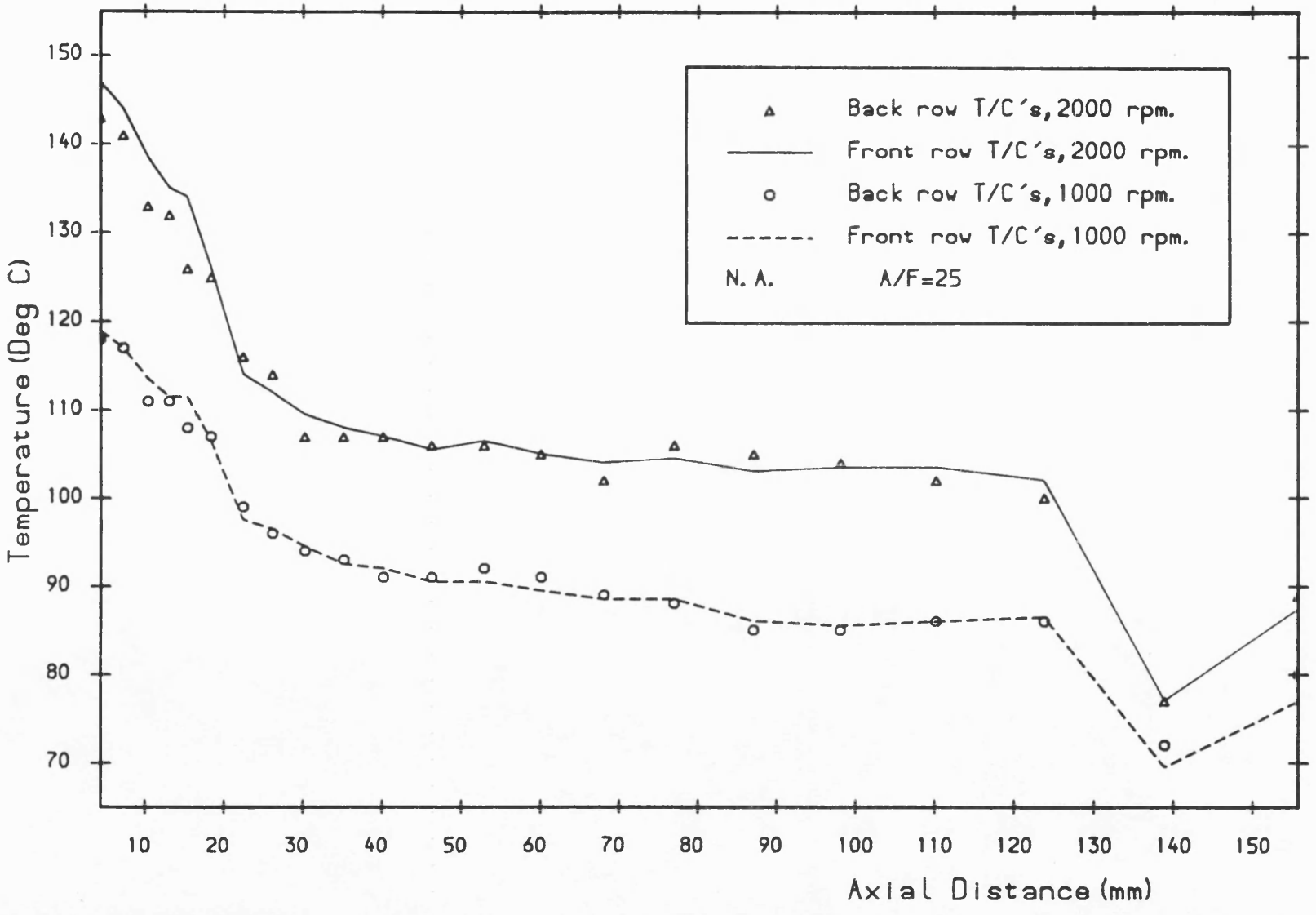

Fig. 8.18 Liner temperature distribution measured by the front and back row T/C's at 1000 and 2000 rpm engine speeds.

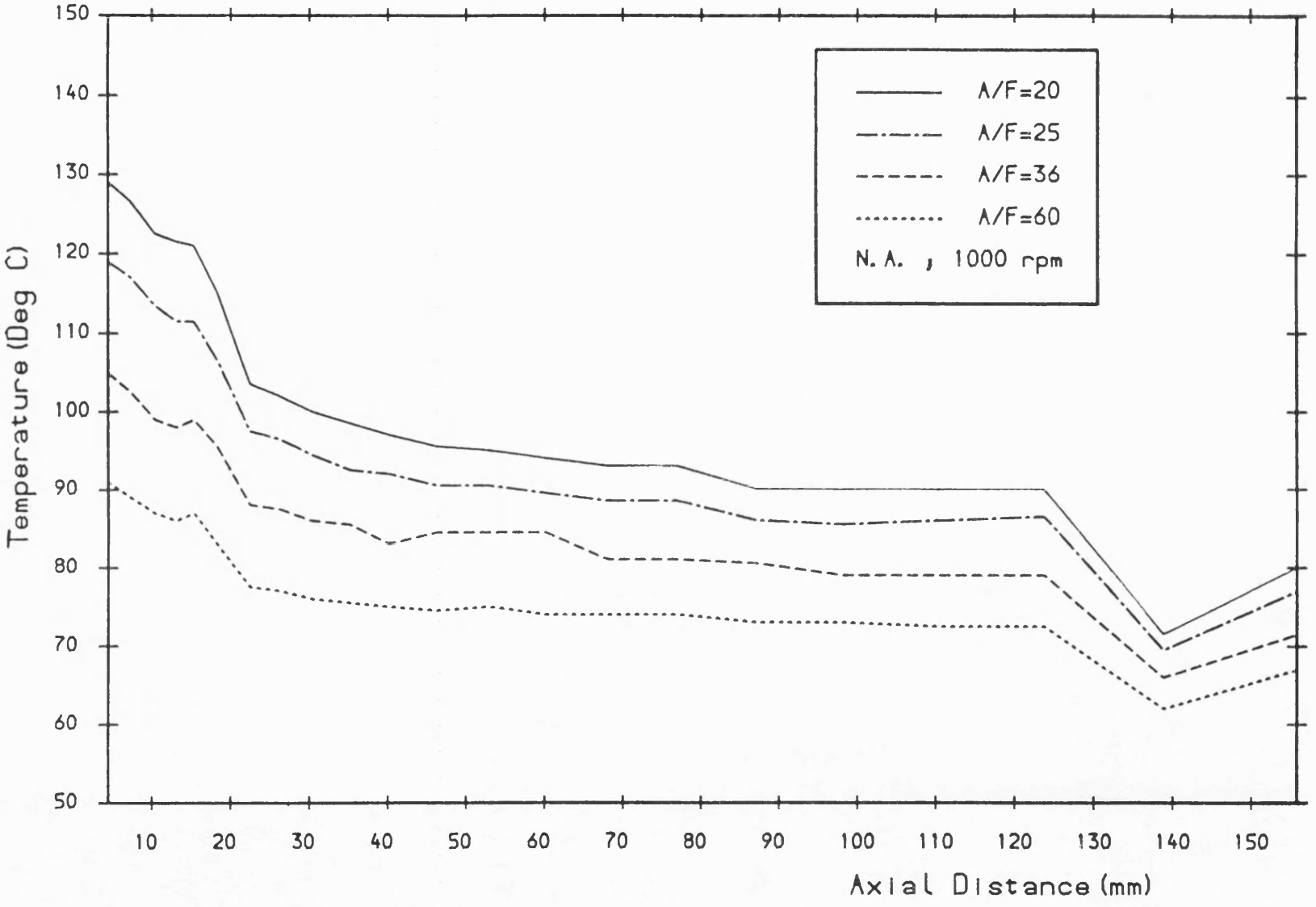

Fig. 8.19 Experimental liner surface temperature distribution at various air/fuel ratios for naturally aspirated engine.

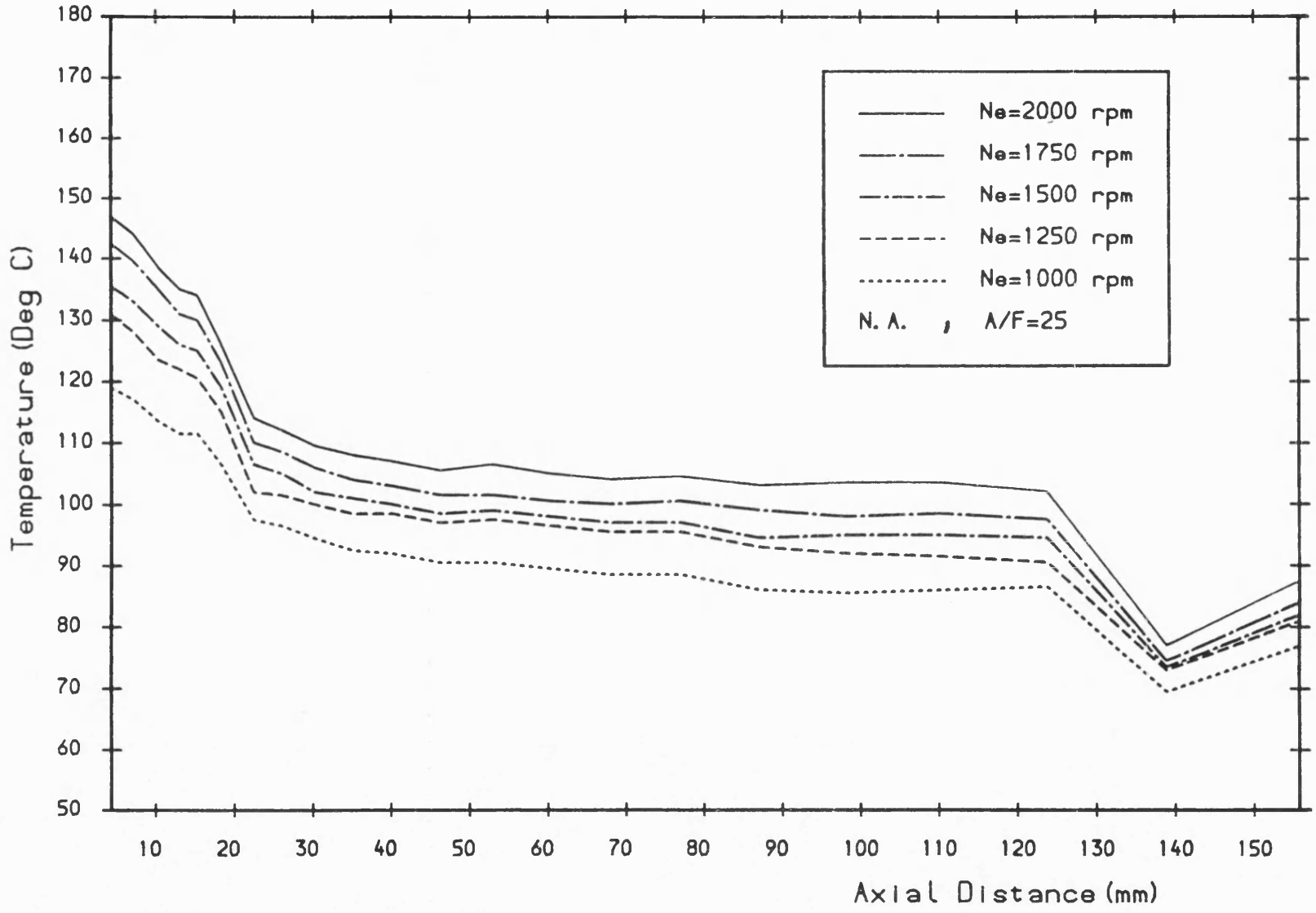

Fig. 8.20 Experimental liner surface temperature distribution at various engine speeds for naturally aspirated engine.

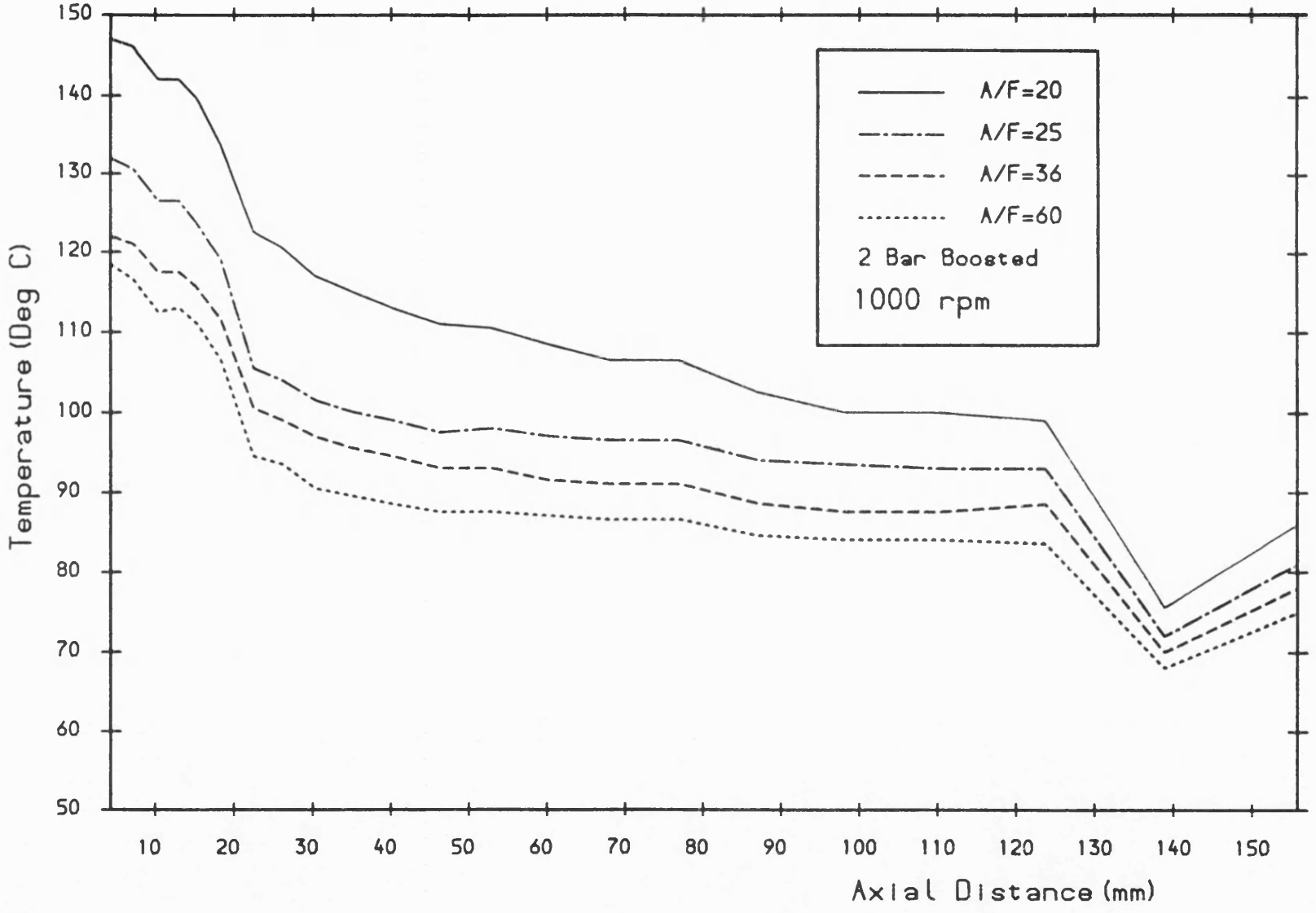

Fig. 8.21 Experimental liner surface temperature distribution at various air/fuel ratios for 2 bar boosted engine.

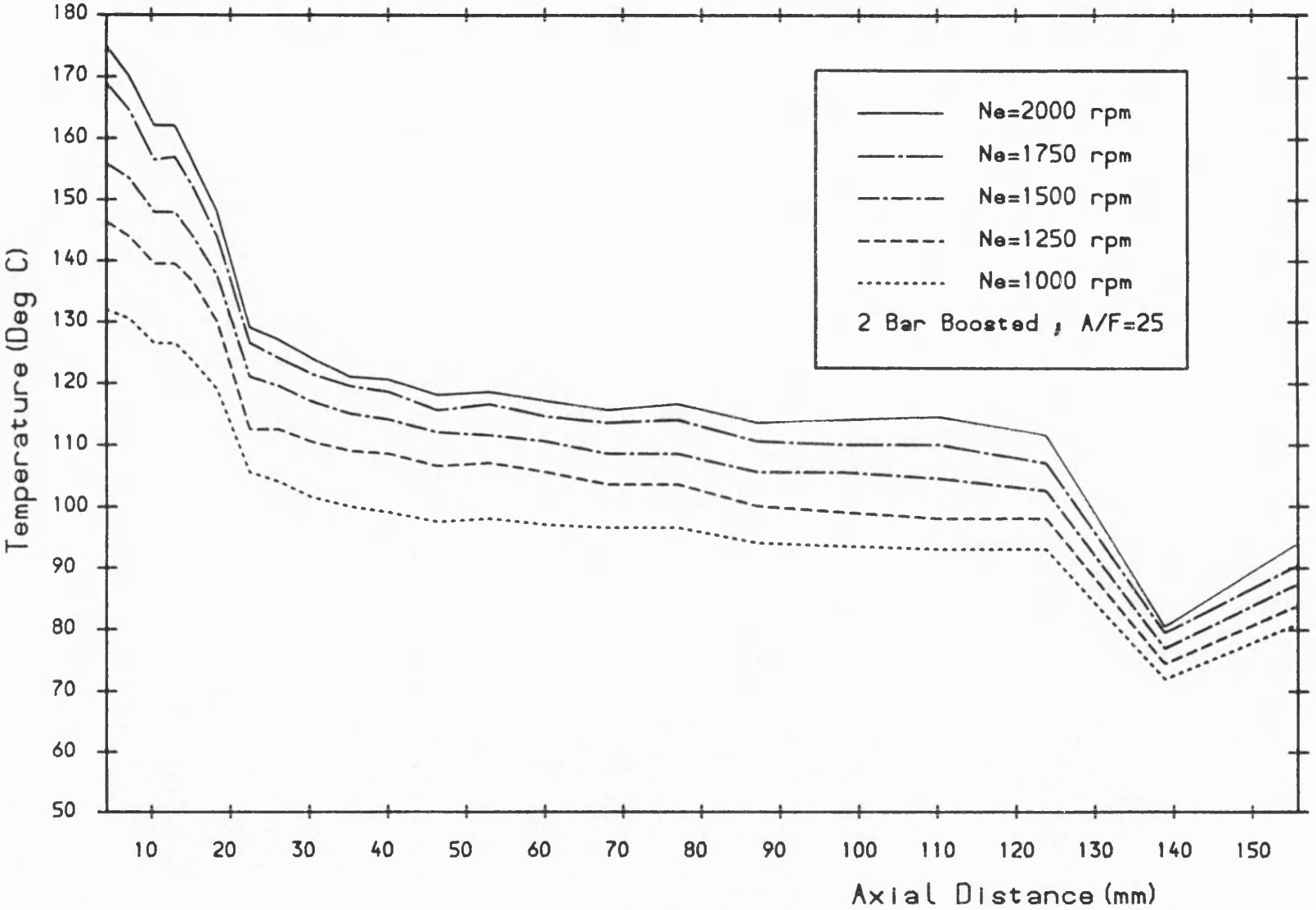

Fig. 8.22 Experimental liner surface temperature distribution at various engine speeds for 2 bar boosted engine.